

AGARD-CP-300

AGARD-CP-300

AGARD

ADVISORY GROUP FOR AEROSPACE RESEARCH & DEVELOPMENT

7 RUE ANCELLE 92200 NEUILLY SUR SEINE FRANCE

AD A105193

AGARD CONFERENCE PROCEEDINGS No. 300

Special Topics in Optical Propagation

OCT 8 1981

This document has been approved
for public release and sale; its
distribution is unlimited.

A

DMC FILE COPY

NORTH ATLANTIC TREATY ORGANIZATION



DISTRIBUTION AND AVAILABILITY
ON BACK COVER

81 10 6 244

NORTH ATLANTIC TREATY ORGANIZATION
ADVISORY GROUP FOR AEROSPACE RESEARCH AND DEVELOPMENT
(ORGANISATION DU TRAITE DE L'ATLANTIQUE NORD)

12/11/81

9

AGARD Conference Proceedings No. 300

6 SPECIAL TOPICS IN OPTICAL PROPAGATION

Edited by

P. Halley
Capitaine de Frégate honoraire
12 rue du Docteur Kurzenne
78350 Jouy en Josas
France

12
Pierre / Halley = 1

1/11 Jul 81

Papers and Discussions presented at the 28th Meeting of the Electromagnetic Wave Propagation Panel held in Monterey, California, USA, 6-10 April 1981.

400043

JOB

THE MISSION OF AGARD

The mission of AGARD is to bring together the leading personalities of the NATO nations in the fields of science and technology relating to aerospace for the following purposes:

- Exchanging of scientific and technical information;
- Continuously stimulating advances in the aerospace sciences relevant to strengthening the common defence posture;
- Improving the co-operation among member nations in aerospace research and development;
- Providing scientific and technical advice and assistance to the North Atlantic Military Committee in the field of aerospace research and development;
- Rendering scientific and technical assistance, as requested, to other NATO bodies and to member nations in connection with research and development problems in the aerospace field;
- Providing assistance to member nations for the purpose of increasing their scientific and technical potential;
- Recommending effective ways for the member nations to use their research and development capabilities for the common benefit of the NATO community.

The highest authority within AGARD is the National Delegates Board consisting of officially appointed senior representatives from each member nation. The mission of AGARD is carried out through the Panels which are composed of experts appointed by the National Delegates, the Consultant and Exchange Programme and the Aerospace Applications Studies Programme. The results of AGARD work are reported to the member nations and the NATO Authorities through the AGARD series of publications of which this is one.

Participation in AGARD activities is by invitation only and is normally limited to citizens of the NATO nations.

The content of this publication has been reproduced directly from material supplied by AGARD or the authors.

Published July 1981

Copyright © AGARD 1981

All Rights Reserved

ISBN 92-835-0295-7



Printed by Technical Editing and Reproduction Ltd
Harford House, 7-9 Charlotte St, London, W1P 1HD



THEME

Recent measurements and developments in optical propagation in the air and in the sea have opened the door to applications of significant importance to military systems.

As an example, transmission measurements in the marine boundary layer have demonstrated that light beams are strongly scattered in the forward direction by hydrometeors; as a result, communication links may be possible beyond line of sight. Another example is improved modeling of the upper atmosphere and related propagation effects, which allows high altitude sensing systems to discriminate between target and background radiance.

Such phenomena and others peculiar to atmosphere and marine environments offer unique possibilities to communicate between space based and submerged platforms as well as pointing the way to remote observations. The resultant applications to communication and surveillance are of great interest to the military.

This meeting reviewed these propagation phenomena to establish their limitations on transmitting and receiving equipment and bring out military implications and applications.



Accession For	
FRIS GR&I	<input checked="" type="checkbox"/>
DTIC TAB	<input type="checkbox"/>
Unannounced	<input type="checkbox"/>
Justification	
Distribution/	
Availability Codes	
Avail and/or	
Special	
A	

ELECTROMAGNETIC WAVE PROPAGATION PANEL

Chairman: Dr J.Aarons
AF Geophysics Laboratory
Hanscom Field
Bedford, Mass.01731
USA

Deputy Chairman: Dr J.Belrose
Communications Research Center
Department of Communications
P.O.Box 11490, Station H
Ottawa K2H 8S2,
Canada

PROGRAMME COMMITTEE

Chairmen: P.Halley, FR -- H.Hodara, US

Programme Committee: R.R.Allan, UK
R.Anderson, US
B.Crosignani, IT
D.H.Hohn, FRG
G.Mooradian, US
E.Schimitschek, US
E.Spitz, FR
A.T.Stair, US
H.Yura, US

PANEL EXECUTIVE

Lt.Col. J.B.Catiller
AGARD/NATO
7, rue Ancelle
92200 Neuilly-sur-Seine
France

CONTENTS

	Page
THEME	iii
PANEL OFFICERS AND PROGRAMME COMMITTEE	iv
EDITOR'S INTRODUCTION (in English and French) by P.Halley	ix
	Reference
<u>SESSION I – PROPAGATION EFFECTS IN AIR AND SEA WATER</u>	
OVER-THE-HORIZON OPTICAL SCATTER PROPAGATION IN THE MARINE BOUNDARY LAYER by G.C.Mooradian and M.Geller	1
MULTIPLE SCATTER OF COLLIMATED IRRADIANCE by W.H.Wells, J.Harris and H.C.Lin	2
GREEN'S FUNCTION CALCULATION OF THE EFFECTS OF THE AIR/SEA INTERFACE ON OPTICAL PROPAGATION by R.F.Lutomirski and D.E.Snead	3
MULTIPLE SCATTERING EFFECTS ON OPTICAL PROPAGATION IN TURBULENCE AND PARTICLES by A.Ishimaru	4
INVESTIGATIONS FOR THE DEVELOPMENT OF A FORECAST SYSTEM FOR UNDERWATER-VISIBILITY IN THE HELIGOLAND BIGHT by E.R.Küsters	5
METEOROLOGICAL DESCRIPTIONS FOR OPTICAL PROPERTIES by K.L.Davidson, G.E.Schacher and C.W.Fairall	6
DEPENDENCE OF AIR TO GROUND (LAND AND SEA) VISIBILITY RANGES ON LOW FLIGHT ALTITUDES IN CONJUNCTION WITH METEOROLOGICAL PARAMETERS by H.-E.Hoffmann	7
DETERMINATION DES PERFORMANCES D'UN SYSTEME COAT EN REGIME DE POURSUITE par G.Roger	8
SUMMARY AND DISCUSSION FOR SESSION I	S1
<u>SESSION II – RECENT ATMOSPHERIC AND SEA WATER MEASUREMENTS</u>	
ATMOSPHERIC MEASUREMENTS IN A COASTAL ENVIRONMENT by T.Bakker	9
ATMOSPHERIC OPTICAL/IR PROPERTIES IN NORTHERN GERMANY – CLASSIFIED†* (Available by request) by R.W.Fenn and E.P.Shettle	10
MEASUREMENTS OF CLOUD DEPOLARIZATION AND MULTIPLE SCATTERING by C.Werner and E.Wolff	11
APPLICATION DES LASERS A LA MESURE A DISTANCE DES GAZ ATMOSPHERIQUES. UTILISATION DE LA DIFFUSION RAMAN RESONNANTE par J.C.Pourny et H. El Naby Salah	12

† Abstract only.

* Paper not available for publication in these Proceedings (may be requested through official channels from AGARD).

	Reference
MULTIWAVELENGTH EXTINCTION AND INDEX FLUCTUATION MEASUREMENTS by E.C.Crittenden, Jr, E.A.Milne, A.W.Cooper, G.W.Rodeback and S.H.Kalmbach	13
MEASUREMENTS OF OPTICAL ATMOSPHERIC QUANTITIES IN EUROPE AND THEIR APPLICATION TO MODELLING VISIBLE SPECTRUM CONTRAST TRANSMITTANCE by R.W.Johnson and W.S.Hering	14
COMPARISON OF UNDERWATER RADIANCE MEASUREMENTS WITH VARIOUS ANALYTICAL TREATMENTS OF THE RADIATIVE TRANSFER EQUATIONS by R.Anderson and L.Stotts	15
DOWNLINK LASER CLOUD PROPAGATION EXPERIMENT by G.R.Hostetter and P.J.Titterton	16
LABORATORY MEASUREMENTS OF LIGHT PROPAGATION IN TURBID MEDIA by A.I.Carswell	17
REMOTE SENSING OF THE DIFFUSE ATTENUATION COEFFICIENT OF OCEAN WATER by R.W.Austin	18
SUMMARY AND DISCUSSION FOR SESSION II	S2
<u>SESSION III – UPPER ATMOSPHERE EFFECTS: THEORY AND EXPERIMENTS</u>	
RECENT AURORAL AND AIRGLOW MEASUREMENTS IN THE INFRARED by A.T.Stair, Jr, R.Nadile, J.C.Ulwick, K.D.Baker and D.J.Baker	19
BACKGROUND MEASUREMENTS FROM A BALLOON-BORNE STARING SENSOR by R.E.Murphy, F.H.Cook and B.K.Yap	20
OPTICAL C_N^2 REMOTE SENSING IN THE UPPER ATMOSPHERE BY MULTIDIMENSIONAL ANALYSIS OF STELLAR SCINTILLATION by J.Vernin and M.Azouit	21
Paper 22 cancelled	
INFRARED RADIANCE MODEL OF THE UPPER ATMOSPHERE by T.C.Degges and H.J.P.Smith	23
Paper 24 cancelled	
MINIMUM DETECTABLE QUANTITIES OF TRACE GASES USING HIGH RESOLUTION SPECTROSCOPY by A.S.Zachor, B.Bartchi and F.P.DelGreco	25
Paper 26 cancelled	
SUMMARY AND DISCUSSION FOR SESSION III	S3
<u>SESSION IV – NOVEL COMMUNICATION TECHNIQUES AND DEVICES</u>	
LINE-OF-SIGHT OPTICAL COMMUNICATION THROUGH LOW-VISIBILITY WEATHER by J.H.Shapiro	27
MERCURIC BROMIDE DISSOCIATION LASERS by E.Schimitschek	28
COPPER VAPOR LASERS: A REVIEW by T.W.Karras	29

RECENT DEVELOPMENT OF HIGH-POWER VISIBLE LASER SOURCES EMPLOYING SOLID-STATE SLAB LASERS AND NONLINEAR HARMONIC CONVERSION TECHNIQUES by Y.S.Liu, W.B.Jones and J.P.Chernoch	30
DOWN-CONVERSION OF RARE GAS HALIDE LASERS FOR BLUE-GREEN APPLICATIONS by R.Burnham, N.Djeu and B.L.Wexler	31
NARROW BANDPASS LARGE FIELD OF VIEW OPTICAL FILTERS by W.J.Rosenberg and A.M.Title	32
OPTICAL RECEIVERS FOR UNDERWATER COMMUNICATION by J.E.Jackson, G.M.Lee and C.M.Ciany	33
OPTICAL FIBER COMMUNICATION AT DIFFERENT TRANSMISSION WAVELENGTHS by K.Hess and H.Haupt	34
SUMMARY AND DISCUSSION FOR SESSION IV	S4

SESSION V – NON-LINEAR OPTICS

NONLINEAR ADAPTIVE OPTICS by C.R.Giuliano	35
PHASE CONJUGATION AND DEGENERATE FOUR WAVE MIXING IN PHOTOREFRACTIVE $\text{Bi}^{12}\text{SiO}_2$ CRYSTAL by J.P.Huignard and J.P.Herriau	36
Paper 37 cancelled	
THEORY OF NONLINEAR PROPAGATION IN MULTIMODE OPTICAL FIBERS by B.Crosignani, P. Di Porto and C.H.Papas	38
THEORY OF NONLINEAR PULSE PROPAGATION IN INHOMOGENEOUS DISPERSIVE MEDIA: APPLICATION TO OPTICAL WAVEGUIDES by N.Tzoar, B.Bendow and P.D.Gianino	39
HOW TO TAP A FIBER-OPTIC LINK AND ELUDE DETECTION – WHAT'S NEW IN QUANTUM COMMUNICATION by J.H.Shapiro	40
USE FOR REMOTELY CONTROLLED INTEGRATED DIRECTIONAL COUPLER SWITCH IN AN OPTICAL FIBER LINK by M.Papuchon, C.Puech and A.Schnapper	41
DISCUSSION FOR SESSION V	S5

SESSION VI – ADAPTIVE OPTICS

Paper 42 cancelled	
RESOLVING POWER EVALUATION OF OPTICAL ADAPTIVE SYSTEMS THROUGH THE ATMOSPHERE by A.Consortini	43
Paper 44 cancelled	
ADAPTIVE OPTICS FOR THERMAL BLOOMING† by W.P.Brown	45

† Abstract only

	Reference
ANISOPLANATISM IN ADAPTIVE OPTICS by D.J.Fried	46
REDUCTION OF ANISOPLANATIC ERRORS by D.W.Hanson and N.Schwartz	47
PHASE MEASUREMENT SYSTEMS FOR ADAPTIVE OPTICS by J.C.Wyant	48
ADAPTIVE OPTICAL SYSTEMS USING DISCRETE COMPONENTS by J.W.Hardy	49
SUMMARY AND DISCUSSION FOR SESSION VI	S6
LIST OF ATTENDEES	A

EDITOR'S INTRODUCTION

1. The purpose of the technical meeting on "Special Topics in Optical Propagation" which was held in Monterey, California, US, was to review the new elements of knowledge which are technically utilizable, and the new elements of development in the field of propagation and optical devices, which have a direct military application to communications and reconnaissance.

Two sessions were devoted to the reconnaissance of sea traffic from surveillance satellites: Session III on "The Effects of the High Atmosphere (theory and experiments)" and Session VI on "Adaptive Optics".

One Session, Session I dealt with strategic communications and, more particularly, communications with submerged submarines, which depend on propagation.

Measurements were the subject of Session II, and instruments, laser sources, special filters, etc. were covered in Session IV.

The new points in the field of optical propagation are concerned with:

the air, for the upper atmosphere,
the water, for radiative transfer,
glass, for non linear effects.

Optical transmission between a satellite and a submerged platform is based on these results.

2. In his opening speech at the AGARD EPP Symposium on "Electromagnetics of the Sea", which took place in Paris in 1970 (see AGARD C.P.77), Vice Admiral O'Grady, from the US Navy General Staff, requested the assistance of AGARD EPP for investigations on non acoustic means of sea surveillance, and especially on electromagnetic means for the detection and location of submarines.

The EPP meeting on "Optical Propagation in the Atmosphere" which convened in Lyngby (Denmark) in 1975 (see AGARD C.P. 183) and the EPP meeting held recently in Monterey, California, on "Special Topics in Optical Propagation" provide partial replies, or elements of replies, to Vice-Admiral O'Grady's request.

However, it should be pointed out that, while the extent of our knowledge on optical propagation in the atmosphere is relatively satisfactory as regards the understanding and modelling of phenomena, the computation of results and their good agreement with experience, the same does not apply to optical propagation in the water, a recently opened field of research where scientific and technical activities have only been developing for a few decades, whereas optical research in the atmosphere has been going on since the beginning of instrument optics.

On the other hand, experiments in sea water, and the acquisition of a sufficient amount of high quality data are certainly more difficult and more costly than in the atmosphere.

A considerable effort should be made in this area, because, as regards the propagation of light, and due to the presence of noise sources, the ocean water varies much more with the location considered than the atmosphere.

Much remains to be done. However, it is already known that interesting possibilities exist when the conditions are favourable in the water, and, if necessary, in the air. The purpose in view is of course to extend these possibilities to less favourable conditions and to determine accurately the natural constraints.

3. In addition, at Monterey, various important contributions were made in the fields of optical propagation, laser sources in the blue-green, detection, on optical fibers and non-linear effects.

In this respect, it should be recalled that the use of the laser has made it possible to obtain electric fields of an intensity comparable to that of the intra-atomic field, that is approximately 10^{10} V/m, and to induce a non-linear polarization in non ferro-electric media, either in the mass of crystals or amorphous bodies, or in solid or liquid core optical fibers.

Thus, the technology of these non-linear effects and mainly of the Brillouin scattering and the stimulated Raman effect has developed during the last few years (see "Fiber and Integrated Optics", NATO Advanced Study Institute Series: B 41 (1978)). It has led to a good understanding of the physical phenomena involved, and to the presentation of a theory confirmed by experience.

Among the various results achieved, that which appears the most important and the most stimulating for the imagination is the phase conjugation response, either by Brillouin backscatter or by a degenerate mixture of four waves.

To make a brief description of this matter, let us say that the medium which receives the field of angular frequency, whose expression is $E = R_e[\psi(x, y, z)e^{j\omega t}]$ produces the field

$$E_{p.c.} = R_e[\psi^*(x, y, z)e^{j\omega t}] \equiv R_e[\psi(x, y, z)e^{-j\omega t}]$$

where ψ^* is the conjugate imaginary quantity of ψ . Hence the appellation of "Reflection by Conjugation of Space Phase". The reflected wave travels back along the path of the incident wave.

For the time being, high reflectivity has been obtained at low power densities, on small size samples. This is only the initial phase of this work, but it seems to hold good promise.

For the production of fusion nuclear energy, activation through the heating of small material pellets containing a mixture of deuterium and tritium could use high intensity u.v. light beams, automatically aimed at the pellets, by phase conjugation, from the light emitted by the pellet itself.

For the transmission of the solar energy between a space station and an earth station. the high intensity beam would be automatically aimed at the earth station by the sounding signal emitted by this station and sent back, amplified, by the space station, along the very same path.

Thus, in the long term, non linear optics seems to be potentially capable of solving many adaptation problems.

In the field of chemistry and pollution, the identification and quantity determination of pollutants such as SO_2 or nitrogen oxides in the atmosphere can be carried out at a distance, in real time, by optical means, for the protection of the environment and for defence purposes.

Such methods utilize the interaction of the light of a laser with the atmospheric molecule to determine the composition at a distance.

New possibilities are being opened for optical fibers, in a new band in the vicinity of 1600 nm, if these hopes are confirmed, it will be possible to leave a space of 100 km or more between repeaters on the cables for sub-marine or ground communications.

It should be pointed out that optical fibers and cables offer a high transmission reliability due to their invulnerability to jamming and the extreme difficulty of interception. In view of these advantages which are to be added to many others, the optical cable is a first-class means of tactical communication.

In the field of optical detection, the use of quantum mechanics formulations applied to photodetection opens new theoretical avenues.

The use of a light source offering a coherent state at two photons (TCS) could make it possible to gain approximately ten decibels on the signal/noise ratio necessary to detection, and, consequently, on the overall power of the link.

The possibility of producing and using a light source offering this coherence remains to be demonstrated experimentally.

4. I would like to add that, among the many papers presented on the occasion of this meeting, most were related to advanced studies.

Although some of these papers had already been published, the fact that they were collected together, associated with their oral presentation and the ensuing discussions, shed some light on the participants' and observers' knowledge and will lead to a better understanding of new topics and to a stimulation of progress.

In these Conference Proceedings, the papers have been arranged by sessions. At the end of each Session the reader will find the participants' questions and comments, then the summary and conclusions of the Session Chairman or his substitute, such as they were presented at the Round Table discussion.

In conclusion, we can state as a certain fact that optics is now a most promising field of research.

P. Halley
Capitaine de Frégate honoraire
12 rue du Docteur Kurzenne
78350 Jouy en Josas
France

INTRODUCTION

de

l'Editeur

1. La réunion technique "Special topics in optical propagation" tenue à Monterey, Californie, Etats-Unis, avait pour but de passer en revue les nouveaux points de la connaissance, techniquement exploitables, et les nouveaux points du développement dans le domaine de la propagation et de l'appareillage optiques, qui ont une application militaire directe pour les communications et la reconnaissance.

Deux sessions ont été dévolues à la reconnaissance, à partir des satellites de surveillance du trafic océanique : la session III sur "Les effets de la haute atmosphère (théorie et expériences)" et la session VI sur "L'optique adaptative".

Une session a été dévolue aux communications stratégiques et, plus particulièrement, aux communications avec les sous-marins en immersion, qui dépendent de la propagation : La session I.

Les mesures ont été rassemblées en session II et l'appareillage, les sources lasers, filtres spéciaux, etc ..., en session IV.

Les points nouveaux sur la propagation optique concernent :

*l'air, pour l'atmosphère supérieure,
l'eau, pour le transfert radiatif,
le verre, pour les effets non-linéaires.*

La transmission optique entre un satellite et une plateforme immergée fait appel à ces résultats.

2. Dans son discours d'ouverture du symposium AGARD-EPP "Electromagnetics of the Sea", tenu à Paris en 1970 (voir AGARD C.P. 77), monsieur le Vice amiral O'GRADY de l'Etat Major de l'U.S. Navy, sollicitait l'activité du comité de propagation des ondes électromagnétiques de l'AGARD, afin que soient recherchés des moyens non-acoustiques de surveillance de la mer et notamment des moyens e. m. de détection et de localisation des sous-marins.

La réunion technique AGARD-EPP "Optical propagation in the atmosphere" tenue à Lyngby (Danemark) en 1975 (voir AGARD-C.P. 183) et la réunion technique qui vient d'avoir lieu à Monterey, comportent des réponses partielles ou des éléments de réponses à la sollicitation du Vice amiral O'GRADY.

Il convient toutefois de souligner que, si le degré de notre connaissance de la propagation optique dans l'air est raisonnablement satisfaisant, tant par la compréhension des phénomènes que par leur modélisation, le calcul des résultats et leur accord avec l'expérience, il n'en est pas de même pour la propagation optique dans l'eau, domaine de recherche récemment ouvert, où l'activité scientifique et technique ne s'est développée que depuis quelques décennies, alors que la recherche optique dans l'air dure au moins depuis le début de l'optique instrumentale.

D'autre part, l'expérimentation dans l'eau des mers et l'acquisition d'une masse suffisante de données de qualité sont certainement plus pénibles et plus coûteuses que dans l'air. Un très important effort devrait être fourni, car, du point de vue de la propagation de la lumière et par la présence de sources de bruit, l'eau de l'Océan est beaucoup plus variable, en fonction du lieu, que l'air de l'atmosphère.

Beaucoup reste à faire. Cependant, on sait déjà qu'il y a des possibilités de transmission intéressantes, lorsque les conditions sont favorables dans l'eau et, si nécessaire, dans l'air. Le but est, bien sûr, d'étendre ces possibilités à des conditions moins favorables et de préciser les limitations naturelles.

3. Par ailleurs, la réunion de Monterey a fourni diverses contributions importantes dans les domaines de la propagation optique, des sources laser dans le bleu-vert, de la détection sur les fibres optiques et surtout des effets non-linéaires.

- Rappelons à ce propos que l'emploi du laser a permis d'obtenir dans la matière des champs électriques d'une intensité comparable à celle du champ intra-atomique, soit environ 10^{10} V/m et de provoquer une polarisation non-linéaire, dans les milieux non ferro-électriques, soit dans la masse de cristaux ou de corps amorphes, soit dans des fibres optiques à coeur solide ou liquide.

Ainsi, la technologie de ces effets non-linéaires et notamment de la diffusion Brillouin et de l'effet Raman stimulé s'est développée au cours des dernières années [voir "Fiber and integrated optics" Nato advanced study institute series : B41 (1978)]. Elle a permis une bonne compréhension des phénomènes physiques qui sont mis en jeu et la présentation d'une théorie confirmée par l'expérience.

Parmi les différents résultats obtenus, celui qui paraît le plus important et le plus stimulant pour l'imagination, est la réponse en conjugaison de phase, soit par rétrodiffusion Brillouin, soit par mélange de quatre ondes, dégénéré.

Pour exprimer la chose sommairement, disons que le milieu, qui reçoit le champ de pulsation ω et d'expression : $E = R_e \left[\psi(x, y, z) e^{j\omega t} \right]$ produit le champ :

$$E_{p.c.} = R_e \left[\psi^*(x, y, z) e^{j\omega t} \right] \equiv R_e \left[\psi(x, y, z) e^{-j\omega t} \right]$$

où ψ^* est l'imaginaire conjugué de ψ . D'où l'appellation de "réflexion par conjugaison de phase spatiale". L'onde réfléchie revient sur le chemin de l'onde incidente.

Pour le moment, de fortes réflectivités ont été obtenues à de faibles densités de puissances, sur des échantillons de petites dimensions. Ce n'est que le début du travail, mais la perspective est très stimulante.

Pour la production de l'énergie nucléaire de fusion, l'activation par échauffement de petites billes matérielles, contenant un mélange de deutérium et de tritium, pourrait utiliser des faisceaux lumineux u.v., très intenses, automatiquement pointés sur la bille, par conjugaison de phase, à partir de la lumière émise par la bille elle-même. Pour la transmission de l'énergie solaire, entre une station spatiale et une station terrestre, le faisceau très intense serait automatiquement pointé sur la station terrestre par le signal de sondage émis par celle-ci et renvoyé, amplifié, par la station spatiale, exactement sur le même trajet.

Ainsi, l'optique non-linéaire paraît potentiellement capable, à terme, de résoudre de nombreux problèmes d'adaptation.

- En chimie-pollution, la reconnaissance et le dosage de polluants tels que SO_2 ou les oxydes d'azote dans l'atmosphère peut être effectuée à distance, en temps réel, par des moyens optiques pour la protection de l'environnement et la défense.

Ces méthodes exploitent l'interaction de la lumière d'un laser avec les molécules atmosphériques pour obtenir, à distance, la composition.

- Les fibres optiques s'ouvrent à de nouvelles possibilités dans une nouvelle bande au voisinage de 1 600 nm, qui, si les espoirs sont confirmés, permettra d'espacer de 100 km, ou davantage, les répéteurs sur les câbles pour les communications sous-marines ou terrestres.

Noter que les fibres et les câbles optiques présentent une grande sécurité de transmission, par l'invulnérabilité au brouillage et la difficulté extrême de l'interception. Ces avantages, qui sont à joindre à beaucoup d'autres, font du câble optique un moyen de communication tactique de choix.

- En détection optique, l'emploi des formulations de la mécanique quantique, appliquées à la photodétection, ouvre de nouvelles perspectives théoriques.

L'emploi d'une lumière présentant un état cohérent à deux photons (TCS) pourrait permettre de gagner une dizaine de décibels sur le rapport signal à bruit nécessaire à la détection et, par conséquent, sur le bilan de puissance de la liaison.

Il reste à montrer expérimentalement, la possibilité de produire une lumière présentant cette cohérence et à l'utiliser.

4. J'ajouterai encore que la réunion a comporté la présentation de nombreuses communications, dont la plupart étaient relatives à des études de pointe.

Bien qu'un certain nombre de ces communications aient déjà fait l'objet d'articles publiés, leur rassemblement, associé à la présentation orale et à la discussion, a permis d'éclairer les connaissances des participants et des observateurs, pour une meilleure compréhension de sujets nouveaux et la stimulation du progrès.

Dans le présent compte rendu, le lecteur trouvera les communications groupées par sessions. A la fin de chaque session, sont rassemblées les questions et les commentaires des participants, puis les appréciations et conclusions du président de session ou de son remplaçant, telles qu'elles ont été présentées à la discussion de table ronde.

Une chose est certaine : L'optique est actuellement un domaine de recherche des plus prometteurs.

Pierre HALLEY

Capitaine de Frégate honoraire
12 rue du Docteur Kurzenne
78350 Jouy en Josas
France

OVER-THE-HORIZON OPTICAL SCATTER
PROPAGATION IN THE MARINE BOUNDARY LAYER

G. C. Mooradian and M. Geller
NAVAL OCEAN SYSTEMS CENTER
San Diego, California 92152
USA

SUMMARY

Measurements of the scattering properties from normal marine atmospheric aerosols for an Over-The-Horizon (OTH) optical propagation channel has been made for two links: The first link involves an overwater range of 63 km with 19-km and 40-km horizons; the second involves an overwater range of 128 km with a 19-km horizon. Pathloss measurements as a function of transmitter-receiver azimuth and elevation angles for a 0.51 μm Ar-ion CW laser, and a 1.06 μm and .53 μm frequency doubled pulsed Nd:YAG laser are reported. Examples of atmospheric ducting are shown with an accompanying large increase of signal and severe scintillations. Two theoretical models are presented, one based on particulate single scatter and the other based on particulate multiple scatter. Comparison between models and the experimental results are made.

1. INTRODUCTION

The use of optical frequencies for communication applications is being pursued in a wide variety of propagation channels in the atmosphere, space, the marine boundary layer and underwater (HOWARTH, 1977; KARP, 1976; MOORADIAN, 1974). The application of the optical scatter channel for atmospheric communications has yet to develop within the optical communication community (CURCIO, 1964). Indeed with few exceptions, most atmospheric laser communication systems are designed for solely line-of-sight operation and consider any interaction with particulate media as degrading (BUCHER, 1973). Unfortunately, there is good basis for this opinion. Recent experimental work (MOORADIAN 1980) has shown varying but never negligible degrees of spatial, angular, and temporal degradation of initial laser characteristics after propagation through clouds, fog, or extended atmospheric paths. The possible utility, however, of atmospheric aerosols or cloud bottoms for Over-The-Horizon (OTH) communications in practical applications will hopefully alter this impression (MOORADIAN 1976, 1971). The purpose of this effort was threefold: (1) to describe the performance of two multiwavelength OTH laser links, one with an overwater range of 63 km (19-km and 40-km horizons) and the other with a range of 128 km (19-km horizon); (2) to describe two associated OTH propagation channel models - one based on particulate single scatter, the other based on particulate multiple scatter; and (3) to compare experimental results with theoretical predictions. A complete and thorough theoretical and experimental description of the OTH optical propagation in the marine boundary layer is given in the Applied Optics paper (MOORADIAN, 1980) and will not be reported here. Instead the results are summarized with details left for the reference.

2. ELOS OPTICAL COMMUNICATIONS

The ELOS (Extended Line-of-Sight) optical communications system utilizes optical aerosol scatter in the marine boundary layer to provide low to moderate data rate communications over-the-horizon ranges of 30 to 300 miles. The driving requirement is an over-the-horizon communication capability without use of a relay (MOORADIAN, 1976).

Over-the-horizon optical propagation can occur by a number of different physical mechanisms. For example, anomalous refractivity gradients and structures in the marine boundary layer and above can result in refractive propagation beyond the geometric horizon (i.e., the horizon computed neglecting refraction), where such propagation manifests itself in the form of either atmospheric ducting or simple downward curvature of the initial beam. The latter circumstance, experienced when the refractivity falls off monotonically and approximately linearly in height, can be accommodated analytically by the effective earth radius concept wherein rectilinear ray paths are used. The result is that the earth's radius is imagined to be somewhat larger than its initial value by an amount that increased as the magnitude of the surface refractivity gradient increases. Thus, it is important to appreciate that, in some situations apparent OTH propagation is not so in fact, because the horizon is being miscomputed based either on underestimating or ignoring the surface refractivity gradient.

In this study only bona fide OTH propagation was considered. That is, only propagation beyond the true optical horizon as computed taking refractivity fully into account. This is not to understate the importance or refractive effects in the atmosphere but rather to emphasize the physical scattering process under investigation. Hence, such propagation, by definition, can occur naturally only through scattering by atmospheric aerosols or clouds (DEIRMENDJIAN, 1969).

A detailed, comprehensive analysis of ELOS propagation has been completed addressing the following (MOORADIAN 1976): relative contributions from single and multiple scattering (as a function of range), wavelength dependence, vertical exponential decrease in aerosol concentration with altitude, effects of refraction, general meteorological parameters (e.g., temperature, humidity, wind speed) multipath time spread, etc. Figure 1 illustrates the performance of two different data communication links in an OTH marine environment. The upper curves give maximum communication range as a function of wind speed and visibility for a teletype data link (75 bits/sec) using the single scatter propagation model. The lower curves depicts maximum communication range as a function of wind speed and visibility for a digital voice link (2400 bits/sec) using the same model. Pertinent system parameters are indicated in the figure. A typical condition of visibility 20 km, wind velocity 5 m/s, and relative humidity of 80% (MCDONNELL DOUGLAS, 1968, NICODEMUS 1972) indicates a voice communications range of 148 km (2400 BPS), and a teletype range of 187 km (75 BPS). This assumes only a modest 10 watt average power Nd:YAG laser employing pulse interval modulation of approximately 10 bits-per-pulse.

3. OTH PROPAGATION AT 63km RANGE

In order to perform any quantitative comparison with the above cited models and gather enough data to determine system feasibility, it was necessary to determine the following optical scatter channel characteristics during each experimental run: (1) the integrated pathloss over the range; (2) the angular brightness distribution of the source as seen by the receiver, and (3) the magnitude of the pulse stretching. These propagation parameters depend critically on both the atmospheric visibility and the elevation-azimuthal angles of the receiver and secondarily on the aerosol size distribution in the path. In this section, the recent experimental results derived from an OTH propagation link between San Diego and Oceanside, California will be described. For this experiment, the integrated pathloss (received power divided by transmitted power) was measured using the 514.5-nm line of a 1-W Ar-ion laser and the 532-nm and 1.06 μm lines of a Q-switched Nd:YAG laser. In the latter both wavelengths transversed the identical propagation path, i.e., if refractive dispersion could be ignored.

The initial scattering channel selected was a 63-km path, almost all of which is over the ocean. The transmitter was at NOSC in Point Loma. The receiver was on the beach at the Marine Base at Camp Pendleton. The geometric horizon was 40 km from the transmitter for the CW experiments and 19 km for the pulsed.

4. EXPERIMENTAL RESULTS

The experimental results for the 63 km link can be summarized as follows:

- For visibilities greater than 10 miles, the path loss was nominally -100 dB to -120 dB (10 log₁₀ of the power received divided by the peak power transmitted)
- Apparent angular source size was very small (<0.25°) indicating very highly peaked forward scattering (WELLS 1977)
- When atmospheric ducting occurred, approximately 100 times more optical energy was received and severe scintillations were observed (>10 dB)
- Without ducting, almost no amplitude fluctuations were observed (<1 dB) due to scattering volume aperture averaging
- Path loss at 1.06 μm was 20 dB less than at 0.53 μm (i.e., the reduced scattering coefficient at 1.06 μm dominates the increased forward scattering phase function at 0.53 μm due to the exponential atmospheric attenuation)
- The single scatter model appears to be in better agreement with the experimental data than the multiply scatter model, though this is not conclusive

- No evidence of pulse dispersion of the 20 ns pulse was observed at either 1.06μ or 0.53μ (STOTTS, 1978)
- No enhancement of received signal with increased transmitter elevation angle was observed
- Electrical signal to noise ratios >90 dB have been measured at 1.06μ (day) with a Nd:YAG laser of ~ 0.05 J/pulse.
- The scattered beam is very sharply peaked in the forward direction (nominally -20 dB at 10 mrad off-axis in azimuth) and falls off more rapidly in azimuth than elevation when there was vertical structure in the aerosol concentration)

5. OTH PROPAGATION AT 128 km RANGE

The following data was also taken over a Pacific Ocean link, but the ground range was increased to 128 km. The transmitter was located on the seaward side of Point Loma (NOSC) at a height of 37 m above the water; the receiver was located on the northern tip of San Clemente Island at a height of 10 m above the water. The experimental setups are similar to those of the 63 km link with the following modifications:

(1) replacement of the Nd:YAG pulsed laser source with one of higher peak power (5 MW vs. ~ 0.8 MW); (2) a Tektronix 7834 storage scope at the receiver instead of the Biomation digitizer; (3) increase of the receiver's diameter from 20 cm to 39 cm; (4) two receiver field-of-views (8 mrad and 35 mrad).

The experimental results for the 128 km link can be summarized as follows:

- Path loss measured was nominally -115 dB to -135 dB.
- Apparent angular source size ($\sim 1^\circ$) was approximately four times larger than at 63 km.
- Significant pulse stretching was not observed (<60 ns) and was less with the 8 mrad receiver field-of-view than with 35 mrad.
- Electrical signal to noise ratios of 35 dB were measured during day time.
- Signals fell off more slowly with angle at 80 miles than at 40 miles in both azimuth and elevation.
- Single scatter theory appears to hold.

6. ACKNOWLEDGEMENTS

The authors would like to thank P.H. Levine, L.B. Stotts, and D.H. Stephens for their invaluable efforts which combined to produce this work.

7. REFERENCES

- Bucher, EA, and Lerner, RM, "Experiments on Light Pulse Communication Through Atmospheric Cloud" Applied Optics, 12, p 2401, 1973
- Curcio, JA, and Drummeter, LF, Jr. 30 September 1964, "Experimental Observations of Forward Scattering of Light in the Lower Atmosphere", NRL Report 6152
- Deirmendjian, D. 1969, "Electromagnetic Scattering On Spherical Polydispersions", New York, American Elsevier Publishing Co. Inc.
- Howarth, RF, Hyde, ME 1977, "Submarine-Aircraft and Submarine-Satellite Optical Communications System Model," NELC Technical Report, TR-2021
- Karp, S. 1976, "Optical Communications Between Underwater and Above Surface (Satellite) Terminals". IEEE Trans Com COM-24, pp 66-81
- McDonnell Douglas, June 1968, "Marine Weather of the World", Report F-063
- Mooradian, GC, March 1974 "Atmospheric and Space Optical Communications for Naval Applications", Proceedings of 6th DoD Conference on Laser Technology

Mooradian, GC, VJ Adrian, PH Levine, and WR Stone, June 1976, "Extended Line of Sight Optical Communications Study", NELC TR 1988

Mooradian, GC M Geller, GJ Barstow, KE Davies, August 1976, "Over the Horizon Optical Communications Channel" Vail, Colorado, Proceedings of Workshop on Remote Sensing of the Marine Boundary Layer

Mooradian, GC, Geller, M, Krautwald, R, and Stephens, DH, 28 January 1977 "Over-The-Horizon Optical Scatter Communication in the Marine Boundary Layer" NELC Technical Report TR-2022

Mooradian, GC, Geller, M, Levine, P, Stotts, Stephens, D. "Over-The-Horizon Optical Propagation in the Maritime Environment," Applied Optics, 19, no 1, pp 11-30, 1980

Mooradian, GC, Geller, M, Stotts, LB, Stephens, DH, and Krautwald, RA. "Blue/Green Propagation Through Maritime Fogs," Applied Optics, 18, no 4, pp 429-441, 1980

Nicodemus, FE, May 1972, "Weather Effects on Infrared Systems for Point Defense", NWC, China Lake, TN 4056-16

Stotts, LB, "The Radiance Produced by Laser Radiation Transversing a Particulate Multiple-Scattering Medium." J of Opt. Soc. of Am. Vol 67, No 6, pp 815, June 1977

Stotts, LB, "Closed Form Expression for Optical Pulse Broadening in Multiple-Scattering Media." Applied Optics, Vol 17. p 504, February 1978

Wells, E, Gal, G, and Munn, MW, 1977, "Aerosol Distributions in Maritime Air and Predicted Scattering Coefficients in the Infrared", Applied Optics vol 16, no 3, p 654-9

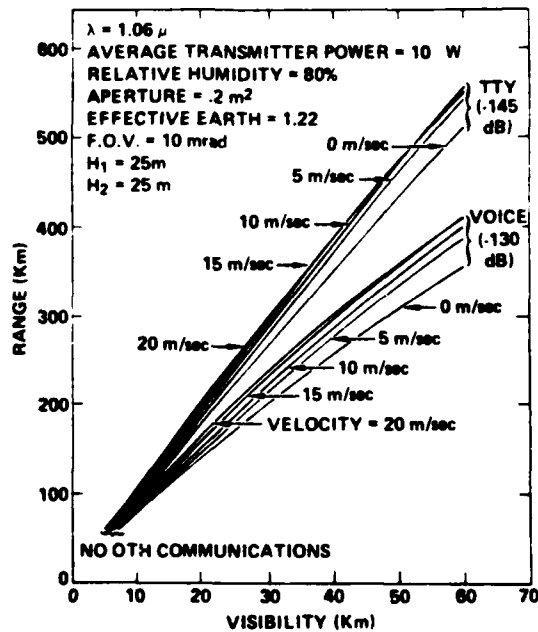


Fig. 1. Maximum communication range as a function of visibility for various wind speeds for teletype data (75-bits/sec) and digital voice (2400-bits/sec) communication links.

MULTIPLE SCATTER OF COLLIMATED IRRADIANCE

W. H. Wells, J. Harris, H. C. Lin
Tetra Tech, Inc., 630 North Rosemead Boulevard, Pasadena, California 91107

ABSTRACT

Using the method of spherical harmonics, we investigate multiple scattering of incoherent light (or other particles) in an optically thick medium with a plane surface. We report techniques that are particularly useful when scattered radiance has a forward peak that generates harmonics of very high degree. Convergence of computations hinges mainly on the small number of harmonics in the backscatter and not so much on the large number in the incident and forward scattered light. The method uses annihilation operators to improve the solution by removing eigenfunctions that propagate the wrong way. Backscattered radiance at the surface may be calculated without solving for interior radiance.

The problem of radiative transfer by multiple scattering in a homogeneous medium has been treated by several mathematical techniques. Prieur and Morel [1973] have reviewed several of these, and Davison and Sykes [1957] have made an extensive review of similar techniques from the old literature of neutron transport.

Unlike diffusion approximations, the method of spherical harmonics gives detailed radiance distributions whose precision is limited only by the effort expended in computation. We report new computational techniques for an optically thick medium with a plane surface at $z=0$. The method is particularly useful when scattered radiance has a forward peak and thus requires many harmonics to represent its distribution. That is, the incident light is quite well collimated, and the scattering function is sufficiently pointed to preserve high harmonics beyond the first scatter. We treat the case in which the radiance is uniform in the x - y plane parallel to the boundary. Sections 1, 2 and 3 develop the theory. Section 4 relates it to some previous work, and Section 5 describes a numerical example.

1. GENERAL FORMATION

The medium in question is characterized by absorption rate a and scattering function σ : a gives fractional loss of light per unit length along any ray, $\sigma(\psi)$ gives the fraction scattered per unit length per unit solid angle in the direction ψ from the ray (independent of the azimuthal angle around the ray). Let S_n denote spherical harmonics of σ :

$$\sigma(\psi) = \sum_{n=0}^{\infty} \frac{2n+1}{4\pi} S_n P_n(\cos\psi), \quad (1)$$

$$S_n = \int_{\text{sphere}} \sigma(\psi) P_n(\cos\psi) d\omega_{\psi}, \quad (2)$$

where P_n is the Legendre polynomial. Let α denote the total beam attenuation rate, and s the total scattering constant S_0 :

$$\alpha = a + s, \quad s = S_0, \quad (3)$$

so that the power lost from a collimated beam of light in the r direction is $dP = -\alpha P dr$, and $P = P_0 \exp(-\alpha r)$.

The angular distribution of light, i.e. radiance L , is in general a function of time, measurement position r , and direction of observation Ω . It gives power per steradian in direction Ω per unit area perpendicular to Ω . In our case, $L(t, r, \Omega) \rightarrow L(z, \theta, \phi)$ since we specialize to the case in which L is independent of t , x , and y , and Ω is specified by spherical angles, which permit expansion in harmonics L_n^m :

$$L(z, \theta, \phi) = \sum_{m \leq n} \frac{2n+1}{4\pi} 2_m \frac{(n-m)!}{(n+m)!} L_n^m(z) P_n^m(\cos\theta) \cos m\phi, \quad (4)$$

$$L_n^m(z) = \int_{\text{sphere}} L(z, \theta, \phi) P_n^m(\cos\theta) \cos m\phi d\omega, \quad (5)$$

$$\text{where } 2_m = \begin{cases} 1, & m = 0 \\ 2, & m > 0 \end{cases}, \quad d\omega = \sin\theta d\theta d\phi.$$

Here we have assumed that ϕ is measured from a plane of symmetry; for asymmetric cases, terms in $\sin m\phi$ must be included. In terms of these harmonics, the well-known Boltzmann equation for radiative transfer is

$$(n-m+1) L_{n+1}^m + (n+m) L_{n-1}^m + (2n+1) A_n L_n^m = 0, \quad (6)$$

where L' denotes dL/dz , $L_{m-1}^m \equiv 0$, and

$$A_n \equiv \alpha - S_n, \quad A_0 = a, \quad A_{\infty} = \alpha. \quad (7)$$

The two limits follow from Eq. (3) and $S_\infty = 0$; the latter in turn follows from Eq. (2). A later discussion shows that A_n may be interpreted more or less as the decay rate of the n th harmonics $L_n^m(z)$. The limit $A_\infty = \alpha$ means that high harmonics decay at the same rate as a collimated beam. However, for moderate values of n the harmonics are unaffected by scattering angles less than the size of their lobe structure, and so the decay rate A_n is correspondingly less.

The form of Eq. (6) obviously suggests an exponential solution:

$$L_n^m = C_n^m e^{-kz} \quad (8)$$

Substitution gives

$$(n-m+1)C_{n+1}^m + (n+m)C_{n-1}^m = (2n+1)(A_n/k)C_n^m \quad (9)$$

where $C_{n-1}^m \equiv 0$. This equation couples different values of the subscripts, but the superscript m is the same throughout. For this reason we shall omit m in nearly all the equations that follow with the understanding that everything except A_n and z depends on m . Equation (9) is an eigenvalue equation for the decay rate k . Solutions of interest have positive k (so that $L(\infty) = 0$) and eigenvectors C (with elements C_i) such that $C_i \rightarrow 0$ as $n \rightarrow \infty$. In all cases, k is real (as can be proved by the standard method of Appendix A in Reference 9); i.e. there is no oscillating solution, which is fortunate because the search for k described below would be difficult to implement in the complex plane. Moreover, the i th eigenvector $C_{(i)}$ has $i-1$ sign changes before decaying to zero (see Appendix C of Reference 9).

The best way to find the i th eigensolution is to choose an arbitrary normalization, say $C_{(i)}^m = 1$, guess a value for k_i , and iterate Eq. (9) as a recurrence relation in C_n until it is apparent that $C_n \rightarrow \pm \infty$, which merely indicates that the guess for k was not exact. Next adjust the trial value of k_i , smaller if C_n changed signs i times or more, larger if otherwise. Repeated trials using a suitable search pattern converge on the critical eigenvalue such that $C_{n(i)} \rightarrow 0$. (There is considerable precedent for truncating Eq. (9) by putting $C_{N+1} = 0$ and solving as a finite matrix eigenvalue problem, but this is less accurate and more difficult.)

The general solution of Eq. (6) is a linear combination of eigensolutions:

$$L(z) = \sum_i B_i C_{(i)} \exp(-k_i z) \quad (10)$$

where L (like C) denotes a column vector of components L_i . There are two problems in using this result. First, it requires a large number of eigensolutions, particularly with collimated illumination that requires many spherical harmonics. Unless $\sigma(\psi)$ contains unusual off-axis peaks, $L_n(z)$ merely decays quite uneventfully and should be expressible in only one or two terms.

The second problem with Eq. (10) concerns boundary conditions. At $z = 0$, the incident light $L_n^{\text{in}}(0, \theta, \phi)$ is given. Actually L_n^{in} denotes light barely inside the scattering medium since surface effects (refraction, reflection, roughness) are not the subject of this paper. However, there is additional back-scattered radiance (diffuse reflection) L_n^{back} that complicates the initial values because it is not given, but rather is part of the solution:

$$L(0, \theta, \phi) = L_n^{\text{in}}(\theta, \phi) + L_n^{\text{back}}(\theta, \phi) \quad (11)$$

In these terms, the surface boundary condition is

$$L_n^{\text{back}}(\theta, \phi) = 0, \quad \theta < \pi/2, \quad (12)$$

which is not easy to apply in terms of spherical harmonics because these functions are orthogonal on the whole sphere, not the hemisphere of Eq. (12). Reference 2 discusses conventional solutions to this problem, Section 2 gives ours.

The condition at the far boundary is simple for an optically thick medium, namely $L(\infty) = 0$, which is already satisfied by choosing positive k for Eqs. (8) and (10). For finite thickness Z we would have $L(Z, \theta, \phi) = 0$, $\pi/2 < \theta \leq \pi$.

The following two sections describe our technique for simplifying the problems just described, the boundary condition in Section 2 and the complexity of Eq. (10) in Section 3.

2. DIFFUSE REFLECTION FROM THE BOUNDARY

In this section we find the boundary values $L_n(0)$ given the incident light L_n^{in} . This accomplishes two things. First, it gives the diffuse reflection L_n^{back} by Eq. (11) without the necessity for finding the interior solution for all z . Second, it facilitates the interior solution also by supplying the initial values for the differential equation, Eq. (6).

The index i in the general solution, Eq. (10), can be assigned in any way, so let positive i denote eigenfunctions with positive k , and negative i denote negative k . Segregating these terms in separate sums gives

$$L(z) = \sum_{i=1}^{\infty} B_i C_{(i)} \exp(-k_i z) + \sum_{i=1}^{\infty} B_{-i} C_{(-i)} \exp(+|k_{-i}|z) \quad (13)$$

As mentioned before, a valid solution requires that the second sum vanish, i.e. all coefficients $B_{-i} = 0$, because the positive exponentials violate the boundary conditions as $z \rightarrow \infty$. However, Eq. (13) shows the second sum anyway, so that we can discuss an iterative solution in which these invalid eigenfunctions

represent the residual error.

We use the transform L^{in} of the incident light as an initial guess for the surface value $L(0)$, which simply neglects L^{back} , Eq. (11). Putting this guess in Eq. (13) with $z = 0$ determines the set of expansion coefficients B_1 and B_{-1} :

$$L(0) \approx L^{in} = \sum_{i=1}^{\infty} B_1 C_{(1)} + \sum_{i=1}^{\infty} B_{-1} C_{(-1)}. \quad (14)$$

Now the second sum, i.e., B_{-1} , does not vanish because the eigenvectors $C_{(-1)}$ comprise part of the complete set for expansion of any arbitrary vector, i.e., L^{in} in our case. If we were to compute this expansion explicitly, we could improve the estimate of $L(0)$ by merely omitting the invalid second sum. However, we do not expand explicitly, and so we eliminate these terms in another way. We develop a set of matrix annihilation operators $N_{(1)}$ that eliminate the i th vector from a sum but have no other effect:

$$N_{(1)} C_{(j)} = (1 - \delta_{ij}) C_j = \begin{cases} C_j, & i \neq j \\ 0, & i = j \end{cases}. \quad (15)$$

Thus successive applications of $N_{(-1)}$, $N_{(-2)}$, etc. improve the estimate of $L(0)$ until it converges to a valid initial vector

$$L(0) = (\dots N_{(-3)} N_{(-2)} N_{(-1)}) L^{in}, \quad (16)$$

which includes diffuse reflection missing from the initial guess L^{in} . This equation describes a vital step in our computations, which require explicit expressions for N_i that we develop shortly.

But why form a valid solution by annihilating invalid eigenvectors instead of building it up from valid ones? The answer lies in convergence rates. The number of annihilation operations required is comparable with the number of spherical harmonics contained in the diffuse reflection, which is typically small since backscatter is broad and featureless from multiple scattering events. By contrast, collimated incident illumination requires many harmonics. Furthermore, when the medium has absorption, the backscatter is small in comparison with incident illumination. Thus any error caused by terminating the annihilation operations is an error in the small backscattered part of the light field and not an error in the large incident illumination.

The annihilation operators are clearly necessary to produce a valid solution, but are they sufficient to satisfy the boundary condition? From the example in Section 5, it appears that they are (the very small error that could result from terminating the sequence of annihilations). However, we are not convinced that this holds in general and suspect that the operations alter the boundary condition in a benign way: the solution obtained is a valid one in which the incident light differs slightly from the intended distribution. That is, $L(0, \theta, \phi)$ derived from Eq. (16) differs from $L^{in}(0, \phi)$ in the hemisphere $\theta < \pi/2$. Further analysis and computations for cases with less absorption and more backscatter may clarify this point. At worst, one or two iterative adjustments may be required to find the initial L^{in} that gives the desired solution. However, consider the practical case in which the boundary is also a refractive discontinuity where Fresnel reflection returns a portion of the backscatter into the medium. This case requires iterative tinkering with the boundary values anyway, and so the problem with the operators causes little or no additional labor.

To develop the annihilation operators, Eqs. (15) and (16), we first define a row vector \bar{C} of elements

$$\bar{C}_n = (2n+1) A \frac{(n-m)!}{n(n+m)!} C_n. \quad (17)$$

When they are properly normalized, the $C_{(1)}$ form an orthonormal set such that

$$\bar{C}_{(1)} C_{(j)} = \delta_{ij}, \quad (18)$$

as proved in Appendix B of Reference 9. Now the required operator is

$$N_{(1)} = I - C_{(1)} \bar{C}_{(1)}, \quad (19)$$

because

$$N_{(1)} C_{(j)} = C_{(j)} - C_{(1)} (\bar{C}_{(1)} C_{(j)}) = C_{(j)} - C_{(1)} \delta_{1j} = (1 - \delta_{1j}) C_{(j)}$$

[compare Eq. (15)].

To complete the theory we need the invalid eigenvectors $C_{(-1)}$ to substitute in Eq. (19) and then use in Eq. (16). For each positive eigenvalue k_i , there corresponds a negative one $-k_{-i}$ whose eigenvector consists of the elements $(-1)^n C_{n(-i)}$. This is evident from Eq. (9) because the sign change in alternate C_n cancels the sign change in k . Thus the invalid eigenvectors have components

$$C_{n(-i)} = (-1)^n C_{n(i)}, \quad k_{-i} = -k_i. \quad (20)$$

In summary, the iterative method described following Eq. (9) gives $C_{(1)}$, and Eq. (20) gives $C_{(-1)}$, which goes into Eq. (19) for the annihilation operator. Equation (16) then supplies the initial values $L(0)$. These may be used in Eq. (4) to find the angular distribution of backscatter without ever solving for radiance in the interior of the scattering medium.

3. INTERIOR SOLUTION

Having established the boundary values $L_n(0)$, we can readily evaluate the coefficients B_1 needed for the general solution, Eq. (10), inside the scattering medium. Using the orthogonality property, Eq. (18), and Eq. (10) at $z = 0$, we have

$$B_1 = \bar{C}_{(1)} L(0). \quad (21)$$

This is quite practical for deep penetration where only a few of the lowest eigenfunctions survive, but for shallow penetration the required number of eigenfunctions is excessive.

We use the first eigenfunction explicitly and lump all the others into a second exponential term that represents them approximately:

$$L_n(z) = B_1 C_{n(1)} \exp(-k_1 z) + Q_n \exp(-q_n z). \quad (22)$$

Obviously, two or more eigenfunctions would give greater accuracy. Evaluation at $z = 0$ readily gives the Q_n coefficients:

$$Q_n = L_n(0) - B_1 C_{n(1)}. \quad (23)$$

Matching first derivatives of Eq. (22) at $z = 0$ determines the decay rates q_n . Let λ_n denote the negative derivative,

$$\lambda_n \equiv -L'_n(0), \quad (24)$$

and then

$$q_n = (\lambda_n - k_1 B_1 C_{n(1)}) / Q_n. \quad (25)$$

The λ_n must be evaluated from the basic differential equation, i.e. Eq. (6), which gives a recurrence formula for λ_n^m :

$$(n-m+1) \lambda_{n+1}^m + (n+m) \lambda_{n-1}^m = (2n+1) A_n L_n^m(0), \quad (26)$$

with $\lambda_{n-1}^m = 0$. Evaluation is perfectly straightforward for the series in which $n - m$ is odd, which begins by putting $n = m$ in Eq. (26):

$$\lambda_{m+1}^m = (2m+1) A_m L_m^m(0). \quad (27)$$

The series in which $n - m$ is even causes a minor problem. When we attempt to find the first member by putting $n = m+1$ in Eq. (26), we find an equation that has two unknowns, λ_m^m and λ_{m+2}^m , and thus fails to start the series. Instead, one must begin with the asymptotic value for large n discussed in the next section [Eq. (33)]:

$$\lambda_n^m = L_n^m(0) A_n \sec \theta_0 P_n^m(\cos \theta_0) \quad (28)$$

and iterate backward until $n = m$. In practice, one watches the convergence of the odd series going up in n , and uses this as an interpolation guide to find a starting value for the even series.

In summary, the λ 's gives the q 's, [Eq. (25)], the q 's complete Eq. (22) for the harmonics, and finally the harmonics are transformed back to radiance, [Eq. (4)]. Practical computations run quickly using the recurrence relation for associated Legendre functions:

$$P_{n+1}^m(x) = \left[(2n+1)xP_n^m(x) - (n+m)P_{n-1}^m(x) \right] / (n-m+1). \quad (29)$$

4. SMALL ANGLE SOLUTION

Consider a collimated beam of light at normal incidence on the plane surface of a medium with small-angle scattering such that $\cos \theta \approx 1$ is an acceptable approximation. Then instead of Eq. (6), Boltzmann's equation for radiative transfer becomes [Wang and Guth (1951)].

$$L'_n + A_n L_n = 0 \rightarrow L_n(r) = L_n(0) e^{-A_n r}. \quad (30)$$

Because of axial symmetry, we have

$$\text{symmetric: } L_n^{m > 0}(r) = 0, \text{ all } n. \quad (31)$$

If, in addition, the light is perfectly collimated, L is a delta function in solid angle, and Eq. (5) gives

$$\text{perfect collimation: } L_n(0) = 1, \text{ all } n; \quad (32)$$

otherwise, $L_n(0)$ gradually decays for large n .

Now suppose that the surface is tilted by an angle θ_0 , as shown in Fig. 1, while keeping the $\theta = 0$ axis aligned with the light source, not perpendicular to the surface. For θ sufficiently small, it is clear that the small path changes $\Delta r \ll 1/\alpha$ make little difference, and so the solution is still valid. (However, the irradiance is now $\cos\theta_0$ instead of 1, and note that $r = z \sec\theta_0$). All high harmonics, say $n > 20$, arise from small angle peaks, say $\theta < \pi/20 = 9^\circ$, and are much more easily computed with the axis tilted to point at the light source, because the asymmetric terms vanish [Eq. (31)]. This is a great saving in the number of harmonics required, of the order N instead of $\frac{1}{2}N^2$, where N may be as large as 100 for a few degrees of angular resolution.

To match the small-angle solution to the large-angle solution at some value of n , say 20, we need to rotate the origin of θ back to the z axis (Fig. 1). The addition theorem of spherical harmonics accomplishes this with the result that

$$L_n^m(z) = P_n^m(\cos\theta_0) \exp(-A_n z \sec\theta_0) L_n^m(0). \quad (33)$$

This independent exponential decay of each harmonic is reminiscent of small-angle theory using Fourier transforms in which each spacial frequency decays exponentially [Wells (1969), Yura (1971) and Arnush (1972)]. The connection between the two follows from the following limit of Legendre functions for large n and small θ :

$$P_n^m(\cos\theta) \sim \frac{(n+m)!}{(n-m)!} (n+\frac{1}{2})^{-m} J_m[(n+\frac{1}{2})\theta].$$

The Bessel function in turn represents Fourier transforms expressed in polar coordinates.

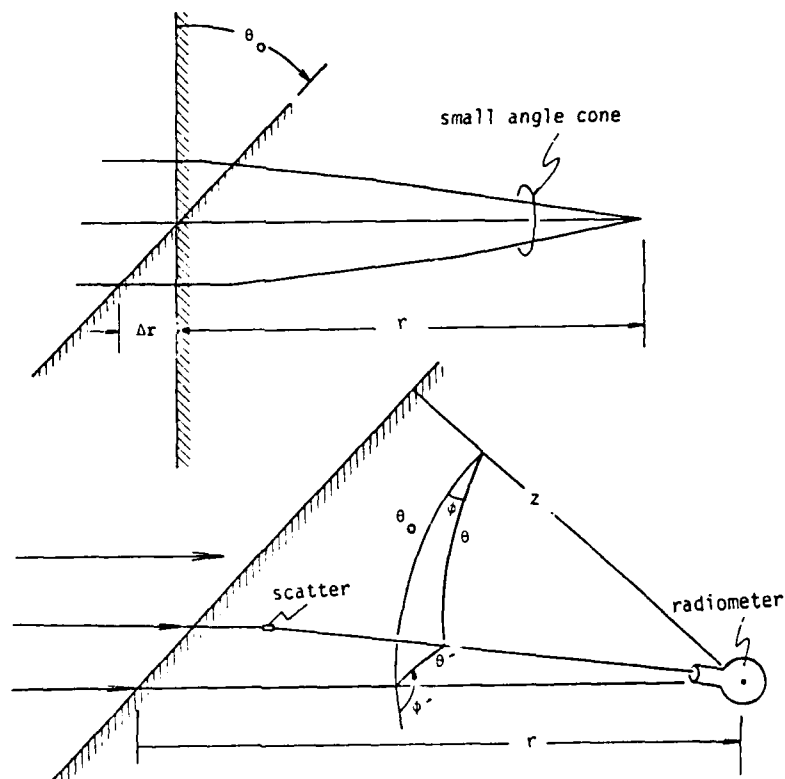


Fig. 1 Geometry of Small-Angle Scatter

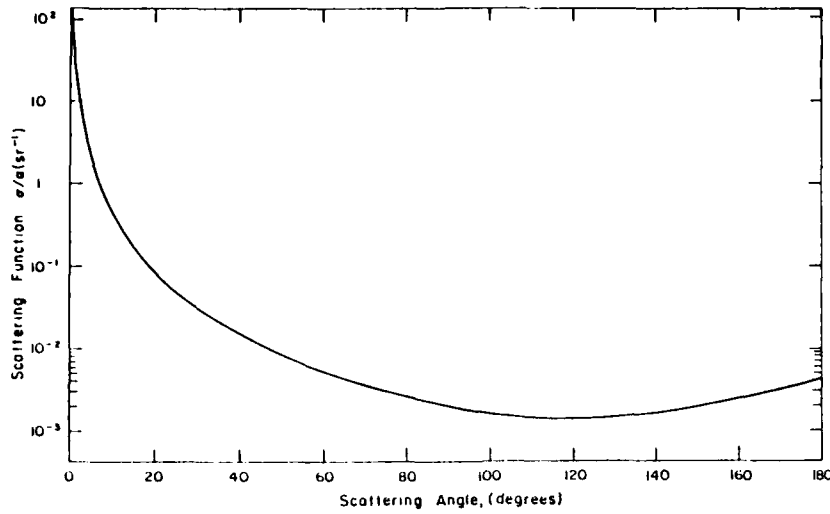


Fig. 2. Scattering Function

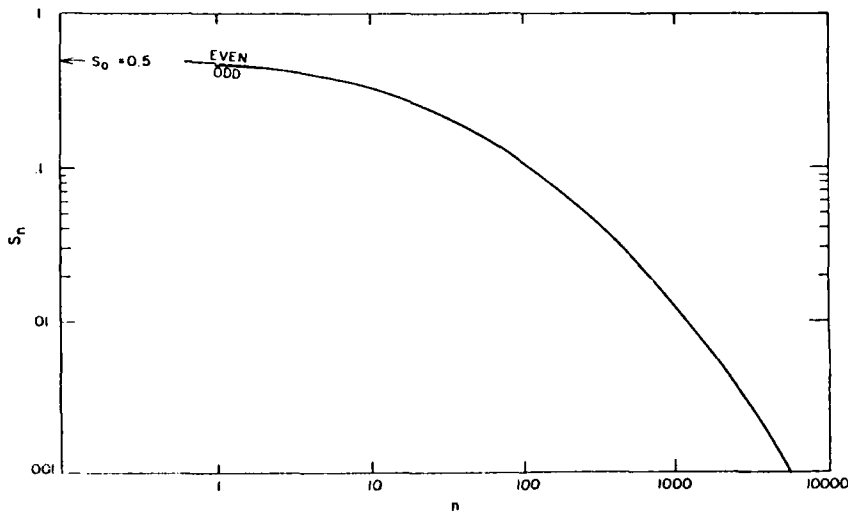


Fig. 3. Spherical Harmonics of Scattering Function

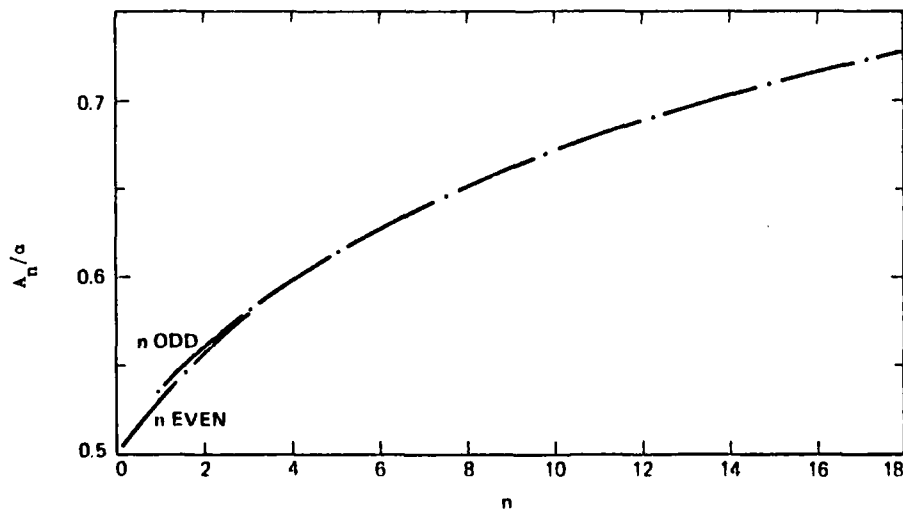


Fig. 4. First Nineteen Attenuation Constants for Spherical Harmonics. $A_0 = a = 0.5$
 $A_\infty = a = 1.0$

Table 1.
First Three Eigenvectors and Eigenvalues

n	$k_1=0.5886$	$k_2=0.6742$	$k_3=0.7230$
	$C_{n(1)}$	$C_{n(2)}$	$C_{n(3)}$
0	1.0000	1.0000	1.0000
1	.8494	.7416	.6915
2	.6591	.3836	.2683
3	.4721	.0332	-.1170
4	.3196	-.2377	-.3654
5	.2060	-.4055	-.4496
6	.1280	-.4798	-.3963
7	.0770	-.4873	-.2538
8	.0450	-.4388	-.0746
9	.0257	-.3721	.0987
10	-.0143	-.2989	.2387
11	-.0078	-.2298	.3334
12	-.0042	-.1705	.3823
13	-.0022	-.1226	.3923
14	-.0012	-.0858	.3734
15	-.0006	-.0587	.3362
16	-.0004	-.0393	.2897
17	-.00015	-.0258	.2407
18	-.00007	-.0167	.1940
19	-.00004	-.0106	.1524
20	-.00002	-.0067	.1169

Table 2.
(Fast) Convergence of Annihilation Operators

n	L_n^{in}	$N_{(-1)}^{in} L_n^{in}$	$N_{(-2)}^{in} N_{(-1)}^{in} L_n^{in}$	$N_{(-3)}^{in} N_{(-2)}^{in} N_{(-1)}^{in} L_n^{in}$
0	1.0	1.00336	1.00393	1.00402
1	1.0	.99714	.99672	.99666
2	1.0	1.00222	1.00243	1.00246
3	1.0	.99841	.99839	.99840
4	1.0	1.00108	1.00094	1.00091

Table 3.
Computed Parameters for the Example

n	A_n	$L_n(0)$	Q_n	q_n
0	.5000	1.0000	-1.4112	.6498
1	.5355	.9967	-1.0807	.6503
2	.5564	1.0025	-.8091	.6510
3	.5800	.9984	-.5558	.6520
4	.5971	1.0009	-.2941	.6533
5	.6147	.9996	-.0959	.6551
6	.6280	1.0000	.1872	.6583
7	.6401	1.0000	.4117	.6597
8	.6513	.9999	.6898	.6624
9	.6617	1.0001	.9373	.6665
10	.6713	.9999	1.1649	.6741
11	.6802	1.0001	1.3710	.6839
12	.6884	1.0000	1.5497	.6894
13	.6962	1.0000	1.6966	.6946
14	.7034	1.0000	1.8172	.7015
15	.7101	1.0000	1.9096	.7092
16	.7164	1.0000	1.9791	.7174
17	.7223	1.0000	2.0296	.7223
18	.7279	1.0000	2.0648	.7278
19	.7332	1.0000	2.0899	.7331
20	.7381	1.0000	2.1000	.7380

$$\theta_1 = 2.45$$

5. EXAMPLE

As an example we choose the scattering function shown in Fig. 2. This results in moments S_n and A_n in Figs. 3 and 4; see Eqs. (2) and (7). We take equal absorption and scattering constants $a = s = 0.5$; thus $\alpha = 1$. The sharp forward peak in σ requires many harmonics and causes A_n to increase slowly and smoothly to its limit $A = \alpha = 1$. The broad backscatter peak, $\sigma(180^\circ)$ in Fig. 2, causes the slight offset of even and odd S_n and A_n (Figs. 3 and 4), since $P_n(\cos 180^\circ) = P_n(-1) = (-1)^n$.

We assume that the incident light is perfectly collimated, which generates an infinite number of high harmonics. To keep the example simple otherwise, we choose normal incidence so that only the harmonics of the incident light are the same as Eqs. (31) and (32);

$$L_n^{in}(0) = 1, L_n^{m>0}(z) = 0, \text{ all } n \quad (34)$$

We solved the eigenvalue problem, Eq. (9), by the means explained following that equation. Results appear in Table 1 for the first three positive k solutions. We form the annihilation operators, Eqs. (17), (19), and (20), and operated in L_n^{in} [Eq. (34)], with the first three to find the boundary values in [Eq. (16)]. Convergence of the process is apparent in Table 2. Computation of the radiance at $z=0$ [Eq. (4)] shows that the boundary condition in Eq. (12) remains quite well satisfied.

$$L(0,10^\circ) = 8 \times 10^{-6}, L(0,30^\circ) = 7 \times 10^{-6}, \\ L(0,60^\circ) = 6 \times 10^{-6}.$$

Equation (22) gives the harmonics as a function of depth inside the scattering medium. The parameters for that equation appear in Table 3, except for $C_{n(1)}$ in Table 1. (Equation (23) gives Q_n , and Eqs. (22) through (28) give q_n .) Note that Q_n is negative for harmonics of low degree, which means that their decay rate $-L'/L$ increases with z . To understand this, consider L_0 . Since it includes all light regardless of direction, its decay depends on absorption a , not scatter, and so $-L'/L = \langle a \sec\theta \rangle$, just the decay rate along each ray average over the radiance distribution. Near the surface, $\sec\theta = 1$ for incident light, but $\sec\theta < 0$ for backscatter, and so $-L'/L < a$. Deep in the medium, most of the light propagates in the forward hemisphere where $\sec\theta > 1$, and so $-L'/L > a$.

The final step is the transform in Eq. (4) that gives radiance $L(z,\theta)$. Results appear in Figs. 5 and 6. The former shows L versus α with discrete θ as parameter; the latter gives polar plots of L versus θ at discrete αz . The straight dashed lines in Fig. 5 show the absorption decay rate a for comparison. From 10° to 60° , the radiance decays slower than a because the central core of slightly scattered light feeds light into this angular range faster than angular scatter removes it. Figure 6 shows a poor result near $z = 0, \theta = 90^\circ$. The dashed line is an estimate of the correction. The use of only three annihilation operators did not produce enough harmonics of backscatter to follow the sharp discontinuity at 90° , and this glitch persists to some depth. Otherwise the results are quite good.

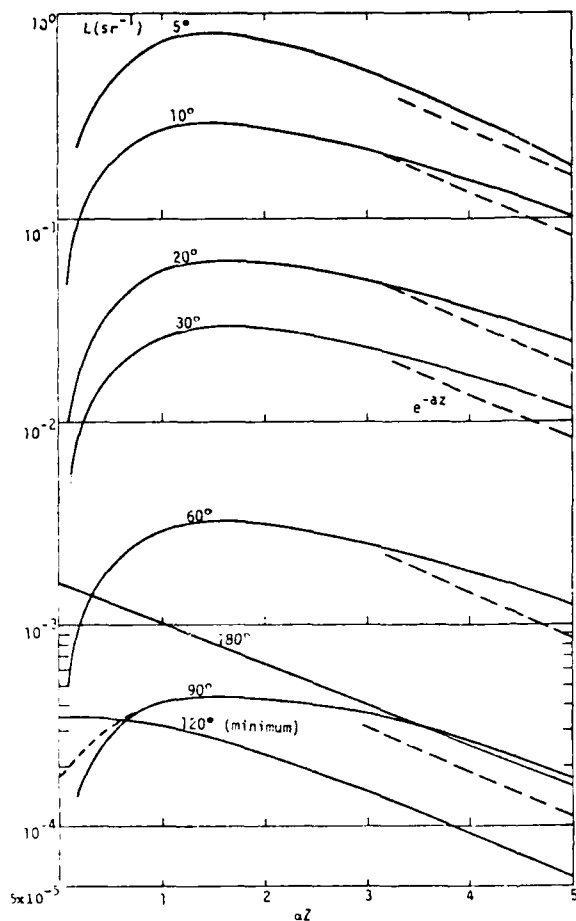


Fig. 5. Radiance as a Function of Penetration Depth

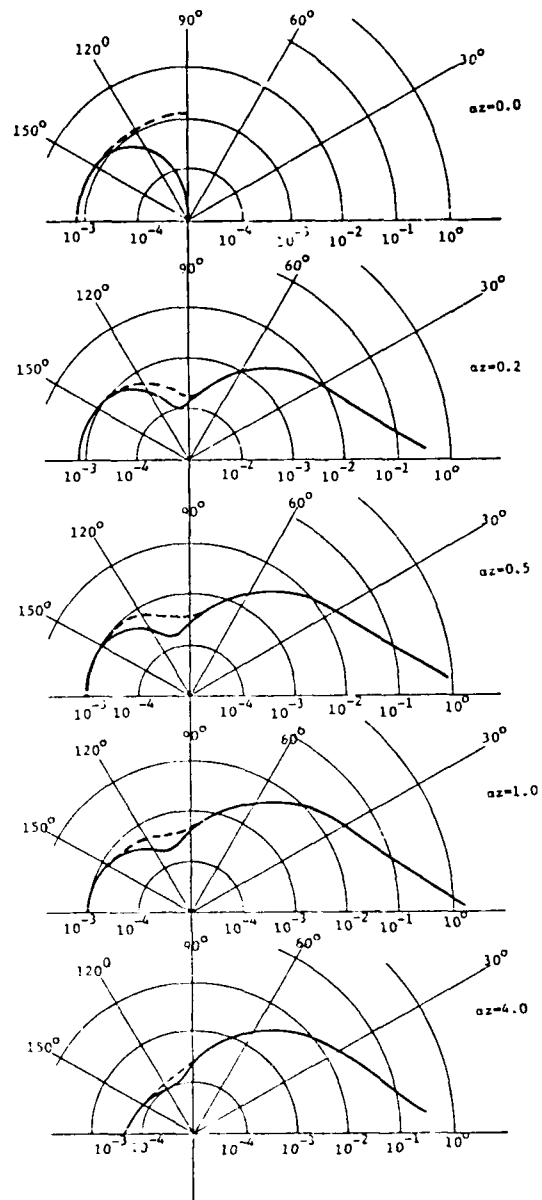


Fig. 6. Radiance as a Function of Observation Angle

The dashed curves in Fig. 6 and on the left of Fig. 5 show our best estimate of the correct radiance calculated for shallow penetration and extrapolated to greater depth. The approximations we made, especially limiting Eq. (16) to three operators, primarily affect the results for small z , and so we have compared to a quasi-single-scatter approximation that is valid only for shallow penetration. This theory by Jerlov [1968], as modified by Gordon [1973], uses a forward-scattering parameter that is (necessarily) defined imprecisely. Within this limitation, the results agree with ours except for the glitch near 90° .

ACKNOWLEDGEMENT

We gratefully acknowledge support by the Office of Naval Research, Code 480.

REFERENCES

1. L. Prieur and A. Morel, AGARD(NATO) Lecture Series #61, Lect. 1.3, 1.3-1-1.3-25, available from Report Distribution Unit, NASA Langley, VA. (1973).
2. B. Davison and J. B. Sykes, Neutron Transport Theory, Oxford, Clarendon Press, 1957.
3. M. C. Wang and E. Guth, "On the Theory of Multiple Scattering, Particularly of Charged Particles," Phys. Rev. 84, 1092-1111.
4. W. H. Wells, "Loss of Resolution in Water as a Result of Multiple Small-Angle Scattering," J. Opt. Soc. Am. 59, 686-691 (1969).
5. H. T. Yura, "Small-Angle Scattering of Light by Ocean Water," Appl. Opt. 10, 114-118 (1971).
6. D. Arnush, "Underwater Light-Beam Propagation in the Small-Angle-Scattering Approximation," J. Opt. Soc. Am. 62, 1109-1111 (1972).
7. N. G. Jerlov, Optical Oceanography, Elsevier, Amsterdam, 1968.
8. H. R. Gordon, "Simple Calculation of the Diffuse Reflectance of the Ocean," Appl. Opt. 12, 2803-2804 (Dec. 73).
9. W. H. Wells, J. Harris, H. C. Lin, "Multiple Scatter of Collimated Irradiance," to be published in J. Opt. Soc. Am. 71, March, 1981.

GREEN'S FUNCTION CALCULATION OF THE EFFECTS OF THE

AIR/WATER INTERFACE ON OPTICAL PROPAGATION

R. F. Lutomirski and D. E. Snead
Pacific-Sierra Research Corporation
1456 Cloverfield Boulevard
Santa Monica, California 90404

SUMMARY

A Green's function formulation has been developed for the propagation of radiance in forward scattering media. The method is used to compute the underwater downwelling radiance and irradiance distributions from a laser source impinging on the ocean surface from above. Calculating the second moment of the irradiance generates an analytic expression for the underwater scintillation in terms of the wave curvature statistics at the surface.

1. INTRODUCTION

The goal of our analysis is to derive approximate closed-form analytic expressions for the radiance distribution and the irradiance fluctuations over a plane at depth z beneath the water resulting from spatially coherent radiation (a laser beam or the sun) incident on the surface from above. The technique proposed is essentially a bookkeeping scheme that keeps track of the radiance as it propagates through the planes of interest. The propagations from the air/water interface down to depth are tracked by means of a Green's function.

The technique in principle allows calculation of the radiance distribution for an arbitrary specification of the wave slope as a function of position on the surface. Averaging over the slope distribution yields the long-term average radiance at depth; calculating the second moment of the irradiance generates an analytic expression for the scintillation in terms of the wave curvature statistics at the surface.

2. ANALYSIS

Figure 1 shows the principal planes at which the radiance is computed. The radiance just above the surface is represented as the product of two terms: an irradiance term I dependent on position in that plane $I(\mathbf{r}')$, and a ray term $R(\mathbf{k})$ dependent on the distribution of ray angles at that point. If the initial irradiance distribution is Gaussian over a plane inclined at angle θ_0 with respect to the zenith (the primed system), then we can represent the radiance f over a horizontal plane just above the surface by

$$f^+ = I^+ R^+ , \quad (1)$$

where

$$I^+(f, y) = \frac{1}{2\pi\sigma_s^2} \exp\left(-\frac{y^2 + x^2 \cos^2 \theta_0}{2\sigma_s^2}\right) \cos \theta_0 \quad (2)$$

and

$$R^+ = \delta(k_y) \delta(k_x - \sin \theta_0) . \quad (3)$$

In Eqs. (2) and (3), we use cartesian coordinates x, y, z , with z denoting depth in the water so k_y, k_x are the projections of unit vectors along the x and y directions, respectively; σ_s is the standard deviation of the Gaussian spot; and δ is the Dirac delta function.

If we use $\mathbf{N}(x, y)$ to denote the upward unit vector normal to the ocean surface at the point (x, y) , then in terms of the local slope components m_x, m_y , we have

$$\mathbf{N} = \frac{-m_x \mathbf{e}_x - m_y \mathbf{e}_y - \mathbf{e}_z}{(1 + m_x^2 + m_y^2)^{1/2}} . \quad (4)$$

Using Snell's law, it can be shown that the transformation of the below-surface values \mathbf{k} is given by

$$\mathbf{k} = n[\mathbf{k} - (\mathbf{N} \cdot \mathbf{k})\mathbf{N}] - n[(\mathbf{N} \cdot \mathbf{k})^2 - (1 - 1/n^2)]^{1/2} \mathbf{N} , \quad (5)$$

where $n = 4/3$. To first order in m_x, m_y , Eqs. (4) and (5) combine to yield

$$k_x = n(K_x - \mu m_x) , \quad (6a)$$

$$k_y = n(K_y - \mu m_y) . \quad (6b)$$

The term

$$\mu(\theta_0) = \sqrt{1 - (\sin \theta_0/n)^2} - (1/n) \cos \theta_0$$

is a downlink coupling factor plotted in Fig. 2. Note that $\mu(0^\circ) = 1/4$ is a reasonable approximation out to 20 deg.

The radiance just beneath the ocean surface is then

$$f^- = I^- R^-, \quad (7)$$

where

$$I^- = T_f(\theta_0) I^+ \quad (8)$$

(T_f being the Fresnel transmission coefficient) and

$$R^- = \delta(K_y - \mu m_y) \delta(K_x - \mu m_x - \sin \theta_0/n) \quad (9)$$

is the ray angle distribution at (x, y) . The slope components m_x, m_y will vary within position (x, y) on the surface. After the radiance just beneath the surface f^- is specified, the radiance over a plane at depth z beneath the surface may be calculated using the Green's function g , derived in the Appendix. The form of the Green's function, which allows us to compute the differential configuration from f^- to the radiance at a point (x, y) at depth z , (\underline{r}, z) , and ray direction \underline{K} , is shown in the Appendix to be

$$df_z(\underline{r}, \underline{K}) = f^-(\underline{r}', \underline{K}') g(\underline{r} - \underline{r}' - z\underline{K}', \underline{K} - \underline{K}') d^2\underline{r}' d^2\underline{K}', \quad (10)$$

and the total radiance of \underline{r}, z in the direction \underline{K} is shown to be

$$f_z(\underline{r}, \underline{K}) = \iint f^-(\underline{r}', \underline{K}') g(\underline{r} - \underline{r}' - z\underline{K}', \underline{K} - \underline{K}') d^2\underline{r}' d^2\underline{K}'. \quad (11)$$

The Appendix derives the relationship between the Green's function g , the diffuse attenuation coefficient and scattering coefficients, the range, and the volume scattering functions. Asymptotic forms are also presented there for certain regions of parameters--in particular, the extinct component--valid for short ranges; and for the multiply scattered component, valid only in an asymptotic sense of many scatterings.

In principle, Eq. (11) completes the solution to the downlink problem in the small-angle scattering approximation. The extent to which the magnitudes of the surface slope m_x, m_y are known, and vary with position x, y , can be inserted into Eq. (7) for f^- , and the extent to which the volume scattering functions of the water are known can be used to determine the Green's function g . The radiance ($W/m^2/sr$) at the point (\underline{r}, z) in the distribution \underline{K} can be found by integrating over all incident directions \underline{K}' and surface positions \underline{r}' . Further, the radiance (W/m^2) at the point (\underline{r}, z) can be found by integrating f_z over all \underline{K} . In particular, integrating both sides of Eq. (11) over \underline{K} yields

$$I_z(\underline{r}) = \int f_z(\underline{r}, \underline{K}) d^2\underline{K} = \iint f^-(\underline{r}', \underline{K}') G(\underline{r} - \underline{r}' - z\underline{K}') d^2\underline{r}' d^2\underline{K}', \quad (12)$$

where

$$G(\underline{r} - \underline{r}' - z\underline{K}') = \int g(\underline{r} - \underline{r}' - z\underline{K}', \underline{K} - \underline{K}') d^2\underline{K} \quad (13)$$

is a pseudo-Green's function that directly relates the irradiance at \underline{r}, z to the radiance $f^-(\underline{r}', \underline{K}')$ just beneath the surface at depth.

The advantage of this formulation, as in all Green's-function-type solutions, is the separation of the geometry of the problem (which is the spatial extent and form of the radiance distribution f^-) from the propagation problem (which is defined by either g or G , which in turn determines how elements of f^- contribute to the radiance or irradiance, respectively).

3. SLOPE-AVERAGED IRRADIANCE

All the slope variations in f^- appear only in the values for the radiance at the underside of the surface f^- and not in the Green's function g , which depends on the scattering properties of the water. Hence, we can propagate the slope-averaged radiance down to depths to obtain f_z using the same Green's function. Assuming a normal distribution for the water slopes,

$$p(m_x, m_y) = \frac{1}{2\pi\sigma_m^2} \exp\left(-\frac{m_x^2 + m_y^2}{2\sigma_m^2}\right), \quad (14)$$

where σ_m^2 is the slope variance, assumed equal in the x and y directions. Then

$$\bar{I}^- = \int \bar{I}^- R^- p(m_x, m_y) dm_x dm_y = T_f(\theta_0) I^+ \frac{1}{2\pi\mu^2\sigma_m^2} \exp \left[-\frac{(K_x - \sin \theta_0/n)^2 + K_y^2}{2\mu^2\sigma_m^2} \right] \quad (15)$$

is the slope-averaged radiance just beneath the surface. Convoluting with the Green's function and carrying out the integration yields approximate expressions for the slope-averaged underwater radiance and irradiance distributions.

The irradiance can be shown to be

$$\bar{I}_z(\underline{r}) = \frac{P_z}{2\pi A_x A_y} \exp \left(-\frac{(x - x_1)^2}{2A_x^2} - \frac{y^2}{2A_y^2} \right), \quad (16)$$

where

$$\frac{P_z}{P} = \frac{T_f(\theta_0) \exp(-\kappa z \sec \theta_1)}{1 + \kappa z \phi^2} \quad (17)$$

is the total power reaching depth z . In Eq. (17), $\theta_1 = \sin^{-1}(\sin \theta_0/n)$ is the refracted angle, κ is the diffuse attenuation coefficient, and

$$\phi^2 = (\mu\sigma_m)^2 + sz\theta_R^2/6, \quad (18)$$

where s is the scattering coefficient and θ_R is the RMS single scattering angle. Then the spatial variance of the irradiance distribution

$$A_x^2 = \sigma_s \sec^2 \theta_0 + \frac{(z \sec \theta_1)^2 \phi^2}{1 + \kappa z \sec \theta_1 \phi^2}, \quad A_y = A_x \text{ with } \theta_1 = 0, \quad (19)$$

and

$$x_1 = \frac{z_1 \sin \theta_1}{1 + \kappa z \phi^2}. \quad (20)$$

Analogous expressions can be derived for the slope-averaged ray direction distribution. These are also algebraic and in closed form, but are rather lengthy and beyond the scope of this paper.

Figures 3 through 5 plot iso-irradiance contours resulting from a Gaussian beam of $\sigma_s = 2$ m inclined at an angle of 30 deg (in air) at the air/water interface. In Fig. 3, the incident angle is 30 deg and the contours are 10 dB apart, with the irradiance increasing as one approaches the surface. The results are normalized to 1 W (CW) incident on the ocean surface. Figure 4 plots the variation of the $I = 10^{-5}$ W/m² contour with incident angle θ_0 . For $\theta_0 = 30$ deg, Fig. 5 plots the variation of the $I = 10^{-4}$ W/m² contour with RMS slope variation $\sigma_{x,y}$. It should be emphasized that, owing to the asymptotic form of the Green's function used in the calculation, these results hold only in the limit of many scatterings.

4. IRRADIANCE FLUCTUATIONS DUE TO AIR/WATER INTERFACE

Wave curvature can produce speckle patterns--such as observed on the bottom of swimming pools--by focusing and defocusing the incident radiation. Over the relatively shallow depths in which this phenomenon is observed, one can use the extinction form of the Green's function given in Eq. (A.10b). Substituting that expression into Eq. (13) yields, for the pseudo-Green's function,

$$G(\underline{r} - \underline{r}' - z\underline{K}') = e^{-\alpha z} \int \delta^2[\underline{r} - \underline{r}' - z\underline{K}' - z(\underline{K} - \underline{K}')] \delta^2(\underline{K} - \underline{K}') d^2\underline{K} = e^{-\alpha z} \delta^2(\underline{r} - \underline{r}' - z\underline{K}'), \quad (21)$$

where $\alpha = a + s$ is the extinction coefficient (a being the absorption coefficient). This equation simply restricts the radiance to propagate along straight lines. For the following example, we assume solar illumination with $I^+ = \text{constant}$ and vertical incidence ($\theta_0 = 0$). Then Eq. (21) implies

$$\begin{aligned} I_z(\underline{r}) &= I^+ T_f(\theta_0) e^{-\alpha z} \iint dx' dK'_x \delta[K'_x - \mu m_x(x')] \delta(x - x' - zK'_x) \\ &\quad \times \iint dy' dK'_y \delta[K'_y - \mu m_y(y')] \delta(y - y' - zK'_y) \\ &= I^+ T_f(\theta_0) e^{-\alpha z} \int \delta[x - x' - \mu z m_x(x')] dx' \int \delta[y - y' - \mu z m_y(y')] dy'. \end{aligned} \quad (22)$$

For small curvatures, the δ function integrals can be evaluated to yield

$$I_z = I^+ T_f(\theta_0) e^{-\alpha z} \frac{1}{1 + \mu z m_x^2} \frac{1}{1 + \mu z m_y^2}, \quad (23)$$

where the curvatures m'_x, m'_y are evaluated just above the observation points. For $\mu z m'_x, \mu z m'_y \ll 1$,

$$I_z = I^+ T_f(\theta_0) e^{-\alpha z} [1 - \mu z(m'_x + m'_y)] . \quad (24)$$

Hence, we have

$$\delta I_z(x, y) = -I^+ T_f(\theta_0) e^{-\alpha z} \mu z(m'_x + m'_y) . \quad (25)$$

If we assume the x and y curvatures to be uncorrelated, then the variance of the irradiance fluctuations at a point is given by

$$\overline{(\delta I_z)^2} = [I^+ T_f(\theta_0)]^2 e^{-2\alpha z} (\mu z)^2 \left[\overline{(m'_x)^2} + \overline{(m'_y)^2} \right] . \quad (26)$$

Now the average irradiance decays as the diffuse attenuation coefficient κ . Hence, the normalized standard deviation of the fluctuations is

$$\frac{\sigma_I}{I_z} = \frac{\left[\overline{(\delta I_z)^2} \right]^{1/2}}{I_z} = \frac{e^{-\alpha z}}{e^{-\kappa z}} \left(\sigma_{c_x}^2 + \sigma_{c_y}^2 \right)^{1/2} , \quad (27)$$

where

$$\sigma_{c_x}^2 = \overline{(m'_x)^2} \quad \text{and} \quad \sigma_{c_y}^2 = \overline{(m'_y)^2}$$

are the variances of the component curvatures of the waves.

It follows from Eq. (25) that, for uncorrelated slopes,

$$R_I(x_1 - x_2) = \frac{\overline{\delta I_z(x_1) \delta I_z(x_2)}}{\overline{\delta I_z^2}} = R_m(x_1 - x_2) . \quad (28)$$

Hence, the correlation function of the underwater speckle pattern is equal to the correlation function of the wave curvature. Both the speckle pattern and the normalized standard deviation decay exponentially with depth, as $\exp[-(\alpha - \kappa)z]$.

APPENDIX

GREEN'S FUNCTION FOR MULTIPLE SCATTERING

The present model is based on finding the Green's function $g(\underline{r}, z, \underline{K}, \underline{r}', 0, \underline{K}')$ for the radiance existing at the point \underline{r}, z (where \underline{r} is transverse to z) and arriving in the (transverse) direction \underline{K} because a point source at $(\underline{r}', 0)$ is emitting flux in the direction \underline{K}' .

In the small-angle scattering approximation, and neglecting absorption in the medium, the equation for the transport of radiance f is

$$\left(\frac{\partial}{\partial z} + \underline{K} \cdot \frac{\partial}{\partial \underline{r}} \right) f = -\alpha f + s \int d^2 \underline{K}' S(\underline{K} - \underline{K}') f(\underline{r}', z, \underline{K}') , \quad (A.1)$$

subject to the specification of f on the plane $z = 0$: $f_0(\underline{r}, \underline{K}) \equiv f(\underline{r}, 0, \underline{K})$. In Eq. (A.1), $\alpha = a + s$ is the extinction coefficient (where a is the absorption coefficient), s is the scattering coefficient, and S is the volume scattering function.

The complete solution is then given by Eq. (9) of Arnush [1972]:

$$f(\underline{r}, z, \underline{K}) = (2\pi)^4 \iint d^2 \underline{Y} d^2 \underline{\beta} e^{i(\underline{Y} \cdot \underline{r} + \underline{\beta} \cdot \underline{K})} F_0(\underline{Y}, \underline{\beta} + z\underline{Y}) G(\underline{Y}, \underline{\beta}) , \quad (A.2)$$

where

$$F_0(\underline{Y}, \underline{\beta}) = \iint d^2 \underline{r} d^2 \underline{K} e^{-i(\underline{Y} \cdot \underline{r} + \underline{\beta} \cdot \underline{K})} F_0(\underline{r}, \underline{K}) , \quad (A.3)$$

$$G(\underline{Y}, \underline{\beta}) = \exp \left[-\alpha z + s \int_0^z d\xi Q(\underline{\beta} + \xi \underline{Y}) \right] = \exp \left[-\alpha z + s z \int_0^1 du Q(\underline{\beta} + u z \underline{Y}) \right] , \quad (A.4)$$

and

$$Q(\underline{\beta}) = \int S(\underline{K}) e^{-i\underline{\beta} \cdot \underline{K}} d^2\underline{K} = 2\pi \int S(K) J_0(\beta K) K dK \quad (A.5)$$

is the Fourier transform of the scattering function.

If we define

$$g(\underline{r}, \underline{K}) = \frac{1}{(2\pi)^2} \iint G(\underline{\gamma}, \underline{\beta}) e^{-i(\underline{\gamma} \cdot \underline{r} + \underline{\beta} \cdot \underline{K})} d^2\underline{\gamma} d^2\underline{\beta}, \quad (A.6)$$

then substituting Eqs. (A.3) and (A.6) into Eq. (A.2) and inverting the order of integration yields

$$f(\underline{r}, z, \underline{K}) = \iint f_0(\underline{r}', \underline{K}') g(\underline{r} - \underline{r}' - z\underline{K}', \underline{K} - \underline{K}') d^2\underline{r}' d^2\underline{K}', \quad (A.7)$$

which is the Green's function solution of the problem.

In the general case, the prescription for computing the Green's function g is to

1. Find the Fourier transform of the volume scattering function [Eq. (A.5)].
2. Integrate and exponentiate the Fourier transform [Eq. (A.4)].
3. Find the inverse transform [Eq. (A.6)].

To obtain approximate expressions for g , we observe from Eq. (A.4) that, because $Q(0) = 1$, $G(0, 0) = 1$, and $J_0(\infty) = 0$, then $Q(\infty) = 0$ and $G(\infty, \underline{\beta}) = G(\underline{\gamma}, \infty) = e^{-sz}$. The behavior of $G(\underline{\gamma}, \underline{\beta})$ about $g(0, 0)$ is obtained by expanding the Bessel function in Eq. (A.5):

$$Q(\underline{\beta}) = \int_0^\infty dK 2\pi K S(K) \left(1 - \frac{\beta^2 K^2}{4} + \dots \right) = 1 - \frac{\beta^2 \theta_R^2}{4} + \dots, \quad \text{for } \beta \theta_R \ll 1, \quad (A.8a)$$

where

$$\theta_R^2 = \int_0^\infty S(K) 2\pi K^3 dK, \quad \left(\int_0^\infty S(K) 2\pi K dK = 1 \right) \quad (A.8b)$$

is the mean square scattering angle and $\theta_R = (K^2)^{1/2}$ is the RMS scattering angle. These expressions become clear if we recognize that $2\pi K dK$ is the small-angle approximation to $2\pi \sin \theta d\theta$.

Substituting Eq. (A.8) into Eq. (A.4), we obtain in the limit of many scatterings ($sz \gg 1$)

$$G_1(\underline{\gamma}, \underline{\beta}) = \exp \left\{ -\frac{-az - sz\theta_R^2}{4} \left[(\beta^2 + z\underline{\beta} \cdot \underline{\gamma} + z^2 \underline{\gamma}^2/3) \right] \right\}, \quad \begin{array}{l} \beta \ll (\theta_R \sqrt{sz})^{-1} \\ \underline{\gamma} \ll (\theta_R z \sqrt{sz})^{-1} \end{array} \quad (A.9a)$$

$$G_2 = e^{-\alpha z}, \quad \text{otherwise.} \quad (A.9b)$$

Then, substituting Eq. (A.9) into Eq. (A.6), the Green's function becomes

$$g(\underline{\theta}, \underline{r}) = \frac{12 e^{-\alpha z}}{\pi^2 s^2 z^2 \theta_R^4} \exp \left\{ -\frac{4}{sz\theta_R^2} \left[(K - 3\underline{r}/2z)^2 + 3\underline{r}^2/z^2 \right] \right\}, \quad \begin{array}{l} K \gg \theta_R \sqrt{sz} \\ \underline{r} \gg \theta_R z \sqrt{sz} \end{array} \quad (A.10a)$$

$$= e^{-\alpha z} \delta^2(\underline{r} - z\underline{K}) \delta^2(\underline{K}), \quad \text{otherwise.} \quad (A.10b)$$

Equation (A.10a) propagates the multiply scattered wave (in the limit of many scatterings), and Eq. (A.10b) propagates the extinct component of the irradiance, both for a source with $\underline{r}' = 0$, $\underline{K}' = 0$.

In addition to the small-angle scattering, there will be absorption and large-angle scattering. The portion of the volume scattering function corresponding to angles greater than 90 deg will contribute very little to the flux in the forward direction, and thus appears much like an effective absorption coefficient for propagation in the forward direction. It is customary to incorporate both effects into a diffuse attenuation coefficient (called κ in our analysis). Experiments suggest that κ can frequently be approximated by the sum of the absorption coefficient and one-sixth of the scattering coefficient.

The portion of the volume scattering function that is less than 90 deg, but greater than, say, 30 deg (where the small-angle absorptions we have used break down), cannot really be treated by the methods outlined above; so the full expression of Eq. (A.5) must be used.

REFERENCE

ARNUSH, D., September 1972, *J. Opt. Soc. Am.*, Vol. 62, No. 9, p. 1109.

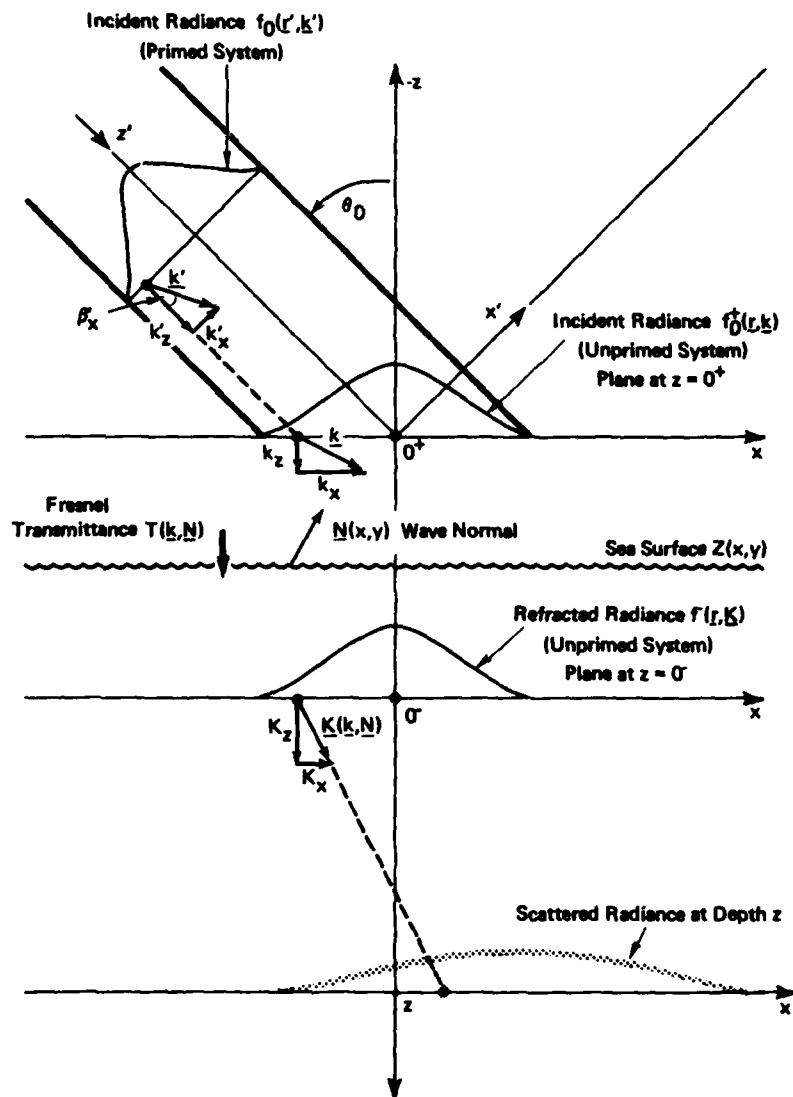


Fig. 1—Principal planes at which radiance is computed

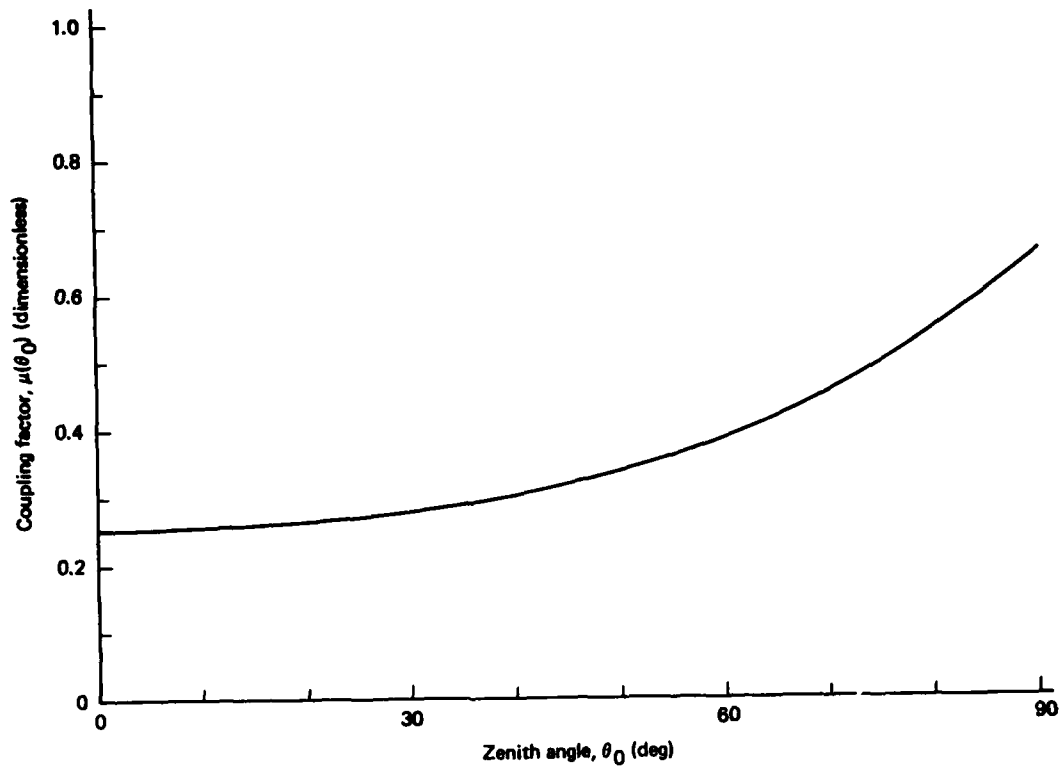


Fig. 2—Downlink coupling factor between ray vector and wave slope

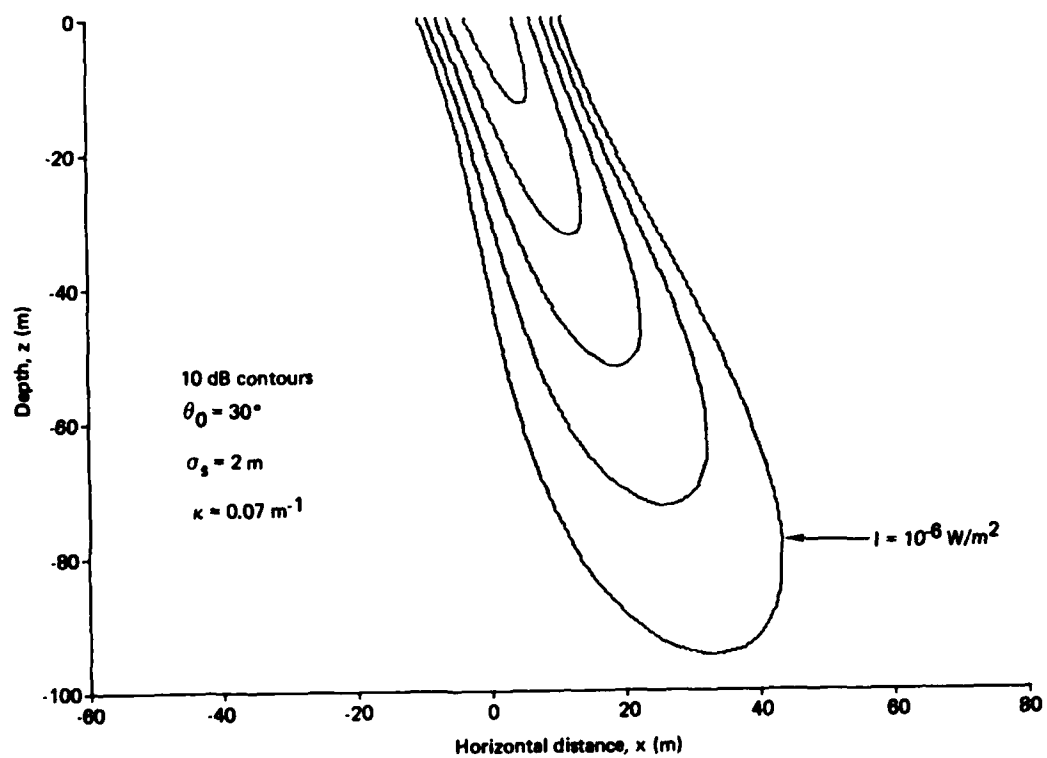


Fig. 3—Iso-irradiance contours in the plane of incidence

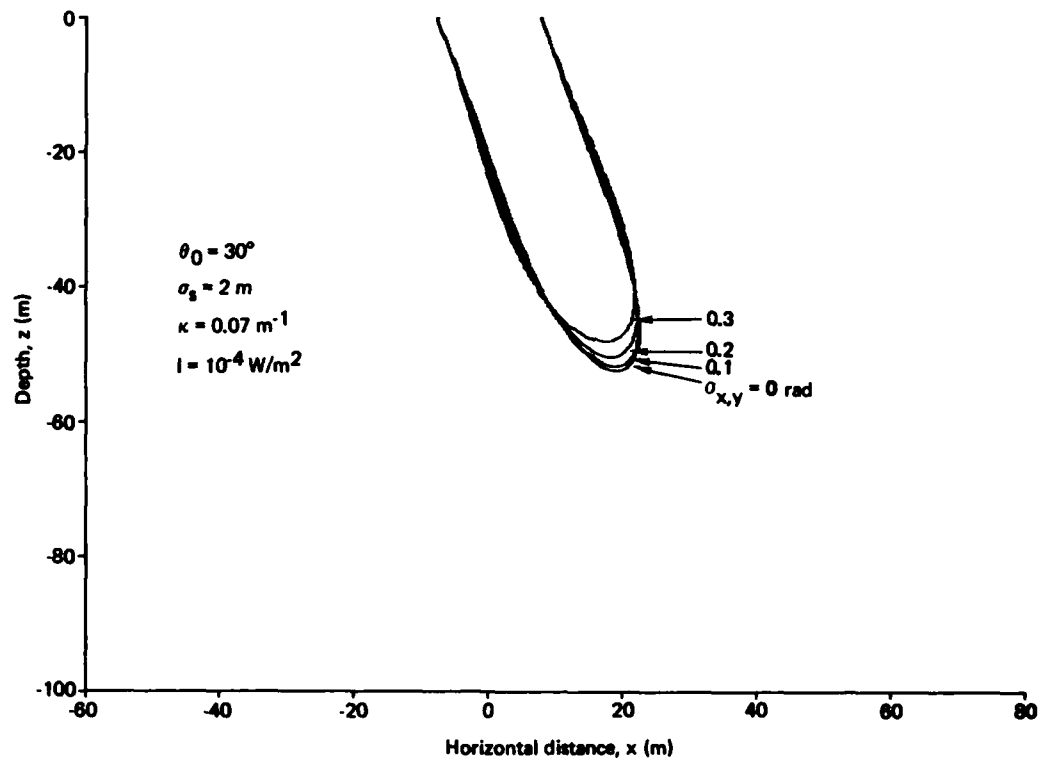


Fig. 4—Sensitivity of iso-irradiance contours to incident angle

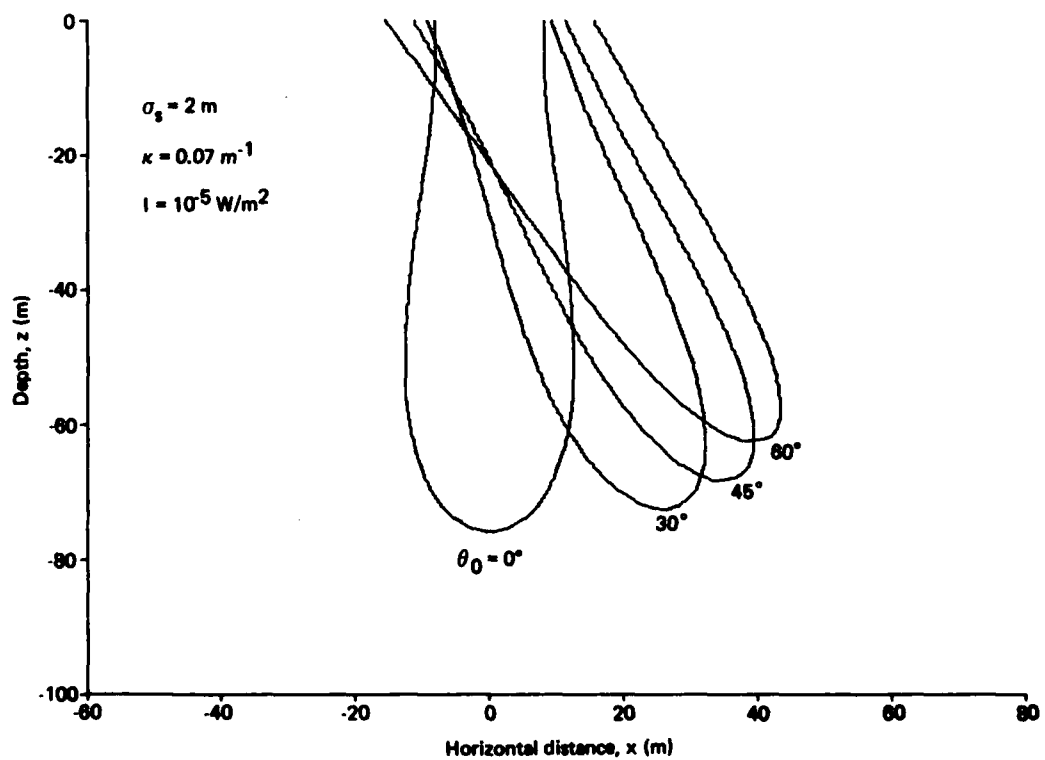


Fig. 5—Sensitivity of iso-irradiance contours to sea slope

MULTIPLE SCATTERING EFFECTS ON OPTICAL PROPAGATION
IN TURBULENCE AND PARTICLES

Akira Ishimaru
Department of Electrical Engineering
University of Washington
Seattle, Washington 98195
U.S.A.

SUMMARY

In recent years, there has been considerable interest in the study of the propagation and scattering characteristics of optical beams in fog and clouds. In contrast with the turbulence, the droplet sizes of fog and clouds are comparable to a wavelength and the scattering is spread over wide angles. Therefore, the wave transmission and scattering exhibit different characteristics depending upon whether the particle sizes are smaller or larger than a wavelength. This paper discusses the following three solutions and their limitations. The forward scatter approximation is used for large particles, while the diffusion approximation is used for small particles. The radiative transfer can be used for all sizes. However, solutions are available only for special wave types and medium geometries.

1. INTRODUCTION

The propagation of optical beams in the turbulent atmosphere has been studied extensively in the past and theoretical expressions for wave fluctuations, beam broadening, angular spectra, and pulse broadening have been obtained. Since the turbulent eddy sizes are much greater than an optical wavelength, all scattering takes place within a narrow forward angle and the angular broadening is very small. For this reason, the forward scatter theory has been extensively used in the study of optical propagation in turbulence. There have also been numerous experimental studies on the optical propagation in the turbulence and the results show good agreement with theoretical predictions. A short summary of these results is given in [Ishimaru, 1981]. For the detailed account of this aspect of optical propagation, the readers are referred to extensive literatures [Ishimaru, 1977, 1978a; Strohbehn, 1977; Tatarski, 1961, 1971; Uscinski, 1977; Fante, 1975, 1980; Barabanenkov et al., 1971; Prokhorov et al., 1975].

In recent years, there has been considerable interest in the study of optical beam propagation in fog and clouds [Mooradian et al., 1979, 1980; Stotts, 1977, 1978; Danielson and Moore, 1969; Furutsu, 1980; Ito and Furutsu, 1980; Bucher, 1973]. A major difference between this problem and the propagation in the turbulence is that while the turbulence scale sizes are much greater than an optical wavelength, the particle sizes are often comparable with a wavelength and the scattering is not always confined within a narrow forward angle. We discuss three theories applicable to optical propagation in fog: the forward scatter theory, the diffusion theory, and the radiative transfer theory. The range of validity of each theory is discussed together with their limitations.

2. OVERVIEW OF OPTICAL PROPAGATION IN FOG

Fog droplets are water or ice particles with size distribution which is usually within 100 μm [Wells et al. 1977; Mooradian et al., 1979]. The number density ρ may be typically 10^8 m^{-3} (100 cm^{-3}) and may vary from $10^6 \sim 10^9 \text{ m}^{-3}$ ($1 \sim 1000 \text{ cm}^{-3}$). Maritime fog reported by Wells et al., [1977] has the number density $\rho = 0.975 \times 10^6 \text{ m}^{-3}$ at wind velocity $V = 1 \text{ m/s}$. The fog in the vicinity of Point Loma reported by Mooradian et al., [1979] has the density $\rho = 0.53 \times 10^9 \text{ m}^{-3}$. The refractive indices of water at 20°C are shown in Table I [Ray, 1972] and the scattering γ_s , absorption γ_a , and extinction coefficients γ_t as functions of wavelength are plotted in Figures 1 and 2. They are defined as follows:

$$\gamma_s = \int_0^\infty \sigma_s(D)n(D)dD \quad \gamma_a = \int_0^\infty \sigma_a(D)n(D)dD \quad \gamma_t = \gamma_s + \gamma_a \quad (1)$$

where $n(D)dD$ is the number of particles with sizes between D and $D + dD$, and $\sigma_s(D)$ and $\sigma_a(D)$ are the scattering and absorption cross-sections of a single particle respectively. Note that for $\lambda < 10 \mu\text{m}$, the scattering is dominant, while for $\lambda > 10 \mu\text{m}$ the absorption becomes more important. Figures 3 and 4 show the scattering patterns $|S_1|^2$ and $|S_2|^2$ of fog with size distributions reported by Mooradian et al., [1979] where S_1 and S_2 are the scattering amplitudes defined by Van de Hulst, [1957]. Note that at $\lambda = 0.5 \mu\text{m}$, the scattering pattern has a sharp forward peak while at $\lambda = 15 \mu\text{m}$, it exhibits a slow variation. In view of these scattering patterns, we consider general characteristics of the optical scattering in fog in terms of the forward scatter and the diffusion phenomena. At $\lambda = 0.5 \mu\text{m}$, the particle sizes are large compared with a wavelength and the scattering pattern is peaked in the forward direction and the forward scatter theory similar to that used for the turbulence may be applicable. This is the case of optical beam with blue-green wavelengths propagating in fog and clouds. Unlike the turbulence case, however, the angular spread is not negligibly small and the effects of field-of-view of the receiver should be taken into account. At $\lambda = 15 \mu\text{m}$, the particle sizes are small compared with a wavelength and the angular spread of the incoherent intensity becomes broad. This is also characteristic of the diffusion phenomena to be discussed later and therefore, it is expected that the diffusion phenomena dominate for the case of small particles. We will discuss these two cases in more detail in the following sections. Completely general formulations for particulate scattering are not available today. However, the radiative transfer theory is considered as being closest to this general formulation, and we discuss this approach in later sections.

3. FORWARD SCATTER THEORY

At visible wavelengths, the scattering takes place mostly in the forward direction and therefore,

the forward scatter theory developed for turbulence is applicable. However, the angular spread is still not as small as in the turbulence case and therefore, approximations valid for turbulence may not be used for particulate scattering.

Let us first consider a collimated beam propagating in fog (Figure 5). Following the analysis given by Ishimaru, [1978a, p. 419], the power received by a receiver located on the beam axis and with the receiving pattern of $\exp[-\theta^2/\theta_r^2]$ is given by

$$I(L) = \int \Gamma(L, \bar{\theta}) \exp\left[-\frac{\theta^2}{\theta_r^2}\right] d\bar{\theta} \quad (2)$$

$$\Gamma(L, \bar{\theta}) = \frac{k^2}{(2\pi)^2} \int \Gamma(L, \bar{\rho}_d) \exp(-ik\bar{\rho}_d \cdot \bar{\theta}) d\bar{\rho}_d$$

where $\Gamma(L, \bar{\rho}_d)$ is the mutual coherence function at two points separated by $\bar{\rho}_d$ and at the distance L from the transmitter. (See Figure 5.)

We, therefore, obtain

$$I(L) = \frac{k^2 \theta_r^2}{4\pi} \int \Gamma(L, \bar{\rho}_d) \exp\left[-\frac{(k\rho_d)^2 \theta_r^2}{4}\right] d\bar{\rho}_d$$

$$\Gamma(L, \bar{\rho}_d) = \frac{W_0^2}{8\pi} \int d\bar{\kappa} \exp[-a\rho_d^2 - b\kappa^2 + c\bar{\rho}_d \cdot \bar{\kappa} - H] \quad (3)$$

where

$$a = \frac{1}{2W_0^2}, \quad b = \frac{W_0^2}{8} \left[1 + \left(\frac{2L}{kW_0^2}\right)^2\right], \quad c = \frac{L}{kW_0^2}$$

$$H = \gamma_a L + \frac{\gamma_s \int_0^L dx K(x, \bar{\rho}_d, \bar{\kappa})}{\int_0^2 \beta(s) s ds}$$

$$K(x, \bar{\rho}_d, \bar{\kappa}) = \int_0^2 \beta(s) [1 - J_0(ks|\bar{\rho}_d + \frac{\bar{\kappa}x}{k}|)] s ds$$

$$\beta(s) = \text{scattering pattern}, \quad s = 2 \sin \frac{\theta}{2}$$

For turbulence, it is possible to approximately evaluate the integral for K since the scattering pattern $\beta(s)$ is limited within a small range of the angle θ . This is not the case for particulate scattering and some comparisons with experimental data show that more exact numerical evaluation of the integral gives a good agreement and the approximations used for turbulence fail to agree with experimental data.

The scattering pattern $\beta(s)$ may be well approximated by the Henyey-Greenstein formula:

$$\beta(s) = \frac{\beta(0)}{[1 + (\frac{s}{s_0})^2]^{3/2}} \quad (4)$$

$$\beta(0) = \frac{\gamma_s}{s_0^2} \left[1 - \left(1 + \frac{4}{s_0^2}\right)^{-1/2}\right]^{-1}$$

For diffusion approximation to be discussed later, the constant s_0 is related to the mean cosine $\bar{\mu}$ of the scattering pattern by the following:

$$s_0^2 = \frac{(1-\bar{\mu})^2}{\bar{\mu}} \quad (5)$$

However, for the forward scatter theory, Equation (5) is not appropriate. It should be related to the scattering pattern of large particles.

$$f(\theta) = \left[\frac{ia}{\sin \theta}\right] J_1(ka \sin \theta) \quad (6)$$

where $D = 2a$ is the diameter of the particle. Comparing (6) with (4), we get approximately:

$$s_0^2 = 2 \left(1 - \left[1 - \left(\frac{1.95}{ka}\right)^2\right]^{1/2}\right) \quad (7)$$

Even though the evaluation of (3) was made numerically giving a good agreement, it is convenient to obtain an approximate solution to (3). For $s_0 \ll 1$ and the following scattering pattern

$$\beta(s) = \frac{\beta(0)}{\left[1 + \left(\frac{s}{s_0}\right)^2\right]^{n/2}} \quad (8)$$

We get the following approximation for H

$$H = \gamma_a L + \gamma_s \int_0^L dx M(x, \bar{\rho}_d, \bar{\kappa}) \quad (9)$$

$$M = - \frac{(n-2)\pi \left[ks_0 \left|\bar{\rho}_d + \frac{\bar{\kappa}x}{k}\right|\right]^{n-2}}{\sin\left(\frac{n\pi}{2}\right) \left[\Gamma\left(\frac{n}{2}\right)\right]^2 2^{n-1}}, \quad 2 < n < 4$$

For Henyey-Greenstein formula, $n = 3$ and M becomes

$$M = \frac{ks_0}{2} \left|\bar{\rho}_d + \frac{\bar{\kappa}x}{k}\right| \quad (10)$$

If $\beta(s)$ is approximated by Gaussian function,

$$\beta(s) = \beta(0) \exp\left(-\frac{s^2}{s_0^2}\right), \quad (11)$$

we get

$$M = \left(\frac{ks_0}{2}\right)^2 \left|\bar{\rho}_d + \frac{\bar{\kappa}x}{k}\right|^2 \quad (12)$$

An analytical solution for $I(L)$ can be obtained using the approximation (12), though these tend to underestimate the total received power. Using (12), we can evaluate (3) and obtain the following:

$$I(L) = F(L, \gamma_s=0) \exp(-\gamma_s L) + F(L, \gamma_s \neq 0) [1 - \exp(-\gamma_s L)] \exp(-\gamma_a L)$$

$$F(L, \gamma_s) = \frac{[\theta_t^2 / (16\theta_t^2)]}{A [B - (C^2/4A)]} \quad (13)$$

where θ_t is the transmitter beamwidth given by $\theta_t^2 = 2/(kW_0)^2$, and $A = k^2 \left[\frac{\theta_t^2}{4} + \frac{\theta_r^2}{4} + \gamma_s L \left(\frac{s_0}{2}\right)^2\right]$,

$$B = \frac{W_0^2}{8} + \frac{\theta_t^2 L^2}{4} + \gamma_s L \left(\frac{s_0}{2}\right)^2 \frac{L^2}{3}, \quad C = (kL) \left[\frac{\theta_t^2}{2} + \gamma_s L \left(\frac{s_0}{2}\right)^2\right].$$

There are some definite limitations on the use of the forward scatter model. In the forward scatter theory, the scattering must be confined within a small forward angle and the backscattering must be negligibly small. This is true only for particles whose sizes are large compared with a wavelength and for a relatively short distance where the large angle scattering is not taking place. The angular spread θ_c is generally given by

$$\theta_c = s_0 \quad \text{if } \tau_s < 1, \quad \text{and} \quad \theta_c = s_0 (\tau_s)^{1/(n-2)} \quad \text{if } \tau_s > 1 \quad (14)$$

Therefore, if $\tau_s > 1$, for the Henyey-Greenstein scattering pattern,

$$\theta_s = s_0 \tau_s \quad (15)$$

and for the Gaussian pattern

$$\theta_s = s_0 \tau_s^{1/2} \quad (16)$$

In general, $\theta_s = s_0 \tau_s^p$ where $1 > p > \frac{1}{2}$. Equation (15) appears to be more reasonable in many practical cases than (16). Equation (15) also shows that since the angular spread θ_c cannot be too large, the forward scatter theory is applicable only within the optical distance limited by

$$\tau_s \ll \frac{1}{s_0^q}, \quad 1 < q < 2 \quad (17)$$

The pulse broadening is generally given by

$$\frac{T_c}{(L/C)} = \frac{\theta_c^2}{8} = \frac{s_0^2}{8}, \quad \text{if } \tau_s < 1 \quad \text{and} \quad \frac{T_c}{(L/C)} = \frac{\theta_c^2}{8} = \frac{s_0^2 (\tau_s)^{2/(n-2)}}{8}, \quad \text{if } \tau_s > 1. \quad (18)$$

For the Henyey-Greenstein case, this becomes

$$\frac{T_c}{(L/C)} = \frac{s_0^2 \tau_s^2}{8}, \quad \tau_s > 1 \quad (19)$$

and for the Gaussian pattern, it is

$$\frac{T_c}{(L/C)} = \frac{s_0^2 \tau_s}{8}, \quad \tau_s > 1. \quad (20)$$

In general,

$$\frac{T_c}{(L/C)} = \frac{s_0^2 \tau_s^{2p}}{8}, \quad 2 > 2p > 1. \quad (21)$$

The angular spread θ_c and the pulse broadening $T/(L/C)$ are sketched in Figures 6 and 7. Note that for fog particles at $\lambda = 0.5 \mu\text{m}$, $ka \approx 20\pi$ and $s_0 \approx 3 \times 10^{-2}$ from (7). Therefore, $\tau_s \ll (33)^q$, $1 < q < 2$ which covers most distances of practical interest in optical propagation in fog.

4. DIFFUSION THEORY

As noted in Figure 6, the diffusion may be dominant if the particle sizes are small compared with a wavelength even at a short optical distance. If the particle sizes are large compared with a wavelength, the diffusion takes place at a relatively large distance. It should also be noted that the more scattering ($\gamma_s > \gamma_a$), the more predominant the diffusion becomes.

A diffusion theory was proposed by Ishimaru, [1978b] to explain the behavior of a short pulse. This will be outlined in this section. Furutsu and Ito, [1980] also proposed a slightly different diffusion theory.

The propagation characteristics of the wave in a random distribution of scatterers can be described by the equation of transfer [Ishimaru, 1978a].

$$\frac{d}{ds} I = -\gamma_t I + \frac{\gamma_t}{4\pi} \int p I' d\Omega' \quad (22)$$

where $I(\vec{r}, \hat{s})$ is the specific intensity and is approximately related to the mutual coherence function $\Gamma(\vec{r}_1, \vec{r}_2)$

$$I(\vec{r}, \hat{s}) = \int \Gamma(\vec{r}_1, \vec{r}_2) \exp(i\vec{k}\hat{s} \cdot \vec{r}_d) d\vec{r}_d \quad \Gamma(\vec{r}_1, \vec{r}_2) = \langle u(\vec{r}_1) u^*(\vec{r}_2) \rangle \quad \vec{r} = (1/2)(\vec{r}_1 + \vec{r}_2) \quad \text{and} \quad \vec{r}_d = \vec{r}_1 - \vec{r}_2 \quad (23)$$

and $U(\vec{r}_1)$ is the field at \vec{r}_1 .

The specific intensity $I(\vec{r}, \hat{s})$ may be expressed as a sum of the coherent and incoherent intensities.

$$I = I_c(\text{coherent}) + I_d(\text{incoherent}) \quad (24)$$

In discrete scatterers, the incoherent (or diffuse) intensity I_d tends to be spread out in all angles and therefore, it is appropriate to expand I_d in a series of Legendre functions:

$$I_d = \sum_{n=0}^{\infty} U_n(\vec{r}) P_n(\cos \theta) \quad (25)$$

where θ is the angle between \hat{s} and the direction of the flux vector \vec{F}_d . The first two terms of (25) constitutes the diffusion approximation:

$$I_d = U_d + \frac{3}{4\pi} \vec{F}_d \cdot \hat{s} \quad (26)$$

where U_d is the average diffuse intensity given by

$$U_d = \frac{1}{4\pi} \int I_d d\Omega \quad (27)$$

The differential equation satisfied by U_d has been obtained [Ishimaru, 1978a,b]

$$[\nabla^2 - 3\gamma_{tr}\gamma_a]U_d = -Q_0 \quad Q_0 = \frac{3\gamma_s}{4\pi} [\gamma_{tr} + \bar{\mu}\gamma_t]F_i \quad (28)$$

where F_i is the incident coherent intensity and the mean cosine of the scattering pattern $\bar{\mu}$ and the transport coefficient γ_{tr} are defined by

$$\bar{\mu} = \frac{\int p(\theta) \cos \theta d\Omega}{\int p(\theta) d\Omega} \quad \gamma_{tr} = \gamma_s(1 - \bar{\mu}) + \gamma_a \quad (29)$$

Note also the optical distance τ and the scattering distance τ_s .

$$\tau = \gamma_t L \quad \text{and} \quad \tau_s = \gamma_s L \quad (30)$$

In the above, we approximated the scattering pattern by a scalar function $p(\theta)$. The more complete representation of the scattering pattern including the polarization effect requires the use of Stokes' parameters and matrix formulations.

For the pulse propagation problem, the output pulse power $P(t)$ is given by the Fourier integral:

$$P(t) = \frac{1}{2\pi} \int_{-\infty}^{\infty} P(\omega) e^{-i\omega t} d\omega \quad (31)$$

where $P(\omega)$ is the frequency spectrum. The received power $P_R(\omega)$ consists of the coherent power $P_C(\omega)$ and the incoherent power $P_I(\omega)$. The incoherent power in the diffusion approximation is given in terms of the spectrum of the average intensity U_d which satisfies the following equation:

$$[\nu^2 - 3\alpha_{tr}\alpha_a]U_d = -Q_0 \quad Q_0 = \frac{3\gamma_s}{4\pi} [\alpha_{tr} + \bar{\mu}\alpha_a]F_1(\omega) \quad (32)$$

where $\alpha_{tr} = \gamma_{tr} - i\frac{\omega}{c}$ and $\alpha_a = \gamma_a - i\frac{\omega}{c}$.

The solutions to (32) and (31) have been obtained for a beam wave incident on a slab of scatterers [Shimizu et al., 1979]. An experiment is conducted on the diffusion of a light beam. An optical beam with a diameter of 0.766 mm is sent into a cylindrical volume with a length of 10 mm and diameter of 22 mm containing latex spheres of 0.481 μm diameter in water. The volume densities of the particles are varied from 10% down to 10⁻³%. The detector has the receiving area of 0.894 mm², and the field-of-view can be varied. The intensity is measured as a function of the radial distance from the beam axis. The measured intensity is compared with the intensity calculated from (32) for the cw case and shows an excellent agreement.

The backscattered pulse shape is calculated by taking the temporal Fourier transform (31). The experiment was performed using pico-second optical pulse [Shimizu et al., 1979]. Excellent agreements are obtained between the theory and experimental results, not only in the pulse shape in time, but also in the relative magnitudes of the pulses for different particle concentrations. It is noted that the transport coefficient γ_{tr} is an important factor characterizing the backscattered pulse.

5. PLANE WAVE INCIDENT ON A SLAB OF SCATTERERS

One of the fundamental problems of optical propagation through fog and clouds is the transmission and backscattering characteristics of a plane optical wave incident on a slab of random distribution of scatterers. In this section, we examine this problem using the equation of radiative transfer. It should be noted that the radiative transfer theory has been developed heuristically and its derivation from Maxwell's equations has not been done to date. Nevertheless, the radiative transfer theory gives good agreement with existing data and is considered as the best of available theories.

Let us consider a plane wave with arbitrary polarization incident on a slab in an arbitrary direction. See Figure 8. We choose the x axis in the plane of incidence. In general, the scatterers can have arbitrary shapes. The equation of transfer can be written in the following general form:

$$\frac{d}{ds} [I] = -[T] [I] + \int [S] [I'] d\omega' + [I_i] \quad (33)$$

where

$$[I] = \begin{bmatrix} I_1 \\ I_2 \\ U \\ V \end{bmatrix} = 4 \times 1 \text{ incoherent specific intensity matrix}$$

$[T] = 4 \times 4$ extinction matrix = $[T_{ij}]$, $[S] = 4 \times 4$ scattering matrix = $[S_{ij}]$, $[I_i] = 4 \times 1$ incident specific intensity matrix. Note that $[I]$ is directed to \hat{n} and $[I']$ is directed to \hat{n}' . Note also that ds is the differential distance along \hat{n} and $d\omega'$ is the differential solid angle in the direction \hat{n}' . See Figure 9. The Stokes parameters (I_1, I_2, U, V) are defined as follows:

$$I_1 = \langle E_1 E_1^* \rangle, \quad I_2 = \langle E_2 E_2^* \rangle, \quad U = 2 \text{Re} \langle E_1 E_2^* \rangle, \quad V = 2 \text{Im} \langle E_1 E_2^* \rangle \quad (34)$$

where E_1 and E_2 are the components of the electric field in the θ and ϕ directions respectively. We now examine the matrices $[T]$, $[S]$, and $[I_i]$.

5.1 Extinction Matrix $[T]$

For spherical particles, the total cross-sections do not depend on the polarization of the incident wave and therefore, the extinction matrix given in (33) is simply scalar. This is also true if the nonspherical particles are randomly oriented. In a general case, however, it should be a 4×4 matrix.

Consider a wave with the components E_1 and E_2 propagating in the direction \hat{n} . The fields E_1 and E_2 consist of the average (coherent) field $\langle E_1 \rangle$ and $\langle E_2 \rangle$ and the fluctuation (incoherent) field E_{1f} and E_{2f} . In general, as the coherent field propagates, there are some depolarization effects due to the nonspherical shape of the particles. We, therefore, write:

$$\frac{d}{ds} \langle E \rangle = [M] \langle E \rangle \quad (35)$$

where $\langle E \rangle = \begin{bmatrix} \langle E_1 \rangle \\ \langle E_2 \rangle \end{bmatrix}$, $[M] = [M_{ij}]$, $i, j, = 1, 2$.

In terms of M_{ij} , the extinction matrix $[T]$ is expressed as follows [Ishimaru and Cheung, 1981]:

$$[T] = \begin{bmatrix} 2 \operatorname{Re} M_{11} & 0 & \operatorname{Re} M_{12} & \operatorname{Im} M_{12} \\ 0 & 2 \operatorname{Re} M_{22} & \operatorname{Re} M_{21} & -\operatorname{Im} M_{21} \\ 2 \operatorname{Re} M_{21} & 2 \operatorname{Re} M_{12} & \operatorname{Re}(M_{11}+M_{22}) & -\operatorname{Im}(M_{11}-M_{22}) \\ -2 \operatorname{Im} M_{21} & 2 \operatorname{Im} M_{12} & \operatorname{Im}(M_{11}-M_{22}) & \operatorname{Re}(M_{11}+M_{22}) \end{bmatrix} \quad (36)$$

The exact determination of the propagation matrix $[M_{ij}]$ has been investigated. However, at present, this is still one of the outstanding problems. For low densities usually encountered in practice, the matrix $[M_{ij}]$ can be well approximated by the Van de Hulst formula. We define the scattering amplitude matrix $[f]$ of a single particle as:

$$[E(\hat{n})] = \frac{ikR}{R} [f] [E(\hat{n}')] \quad (37)$$

where

$$[E(\hat{n})] = \begin{bmatrix} E_1(\hat{n}) \\ E_2(\hat{n}) \end{bmatrix}, \quad [E(\hat{n}')] = \begin{bmatrix} E_1(\hat{n}') \\ E_2(\hat{n}') \end{bmatrix}, \quad [f] = \begin{bmatrix} f_{11}(\hat{n}, \hat{n}') & f_{12}(\hat{n}, \hat{n}') \\ f_{21}(\hat{n}, \hat{n}') & f_{22}(\hat{n}, \hat{n}') \end{bmatrix}.$$

Then $[M]$ is given by:

$$[M] = [M_0] + [M'], \quad [M_0] = ik \begin{bmatrix} 1 & 0 \\ 0 & 1 \end{bmatrix}, \quad [M'] = i \frac{2\pi}{k} \begin{bmatrix} \rho f_{11}(o) & \rho f_{12}(o) \\ \rho f_{21}(o) & \rho f_{22}(o) \\ \rho f_{11}(o) & \rho f_{12}(o) \\ \rho f_{21}(o) & \rho f_{22}(o) \end{bmatrix} = [M_{ij}], \quad (38)$$

where $\rho f_{ij}(o)$ denotes the integration over the size distribution $n(D)$.

$$\rho f_{ij}(o) = \int_0^\infty f_{ij}(o) n(D) dD \quad (39)$$

Note that there are no contributions of $[M_0]$ to (36) and therefore, only the elements of $[M']$ are used in (36). If all the particles are spherical, then the scattering matrix $[f]$ becomes diagonal:

$$M_{11} = M_{22}, \quad M_{12} = M_{21} = 0. \quad (40)$$

Therefore, the extinction matrix can be replaced by the scalar extinction coefficient c .

$$c = \rho \sigma_t = \int_0^\infty \sigma_t(D) n(D) dD \quad (41)$$

where $\sigma_t(D)$ is the total (extinction) cross-section of a single particle with size D and is given by

$$\sigma_t = \frac{4\pi}{k} \operatorname{Im} f_{11}(o) = \frac{4\pi}{k} \operatorname{Im} f_{22}(o) \quad (42)$$

5.2 Scattering Matrix $[S]$

The scattering matrix $[S]$ can be expressed in terms of the elements of the scattering amplitude matrix $[f]$ in (5).

$$[S] = \begin{bmatrix} \rho |f_{11}|^2 & \rho |f_{12}|^2 & \rho \operatorname{Re}(f_{11} f_{12}^*) & -\rho \operatorname{Im}(f_{11} f_{12}^*) \\ \rho |f_{21}|^2 & \rho |f_{22}|^2 & \rho \operatorname{Re}(f_{21} f_{22}^*) & -\rho \operatorname{Im}(f_{21} f_{22}^*) \\ \rho 2 \operatorname{Re}(f_{11} f_{21}^*) & \rho 2 \operatorname{Re}(f_{12} f_{22}^*) & \rho \operatorname{Re}(f_{11} f_{22}^* + f_{12} f_{21}^*) & -\rho \operatorname{Im}(f_{11} f_{22}^* - f_{12} f_{21}^*) \\ \rho 2 \operatorname{Im}(f_{11} f_{21}^*) & \rho 2 \operatorname{Im}(f_{12} f_{22}^*) & \rho \operatorname{Im}(f_{11} f_{22}^* + f_{12} f_{21}^*) & \rho \operatorname{Re}(f_{11} f_{22}^* - f_{12} f_{21}^*) \end{bmatrix} \quad (43)$$

where $\rho[\]$ means the integration over the size distribution and $\rho[\] = \int_0^\infty [\] n(D) dD$.

In general, f_{ij} depends on \hat{n}, \hat{n}' , the polarization dependence of the scatterers. However, for spherical particles, f_{ij} can be simplified considerably. Following Sekera, [1966], we write

$$\begin{aligned} f_{11} &= (e, e)T_1 + (r, r)T_2 \\ f_{12} &= -(r, e)T_1 + (e, r)T_2 \\ f_{21} &= -(e, r)T_1 + (r, e)T_2 \\ f_{22} &= (r, r)T_1 + (e, e)T_2 \end{aligned} \quad (44)$$

with the following notations introduced by Chandrasekhar, [1960],

$$\begin{aligned}
 (\ell, \ell) &= [(1-\mu^2)(1-\mu'^2)]^{\frac{1}{2}} + \mu\mu' \cos(\phi'-\phi), \\
 (\ell, r) &= -\mu' \sin(\phi'-\phi), \quad (r, \ell) = \mu \sin(\phi'-\phi), \quad (r, r) = \cos(\phi'-\phi),
 \end{aligned} \tag{45}$$

and

$$T_1(x) = \frac{A_{rr}(x) - xA_{\ell\ell}(x)}{1-x^2}, \quad T_2(x) = \frac{A_{\ell\ell}(x) - xA_{rr}(x)}{1-x^2},$$

where $x = \cos H = [(1-\mu^2)(1-\mu'^2)]^{\frac{1}{2}} \cos(\phi'-\phi) + \mu\mu'$, $\mu = \cos \theta$, $\mu' = \cos \theta'$. (θ', ϕ) and (θ, ϕ) correspond to the incident and scattered wave directions respectively, and H is the angle between the incident and scattered waves. $A_{\ell\ell}$ and A_{rr} are functions of H , and they are related to the scattering functions S_2 and S_1 respectively, used by Van de Hulst, [1957] for the Mie solution.

$$A_{\ell\ell} = \frac{i}{k} S_2 \quad \text{and} \quad A_{rr} = \frac{i}{k} S_1 \tag{46}$$

5.3 Incident Intensity Matrix $[I_i]$

We write Stokes' parameters for the incident coherent field $\langle E_1 \rangle$ and $\langle E_2 \rangle$ as $[I_{inc}(i)] \delta(\hat{n}-\hat{i})$, where \hat{i} is the unit vector in the direction of the incident wave. We then get

$$[I_i] = [S(\hat{n}, \hat{i})][I_{inc}(\hat{i})] \tag{47}$$

In the next section, we examine several special cases.

6. UNPOLARIZED WAVE NORMALLY INCIDENT ON A SLAB

In the preceding section, we presented general formulations of the radiative transfer for a plane wave incident on a slab of scatterers. In this section, we examine the case of unpolarized waves. Other cases including circular polarization and linear polarization can be obtained in a similar manner.

If the incident wave is unpolarized, their Stokes' parameters are given by

$$[I_{inc}] = I_0 \begin{bmatrix} 1 \\ 1 \\ 0 \\ 0 \end{bmatrix} \tag{48}$$

where $I_0 = |\langle E_1 \rangle|^2 = |\langle E_2 \rangle|^2$. The equation of transfer is then simplified to the following form:

$$\mu \frac{d}{d\tau} \begin{bmatrix} I_1 \\ I_2 \end{bmatrix} = - \begin{bmatrix} I_1 \\ I_2 \end{bmatrix} + \int_{-1}^1 \begin{bmatrix} S_{11} & S_{12} \\ S_{21} & S_{22} \end{bmatrix} \begin{bmatrix} I_1' \\ I_2' \end{bmatrix} d\mu' + \begin{bmatrix} F_1 \\ F_2 \end{bmatrix} e^{-\tau} \tag{49}$$

where I_1 and I_2 are the incoherent specific intensities for the field component parallel and perpendicular to the plane including the z-axis respectively. The scattering matrix elements S_{ij} used in (49) are normalized with respect to the extinction coefficient and are given by

$$S_{11} = \frac{\int_0^{2\pi} \rho |f_{11}(\hat{n}, \hat{n}')|^2 d\phi}{\rho\sigma_t} \tag{50}$$

Similarly, S_{12} , S_{21} , and S_{22} are expressed in the same form with $|f_{11}|^2$ replaced by $|f_{12}|^2$, $|f_{21}|^2$, and $|f_{22}|^2$ respectively. Note also that we used the optical distance τ defined by

$$\tau = \rho\sigma_t z \tag{51}$$

F_1 and F_2 are given by

$$F_1 = \frac{\rho |A_{\ell\ell}(\mu)|^2}{\rho\sigma_t} \quad \text{and} \quad F_2 = \frac{\rho |A_{rr}(\mu)|^2}{\rho\sigma_t} \tag{52}$$

Note that I_1 and I_2 are the incoherent specific intensity and that the boundary conditions are $I_1 = I_2 = 0$ for $\mu > 0$ at $\tau = 0$ and $I_1 = I_2 = 0$ for $\mu < 0$ at $\tau = \tau_0 = \rho\sigma_t d$.

In Figure 10, the received powers for different fields-of-view are shown as functions of the optical distance and in Figure 11, the ratio of the incoherent to coherent power is shown for the optical wave with $\lambda = 15 \mu\text{m}$.

7. CONCLUSIONS

In this paper, we examined three theoretical approaches to the optical propagation in fog. The forward scatter theory is applicable to the case where the particle sizes are large compared with a wavelength. The diffusion theory is applicable to the case where the particle sizes are small compared with a wavelength. The equation of transfer is applicable to all particle sizes, but the solutions are available only for limited geometry and wave types. Some general characteristics of the received power are shown together with several numerical calculations.

ACKNOWLEDGEMENT

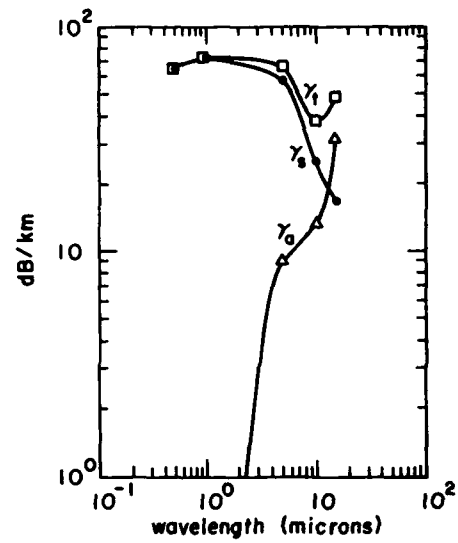
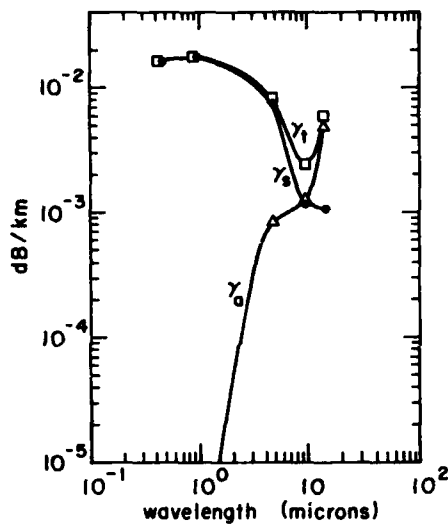
This work has been supported by the Office of Naval Research.

REFERENCES

1. Barabanenkov, Y. N., Y. A. Knavtsov, S. M. Rytov, and V. I. Tatarski, 1971, "Status of the Theory of Propagation of Waves in a Randomly Inhomogeneous Medium," *Sov. Phys. Usp.*, 13, 551-580.
2. Bucher, E. A., 1973, "Computer Simulation of Light Pulse Propagation for Communication Through Thick Clouds," *Applied Optics*, 12, 10, 2391-2400.
3. Chandrasekhar, S., 1960, *Radiative Transfer*, Dover, New York.
4. Danielson, R. E., and D. R. Moore, 1969, "The Transfer of Visible Radiation Through Clouds," *J. Atmos. Sciences*, 26, 1078-1087.
5. Fante, R. L., 1975, "Electromagnetic Beam Propagation in Turbulent Media," *Proc. IEEE*, 63, 12, 1669-1692.
6. Fante, R. L., 1980, "Electromagnetic Beam Propagation in Turbulent Media: An Update," *Proc. IEEE*, 68, 11, 1424-1443.
7. Furutsu, K., 1980, "Diffusion Equation Derived from Space-Time Transport Equation," *J. Opt. Soc. Amer.*, 70, 4, 360-365.
8. Ishimaru, A., 1977, "Theory and Application of Wave Propagation and Scattering in Random Media," *Proc. IEEE*, 65, 1030-1061.
9. Ishimaru, A., 1978a, *Wave Propagation and Scattering in Random Media*, Vols. I and II, Academic, New York.
10. Ishimaru, A., 1978b, "Diffusion of a Pulse in Densely Distributed Scatterers," *J. Opt. Soc. Amer.*, 68, 1045-1050.
11. Ishimaru, A., 1981, "Theory of Optical Propagation in the Atmosphere," *Optical Engineering*, to appear.
12. Ishimaru, A., and R. L-T Cheung, 1981, "Multiple Scattering Effects on Wave Propagation Due to Rain," *Annales des Télécommunications*, to appear.
13. Ito, S., and K. Furutsu, 1980, "Theory of Light Pulse Propagation Through Thick Clouds," *J. Opt. Soc. Amer.*, 70, 4, 366-374.
14. Mooradian, G. C., M. Geller, L. B. Stotts, D. H. Stephens, and R. A. Krautwald, 1979, "Blue-Green Pulsed Propagation Through Fog," *Applied Optics*, 18, 4, 429-441.
15. Mooradian, G. C., M. Geller, P. H. Levine, L. B. Stotts, and D. H. Stephens, 1980, "Over-the-Horizon Optical Propagation in a Maritime Environment," *Applied Optics*, 19, 1, 11-30.
16. Prokhorov, A. M., F. V. Bunkin, K. S. Gochelashvily, and V. I. Shiskov, 1975, "Laser Irradiance Propagation in Turbulent Media," *Proc. IEEE*, 63, 790-811.
17. Ray, P. S., 1972, "Broadband Complex Refractive Indices of Ice and Water," *Applied Optics*, 11, 1836.
18. Sekera, Z., 1966, "Scattering Matrices and Reciprocity Relationships for Various Representations of the State of Polarization," *J. Opt. Soc. Amer.*, 56, 1732-1740.
19. Stotts, L. B., 1977, "The Radiance Produced by Laser Radiation Transversing a Particulate Multiple-Scattering Medium," *J. Opt. Soc. Amer.*, 67, 815-819.
20. Stotts, L. B., 1978, "Closed-Form Expression for Optical Pulse Broadening in Multiple-Scattering Media," *Applied Optics*, 17, 504-505.
21. Strohbehn, J. W., 1977, "Laser Beam Propagation in the Atmosphere," *Topics in Applied Physics*, Springer-Verlag, Berlin and New York.
22. Tatarski, V. I., 1961, *Wave Propagation in a Turbulent Medium*, McGraw-Hill, New York.
23. Tatarski, V. I., 1971, "The Effects of the Turbulent Atmosphere on Wave Propagation," Acc. No. TT-68-50464, National Technical Information Service, Springfield, Virginia.
24. Uscinski, B. J., 1977, *The Elements of Wave Propagation in Random Media*, McGraw-Hill, New York.
25. Van de Hulst, H. C. 1957, *Light Scattering by Small Particles*, John Wiley and Sons, New York.
26. Wells, W. C., G. Gal, and M. W. Munn, 1977, "Aerosol Distributions in Maritime Air and Predicted Scattering Coefficients in the Infrared," *Applied Optics*, 16, 3, 654-659.
27. Shimizu, K., A. Ishimaru, L. Reynolds, and A. P. Bruckner, 1979, "Backscattering of a Picosecond Pulse from Densely Distributed Scatterers," *Applied Optics*, 18, 3484-3488.

Table I
Refractive and Absorption Indices
for Water at 25°C

Wavelength (μm)	$n = n_1 - jn_2$	
	n_1	n_2
0.5	1.335	0.1×10^{-8}
1	1.327	0.289×10^{-5}
5	1.325	0.0124
10	1.218	0.0508
15	1.27	0.402



Figs. 1 and 2: The scattering γ_s , absorption γ_a , and extinction coefficients γ_t . Fig. 1 is from Wells et al. and Fig. 2 is from Mooradian.

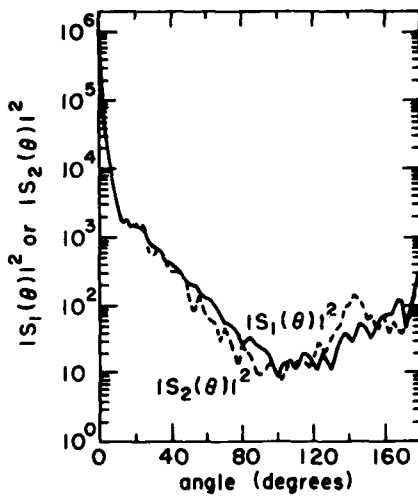


Figure 3

Scattering patterns at $\lambda = 0.5 \mu$

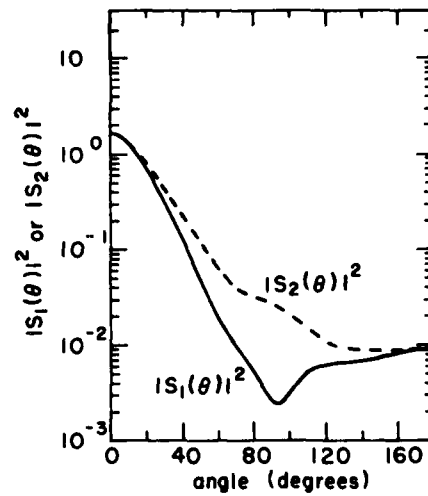


Figure 4

Scattering patterns at $\lambda = 15 \mu$

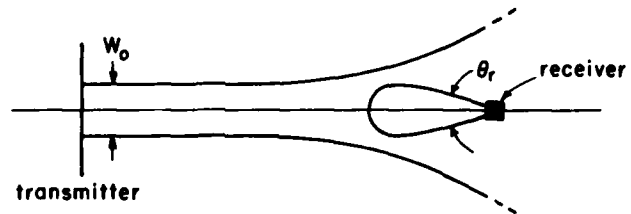


Figure 5
Collimated beam in fog

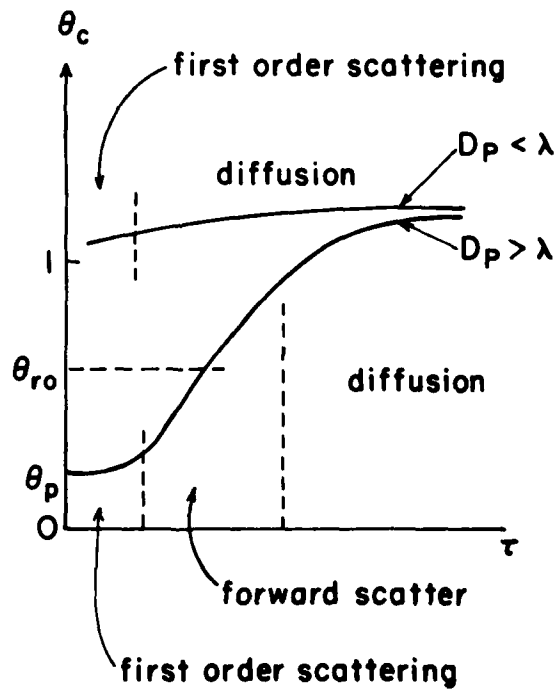


Figure 6
Angular broadening

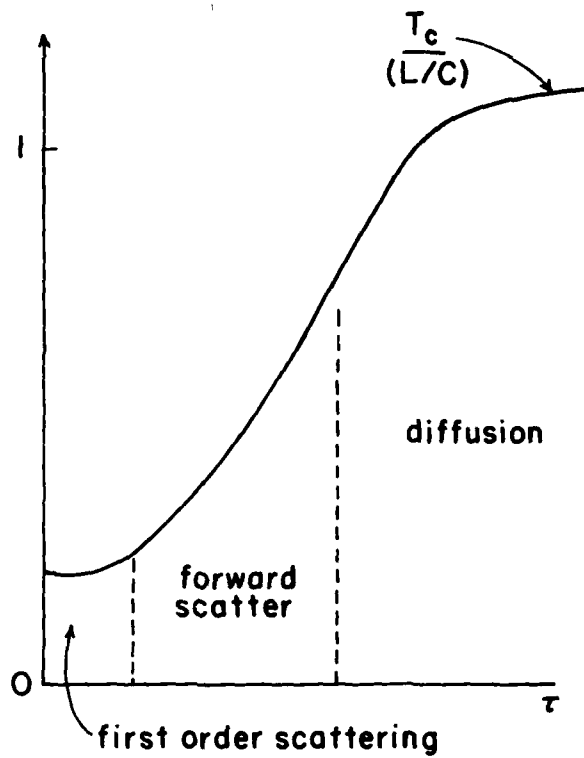


Figure 7
Pulse broadening

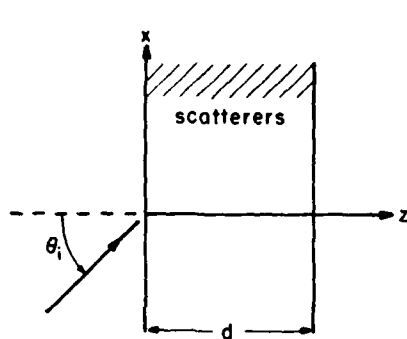


Figure 8
Plane wave incident on a slab of scatterers

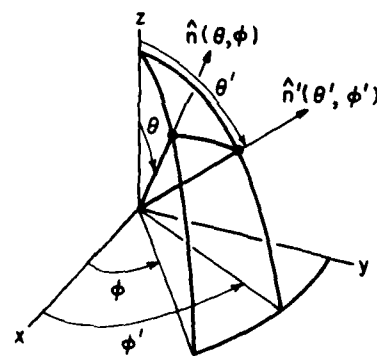
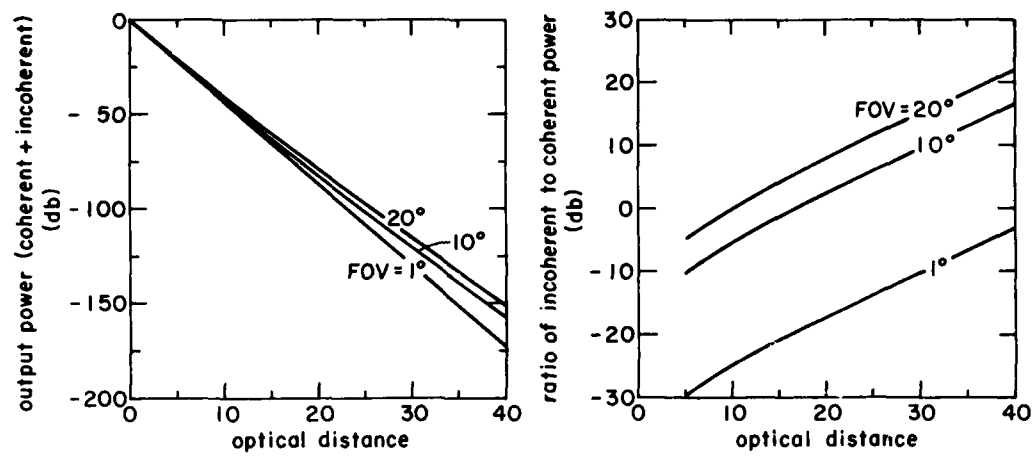


Figure 9
Incident \hat{n}' and scattered \hat{n} directions

Figs. 10 and 11: Received power at $\lambda = 15 \mu\text{m}$

INVESTIGATIONS FOR THE DEVELOPMENT OF A FORECAST SYSTEM FOR
UNDERWATER-VISIBILITY IN THE HELIGOLAND BIGHT

Ekkehard R. Küsters

German Military Geophysical Office
D - 5580 Traben-Trarbach
Germany

SUMMARY

In the Heligoland Bight, a shallow part of the North Sea, investigations are being carried out in order to get informations about correlations between meteorological/oceanographic parameters and turbidity. There are two components that influence underwater visibility: inorganic material and plankton. During most of the year a reduction of the visibility is caused by sediment particles stirred up by strong winds. In summer, however, especially in August, plankton can reach such densities that its influence is greater than that of inorganic material. The vertical extension of the layer rich in plankton is limited by salinity stratifications. During calm periods internal tides make the salinity boundary layer oscillate up and down. The drastic reduction in transparency by sediment particles normally lasts until the third day after the end of a storm, then a pronounced improvement can be noticed.

1. INTRODUCTION

The main operation areas of the German Navy are the western part of the Baltic and the south-eastern part of the North Sea. That makes it necessary to get thorough knowledge of all environmental factors that might influence the execution of missions.

The Heligoland Bight is a very shallow part of the North Sea, almost the entire region has a depth of less than 40 m (fig. 1). So there are no technical problems for divers to reach the bottom of the sea and work there. But what may cause difficulties - apart from stormy weather - s.e the optical conditions under water. Under certain circumstances the visibility is that bad, that it is very hard if not impossible to locate objects optically under water, even if they are very close.

VISSER, M.P. (1978), who made intensive literature studies on data concerning the turbidity of the North Sea, found out that though there exist a lot of data about the conditions in the area between the British and Dutch coast, very little is known about the Heligoland Bight apart from the Elbe estuary and the vicinity of some islands.

In order to get some informations about how the factors that influence the visibility vary in the Heligoland Bight, the German Military Geophysical Office has been carrying out oceanographic, biological, and meteorological investigations since 1978. To avoid falsifications of the results by coastal effects, the measurements were made from a ship anchored in the position 54°42'N, 07°11'E (40 nautical miles northwest of Heligoland; see fig. 1).

The two factors that may be responsible for turbidity of the water are the sediment being stirred up by currents or strong winds and planktonic organisms, the development of which is a function of the seasons, that means of temperature and light irradiation.

In literature it is often denied that unless in the deep open ocean far from the coast, plankton has any major effect upon the light attenuation (WRTKI, K., 1950, HEIDÖTTING, J. & OSSMANN, H.-J., 1978). Despite this opinion special attention was paid to the occurrence of planktonic organisms.

The programme comprehended measurements of temperature and salinity on a vertical profile, sampling of plankton, determination of the visual depth with the Secchi-disk, and in November 1980 measurements of the attenuation. Moreover wind velocity and direction, air temperature and cloud amount were measured/estimated.

In the laboratory the plankton samples were examined under the inverted microscope using the technique of UTERMÖHL, H. (1958) to find out the relation between plankton and sediment particles; the plankton species were determined, counted, and measured to be able to calculate their importance for the visibility.

2. GENERAL CONSIDERATIONS

By definition "plankton" are organisms that are unable to move over greater distances by their own. As they are subject to the gravity, they therefore would sink down to the bottom sooner or later, according to the law of Stokes. Most of the planktonic organisms are algae, and so they need light for their development. That means that they cannot survive unless they stay in the upper regions of the sea. To provide this, several ways have been developed to avoid or at least slow down sinking: the specific weight can be reduced by storing oil or gas in the plasma, or the frictional resistance can be raised by enlarging the surface. There are stick-shaped diatoms forming colonies that look like stars and have the effect of parachutes, others have long needles at each end. Barrel-shaped diatoms form long chains, sticking together with some kind of jelly, or they are equipped with groups of bristles, about ten times as long as their body is. Moreover, some organisms, the flagellates, possess a flagellum that enables them to move a little bit.

All these aids have an influence on the propagation of light under water: oil and gas changes the refraction index in an other way than plasma does, the needles cause diffraction effects.

The projection of the outline of the planktonic organisms, that means their optical effective surface, varies depending on the point of view. E.g. the surface of a Ceratium looked at from one side is $3500 \mu\text{m}^2$, the vertical projection covers merely $2000 \mu\text{m}^2$. A star formed of eight Asterionella cells may cover $1600 \mu\text{m}^2$ or $300 \mu\text{m}^2$ only, depending on the point of view.

As all these organisms try to gain an optimum of light for assimilation, their position in space is not a random one. That means when looking at a large number of planktons, their distribution between showing the minimum and the maximum surface is not Gaussian, but shifted to either end, depending on whether they are looked at horizontally or vertically. Consequently especially at times when plankton influences the turbidity of the water there are differences between horizontal and vertical visibility.

At night, however, those organisms that are able to change their positions arbitrarily, are distributed randomly, because then the reason for taking special positions - the light - is lacking.

3. RESULTS

3.1. Spring

The investigations were carried out in the second half of April 1980. This time of the year is characterized by decreasing wind intensities (end of the winter storms) and, due to the increase in the daily insolation, by the beginning of the plankton development (HAGMEIER, E., 1978).

As a relict of the winter aspect, at the beginning of the investigation period the water revealed high salinity without any stratification. The Secchi-depth varied between 7.5 and 8.5 m. The initial phase of relatively calm weather was interrupted by a storm with wind velocities up to more than 50 knots, lasting for two days. This led to a drastic reduction of the transparency: 60 hours after the end of the storm the visibility still was 3.5 m only. But the further improvement took place rapidly: after six more hours visibility had increased to 5.5 m. This value did not change very much anymore until the end of April, because from this time on plankton influenced the transparency almost as much as the inorganic particles did: the ratio between plankton and sediment was about 1 : 1 to 1 : 2.

The transition from wintry conditions to the spring aspect appeared in salinity, too. The first stage was a difference in salinity between high tide and low tide with a stratification at low tide. Later on even at high tide a stratification could be observed, yet it was less distinct than at low tide.

3.2. Late spring

In 1978 the investigations were made during the second half of May. The weather was calm and sunny almost all the time, and so it could be observed what happens under undisturbed conditions.

During the first few days salinity did not show any stratification, there was a gradual increase from top to bottom, sometimes interrupted by upwelling of water with high salinity. The Secchi-visibility varied between 6.5 and 9 m. Though after HAGMEIER, E. (1978) by this time of the year the plankton used to be twice as numerous as in April, in this case the plankton density was that low, that it had almost no effect on the visibility. (The theoretical minimum free pathlength of light lay between 100 and 130 m.) The ratio between planktons and inorganic particles was about 1 : 3 to 1 : 4, so mainly sediment was responsible for the turbidity,

On May 24 and 25 the calm weather was interrupted by strong northwesterly winds that caused wave heights of more than 4 m. By this the stratification of water bodies of different salinities, that had begun to develop on the sixth calm day, was destroyed, but with the wind calming down again, it reestablished quickly and remained until the end of the observation period. Two water bodies, one with a salinity of about 32 ‰, the other one with almost 34 ‰ were separated by a transition layer that was between 2 and 5 m thick (fig. 2). During this calm period an internal tide established, showing the same frequency but thrice the amplitude of the normal tide. On the first three days following the storm the visibility depth estimated with the Secchi-disk ranged from 6.7 to 8 m. Later on it increased to 9.5 - 10 m during daytime (clear sky) with values between 6.5 and 8 m at dawn and dusk.

As figure 2 shows, visibility was not influenced by plankton, because the surface water contained very few organisms, still less than deeper layers. The figure does not give their numbers, but the surface of the planktons found in one cm^2 . (A surface of $25000 \mu\text{m}^2$ means, that the theoretical minimum free pathlength is about 100 m.) The concentration of sediment particles had decreased compared with the first days of the investigation period and thus the factors influencing the underwater visibility had reached values that probably will be the optimum for this part of the North Sea.

3.3 Summer

During the summer investigation period in 1979 there was no such sharp boundary between layers of different salinity as it had appeared in May (fig. 3). Again an internal tide could be observed, but it was much less distinct than during the calm period, because the influence of the wind from time to time caused up - or downwelling of different water bodies.

Such alternations between nutrient renewal by upwelling and mixing, and surface stratification during settled weather, as they occur in the transitional zone between coastal regions and deep

sea, create optimum conditions for plankton growth (PINGREE, R.D. et. al, 1978). So this time the plankton really reached densities that made it become an important factor for underwater visibility (in accordance with the results of a thirteen years observation period near Heligoland, where the plankton maximum was found in August, too (HAGMEIER, R., 1978), but in contrast to VISSER, M.P., (1978), who found the maximum in March/April).

The minimum Secchi-depth registered was 3.3 m. This did well agree with the minimum theoretical visibility calculated by the effective surface of the planktons when they had reached their maximum density.

But the reduction of the visibility by plankton was limited to the layer close to the surface; in greater depths the number of algal cells decreased enormously (fig. 4). The boundary between water bodies rich and poor in plankton correlated well with the isohaline of 32 ‰. However in the water body with more than 32 ‰ salinity the turbidity by inorganic (sediment) material was greater than in the upper layer: on August 24 at noon, during a period of upwelling, the visibility was almost the same as it was at 18 hours, though the surface of the planktons differed by the factor 1.55. The difference between theoretical and actual visibility must have been caused by the greater portion of sediment particles in the water body coming up from below.

3.4 Autumn

Due to strong winds over almost all the investigation period in November 1980 there was no stratification in the water. Plankton was distributed almost homogeneously over the water column. The algae had very little influence on turbidity, the theoretical visibility regarding just the organisms was more than 45 m all the time.

The ratio between plankton and sediment was in the magnitude of 1 : 20 to 1 : 30. That means that the reduction of the visibility in autumn is merely a function of wind velocity and the duration of strong winds.

4. CONCLUSIONS

In the investigated part of the Heligoland Bight even under most favourable conditions (calm weather that prevents the raise of sediment particles, minimum in plankton density) the visual depth (Secchi-depth) hardly ever exceeds 10 m. This "rest turbidity" must be caused by yellow substance and inorganic particles of such small size that their sinking rate is that low that the sinking time is longer than the duration of periods calm enough not to bring up new sediment to the surface.

During most of the year sediment particles are responsible for further increase in light extinction/attenuation because of the shallowness of the Heligoland Bight that enables the wind to stir up sediment.

Within three days after a storm most of the inorganic particles have settled again and visibility increases significantly.

Due to tidal currents a thin layer above the bottom always contains such a great quantity of sediment particles that it is nearly nontransparent.

During calm periods internal tides develop at the boundary between water bodies with different salinity. These internal tides periodically alter the thickness of layers of equal attenuation.

In summer plankton is responsible for losses in transparency. Stratification of the organisms is not correlated with the thermocline but with differences in salinity. The thickness of the layer rich in plankton may vary between 5 and 15 m.

To be able to give forecasts about underwater visibility, it is necessary to correlate wind velocity and duration of strong winds with the amount of sediment particles stirred up.

As plankton is a relevant factor in summer only, it must be found out, under which meteorological and oceanographic conditions a mass development or a breakdown of the population takes place.

Furthermore correlations have to be made between attenuation coefficients and in situ observations of the actual vertical and horizontal visibility with respect to objects of different contrast. These correlations are necessary for the human eye with and without optical aids and for various optical instruments.

The aim of the forecast system is not to say whether visibility will be 3 or 3.2 m, but to distinguish several degrees, for example "visibility less than 2 m", "visibility between 2 and 5 m", "visibility more than 5 m", respectively the equivalent values for e.g. underwater - t.v..

5. ACKNOWLEDGEMENT

I am obliged to Mrs. Petra Oudhoff for carrying out the strenuous task of determining, measuring, and counting the plankton organisms, and also for her assistance in the measurement of the salinity.

6. REFERENCES

- HAGMEIER, E., 1978, "Variations in Phytoplankton near Heligoland", Rapp.R.-v.Réun. Cons.int.Explor.Mer, 172, p. 361-363.
- HEIDÖTTING, J. & OSSMANN, H.J., 1978, "In-situ Light Attenuation Measurements in the Sea". mt (MarTechnol), 2 (5), p. 151-156.

- PINGREE, R.D., HOLLIGAN, P.M. & MARDELL, G.T., 1978, "The Effects of Vertical Stability on Phytoplankton Distributions in the Summer on the Northwest European Shelf". *Deep-Sea Res.* 25, p. 1011-1028.
- UTERMÖHL, H., 1958, "Zur Vervollkommnung der quantitativen Phytoplankton-Methodik". *Mitt.Int.Ver. Limnol.*, 9, p. 1-38.
- VISSER, M.P., 1970 "The Turbidity of the Southern North Sea". *Dt. Hydrograph. Zeitschr.*, 23, p. 97-117.
- WYRTKI, K., 1950 "Über die Beziehungen zwischen Trübung und ozeanographischem Aufbau". *Kieler Meeresforsch.* 2, p. 87-107.

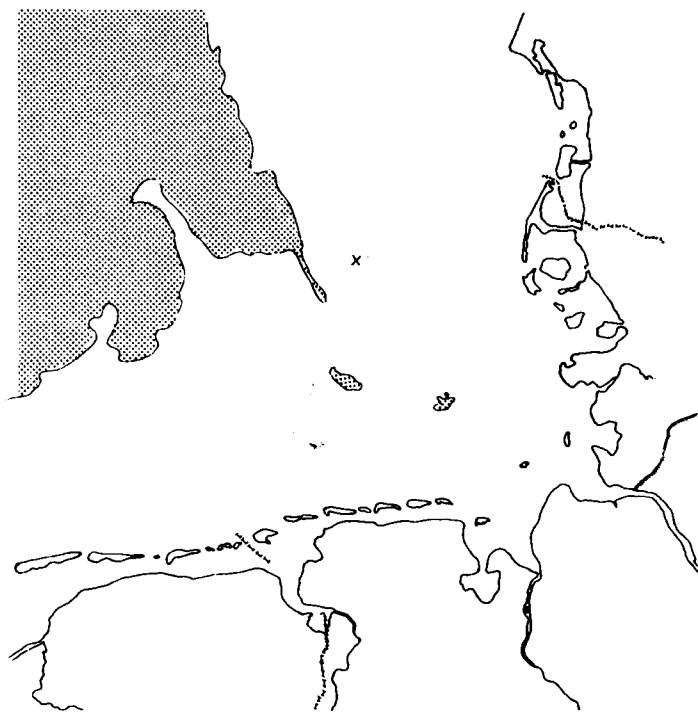


Figure 1
 South - eastern North Sea.
 Dotted area: water depth greater than 40 m.
 X: Position of the ship.

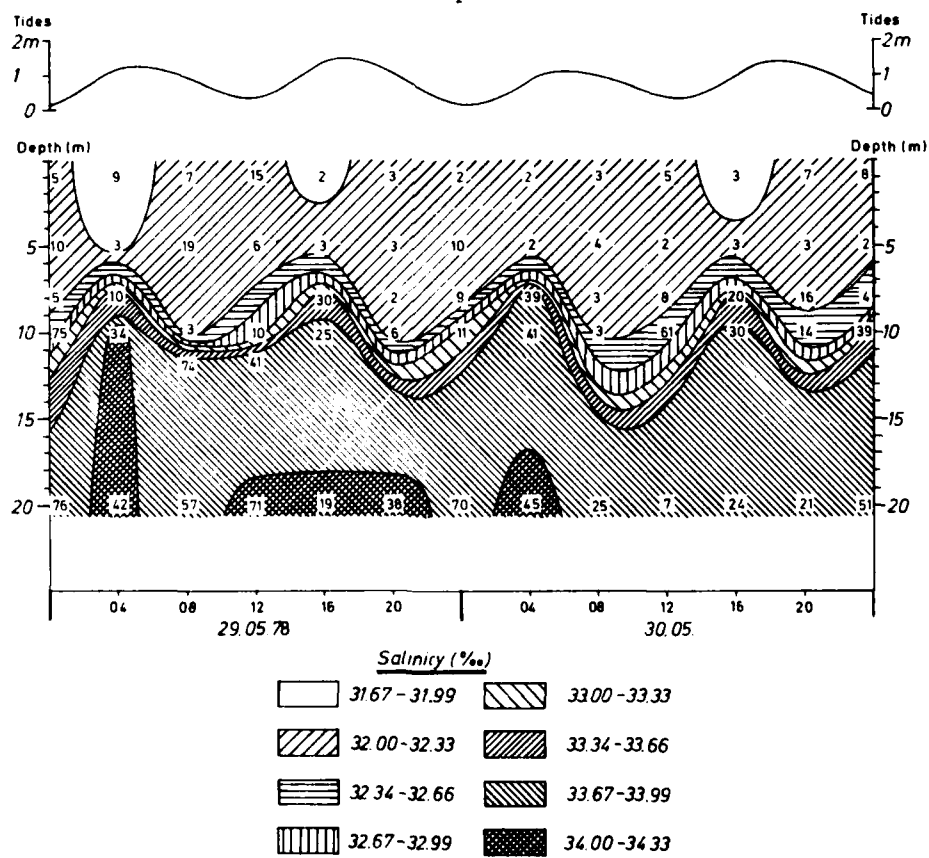


Figure 2
 Salinity and plankton density in the Heligoland Bight in May 1978.
 Numbers indicate the effective surface of planktons per cm^2
 (in $1000 \mu\text{m}^2$).

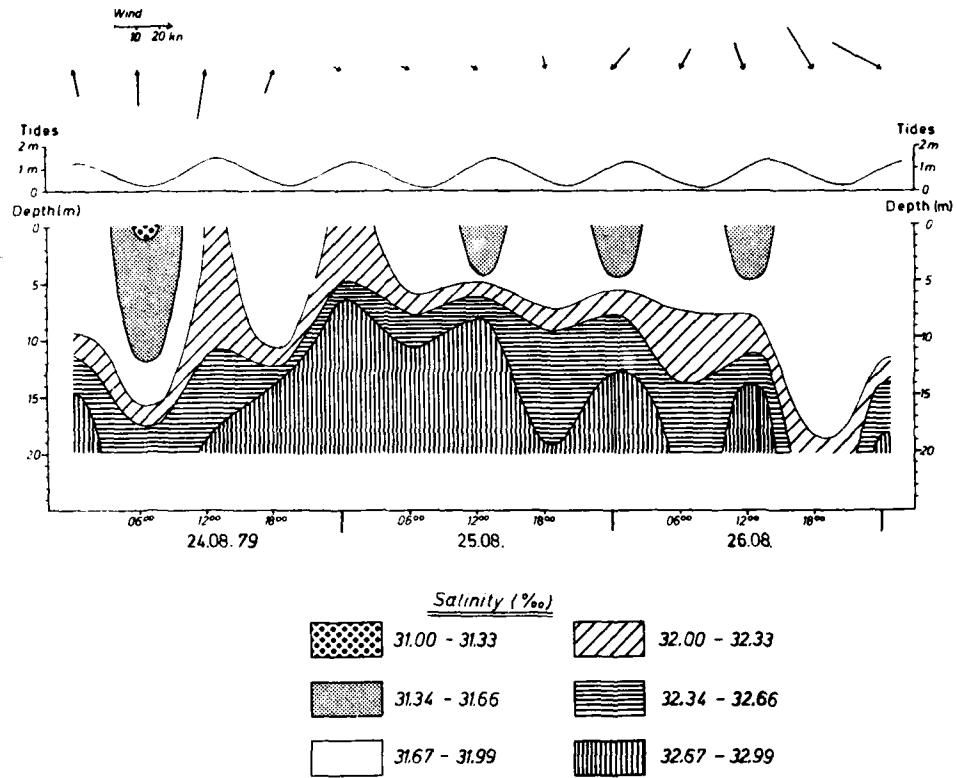


Figure 3
Wind and salinity in the Heligoland Bight in August 1979.

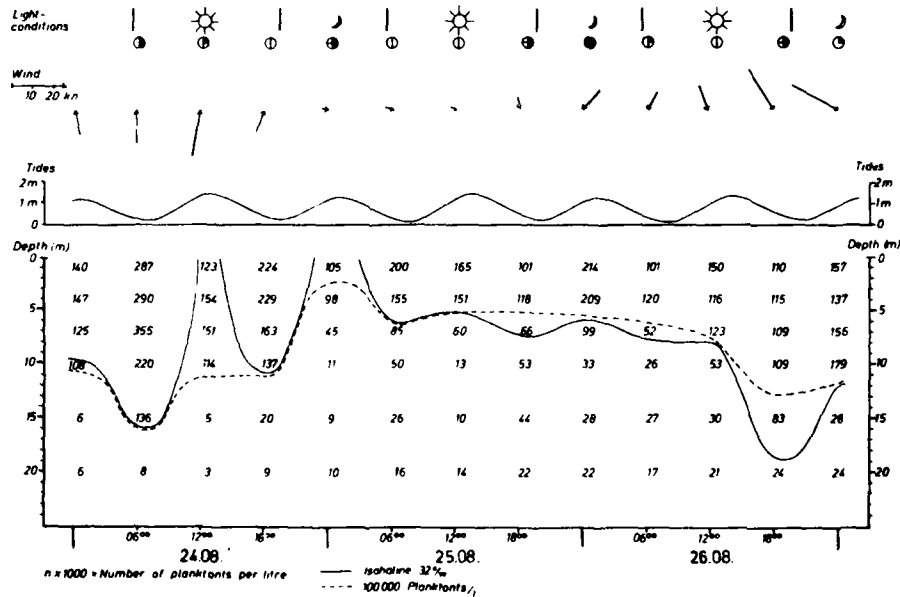


Figure 4
Plankton density in the Heligoland Bight in August 1979.

METEOROLOGICAL DESCRIPTIONS FOR OPTICAL PROPERTIES

K. L. Davidson and G. E. Schacher
Naval Postgraduate School
Monterey, California 93940

C. W. Fairall
BDM Corporation
Monterey, California 93940

SUMMARY

Observational experiments on turbulent intensities and aerosol distributions in the marine atmospheric boundary layer (MBL) have been performed over several years. Objectives have been to relate optical properties to bulk meteorological parameters. Our approach has been to incorporate parameters which define the surface fluxes of momentum, heat, and moisture, the processes at the inversion and the profiles within the intervening convectively mixed layer. We have found that optical turbulence (C_N^2) can be accurately estimated from measured values of wind, temperature, and humidity and recent bulk formulae. A bulk model for estimating C_N^2 values was evaluated on the basis of optically determined values with good agreement. Good agreement has also been observed between extinction values obtained from transmission measurements and those obtained from measured aerosol distributions. However, an existing empirical expression to relate the latter to wind speed and relative humidity appears to be inadequate. Reformulations should include the height of the inversion and stability dependent transport.

1. INTRODUCTION

Three atmospheric processes are primarily responsible for the degradation of the transmission of optical images and electro-optical energy: aerosol extinction, molecular absorption, and turbulent distortion (scintillation and beam wander). Optical energy propagation through the atmosphere is scattered and absorbed by aerosols and molecules and optical wave fronts are deflected and distorted by turbulent fluctuations in the refractive index. Tested physical models of these atmospheric effects and approaches to estimate them from routine meteorological data are required for applications of optical and electro-optical systems. Naval Postgraduate School (NPS) investigators have participated in field experiments designed to improve and verify such models and approaches for the overwater regime. These have been performed for U. S. Navy research programs over the past seven years.

One part of the experiments dealt with the compatibility of optical and meteorological propagation theories. For this, direct optical measurements of extinction and scintillation across an overwater path were compared to values calculated from aerosol and turbulence data obtained at the midpoint of the optical path from an instrumented research vessel.

A second part of the experiments involved attempts to apply existing models for the marine atmospheric surface layer and mixed layer to describe the optically relevant turbulent and aerosol properties. The surface layer is considered to be the region extending from the air-sea interface to heights of 40-50 meters. Its mean and turbulent properties are closely related to surface fluxes of momentum, temperature and moisture and, hence, the air-surface (bulk) differences of the mean properties. The fluxes themselves are often assumed to be independent of height within the surface layer. The mixed layer extends from the top of the surface layer to the base of the capping inversion. Properties of the mixed layer are determined by both the underlying surface fluxes and entrainment at the inversion. The latter is influenced further by the existence of clouds. In general, understandings and models for the boundary layer range from very good for the surface layer to good for the convectively forced clear mixed layer to fair for convectively forced cloud covered mixed layer.

The purpose of this paper is to present observational results which address the compatibility of optical and meteorological theories and the validity of models for estimating the optical parameters from bulk meteorological data. For this purpose we include brief reviews of the expected relationship between optical and meteorological parameters and of the scaling laws for turbulence in the boundary layer.

2. RELATIONSHIPS BETWEEN OPTICAL AND METEOROLOGICAL PARAMETERS

The two atmospheric optical parameters of primary interest are the total extinction coefficient and the refractive-index structure function parameter, C_N^2 . The total extinction coefficient ($\beta + \alpha$) parameterizes the loss of optical energy as it is scattered out of the beam or absorbed by molecular and particulate constituents of the atmosphere. Thus, it has four components: molecular scattering and absorption ($\beta = \beta_s + \beta_a$) and aerosol scattering and absorption ($\alpha = \alpha_s + \alpha_a$). The refractive-index structure function parameter parameterizes the intensity of refractive-index spatial inhomogeneities which distort and tilt image wave fronts. Both of these parameters can be related to meteorological parameters: 1) C_N^2 to the intensity of small scale turbulent fluctuations and 2) total extinction to the concentration of certain gases and to the size distribution of aerosols.

C_N^2 for optical wavelengths is related to the temperature (C_T^2), water vapor (C_Q^2) and temperature-water vapor (C_{TQ}) structure function parameters as

$$C_N^2 = (79 \times 10^{-6} P/T^2)^2 (C_T^2 + 0.113 C_{TQ} + 3.2 \times 10^{-3} C_Q^2) \quad (1)$$

where P is the pressure in mb, T the absolute temperature. Meteorological estimates of C_N^2 can be obtained in two ways: 1) direct measurement of C_T^2 , C_T , and C_Q^2 ; and 2) calculation of C_T^2 , C_{TQ} , and C_Q^2 from bulk meteorological data (water temperature, air temperature, humidity and wind speed).

The separate components of total extinction ($\beta + \alpha$) can be calculated from meteorological data. Molecular extinction (β) can be obtained using existing models, such as the LOWTRAN model developed by the Air Force Geophysics Laboratory (Selby et al, 1978), with observed temperatures and water vapor concentrations. Aerosol total extinction (α) can be calculated from the aerosol spectral density, $N(r)$, as

$$\alpha = \int_0^{\infty} \pi r^2 E(n, \lambda) N(r) dr \quad (2)$$

where r is the particle radius, $E(n, \lambda)$ the total scattering efficiency at wavelength, λ , and refractive-index, n . Therefore, meteorological estimates of aerosol extinction (scattering) can also be obtained in two ways: 1) direct measurement of $N(r)$ over a sufficiently wide radius range and 2) calculation of $N(r)$ from bulk meteorological data (relative humidity, wind speed and any other routinely measured parameter proven to be a factor).

In the next two sections we evaluate results on scintillation and aerosol scattering extinction. The first set of results are comparisons of optical and measured meteorological values. The second set of results are of the directly measured and the bulk derived meteorological values.

3. COMPARISON OF OPTICAL AND METEOROLOGICAL VALUES FOR C_N^2 AND AEROSOL SCATTERING EXTINCTION COEFFICIENT

Results for these comparisons were obtained during a combined meteorological and optical propagation experiment conducted in Monterey Bay from 28 April to 9 May 1980. The optical measurements were made over a 13 km overwater path and are described by Crittenden et al (1981) in this proceeding. The meteorological measurements were made from the R/V Acania (operated by the Department of Oceanography of NPS) which was stationed near the midpoint of the optical path.

The R/V Acania was equipped with multi-level measurement systems to measure mean and turbulent wind, temperature and humidity and aerosol size distribution (.09 μ m to 14 μ m radius). Descriptions of the measurement and analyses systems and procedures are given by Schacher et al (1980). Two measurements requiring further description for these comparisons are those of the temperature structure function parameter, C_T^2 , and of the aerosol size distributions.

Meteorological values for C_N^2 in this comparison were determined primarily from C_T^2 measurements with minor (less than 15%) adjustments for the water vapor contributions, C_{TQ} and C_Q^2 . The C_T^2 measurements were made with two resistance wires, 2.5 μ m platinum sensors, separated a distance of 30 cm in the crosswind direction. C_T^2 values were obtained from RMS values of the sensed temperature differences. The RMS values were calculated with an analog circuit with a 30 second time constant and the C_T^2 values used for the comparisons were obtained with 30 minute averages of the RMS values.

The aerosol spectra were measured with optical particle counters made by Particle Measurement Systems (PMS) of Boulder, Colorado. The total system consisted of two probes, the classical scattering (CSAS) and the active scattering (ASAS), controlled by a DAS-32 with computer interfacing. This system measures aerosols in 90 size channels from 0.09 μ to 14.0 μ radius. The $N(r)$ spectra were determined for half-hour periods. Each spectrum was fit in $\text{LOG}(N(r))$, $\text{LOG}(r)$ space with a seventh order polynomial for $0.09 \mu < r < 7 \mu$, with a linear fit for $r > 7 \mu$. The extinction was then calculated using these fits for $0.03 \mu < r < 30 \mu$.

An additional consideration of these optical-meteorological comparisons is that the meteorological measurements were point averages over a one half hour period and the optical measurements were path averages of instantaneous occurrences. As such, we are comparing a time average with a space average and the two are not exactly equivalent. The effect of this on the comparisons cannot be determined without detailed knowledge of the local wind and temperature patterns.

Comparisons of optically measured C_N^2 with meteorological measured C_N^2 (calculated from C_T^2 measurement with correction for probable water vapor contributions) are shown in Figure 1. These results are presented in Davidson et al (1981) in which data from non-equilibrium condition are included which are not shown here. These turbulent C_N^2 values have also been corrected for a known salt loading effect (Fairall et al, 1979). The salt loading effect increases measured C_T^2 values for general conditions during these measurements.

The solid line in Figure 1 indicates perfect agreement and the two dashed lines are for factors of two disagreements. For all but two of the 20 compared values the agreement is within a factor of two. The meteorological C_N^2 values are generally larger by an average factor of 50% and we believe this is due to the salt loading effect. In general, the agreement is very good in view of the difficulties in both optical and meteorological measurements. For purposes of the general objective of this paper, these results show that small scale temperature fluctuations determining overwater scintillation can be satisfactorily measured from the R/V Acania with the system used.

Comparisons of optically measured aerosol extinction values with extinction values calculated from measured aerosol spectra (Eq. 2) are shown in Figure 2. These results are presented in Fairall

et al (1981) along with results from other intermediate wavelengths. For this comparison, optically measured extinction values were reduced for the molecular absorption and scattering using the LOWTRAN model and shipboard measured relative humidity and temperature.

The agreement between optical and meteorological extinction results is surprisingly good in view of the fact that these were obtained in a field experiment and the aerosol spectra were extrapolated beyond $r = 14 \mu$. Again, the significance of these results is that the necessary meteorological measurement for optical extinction (aerosol and molecular) can be made from shipboard (provided the aerosols are measured over all parts of the spectrum that contribute significantly to the extinction at the wavelength of interest).

4. BULK DESCRIPTIONS OF C_N^2

We are interested in evaluating models and approaches for estimating the C_N^2 from bulk parameters such as the wind speed, temperature and humidity on a single level and the surface temperature. From Eq. 1, the meteorological parameters involved are the variance and covariance structure function parameters; C_T^2 , C_{TQ} and C_Q^2 . Existing surface layer scaling on the basis of the surface fluxes enables the latter to be related to bulk parameters. This scaling is often referred to as Monin-Obukhov Scaling (MOS).

Since the details of MOS surface layer scaling are covered in previous papers this discussion will be limited to a few basic definitions. Near the surface, the height above the surface, Z , can be normalized by the Monin-Obukhov stability length, L . We can then represent the micrometeorological properties in terms of height (Z), scaling parameters (T_* and U_*) and dimensionless functions of $\xi = Z/L$,

$$C_T^2 = T_*^2 Z^{-2/3} f(\xi) \quad (3a)$$

$$C_Q^2 = Q_*^2 Z^{-2/3} Af(\xi) \quad (3b)$$

$$C_{TQ} = r_{TQ} T_* Q_* Z^{-2/3} A^{1/2} f(\xi) \quad (3c)$$

where T_* and Q_* are the temperature and humidity scaling parameters, $f(\xi)$ is a dimensionless function (Wyngaard et al, 1971), r_{TQ} is the temperature-humidity correction parameter (about 0.8) and A is a constant (about 0.6). The scaling length, L , is given by

$$L = \frac{\kappa}{Kg} \frac{u_*^2}{T_* + 0.61 T_{Q_*}/\rho} \quad (4)$$

where u_* is the friction velocity, κ is Von Karman's constant (0.35), g is the acceleration of gravity and ρ is the density of air.

Note that the scaling parameters are related to the surface fluxes of momentum ($\tau = \rho u_*^2$), temperature ($Q_* = -u_* T_*$) and water vapor ($M_{Q_*} = -u_* Q_*$). The difficulty of direct flux measurements led to the development of a method that utilizes bulk meteorological quantities (wind speed, u , temperature, T , and water vapor density, Q). In this case, the scaling parameter for $X(X = u, T, Q)$ is obtained from the difference in X from the sea surface (X_S) to some reference height (usually 10 m) in the atmosphere.

$$X_* = c_x^{1/2} (X_{10} - X_S) \quad (5)$$

where c_x is the drag coefficient for X (typically, $c_x = 1.3 \times 10^{-3}$ over the ocean). Further details on our use of the bulk method can be found in Davidson et al (1980).

We have evaluated numerous observational results with respect to the bulk approach which includes both the validity of general scaling expressions given by Eqs. 3a-b and the bulk derivation of the scaling parameters as accomplished by Eq. 5. Our bulk comparison results for C_T^2 (Eq. 3a) are presented in Davidson et al (1978), results for C_Q^2 and C_{TQ} as well as C_N^2 are presented in Fairall et al (1980) and results for another small scale parameter, the turbulent kinetic energy dissipation rate, are presented in Schacher et al (1981).

The comparison for this discussion will be between bulk derived C_N^2 and optically measured C_N^2 for the Monterey Bay experiment described in Section 3. These comparisons are shown in Figure 3 which includes equilibrium cases presented by Davidson et al (1981). In this comparison all but three of 26 pairs of values are within a factor of two of perfect agreement. The mean percent error, taking the optical values to be correct, is 33% which is extremely good agreement. This agreement is better than that obtained in the comparison with C_N^2 derived from C_T^2 measurements. Such a result is partially expected because of inherent measurement errors in the latter.

Results of these comparisons and results of comparison of bulk and turbulence derived parameters in above referenced papers clearly demonstrates that surface layer optical turbulence, C_N^2 , is very satisfactorily described by existing bulk formulae and scaling expressions. In fact, over the ocean C_N^2 can be more accurately determined from bulk model calculations than from the more difficult direct measurements of small scale temperature and humidity fluctuations.

5. BULK DESCRIPTIONS OF AEROSOL EXTINCTION

5.1 The Model

Over the ocean, sea-salt aerosols ($0.1 \mu < r < 20 \mu$) generated by whitecaps are usually the dominant component of the aerosol extinction coefficient at IR wavelengths. Because the whitecap generation of sea-salt aerosols is related to the sea state, the wind speed is an important factor in the marine aerosol component. Another important factor is the relative humidity (RH) since aerosol particles (which are actually droplets at $RH > 50\%$) change their size in response to humidity changes. For example, if $r(S)$ is the radius of an aerosol particle at saturation S ($S = RH/100$) and r_0 is the particle radius at some reference humidity ($S_0 = 0.8$), then

$$r(S) = r_0 a(S) \quad (6)$$

where $a(S)$ is a function that describes the humidity size dependence.

We must also consider the fact that, even over the ocean, the total aerosol spectrum is due to both continental ($N_C(r_0)$) and locally generated sea-salt ($N_S(r_0, u)$) aerosol particles

$$N(r_0) = N_C(r_0) + N_S(r_0, u) \quad (7)$$

where only the sea-salt component depends on the wind velocity, u . Since $r_0 = r/a$ and $N(r_0) = N(r)a$, we can write the aerosol spectrum at ambient saturation and wind speed as

$$N(r) = (N_C(r/a) + N_S(r/a, u))/a \quad (8)$$

We have used aerosol data from the Joint Air-Sea Interaction Experiment (JASIN) to examine the Wells-Munn-Katz (WMK) model B as given by Noonkester (1980). The WMK model B uses

$$a(S) = 0.81 \exp(.066*S/(1.058 - S)) \quad (9)$$

and a continental aerosol of the form

$$N_C(r_0) = B r_0^{-4} \quad (10)$$

where $B = 1.7$ is the continental "Junge" coefficient. Since $N_S(r_0, u)$ is a rather complicated empirical expression we simply refer those interested in more detail to Noonkester (1980).

5.2 Model Evaluation

This evaluation is basically a comparison of WMK model predictions of aerosol extinction based on measurements of relative humidity and wind speed with extinctions obtained from measurements of aerosol spectra. A twenty minute averaging period was used for RH and aerosol spectra. The wind speed used in Eq. 8 was an average over the 12 hours preceding the aerosol data in order to take into account the long response times required for sea-salt aerosol generation. This comparison (Figure 4) asks "given a wind speed and relative humidity, how well does the model predict the observed extinction?" Clearly, the WMK model predicts very well on the average with a rather large standard deviation (about half an order of magnitude, or a factor of 3). A considerably more stringent comparison asks "given an observed extinction, how well does the model predict this extinction?" This comparison (Figure 5) is considerably less favorable, particularly in the extremes of good visibility and low visibility conditions. A certain amount of disagreement of this type is expected when comparing quantities that are subject to experimental error. However, we found that a considerable part of the discrepancy is due to overestimation of the continental aerosol component (WMK assume $B = 1.7$ while JASIN gives $B = 0.24$). If we change B to 0.24 and repeat the comparison (X's in Figure 5), we get some improvement. Furthermore, there is considerable correlation between visible extinction and the amount of continental aerosol; the high visibility conditions are characterized by relatively much smaller continental aerosol densities while the low visibility conditions have relatively greater continental aerosol densities. The disagreement at high extinction values is due to the inaccuracy of the relative humidity measurement which is critical under near fog and heavy haze conditions where $RH = 100\%$.

It is important to realize that the WMK model is an average continental, equilibrium surface generation model. Deviations of the continental aerosol were more than an order of magnitude during JASIN. The sea salt component is also subject to considerable deviations from equilibrium (this is one of the reasons for the 12 hour average wind speeds). The deviations from average and equilibrium values are more important for operational usage and somewhat less important for climatological and spectrum evaluation usage. An example where both usages are affected is the estimation of IR extinction using visible extinctions (visibility observations) and empirical assumptions about their relationship. We have plotted the visible to IR extinction ratio in Figure 6 with lines indicating the WMK model predictions using two different continental aerosol coefficients. Since the continental aerosol coefficients are correlated to visibility, the correct ratio depends not only on wind speed but also the visibility observation.

Although we have dealt with the stochastic properties of ensemble averages of the aerosols, variations about the average are not necessarily random but are primarily due to changes in synoptic and mesoscale weather patterns. In the case of the continental aerosol component, this is basically a question of air-mass history. In the case of the sea salt aerosol, it is a question of changing surface generation rates (wind speed) and the production, removal and mixing mechanisms in the marine atmospheric boundary layer. Since the surface generated aerosols are quickly mixed vertically to fill the boundary layer up to the capping inversion, rapid changes in the inversion height, h , will be reflected in changes in the sea salt aerosol density and, therefore, the extinction coefficient. In Figure 7 we can see that the fractional variations in h are highly correlated with variations in the visible extinction. The correlation with 10.6μ extinction is considerably less because the large size aerosols (which are heavier contributors to IR extinction) reach equilibrium more quickly after changes in surface conditions.

6. ACKNOWLEDGEMENTS

We are indebted to members of the Naval Postgraduate School Optical Propagation Group for providing the optical measurements for these comparisons.

This research was supported by the following U.S. Navy Commands; NAVSEA (HEL), NAVMAT (EOMET) and NAVAIR (AIR-370).

7. REFERENCES

- Crittenden, E. C., E. A. Milne, A. W. Cooper, G. W. Rodeback and S. Kalmbach, 1981, "Multiwavelength extinction and index fluctuation measurements", Proc. AGARD Conf., Monterey, Calif. (NATO).
- Davidson, K. L., T. M. Houlihan, C. W. Fairall and G. E. Schacher, 1978, "Observation of temperature structure function parameter, C_T^2 , over the ocean", Bound.-Layer Meteor., 15, 507-523.
- Davidson, K. L., G. E. Schacher, C. W. Fairall and A. Goroch, 1981, "Verification of the bulk method for calculating overwater optical turbulence", Applied Optics, submitted.
- Fairall, C. W., K. L. Davidson and G. E. Schacher, 1979, "Humidity effects and sea salt contamination of atmospheric temperature sensors", Applied Meteor., 18, 1237-1239.
- Fairall, C. W., G. E. Schacher and K. L. Davidson, 1980, "Measurements of the humidity structure function parameters, C_q^2 and C_{Tq} , over the ocean", Bound.-Layer Meteor., 19, 81-92.
- Fairall, C. W., G. E. Schacher and K. L. Davidson, 1981, "Atmospheric optical propagation comparisons during MAGAT-80", Tech. Report NPS-61-81-002.
- Noonkester, V. R., 1980, "Offshore aerosol spectra and humidity relations near Southern California", Proc. Sec. Conf. on Coastal Meteorology, Los Angeles, Calif. (AMS), 113-120.
- Schacher, G. E., C. W. Fairall, D. E. Spiel and K. L. Davidson, 1980, "NPS shipboard and aircraft meteorological equipment", Tech. Report NPS-61-80-017.
- Schacher, G. E., K. L. Davidson, T. M. Houlihan and C. W. Fairall, 1981, "Measurements of the rate of dissipation of turbulent kinetic energy, ϵ , over the ocean", Bound.-Layer Meteor., to be published.
- Selby, J. E., F. X. Kneizys, J. H. Chetwynd and R. A. McClatchey, 1978, "Atmospheric transmittance/radiance: Computer code LOWTRAN-4", Tech. Report AFGL-TR-78-0053.
- Wyngaard, J. C., Y. Izumi and S. A. Collins, 1971, "Behavior of the refractive index structure parameter near the ground", J. Opt. Soc. Am., 61, 1646-1650.

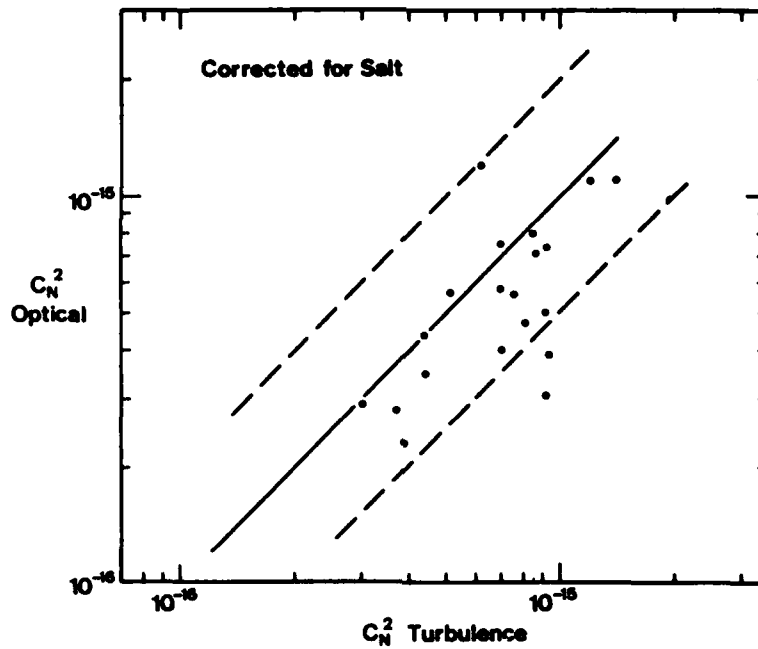


Figure 1 Refractive-index structure function, C_N^2 , determined from direct optical measurement versus C_N^2 determined from microthermal point measurements of C_T^2 (Eq. 1) assuming C_q^2 and C_{TQ} are negligible. The dashed lines represent factors of 2 disagreement.

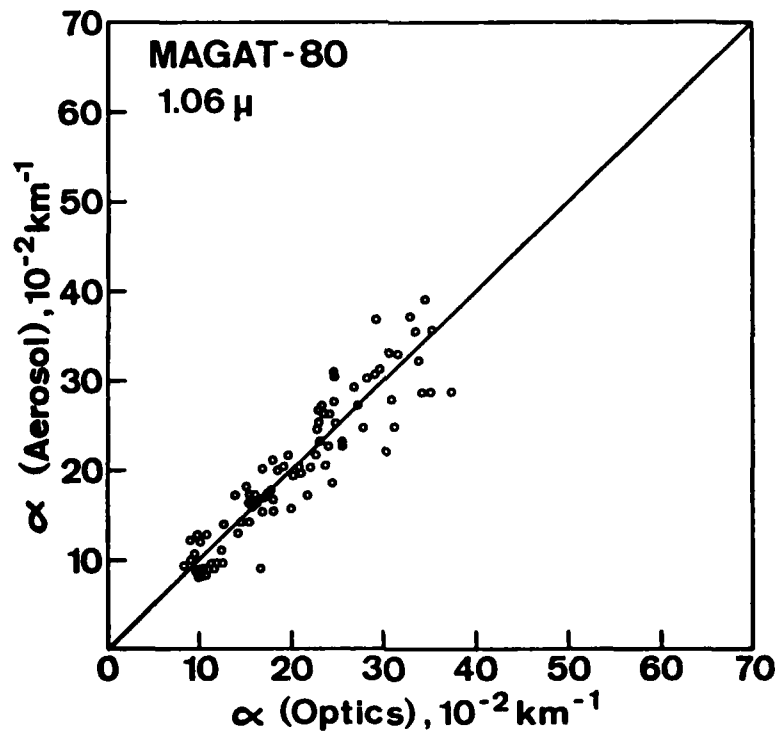


Figure 2 Aerosol extinction coefficient, α , determined from direct optical measurement versus α determined from point measurements of aerosol spectral density, $N(r)$, and Eq. 2.

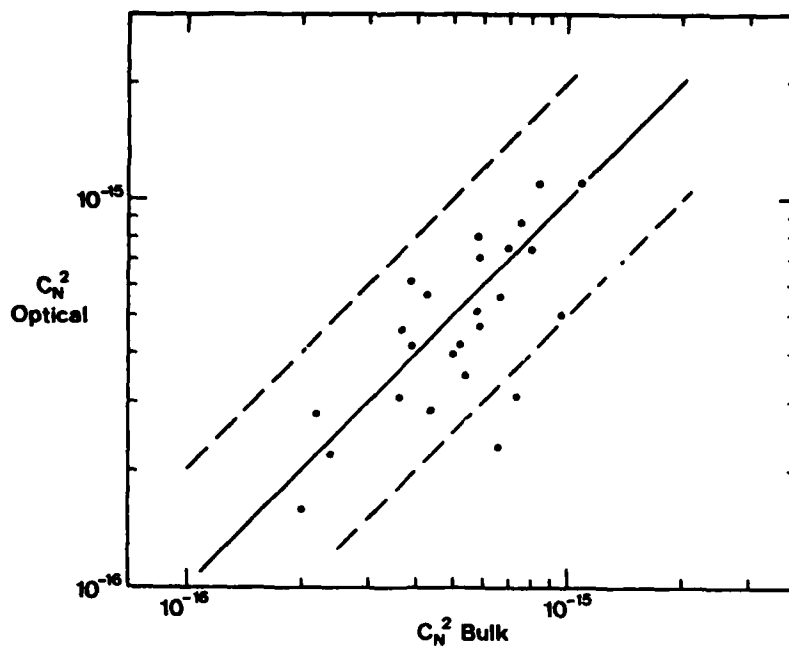


Figure 3. Similar to Figure 1 but the horizontal axis is C_N^2 determined from bulk model calculations (Eq. 1 and Eq. 3).

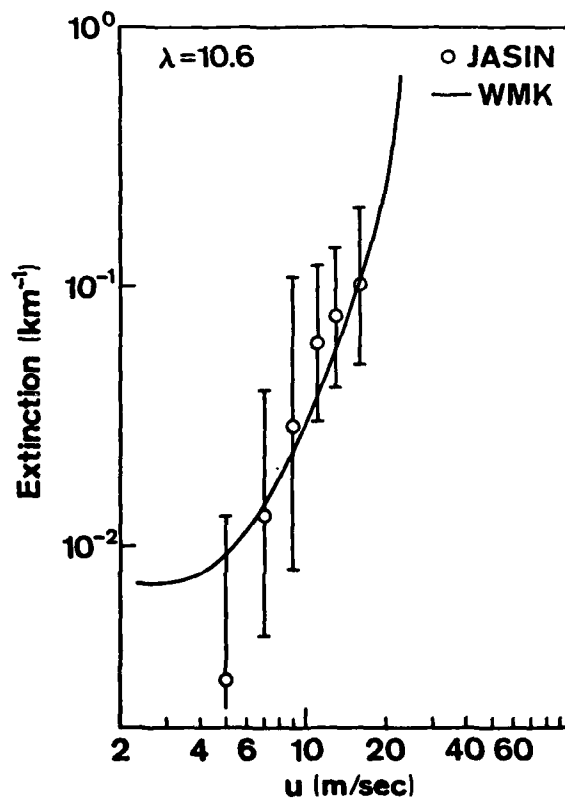


Figure 4 Aerosol extinction coefficient (circles) and WMK model predictions (line) at $\lambda = 10.6 \mu$ and RH = 87% as a function of 12 hour average wind speed.

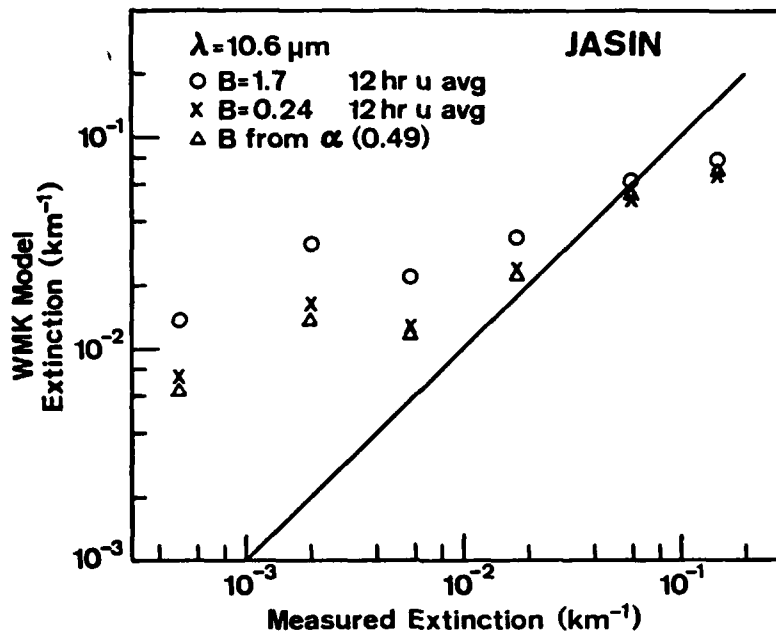


Figure 5 WMK model predictions of aerosol extinction at $\lambda = 10.6 \mu$ as a function of observed extinction (circles are $B = 1.7$, X's are $B = 0.24$ and triangle are B obtained from average correction with visibility).

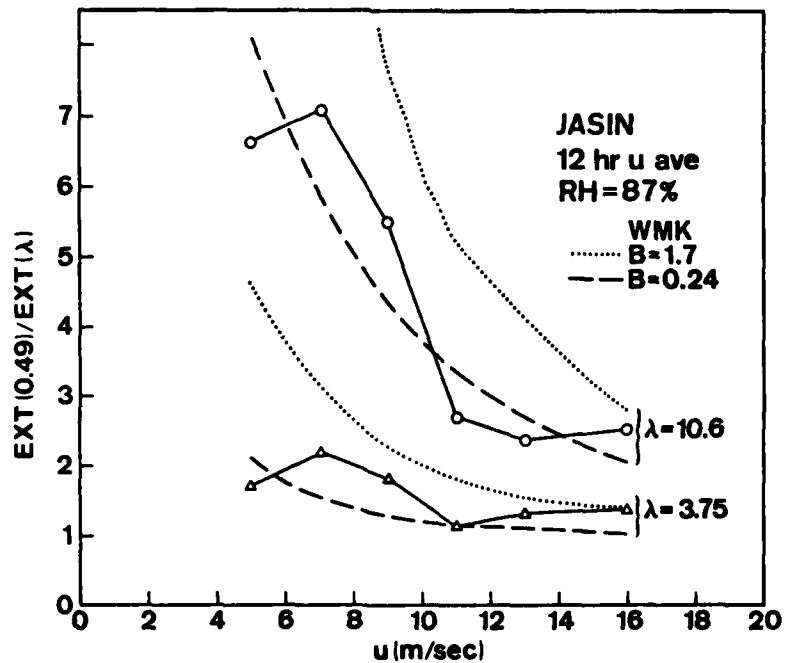


Figure 6 Ratio of aerosol extinction coefficient at $\lambda = 0.49 \mu$ to that obtained at $\lambda = 3.75 \mu$ and 10.6μ . The circles are the JASIN data at $\lambda = 10.6 \mu$, the triangles are the JASIN data at $\lambda = 3.75 \mu$. The dashed line is the WMK model with $B = 0.24$ while the dotted line is $B = 1.7$.

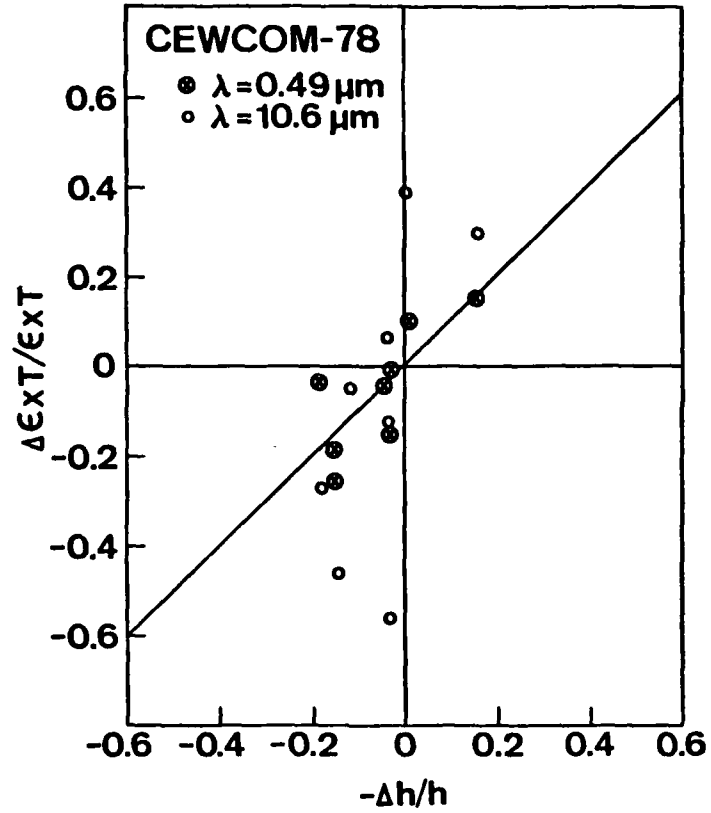


Figure 7 Fractional changes of aerosol extinction coefficient versus fractional changes in mixed layer height h for successive 4 hour periods.

DEPENDENCE OF AIR TO GROUND (LAND AND SEA) VISIBILITY
RANGES ON LOW FLIGHT ALTITUDES IN CONJUNCTION WITH
METEOROLOGICAL PARAMETERS

H.-E. Hoffmann

German Aerospace Research Establishment (DFVLR)
Institut für Physik der Atmosphäre
8031 Wessling-Oberpfaffenhofen, W. Germany

Summary

In outdoor tests the influence of different observation and environmental parameters on the visibility of objects observed from a helicopter was determined. During these tests it has also been researched how distances for detection, recognition and identification change for observations with the naked eye, when these observations are made from different altitudes in the lower atmosphere. In one case it showed up that an increase of the flight altitude by 100 m caused a decrease of the maximum identification range from 2 to 0.8 km, and of the maximum detection range from 15 to 13 km. This might be explained by layers of increased aerosol extinction within the range of temperature inversion or below the cumulus condensation level.

1. Introduction

A series of tests regarding the air to ground visibility has been made during the last few years. In these tests it was to be found out in which distance objects on the ground (land, water) can be detected, recognized and identified by an observer in an aircraft and how these visibility ranges are influenced by various observation and environmental parameters. By environmental parameters, among others, we understand:

- Inherent contrast of the observed object
against its background
- Surrounding (adaptation) luminance
- Sky-ground ratio
- Degree of turbidity of the atmosphere.

The environmental parameter "Degree of turbidity of the atmosphere" mentioned at last is one of the parameters having a strong influence on visibility of objects. It is subject to strong local and temporal fluctuations and usually also changes together with the altitude. The standard visibility (Middleton, 1963; Hoffmann, 1971; Hoffmann and Kuehnemann, 1979a) resp. the meteorological visibility (Ruppersberg and Schellhase, 1979) is a measure for the degree of turbidity of the atmosphere.

Fig. 1 shows how standard visibility between an aircraft flying in different altitudes and the ground can change. Here mean standard visibility air to ground up to an altitude of 5 km for the same airspace is shown, however at three different times. Values for the mean standard visibility have been calculated according to the values for the scattering coefficient for different altitudes found out by Duntley (Duntley, 1976). The scattering coefficient was measured by Duntley by means of a nephelometer installed in an aircraft. The values for the scattering coefficient thus measured in different altitudes were, by means of equation 1,

$$V_N(a) = 3,91/\sigma \quad (1)$$

$(V_N(a))$ = standard visibility in the altitude a (km).
 σ = scattering coefficient (km^{-1})

converted to values for the standard visibility in the different altitudes. The determination of a mean standard visibility \bar{V}_N between a certain altitude and the ground was then made by forming the arithmetic mean value from the individual values for the standard visibilities up to the respective altitude.

Whereas above a height of 2 km the mean standard visibility air to ground \bar{V}_N increases during the three test times in accordance with the height, the course of this standard visibility in dependence on the altitude below a height of 2 km varies considerably. In the one measurement (●) the mean standard visibility \bar{V}_N decreases up to a height of approx. 0.5 km, then remains nearly constant up to a height of 1 km. It then increases continuously in higher altitudes. The curve of the mean standard visibility \bar{V}_N in the measurement shown in Fig. 1 by (▲) is different. Here the mean standard visibility has approx. constant values in heights between 0 and 1.5 km, then increases together with the height. The third measurement in Fig. 1 (○) finally shows that the mean standard visibility from the ground to a maximum height of 5 km increases nearly continuously.

The tests made by the DFVLR yielded answers to quite special questions regarding the visibility air to ground (Hoffmann et al., 1979b; Hoffmann, 1979c). Some of the results obtained are used in the following in order to give statements as to which influence the flight altitude in connection with meteorological parameters has on the visibility of objects on the ground. The meteorological parameters thought of here are the vertical run of air temperature, altitude of temperature inversions and cumulus condensation levels.

2. Performance of the tests for determination of the visibility air to ground

Observers in a helicopter approaching in different altitudes the viewing objects on the ground, had to inform about the moments in which they could "just see" the respective object resp. in which they were able to "distinguish" certain details in the viewing object. By coordination these times to the flight path of the helicopter which was determined by means of a radar set, the maximum detection range, recognition range or identification range could then be calculated. The 4 or 5 observers in the helicopter

were placed to have normal sight so that their observation results were not influenced by a limited field of view, dirty windows or vibrations. All observation results given in the next paragraph have been found out with the naked eye, i.e. without using any special observation devices.

The meteorological parameters discussed here were measured either during the test sections that lasted up to 1 hour, in which observation flights were made, or shortly before or after them. The horizontal standard visibility on the ground was determined by contrast measurements of natural objects in different directions, in an approx. 20-minute rhythm (Hoffmann, 1971). Values for the air temperature in dependence on the altitude and the cloud base were found out by balloon ascents.

3. Test results

The following figures show the results of observations made from 3 - 6 different altitudes. Each point of these observation results - results for the maximum detection range, the maximum recognition range or the maximum identification range - represents a mean value of 3 - 5 individual values independent of each other. Each figure shows the result of a test section which lasted between 30 and 60 minutes.

In addition to the observation results also values for the mean standard visibility air to ground for different altitudes are given in each figure. The ground value here - i.e. the value for the altitude 0 km - is the one that in the tests was obtained for the standard visibility by contrast measurements at natural visibility objects, whereas the other values were calculated by means of equation (2):

$$V_N(a) = V_0 \cdot \exp(c \cdot a) \quad (2)$$

The meaning here is:

$$\begin{aligned} V_N(a) &= \text{standard visibility in the altitude } a \text{ (km)} \\ V_0 &= \text{standard visibility on the ground (km)} \\ c &= \text{constant} = 1 \\ a &= \text{altitude (km)} \end{aligned}$$

The calculations were based on the supposition that the scattering coefficient exponentially decreases in the planetary boundary layer along with the altitude in the ideal case, i.e. in an unstratified atmosphere with regard to temperature and aerosol concentration, resp. that standard visibility exponentially increases along with the altitude. This supposition was in one case confirmed by the course of the scattering coefficient measured by Duntley for different heights resulted in curve (o) of Fig. 1.

The assumption on exponentially increasing of standard visibility with the height here was made as - in contrast to the tests made by Duntley - the scattering coefficient resp. the standard visibility could not be measured directly for different height. The determination of the mean standard visibility between the height = 0 and the height a is then effected in the same way as for Fig. 1 by producing mean values out of the values for standard visibilities in the different heights. Besides the visual ranges and the mean standard visibilities between the ground and certain altitudes in the left part of Fig. 2 - 6, in the right parts of these figures the meteorological data regarded here, such as air temperature, cloud base, type of cloud, and degree of cloud, so far as existent, have been plotted.

Fig. 2 and 3 show visual ranges to be expected if the mean standard visibility air to ground V_N shows the plotted course. The maximum detection range when observing a ship increases (see Fig. 2) in a similar way as the mean standard visibility air to ground.

The maximum detection range when observing a truck, (see Fig. 3) however, at the beginning increases more than the mean standard visibility air to ground, but from a height of approx. 300 m the increase is rather unimportant.

The variable curve of the maximum detection ranges of Fig. 2 and 3 is due to the differing sizes of the objects observed and can be explained by physiologic-optical interrelationships regarding the contrast threshold of the human eye (Hoffmann 1972, 1976). During the tests of Fig. 3 the base of the clouds was somewhat above the heights up to which approaches were effected in order to determine the maximum detection ranges.

Contrary to the foregoing figures, the results of Fig. 4 to 6 for the visual ranges show curves which can not be explained by assumed exponential change of the standard visibility in dependence on the altitude and a therefrom resulting curve of the mean standard visibility air to ground. As physiologic-optical interrelationships do not furnish any explanation, too, only changes of the scattering coefficient resp. of the standard visibility along with the height and thus changes of the aerosol concentration can have been the reasons.

Three visual ranges that have been determined from 3 different altitudes are plotted in Fig. 4. On the one hand, the maximum identification range and the maximum detection range in observing a ship from a helicopter, and on the other hand the maximum detection range in observing this helicopter from the ship have been plotted. Up to a height of approx. 190 m the changes of the visual ranges correspond to the assumed course of the changes of the mean standard visibility V_N . Above 190 m two of the visual ranges plotted in Fig. 4 then become smaller. The increase of the aerosol concentration being the reason for this may be explained by the temperature inversion beginning at approx. 170 m and the cloud base situated in the same height.

The assumed changes of aerosol concentration in cloud condensation levels become even more apparent, and also more systematically, in the test results plotted in Fig. 5.

Cumulus clouds in a height of approx. 450 m and 600 m can be related to a decrease of the maximum identification range and the maximum detection range in observing a ship at an approach level of about 350 and 450 m; they can also be related to a constancy resp. to a decrease between approx. 600 and 750 m approach level. During these tests no temperature inversions were measured.

In the left half of Fig. 6 the maximum identification range observing a 1.5 t truck has been plotted for heights between 200 and 1000 m. Here the course between a height of approx. 750 m up to 1000 m shows a decrease of the maximum identification range. A temperature inversion has not been registered during these tests, either. The decrease of the maximum identification range most probably is due to the 3/8 stratocumulus clouds here as well, under which an increased aerosol concentration has developed.

4. Conclusions

Small changes of the flying altitude can cause stronger decreases of the visual ranges differing from the normal run of curve. For example, an increase of the flight altitude by about 100 m was able to cause a decrease of the maximum identification range from 2 to 0.8 km and of the maximum detection range from 15 to 13 km when observing a ship (see Fig. 5).

In the test results discussed in this report, the heights in which the changes of the visual ranges appeared were closely related to the height of the temperature inversion or the cloud condensation level. We have to lay emphasis on the fact that the observations in order to determine the visual ranges in the tests discussed here, were not made through the clouds, but in the cloudless interfaces.

Obviously the visual ranges were influenced by layers of increased aerosol concentration below temperature inversions or below cumulus condensation levels.

References

- | | |
|--|---|
| Duntley, S.Q. (1976) | Measured Visible Spectrum Properties of Real Atmospheres. AGARD Conference Proceedings No. 183 on Optical Propagation in the Atmosphere, Lyngby, Denmark, 27-31 October 1975, 39-1-19-14. |
| Hoffmann, H.-E. (1971) | Concerning some experiments obtained during the determination of the horizontal standard visibility by contrast measurements of natural targets. Royal Radar Establishment, Malvern, Wores. RRE. Translation No. 352. |
| Hoffmann, H.-E. (1972) | The visibility range when observing an aircraft with and without field-glasses. Optica Acta, Vol. 19, No. 5, 463-466. |
| Hoffmann, H.-E. (1976) | A Review of the most important established Facts about the Visibility (Maxim. Detection Range) of Aircraft. Royal Aircraft Establishment, Farnborough, Hants, Library Translation No. 1895. |
| Hoffmann, H.-E. (1979a)
Kuehnemann, W. | Comparison of the results of two measuring methods determining the horizontal standard visibility with the visual visibility range. Atmospheric Environment Vol. 13, No. 12, 1629-1634. |
| Hoffmann, H.-E. (1979b)
Buell, R.H.
Kuehnemann, W. | Summaries of some Reports of 1978 Concerning Results of Field Experiments for Visibility. DFVLR-Mitt. 79-11 (1979). |
| Hoffmann, H.-E. (1979c) | Influence of the flight altitude and limitation of the field of view on the visibility of targets on the ground and the maximum visibility flight altitude.
European Space Agency
ESA-TT-654, 1980. |
| Middleton, W.E.K. (1963) | Vision through the Atmosphere. Toronto, University of Toronto Press, 250 pp. |
| Ruppersberg, G.H. (1979)
Schellhase, R. | Slant meteorological visibility. Optica Acta, Vol. 26, No. 5, 699-709. |

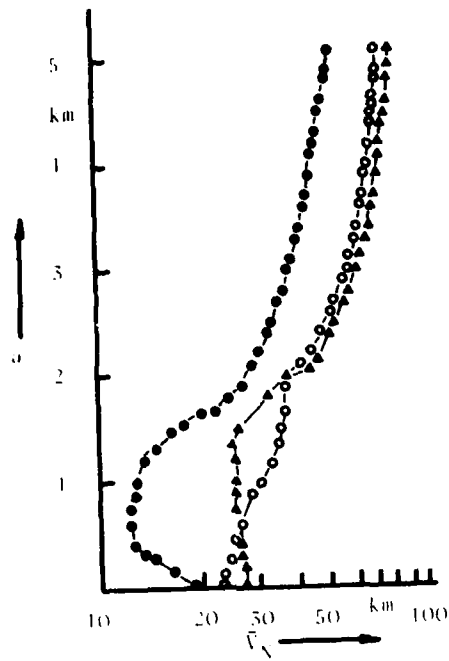


Fig. 1

the mean standard visibility \bar{V}_N between different altitudes a and the ground for three test periods ●▲○ derived from measurements by Duntley, 1970

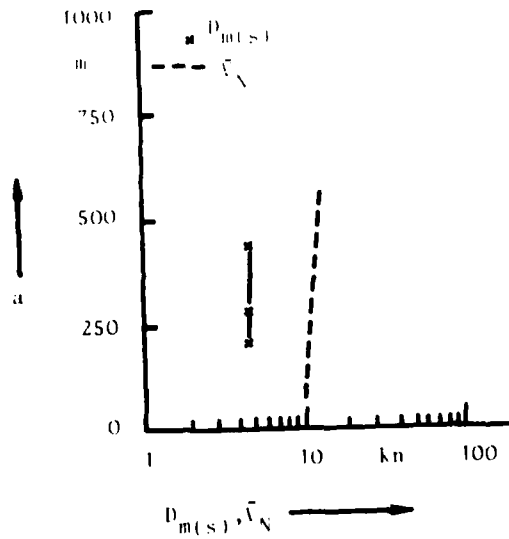


Fig. 2

The maximum detection range $D_{m(s)}$ when observing a ship and the mean standard visibility \bar{V}_N for different altitudes a

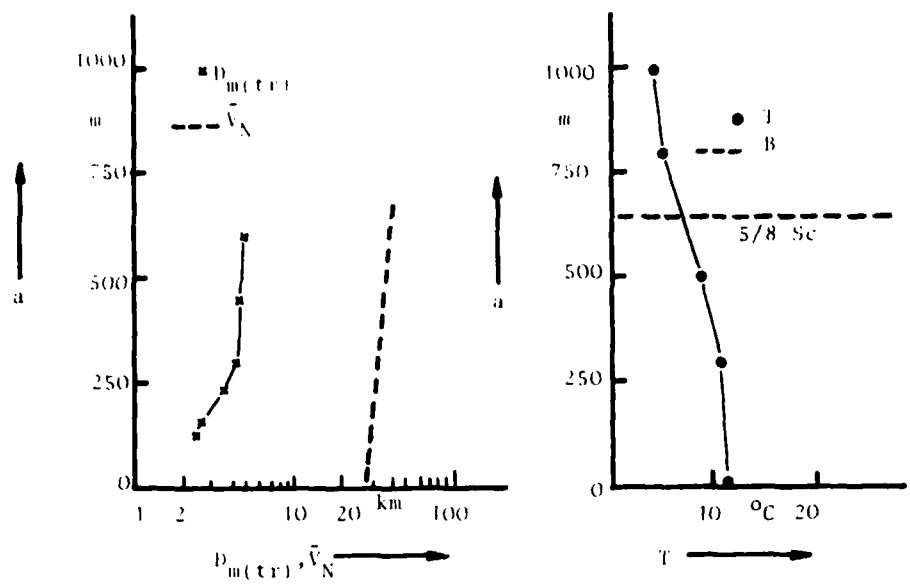


Fig. 3

The maximum detection range $D_{m(tr)}$ when observing a LSt-truck, the mean standard visibility \bar{V}_N , and the temperature T for different altitudes a and the base of clouds B

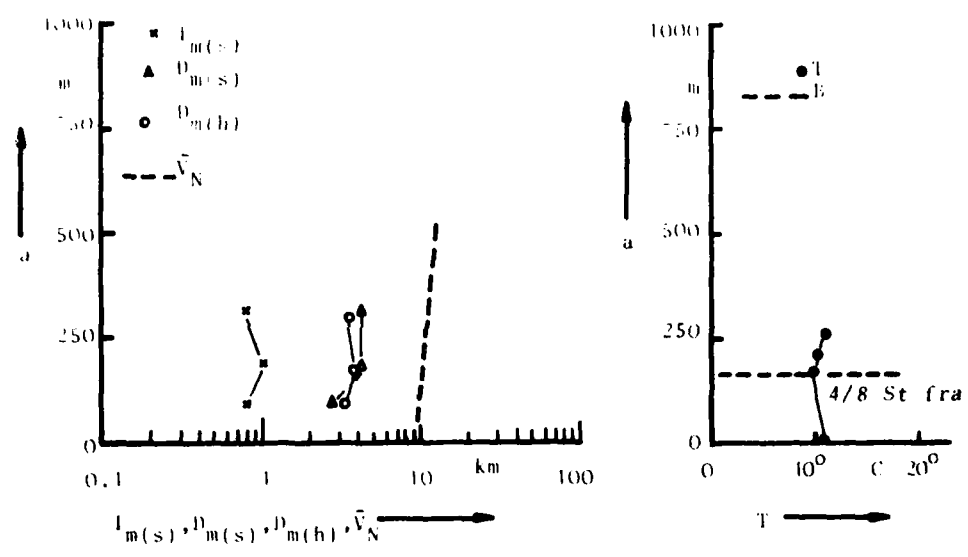


Fig. 4

The maximum identification range $I_{m(s)}$ and the maximum detection range $D_{m(s)}$ when observing a ship, the maximum detection range when observing a helicopter $D_{m(h)}$, the mean standard visibility \bar{V}_N , and the temperature T for different altitudes a and the base of clouds B

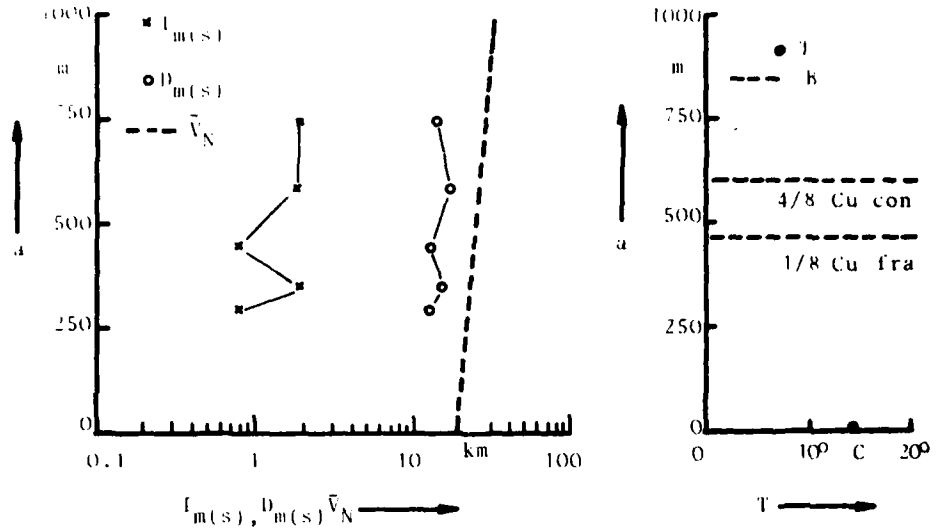


Fig. 5

the maximum identification range $I_m(s)$ and the maximum detection range $D_m(s)$ when observing a ship and the mean standard visibility \bar{V}_N for different altitudes a and the base of clouds B

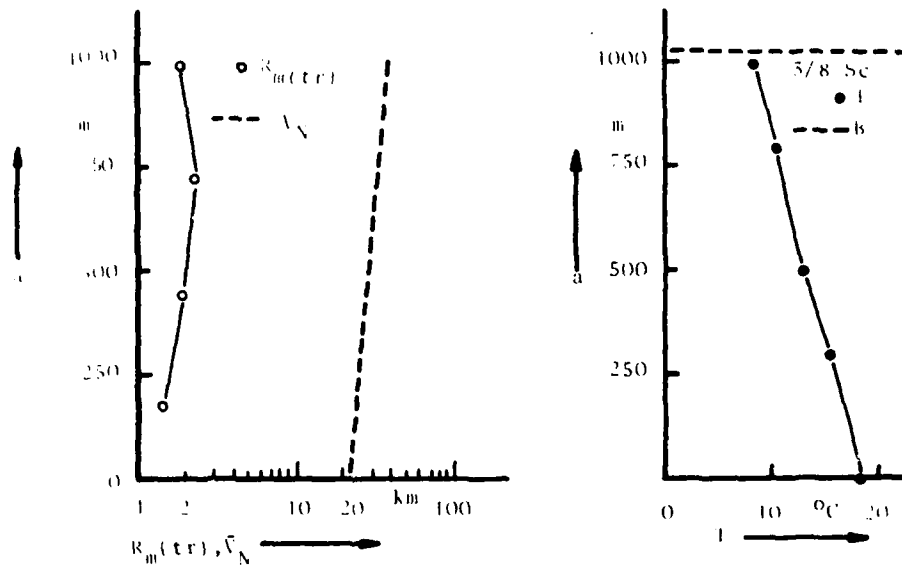


Fig. 6

the maximum recognition range $R_m(tr)$ when observing a 1.5t-truck the mean standard visibility \bar{V}_N , and the temperature T for different altitudes a and the base of clouds B

DETERMINATION DES PERFORMANCES D'UN SYSTEME COAT

EN REGIME DE POURSUITE**

G. ROGER

Laboratoires de Marcoussis
Centre de Recherches
de la Compagnie Générale d'Electricité
F - 91460 MARCOUSSIS

** Travail réalisé sous contrats D.R.E.T. 78/133 et 79/204.

SUMMARY

The paper concerns the computation of the performances of a COAT system when the phase tracking is operating. Phases errors are detected by "dithering" so the system uses two deformable mirrors of any type, one for correction, one for modulation. We suppose that the phase errors which must be corrected, the characteristics of the mirrors used for correction and modulation, the noise spectral density of the receiver and the gain matrix are known. We determine an expression which represents the gain loss due to the phase errors and we define a vector space of surfaces with an inner product such that the loss appears as the squared norm of a vector in that space. Changing the basis of the vector space permits to express the shape of the wave front as a combination of simple shapes, which may guide the choice of the mirrors structure. We compute the minimal loss corresponding to the correcting mirror, then the loss corresponding to the combination of the correcting mirror and the modulating mirror. At last, we introduce the gain matrix and obtain the general loop equation of the complete system.

RESUME

L'exposé est consacré au calcul des performances d'un système COAT en régime de poursuite. Le système est à miroirs déformables de type quelconque. La détection des erreurs de phase se fait par modulation (dithering). On suppose que l'on connaît les erreurs de phase à compenser, les équations des déformées des miroirs de correction et de modulation, la densité spectrale du bruit du récepteur et la matrice de gain. On détermine une expression caractéristique de la perte de gain due aux erreurs de phase. On définit un espace vectoriel de surfaces muni d'un produit scalaire tel que la perte de gain apparaît comme le carré de la norme d'un vecteur de cet espace. Les changements de base permettent d'interpréter la forme d'une surface comme une superposition de formes simples, ce qui peut guider le choix de la structure des miroirs. On calcule la perte minimale correspondant aux déformées du miroir de correction, puis celle qu'autorise l'association du miroir correcteur et du miroir de modulation. Enfin, on fait intervenir la matrice de gain et l'on aboutit aux formules générales du système asservi.

NOTATIONS

Elles sont précisées dans le texte. Voici les principales.

σ	surface de l'ouverture (normée à 1)	\vec{a}, \vec{b}	vecteurs de composantes a_i, b_i
$e(m)$	champ relatif au point m de l'ouverture	\vec{e}^T	vecteur transposé de \vec{e}
$\epsilon(m)$	phase au point m de l'ouverture	$\vec{\epsilon}^*$	vecteur transposé conjugué de \vec{e}
$q(\epsilon)$	perte relative liée à la phase	$\bar{q}(\epsilon)$	le trait supérieur désigne la valeur moyenne, donc : valeur moyenne de $q(\epsilon)$
$\vec{\varphi}, \vec{\psi}, \vec{\theta}, \vec{e}$	vecteurs représentant des phases $\varphi(m)$, etc., mesurées sur l'ouverture	$ \vec{\theta} \vec{\theta}^T $	matrice de covariance de θ
\vec{u}	vecteur correspondant au plan de cote 1 par rapport à l'ouverture	$ \vec{\theta} \vec{\theta}^* $	transformée de Fourier de la précédente
$\vec{\delta}_i$	vecteur de la base initiale où sont représentés les vecteurs précédents	Φ, Ψ	matrices des vecteurs correspondant aux déformées de R1 et R2, respectivement
$B(\varphi), E(\varphi)$	base et sous-espace vectoriels correspondant à un ensemble de vecteurs $\vec{\varphi}_i$	G	matrice de gain
$\vec{\varphi}', \vec{e}'$	le " ' " désigne la valeur centrée si c'est nécessaire	$ \Psi^T \Phi ^{-1}$	inverse du produit des matrices Ψ^T et Φ
		$ \Psi^T \Phi ^{-}$	inverse généralisée
		\vec{e}_r, \vec{v}	vecteur d'erreur et vecteur de bruit

1. INTRODUCTION

La figure 1 représente le schéma d'un système optique auto-adaptatif (COAT) dont le but est de concentrer sur une cible ponctuelle T la puissance émise par le laser L. La longueur des chemins optiques compris entre la surface d'onde Σ , en sortie du laser, et la cible peut être perturbée par des déformations de Σ , par les turbulences atmosphériques, ou par des défauts du système.

Le miroir R1, dont la surface peut être déformée sous l'action des signaux de commande a_j (notés \vec{a} sur la figure) a pour rôle de compenser ces perturbations.

Le miroir R2 est destiné à mettre en évidence les erreurs de phase. Il est déformé sous l'action des signaux b_j (notés \vec{b}). Ces signaux sont orthogonaux entre eux, c'est-à-dire que la moyenne $b_j(t) \cdot b_k(t)$, calculée sur un court intervalle de temps, est nulle si $j \neq k$. Ce sont par exemple des signaux sinusotiaux de fréquences différentes, ou des impulsions survenant à des instants distincts, etc. Ils sont fournis par un générateur (Mod).

Le récepteur optique "Rec" capte une fraction de la puissance réémise par la cible. Une batterie de démodulateurs (indiqués par des "x"), alimentés par les mêmes signaux b_j , permet d'extraire les signaux d'erreur E_j (notés \vec{E}_r) à partir du signal détecté.

Une matrice de commande G complète le système.

Les miroirs R1 et R2 peuvent être construits de différentes façons :

- ensemble de miroirs plans contigus déplacés par des moteurs piézo-électriques ;
- membrane souple déformée par des "actuateurs" ;
- combinaison d'un miroir déformable et d'un miroir plan orientable, etc.

Nous supposons que toute commande a_j ou b_j provoque une déformation proportionnelle à son amplitude, et que les déformations s'ajoutent linéairement.

Dans certaines réalisations, les fonctions attribuées à R1 et R2 sont assurées par un seul miroir déformable, ce qui est préférable théoriquement, mais peut conduire à des difficultés techniques puisque R1 doit subir des déformations lentes (quelques dizaines ou centaines de hertz) mais d'amplitude notable (quelques longueurs d'onde), alors que R2 sera appelé à vibrer avec des amplitudes d'une fraction de longueur d'onde, mais à des fréquences plus élevées.

Notre but est d'analyser le comportement du système et d'en évaluer les performances lorsque l'asservissement fonctionne, c'est-à-dire lorsque les erreurs de phase sont faibles.

2. DEFINITION DE LA PERTE RELATIVE

Soit $\epsilon(m)$ la phase traduisant le chemin optique parcouru par le rayon passant au point m de l'ouverture S. La perte de gain due aux erreurs de phase ϵ est mesurée par la quantité $q(\epsilon)$ telle que :

$$1 - q(\epsilon) = \frac{\int_S \mathcal{E}(m_1) e^{j\epsilon(m_1)} dS_1 \cdot \int_S \mathcal{E}(m_2) e^{-j\epsilon(m_2)} dS_2}{\left[\int_S \mathcal{E}(m) dS \right]^2}$$

si $q(\epsilon) = 0,25$, par exemple, la perte est de 1 dB (\mathcal{E} est le champ sur l'ouverture).

On pose :

$$\frac{dS}{S} = d\sigma \quad \text{donc} \quad \int_{\sigma} d\sigma = 1$$

et :

$$e_i = e(\epsilon_i) = \frac{\mathcal{E}(m_i)}{\frac{1}{S} \int_S \mathcal{E} dS} \quad \text{donc} \quad \int_{\sigma} e d\sigma = 1$$

d'où :

$$1 - q = \iint_{\sigma} e_1 e_2 e^{j(\epsilon_1 - \epsilon_2)} d\sigma_1 d\sigma_2$$

Lorsque le système fonctionne correctement, l'écart $\epsilon_1 - \epsilon_2$ est petit quels que soient m_1 et m_2 . Alors, en développant l'exponentielle,

$$q(\epsilon) \neq \frac{1}{2} \iint_{\sigma} e_1 e_2 (\epsilon_1 - \epsilon_2)^2 d\sigma_1 d\sigma_2 \quad (2.1)$$

$$= \int_{\sigma} e_1 \left(\epsilon_1 - \int_{\sigma} e_2 \epsilon_2 d\sigma_2 \right)^2 d\sigma_1 \quad (2.2)$$

L'équation (2.1) montre que $q(\epsilon)$ est indépendant de l'origine des phases et l'équation (2.2) que c'est la moyenne quadratique centrée de la phase ϵ , pondérée par le champ relatif e . Si l'on choisit l'origine des phases de façon que $\int_{\sigma} e \epsilon d\sigma = 0$,

$$q = \int_{\sigma} e \epsilon^2 d\sigma \quad (2.3)$$

3. INTERPRETATION VECTORIELLE

Nous donnerons à $q(\epsilon)$ une autre interprétation en considérant que l'ensemble des surfaces de contour σ , associé au corps des réels, constitue un espace vectoriel. Nous noterons par exemple $\vec{\epsilon}$ l'ensemble des valeurs $\epsilon(m)$. D'autre part, nous munissons cet espace vectoriel d'un produit scalaire en posant :

$$\int_{\sigma} e(m) \varphi(m) \psi(m) d\sigma = \vec{\varphi} \cdot \vec{\psi} \quad (3.1)$$

$\varphi(m)$ et $\psi(m)$ représentant deux surfaces quelconques.

Ainsi on a, par exemple, \vec{u} désignant la surface d'onde de cote égale à 1 sur σ :

$$\int_{\sigma} e_2 \epsilon_2 d\sigma_2 = \int e_2 \epsilon_2 \cdot 1 d\sigma = \vec{\epsilon} \cdot \vec{u}$$

La formule (2.2) s'écrit alors :

$$q(\epsilon) = \left[\vec{\epsilon} - (\vec{\epsilon} \cdot \vec{u}) \vec{u} \right]^2 \quad (3.2)$$

et si $\vec{\epsilon}$ est centré ($\vec{\epsilon} \cdot \vec{u} = 0$), l'expression (2.3) devient :

$$q(\epsilon) = \vec{\epsilon}^2 \quad (3.3)$$

$q(\epsilon)$ est le carré de la distance de l'extrémité du vecteur $\vec{\epsilon}$ à la droite qui porte \vec{u} (figure 2) (la formule (2.1) l'exprime comme le carré de la norme du produit extérieur $\vec{u} \wedge \vec{\epsilon}$). La valeur centrée de $\vec{\epsilon}$ (marquée $\vec{\epsilon}'$ sur la figure) est la projection de $\vec{\epsilon}$ sur le plan orthogonal à \vec{u} . Dans une base constituée de \vec{u} et de vecteurs $\vec{\varphi}_i$ qui lui sont orthogonaux, seules les composantes de $\vec{\epsilon}$ suivant ces derniers interviendront dans le calcul. De telles bases seront dites "centrées" ($\vec{\varphi}_i \cdot \vec{u} = 0$).

4. BASES

4.1. Généralités

Une base est un ensemble de surfaces d'équation $z = \varphi_i(m)$ à partir desquelles on peut construire la famille de surfaces :

$$z = \epsilon(m) = \sum a_j \varphi_j(m)$$

relation qu'on écrira :

$$\vec{\epsilon} = \sum a_j \vec{\varphi}_j$$

Les coefficients a_j sont les coordonnées (contravariantes) de $\vec{\epsilon}$ dans la base φ_j . Nous noterons B (φ) et E (φ) la base et le sous-espace relatifs à l'ensemble des vecteurs $\vec{\varphi}_j$.

Par exemple, la déformation que subit le miroir R1 (ou R2) lorsqu'une de ses commandes est positionnée à 1 et les autres à 0 est un vecteur de base et l'ensemble de ces déformations engendre un sous-espace qui contient toutes les formes que peut prendre R1 (ou R2).

Les vecteurs de la base sont dépendants s'il existe des nombres α_i non nuls tels que $\sum \alpha_j \vec{\varphi}_j = \sum \alpha_j \varphi_j(m) = 0$, c'est-à-dire si une combinaison des surfaces représente le plan de cote nulle.

Si les équivalents centrés $\vec{\varphi}_i$ des vecteurs ou surfaces de base sont dépendants, alors ces surfaces permettent de représenter le plan de cote constante.

Une base est orthogonale si $\vec{\varphi}_i \cdot \vec{\varphi}_j = \int e \varphi_i \varphi_j d\sigma = 0$ pour $i \neq j$. Elle est orthonormée si $\vec{\varphi}_i \cdot \vec{\varphi}_j = \delta_{ij}$.

Notons que deux surfaces "orthogonales" ne sont pas en général "perpendiculaires" au sens géométrique du terme.

4.2. Base initiale

La base que nous considérerons en premier est celle qui permet de représenter les surfaces par leurs cotes en différents points de σ . Elle est indispensable pour effectuer les calculs numériques. Nous supposons, par exemple, qu'elle est constituée d'un ensemble de surfaces δ_i , qui sont des prismes de hauteur d_i , élevés sur N éléments égaux σ_i d'une partition de σ . Les surfaces δ_i sont évidemment orthogonales. La base est orthonormée si l'on choisit les hauteurs d_i de façon telle que :

$$\int_{\sigma_i} e d_i^2 d\sigma = d_i^2 \int_{\sigma_i} e d\sigma = d_i^2 e_i \sigma_i = \frac{d_i^2 e_i}{N} = 1$$

e_i étant la valeur moyenne de e à l'intérieur de σ_i .

Elle est "incomplète" dans la mesure où elle est de dimension finie et ne permet pas de représenter n'importe quelle surface. Nous dirons qu'elle est suffisante, si pour tout vecteur \vec{e} intervenant dans nos calculs, la valeur minimale q_{\min} de :

$$q(\vec{e} - \sum a_i \delta_i^*)$$

qui s'obtient pour un choix convenable des a_i , est inférieure à une limite déterminée.

Les surfaces $\sum a_i \delta_i^*$ sont évidemment définies à une translation près.

Nous choisissons celle qui est centrée, pour laquelle

$$a_i = \frac{\delta_i^* \vec{e}'}{\delta_i^{*2}}$$

avec

$$q_{\min} = e'^2 - \sum \frac{(\vec{e}' \cdot \delta_i^*)^2}{\delta_i^{*2}}$$

Remarque

Ces formules s'appliquent pour toute base orthogonale permettant de représenter le plan de cote constante.

Fin de remarque

Dans le cas particulier de l'ensemble de prismes $B(\delta)$ que nous avons décrit, on obtient :

$$a_i = e'_i \sqrt{\frac{e_i}{N}}$$

et

$$q_{\min} = \sum_i \int_{\sigma_i} e' \left(e - \frac{\int_{\sigma_i} e d\sigma}{\int_{\sigma_j} e d\sigma} \right)^2 d\sigma$$

où e'_i et e_i sont des valeurs moyennes de e et e dans l'élément σ_i . On notera que les coordonnées a_i sont proportionnelles à la phase au point i et à la racine carrée du champ relatif en ce point.

La valeur q_{\min} est la somme des pertes relatives aux divers éléments de surface σ_i .

4.3. Notations et formules

Par la suite, nous ne distinguerons plus les vecteurs de l'espace des surfaces de leur représentation "centrée" dans $B(\delta_i)$ et \vec{e} , par exemple, désignera la matrice à une colonne des coordonnées du vecteur dans cette base. La matrice transposée sera notée \vec{e}^T .

On écrira la perte $q(\epsilon)$ sous deux formes, qui présentent chacune leurs avantages :

$$q(\epsilon) = \vec{e}^T \vec{e} \quad \text{ou} \quad q(\epsilon) = T_r(\vec{e} \vec{e}^T) \quad (T_r = \text{Trace de})$$

et sont équivalentes à $q(\epsilon) = \sum a_i^2$.

Au vecteur fonction du temps $\vec{e}(t) = \sum a_i(t) \delta_i^*$ correspondent les transformées de Fourier, Laplace, en z , etc., telles que, par exemple :

$$\vec{e}(\omega) = \sum a_i(\omega) \delta_i^*$$

où $a(\omega)$ est la transformée de Fourier de $a_i(t)$. \vec{e}^{*} désignera la transposée conjuguée.

L'espérance mathématique de q s'écrira \bar{q} et pourra être calculée à partir de la densité spectrale de ses coordonnées :

$$\begin{aligned} \bar{q} &= \int_{-\infty}^{+\infty} \sum_i a_i(\omega) a_i^*(\omega) \frac{d\omega}{2\pi} \\ &= \int_{-\infty}^{+\infty} \overline{\epsilon(\omega)^* \epsilon(\omega)} \frac{d\omega}{2\pi} = \int_{-\infty}^{+\infty} T_r \left(\overline{\epsilon(\omega)^* \epsilon(\omega)} \right) \frac{d\omega}{2\pi} \end{aligned}$$

4.4. Changements de base. Représentation des perturbations

En général, les perturbations que le système COAT doit corriger sont connues dans $B(\delta)$, c'est-à-dire que l'on dispose d'une mesure des phases θ_j aux différents points de l'ouverture du système, ou de l'intercorrélation $\theta_j(\bar{t}) \theta_j(\bar{t} - \tau)$ entre deux points distincts, ou de la densité spectrale $\theta_j(\omega) \theta_j^*(\omega)$, transformée de Fourier de la précédente. Les changements de base nous permettent d'exprimer ces perturbations comme une superposition de déformations d'allure simple, par exemple : inclinaison d'un plan d'onde, sphéricité, etc., d'amplitude variable dans le temps. Souvent, le nombre des surfaces qui interviennent de façon significative est inférieur au nombre N des points donnés initialement. On pourra ainsi avoir une représentation simplifiée et imagée du phénomène à compenser et on en déduira le nombre et la forme des surfaces correctrices à introduire dans le miroir R1. Les coordonnées du vecteur $\bar{\theta}$ dans la nouvelle base représenteront les amplitudes des corrections à apporter. La densité spectrale de ces coordonnées indiquera la bande passante que doit couvrir l'asservissement, la puissance nécessaire à la commande du miroir, etc. Les bases les plus agréables à manier sont orthonormées et "centrées".

Nous supposons dans ce qui suit que le vecteur $\bar{\theta}$ représentant le front d'onde perturbé est "centré" ($\bar{\theta} \cdot \bar{u} = 0$).

La nouvelle base, constituée de N vecteurs $\bar{\psi}_j$, est représentée par la matrice carrée ϕ , dont les colonnes sont les coordonnées des $\bar{\psi}_j$ dans $B(\delta_j)$, donc :

$$\bar{\theta} = \sum_j b_j \bar{\psi}_j = \phi \bar{b}$$

\bar{b} étant le vecteur des nouvelles coordonnées. Si ϕ est régulière, $\bar{b} = \phi^{-1} \bar{\theta}$.

Les éléments de la matrice $|\bar{b} \bar{b}^T| = \phi^{-1} |\bar{\theta} \bar{\theta}^T| \phi^{-1 T}$ ou $|\bar{\theta} \bar{\theta}^T|$ est la matrice de covariance des perturbations, fournissent les covariances des nouvelles coordonnées et ceux de la matrice $|\bar{b} \bar{b}^*| = \phi^{-1} |\bar{\theta} \bar{\theta}^*| \phi^{-1 T}$ leurs densités spectrales.

Si la nouvelle base est orthonormée, $\phi^T \phi = 1$ $|\bar{b} \bar{b}^T| = \phi^T |\bar{\theta} \bar{\theta}^T| \phi$ alors $q = \tau_r |\bar{\theta} \bar{\theta}^T| = \tau_r |\bar{b} \bar{b}^T|$ et l'on obtient directement la participation de chaque surface de base à la perte totale, par exemple dépointage, convergence, etc. On en déduira le nombre de surfaces correctrices que doit comporter le système pour ramener la perte à une valeur acceptable.

En particulier, si les surfaces de base correspondent aux vecteurs propres de la matrice $|\bar{\theta} \bar{\theta}^T|$, alors la matrice $|\bar{b} \bar{b}^T|$ se réduit à une matrice diagonale constituée des valeurs propres de $|\bar{\theta} \bar{\theta}^T|$. Ce cas présente l'intérêt, au moins théorique, de permettre le maximum de correction avec le minimum de surfaces. Il permet surtout, comme nous le disons, d'avoir une représentation très condensée des caractéristiques du phénomène à corriger.

A titre d'exemple, les figures 3 a, 3 b et 3 c donnent les formes de surfaces propres, leur participation à la perte totale, et les densités spectrales obtenues pour un cas très simple, celui de cinq points alignés recevant une onde qui a traversé une atmosphère perturbée.

5. SURFACES CORRECTRICES

Soit $\bar{\psi}_j$ le vecteur correspondant à la déformation que subit le miroir R1 sous l'action de la commande a_j positionnée à 1. L'ensemble des déformées $\bar{\psi}_j$, en nombre M , constitue une base. Nous appelons ϕ la matrice à N lignes et M colonnes ($M < N$) constituées des coefficients des vecteurs $\bar{\psi}_j$ dans $B(\delta)$, \bar{a} le vecteur des commandes a_j . Les vecteurs de $E(\psi)$ s'écrivent alors :

$$\sum a_j \bar{\psi}_j = \phi \bar{a}$$

La perte liée à la perturbation $\bar{\theta}$ compensée par R1 est :

$$q = (\bar{\theta} - \phi \bar{a})^2 = (\bar{\theta}^T - \bar{a}^T \phi^T) (\bar{\theta} - \phi \bar{a})$$

On cherche le vecteur \bar{a} qui minimise q , ce qui permettra de connaître l'efficacité de R1.

La condition d'extremum s'écrit :

$$d \bar{a}^T (\phi^T \phi \bar{a} - \phi^T \bar{\theta}) = 0$$

Si la matrice $\phi^T \phi$ est régulière :

$$\bar{a} = |\phi^T \phi|^{-1} \phi^T \bar{\theta} \quad \text{et} \quad \phi \bar{a} = \phi |\phi^T \phi|^{-1} \phi^T \bar{\theta} = P \bar{\theta}$$

$P = \phi |\phi^T \phi|^{-1} \phi^T$ est un projecteur ($P^2 = P$), $\phi \bar{a}$ est la projection orthogonale de $\bar{\theta}$ sur $E(\psi)$, $\phi^T \phi$ est le tenseur fondamental de ce sous-espace, q est le carré de la différence entre $\bar{\theta}$ et sa projection $P \bar{\theta}$.

La valeur minimale de q est :

$$q = \bar{\theta}^T (1 - P) \bar{\theta} = \tau_r ((1 - P) |\bar{\theta} \bar{\theta}^T| (1 - P))$$

d'où

$$\bar{q} = \tau_r ((1 - P) |\bar{\theta} \bar{\theta}^T| (1 - P))$$

expression qui fait intervenir la matrice de covariance $|\bar{\theta} \bar{\theta}^T|$. La perte résiduelle est nulle si la base est complète ou si $\bar{\theta}$ est dans $E(\psi)$.

Si les vecteurs $\vec{\varphi}_i$ sont orthonormés, $\Phi^T \Phi = \mathbb{1}_M$ (matrice unité de rang M). Alors :

$$\begin{aligned} q &= \vec{\delta}^T \vec{\delta} - \vec{\delta}^T \Phi \Phi^T \vec{\delta} = \text{Tr} \left(\vec{\delta} \vec{\delta}^T - \Phi^T \vec{\delta} \vec{\delta}^T \Phi \right) \\ &= \sum_{i=1}^N a_i^2 - \sum_{j=1}^M b_j^2 \end{aligned}$$

où a_i est la coordonnée de $\vec{\delta}$ dans B (δ) et b_j la coordonnée de $\vec{\delta}$ dans B (φ).

Si la matrice $\Phi^T \Phi$ est singulière, c'est que les vecteurs $\vec{\varphi}_i$ ne sont pas indépendants. Il existe alors un vecteur $\vec{\alpha}$ non nul tel que $\Phi \vec{\alpha} = 0$, c'est-à-dire que E (φ) contient le plan de cote nulle.

Le cas n'est pas "pathologique". C'est par exemple celui des systèmes COAT à miroir segmenté. Il suffit alors de remplacer $|\Phi \Phi^T|^{-1}$ par $|\Phi^T \Phi|^{-1}$, inverse généralisée, obtenue en inversant les valeurs propres non nulles de $|\Phi^T \Phi|$. On a alors la solution particulière :

$$\vec{a} = |\Phi^T \Phi|^{-1} \Phi^T \vec{\delta}$$

telle que :

$$\vec{\alpha}^T \vec{a} = 0$$

car $\vec{\alpha}^T$, comme \vec{a} , est vecteur propre de $|\Phi^T \Phi|^{-1}$ avec la valeur propre zéro, de même qu'il est vecteur propre de $|\Phi^T \Phi|$ avec la même valeur zéro.

En résumé, B (φ) doit être choisie pour que les vecteurs $\vec{\delta}$ en soient "proches". Ce choix est facilité par l'étude de l'espace des $\vec{\delta}$ dont les principes ont été décrits précédemment. La perte résiduelle instantanée ou moyenne s'obtient ensuite à l'aide des diverses formules que nous avons données.

6. SIGNAUX D'ERREUR

6.1. Extraction des signaux d'erreur

Soit $\vec{\psi}_i$ l'ensemble des M surfaces utilisées pour l'obtention des signaux d'erreur. Chacune est déplacée par un signal $b_i(t)$. Nous appelons Ψ la matrice constituée par les m vecteurs colonne $\vec{\psi}_i$ et \vec{b} le vecteur ayant les b_i pour coordonnées. Nous ajoutons la distorsion de phase causée par les $\vec{\psi}_i$ et la distorsion $\vec{\epsilon}$, et nous obtenons :

$$\begin{aligned} q(\vec{\epsilon} + \Psi \vec{b}) &= (\vec{\epsilon} + \Psi \vec{b})^T (\vec{\epsilon} + \Psi \vec{b}) \\ &= \vec{\epsilon}^2 + 2 \vec{b}^T \Psi^T \vec{\epsilon} + \vec{b}^T \Psi^T \Psi \vec{b} \end{aligned}$$

Nous négligeons le dernier terme écrit, car $b_i(t)$ est petit.

q est contenu dans le signal fourni par le récepteur optique, que nous multiplions par \vec{b} dans la batterie de démodulateurs. Nous supposons que les signaux sont orthogonaux, c'est-à-dire par exemple que :

$$\overline{b_i(t) b_j(t)} = \frac{\delta_{ij}}{2}$$

et de moyenne nulle ($\overline{b_i(t)} = 0$), les moyennes étant calculées sur un temps court par rapport aux temps de réponse du système. L'intégration nécessaire au calcul de cette moyenne est assurée par un filtre qui peut être intégré au réseau de commande et nous considérerons donc que les signaux issus des démodulateurs constituent le vecteur d'erreur :

$$\vec{\epsilon}_r = \overline{q \vec{b}} = \vec{\epsilon}^2 \vec{b} + \vec{b} \vec{b}^T \Psi^T \vec{\epsilon} = \Psi^T \vec{\epsilon} \quad (6.1)$$

dont les composantes sont les projections de $\vec{\epsilon}$ sur les différents vecteurs $\vec{\psi}_i$. En particulier, si les vecteurs $\vec{\psi}_i$ sont identiques aux vecteurs de correction $\vec{\varphi}_i$ (miroirs R1 et R2 identiques), on est en mesure d'annuler la projection de $\vec{\epsilon}$ sur l'espace des $\vec{\varphi}_i$ et d'obtenir la perte minimale que permet le miroir R1.

Le vecteur $\vec{\epsilon}$ contient la perturbation à compenser, $\vec{\delta}$, et l'effet correcteur du miroir R1. On a donc :

$$\vec{\epsilon}_r = \Psi^T (\vec{\delta} - \Phi \vec{a})$$

6.2. Annulation des erreurs

Le vecteur d'erreur sera nul si $\Psi^T \Phi \vec{a} = \Psi^T \vec{\delta}$ d'où, si $|\Psi^T \Phi|$ est régulière :

$$\vec{a} = |\Psi^T \Phi|^{-1} \Psi^T \vec{\delta} \quad (6.2)$$

et

$$\vec{\epsilon} = \vec{\delta} - \Phi |\Psi^T \Phi|^{-1} \Psi^T \vec{\delta} = (\mathbb{1} - Q) \vec{\delta} \quad (Q \text{ est, comme } P, \text{ un projecteur}).$$

Si elle ne l'est pas, c'est qu'il existe (au moins) un vecteur $\vec{\alpha}$ et un vecteur $\vec{\beta}$, non nuls, tels que :

$$|\Psi^T \Phi| \vec{\alpha} = 0 \quad \text{et} \quad \vec{\beta}^T |\Psi^T \Phi| = 0$$

Les éléments de $|\Psi^T \Phi|$ sont $\psi_i^* \cdot \varphi_j$, donc :

$$\psi_i^* \cdot \sum \varphi_j \alpha_j = 0 \quad \text{et} \quad (\sum \beta_i \psi_i^*) \varphi_j = 0 \quad (6.3)$$

Donc, ou bien :

- B (φ) ou B (ψ), ou les deux, sont de dimension inférieure à M (vecteurs dépendants). Si le rang de B (φ) est inférieur à celui de B (ψ) il est impossible d'annuler les erreurs : on ne dispose pas d'un nombre suffisant de paramètres indépendants. Si c'est le contraire, il faut imposer une contrainte aux commandes car on a un paramètre en trop par rapport au nombre de signaux d'erreur (on peut alors utiliser l'inverse généralisée de $\Psi^T \Phi$ pour déterminer \hat{a}) ;
- ou encore, il existe un vecteur de E (φ) orthogonal à E (ψ), donc "invisible" pour le système de détection d'erreur, ce qui est fâcheux.

7. ASSERVISSEMENT

7.1. Equations des boucles

Il reste, pour finir, à "boucler la boucle".

Avant de le faire, nous devons tenir compte du bruit du récepteur en ajoutant au vecteur d'erreur un vecteur de bruit, \vec{v} , auquel on peut attribuer des propriétés simplificatrices : moyenne nulle et matrice de covariance diagonale. On a donc :

$$\vec{e}_r = \Psi^T (\vec{\theta} - \Phi \hat{a}) + \vec{v}$$

On ferme la boucle grâce à la matrice G en écrivant :

$$\hat{a} = G \cdot \vec{e}_r = G \left[\Psi^T (\vec{\theta} - \Phi \hat{a}) + \vec{v} \right]$$

ce qui sous-entend que les grandeurs sont fonction de p, ω ou z. Donc :

$$\left(\Pi + G \Psi^T \Phi \right) \hat{a} = G \Psi^T \vec{\theta} + G \vec{v}$$

et si

$\Pi + G \Psi^T \Phi$ n'est pas singulière,

$$\hat{a} = \left(\Pi + G \Psi^T \Phi \right)^{-1} \left(G \Psi^T \vec{\theta} + G \vec{v} \right)$$

d'où finalement l'erreur de phase résiduelle sur l'ouverture :

$$\begin{aligned} \vec{e} &= \vec{\theta} - \Phi \hat{a} \\ \vec{e} &= \vec{\theta} - \left(\Pi + G \Psi^T \Phi \right)^{-1} G \Psi^T \vec{\theta} + \left(\Pi + G \Psi^T \Phi \right)^{-1} G \vec{v} \end{aligned} \quad (7.1)$$

Les conditions de stabilité sont bien connues. Il est nécessaire par exemple que les valeurs de p, racines du déterminant de $\Pi + G \Psi^T \Phi$ aient leurs parties réelles négatives. Il peut être difficile de le vérifier, dans le cas général, pour des systèmes de rang élevé, 20 par exemple.

Si la matrice $\Psi^T \Phi$ admet un inverse, alors :

$$\left(\Pi + G \Psi^T \Phi \right)^{-1} G = |\Psi^T \Phi|^{-1} - \left(\Pi + G \Psi^T \Phi \right)^{-1} |\Psi^T \Phi|^{-1} \quad (7.2)$$

d'où

$$\begin{aligned} \vec{e} &= \left(\Pi - \Phi |\Psi^T \Phi|^{-1} \Psi^T \right) \vec{\theta} + \left\{ \Phi \left(\Pi + G \Psi^T \Phi \right)^{-1} |\Psi^T \Phi|^{-1} \Psi^T \right\} \vec{\theta} \\ &\quad + \left\{ \Pi + G \Psi^T \Phi \right\}^{-1} G \vec{v} \\ &= \left(\Pi - Q \right) \vec{\theta} + \Gamma_\theta \vec{\theta} + \Gamma_v \vec{v} \end{aligned} \quad (7.3)$$

Cette expression a l'intérêt de mettre en évidence :

- le terme $(\Pi - Q) \vec{\theta}$ qui ne dépend que du choix des surfaces φ et ψ . Pour un choix des surfaces φ , il est minimal si les surfaces ψ leur sont identiques ;
- un terme Γ_θ qui décroît lorsque le gain augmente ;
- un terme Γ_v qui croît lorsque le gain augmente.

7.2. Cas particuliers

Examinons deux cas particuliers :

- 1) $G = g(p) |\psi^T \phi|^{-1}$, où g est un scalaire.

$$\vec{\varepsilon} = (\Pi - Q) \vec{\delta} + \frac{\phi |\psi^T \phi|^{-1} \psi^T}{1+g} + \frac{g}{1-g} |\psi^T \phi|^{-1} \vec{v}$$

La stabilité du système est alors très simple à étudier. De plus, toutes les commandes ont la même rapidité.

- 2) Si les miroirs R1 et R2 sont identiques ($\psi = \phi$) et si B (φ) est orthonormée ($\psi^T \phi = \Pi_M$) :

$$\begin{aligned} \vec{\varepsilon} &= (\Pi - \phi \phi^T) \vec{\delta} + \phi (\Pi + G)^{-1} \phi^T \vec{\delta} + (\Pi + G)^{-1} G \vec{v} \\ \vec{\varepsilon}^* \vec{\varepsilon} &= \vec{\delta}^* (\Pi - \phi \phi^T) \vec{\delta} + \vec{\delta}^* \phi (\Pi + G)^{-1} (\Pi + G)^{-1} \phi^T \vec{\delta} \\ &\quad + \vec{v}^* G^* (\Pi + G)^{-1} (\Pi + G)^{-1} G \vec{v} \\ \bar{q} &= T_r \left[(\Pi - \phi \phi^T) \vec{\delta} \vec{\delta}^* (\Pi - \phi \phi^T) + (\Pi + G)^{-1} \phi^T \vec{\delta} \vec{\delta}^* \phi (\Pi + G)^{-1} \right. \\ &\quad \left. + (\Pi + G)^{-1} G \vec{v} \vec{v}^* G^* (\Pi + G)^{-1} \right] \end{aligned}$$

Les éléments de la diagonale de la matrice $\phi^T \vec{\delta} \vec{\delta}^* \phi$ sont les densités spectrales des coordonnées de $\vec{\delta}$ dans la base B (φ). Appelons-les $C_i C_i^*$.

Si la matrice G est diagonale, d'élément g_i , on a donc :

$$T_r \left[(\Pi + G)^{-1} \phi^T \vec{\delta} \vec{\delta}^* \phi (\Pi + G)^{-1} \right] = \sum_i \frac{C_i C_i^*}{(1+g_i)(1+g_i^*)}$$

et

$$T_r \left[(\Pi + G)^{-1} G \vec{v} \vec{v}^* G^* (\Pi + G)^{-1} \right] = \sum_i \frac{\vec{v}_i^* \vec{v}_i \cdot g_i g_i^*}{(1+g_i)(1+g_i^*)}$$

La stabilité est également facile à étudier. On peut d'autre part choisir chacune des fonctions de gain g_i afin de minimiser la somme des erreurs dues aux perturbations et au bruit pour chaque coordonnée.

7.3. La matrice $\psi^T \phi$ n'est pas régulière

On peut remplacer $|\psi^T \phi|^{-1}$ par $|\psi^T \phi|^{-}$ dans la relation (7.2) qui reste exacte si $G \vec{\alpha} \vec{\beta}^T = 0$. Il faut donc pour cela que $\vec{\alpha}$, vecteur propre à droite à valeur propre nulle de $\psi^T \phi$ ait la même propriété vis-à-vis de G et, dans ce cas, la formule (7.3) demeure valable.

8. CONCLUSIONS

L'interprétation vectorielle que nous avons donnée des systèmes COAT présente divers avantages :

- 1) Elle est très générale.
- 2) Les calculs sont systématiques, facilement programmables avec des algorithmes existants.
- 3) Une fois que les diverses surfaces sont traduites sous forme de coordonnées dans le système orthonormé δ , centrées et normées, les diverses relations que l'on est amené à écrire correspondent à des propriétés géométriques simples qui en facilitent la compréhension.

REMERCIEMENTS

Je remercie la D.R.E.T. et en particulier M. SECHAUD pour l'intérêt porté à cette étude.

BIBLIOGRAPHIE :

- G. ROGER : Vector interpretation of deformable mirror C.O.A.T. system. Third International Symposium on Gas-Flow and Chemical Lasers (Marseille September 8 - 12 1980), Journal de Physique, Colloque n° 9, Supplément au Journal de Physique, FASC. 11, C9-1980, C9-399-C9-403.

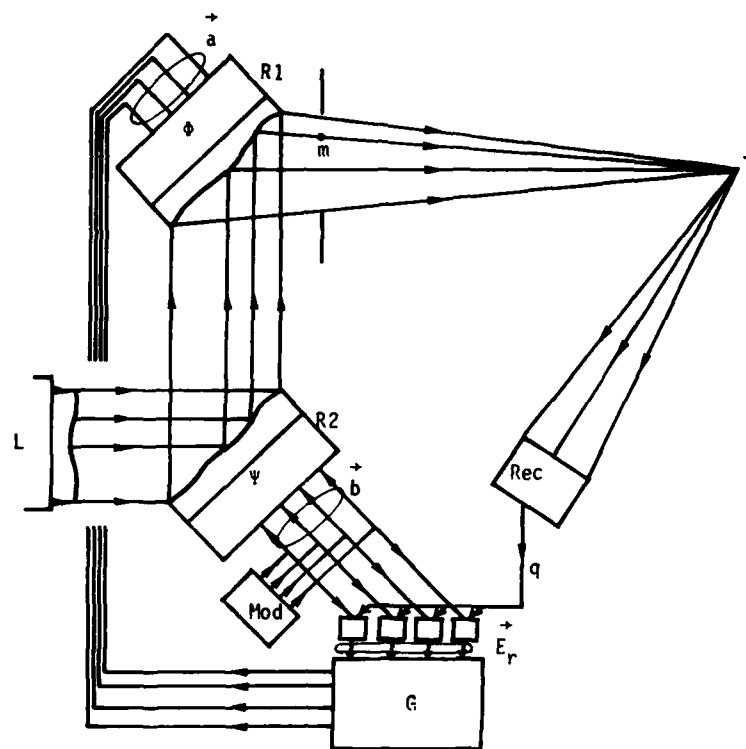


FIGURE 1 - Schéma de principe d'un COAT à modulation

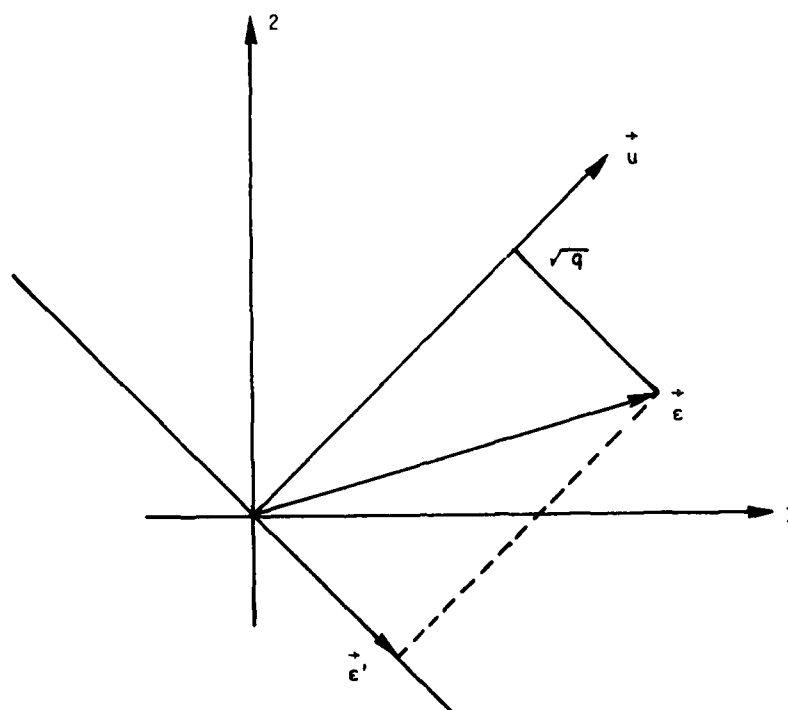


FIGURE 2 - Représentation vectorielle de la perte $q(\epsilon)$

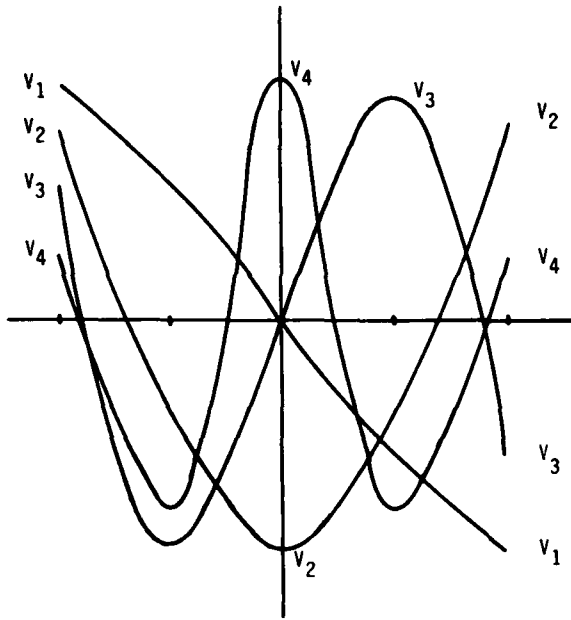


FIGURE 3 a - 5 points alignés. Forme des surfaces associées aux vecteurs propres

Figure 3 b - 5 points alignés. Variances cumulées correspondant aux diverses valeurs propres

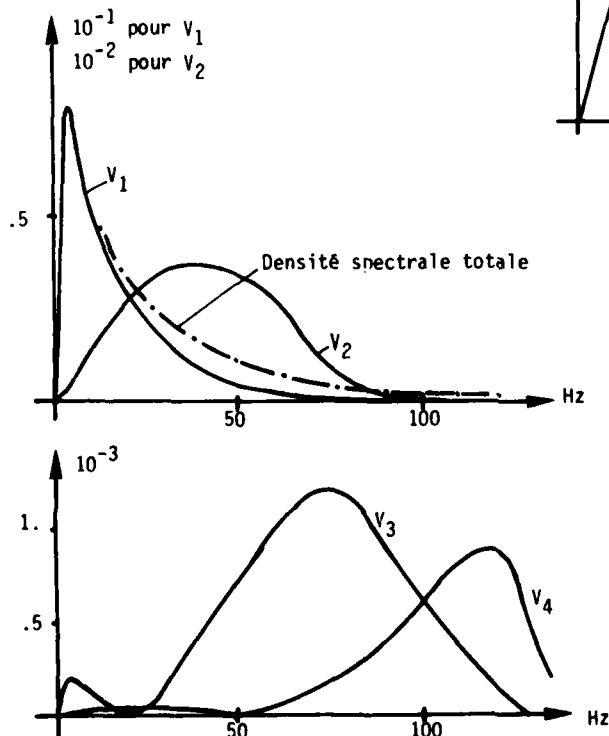
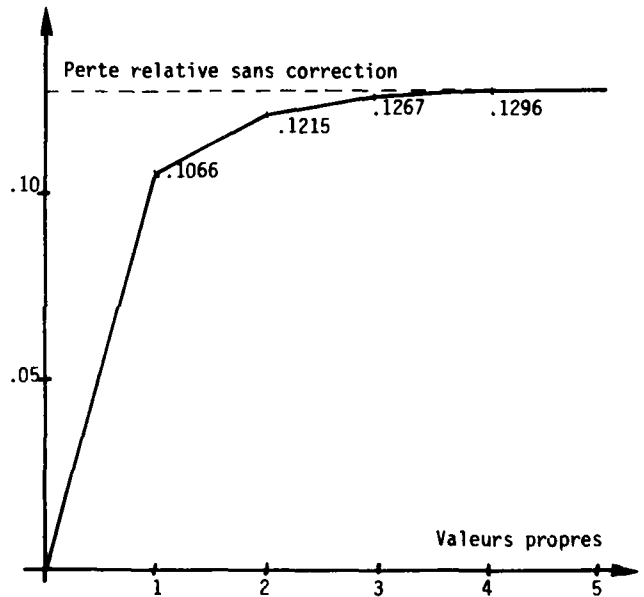


FIGURE 3 c - 5 points alignés. Densités spectrales des pertes liées aux différents vecteurs propres. Noter les différentes échelles verticales (unités proportionnelles à des radians carrés par hertz).

SUMMARY OF SESSION I

PROPAGATION EFFECTS IN AIR AND SEA WATER

by

Dr. Richard Anderson, Chairman

In this session we have examined the status of theoretical modelling of the radiative transfer problem through scattering and absorbing mediums and the experimental measurement of the most interesting and critical parameters involved in the theory.

Modelling of atmospheric transfer of radiant energy appears to be well in hand. The theory has been tested and accepted and, at this time, efforts are being directed to the measurement of the structure constants in these models, such as C_n^2 and C_T . Experiments are being performed to determine the structure constants in the marine boundary layer to predict visibility, contrast reduction and so forth.

One interesting experiment is described which relies on multiple scattering to propagate optical energy over the horizon. All of the above indicates a well developed understanding of the optical atmosphere.

The underwater models of radiative transfer are not nearly as well based in scientific theory and are, in comparison, only first order approximations. Workers in this field have produced neat and convenient forms which are easily interpreted in systems studies. Typically, the underwater models employ gaussian approximations for the phase functions and spatial distribution, for example, to produce forms which are easily analyzed.

As an example of the difference in the level of development between atmospheric and underwater radiant propagation, those working in atmospheric optics are measuring scintillation and turbulence. Similar phenomenological quantities are not yet defined in studies of underwater propagation though they are known to exist.

This situation derives from at least two sources. The first is the greater difficulty in the acquisition of detailed propagation parameters in the water masses. Secondly, the history of visibility and atmospheric optics is much older and more relevant to human endeavour resulting in a more sophisticated state of development.

QUESTIONS AND COMMENTS
ON SESSION I

PROPAGATION EFFECTS IN AIR AND SEA WATER

- Paper 2 : Multiple scatter of collimated irradiance.

Dr. H. T. Yura : Which source do you point at for the off-axis case, the true or apparent ?

Dr. W. H. Wells : The apparent source. The problem treated here begins just beneath the surface. Various surface effects, refraction, reflection and roughness, must be treated separately to establish what we call incident radiance.

Prof. A. Ishimaru : Can this technique be applied to two boundary problems ?

Dr. W. H. Wells : Yes but with some difficulty. We can no longer dismiss the increasing exponential functions as unphysical. Much more algebra is required to fit boundary conditions. If light is incident at $z = 0$ but not on surface $z = Z$ then $L(0, \theta < 90^\circ, \phi) = L^{in}$ and $L(Z, \theta > 90^\circ, \phi) = 0$.

- Paper 7 : Dependence of air to ground (land and sea) visibility ranges on low flight altitudes in conjunction with meteorological parameters.

Dr. C. Werner : Comment :

After reading the paper of M^r Hoffmann. I like to add that we developed and tested a slant range visibility device based on the lidar technique (1). This technique allows an on - line determination of the visibility in any direction of the atmospheric boundary layer. Test reports are available (2).

(1) Werner C. H. R. "Slant range visibility determination from lidar signatures by the two - point - method". Optics and laser technology. Feb. 1981 p. 27 - 36.

(2) D F V L R Mitt. 81 - 01, 1981.

General comment (Round table discussion)

Dr. W. Wells : The boundary conditions in light entering the ocean are such that the ocean is really a dark medium unless you look at the sun glint. In mathematically setting up the boundary conditions at the surface of the sea you could neglect backscatter and simply take the radiance of the surface to be equal to the insidious radiance without much error, unless backscatter is the thing you are interested in measuring specifically. On the other hand are the clouds in the atmosphere. You have huge percentages of the light coming back out of the boundary and making the mathematical solution quite different in nature and a different set of approximations because of the fact that the downwelling light is part of the "given" and the "upwelling" light is part of the "solution" and here you have to reconcile them at the boundary.

Mr. R. Anderson : That is true. That is one of the fundamental differences. The scattering albedo is so much lower in water than in a cloud, for instance. It is a different problem, it is much further from a complete solution than the atmospheric problem.

ATMOSPHERIC MEASUREMENTS IN A COASTAL ENVIRONMENT

T. Bakker
 Physics Laboratory NDRO-TNO, P.O.Box 96864
 2509 JG, The Hague, The Netherlands

SUMMARY

In this paper the results of measurement projects, concerning atmospheric limitations for the application of electro-optical equipment are reviewed. Results of simultaneous transmission measurements along close parallel tracks in the visible, the infrared as well as the mm-wave (94GHz) region are compared. Long-range (5 km) laser transmission measurement results are given. Remote-measurement techniques as well as aerosol counters were applied in order to determine the relevant atmospheric characteristics. The measurements were carried out in a coastal environment and on the North Sea. In order to study mutual relationships meteorological measurements were done simultaneously.

1. INTRODUCTION

During several years atmospheric measurements are being performed by the Physics Laboratory TNO, The Hague. The main objectives of these measurements are to determine the limitations imposed by the atmosphere on the application of electro-optical equipment for military purposes (image-intensifiers, TV-camera's thermal infrared equipment and lasers). Besides the extinction and scattering coefficients of the atmosphere, the meteorological parameters and aerosol properties are measured as well in order to determine the mutual physical relationships between all these parameters and with the hope in mind that suitable methods could be developed for forecasting the performance of electro-optical systems under predicted weather conditions. For those purposes the following projects have been carried out:

1.1 The project OPAQUE

An OPAQUE measurement site was installed and in operation at the Airbase Ypenburg, located in the South East direction of the Hague.

1.2 The project LASERLINK

In between the measurement towers of the Physics Laboratory TNO and the tower of the Post-Office Laboratory, located at a distance of 5 km, measurements have been carried out using CO₂ lasers and Helium-Neon lasers as sources. The measurement track was at a height of 35 m above ground level.

1.3 AEROSOL and LIDAR project

At a later stage our efforts were more and more directed towards the development of remote-measurement techniques. For that reason lidar measurement equipment has been developed. Routine measurement programmes have been carried out at the Physics Laboratory, resulting in a small data base. In order to relate the measured results the aerosol-characteristics of the atmosphere were measured at the same time.

1.4 NORTH SEA project

In order to determine the differences between the overland, coastal and maritime environments, measurements have been carried out aboard the oceanic survey vessel of the Royal Netherlands Navy: H.Nl.Ms. Tydeman. Various trips across the North Sea were made.

2. MEASUREMENT LOCATIONS AND PHYSICAL ENVIRONMENT

Before dealing with details and results of the measurements, the environments where these measurements were done will be described. The locations itself have been indicated on the map, given in fig. 1. In fig. 2 the visibility is given as a function of the wind direction in a polar diagram. In fig. 3 the particle concentration, as measured by Knollenberg counters has been plotted in a polar diagram against wind direction. From these figures it becomes clear, that visibility is low and particle concentrations are high when the winds are blowing from the South-East direction. This dependence on wind direction can be explained from the presence of the heavy polluted industrial area around Rotterdam and Europort Harbour. When the wind is blowing from the North-West direction on the contrary the highest visibilities have been measured and the particle concentrations are lowest then. The measurements were performed at the Physics Laboratory TNO, located North of the Hague at a distance of about 2 km from the sea shore. The prevailing wind direction is South-West.

3. THE PROJECT OPAQUE

As mentioned already a complete OPAQUE station was installed at Ypenburg Airbase, located South-East of the Hague. For a description of the OPAQUE programme the reader is referred to [1]. In this paper the results of the transmission measurements in the visible, the thermal infrared wavelength regions (3-5 μm and 8-12 μm) and at a frequency of 94 GHz will be discussed. These measurements were done every hour on the hour along close parallel tracks, [2]. [3].

The infrared transmission measurements were carried out by means of the Barnes Infrared Transmissometer, type 17-708. The source and receiver were mounted at a height of 1.5 m above the ground; the measurement base was 500 m. For the visible transmission measurements an Eltro transmissometer was used. At a distance of 500 m from the source a retroreflector was placed, resulting in an effective measurement base of 1000m. The 94 GHz source was situated at about 1 m above the ground at a distance of 935 m from the receiver, which was mounted at a height of 3.5 m above ground level. Rain-intensity meters, rain-rate meters, meteo equipment, humidity meters, aerosol counters (Royco, type 225 and Kratel type Partoscope R) were installed along the measurement track or in its immediate neighbourhood.

In fig. 4 and 5 histograms are given of the transmission in the 8-12 μm wavelength region for the months of September and November 1978. In November we had frequently fogs resulting in a high cumulative probability (18%), that the infrared transmission dropped below 50% over 500 m. From these type of histograms annual surveys have been made, see figs. 6 and 7. Along the horizontal axis the month of the year has been plotted. Along the vertical axis the probability is given that the transmission is lower than the value of the parameter, associated with the corresponding curves. One can immediately conclude from these surveys, that the probability for low transmission values in the 8-12 μm wavelength region is high during Fall and in Winter and is smaller in Spring and Summer.

Annual surveys have been made now for three years of validated infrared transmission data in the 8-12 μm as well as in the 3-5 μm wavelength region. The same type of histograms and surveys have been made for the visual transmission and the transmission at 94 GHz. [4]

Besides histograms and annual surveys scatterplots were made. In fig. 8 the transmission in the 8-12 μm region has been plotted in the vertical direction against the transmission in the visible region in the horizontal direction. These measurements were made in the period Sept.- Nov. 1978. From this figure the following general conclusions can be drawn:

- With only a few exceptions the transmission in the 8-12 μm region is equal to or greater than in the visible region.
- When it is not raining the infrared transmission does hardly depend on the transmission in the visible region, as long as the visual transmission is larger than 0.2. (Visibility larger than 1 km).
- During rain the infrared transmission is decreasing and tends to become equal to the visual transmission. The same conclusions apply to the dependence of the transmission in the 3-5 μm region on the visual transmission.

In fig. 9 the transmission in the 8-12 μm region over 500 m has been plotted along the vertical axis against the transmission at 94 GHz over 935 m along the horizontal axis. These measurements were also done in the period Sept. - Nov. 1978. For active mm-wave devices the radiation has to pass through the atmosphere twice. So the plot gives a good comparison between active mm-wave and passive infrared systems, with respect to atmospheric limitations. From fig. 9 it may be concluded, that under no rain conditions the transmission at 94 GHz over 935 m is superior or equal to the transmission in the 8-12 μm band. During rain the transmissions tend to become more equal.

Very interesting results were found once the dependence of the infrared transmission on humidity was studied. In fig. 10 the transmission in the 8-12 μm band has been plotted against absolute humidity. Although in general the infrared transmission decreases slowly with increasing water vapour density quite a number of measurements correspond to much lower transmission values. A much better relation results when the infrared transmission is plotted against relative humidity. From fig. 11 it follows that for values of relative humidity ≤ 0.90 the infrared transmission slowly decreases with increasing relative humidity. When the relative humidity is larger than 0.90, the infrared transmission can take all values between 0 and 0.95. Until some years ago it was assumed in infrared systems analysis studies, that the infrared transmission could reasonably well be described by the amount of precipitable water present in the transmission path. This amount is proportional to absolute humidity. A possible interpretation of our results is that for values of relative humidity ≥ 0.90 it is the amount of liquid water, present in the form of drops in rain or aerosols in fog that determines the infrared transmission of the atmosphere.

A major achievement was the introduction of the LOWTRAN models [5]. Besides gaseous absorption the extinction due to aerosols was included. At Ypenburg Airbase aerosol measurements were carried out every hour on the hour by the Prins Maurits Laboratory TNO. Some results of the measurements on 7 February 1979 have been given in fig. 12, 13, 14, 15. [6] Along the horizontal axis the size D of the particles is given on a logarithmic scale. Along the vertical axis the density $N(D)$ of the particles corresponding to a given interval is given also on a logarithmic scale $\left\{\frac{dN(D)}{dD}\right\}$.

From the measurement on 17.00 h one might conclude that in particular the larger particles have a marked influence on the infrared transmittance.

4. THE PROJECT LASERLINK [7]

As mentioned already laser transmission measurements were carried out at an altitude of 35 m over a base-length of 5 km. The CO_2 laser used was a Sylvania type 341 P, delivering a continuous power of 2-4 W. It was cooled by running tap-water; neither the temperature nor the pressure of this cooling water was stabilized. The power supply was not stabilized as well. As a consequence a haphazard switching of the laserline occurred from time to time. As the wavelength of the transmitted radiation was not monitored the exact wavelength during the transmission measurement was not known. This CO_2 laser was designed to operate in the TEM₀₀ mode. The output beam passed through a 7 x magnifying telescope, resulting in a beam divergence of 1 mrad. The CO_2 laser radiation was collected by a Germanium lens with a diameter of 7.5 cm and a focal length of 15 cm. The detector was an uncooled pyroelectric one (Barnes Engineering, type T-300), integrated with a FET amplifier. The Noise Equivalent Power amounts to 10^{-9} $\text{WHz}^{-\frac{1}{2}}$.

The Helium-Neon laser was a Spectra Physics, model P36. It delivered an output beam with a continuous power of 2 mW and a beam divergence of 1.5 mrad. This radiation was collected at a distance of 5 km by a Fresnel lens with a diameter of 24 cm and a focal length of 32 cm. A Silicon photovoltaic detector was used. The Noise Equivalent Power amounts to 10^{-13} $\text{WHz}^{-\frac{1}{2}}$. No provisions were made for the absolute calibration of the transmission measurements. Instead the excess loss due to atmospheric extinction was measured. So the 0 db loss is arbitrary and simply refers to specific values of the receiver signals. The rain rate, humidity and temperature were measured at the transmitter as well as the receiver side of the link. In fig. 16 and 17 this excess loss has been plotted against relative humidity for Helium-Neon as well as CO_2 laser radiation respectively. In particular for CO_2 laser radiation we see that for relative humidities smaller than 0.90-0.95 the extinction is almost independent of relative humidity. For values of the relative humidity larger than 0.95 there is a steep rise in the extinction. The same arguments apply to the extinction of Helium-Neon radiation. These results confirm the results of our OPAQUE measurements.

A second objective of these measurements was to study the scattering of radiation in the atmosphere under small angles in the forward direction. For that reason both beams were scanned in a horizontal direction by means of a stepping motor over 9 m in steps of 0.9 m. Figs. 18 and 19 give the average beam profile of the Helium-Neon and the CO_2 laser respectively after transmission over a 5 km path through the atmosphere at an altitude of 35 m above ground level.

We never measured a significant change in these profiles under various weather conditions. It was planned to perform aerosol- and lidar measurements during these laser experiments. Unfortunately either the laserlink or the lidar and aerosol equipment turned out to be inoperative, so that no simultaneous measurements have been carried out. Because of manpower problems the laser transmission experiments were stopped in 1979.

5. AEROSOL AND LIDAR PROJECT

Already in an early stage (1974) lidar investigations were performed at the Physics Laboratory TNO. Experimental feasibility studies were carried out concerning the application of the vibrational and rotational Raman effects for the remote-measurement of the concentrations of specific gases and the temperature in the atmosphere respectively. Both methods turned out to be too insensitive for our purposes. In our experimental set-up besides the Raman-shifted backscattered radiation the unshifted Mie-scattered radiation could be measured as well. The results were so promising that a more definite lidar equipment was developed, see fig. 20 with the following specifications:

laser	: Neodymium/YAG
wavelength	: 1.06 μm
pulse energy	: 30 mJ
pulse width	: 20 ns
beam divergence	: 2.5 mrad
pulse repetition frequency:	1 Hz
receiver	: plastic Fresnel lens
aperture	: 39 cm
focal length	: 60 cm
detector	: YAG 444 (E.G & G.), Silicon photodiode.
rise time	: 100 ns
optical bandwidth	: 50 nm
overall transmission	: 0.49

The range of this monostatic configuration is approximately 1.5 km. The output of the detector was connected to a Tektronix WP 2221 waveform processing system, including a dual floppy disk unit. In order to improve the signal to noise ratio the output signals of 4-5 successive shots were summed.

The aerosol measurements were performed with two optical particle counters from Particle Measuring Systems: an active scattering aerosol spectrometer probe ASASP-300A and a classical scattering probe CSASP-300A. The total size interval covered with this equipment ranges from 0.16 μm to 18 μm . In order to reduce errors in the sample volumes the inlet horns were turned towards the wind direction. [8] The aerosol data were recorded and processed. The resulting aerosol size distributions $\log \frac{dN(D)}{dD}$ as a function of $\log D$ were approximated

by a first degree polynomial (Junge distribution) and a fifth degree polynomial.

All the measurements were carried out at the Physics Laboratory. The lidar was situated at ground level. The lidar soundings were done in a fixed direction (74° eastwards with respect to North). The elevation angle of the lidar was only 5°. So the measurement path was completely within the lower atmosphere. The signal originates from a range interval between 200 and 1500 m. The aerosol and meteorological equipment were located at our measurement tower, approximately 35 m above ground level.

All the data were recorded on datafiles. During 1978 a data base of 181 complete files has been acquired. Every single datafile comprises 160 elements with measured and calculated lidar- and aerosol data, meteorological and environmental parameters, equipment characteristics etc. In a second phase these datafiles have been used in a statistical analysis in order to determine whether or not useful numerical information concerning atmospheric parameters can be derived from the results of these remote-measurements [10, 11]. The most important questions, to be answered are:

- Is it possible to derive the extinction parameters (absorption as well as scattering coefficients)?
- Is it possible to derive the aerosol characteristics?

From the lidar equation one can easily derive, that in a homogeneous atmosphere the received signal V_D varies as a function of range R, according to:

$$\ln(V_D R^2) = -2AR + \ln B + C.$$

A: extinction coefficient

B: volume backscatter coefficient

C: constant, dependent on transmitter and receiver characteristics.

From the slope of the curve A can be determined. Knowing C from calibrations B is found after substitution of A. An inhomogeneous atmosphere can be dealt with by dividing the total range interval of 200 till 1500 m into at most 4 subranges, that can be considered as homogeneous. This technique has been applied e.g. in a horizontally stratified and layered atmosphere.

Amongst the atmospheric and meteorological parameters, being measured is the visibility, measured with an AEG scatterometer as well as by a human observer, looking at distant targets (further indicated as estimated visibility ESTVIS). It is known that this estimated visibility depends, amongst other parameters, strongly on the scattering characteristics of the atmosphere. In fig. 21 \ln ESTVIS has been plotted against $\ln B$ as measured by lidar. In the following we will use the correlation coefficient as a possible indicator whether or not a relationship between the parameters exists. In the case of the \ln ESTVIS vs- $\ln B$ dependence this correlation coefficient amounts to 0.95. When \ln ESTVIS is plotted against $\ln A$, fig. 22, as determined from lidar measurements the relation is not as good (correlation coefficient 0.85). One of the reasons is that as a result of the relatively short measurement interval (1300 m) the accuracy in the derivation of small A values is rather limited.

In fig. 23 $\ln C$, being the constant in the first order polynomial approximation of the aerosol distribution, has been plotted against $\ln B$, as derived from lidar soundings. A relationship is apparent.

In fig. 24 the \ln of the total particle area $\ln(A_T)$ is given as a function of $\ln B$. It turned out that the particle area is a better measure for atmospheric scattering than the total particle number N_T . An even better relation has been found when $\ln A_T$ is plotted against a linear combination of $\ln B$ and \ln ESTVIS, fig. 25. Of particular interest is of course the relation between the backscatter coefficient B as measured by lidar and the value B_{MIE} as calculated from the aerosol measurements by applying Mie-theory. In fig. 26

these quantities have been plotted for Spring 1978 (the relation turns out to be season dependent). A correlation coefficient of 0.83 was found.

A rather practical relation was found between the measured aerosol parameters C_j and v (Junge exponent) in combination with the relative humidity H on the one side and the calculated backscatter coefficient B_{MIE} on the other side. This relation has been depicted in fig. 27. The correlation coefficient amounts to 0.97. This might be an interesting method to derive backscatter coefficients from aerosol measurements without applying the time consuming Mie calculations on a computer.

In conclusion we consider the lidar as a promising tool to provide numerical information on the relevant atmospheric parameters. In particular in slant path directions, at open sea and in an operational environment the lidar offers unique possibilities. In fig. 28 the result of an early lidar measurement in ground fog is given. Although the lidar itself was located in the fog one could measure the thickness of the particular fog (190 m). For the study of interaction layers as exist above sea surfaces the lidar technique is very promising. We hope to apply lidar for that purpose in the future.

6. THE NORTH SEA PROJECT

In fall 1980 aerosol measurements were performed at the North Sea aboard the oceanic survey vessel H.N1.Ms. Tydeman [12]. Besides the aerosol counters mentioned in Ch. 5 also a PMS high-volume probe, type CSAS 100 HV was installed aboard this ship. The total range of aerosol diameters that could be measured was 0.16 μm -32 μm . These counters, together with an AEG scatterometer were installed at a height of about 8 m above sea-level. In fig. 29 the equipment is shown. The meteorological parameters and the navigation data were provided by the ships facilities. The measurements were reduced and combined on data files.

The main objective of these measurements was to investigate whether there are significant differences between the aerosol-sizedistributions, as measured overland, in harbour, near-coast and at open sea. For that purpose a number of trips were made, starting in the naval base Den Helder in various directions across the North Sea. A trip of 1 week was made to Devils Hole, see fig. 30. Unfortunately at Devils Hole we could measure only for 1 day because of gales and backwater, resulting in equipment failure.

Fig. 31 shows the averaged aerosol-volume distribution (MVDF) $\log \frac{dV(D)}{dD}$ ($\mu\text{m}^2 \text{cm}^{-3}$) as a function of $\log D$ (μm), measured at Devils Hole. The length of the vertical bars indicates the spread in the measurement results. Note the maximum at a diameter of about 5 μm . This curve is representative for the ones found at open sea. In fig. 32 the results of aerosol-volume distribution measurements near the coast of Holland are given. Curve 1 corresponds to measurements in the neighbourhood of platform NOORDWIJK, located 10 km outside the coast. Curve 2 was measured on a trip from Den Helder to Scheveningen. Curve 3 was measured 2 km from the coast of the Hague and curve 4 was measured near the oil rig of Placid Field in the North Sea. One notices a significant gradual change from a Junge type of distribution near the coast to a curve with a maximum at a diameter of about 5 μm at open sea. In table 1, the meteorological and environmental conditions during these measurements are given. In fig.33 the calculated extinction factors, corresponding to the curves of fig.32 are given.

curve	location	visibility	windspeed	winddirection	sea state	humidity
fig. 31	Devils Hole	18 km	11 M/S	215° (N=0)	4	0.84
fig. 32,1	NOORDWIJK	30 → 10	7	200	3	0.94
fig. 32,2	den Helder-Schev.	7	6	215	3	0.97
fig. 32,3	the Hague coast	7	6	215	3	0.97
fig. 32,4	Placid Field	30	6	290	2	0.77

table 1 Meteorological and environmental conditions.

The curves presented are only a few examples. A total of 120 individual measurements have been done. A first conclusion is, that indeed a gradual change in the particle volume distribution occurs between the coastal and the open-sea environment. Of course more measurements need to be done before a definite statement can be made.

These measurements have been carried out within the framework of the NATO Defence Research Study Group AC/243(Panel IV/RSG.8) on: "Atmospheric Optical and Infrared Effects". During the same period aerosol and meteorological measurements were carried out by a German team from the measurement platform: NORDSEE, by a British team at the Royal Aircraft Establishment in Farnborough and by a Danish group at the former OPAQUE site in Lolland. Further investigations have been planned. The application of lidar systems is under consideration.

Of particular interest of course are the physical mechanisms, that are responsible for these marked differences in the particle volume distributions and its effects on the propagation characteristics for visible and infrared broadband as well as laser radiation. The influence of sea spray on these characteristics has to be studied in detail.

ACKNOWLEDGEMENT

The author, being Head of the Physics Group, is much indebted to the collaborators of this group who performed the measurements and reduced the data. In particular the principal investigators, Ir. J.v. Schie and Drs. F. Oeseburg (project OPAQUE), Drs. R.J.L. Lerou (project LASERLINK), Drs. C.W. Lamberts (AEROSOL, LIDAR and NORTH SEA projects) are gratefully mentioned.

References

1. Bakker T.
The Measurement Programme OPAQUE of AC/243(Panel IV/RSG.8) on Sky and Terrain Radiation. AGARD Conference Proceedings CP183 on Optical Propagation in the Atmosphere, 14-1, 1976.
2. Buys, J.H., and L.H. Janssen.
Comparison of simultaneous atmospheric attenuation measurements at visible light, mid-infrared (3-5 μm) and mm-waves (GHz).
Proceedings IEE, part H to be published.

3. Buys, J.H., and L.H. Janssen.
Comparison of simultaneous atmospheric attenuation measurements at visible light, mid-infrared (3-5 μm) and mm-waves (94 GHz).
Physics Laboratory TNO, Report PHL 1981- (to be published).
4. Janssen, L.H.
A comprehensive survey of the OPAQUE transmittance measurements.
Physics Laboratory TNO, Report PHL 1981- (to be published).
5. Selby, J.E.A., and R.A. Mc Clatchey et al.
Atmospheric Transmittance from 0,25 to 28,5 μm : Computer Code LOWTRAN.
Air Force Geophysics Laboratory Reports
AFCRL-TR-75-0255 LOWTRAN 3
AFGL -TR-76-0258 LOWTRAN 3B
AFGL -TR-78-0053 LOWTRAN 4
AFGL -TR-80-0067 LOWTRAN 5
6. Oeseburg, F.
Prins Maurits Laboratorium TNO, private communication.
7. Lerou, R.J.L.
Long range transmission measurements of laser radiation through the atmosphere.
Physics Laboratory TNO, Report PHL- 1980-35.
8. Ven, van de, M.J.M.
Aerosol measurements during Spring 1978.
Physics Laboratory TNO, Report PHL 1978-41.
9. Ven, van de, M.J.M., C.J. Noorman and C.W. Lamberts.
Coastal Aerosol Measurements.
Journal of Aerosol Science, Vol. 11 (1980) pp 281-292.
10. Lamberts, C.W.
LIDAR, a statistical approach.
Physics Laboratory TNO, Report PHL 1978-31.
11. Lamberts, C.W.
Statistical Analysis of the 1978 lidar measurements.
Physics Laboratory TNO, Report PHL 1980-41.
12. Dielis, J.W.H.
Aerosol measurements on the North Sea.
Physics Laboratory TNO, Report PHL 1980- (to be published).

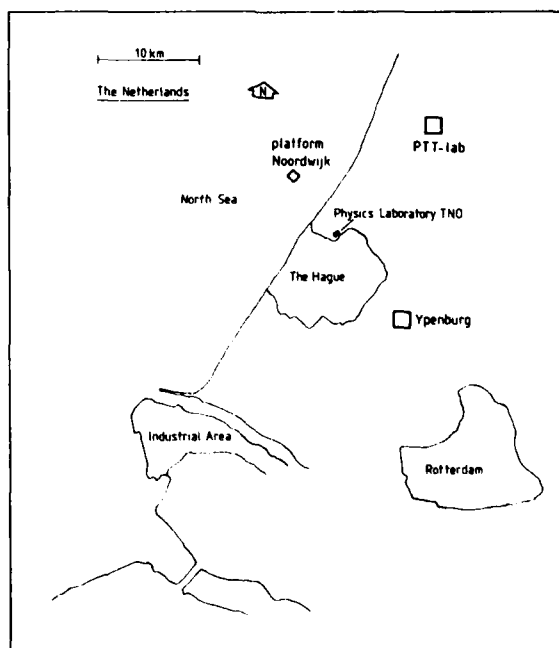


Fig.1 Map of the measurement locations

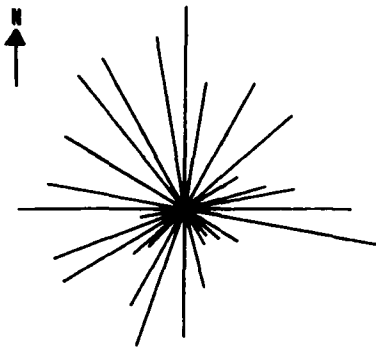


Fig.2 Visibility as a function of winddirection

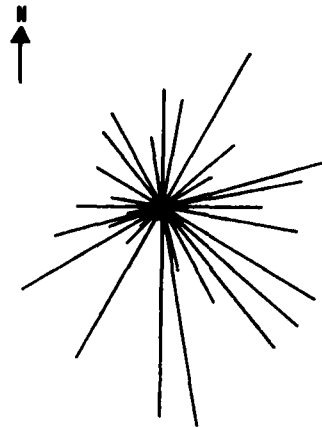


Fig.3 Particle concentration as a function of winddirection

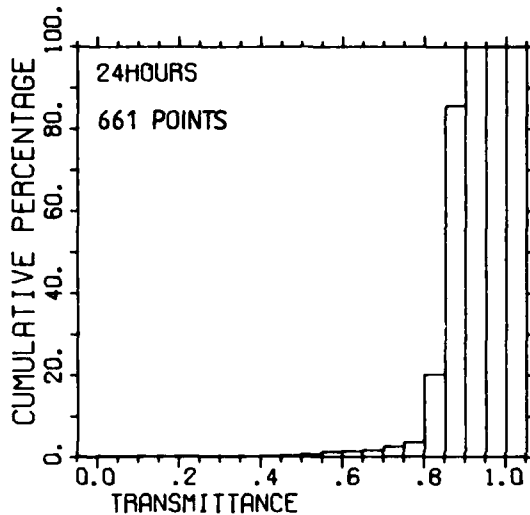


Fig.4 Cumulative probability of the transmission in the 8-12 μm region during September 1978

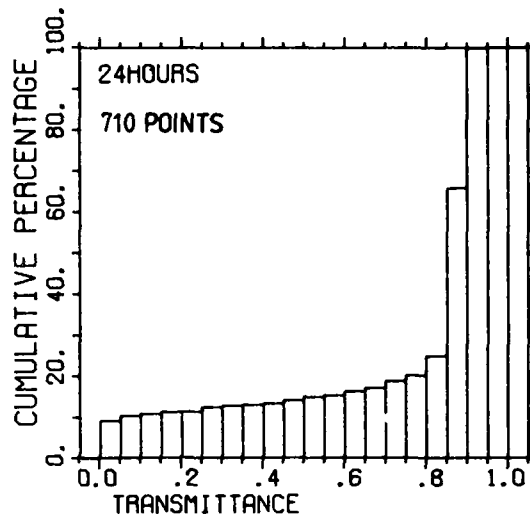


Fig.5 Cumulative probability of the transmission in the 8-12 μm region during November 1978

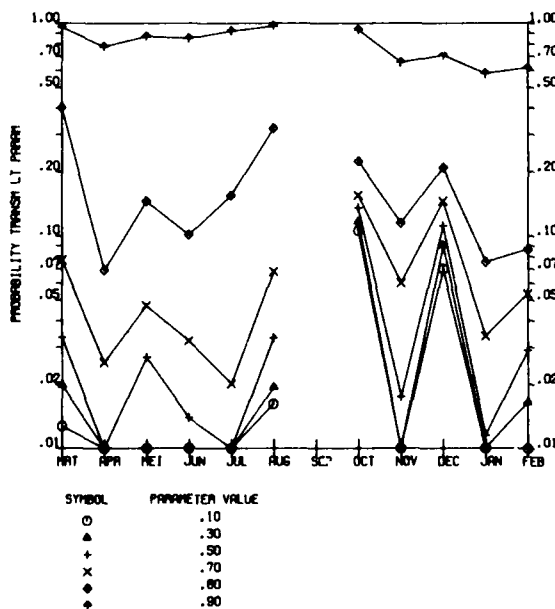


Fig.6 Probability that the transmission in the 8-12 μm region is lower than the parameter value, associated with the curves (March 1977 - February 1978)

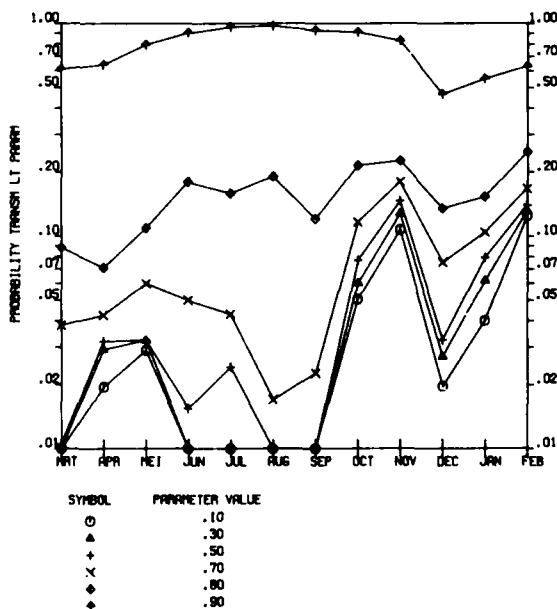


Fig.7 Idem for the period March 1978 - February 1979

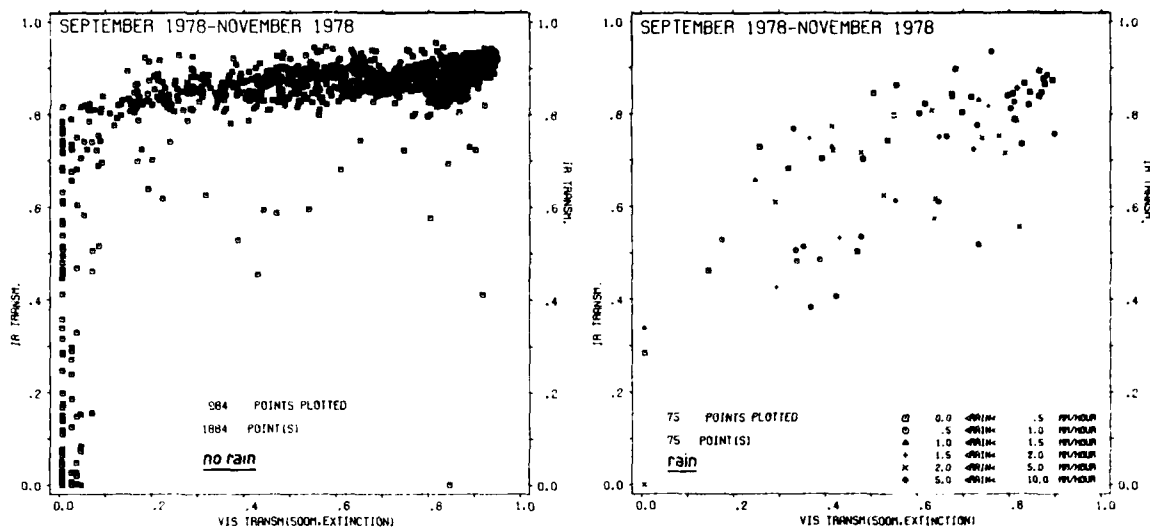


Fig.8 Transmission in the 8-12 μ m region vs transmission in the visible region (baselength 500 m)

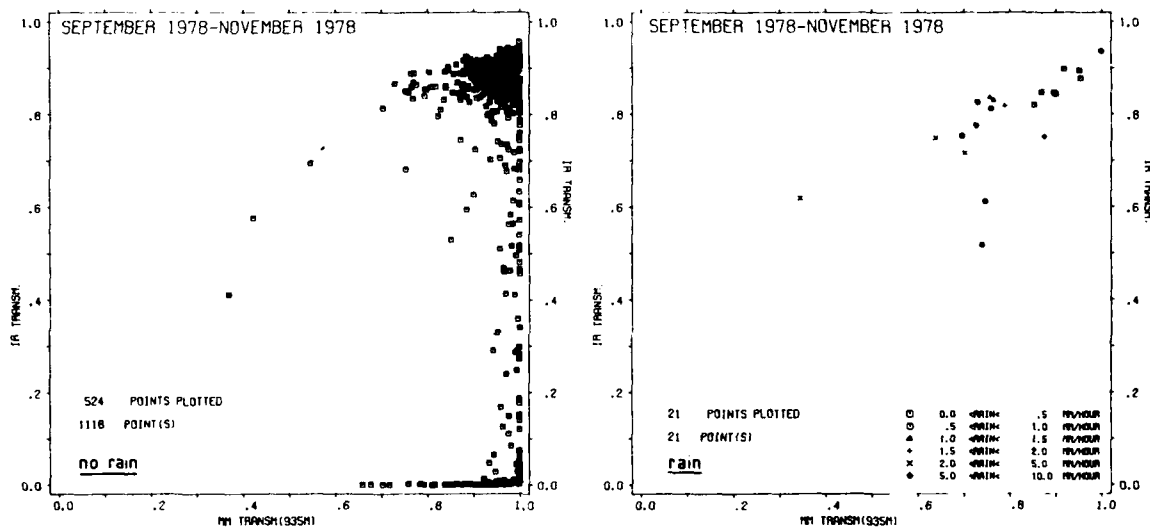


Fig.9 Transmission in the 8-12 μ m region over 500 m vs transmission at 94 GHz over 935 m

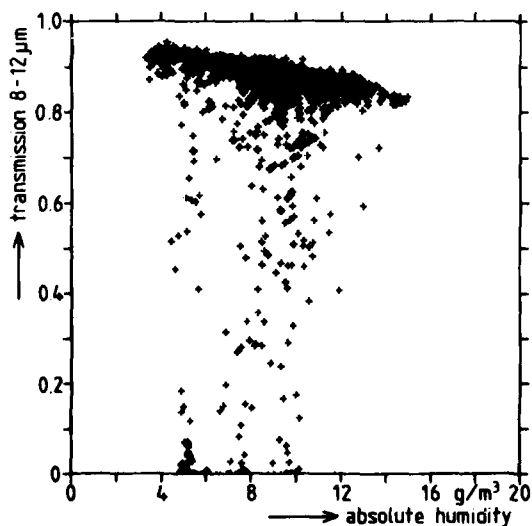


Fig.10 Transmission in the 8-12 μ m region vs absolute humidity

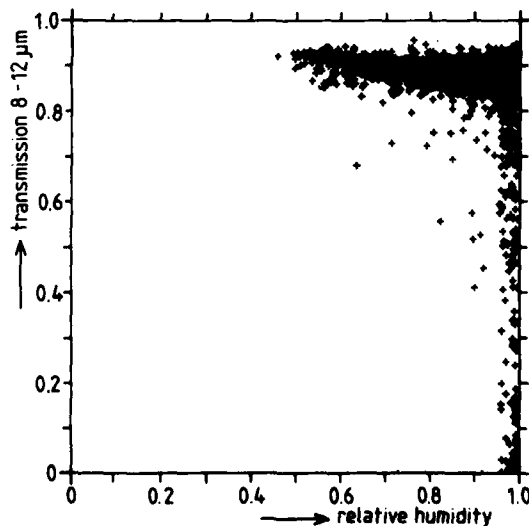


Fig.11 Transmission in the 8-12 μ m over 500 m vs relative humidity

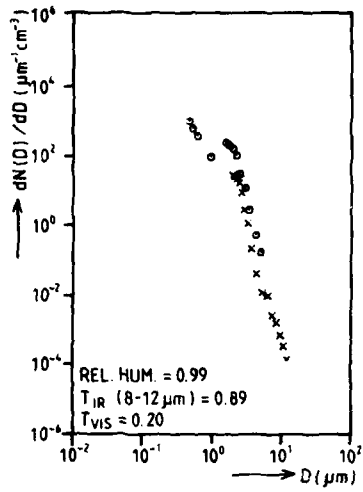


Fig.12 Aerosol size distribution, measured on Ypenburg Airbase on 7 Febr.79 at 11.00 h

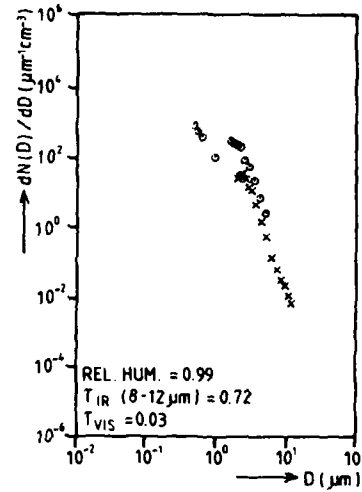


Fig.13 Idem, measured at 14.00 h.

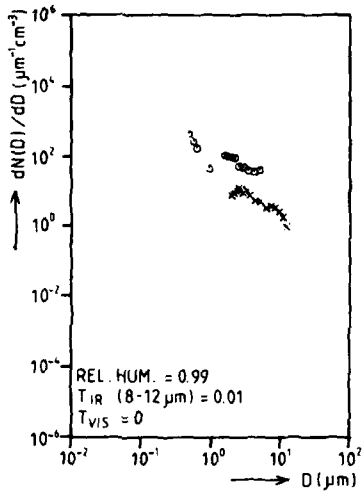


Fig.14 Idem, measured at 17.00 h.

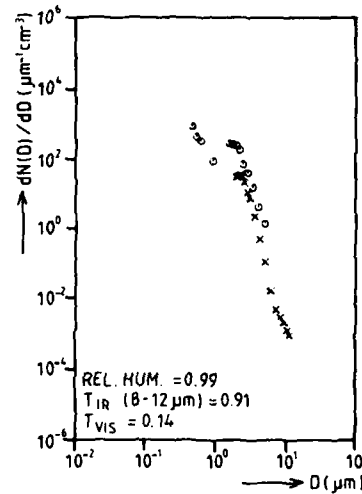


Fig.15 Idem, measured at 20.00 h.

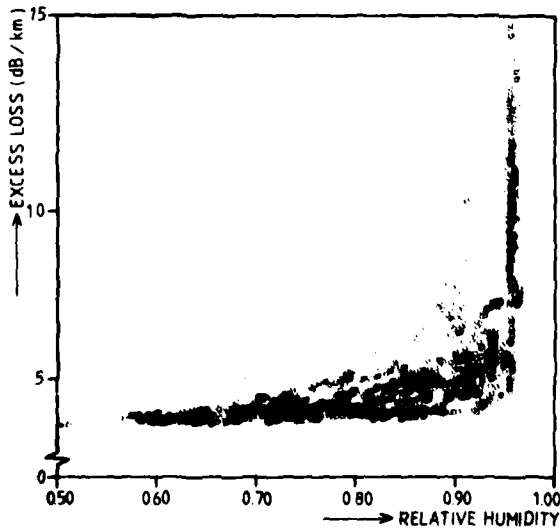


Fig.16 Excess transmission loss for Helium-Neon laser radiation over 5 km as a function of relative humidity

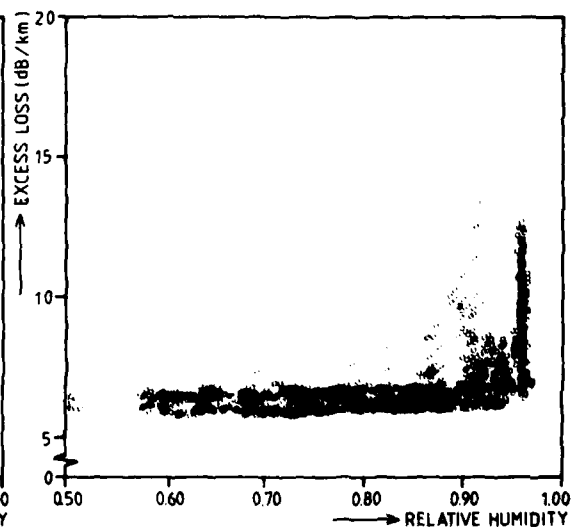


Fig.17 Excess transmission loss for CO₂ laser radiation over 5 km as a function of relative humidity

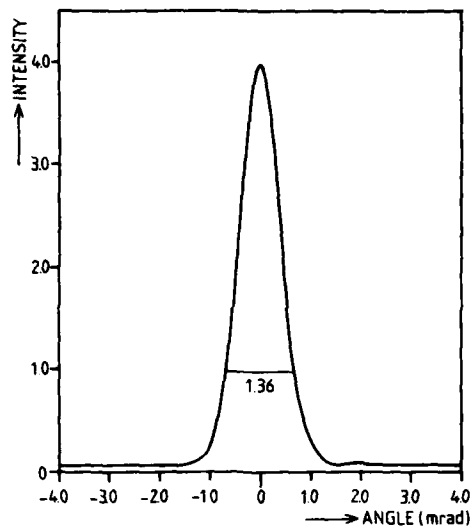


Fig. 18 Averaged beam profile of the Helium-Neon laser after transmission over 5 km through the atmosphere

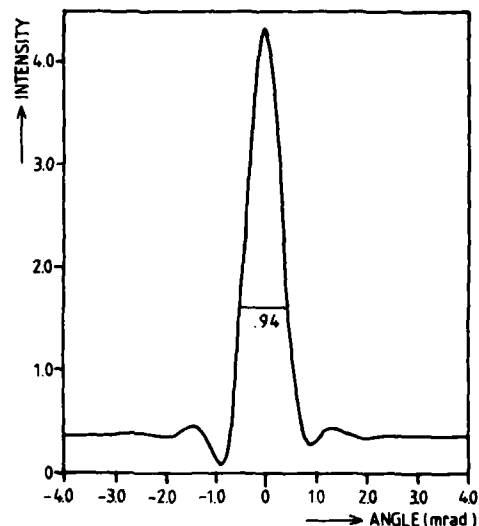


Fig. 19 Averaged beam profile of the CO₂ laser after transmission over 5 km through the atmosphere

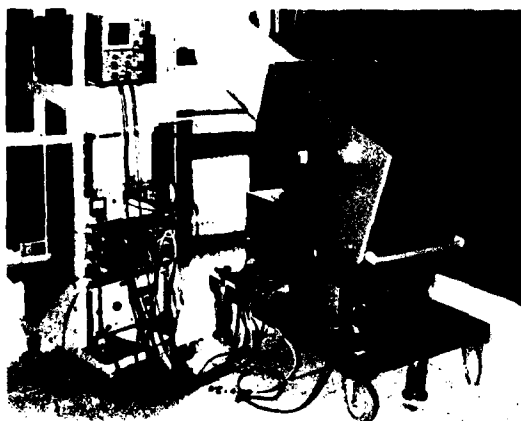


Fig. 20 Lidar measurement equipment

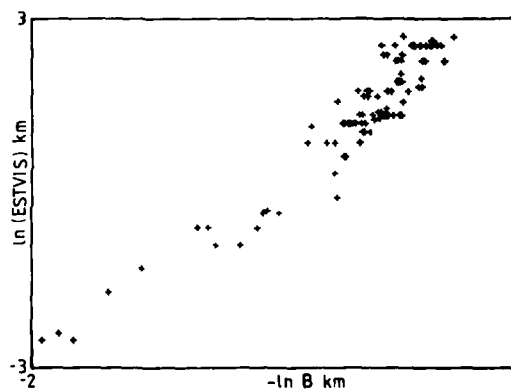


Fig. 21 Estimated Visibility vs lidar backscatter coefficient B

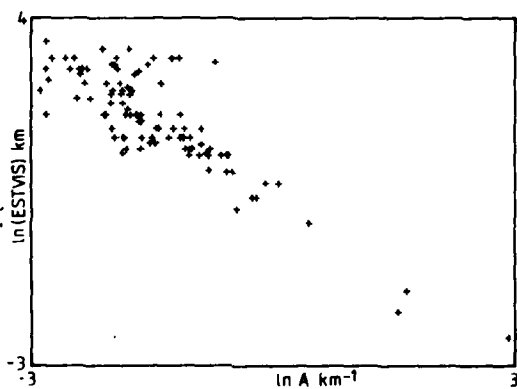


Fig. 22 Estimated Visibility vs lidar derived extinction coefficient A

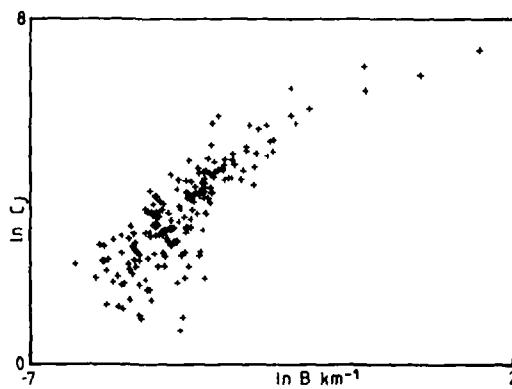


Fig. 23 Junge constant $\ln C_j$ vs $\ln B$ the lidar backscatter coefficient

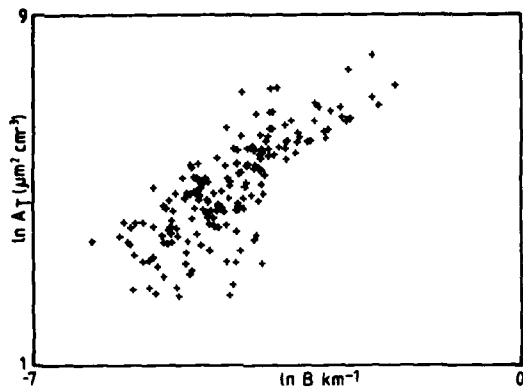


Fig.24 Total aerosol particle area $\ln A_T$ vs lidar backscatter coefficient $\ln B$

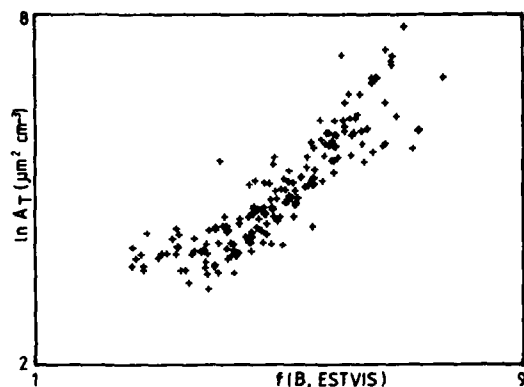


Fig.25 Aerosol particle area $\ln A_T$ vs linear combination of $\ln B$ and $\ln \text{ESTVIS}$

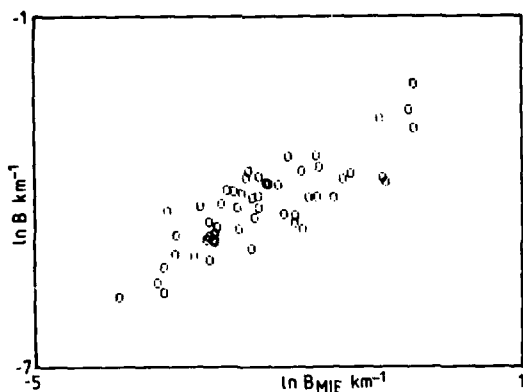


Fig.26 Lidar measured backscatter coefficient B vs B_{MIE} , calculated from aerosol measurements for Spring 1978

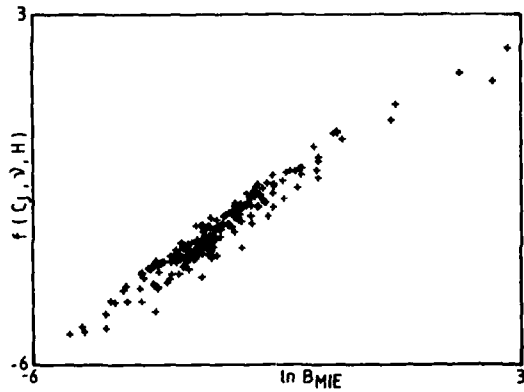


Fig.27 Backscatter coefficient B_{MIE} calculated from aerosol measurements vs linear combination of Junge constant C_j , Junge exponent ν and relative humidity H

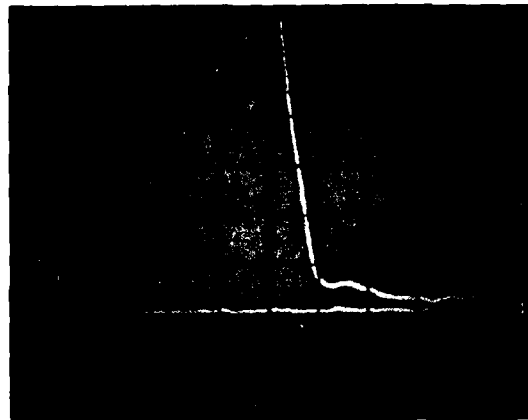


Fig.28 Lidar measurements in ground fog; the apparent height of the fog amounts to 190 m

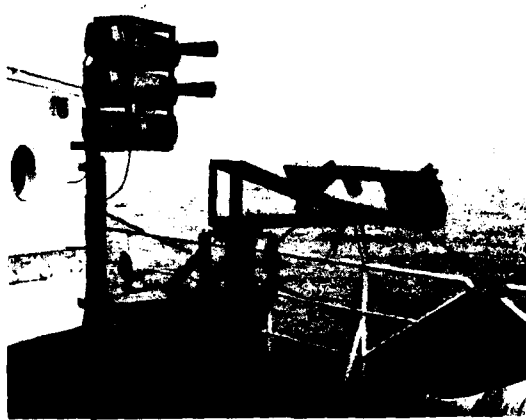


Fig.29 Aerosol counters and AEG scatterometer installed aboard H.N.I.Ms. Tydemann

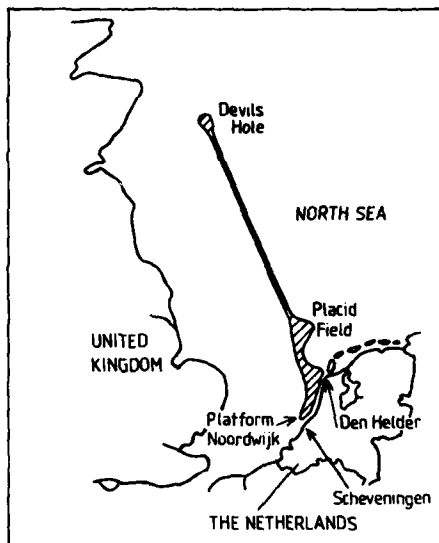


Fig.30
Map of the North Sea measurements area

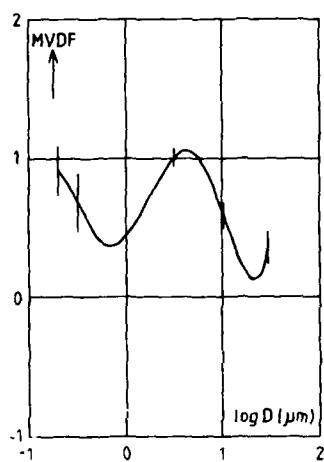


Fig.31 Mean aerosol-volume distribution (MVDF) measured at Devils Hole
 $\log \frac{dV(D)}{dD} (\mu\text{m}^2 \text{cm}^{-3})$ vs $\log D (\mu\text{m})$, measured at Devils Hole

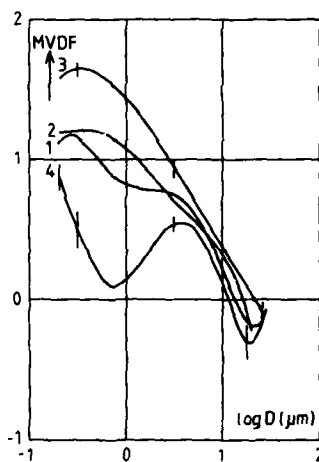
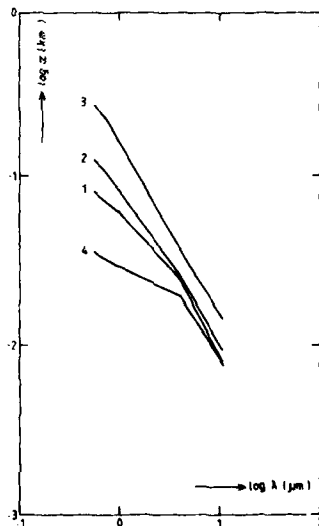


Fig.32 Mean aerosol-volume distribution (MVDF) measured near the coast of Holland
curve 1: near platform NOORDWIJK
curve 2: from Den Helder to Scheveningen
curve 3: 2 km from the coast
curve 4: at Placid Field

Fig.33 Extinction factors as a function of wavelength. These extinction factors have been calculated from the corresponding aerosol sizedistributions given in fig.32 by applying MIE-theory.



ATMOSPHERIC OPTICAL/IR PROPERTIES IN NORTHERN GERMANY

by

R.W.Fenn and E.P.Shettle
Air Force Geophysics Laboratory
Hanscom AFB, MA, USA

ABSTRACT

This paper describes results from the NATO measurement program OPAQUE (Bakker, 1976, AGARD Proceedings 183, pages 14-). The results presented cover the first three years of regular measurements of optical and infrared propagation properties at one of seven OPAQUE stations, located near Meppen in North West Germany.

Hourly measurements of visible and infrared transmittance in the 3-5 and 8-12 μm band, of day- and night-time illuminance, of contrast reduction (path radiance) as well as the meteorological quantities, temperature, dewpoint, and windspeed have been reduced and analyzed. During limited time periods of the three-year measurement program also optical/IR turbulence and laser scattering intensity (at 10.6 μm) have been measured.

This paper presents results of the analysis of monthly and seasonal frequency of occurrence of different levels of these quantities. We present probabilities of occurrence of visibility, 3-5 and 8-12 μm transmittance as a function of time of day and for different seasons. For this data base we have also derived the frequency of occurrence of various levels of day- and night-time illumination levels, indicating the dependence on cloud cover and other factors.

This limited climatology of atmospheric optical/IR properties is directly applicable to studies on the effectiveness of various E/O systems in the European environment.

This data base is also a source for deriving empirical correlations between atmospheric optical/IR properties and meteorological parameters and conditions. E.g., the relationships between transmittance properties in the visible and infrared and atmospheric humidity can be demonstrated.

The OPAQUE data also have been a unique data base for testing and validating atmospheric optical models. Results of comparisons with transmittance model (LOWTRAN) calculations and with illuminance model calculations are shown.

From this large data base, empirical correlations between the optical/IR atmospheric properties and the meteorological conditions have been developed which can aid in prediction schemes.

The data also have provided a unique source for comparison with and validation of atmospheric optical propagation models. Results of comparisons with transmittance and illuminance model calculations are shown.

The validation and analysis of the OPAQUE data is being performed as a cooperative effort between the eight OPAQUE nations and is coordinated within RSG-14 of Panel IV (AC243).

NOTE: This paper may be requested in Classified form from AGARD until June, 1982 through official national channels.

Measurements of Cloud Depolarization and Multiple Scattering

by

Christian Werner and Egmont Wolff

Institute of Optoelectronics

German Aerospace Research Establishment (DFVLR)

D-8031 Wessling/Oberpfaffenhofen

Federal Republic of Germany

SUMMARY

To get values of backscatter coefficients, depolarization ratios and multiple scattering effects a calibrated lidar system is necessary. The DFVLR-lidar-system IV was used for the measurements. Polarization characteristics and beam properties of the system are calibrated. An on-line data handling system is added. There are different aperture sizes available, also with a field stop for the single scattering component.

The measurements of cloud depolarization and multiple scattering effects were started in 1979. The first observation set on different cloud types is available. An anisotropy of the depolarization with the azimuth angle θ was determined. This anisotropy depends on the size of the cloud droplets.

1. INTRODUCTION

Remote sensing of atmospheric parameters by means of lidar methods has become of great interest. This methods are used to examine the scattering of transmitted pulse by the atmospheric molecules and particles. This examination is based on single scattering.

The transmissivity, which has been determined by lidar measurements of clouds and fog layers, turned out to be higher than the theoretically expected one for a single scattering process of the direct laser beam. Estimations carried out by different authors of multiple scattering show that this process could not be neglected [1, 2, 3, 4]. If a laser beam impinges on a thick scattering medium, after penetration through it, it becomes (1) physically wider, (2) decollimated, and (3) less intense. Figure 1 shows this principle. The laser pulse is propagating through some cloud levels. The telescope receives the backscattered radiation. In position 1 the telescope receives single backscattered radiation and also an increasing portion of multiple backscattered radiation due to spatial and angular spreading, in position 2 the multiple scattered radiation increases.

If the laser beam is linearly polarized the backscattered radiation will be partially depolarized.

To measure the effects described above, we constructed a new lidar system: The lidar system IV consisting of a ruby laser and two Newtonian telescopes with 25 and 40 cm mirror diameter. By changing the aperture angle of one telescope, the other has a constant aperture angle, the influence of multiple scattering can easily be revealed.

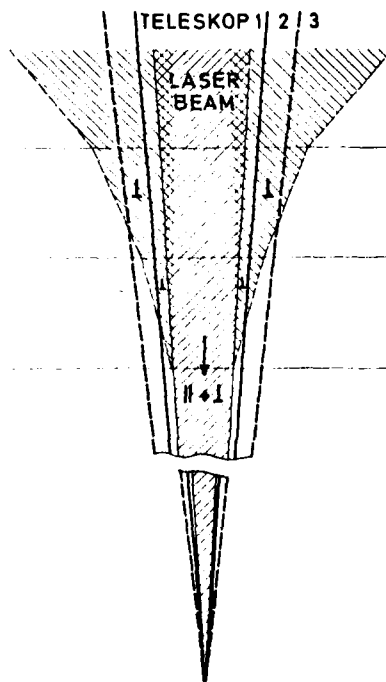


Figure 1: Principle of laser pulse propagation through a thick scattered medium

There are two research goals for the described cloud measurements: 1) the determination of the liquid water content of a cloud remotely, and 2) statistical values of cloud multiple scattering for optical communication.

2. BACKGROUND

It is known that cloud droplets scatter a considerable fraction of visible laser light into a narrow angular lobe in the forward direction [5, 6]. Some light which would for single scattering be lost from the transmitted beam is scattered back into the beam and reduces the effective extinction coefficient of the medium. This is important for problems concerned with measuring atmospheric transmittance using laser light. The relation between extinction and liquid water content is valid for single scattering only. Pinnick et al [7] showed for ruby-and Nd:YAG-laser wavelengths the cloud backscatter coefficient β has a simple relation to the extinction coefficient σ : $\sigma = 15.8 \beta$, independent of the form of the cloud drop size distribution.

Dense clouds along a transmission path can produce spatial and temporal spreading of a laser pulse [1,2]. If the radiation is linearly polarized, the multiple scattering produces a depolarization [8,9]. It was known from previous measurements - i.e. with the micro-wave radar - that iceparticles produce a strong depolarization. The depolarization can be used to distinguish between ice and water clouds [10,11]. To determine the liquid water content in the mixed phase, both effects of depolarization are mixed [12].

For optical communication it is necessary to know something about the angular behaviour of the depolarization [13,14]. The theoretical calculations do not assume a dependence of the depolarization on the azimuth angle θ [15,16,17,18,19]. With the measurements we will describe, we will present results for three items:

- 1) The experimental test of the multiple scattering.

The multiple scattering correction factor $(1-F(\tau))$ using Shipley's [17] theory is

$$1 - F(\tau) \sim \begin{cases} 0.62 - 0.02 \tau & \tau < 3.5 \\ 0.55 & 3.5 < \tau \leq 5.5 \\ 0.55 + 0.02 (\tau - 5.5) & 5.5 < \tau \leq 7.5 \end{cases}$$

τ = optical thickness

In the lidar equation

$$P_r = P_t \cdot \frac{K}{R^2} \cdot \beta \cdot e^{-2\tau}$$

where

P_r = received power

P_t = transmitted power

K = system constant including the effective receiver area

R = range

the multiple scattering is placed in

$$P_{rm} = P_t \cdot \frac{K}{R^2} \cdot \beta \cdot e^{-2 \int_0^R \sigma(1-F(\tau)) dr}$$

where the optical thickness τ is explained as $\int \sigma dr$.

Other authors give similar corrections. Bucher [1] made experimental tests and determined a pulse lengthening depending on the diffusion depth and the cloud thickness. The following expression should be valid [2,13]

$$T = \frac{\Delta R}{\tau(1 - \omega_0) \cdot c}$$

with T = multipath time spreading

ΔR = cloud thickness

$\tau = \tau_D (1 - \langle \cos \theta \rangle)^{-1}$

τ_D = diffusion depth

$\langle \cos \theta \rangle = 0.97$

$\omega_0 = 0.96$ = single scattering albedo = $\sigma_{scatt} / \sigma_{ext}$

c = velocity of light

- 2) To get a statistical data base on the depolarization for different clouds, and
- 3) to test the angular dependency of the depolarization.

Many authors made lidar experiments with clouds by varying the receiver field of view, the polarization orientation, and using field stops to eliminate the single backscatter component [20]. Carswell et al [21] made laboratory measurements using a fog chamber and determined a "strongly spatially inhomogeneous radiation field" for the pure multiply backscattered radiation.

3. LIDAR SYSTEM

The DFVLR-lidar-system IV is a ruby lidar system constructed for meteorological application. There is a possibility to determine the water vapor distribution in the boundary layer using two ruby lasers, and there is a possibility to study cloud parameters by using one ruby laser and two telescopes. Table 1 shows the parameters of the system [22].

Table 1: Parameters of the DFVLR-lidar-system IV

Transmitter 1		
Ruby laser (Impulsphysics)		
Wavelength	0.69428	μm
Linewidth	< 0.00001	μm
Stability	≈ 0.00001	μm
Output energy	1	Joule
Pulse duration	20	ns
Pulse repetition rate	1	Hz
Transmitter 2		
Ruby laser (Laser Associates Ltd.)		
Wavelength	0.6942-0.69428	μm
Linewidth	< 0.00001	μm
Stability	≈ 0.00001	μm
Output energy	1	Joule
Pulse duration	20	ns
Pulse repetition rate	5/100	Hz
Receiver 1 / Receiver 2		
Mirror diameter	40/25	cm
Focal length	250/150	cm
Photodiode	YAG 444 / YAG 444	

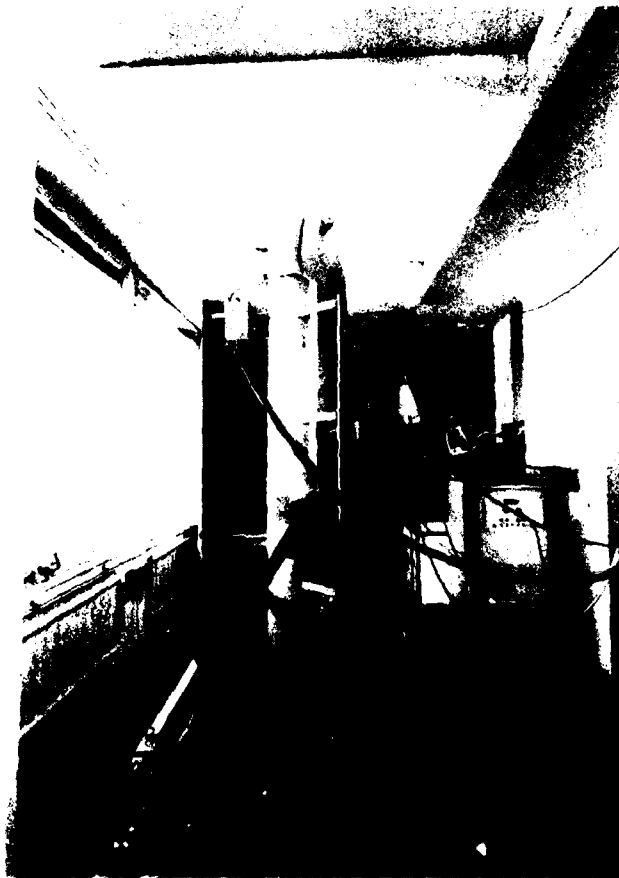


Figure 2: Lidar system IV

Figure 2 shows the system, which is installed on the top of the DFVLR-Institute of Atmospheric Physics. Measurements in vertical direction are possible. To be independent of the sky background radiation photodiodes are used especially for the water vapor detection. Photodiodes are thermal noise limited detectors and the thermal noise is higher than the daylight sky background noise. Therefore no interference filter is necessary to block the sky background radiation. The received backscatter radiation reaches the photodiode after

penetrating a field lens and a polarization filter. For cloud measurements photodiodes have an additional advantage compared to photomultipliers: there is no overload effect!

Two similar units are used in both telescopes. The polarization filters can be turned from parallel to perpendicular polarization direction according to the transmitted beam polarization.

For the cloud studies the small telescope 2 is used with the parallel polarization direction, telescope 1 receives the perpendicular polarized component.

The geometry of the system was tested. Laser 1 has a determined beam divergence shown in figure 3. Therefore, the telescopes are used with 5 mrad aperture size. To use the lidar system for multiple scattering determinations, there was a need for a blocking aperture. The required field of view corresponding to the diverging transmitted beam has to be blocked. Figure 4 shows an example for such a blocking aperture (field stop). The measured signal caused by scattering processes outside the blocked spatial volume.

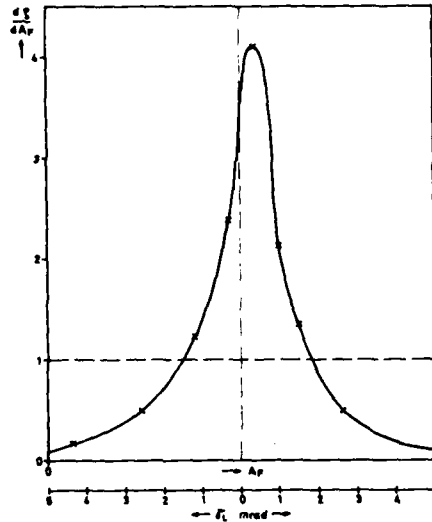


Figure 3: Determined beam divergence of Laser 1 (appr. 5 mrad)

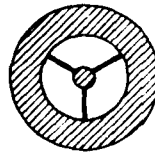


Figure 4: Example of a spatial filter (5 mrad blocking aperture and 13 mrad aperture)

AD-A105 193

ADVISORY GROUP FOR AEROSPACE RESEARCH AND DEVELOPMENT--ETC F/G 17/2
SPECIAL TOPICS IN OPTICAL PROPAGATION.(U)

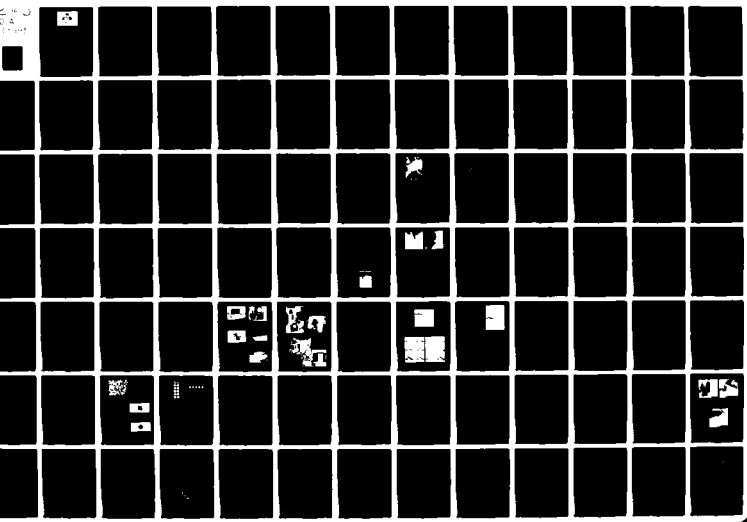
JUL 81 P HALLEY

AGARD-CP-300

NL

UNCLASSIFIED

2 4 3
4 2 3
1 2 3



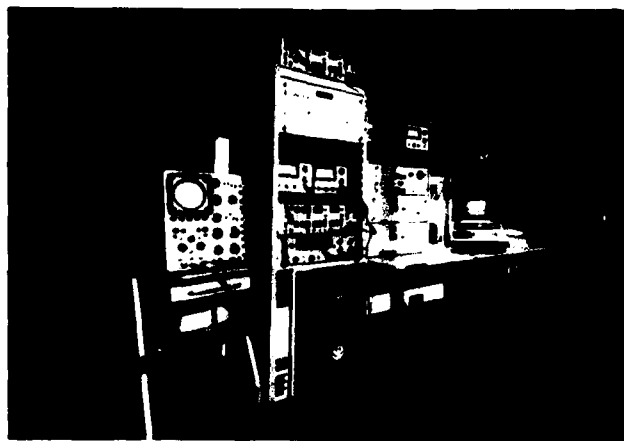


Figure 5: Data handling system

There is an on-line data handling system added to the lidar. Figure 5 shows the data system which is installed in another room to avoid electromagnetic interference from the laser ignition to the data transfer. The lidar signals are stored in two Biomation 8100 transient digitizers. The energy of each single laser pulse is measured and stored. In order to avoid short time variations of the cloud structure, the signals are given to two averaging units connected to the transient digitizers. These averaging units can average up to 500 signals from the Biomations per second. They offer a 16 bit memory for 2048 words. The averaging units are controlled via the IEEE-488-bus system by a personal computer Commodore 3016. The operator gives the transient digitizer values of sample interval and input range, the laser output energy and the amplifier stages into the computer and the computer calculates the backscatter values and the ratios for interested range intervals. Parallel to this, the calculated values can be stored on a mini-discette. The program language is BASIC, so students can handle the system.

4. CLOUD BACKSCATTER AND DEPOLARIZATION MEASUREMENTS

During half a year at different days lidar measurements of cloud backscatter coefficient was made [23]. This was the start of a serie of measurements to get a statistic of mid-European cloud data. Table 2 gives the result with date, time, mean temperature in cloud level from a nearby radiosonde station, the height above ground, and the maximum backscatter value in $m^{-1}sr^{-1}$.

Table 2: Data of measured clouds

date	local time	Temp. °C	R km	$\frac{S(R)_{max}}{m^{-1}sr^{-1}}$
6.2.80	10.27	-14,8	2,76	3,0 10 ⁻⁵
6.2.80	10.37		1,10	6 10 ⁻⁵
6.2.80	11.23		2,24	1,4 10 ⁻⁵
6.2.80	11.23	-14,8	2,68	5 10 ⁻⁵
6.2.80	11.29	-14,8	2,70	6,4 10 ⁻⁵
6.2.80	13.15		1,09	2,0 10 ⁻⁵
6.2.80	13.15	- 4,1	1,21	4 10 ⁻⁵
6.2.80	13.21	- 4,1	1,42	5,5 10 ⁻⁵
6.2.80	14.17	- 3,8	1,76	9 10 ⁻⁵
6.2.80	14.58		2,19	6 10 ⁻⁵
6.2.80	15.21		1,99	4,5 10 ⁻⁵
7.2.80	12.25	- 2,2	0,80	3 10 ⁻⁴
7.2.80	12.36		0,89	1,5 10 ⁻⁴
7.2.80	13.15		0,77	2,5 10 ⁻⁴
7.2.80	13.23	- 2,2	0,97	5 10 ⁻⁴
6.3.80	9.51	- 1,1	1,39	1,3 10 ⁻⁴
6.3.80	9.51	- 1,1	1,01	2 10 ⁻⁵
17.4.80	15.49	-23,7	5,10	5,3 10 ⁻⁴
17.4.80	15.49	-53,9	8,87	1 10 ⁻⁴
17.4.80	16.22	- 1,1	2,06	1 10 ⁻⁴
28.5.80	12.14	+10,3	0,41	1 10 ⁻⁴
28.5.80	12.14	+ 8,5	0,63	2 10 ⁻⁴
28.5.80	12.28	+10,3	0,40	4 10 ⁻⁴
28.5.80	12.28	+ 8,5	0,53	7 10 ⁻⁵
28.5.80	12.52	+ 6,0	1,15	4,0 10 ⁻⁴
28.5.80	13.06	+ 6,0	0,99	5,0 10 ⁻⁴
28.5.80	13.06		1,45	2,0 10 ⁻⁴
28.5.80	13.06		1,61	1,0 10 ⁻⁴
28.5.80	13.06		1,73	2,0 10 ⁻⁴
19.6.80	16.21		2,14	1,4 10 ⁻³
19.6.80	16.24		2,37	8,3 10 ⁻⁴
19.6.80	16.39		1,72	9,7 10 ⁻⁴

Table 2: (cont.)

date	local time	$\frac{R}{\text{km}}$	$\frac{S(R)_{\text{max}}}{\text{m}^{-1} \text{sr}^{-1}}$
19.6.80	16.49	1,67	$5,9 \cdot 10^{-4}$
19.6.80	17.06	2,13	$1,0 \cdot 10^{-3}$
19.6.80	18.08	2,28	$5,6 \cdot 10^{-4}$
19.6.80	18.12	2,21	$8,8 \cdot 10^{-4}$

The depolarization δ ($\delta = \frac{S(R)_{\perp}}{S(R)_{\parallel}}$ where $S(R)$ is the lidar signature $\equiv \beta \tau^2$) was measured simultaneously. Table 3 gives some examples with date, height above ground, maximum backscatter value β and depolarization δ .

Table 3: Examples of depolarization measurements

Date	R (km)	$S(R)_{\text{max}}$	δ_{max}
6.2.80	1,10	$6 \cdot 10^{-5}$	0,11
6.2.80	1,37	$1 \cdot 10^{-5}$	0,13
6.2.80	1,42	$5 \cdot 10^{-5}$	0,14
6.2.80	1,20	$2,5 \cdot 10^{-5}$	0,42
7.2.80	0,7	$1 \cdot 10^{-5}$	0,45
7.2.80	1,0	$4,5 \cdot 10^{-4}$	0,18
17.4.80	8,9	$2 \cdot 10^{-5}$	0,42

Figure 6 shows an example of a received lidar signal (single echo) for graupel precipitation.

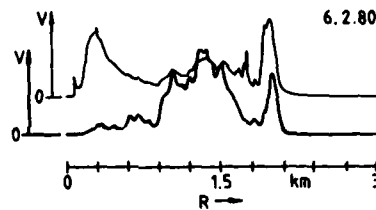


Figure 6: Example of depolarization measurement during precipitation (graupel)
 upper trace: lidar signal (voltage versus time \approx range) of the parallel polarized backscatter
 lower trace: perpendicular polarized backscatter component.

The very large depolarization was measured also by Platt [20]. Figure 7 shows the averaged profile of the same precipitation. The lidar signatures ($\beta \tau^2 = S(R)$) for both telescopes are shown versus altitude. The quotient Q represents the depolarization δ . There is again a very large depolarization in the precipitation regime and comparable low depolarization within the cloud (above 1.6 km).

There is in general always a depolarization within the cloud which exceeds the clear air depolarization ($\delta=0.05$) by a factor of two and more.

For mixed clouds the value $\delta = 0.2$ is possible. Ice-clouds have values of $\delta = 0.4$.

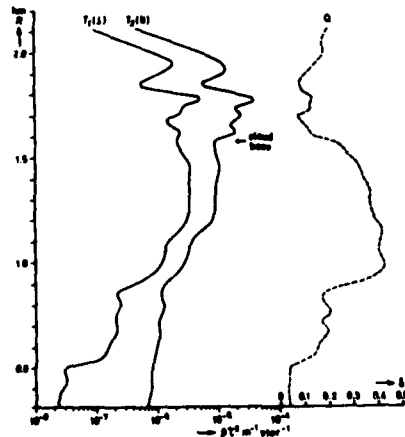


Figure 7: Lidar signatures for the graupel precipitation shown in figure 6. The depolarization Q shows the precipitation.

5. MEASUREMENTS OF MULTIPLE SCATTERING EFFECTS

5.1 Measurements in 1974

During 1974 we made the first multiple scattering measurements with a similar lidar to that described above using photomultipliers as detectors and polaroid pictures of the oscilloscope as signals. Different aperture sizes and different polarization direction was used as well as the Raman nitrogen component for determination of effects caused by the multiple scattering. The measurements were carried out under 30° elevation.

Figure 8 shows signals backscattered by a cloud and received with different telescope aperture angles. The upper beam is the reference signal from telescope 2 with 4 mrad aperture, the lower beam is the signal from the 40 cm telescope 1 at 2 mrad and 20 mrad. A pulse lengthening at the 20 mrad signal is observed. In figure 9 the computed values of $\delta\tau^2$, at different aperture angle, are plotted versus range R or the height above ground H. The upper scale shows the depolarization ratio measured at 4 mrad. Each curve represents the mean value of 10 received signals. The pulse lengthening effect, which shows the influence of the multiple scattering, is clearly to be seen [1,2].

Figure 10 shows signals backscattered by a cloud at different positions of the depolarization filters. These signals are similar to those reported by CARSWELL [5]. Figure 11 represents the computed values of $\delta\tau^2$ obtained at different polarization (parallel and perpendicular component) and plotted versus range R or height above the ground H. The upper scale shows the depolarization ratio for this single lidar measurement.

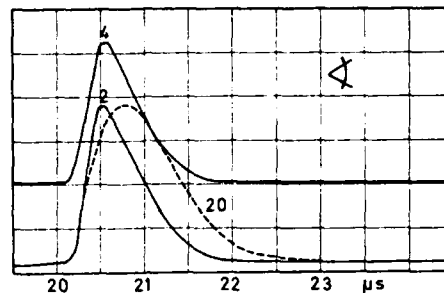


Figure 8: Signals backscattered by a cloud at different aperture angles (upper beam: 4 mrad constant, lower beam; 2, 20 mrad)

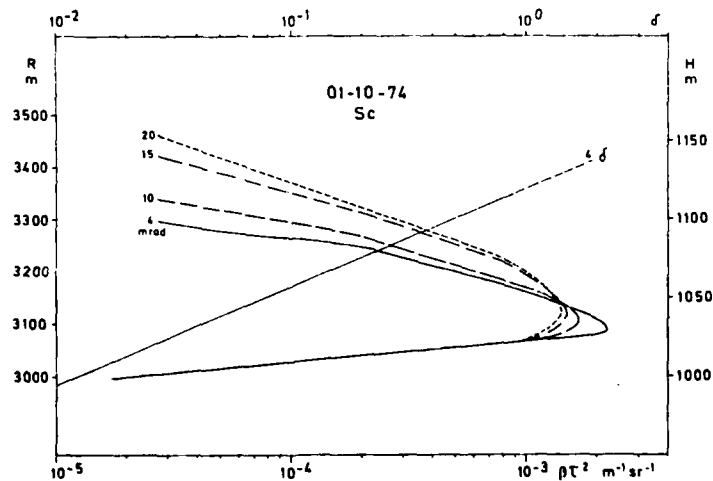


Figure 9: Values $\delta\tau^2$ versus range R or height above ground H measured at different aperture angles. The upper scale shows the depolarization ratio δ .

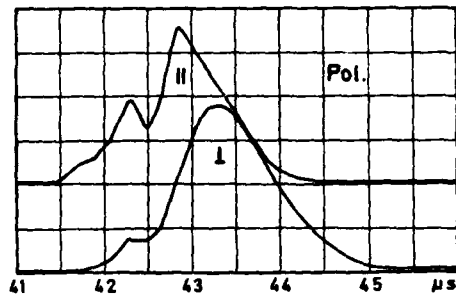


Figure 10: Signals backscattered by a cloud at parallel (upper beam) and perpendicular (lower beam) polarization.

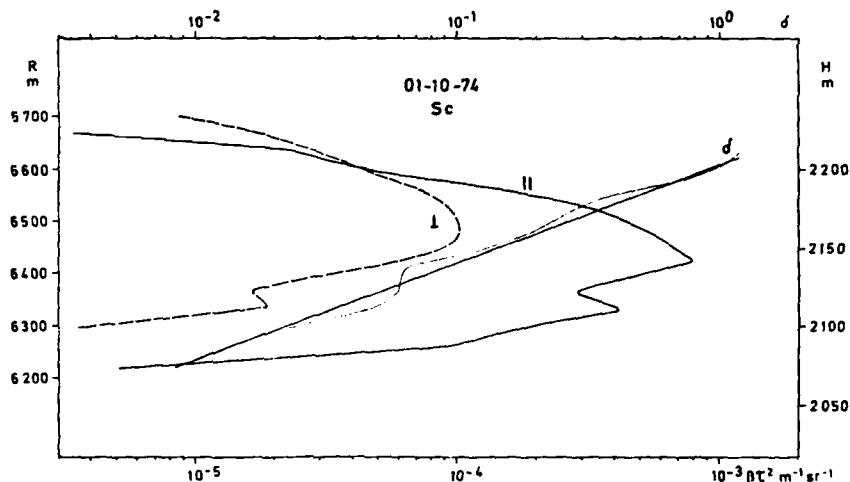


Figure 11: Values $B\tau^2$ versus range R or height H from figure 10. The upper scale shows the depolarization ratio δ .

At cloud top due the pulse lengthening process the perpendicular component will be greater than the parallel one.

Figure 12 shows measurements of the Raman nitrogen component. The curve $B_r \tau'^2$ represents the computed cloud signal at 694.3 nm. The curve $B_{R_n} \tau'^2$ is the computed signal from the Raman nitrogen component at 828.3 nm received with the 40 cm telescope. The computation was carried out with the same system constant as for the aerosol measurements, therefore the values $B_{R_n} \tau'^2$ are too large. The extinction, which is the influence of the cloud on the Raman signal, can be seen. This is very small compared with the single scattered shape of the cloud signal $B_r \tau'^2$ (dashed line).

By lidar measurements of water clouds (mostly stratocumulus clouds) we determined the influence of the pulse lengthening mechanism. The relation between the single volume scattering coefficient σ and the multiple volume scattering coefficient σ' could be determined by calculations and by comparison with measurements of the Raman-nitrogen component [24].

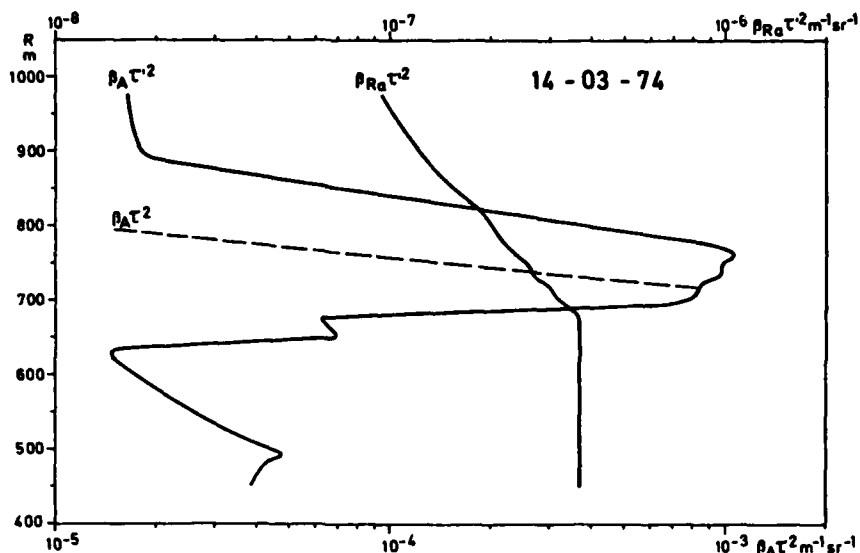


Figure 12: Values $\beta \tau^2$ versus range R
 lower scale: $\beta_A \tau^2$, $\beta_{Ra} \tau^2$ for $\lambda = 694.3$ nm
 upper scale: $\beta_{Ra} \tau^2$ for Raman-nitrogen component at $\lambda = 828.3$ n.

5.2 Beam spreading

After some necessary changes in the lidar system we renewed these measurements shown in section 5.1. Telescope 1 was used with a field stop of 5 mrad (13 mrad aperture), telescope 2 has the 5 mrad aperture. Polarization direction for both telescopes was parallel. Both signals together would give the 13 mrad signature. Figure 13 shows the result. The measured signatures $\beta \tau^2$ are drawn versus cloud altitude. The quotient q is the ratio for both signatures $S_{5-13}(R)/S_5(R)$. There is a linear increasing of the multiple scattering starting at the cloud base.

The dashed curve gives the theoretical expected values for an assumed homogeneous cloud with $\beta = 10^{-3} \text{m}^{-1} \text{sr}^{-1}$ ($\tau \approx 4$). The slope of this dashed curve is in good agreement with the measurements and this demonstrates, that Shipley's correction can be used for cloud measurements [17, 25].

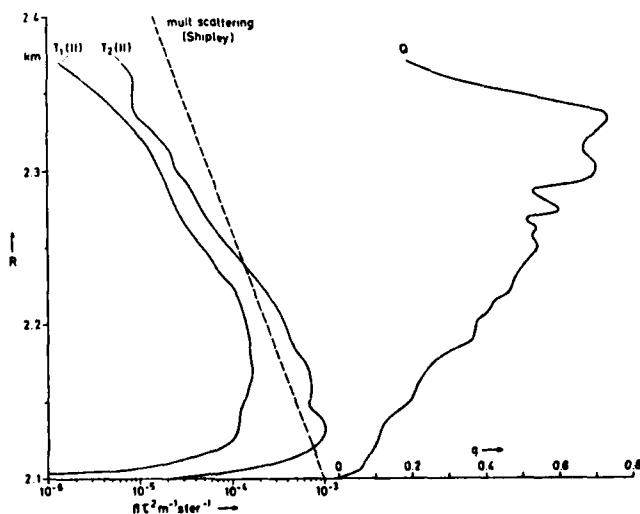


Figure 13: Example for beam spreading, measured cloud lidar signatures versus altitude.
 T1(II): 5 mrad field stop, 13 mrad aperture, parallel pol.
 T2(II): 5 mrad aperture, parallel pol.,
 dashed curve using Shipley's relation,
 Q = ratio of signature T1(II)/T2(II).

5.3 Pulse lengthening

The pulse lengthening could be studied by measuring the perpendicular polarized component using telescope 1 with 5 mrad field stop and 13 mrad aperture. Telescope 2 measures the parallel polarized component with 5 mrad aperture. Figure 14 shows the result. The signatures are drawn versus cloud altitude. The cloud base height was 200 m lower than that of figure 13. Contrary to the behaviour of the quotient Q shown in figure 13, there is an exponential increase of the depolarization with penetration. This caused by multiple scattering processes which change the polarization direction. This effect is direct related to the pulse lengthening.

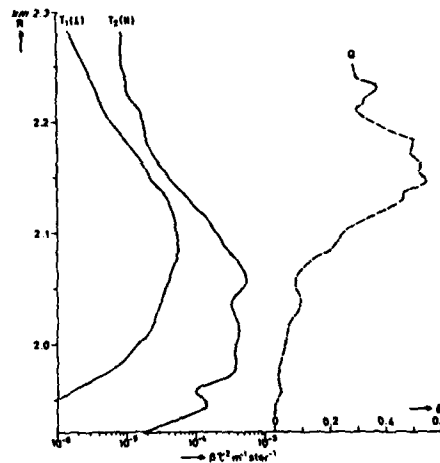


Figure 14: Example for pulse lengthening, measured cloud lidar signatures versus altitude.

T1 (I): 5 mrad field stop, 13 mrad aperture, perpend.pol.

T2 (II): 5 mrad aperture, parallel pol.

Q : ratio of signatures T1(I)/T2(II)

5.4 Dependency of the multiple scattering on the azimuth angle θ

It was assumed that the intensity of the multiple scattering is independent of the azimuth angle θ . First laboratory measurements of assymmetric behaviour were reported by Carsell [21]. There should be a dependency of the drop size and of the polarization direction.

Because the depolarization is also a value for the angle dependency, we could rotate the polarizer and measure the value $q_{S_{\parallel} \rightarrow \perp}$ where

$$q_{S_{\parallel} \rightarrow \perp} = \frac{\int_{R_1}^{R_2} S_{S_{\parallel} \rightarrow \perp}(R) dr_{\parallel} / \int_{R_1}^{R_2} S_S(R) dr_{\parallel}}{\int_{R_1}^{R_2} S_S(R) dr_{\parallel}}$$

is the quotient of the integral backscattering signature of the cloud. Table 4 gives the results. The values q_S are listed versus the polarization direction. The mean backscatter value $\int_{R_1}^{R_2} S_S(R) dr_{\parallel}$ is listed for comparisons.

Figure 15 shows the quotient q_S for measurement B in polar coordinates (1st quadrant). There is an inhomogeneous behaviour. A large portion of the multiple scattering is in forward direction as known from section 5.2. This represents the beam spreading. But there is an increasing also at $30^\circ \rightarrow 60^\circ$ before decreasing for the perpendicular component. Measurement C was made at optical thin ice cloud. There is an homogeneous behaviour caused by low multiple scattering.

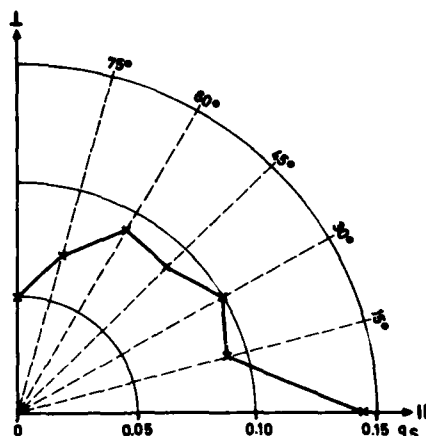


Figure 15: Angular behaviour of the multiple scattering, quotient q_s versus the polarizer angle for telescope 1 (5 mrad field stop, 13 mrad aperture)

Table 4: Results of measurements by varying the receiver polarization direction

Polarization direction	0	15	30	45	60	75	90
q_s for measurement A	24	23	15	24	16	13	11
B	15	9	10	9	9	7	5
C	9	9		5		5	7
D	5	8		5		5	4

6. CONCLUSION

With the described lidar system we could show the effects of multiple scattering from clouds. The beam spreading and the pulse lengthening could be measured separately. Additional measurements of signatures for different polarizing direction showed an effect of anisotropy of the multiple scattering.

These measurements should be repeated in the forthcoming years to get a statistic for different clouds in mid-Europe.

7. REFERENCES

- 1 BUCHER, E.A., 1973, "Computer Simulation of Light Pulse Propagation Through Thick Clouds", *Applied Optics*, 12, 2391-2400
- 2 BUCHER, E.A., and LERNER, R.M., 1973, "Experiments on Light Pulse Communication and Propagation Through Atmospheric Clouds", *Applied Optics*, 12, 2401-2414
- 3 ELORANTA, E.W., 1973, "An Approximate Equation for the Multiply Scattered Contribution to Lidar Return", 5th Conference on Laser Radar Studies, Williamsburg, Va., June 4-6
- 4 LIOU, K., and SCHOTLAND, R.M., 1971, "Multiple Backscattering and Depolarization from Water Clouds for a Pulsed Lidar System", *J. Atm. Sci.*, 28, 772
- 5 PAL, S.R., and CARSWELL, A.I., 1973, "Polarization Properties of Lidar Backscattering from Clouds", *Applied Optics*, 12, 1530-1536
- 6 VAN DE HULST, H.C., 1957, "Light Scattering by Small Particles", Wiley, New York
- 7 PINNICK, R.G., JENNINGS, S.G., CHYLEK, P., and HAM, C., "Backscatter and Extinction in Water Clouds", Abstract 10th International Laser-Radar Conference, Silver Spring, MD, Oct. 6-9, 1980, U.S.A.

- 8 PAL, S.R., and CARSWELL, A.I., 1976, "Multiple Scattering in Atmospheric Clouds", Applied Optics, 15, 1990-1995
- 9 RYAN, J.S., and CARSWELL, A.I., 1978, "Laser Beam Broadening and Depolarization in Dense Fog", J.Opt.Soc.Am., 68, 900-908
- 10 HARRIS, F.S., Jr., 1969, "Changes in Polarization and Angular Distribution of Scattered Radiation during Cloud Formation", Applied Optics, 8, 143-145
- 11 HARRIS, F.S., Jr., 1971, "Water and Ice Cloud Discrimination by Laser Beam Scattering", Applied Optics, 10, 732-737
- 12 SASSEN, K., 1980 "An Initial Application of Polarization for Orographic Cloud Seeding Operations", J.Appl.Meteor., 19, 298-304
- 13 MOORADIAN, G.C., GELLER, M., STOTTS, L.B., STEPHANS, D.H., KRAUTWALD, R.A., 1979, "Blue-green Pulsed Propagation through Fog", Applied Optics, 18, 429-441
- 14 STOTTS, L.B., 1977, "The Radiance Produced by Laser Radiation Transversing a Particulate Multiple-scattering Medium", J.Opt.Soc.Am., 67, 815-819
- 15 BOGDANOV, R.I., TJABATOV, A.E., SLJACHOV, V.I., Subjackij, A.B., 1979, "On Multiple Scattering in Turbid Medium Consisting of Spherical Particles", Meteorologija i Hidrologija, 2, 110-113
- 16 ELORANTA, E.A., 1972, "Calculations of Doubly Scattered Lidar Returns Thesis", Univ. of Wisconsin, Ph.D., Physics, Meteorology
- 17 SHIPLEY, S.T., 1978, "The Measurements of Rainfall by Lidar Thesis", Univ. of Wisconsin, Ph.D., Physics, Meteorology
- 18 WEINMAN, J.A., "Effects of Multiple Scattering on Light Pulses Reflected by Turbid Atmospheres", J.Atmosciences, 33, 1763-1771
- 19 KUNKEL, K.E., and WEINMAN, J.A., "Monte Carlo Analysis of Multiply Scattered Lidar Returns", J.Atmosciences, 33, 1772-1781
- 20 ALLEN, R.J., and PLATT, C.M.R., "Lidar for Multiple Backscattering and Depolarization Observations", Applied Optics, 16, 3193-3199
- 21 CARSWELL, A.I., PAL, S.R., and SMITH, R.B., 1980, "Multiple Scattering in Clouds measured by Laser Backscatter", Abstract 10th International Laser Radar Conference, Silver Spring, MD Oct. 6-9, U.S.A.
- 22 WERNER, Ch., and HERRMANN, H., 1981, "Lidar Measurements of the vertical absolute Humidity Distribution in the Boundary Layer", J.Appl.Meteor., in press
- 23 WOLFF, E., 1980, "Lidar-Rückstreuungsmessungen an Wolken, DFVLR-Mitt.80-12
- 24 WERNER, CH., 1974, "Determination of Multiple Scattering by Means of Laser Radar Rechniques", Abstract 6th International Laser-Radar-Conference, Sendai, Sept. 3-6, Japan
- 25 DERR, V.E., 1980, "Estimation of the Extinction Coefficient of Clouds from Multiwave-length Lidar Backscatter Measurements", Applied Optics, 19, 2310-2314

APPLICATION DES LASERS A LA MESURE A DISTANCE DES GAZ ATMOSPHERIQUES.
UTILISATION DE LA DIFFUSION RAMAN RESONNANTE.

Pourny J.C. - Hassab El Naby Salah.
Laboratoire d'Optique Appliquée, Palaiseau (France)

Résumé :

L'application des lasers à la télédétection des composés gazeux de l'atmosphère a été développée dans différentes techniques lidar faisant appel à plusieurs types d'interaction de la lumière monochromatique du laser avec les molécules atmosphériques.

Les mesures par absorption, principalement dans l'infra-rouge, permettent d'atteindre des sensibilités de l'ordre du ppb, sur un trajet de mesure de quelques centaines de mètres. La mesure lidar à absorption différentielle, moins sensible, apporte la possibilité d'une exploration dans toutes les directions avec une résolution en distance.

La mesure par lidar, basée sur la diffusion Raman, permet le sondage de nombreux constituants moléculaires avec une raie laser unique. Son emploi est toutefois limité à la mesure de composés de forte concentration.

L'utilisation de lasers accordables permet de mettre à profit des cas de résonance où la section de diffusion Raman augmente fortement. Le cas a été étudié pour NO_2 , SO_2 et O_3 .

On montre que la méthode est intéressante dans la détection de ces constituants dispersés en nuages.

I. INTRODUCTION

La détection et le dosage à distance en temps réel des composés de l'atmosphère intéressent plusieurs secteurs de recherche atmosphérique : la météorologie, la protection de l'environnement, la défense.

Bien que les mesures par prélèvement soient précises, elles sont pratiquement inadaptées à la surveillance permanente d'un grand volume d'air.

Des méthodes optiques actives qui exploitent l'interaction de la lumière d'un laser avec les molécules atmosphériques ont été appliquées avec succès à la mesure à distance de la composition de l'atmosphère.

Le système de télédétection est inspiré du radar transposé dans le domaine des longueurs d'ondes optiques. Il est dénommé LIDAR (Light Detection And Ranging). L'émetteur du lidar est un laser à impulsions. Le récepteur placé à côté de l'émetteur est un télescope qui collecte la lumière du laser rétrodiffusée par l'atmosphère. La lumière reçue est analysée en fréquence et en intensité. Le temps de trajet aller-retour de la lumière permet une analyse résolue en distance des intensités rétrodiffusées, lorsque la diffusion est instantanée.

Les phénomènes optiques principalement utilisés sont l'absorption moléculaire et les diffusions de la lumière (Rayleigh, Mie, Raman).

II. ABSORPTION SUR UN LONG TRAJET

II.1. La méthode par absorption consiste à mesurer la transmission par une épaisseur d'air à une longueur d'onde qui est absorbée par la molécule recherchée. En appliquant la loi de Beer-Lambert

$$T = \exp \left(- k(\nu) \int_0^L \frac{C}{N_0} dl \right)$$

On déduit de la transmission T la valeur intégrale de la concentration du composé sur le trajet de mesure de longueur L. $k(\nu)$ est le coefficient d'absorption différentiel, qui est relié à la section d'absorption par :

$$k [\text{cm}^{-1} \cdot \text{atm}^{-1}] = N_0 (\text{cm}^{-3} \cdot \text{atm}^{-1}) \sigma (\text{cm}^2)$$

avec $N_0 = 2,55 \cdot 10^{19} (\text{cm}^{-3} \cdot \text{atm}^{-1})$.

Comme les sections d'absorption sont élevées ($\sigma \approx 10^{-19} \text{ cm}^2$), la méthode est sensible.

Le tableau (1) montre quelques mesures faites par ce procédé sur des trajets de quelques centaines de mètres, généralement en absorption infra-rouge.

Les sensibilités sur la concentration moyenne sont de l'ordre du ppb.

Tableau 1

Détection de polluants gazeux par absorption sur un long trajet (ref. 1)

Polluant	Laser	λ μm	Trajet de mesure (km)	sensibilité
NO_2	Argon ionisé	0,5	3	
CH_4	He Ne	3,39	0,3	0,15 ppm
CO	diode	4,7	1	
NO	diode	5,3	0,22	
NO	CO	5,3	0,5	
O_3	CO_2	9,5	0,7	
C_2H_4	diode	10,5	0,25	
O_3	CO_2	9,5 10,3	0,08	0,02 ppm
O_3	CO_2	9,5	0,5	

Les installations de surveillance peuvent être équipées de multiples miroirs de renvoi permettant ainsi une couverture accrue (fig. 1, a). Dans le cas où la coopération d'un miroir de renvoi n'est pas possible, les objets diffusants qui sont en relief sur le terrain peuvent servir, mais la calibration de leur facteur de diffusion est difficile et l'installation doit être plus puissante (fig. 1, b).

II.2. Lidar à absorption différentielle

Les gaz et aérosols de l'atmosphère peuvent aussi servir de "réflecteurs" dans une mesure basée sur l'absorption moléculaire (fig. 1, c).

Ce principe a été appliqué dans le lidar à absorption différentielle (ref. 2, 3). L'utilisation de lasers pulsés puissants compense la faiblesse des rétrodiffusions et permet des mesures résolues en distance à partir d'une installation à une seule terminaison.

Le profil de concentration d'une molécule présente sur le trajet du laser est calculé à partir des signaux rétrodiffusés par l'air en diffusion Rayleigh-Mie pour deux longueurs d'onde voisines. Les longueurs d'onde sont choisies de telle façon que les coefficients de rétrodiffusion soient identiques dans les deux cas ; seule, l'absorption par la molécule intéressante diffère pour les deux raies utilisées.

L'exploitation des signaux rétrodiffusés fait appel à l'équation du lidar suivante :

$$n(R) = E_0 \cdot \frac{\lambda}{hc} \cdot \beta(\lambda, R) \cdot \frac{A}{R^2} \cdot \Delta R \cdot \exp - 2(\tau_e(\lambda, R) + \tau_i(\lambda, R)) \cdot \eta$$

$n(R)$ est le signal reçu exprimé en photoélectrons.

E_0 est l'énergie émise par le laser à la longueur d'onde λ .

β le coefficient de rétrodiffusion élastique à la distance R

A la surface de collection

$\Delta R = \frac{c\Delta T}{2}$ la résolution en distance déterminée par le temps d'intégration du récepteur

$\tau_e(\lambda, R)$ et $\tau_i(\lambda, R)$ sont les épaisseurs optiques de l'atmosphère sur le trajet du faisceau laser entre le lidar et le point situé à la distance R.

τ_e est la partie qui concerne l'atmosphère en l'absence de la molécule absorbante.

τ_i le terme dû uniquement à l'absorption par la molécule.

η est un facteur d'efficacité du récepteur.

Quatre valeurs sont nécessaires pour déterminer la concentration à une distance R

$$n(R, \lambda_1), n(R, \lambda_2), n(R + \Delta R, \lambda_1), n(R + \Delta R, \lambda_2)$$

en appliquant la loi de Beer-Lambert, on déduit la concentration C à la distance R

$$C = \frac{N_0}{2(K_2 - K_1)\Delta R} \cdot \log \left(\frac{n(R + \Delta R, \lambda_1) n(R, \lambda_2)}{n(R + \Delta R, \lambda_2) n(R, \lambda_1)} \right)$$

La sensibilité de la mesure par lidar à absorption différentielle peut être de quelques dizaines de ppb pour une résolution en distance de 100 m dans la mesure de NO_2 , SO_2 , O_3 à l'aide de lasers émettant dans le visible ou le proche U.V. (ref. 1).

II.3. Lidar Raman

Une technique lidar qui utilise un laser unique à longueur d'onde fixe, est applicable à la plupart des espèces moléculaires. C'est le lidar Raman.

L'effet Raman est une diffusion inélastique de la lumière par les molécules. La lumière Raman est diffusée avec un décalage de fréquence égal à une fréquence de vibration-rotation de la molécule. La fig. (2) montre les transitions possibles qui conduisent à la diffusion Raman.

À la température ambiante, seules les raies Stokes, correspondant à $\Delta v = 1$, sont utilisables. Les sections de diffusion sont de l'ordre de $10^{-3} \text{ m}^2/\text{sr}$. et varient avec la fréquence d'excitation suivant une loi en ν^4 .

L'effet Raman a été choisi pour les facilités qu'il apporte dans l'exploitation du lidar.

- Le choix de la raie laser est libre, mais un laser ultra-violet présente les avantages suivants :

- . meilleure sensibilité des détecteurs photoélectriques, bruit d'obscurité plus faible.
- . une section de diffusion Raman plus forte.
- . la possibilité de mesures de jour en l'absence de bruit de fond solaire si le laser a une longueur d'onde voisine de 2600 Å.

- Les raies Raman de vibration sont spécifiques des espèces moléculaires et facilement sélectionnées avec un monochromateur sur une plage spectrale de 4000 cm^{-1} à partir de la raie laser excitatrice.

- La diffusion est instantanée, ce qui permet d'obtenir des mesures résolues en distance avec un laser pulsé, en analysant la variation temporelle de l'intensité de la lumière rétrodiffusée.

- Enfin, la linéarité de l'effet Raman facilite les mesures de concentration.

L'inconvénient est la faible section efficace de la diffusion Raman.

L'équation du lidar Raman permet d'établir les profils de concentration d'une molécule N (R) à partir des signaux reçus à la fréquence Raman décalée $\nu = (\nu_0 - \Delta\nu)$. σ_r est la section de rétrodiffusion Raman. L'intensité du signal en photons reçus par incrément de distance ΔR s'écrit :

$$n(R) = \frac{E_0}{h\nu} N(R) \cdot \sigma(r) \cdot \frac{A}{R^2} \Delta R \exp -(\tau(\nu_0) + \tau(\nu)) \cdot \eta$$

- Le terme d'atténuation est composé d'un terme d'atténuation du faisceau laser à l'aller et un terme d'atténuation au retour de la lumière rétrodiffusée Raman dont la longueur d'onde est différente. Ces deux termes sont mal connus et demandent une calibration du lidar en temps réel. La méthode consiste à mesurer en plus les signaux rétrodiffusés Raman de molécules de référence telles que O_2 et N_2 dont les profils de concentration sont connus.

Dans le cas de la mesure de jour, on met à profit la forte absorption de la lumière solaire par l'ozone atmosphérique pour observer les signaux Raman en l'absence de bruit de fond de lumière solaire. Ces mesures sont affectées d'un terme d'absorption dû à l'ozone présent sur le trajet de mesure. Comme cette absorption est rapidement variable dans la région 2660 - 3000 Å, l'exploitation des signaux de O_2 et N_2 dont on connaît le rapport de mélange permet d'apporter un terme correctif qui tient compte de la concentration de O_3 .

Une installation lidar Raman adaptée à la mesure de faibles concentrations de gaz doit être équipée d'un laser U.V. très puissant et d'un télescope de grande surface. Une cadence d'émission rapide permet d'améliorer la sensibilité et de se rapprocher d'une mesure en temps réel. Si l'on accepte de perdre en résolution de distance, la sensibilité peut être augmentée.

Une étude expérimentale de la mesure de jour de l'humidité atmosphérique par lidar Raman nous a permis de définir une installation équipée de composants très performants dont on peut citer les spécifications à titre d'exemple (ref. 4).

- laser YAG quadruplé en fréquence : 80 mJ à 10 Hz à 266 nm
- télescope de 60 cm de diamètre
- monochromateur avec une transmission de 10 %
- rendement quantique du détecteur 25 %.

Compte tenu de la transmission de l'atmosphère dans le proche U.V., (fig. 3) les profils de vapeur d'eau atmosphérique peuvent être obtenus jusqu'à 1,8 km en 300 secondes avec une résolution verticale de 30 m. La précision de la mesure est encore de 10 % pour une concentration de 10000 ppm de vapeur d'eau. Une même précision peut être obtenue jusqu'à 3 km avec une durée de mesure de 10 minutes.

Le lidar Raman est un moyen pratique pour le dosage à distance des composés gazeux présents dans l'atmosphère à des concentrations de l'ordre de 1000 ppm. Une sensibilité de détection de l'ordre du ppm peut être obtenue à faible distance (ref. 5).

La sensibilité du lidar Raman peut être améliorée en recherchant l'augmentation des sections de diffusion. Comme il a été dit précédemment, on peut choisir des lasers U.V., mais dans certains cas, la valeur de la section de diffusion dépasse de beaucoup celle prévue par la loi en ν^4 . Ce sont des cas de résonance.

II.4. La diffusion Raman résonnante

La fluorescence résonnante ou diffusion Raman résonnante se présente lorsque l'énergie des photons de la source d'excitation approche celle d'une transition électronique permise de la molécule. L'effet s'accompagne d'une absorption de la lumière d'excitation et parfois de la lumière diffusée.

On distingue trois cas dont le schéma de transition est représenté dans la fig. 4

- fluorescence résonnante (fig. 4,d). La transition a lieu entre des niveaux discrets. Le laser est accordé exactement sur la raie d'absorption correspondante. Le niveau excité a une durée de vie longue. L'effet résonnant est faible en raison des désexcitations par collision. L'application quantitative est compliquée.
- la diffusion Raman résonnante (fig. 4,b et c) a lieu lorsque la longueur d'onde incidente s'approche d'une raie d'absorption électronique de la molécule ou entre dans le continuum d'absorption d'une molécule. On peut observer une forte augmentation de la diffusion Raman qui est instantanée, et dont l'intensité ne sera pas affectée par l'effet de "quenching" rencontré en fluorescence résonnante.
- les progrès des lasers accordables pulsés permettent d'exploiter ces cas de résonance avec la technique de détection par lidar.

III. DIFFUSION RESONNANTE DE NO₂, O₃, SO₂

La diffusion Raman résonnante de NO₂, O₃, SO₂ a été étudiée en vue de l'application à la mesure à distance par lidar de ces polluants de faible concentration.

- NO₂ a une bande d'absorption étendue de 320 à 1000 nm. L'analyse systématique de l'intensité de la raie de vibration de SO₂ à 750 cm^{-1} en utilisant un laser accordable entre 420 et 610 nm a permis à Rosen et al (ref. 6) de montrer que la section de diffusion Raman de NO₂ dépasse la valeur prévue pour la diffusion Raman ordinaire.

Un gain maximum de 10^2 est atteint avec une excitation à 454,7 nm. Les mesures faites sur notre installation de spectroscopie Raman (ref. 7) nous ont confirmé ce résultat. On a pu noter que la nature du spectre diffusé dépend de la longueur d'onde d'excitation et que la raie Raman apparaît nettement pour $\lambda = 444,4 \text{ nm}, 445,5 \text{ nm}, 447,7 \text{ nm}$.

Pour les autres longueurs d'onde, on observe un continuum de fluorescence qui masque la raie Raman.

L'utilisation d'une raie d'excitation très étroite devrait améliorer le contraste entre la raie Raman de résonance et la fluorescence.

- O₃ : l'ozone absorbe fortement la lumière entre 200 et 300 nm, et subit une dissociation. Ce continuum d'absorption est la bande de Hartley, (fig. 5). Penney (ref. 8) a montré qu'une diffusion Raman résonnante se produit si l'on excite l'ozone dans cette bande.

Dans le cas d'un continuum, l'ajustement de la raie du laser d'excitation n'est pas très critique : le gain en section efficace est lié au coefficient d'absorption de la molécule en fonction de la longueur d'onde. Un compromis doit être fait pour tenir compte de l'absorption de la lumière diffusée Raman.

Une mesure de la section de diffusion de l'ozone comparée à celle de l'oxygène a été faite pour la raie de vibration de O₃ à 1105 cm^{-1} en utilisant comme source d'excitation un laser YAG quadruplé émettant à 266 nm.

La diffusion Raman résonnante a été observée et le rapport des sections de diffusion évalué à 1200. Compte tenu d'un effet de prérésonance pour O_2 , la section de diffusion de O_3 est évaluée à $2,4 \cdot 10^{-30} m^2/sr$.

$-SO_2$ a une bande d'absorption électronique forte qui s'étend entre 260 et 340 nm, elle a une structure de raie (fig. 6). Les mesures de la section de diffusion Raman ont été faites par rapport à celle de l'azote. Un laser à colorant à rhodamine doublé en fréquence est utilisé et les raies laser sont ajustées sur les minimums et maximums de la bande d'absorption entre 292 et 298 nm. La raie Raman de SO_2 à 1151 cm^{-1} est accompagnée d'un fond de fluorescence.

Le tableau 2 montre les variations de la section de diffusion Raman résonnante de SO_2 ainsi que le rapport R entre l'intensité de la raie Raman et le fond de fluorescence. La valeur de la section de diffusion de N_2 à 300 nm est de $9,7 \cdot 10^{-34} m^2/sr$.

Un facteur de 10^3 apparaît entre la diffusion Raman résonnante de SO_2 et la diffusion Raman de N_2 .

Tableau 2

Section de diffusion Raman résonnante de SO_2

λ_K [nm]	position	C [ppm]	$\left(\frac{d\sigma}{d\Omega}\right) \cdot 10^{-30} m^2/sr$	Erreur %	R
292.1	max.	9596.6	1.066	23.1	1.01
292.5	-	9876.7	1.075	24.6	1.14
293.1	min.	9493.8	1.5441	22.2	1.04
293.9	max.	7886	1.926	21.0	1.7
295.2	min.	9000.8	1.087	23.8	1.58
295.9	max.	6047	3.093	18.7	1.83
297.1	min.	6697.7	1.964	20.3	1.8
298.1	max.	9221.7	1.323	22.6	1.4

IV. ESTIMATION DES PERFORMANCES D'UN LIDAR RAMAN RESONNANT

L'application de l'équation du lidar permet d'évaluer les performances d'un lidar Raman résonnant.

Les mesures qui ont été faites sur la diffusion résonnante de NO_2 , SO_2 et O_3 nous permettent d'évaluer les performances d'installation lidar réalistes, adaptées à chaque cas.

Pour O_3 , on envisage un lidar dont les caractéristiques sont celles du lidar diurne décrites plus haut. On distingue deux éventualités :

- mesure d'une concentration uniforme de 35 ppb d'ozone
- mesure d'un nuage d'ozone de 1 ppm sur un fond naturel de 35 ppb.

Pour NO_2 et SO_2 , on se base sur un lidar de caractéristiques suivantes :

- énergie des impulsions laser 50 microjoules
- cadence 10 Hz
- surface du récepteur $0,8 m^2$
- transmission de l'optique 10 %
- rendement quantique du détecteur 25 %

Tableau 3

Estimation des performances d'un lidar Raman résonnant pour NO₂, O₃, SO₂.

Molécule	NO ₂	O ₃	SO ₂
Décalage Raman cm ⁻¹	(v ₂) 750	1105	(v ₁) 1151
Laser d'excitation nm	454.7	266	299.9
σ_R m ² /sr	5.6.10 ⁻³¹	2.4 10 ⁻³⁰	1.10 ⁻²⁹
Section d'absorption à λ_0	3 10 ⁻²³	9 10 ⁻²²	5 10 ⁻²³
Section d'absorption à λ_R	3 10 ⁻²³	6 10 ⁻²²	-
Energie laser et nombre de tirs	50 μ J x 750	80 mJ x 3000	50 μ J x=1000
Surface du récepteur m ²	0.8	0.28	0.8
Résolution en distance m.	10	30	10
Concentration	5 ppm	35 ppb nuage de uniforme 1 ppm	5 ppm
Précision de la mesure à 100 m	de nuit uniquement 10 %		de jour 10 %
Précision à 500 m		8 %	2 %

V. CONCLUSION

Le lidar basé sur l'effet Raman de résonance permet la détection à distance de polluants peu concentrés, à l'aide de lasers de faible puissance accordés à la longueur d'onde correspondant à une transition électronique de la molécule considérée.

Ce type de lidar est bien adapté à la détection de nuages de polluants, mais la détermination de profils de concentration du polluant est plutôt malaisée. Cette difficulté provient de l'absorption par cette molécule de la lumière du laser et aussi de la lumière diffusée Raman.

La méthode n'est pas générale, mais elle a le mérite d'être applicable à quelques polluants importants tels que NO₂, SO₂ et O₃.

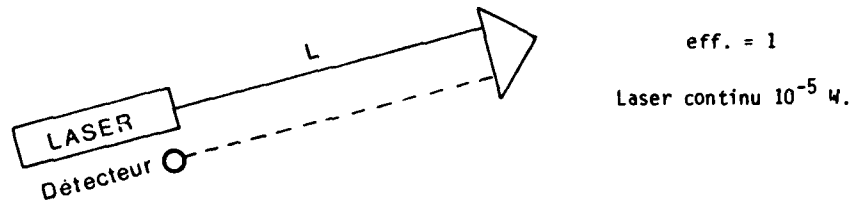
Cette étude a été faite avec le soutien de :

- la DIRECTION DES RECHERCHES ETUDES ET TECHNIQUES (D.R.E.T.) Contrat 78/045
- le MINISTRE DU CADRE DE VIE (M.C.V.) Contrat 74/29
- la METEOROLOGIE NATIONALE, Contrat 2/75.

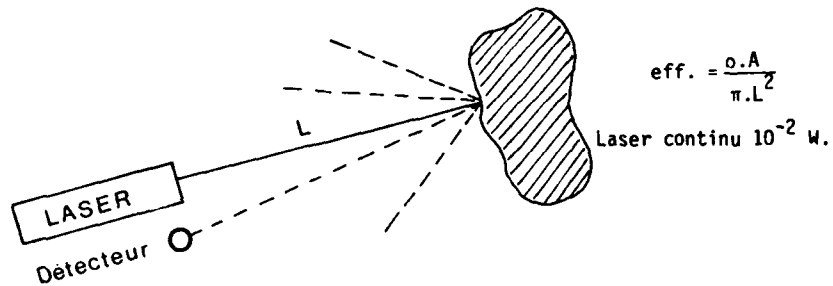
REFERENCES

1. R.H.T. Collis and P.B. Russel
"Lidar measurement of particle and gases"
Topics in Applied Physics, n° 14, Springer Verlag Berlin Heidelberg N.Y. (1976).
2. R.M. Schotland
"Errors in the lidar measurement of atmospheric gases by differential absorption"
J. App. Meteor. 13, 71 (1974).
3. G. Megie and R.T. Menzies
"Complementarity of U.V. and I.R. differential absorption lidar for global measurements of atmospheric species"
Applied Optics 19, 7 pp. 1173-1182 (1980).
4. D. Renaut, J.C. Pourny, R. Capitini
"Daytime Raman-lidar measurement of water-vapor"
Optics Letters 5, 6 pp. 223-235 (1980).
5. T. Hirschfeld et al.
"Remote spectroscopic analysis of ppm-level air pollutants by Raman spectroscopy"
Appl. Phys. Lett. 22, 1, pp. 38-40 (1973).
6. H. Rosen, P. Robrish, O. Chamberlain
"Remote detection of pollutants using resonance Raman scattering"
Applied Optics 14, 11, p 2703 (1975).
7. S. Hassa El Naby
"Etude de la diffusion Raman résonnante de NO₂ et SO₂ aux fins de détection par lidar dans l'atmosphère"
Thèse de Docteur-Ingénieur (1980).
8. C.M. Penney
Laser Raman Diagnostics, Plenum Press, (1974).

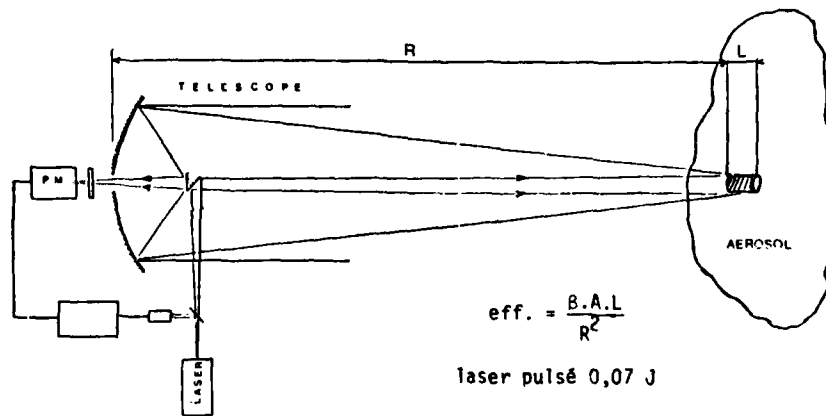
Fig. 1



1.a. absorption sur une longue distance avec réflecteur



1.b. absorption sur une longue distance avec réflecteur topographique



1.c. rétrodiffusion par les aérosols. Absorption différentielle

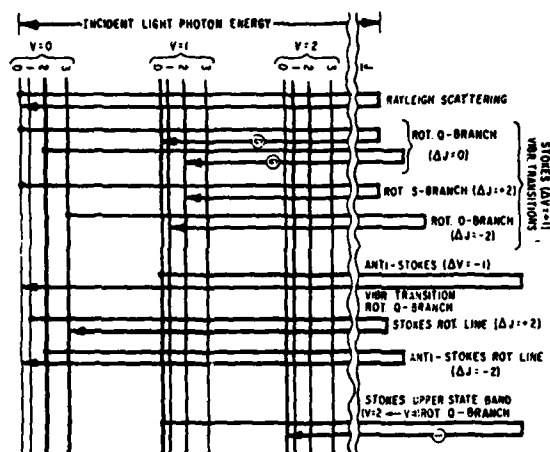


Fig. 2 : quelques transitions Raman permises pour une molécule diatomique (d'après C.M. Penney, 8th international laser Radar Conference, Philadelphia 1977).

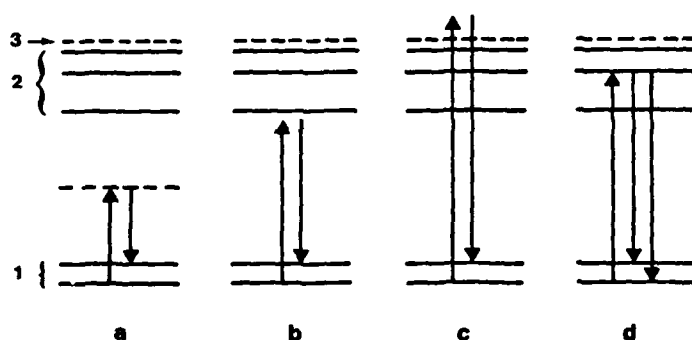
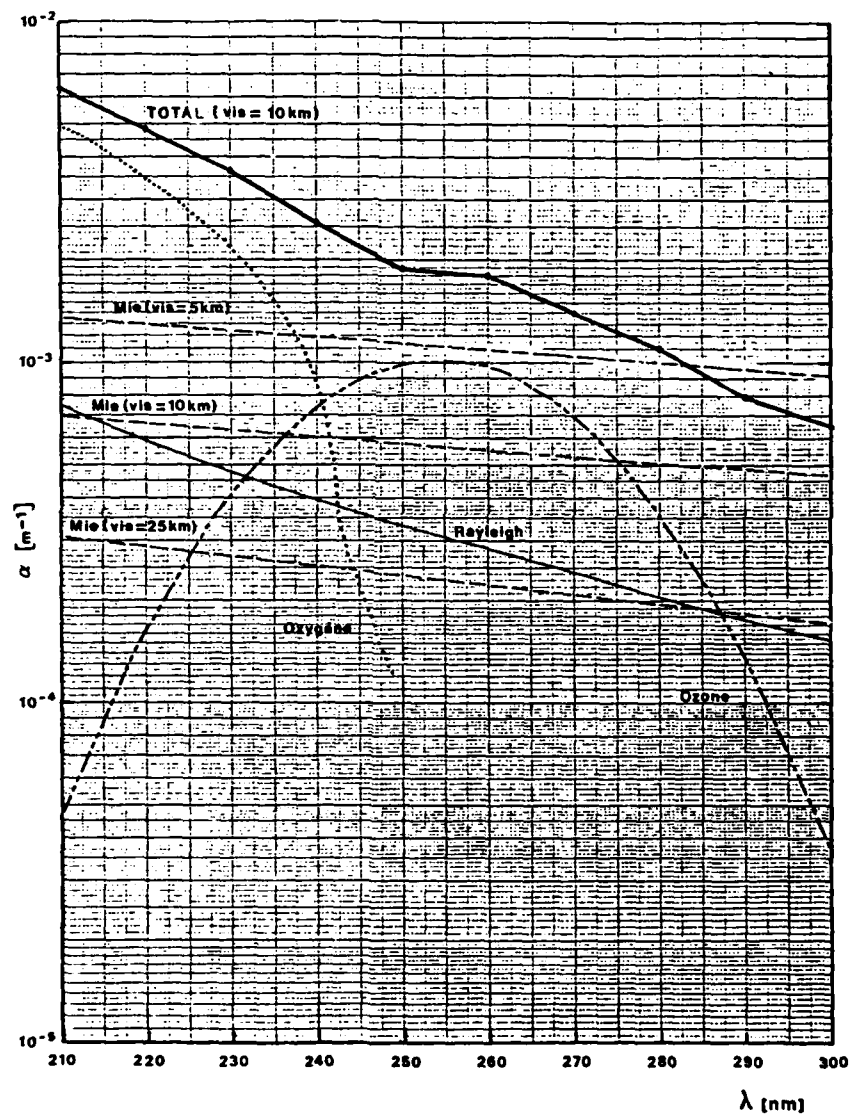


Fig. 4 : Schémas quantiques de deux états électroniques de la molécule et des interactions possibles avec un photon

- a) diffusion Raman ordinaire
 - b) diffusion Raman résonnante à proximité d'une raie
 - c) diffusion Raman résonnante dans un continuum
 - d) fluorescence résonnante
- 1) état électronique fondamental (2 niveaux de vibration)
 - 2) état excité (plusieurs niveaux de vibration)
 - 3) seuil de photodissociation.

Fig. 3 : Coefficients d'atténuation atmosphérique au sol dans l'ultra-violet pour des conditions standard.

(Pour la diffusion de Mie, la concentration en aérosols est paramétrée par la visibilité ; pour l'ozone on a supposé une concentration de 35 ppb).



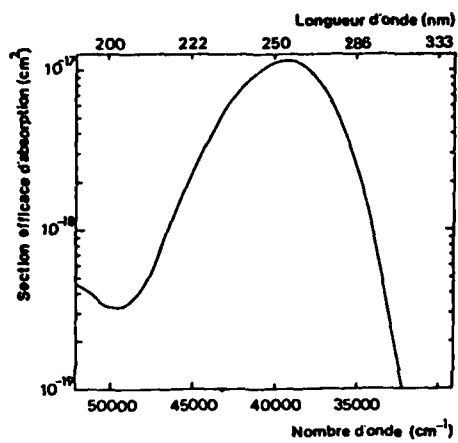


Fig. 5. Absorption de O_3 (bande de Hartley)

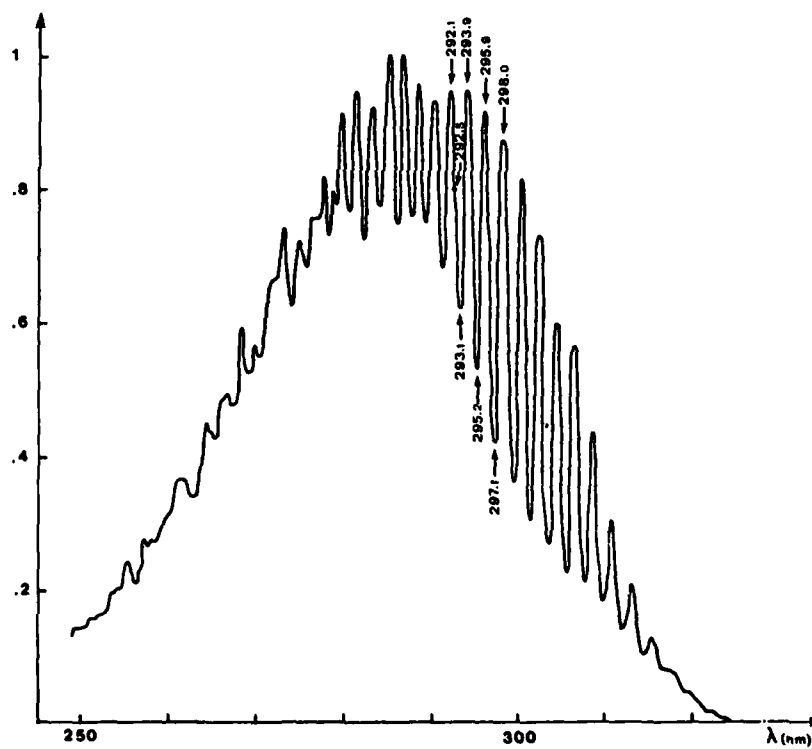


Fig. 6. Absorption de SO_2 (250 - 320 nm)

MULTIWAVELENGTH EXTINCTION AND INDEX FLUCTUATION MEASUREMENTS

E. C. Crittenden, Jr, E. A. Milne, A. W. Cooper,
G. W. Rodeback, and S. H. Kalmbach
Department of Physics and Chemistry
Naval Postgraduate School
Monterey, California, 93940

SUMMARY

Techniques have been developed at the Naval Postgraduate School for measurement of the effects of aerosols and turbulence on optical propagation through the atmosphere. The measurements are made with double ended systems. Path lengths up to 15 km have been utilized. For horizontal paths, the length is limited by the curvature of the earth. Both band-filtered grey body and laser sources are used for extinction measurements at 16 wavelengths, from 0.4 to 10 micrometers. A chopped beam is used with synchronous detection, to improve signal-to-noise ratio. Detection and digitization of the received signal are triggered by means of a small-divergence pulsed pilot laser beam, located at the center of the main beam. This also provides continuous verification of centering of the beam on the detector and permits extinction measurements with moving platforms. The pilot beam also functions as a laser rangefinder. Experiments have been carried out with ship-mounted and aircraft-mounted sources, and with ship-mounted receivers. Measurement of the effects of turbulence on the index of refraction, expressed in terms of C_n^2 , have been made by means of scintillation and Optical Transfer Function (OTF). The scintillation method preferentially weights the middle of the path relative to the ends, while the OTF method preferentially weights the telescope end of the path. Equipment has been developed to make OTF measurements with a pulsed source on an aircraft during a fly-over. Agreement between predicted and observed values of extinction and C_n^2 has been steadily improving, with quite good agreement achieved in the most recent two-week field experiment, MAGAT-1980 (Monterey Aerosol Generation and Transport) experiment, reported in another paper at this meeting. (Davidson, et. al. 1981)

1. INTRODUCTION

This paper reports experimental techniques for measurement of effects of turbulence and turbidity on optical propagation through the atmosphere. The measurements are made concurrently with large scale and micrometeorological measurements, and with measurements of aerosol particle size spectra.

2. TURBULENCE

The turbulence structure constant for refractive index, C_n^2 , can be obtained from measurements of the atmospheric optical transfer function (OTF) for imaging through the atmosphere, or from measurements of scintillation. Of the two methods, the OTF is subject to fewer complicating problems in interpretation. However, for situations in which the value of C_n^2 is not uniform along the path, the values of C_n^2 obtained by the two methods have different path-position weighting. The OTF method weights the end nearest the measuring instrument most heavily. Scintillation, for the case of a point source and a small aperture receiver, and nonsaturated conditions, weights the center of the path most heavily. The relative weightings, as a function of path position are shown in Figure 1. The weighting for scintillation can be somewhat modified by spatial filtering to shift the maximum toward either end (Ochs, et. al. 1976), and the curves flatten for saturation conditions (Wang, 1978).

3. RESOLUTION (OTF)

In the technique utilized at the Naval Postgraduate School (NPS), a laser at the far end of the optical path is diverged to illuminate a fairly large region at the instrument end of the path, serving as a point source for viewing by the measuring instrument. The instrument is a high magnification telescope, with the image scanned across a slit by means of a moving mirror. The signal as a function of time resulting from the light passing through the slit, the line spread function, is digitized and signal-processed. The digitized scans can be directly averaged to obtain a long-term line spread function, or each scan can be centered before averaging to produce an image-centered line spread function. The centering shifts are also tallied and the root mean square deviation calculated to yield "image wander".

The stored average of a number of scans is processed to yield the Fourier transform. This in turn is divided, point by point, by the Fourier transform of the ideal image for the telescope, to yield the OTF of the atmosphere. C_n^2 is obtained by fitting the OTF curve to a theoretical expression by Fried (1966):

$$\text{OTF} = \exp \left\{ -21.6 C_n^2 z_0 (f)^{5/3} - 1/3 \left[1 - \alpha \left(\frac{f\lambda}{D} \right)^{1/3} \right] \right\}$$

Where: z_0 is the range; f is the angular spatial frequency in cycles per radian; λ is the wavelength; α is unity for image centered near field, but decreases to 1/2 for far field; α is zero for the uncentered average; D is the diameter of the optics.

This expression has been found to fit the experimental data over a wide range of the parameters, in measurements carried out here (Crittenden, et. al., 1978) As a result, measurements at a single wavelength can be safely scaled to other wavelengths. Since the effects of turbulence are larger at shorter wavelength, and the required optical systems are smaller, the measurements are now usually made in the red or near IR.

A long-term average OTF and an image-centered OTF curve are shown in Figure 2. The solid lines are the theoretical curves, fitted with C_n^2 as the single fitting parameter.

A value of C_n^2 is also available from the image wander by:

$$C_n^2 = 0.914 \sigma^2 D^{1/3} z_0$$

where: σ^2 is the variance of the angle of arrival, i.e., the image wander, squared.

When either the source or the instrument is on an unstable platform, only the image-centered OTF can be obtained. However, by use of the above equations, the expected wander due to the atmosphere can be calculated.

Measurement of C_n^2 by the OTF method has the advantage that the results are very insensitive to intensity fluctuation at the source. As a result it is readily adaptable to use of a source on an unstable platform. For example, a broadened laser beam from an aircraft can be utilized as a source with little or no orientation stabilization required. Another advantage is that the phenomenon does not appear to saturate in high C_n^2 conditions, as is typical of scintillation, although saturation-resistant scintillation measurements can be made with incoherent sources under specialized conditions (Wang, et. al., 1978). The effect of finite aperture size is well understood for OTF, in contrast with scintillation, for which aperture averaging correction shows rather poor consistency, especially under saturation conditions.

4. SCINTILLATION

Measurement of C_n^2 by means of scintillation can be accomplished using relatively unsophisticated techniques, especially where the source and instrument are at fixed locations, and either the range is short or C_n^2 is small. The instrument used is a photodetector behind a small circular aperture, and the source a distant diverged laser. The variance, $\sigma_{\ln I}^2$, of the logarithm of the intensity is given by:

$$\sigma_{\ln I}^2 = 0.496 C_n^2 k^{7/6} z_0^{11/6}$$

where $k = 2\pi/\lambda$

The value of $\sigma_{\ln I}^2$ saturates as the value of C_n^2 , or of the range, increases, with $\sigma_{\ln I}^2$ reaching a maximum value of approximately unity, and falling off slowly, for higher values of C_n^2 or range. It is usually considered impractical to measure C_n^2 by this method when the log-intensity variance exceeds about 0.4.

A saturation resistant technique for measuring C_n^2 has been developed by Wang et. al. (1978) utilizing incoherent sources, and large aperture sources and receivers. However, the aperture sizes become prohibitively large for the long ranges often needed to avoid shore or ship influence in overwater measurements. For Monterey Bay, with ranges up to 15 km, the simpler coherent source technique has been used, with long wavelength to minimize saturation (10.6 micrometer CO₂ laser). Saturation was not encountered in the data reported in paper 06 at this meeting. (Davidson, et. al. 1981). Aperture averaging has been eliminated in those data by using small receiver aperture, usually 2.5 cm diameter, less than one tenth of the first Fresnel zone. The absence of aperture averaging was also routinely verified by check measurements made at larger apertures up to 12 cm diameter.

Scintillation has been measured here by using a laser source, pulsed at about 1-2 kHz to eliminate the background radiation, which is always present in daylight conditions even through a narrow band interference filter. The frequency is high enough to include the highest scintillation frequency components, occurring in the nonsaturated regime. The signal is synchronously detected, with the receiver triggered by means of a telemetered radio signal from the source. The difference of the beam-on and background signals is used to reconstruct a "cw" signal. This is processed through a logarithmic amplifier to produce a log-intensity signal. That signal is digitized at each update of the log signal at the 1-2 kHz rate. An on-line minicomputer stores the data to produce a probability density curve such as shown in Figure 3. The minicomputer then calculates the best-fit of a Gaussian distribution to obtain the variance, σ_{log}^2 , and from it C_n^2 . During most of the measurements the probability density curve is viewed directly on an oscillograph screen before the value of C_n^2 is accepted. Anomalous distributions sometimes occur due to shifts in laser intensity. Saturation also is detectable because the distribution then shifts toward exponential, which on a log-intensity probability density plot looks a bit like a Gaussian but does not approach zero at low log-intensity.

In seaborne or airborne experimental equipment, a serious problem is the instability of the platform, often coupled with a rapid change of range. Such systems also are not amenable to use of retroreflectors because of the large variation of reflectivity with incidence angle exhibited by most retroreflectors.

One method, used here, to minimize the effects of the above problems, utilizes a fanned beam source, with the fanned beam oscillated perpendicular to the fan, so that the receiver sees a pulsed signal. This has the effect of increasing the practical beam width in the direction of the long dimension of the fan, for given central intensity. The motion in the direction perpendicular to the fan sweeping across detector gives pulses whose intensities are not affected by small movements of the source. The problem of saturation can be reduced by increasing the wavelength; this led to the selection of a CO_2 laser source at 10.6 micrometers for the data reported in paper 06 (Davidson, 1981) at this meeting.

As mentioned earlier, the values of C_n^2 obtained by the scintillation method emphasize the path center. This was the driving reason for use of scintillation rather than OTF to obtain the MAGAT-1980 results reported in paper 06. The values of C_n^2 at the center of Monterey Bay were desired, as these would be more representative of open water than values near shore. Since source and receiver were on shore on opposite sides of the bay, scintillation was indicated as the preferred technique. Fortunately, C_n^2 remained sufficiently small that saturation of did not cause a serious problem.

5. EXTINCTION

Measurement of extinction is accomplished with a double-ended system and is straightforward in principle, although the experimental difficulties are more demanding than for measurement of C_n^2 . The techniques include some novel methods for assuring precision in the face of platform instability, source calibration drift, and atmospheric turbulence. The sources are lasers or grey bodies with wavelengths from 0.4 to 10.6 micrometers. In general, the grey bodies are more stable than the lasers, and lasers are only used because data at specific laser wavelengths are required for some applications.

6. GREY BODY SOURCES

Two types of grey body source are in use, a ribbon filament glass-enclosed tungsten lamp, for the wavelength region from 0.4 to 2.5 micrometers, and an electrically heated ceramic cylinder, open to the atmosphere, for wavelengths from 2 to 14 micrometers. These sources are, respectively, at the foci of 10 inch and 18 inch diameter Cassegrain telescope transmitter systems. The systems are all-reflective, except for the envelope of the tungsten lamp. In each system a chopper wheel interrupts the light to give a square-wave modulated signal at a frequency of about one kilohertz. The optical beams transmitted by these sources produce real images of the source emitters at the plane of the receiver, at a range that usually lies between 2 and 15 kilometers during measurements. The image width at the receiver is correspondingly between 4.6 and 34 meters. More importantly, the width of the projected image at the receiver, on a calibration range of 335 meters is wide enough to span the 18 inch diameter aperture of the receiving telescope. That receiver is an all-reflective Cassegrain, forming a real image of the finite width source on a pinhole

aperture ahead of the detector. This wavelength is selected by interference filters, as indicated in Table I. These wavelengths were chosen to lie in the relatively transparent windows of the atmosphere, since the principal interest here has been in evaluating the extinction due to aerosols, rather than molecular absorption. The detectors used are also listed in Table I. The detectors are interchanged by means of a fast interchange system using a rotatable mirror. The optical systems of the transmitters and receiver are such that any small off-focus maladjustment does not alter the received power through the pinhole. Alignment and focus of the transmitter and receiver are verified by angular scanning to ensure that a flat-topped variation with sharp edge cut-off is observed. The grey body sources are current-regulated and the voltage is monitored. Source emission is monitored with a photocell mounted in the central obscuration of each telescope. The reflectivity of each optical system can be internally monitored with a local LED, transmitting through the system to a photo cell. This is significant for measurements made in a marine environment where sea spray is a constant problem.

Calibration of the systems is accomplished by bringing the complete transmitter system to close range. The transmitter system is mounted on a ground-supported platform with the upper part of the platform within the body of a 3/4 ton truck. The legs of the platform can be hydraulically retracted and the truck driven to a calibration site near the receiver. The minimum range for which the projected real images of the sources will span the receiver aperture is about 250 meters. Calibration ranges of about 350 meters were usually used. Signals measured at this range are attenuated, with careful attention to linearity, and the signals processed through the same system as for the long range measurements. Reference unattenuated signal levels for the long range data are then inferred by application of the inverse square law.

The square-wave signals received over the long path are digitized sixteen times per cycle. Synchronization of the digitization with the source pulses is provided by a trigger signal, generated at the source from the square-wave output of the monitoring photocell. This trigger is relayed over a uhf radio telemeter link from the source to the receiver end of the range. Four values sampled from the center of the beam-on portion of the received signal are stored in the computer memory, and four values from the beam-off portion are similarly stored, to record the background level. The difference of the averages of the signal and background is then used to determine the received intensity. The ratio of this to the calculated unattenuated intensity is the transmittance. This longterm averaging removes the fluctuations due to scintillation in the atmospheric turbulence.

7. LASER SOURCES

Extinction measurements with laser sources are more difficult, since lasers tend (at least for TEM₀₀ lasers) to have Gaussian beam profiles in place of the "flat-topped" real image formed with a finite source. Lasers also tend to be less stable in intensity than grey bodies. The problem of temporal fluctuations in intensity can be overcome by telemetering a synchronous reference measurement made at the source. The gaussian beam profile necessitates very accurate location of the beam center on the receiver aperture. For the measurements described in this paper, the beam location is achieved by using a scanning system consisting of two counter-rotating small angle prisms at the source to produce a cyclic deflection of the beam. This system also produces two electrical pulses each cycle, at the times of maximum beam deflection. These pulses are telemetered to the receiver end of the optical path by radio and used to trigger the sweep of an oscillograph displaying the intensity of the received optical signal. If the beam is centered, the forward and back scans of the beam across the receiver are superimposed on the oscillograph screen. The operator at the receiver end relays the position information by voice radio to the operator at the source end, to optimize the alignment. Rotation of the scanning system by 90° permits alignment in the perpendicular plane. Since alignment is so critical in the case of the Gaussian beam, the overall accuracy of extinction data obtained with laser sources is less than with grey body sources.

8. MOVING PLATFORM - PILOT BEAM

Extinction measurements made with moving platforms are more difficult, because of the problem of assuring that source and receiver are properly aligned. This difficulty has been surmounted by using a pilot beam. This is a GaAs pulsed laser beam collimated to a small divergence and aligned to lie in the center of the beam from a grey body source transmitter. The laser pulse is triggered to occur synchronously with the square-wave modulated grey body beam. The receiver, which may be mounted

on a gyro-stabilized platform on shipboard, is collimated parallel and coaxial with a small receiver for the GaAs pulse. The GaAs pulse is used to trigger digitizing of the main receiver pulse. Thus a signal is digitized and recorded only if the receiver is in the center of the transmitted optical beam and only if the receiver is pointing in the proper direction. Angular deviations of the tracking on shipboard, or at the source transmitter, only lead to reduction in the number of accumulated data points, but not to erroneous data.

The pilot beam pulses, returned to the transmitter by a retroreflector, also serve as a laser rangefinder to provide continuous values of the range, when the range is varying.

9. CORRECTION FOR ABSORPTION

The transmittance obtained directly from the ratio of the corrected received and transmitted intensities leads directly to the overall extinction coefficient. This extinction includes the effects of absorption by molecules and aerosol particles, and the scattering loss due principally to the aerosol. The aerosol extinction is extracted from the total extinction using a LOWTRAN calculation of molecular absorption based on the meteorological conditions determined on shipboard.

10. RESULTS

Results obtained during MAGAT-1980, using the techniques described above, are reported in paper 06 at this meeting, where they are used to make direct comparisons with model predictions.

11. ACKNOWLEDGEMENTS

This research was supported by NAVSEA (HEL), NAVAIR, and U.S. Army MICOM.

12. REFERENCES

Crittenden, E. C., Cooper, A. W., Milne, E. A., Rodeback, G. W., Armstead, R. L., Kalmbach, S. H., Land, D., and Katz, B. "Optical Resolution in the Turbulent Atmosphere of the Marine Boundary Layer", Naval Postgraduate School Report, NPS61-78-003, 1978

Davidson, K. L., Schacher, G. E., Fairall, C. W., "Meteorological Descriptions for Optical Properties", Proc. AGARD Conf., Monterey, California (NATO), 1981.

Fried, D. L., "Optical Resolution through a Randomly Inhomogeneous Medium for Very Long and Very Short Exposures", J. Opt. Soc. Am., 56, 10, 1372, 1966.

Ochs, G. R., Ting-i Wang, Lawrence, R. S., and S. F. Clifford, "Refractive Turbulence Profiles Measured by One-Dimensional Spatial Filtering of Scintillations", Applied Optics, 15, 10, 2504, 1976.

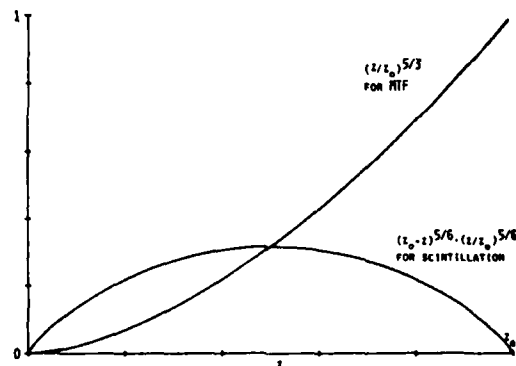
Selby, J. E., Shettle, E. P., and McClatchey, R. A., "Atmospheric Transmittance from 0.25 to 28.5 Micrometers: Supplement LOWTRAN IIIB", Airforce Geophysical Laboratory Report AFGL-TR-76-0258, 1976.

Wang, T., Ochs, G. R., Clifford, S. F., "A Saturation-Resistant Optical Scintillometer to Measure C_n^2 ", J. Opt. Soc. Am., 68, 3, 334, 1978.

TABLE I.
SUMMARY OF LASER AND GREY BODY SYSTEMS

LASER SYSTEMS				
Wavelength, micrometers	Source	Detector	Comments	
0.4880	Ar ion laser	Si avalanche	Stable	
0.6328	He-Ne laser	"	Very stable	
1.06	Nd-YAG laser	"	Unstable, marginal for extinction	
3.8	DF laser	InSb 77K PV	Laser too bulky for field use	
10.6	CO ₂	HgCdTe 77K PC	Unstable, but suitable for scintillation data	

GREYBODY SYSTEMS				
Wavelength micrometers	Filter bandwidth micrometers	Source	Detector	Comments
0.49	.010	10 inch aperture, 2800K grey body, glass enclosed	Si avalanche	Matches laser
0.63	.010	"	"	"
0.84	.010	"	"	Window peak
1.03	.010	"	"	"
1.06	.010	"	"	Matches laser
1.60	.098	"	Ge p-i-n PV	Window peak
2.15	.097	"	InSb 77K PV	"
3.80	.40	18 inch aperture, 1800K grey body, open to atmosphere	"	Window peak matches laser
3.835	.14	"	"	Narrow band
10.66	2.85	"	HgCdTe 77K PC	Window Peak Matches laser
11.02	.72	"	"	Narrow band



RELATIVE WEIGHTING OF C^2 AS A FUNCTION OF POSITION ALONG THE PATH, FOR RTF AND FOR SCINTILLATION. THE TELESCOPE END OF THE PATH IS AT THE RIGHT.

Figure 1.

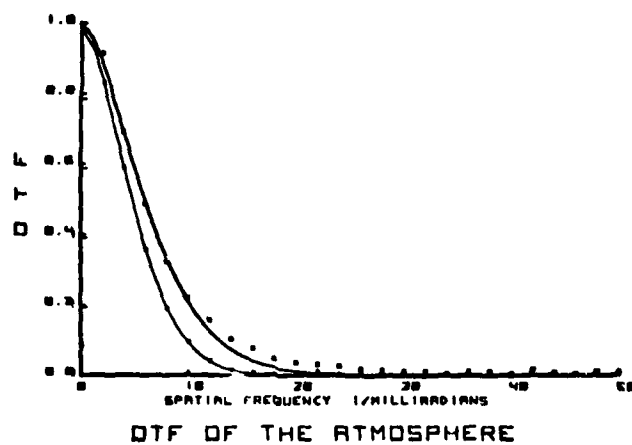


Figure 2. Typical long-term average OTF (lower curve) and image-centered OTF (upper curve) for a path through the atmosphere. The points are experimental; the solid curves are theoretical with the Fried model, with C_n^2 chosen for best fit.

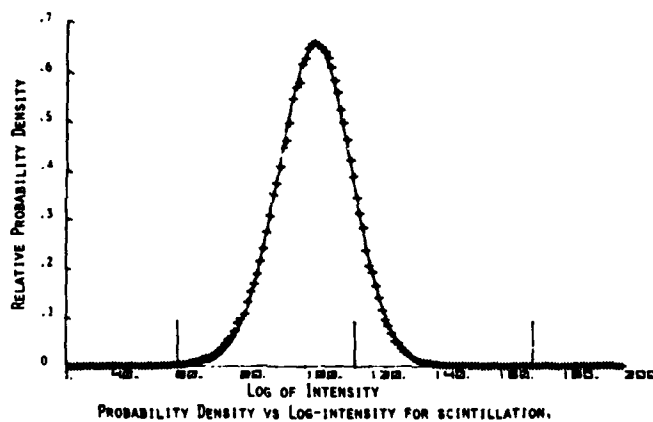


Figure 3.

MEASUREMENTS OF OPTICAL ATMOSPHERIC QUANTITIES IN EUROPE AND
THEIR APPLICATION TO MODELLING VISIBLE
SPECTRUM CONTRAST TRANSMITTANCE

Richard W. Johnson and Wayne S. Hering
University of California, San Diego
Scripps Institution of Oceanography
Visibility Laboratory

ABSTRACT

An 80 flight series of simultaneous optical and meteorological measurements between ground level and an altitude of 6 km has been gathered by the Visibility Laboratory under the sponsorship of the Air Force Geophysics Laboratory. These flights were conducted as an independent but related adjunct to the NATO Program OPAQUE. Data flights were conducted over several European sites during each of five separate two month periods selected to be representative of each of the four temporal seasons.

Illustrative data representing altitude profiles of visible spectrum scattering characteristics are presented, as are the simultaneous measurements of ambient and dewpoint temperatures. In addition to these profile data, several contemporaneous sets of multi-spectral directional volume scattering function measurements at scattering angles of 30 and 150 degrees are presented. The use of these data as a basis for the development of a technique for estimating atmospheric path radiance and contrast transmittance is discussed.

A computer model for the estimation of these atmospheric properties that is relatively fast and easy to apply is described with examples of its performance. The model input parameters are wavelength, extra-terrestrial solar irradiance, solar zenith angle, the number of atmospheric layers selected and their altitude limits, the average optical scattering ratio and the single scattering albedo for each layer, and the terrain reflectance. Using a modelling approximation that relates the directional distribution of single scattering to the total volume extinction coefficient, and using the delta-Eddington method for calculating the diffuse radiative fluxes, the model predicts the directional path radiance and contrast transmittance of any slant atmospheric path as a function of wavelength.

1. INTRODUCTION

In the increasingly sophisticated world of electro-optical detection, search, and guidance, the requirement for establishing and predicting atmospheric influences on system performance continues to be a primary operational necessity. It is in this general context that the techniques discussed in this paper can most usefully be addressed. Thus, though the instrument development and data collection portions of this experimental program have been complete for some time, the analysis of the data is continuing, and the application of these analytic results is both timely and specifically germane to the problems of E/O performance within the lower troposphere.

The Visibility Laboratory has for a good number of years conducted an airborne measurement program in cooperation with, and under the sponsorship of the United States Air Force Geophysics Laboratory. For the past several years the program has been conducted as an independent but cooperative effort, Johnson, *et al.* (1979), in conjunction with the NATO program OPAQUE (Optical Atmospheric Quantities in Europe), Penn. (1978).

In the remainder of this note we will discuss briefly the measurement program, its resulting data base, and in more detail, the application of these data to the task of modelling tropospheric visible spectrum contrast transmittance.

2. AIRBORNE INSTRUMENTATION

The nephelometer system, designed and built at the Visibility Laboratory, Duntley, *et al.* (1977) provides measurements of both the total and directional volume scattering properties of its captured aerosol in four discrete spectral bands, as illustrated in Fig. 1. The measurements of total volume scattering coefficient are produced by optical integration over all scattering angles between 5° and 172° which are then corrected for potential truncation losses via the systems simultaneous directional scattering measurements. The measurements of directional volume scattering function are made at scattering angles of 30° (*i.e.* forward scatter) and 150° (*i.e.* backscatter). These narrow angle directional measurements provide the forward to backscattering ratios which are used to more thoroughly characterize the sample aerosol.

Upper and lower hemisphere scanning radiometers were designed for the measurement of sky and terrain radiance distributions. They operate in the same spectral bands as the nephelometer system, and provide 4 μ radiance maps processed to yield an average (5 $^{\circ}$ field of view) radiance value for each 6 $^{\circ}$ in azimuth and each 5 $^{\circ}$ in zenith angle. These automatic scanner systems were initially described in Duntley, *et al.* (1970) and since were equipped with remotely controlled neutral density filters to enhance their near sun measurement capabilities.

3. AIRBORNE MEASUREMENTS

Although there were nearly ninety data missions flown by the instrumented C-130 during the OPAQUE episode, as illustrated in Fig. 2 and Table 1, the general thrust of these data must be considered in the case study context rather than in the broader climatological context associated with the host nation's far more extensive set of surface measurements. Johnson, *et al.* (1979). Nonetheless, there are sufficient airborne measurements to clearly establish the essential aerosol scattering characteristics required for modelling those tropospheric optical properties most influencing slant path contrast transmittances. Selected samples of these data which have been used as validation data throughout the model development process are illustrated in Figs. 3 through 7 and discussed briefly in the following paragraphs.

3.1. Meteorological Properties

Measurements of atmospheric pressure, temperature and dewpoint temperature were made throughout each data mission in both the fixed altitude and ascent/descent flight modes. These data are illustrated in Figs. 3 and 4 which have been reproduced from Johnson and Gordon (1980). In each of these plots, the data represent four separate ascents or descents. Each profile is coded with a symbol that links it with its simultaneous optical data set. (see Fig. 1). There is good temporal stability within the temperature regime during the data interval as is indicated by the generally good reproducibility among the four separate profiles shown in Fig. 3. Additionally, and as will become apparent more importantly, one can see from the overlaid 1200z RAOB data that the vertical structure of the temperature profiles can be readily identified from either the fine structured aircraft data, or the more coarsely defined RAOB data.

In Fig. 4, relative humidity, as computed from the measured values of ambient and dewpoint temperature, has been plotted in the same format as used to display the temperature data. Whereas these derived values exhibit a significantly higher degree of temporal variability, the general reproduction of major structural characteristics, *i.e.* layers and trends, is maintained. It is immediately apparent however, from an examination of the RAOB data in Fig. 4, that major structural artifacts in derived properties can be missed if one uses measurements reported at inappropriate altitude increments. For example, note the strong moist layer in the Soesterberg data which is completely undetected in the RAOB profile. An immediate recommendation then for enhancing the utility of this type data for model development and/or tactical decision input would be to provide the basic RAOB data at standardized and relatively fine altitude increments similar to those inherent in aircraft soundings.

3.2. Optical Properties

The variation in scattering coefficient as a function of altitude is one of the essential requirements for accurate computations of slant path tropospheric contrast transmittance, and thus must be reliably modelled if one presumes to develop predictive capabilities. Profile measurements such as those illustrated in Fig. 5 can provide the data base required for this model development within the visible spectrum, and conceivably provide the necessary insights for extrapolation to longer optical wavelengths. The profile characteristics requiring specific attention are the number and depth of well defined and reasonably well mixed aerosol layers, the most representative value of scattering coefficient within each layer, and the directional scattering properties of the aerosol within each layer. The data in Fig. 5 identify the first two characteristics. In each case there are two well defined layers with the boundary at about 1200-1500 meters. The average value of scattering coefficient within each layer can be readily established subsequent to upper altitude stray light corrections based upon directional scattering and sky radiance measurements.

There is strong evidence that the specification of the directional scattering properties within each aerosol layer can be reasonably deduced from a knowledge of the total volume scattering coefficient alone. Johnson, *et al.* (1979) and Johnson (1981). An example of the data supporting this contention is illustrated in Fig. 6 from Johnson and Gordon (1980). In these data, directional scattering function measurements made by the Visibility Laboratory ground based nephelometer system are compared with similar data from Barteneva (1960). Whereas the Barteneva data represent over 600 sets of directional scattering measurements using photopic spectral response, the Visibility Laboratory data

represent measurements made in all four of the responses defined in Fig. 1.

The data shown in Fig. 6 have been normalized to reflect only aerosol scattering characteristics by using a ratio display format. Thus the vertical axis, Volume Scattering Function Ratio, represents the ratio of the volume scattering function $\sigma(z, \beta)$ to the Rayleigh (i.e. molecular) volume scattering function ${}_R\sigma(z, \beta)$ at the same scattering angle β . i.e. $Q(z) = \sigma(z, \beta) / {}_R\sigma(z, \beta)$ where z is the altitude parameter. Likewise, the horizontal axis, Optical Scattering Ratio, represents the ratio of the total volume scattering coefficient $s(z)$ to the Rayleigh volume scattering coefficient ${}_R s(z)$. i.e. $Q(z) = s(z) / {}_R s(z)$. These data and their airborne equivalents specifically support the contention that one can develop a parameterization that will adequately represent the directional scattering properties of an atmospheric aerosol once the optical scattering ratio $Q(z)$ is specified, a fundamental simplification in any modelling attempt.

Our second major data set appropriate to the determination of tropospheric slant path contrast transmittances contains simultaneous measurements of sky and terrain radiances as determined from each of several different flight altitudes. In Fig. 7, the apparent radiances throughout the combined upper and lower hemispheres which surrounded the aircraft during flight C-466 are defined in one graph. Each of the four individually coded plots represents the observed radiance along a vertical sweep from the zenith through the horizon to the nadir and is at a fixed and constant azimuth from the sun.

The multi-spectral data typified by those illustrated in Fig. 7 provide a complete magnitude specification of the directional radiance field surrounding the aircraft. Thus they represent the net effects of the solar irradiance upon the total atmosphere within which the aircraft is implanted, including the influence of the underlying terrain. It is these data then, that allow one to close the modelling loop, in that they represent an essential intermediate step that a model must duplicate if it is to proceed to the subsequent determination of slant path contrast transmittance.

4. EXPRESSIONS FOR PATH RADIANCE AND CONTRAST TRANSMITTANCE

The analytic expressions relating the fundamental equation of radiative transfer to the apparent spectral radiance of a distant target, and the apparent contrast of that target as observed against its background are well developed by Duntley, et al. (1957). Those most directly related to the development of the modelling concepts discussed herein are summarized below.

The apparent spectral radiance of a target t at a range r , as measured from an altitude z in a direction defined by zenith angle θ and azimuth angle ϕ is

$${}_t L_r(z, \theta, \phi) = T_r(z, \theta, \phi) L_o(z, \theta, \phi) + L_r^*(z, \theta, \phi) \quad (1)$$

where L_o is the inherent spectral radiance of the target, T_r is the spectral transmittance of the path, and L_r^* is the directional path radiance.

As discussed in Duntley, et al. (1957), the directional path radiance is derived from the integration along the path of sight of the directional path function $L_r(z, \theta, \phi)$ which is defined as the point function component of path radiance generated by the scattering of light reaching that point from all points within its surrounding field.

The expression for the path function is

$$L_r(z, \theta, \phi) = \epsilon(z) \sigma(z, \beta_r) + \int_{\Omega} L_r(z, \theta', \phi') \sigma(z, \beta') d\Omega \quad (2)$$

where $\sigma(z, \beta)$ is the directional volume scattering function at a scattering angle β , and $\epsilon(z)$ is the solar scalar irradiance at altitude z .

The development from these fundamentals to expressions for the inherent and apparent spectral contrasts C_r and C_o of a target t against its background b is straight forward and results in the directional contrast transmittance along the path r as given by

$$C_r(z, \theta, \phi) / C_o(z, \theta, \phi) = T_r(z, \theta, \phi) L_o(z, \theta, \phi) / L_o(z, \theta, \phi) \quad (3)$$

As emphasized by Duntley, et al. (1957), Eq. (3) does not involve restrictive assumptions and defines the law of contrast reduction in its most general form. It should be noted that Eq. (3) is expressed in terms of inherent and apparent background radiances L_o and L_r , and is thus independent of target characteristics.

5. MODEL FOR ESTIMATING SLANT-PATH CONTRAST TRANSMITTANCE

The inherent variability of atmospheric structure and behavior and the complexities of radiative transfer processes require effective simplifying assumptions in order that estimates of contrast transmittance along any slant path in the atmosphere can be made rapidly and consistently. In pursuit of this objective, a series of modelling approximations relating optical properties to meteorological variables were derived from the broad experimental data base generated by airborne and surface measurement program. These relationships were combined with available analytic approximations for radiative transfer calculations to develop an operational technique for the estimation of directional path radiance and contrast transmittance. A detailed description of the model development and validation are presented in a report now being prepared for publication. A brief summary of the technique and several examples of model performance are given in the following paragraphs.

The calculation of the slant-path contrast transmittance with Eq. (3) requires consistent estimates of interrelated physical parameters. These include: (a) the vertical profile of total volume scattering coefficient, $s(z)$, (b) the vertical profile of the phase function for single scattering, $[\sigma(z,\beta)/s(z)] = P(z,\beta)$, and (c) vertical profile of single scattering albedo, $\omega(z) = s(z)/\alpha(z)$, where $\alpha(z)$ is the total volume attenuation coefficient. It should be emphasized that the contrast transmittance along any slant path depends primarily upon the extinction coefficient distribution both along the path and in the surrounding atmosphere. Accordingly, an attempt was made to condition the approximation procedures for all parameters on the existing capability to model and predict the extinction coefficient structure and behavior from conventional meteorological measurements and observations.

5.1. Estimates of the scattering ratio profile

For profile modelling purposes, it is important to consider a conservative measure of scattering coefficient that in the absence of local sources or sinks does not change appreciably following the air motion. The photopic scattering mixing ratio, $Q(z)$, is such a parameter. As the vertical mixing within an identifiable atmospheric layer becomes more complete, $Q(z)$ becomes more constant with height within the layer. The optical scattering ratio is defined $Q(z) = s(z)/s_R(z)$, where $s_R(z)$ is the total volume coefficient for Rayleigh scattering at altitude z .

Profiles of $Q(z)$ derived from the extensive series of airborne optical measurements made by the Visibility Laboratory, reveal large variability depending upon the aerosol source strength and the nature of the convective and turbulent mixing processes. The problem is to model the essential characteristics of the $Q(z)$ profiles in a way that recognizes the operational observing and forecasting limitations yet takes maximum advantage of existing capabilities. A prominent feature of the daytime aircraft soundings of optical scattering is the marked tendency for $Q(z)$ to remain essentially constant with height in the troposphere above the haze layer and also within the low-level haze layer. The difference in $Q(z)$ between adjacent tropospheric layers is typically much larger than the vertical variability within each layer. It should be emphasized that the assumption of constant scattering ratio with height does not hold well for ground-based stable layers with little vertical mixing such as those associated with the nocturnal formation of fog. The computer code developed for this modelling effort has provision for up to 20 atmospheric layers for use in complex situations when detailed information about the extinction coefficient profile is available. However, for application to problems of contrast transmittance in hazy atmospheres in the daytime following the dispersion of any surface inversion existing at sunrise, it is reasonable to employ a model consisting of a stratospheric layer and two or three tropospheric layers of constant optical scattering ratio. Thus, the forecasting problem is reduced to the prediction of the altitude limits of the atmospheric layers and the scattering ratio within each layer.

5.2. Specification of the phase function for single scattering

The asymmetry of the phase function for single particle scattering depends in a complex way on the size distribution and refractive index of the aerosols present in the atmosphere and the wavelength of incident light. The prominent feature of aerosol scattering is that as the particle size increases with respect to the wavelength, the amount of energy scattered in directions close to that of the incident radiation increases markedly causing larger asymmetry in the phase function. Since the total volume scattering coefficient varies approximately as the square or cube of the particle radius depending upon the size parameter, we might expect that the scattering coefficient or scattering ratio, $Q(z)$, might provide, through analytic representation, a good first approximation for the single scattering phase function. Experimental evidence shows this to be true.

The approach used herein for model development was first to represent the single scattering phase function for Mie scattering $P_M(z, \beta)$ by two term Henyey-Greenstein functions (Kattawar, 1975) as follows,

$$P_M(\beta, g_1, g_2, c) = c P_1(\beta, g_1) + (1-c) P_2(\beta, g_2), \quad (4)$$

and

$$P(\beta, g) = (1 - g^2) / [4\pi(1 - 2g\cos\beta + g^2)^{3/2}], \quad (5)$$

where the asymmetry factor, g , is given by

$$g = \frac{1}{2} \int_0^\pi P(\beta) \cos\beta \sin\beta d\beta. \quad (6)$$

The phase function for single scattering has the normalized form,

$$\int_{4\pi} P(z, \theta, \phi) d\Omega = 1. \quad (7)$$

In turn, each of the Henyey-Greenstein parameters, $g_1(z)$, $g_2(z)$ and $c(z)$ were approximated as continuous functions of the Mie scattering ratio, $Q(z)-1$. The relationships between the phase function for combined aerosol and molecular scattering and the scattering ratio are bounded by the Rayleigh phase function ($Q=1, g=0$) for a clear atmosphere and by a phase function representative of dense clouds or fog for very large $Q(z)$. Combined analysis of the asymmetry parameters (g_1, g_2, c) as derived from a least-squares fit of the Henyey-Greenstein functions to the average phase functions measured by Barteneva (1960) and to the phase functions derived from Mie calculations using typical aerosol distributions in haze and fog led to a consistent set of empirical equations expressing the asymmetry parameters as a function of the logarithm of the Mie scattering ratio, ($Q-1$).

Independent evidence of the general applicability of the model estimates of $P(\beta)$ with respect to wavelength and altitude is given by a comparative study of directional scattering functions that were measured by the Visibility Laboratory airborne nephelometer and the Barteneva (1960) phase function measurements (see Section 3 and Fig. 6). In addition to the measurement of total volume scattering coefficient, the integrating nephelometer measured, separately, the directional scattering function at nominal scattering angles of 30° and 150° in four wavelength bands centered near 475, 550, 660, and 750 nm. The analysis by Johnson, et al. (1979) of the airborne data gathered by the Visibility Laboratory in Europe and the United States over all seasons indicates that the derived relationship between the phase functions scattering ratio holds well over all visible wavelengths and over all altitudes up to the highest levels sampled by the instrumented aircraft (usually near 6 km). Figures 8 and 9 show a comparison of phase functions as calculated from the model, calculated from Mie theory, and measured by Barteneva.

To the extent that more accuracy is desired and more complete information is available to define $P(z, \beta)$, the overall computer code for calculating path radiance and contrast transmittance was made general in that it will accept as input for each atmospheric layer any specified $P(z, \beta)$. However, in the absence of information other than an estimate of $Q(z)$, calculation of $P(z, \beta)$ from the system of model equations is recommended for haze only atmospheres. Important details typical of phase functions for fog conditions such as the prominent minimum near $\beta = 100^\circ$ and the secondary maximum near 140° (see Fig. 9) are smoothed out by the representation with Henyey-Greenstein functions. It should be emphasized that important additional evidence of the applicability of the model for estimating $P(z)$ from $Q(z)$ will be obtained as we employ the technique more extensively for the specification of the sky and terrain radiances as measured in various deployments of the instrumented aircraft. Sample comparisons of measured and computed radiances are given in the following section.

5.3. Calculation of the path radiance component due to scattering of diffuse irradiance

As given by the first term on the right hand side of Eq. (2), the component of the directional path function produced by the scattering of direct solar irradiance incident on the path is calculated from estimates of the single scattering phase function determined by the technique described in the previous paragraphs. The second term on the right hand side of Eq. (2) is the component of path function resulting from the scattering of diffuse irradiance reaching the path from the surrounding sky and terrain. As in the case of the direct solar component, the directional dependence of the diffuse background contribution to the path radiance must be considered. Precise numerical

calculation of the radiance distribution resulting from the complex multiple scattering processes requires large amounts of computer time. For this reason, great emphasis has been placed upon the development of rapid approximate methods for radiation transfer calculations (Meador and Weaver, 1980). The appropriate choice of computational method from among the variety of available methods depends upon the results desired for the application at hand.

While it is important to retain complete directionality for calculation of the path radiance component due to single scattering of direct solar irradiance, approximate two stream methods often can be used effectively for fast calculation of the component due to scattering of diffuse irradiance provided that the asymmetric influence of the prominent forward scatter peak is managed adequately. The delta-Eddington approximation introduced by Joseph, Wiscombe and Weinman (1976) satisfies the requirement. It differs from the standard Eddington approximation, which assumes a simple cosine dependence of the single scattering phase function, in that it approximates the phase function by a truncated forward scatter peak and a two-term phase function expansion,

$$P_0(\beta) = 2f\delta(1 - \cos\beta) + (1 - f)(1 + 3g'\cos\beta), \quad (8)$$

where f is the fractional scattering represented by the forward peak and g' is the asymmetry factor of the truncated phase function. In effect, the delta-Eddington approximation transforms most of the scattered radiation in the solar aureole into the direct solar flux component, and assumes that

$$f'(z) = g^2(z). \quad (9)$$

As an integral part of the technique for estimating directional contrast transmittance, the approximate diffuse radiance, $[L_D(z) + L_{D'}(z)\cos\theta]$, calculated by the Eddington computer code (Shettle and Weinman, 1979), as modified by the delta-Eddington approximation, is used directly to obtain the second term on the right hand side of Eq. (2); so that this component of the path function generated by the scattering of diffuse irradiance is given by

$$\int_{\pi} L(z, \theta', \phi') \sigma(z, \beta') d\Omega = L_D(z) + \frac{2}{3} L_{D'}(z) \cos\theta. \quad (10)$$

5.4. Calculation of directional path radiance and contrast transmittance

With the procedures for estimating the direct and diffuse components described above, the directional path radiance L_p^* can be calculated from Eqs. (2) and (3) by finite summation over successive atmospheric layers using the trapezoidal rule. The computer code for calculation of directional path radiance and contrast transmittance along any slant path in accordance with Eqs. (1) through (8) requires the following input:

- 1) a representative wavelength λ that is commensurate with the spectral response of the sensor in μm
- 2) the solar irradiance $E_s(\infty)$ at the upper limit of the atmosphere in $\text{w/m}^2\mu\text{m}$ corresponding to spectral response of the sensor
- 3) the number of atmospheric layers n and the altitude z_n of the base of each layer in km
- 4) the average optical scattering ratio $Q(z)$ for each atmospheric layer
- 5) the average single scattering albedo $\omega(z)$ for each atmospheric layer
- 6) the average surface reflectance $R(\theta, \phi)$ and the reflectance of the immediate background of the viewed object if significantly different than the albedo of the general background
- 7) the object and observer altitudes in km and the viewing angle with respect to the sun, β , and zenith, θ , in degrees
- 8) the solar zenith angle θ , in degrees.

6. RESULTS OF MODEL CALCULATIONS

Model calculations based upon the extensive data gathered by the airborne measurement program make possible a close analysis of the dependence of optical properties on meteorological conditions. Comparative analyses of observed data with the model calculations are being used to improve techniques for the prediction of image transmission properties from conventional meteorological observations. Some examples of

trial model calculations are illustrated in the following paragraphs.

Comparisons of the sky and terrain radiance distribution measured by the scanning radiometers and the model calculations of the radiance distribution from the observed input parameters are shown in Figs. 10 and 11 for the flight made on 15 August 1978 in northwestern Germany near Meppen. A 3-layer atmosphere was assumed for model calculations with the top of the haze layer at 1.3 km (see scattering coefficient profile in Fig. 5) and a tropopause height of 10 km. The observed features of the radiance distribution are typical of rural clear sky conditions observed in western Europe in the summer months. At the observation altitude deep within the haze layer at 200m, the sky radiance in the upsun direction, $\phi = 0^\circ$, is substantially larger than the view angle away from the sun, $\phi = 180^\circ$. However, the disparity in sky radiances in the upsun and downsun directions is much smaller looking upward from an altitude well above the haze layer near 6 km. The rather large fluctuations in measured radiance looking downward from the low altitude of 200m are caused by differences in the reflectivity of various terrain pattern features such as the green and brown fields and small wooded areas.

For the same experimental flight, Fig. 12 shows the contrast transmittance distribution for downward view angles from an observation level of 6 km and target altitude of 0.2 km that were calculated from the radiance distribution given by both the aircraft measurements and the model calculations. Looking overhead, Fig. 13 shows the apparent contrast as a function of zenith angle for an object at 20 km viewed from 0.2 km as calculated from the observed and model sky radiance distributions.

The model calculations can be used to assess quantitatively the changes in contrast transmittance associated with incremental changes in the individual environmental factors governing image transmission in the atmosphere. For purposes of illustration, the reference atmosphere as described in Table 2 was derived from the measurements made on 15 August 1978 near Meppen, Germany (see Fig. 5). As discussed above, the meteorological conditions observed on this flight are representative of clear sky conditions for this geographical area and time of the year. An optical scattering ratio of 16 for the haze layer converts to a horizontal visual range of about 16 km at the surface assuming an inherent target contrast of -1, no absorption and an apparent contrast threshold for detection of 5 percent. The single scattering albedo of 0.83 assumed for the haze layer is commensurate with measurements in rural areas in the United States by Weiss, *et al.* (1980).

For a specified azimuth angle, the slant range between the sensor and target altitudes where the apparent contrast of the target and background reduces to a fixed threshold value can be determined from systematic model calculations for successive zenith view angles. Calculation of the slant range corresponding to 5 percent apparent contrast for the reference atmosphere specified in Table 2 and for a series of individual incremental changes in various atmospheric variables are illustrated in Fig. 14. It should be emphasized that the indicated changes in slant range as a function of changes in the input variables are specific only for the variations about the given set of conditions, *i.e.* observation level at 20 km, target at surface, target reflectivity of 50 percent, azimuth view angle of zero with respect to the sun, and atmospheric structure as given by the reference atmosphere. However, the results illustrated here do provide insight into the relative impact of the parameter changes on contrast transmittance. Using approximate interpolation methods under the same prescribed conditions, we have calculated the changes in individual parameters which produce a family of equivalent effects. Thus, Table 3 illustrates those changes in conditions, any one of which will result in a corresponding 20% decrease in apparent contrast.

7. SUMMARY

The computer model developed during the course of the experimental optical measurement and analysis program can provide relatively fast and consistent estimates of optical atmospheric properties over any slant path as a function of wavelength in the visible spectrum. To the extent that a climatological data base of conventional meteorological observations exists, the technique in its present form can be used to estimate readily the frequency distributions of such quantities as spectral contrast transmittance as a function of location and season.

Refinements in the model are being made as validation tests and experiments continue. Early results indicate that further parameterization of selected components of the model can be made which will improve computational efficiency and at the same time retain the capability to take advantage of any and all relevant observational and forecast information. A realistic goal is to employ the computer model as part of a data acquisition and microprocessing system for real time estimates of image transmission properties. Future experiments are planned to examine the tradeoffs between the type, accuracy, frequency and density of optical/meteorological observations and the reliability of the estimates of spectral contrast transmittance.

8. ACKNOWLEDGEMENTS

The studies conducted prior to and during the preparation of this paper have involved the talents and skills of many persons associated with both the Air Force Geophysics Laboratory and the University of California, Visibility Laboratory. The authors gratefully acknowledge these contributions, and in particular would like to thank Dr. Robert Fenn and Mr. Eric Shettle of the Geophysics Laboratory and Ms. Jacqueline I. Gordon of the Visibility Laboratory for many constructive discussions, comments and suggestions.

This effort has been supported by the Air Force Geophysics Laboratory under Contract No. F19628-78-C-0200.

9. REFERENCES

- Barteneva, O. D. (1960), "Scattering Functions of Light in the Atmospheric Boundary Layer," Bull. Acad. Sci. U.S.S.R., Geophysics Series, 1237-1244.
- Duntley, S. Q., A. R. Boileau, and R. W. Preisendorfer (1957), "Image Transmission by the Troposphere I", J. Opt. Soc. Amer., 47, 499-506.
- Duntley, S. Q., R. W. Johnson, J. I. Gordon, and A. R. Boileau (1970), "Airborne Measurements of Optical Atmospheric Properties at Night," University of California, San Diego, Scripps Institution of Oceanography, Visibility Laboratory, SIO Ref. 70-7, AFGL-70-0137. NTIS, Ad 870 734.
- Duntley, S. Q., R. W. Johnson, and J. I. Gordon (1977), "Airborne Measurements of Atmospheric Volume Scattering Coefficients in Northern Europe, Spring 1976," University of California, San Diego, Scripps Institution of Oceanography, Visibility Laboratory, SIO Ref. 77-8, AFGL-TR-77-0278. NTIS, ADA 046 290.
- Duntley, S. Q., R. W. Johnson, and J. I. Gordon (1978a), "Airborne Measurements of Optical Atmospheric Properties, Summary and Review III," University of California, San Diego, Scripps Institution of Oceanography, Visibility Laboratory, SIO Ref. 79-5, AFGL-TR-78-0286. NTIS, ADA 073 121.
- Duntley, S. Q., R. W. Johnson, and J. I. Gordon (1978b), "Airborne Measurements of Atmospheric Volume Scattering Coefficients in Northern Europe, Fall 1976," University of California, San Diego, Scripps Institution of Oceanography, Visibility Laboratory, SIO Ref. 78-3, AFGL-TR-77-0239. NTIS, ADA 057 144.
- Fenn, R. W. (1978), "OPAQUE - A Measurement Program on Optical Atmospheric Properties in Europe, Vol. I. The NATO OPAQUE Program," Special Reports No. 211, AFGL-TR-78-0011.
- Johnson, R. W. and J. I. Gordon (1980), "Airborne Measurements of Atmospheric Volume Scattering Coefficients in Northern Europe, Summer 1978," University of California, San Diego, Scripps Institution of Oceanography, Visibility Laboratory, SIO Ref. 80-20, AFGL-TR-80-0207.
- Johnson, R. W., W. S. Hering, J. I. Gordon, B. W. Fitch and J. E. Shields (1979), "Preliminary Analysis and Modelling Based Upon Project OPAQUE Profile and Surface Data," University of California, San Diego, Scripps Institution of Oceanography, Visibility Laboratory, SIO Ref. 80-5, AFGL-TR-79-0285. NTIS, ADB 052 172L.
- Johnson, R. W. (1981), "Daytime Visibility and Nephelometer Measurements Related to its Determination," Paper presented at Environmental Protection Agency Symposium on Plumes and Visibility, Grand Canyon, Arizona, Nov. 1980. Accepted for publication, ATMOSPHERIC ENVIRONMENT, Dec. 1980.
- Joseph, J. H., W. J. Wiscombe, and J. A. Weinman (1976), "The delta-Eddington Approximation for Radiative Flux Transfer", Atmos. Sci., 33, 2452-2459.
- Kattawar, G. W. (1975), "A Three-Parameter Analytic Phase Function for Multiple Scattering Calculations", J. Quant. Spectrosc. Radiant. Transfer, 15, 839-849.
- Meador, W. E., and W. R. Weaver (1980), "Two Stream Approximations to Radiative Transfer in Planetary Atmospheres: A Unified Description of Existing Methods and a New Improvement", J. Atmos. Sci., 37, 630-643.
- Shettle, E. P., and J. A. Weinman (1970), "The Transfer of Solar Irradiance Through Inhomogeneous Turbid Atmospheres Evaluated by Eddington's Approximation", J. Atmos. Sci., 27, 1048-1055.
- Weiss, R. E., R. J. Chankin, A. P. Waggoner, N. Sadler, and J. Ognen (1980), "An Assessment of Light Absorption by Aerosol Particles in Urban, Rural and Remote Troposphere and Stratospheric Air", 1980 International Radiation Symposium Extended Abstracts, International Association of Meteorology and Atmospheric Physics, IUGG, 178-180.

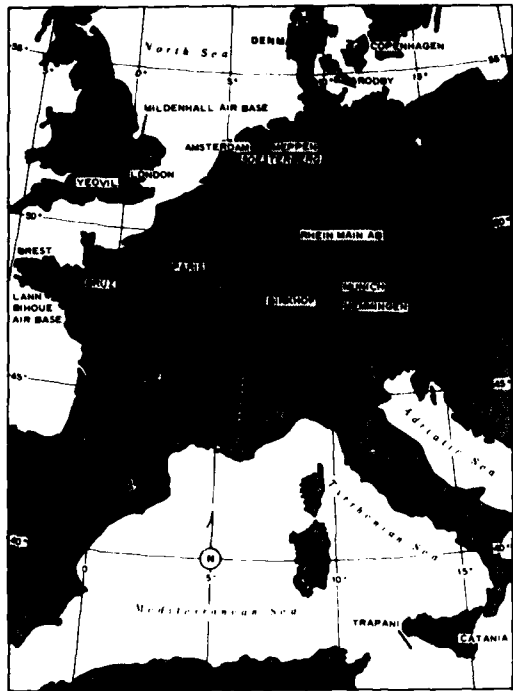


Fig. 2. Typical OPAQUE Flight Tracks.

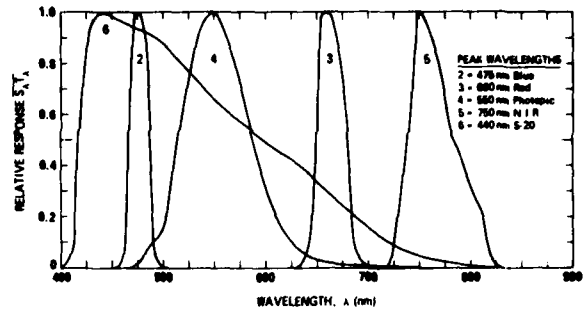


Fig. 1. Standard Spectral Responses.

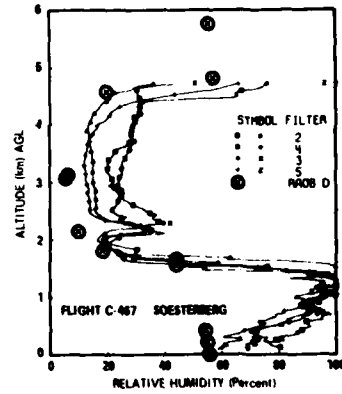


Fig. 4. Relative Humidity Profiles, Flight C-467.

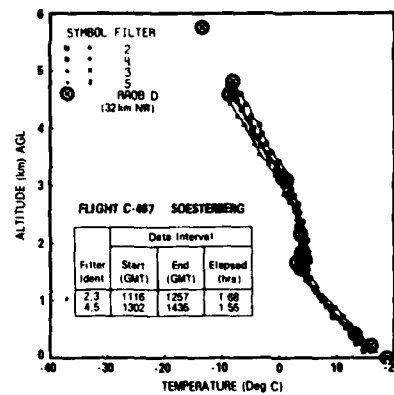
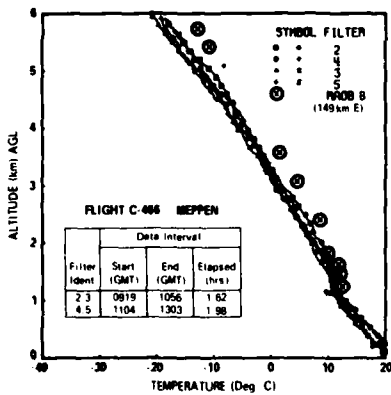


Fig. 3. Temperature Profiles, Flights C-466 & C-467.

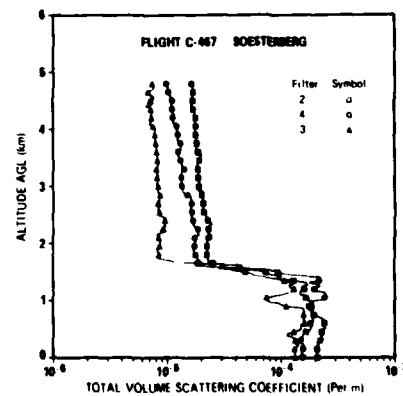
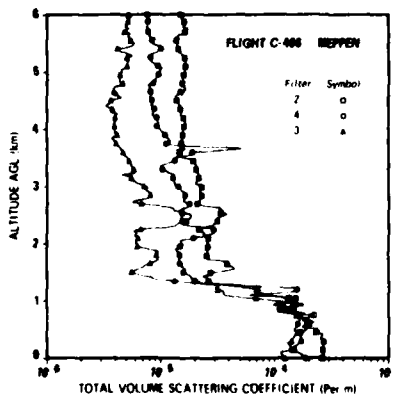


Fig. 5. Total Volume Scattering Coefficient Profiles, Flights C-466 & C-467.

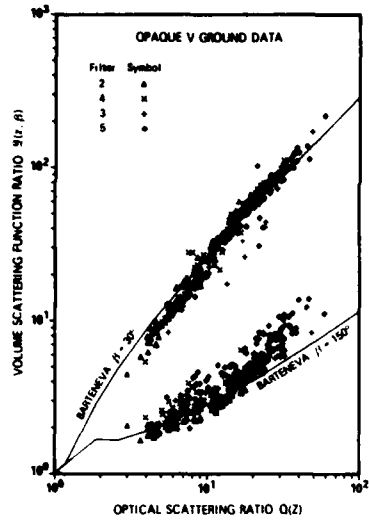


Fig. 6. Multi-Spectral Directional Scattering Measurements.

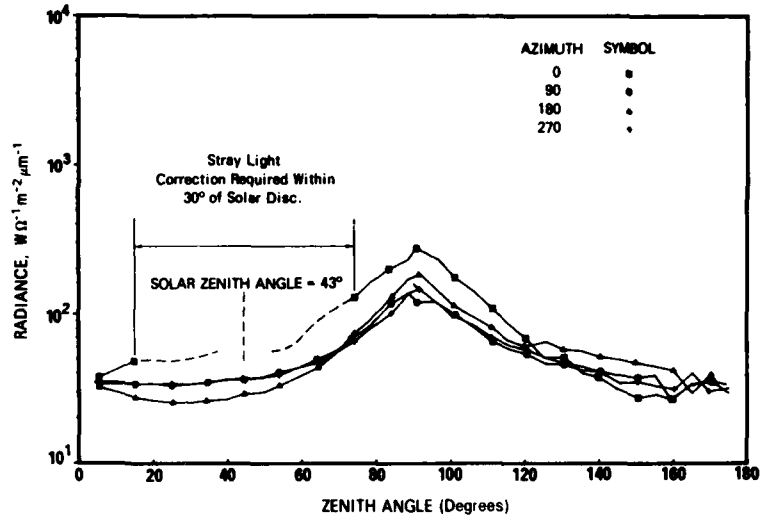


Fig. 7. Measured Sky and Terrain Radiance Distributions for Flight C-466, filter 2, 2953m AGL.

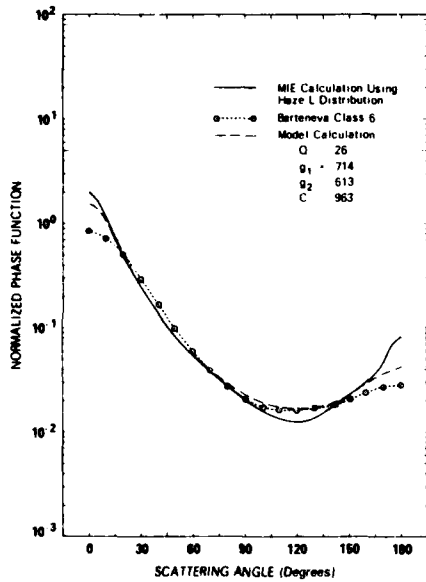


Fig. 8. Single scattering phase functions (a) calculated from Mie theory by Kattawar (1975) using Diermndjian (1969) Haze L distribution with a refractive index of $1.55-0.0i$; (b) observed by Barteneva (1960) (class 6); and (c) calculated for scattering ratio of 26.

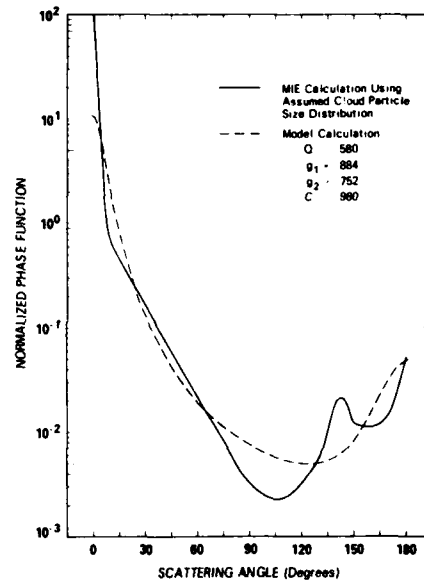


Fig. 9. Single scattering phase functions (a) calculated from Mie theory by Kattawar (1975) for cloud drop distribution $n = kr^{6e-1.5r}$ and refractive index of $1.33-0.0i$, and (b) calculated for scattering ratio of 580.

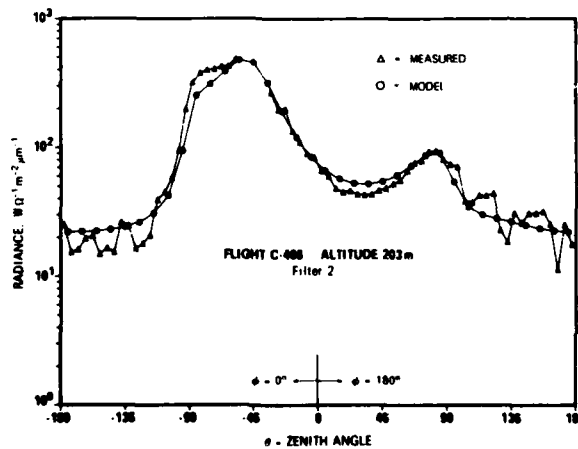


Fig. 10. Comparison of Measured and Calculated Sky and Terrain Radiance Distributions at 200m.

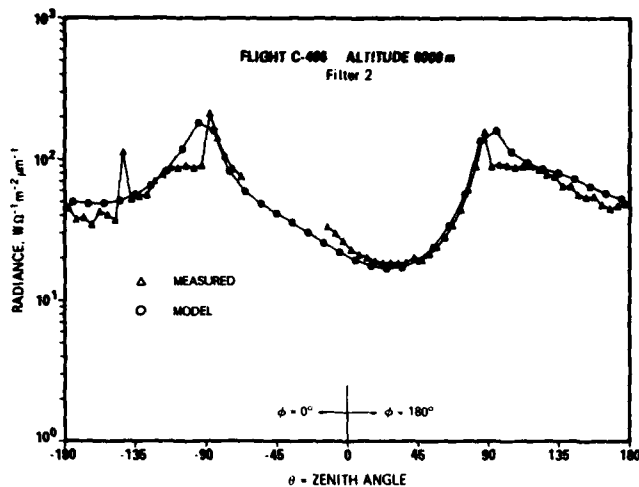


Fig. 11. Comparison of measured and calculated sky and terrain radiance distributions at 6000m.

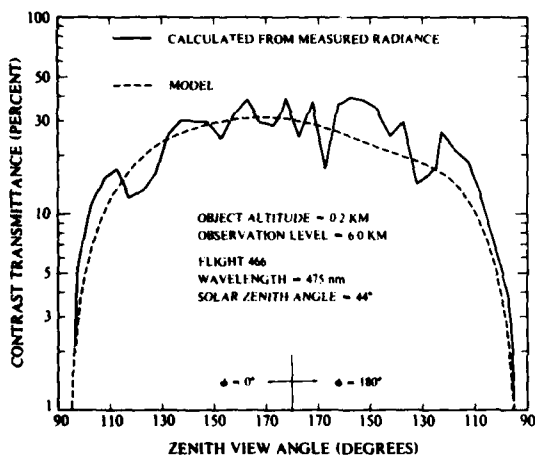


Fig. 12. Comparison of contrast transmittance distributions calculated from measured and observed sky and terrain radiance distributions.

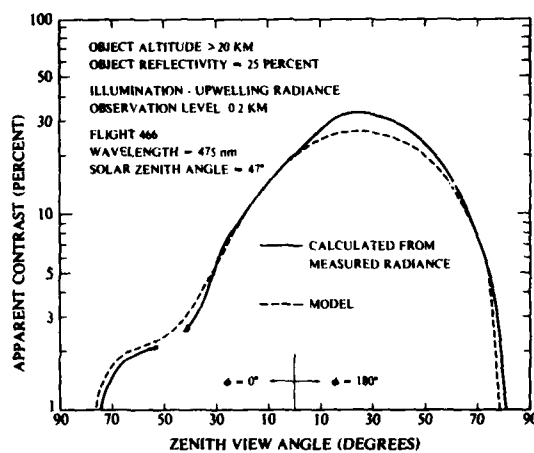


Fig. 13. Comparison of apparent contrast distributions calculated from measured and model sky radiance distributions.

OBJECT AT SURFACE INHERENT CONTRAST = 50%
 OBSERVATION LEVEL = 20 KM AZIMUTH VIEW ANGLE = 0°
 WAVELENGTH = 550 nm (PHOTOPIC)

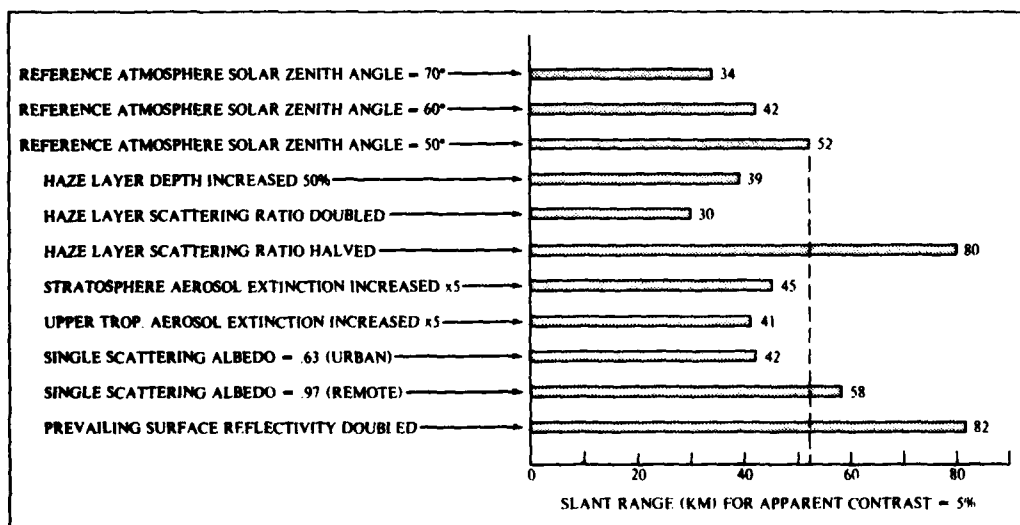


Fig. 14. Comparison of the slant range corresponding to apparent contrast of 5 percent for reference atmosphere and selected changes in the reference atmosphere.

Table 1.
Geographical and Seasonal Distribution of OPAQUE Related Data Flights

Flight Location (Fig. 1)	Attempted Data Sequences				Totals
	Spring 1976	Fall 1976	Summer 1977 & 1978	Winter 1978	
Sicily	0	0	4	5	9
France	0	5	3	0	8
So. Germany	0	0	5	8	13
No. Germany	5	4	9	3	21
Netherlands	1	0	3	2	6
England	5	0	3	7	15
Denmark	2	4	6	2	14
Totals	13	13	33	27	86
Data Reports	AFGL-TR-77-0078	AFGL-TR-77-0239	AFGL-TR-78-0168 AFGL-TR-80-0207	AFGL-TR-79-0159	AFGL-TR-79-0285

Table 2.
Reference Atmosphere (Photopic, $\lambda = 550m$)

NUMBER OF LAYERS	3
ALTITUDE OF TROPOPAUSE	10 km
DEPTH OF HAZE LAYER	1.3 km
OPTICAL SCATTERING RATIO	
STRATOSPHERE	1.3
UPPER TROPOSPHERE	1.3
HAZE LAYER	16.0
SINGLE SCATTERING ALBEDO	
STRATOSPHERE	0.99
UPPER TROPOSPHERE	0.97
HAZE LAYER	0.83
SURFACE REFLECTANCE	0.07

Table 3.
Parametric Changes Inducing 20% Decrease in Apparent Contrast

Item	Parameter	Change	Amount
a	Haze layer depth, Z	increase	30%
b	Haze layer scattering ratio, $Q(z)$	increase	25%
c	Haze layer single scattering albedo, $w(z)$	decreased	24%
d	Mid-Troposphere Aerosol Scattering Coeff. $s(z)$	increase	factor of 3
e	Stratosphere Aerosol Scattering Coeff. $s(z)$	increase	factor of 5.7

COMPARISON OF UNDERWATER RADIANCE MEASUREMENTS WITH VARIOUS ANALYTICAL TREATMENTS OF THE RADIATIVE TRANSFER EQUATIONS

R. Anderson and L. Stotts
Naval Ocean Systems Center
San Diego, California 92152

ABSTRACT

In situ experimental data are presented on the off-axis radiance produced by a pulsed underwater laser operating at a wavelength of 520 nanometers. Path lengths in homogeneous seawater range up to 50 meters with separations of up to more than 6 meters from the path. Absorption and scattering lengths in the water are about 6 and 4 meters, respectively. These results are compared with the predictions provided by popular models derived from radiative energy theory. Limitations are clearly shown on the accuracy of the radiance predicted by these models.

INTRODUCTION

With the introduction of optical and infrared technologies in the areas of communications and surveillance, it has become necessary to account for the atmospheric and oceanic influences on such systems and, in particular, to improve our knowledge of the effects of particulate multiple scattering on laser beam propagation. Particulate multiple scatter will, in general, inhibit optimum system performance by inducing additional beam spread, attenuation, dispersion in the angle of arrival, degradation of spatial coherence, and dispersion in time and frequency of the signal encoding desired information. Several analytical¹⁻¹¹ and Monte Carlo based¹²⁻¹⁵ treatments of Mie-type multiple scatter have been reported in the literature. Unfortunately, very little experimental data are available to verify or refute these models.¹⁶⁻¹⁹ For the first time, the opportunity has presented itself to compare all proposed models with experimental in situ data, and several of the approximate solutions are examined and compared to these measurements.

For three months through the summer of 1975 a sophisticated array of ocean optics experiments was conducted from a barge platform moored in the Southern California bight north of Santa Catalina Island. These tests yielded a prodigious quantity of data on underwater optics and propagation through the air-sea interface.²⁰

The necessity of issuing timely reports on the results of the experiment and their direct application in the sponsoring project left much of the data unreduced. Indeed, there is still a large quantity of potentially interesting data with no present prospect of review or closer examination.

This paper will present and discuss the results of an experiment which measured the off-axis radiance in situ from a blue-green laser underwater. While the basic data were acquired several years ago, the opportunity to reduce the data and examine the results is recent.

EXPERIMENTAL APPROACH

To acquire off-axis radiance measurements, an adequate surface support platform was moored in 122 meters (400 feet) of water. Two optical benches lying in a plane were deployed from the platform, a horizontal bench just above the water surface and a vertical bench.

A laser light source was carried on the vertical bench by an elevator platform down to depths of 55 meters. The axis of the laser was inclined 12.5 degrees from the zenith in the plane of the experiment toward the horizontal optical bench.

A submerged radiance receiver traveling along the horizontal optical bench could scan an angle ± 80 degrees from the nadir in the plane of the experiment. No data were taken with the receiver axis oriented out of the experimental plane.

MECHANICAL

As depicted in figure 1, the optical benches were attached to the barge in the form of a suspended pipe and an H-beam guide rail lying in the same plane. Experiments could be conducted through an underwater path from equipment mounted on both benches. The vertical optical bench was also used to deploy other equipments for other test objectives.

Several techniques were considered for deploying equipment to the desired depths, and a procedure was devised which would not require divers and which would reduce boat operations to a minimum. It involved the fabrication of a single piece of pipe 55 meters long and 0.2 meter (approximately 8 inches) in diameter. Deployment of the vertical bench was reduced to fabricating, floating, and towing the pipe to the desired location. At the test location, it was necessary only to attach one end of the pipe to the barge and to sink the other. The port aft corner of the barge was fitted with an A-frame support designed to support a vertical load of 9000 kg at an angle of 30 degrees from the vertical. The vertical pipe and test instrument platform represented a maximum load of approximately 3 tons.

Barge trim recorded during the tests was 0.15 meter, or a tilt of approximately 5 milliradians fore and aft. The position of the barge remained relatively stable during the tests. The orientation of the barge and all equipment was known and varied by less than ± 50 milliradians.

The horizontal optical bench was provided by suspending a guide rail along the side of the barge. Both sides of the barge were first fitted with wooden fenders (0.2 by 1 meter cross section). The barge draft was such that the bottom edge of the fenders was in contact with the surface of the water. An H-beam (0.15 meter), 18 meters long, was then suspended with L-brackets and angle iron 0.1 meter up from the bottom of the fender. The supports were attached to the top flange of the H-beam, leaving the bottom flange to support and guide a subsurface radiance receiver positioning carriage.

The positioning carriage (fig 2) was fitted with nylon top runners inside the flanges of the H-beam and a spring-loaded roller which pressed up against the bottom of the beam. A yoke assembly around the underwater radiance receiver housing was attached to bearings on both sides of the positioning carriage. The outboard side of the yoke (fig 2) provided a control arm for pointing the instrument. A protractor was fitted to the outboard side of the positioning carriage. Drilled holes in the protractor aligned with a pin in the control arm and allowed adjustments of the instrument pointing angle of ± 80 degrees in 5-degree increments. The operator could easily control the angle to every 2.5 degrees by manually holding the arm. Brakes were provided to lock the unit in position and eliminate wave-induced sway.

The platform had the following features (among others):

- (1) It was sufficiently stable for experiments under a variety of ocean conditions. It provided a work area for up to 7 people and was equipped to support electrical, mechanical, and electronic equipments;
- (2) It provided vertical access to depths of approximately 50 meters in the form of an assembly which could be raised, lowered, and rotated and upon which various instruments could be mounted. The assembly position was fixable to within 3 degrees (an allowable swing of 2.5 meters at 50 meter depth);
- (3) It provided a method to traverse a submerged optical radiance receiver along a horizontal path slightly below the surface of the water. It was necessary that orientation of the horizontal path and the pointing of the detector with respect to the vertical elements (described in 2 above) be well defined;
- (4) It provided support to personnel of the Scripps Institution of Oceanography Visibility Laboratory for the deployment and operation of the instruments for measuring ocean optical properties; and
- (5) It enabled mooring, deployment, upkeep, support, watchstanding, small-boat platform-to-shore transportation, and correction of equipment break-downs.

The instrument platform which carried the laser on the vertical optical bench consisted of a 1.5-meter-long tubular guide to which was welded a horizontal table or platform. The guide section was fitted on its inside surface with a set of runners of a UHFM polymer designed to glide along the pipe and guide rail. Once installed on the pipe at the test site, the half-ton assembly was raised and lowered through its 55-meter operating range by an automatic winch. The submerged instrument platform is shown on the vertical pipe in figure 3. The laser mount was constructed so as to hold the laser securely in place and to permit it to be tilted in 10-degree intervals from zenith to 50 degrees.

The platform was also fitted with a 2-axis tilt sensor to measure deviations in platform position caused by pipe sway. No significant changes in platform position were observed during the tests.

LASER

The underwater light source used in the field tests is a flashlamp-pumped dye laser system, visible in figure 3, specifically designed and built for the project at the Naval Ocean Systems Center (NOSC). The system consists of three main parts — the laser proper in a submersible canister, a topside control panel, and 250 feet of interconnecting cable. The general system specifications are given in table 1.

Other features of the laser system are:

- Automatic control of pulse amplitude
- Leak-initiated shutdown
- Pressure and temperature interlocks
- Stable pulse rate
- Telemetry sync output
- Rapid dye solution and flashlamp replacement

Table 1. System Specifications

Mechanical	
Canister size	41 cm dia X 84 cm height (16 X 33 in) 46 cm dia flange (18 in)
Weight	109 kg (240 lb)
Displacement	114 kg (250 lb)
Depth limit	180 m (600 ft)
Electrical	
Input power	1 kW, 3 phase, 400 Hz, Y
Lamp energy	up to 10 joules
Operating Parameters	
Pulse repetition rate	20 p/s
Peak pulse amplitude	5 kW ($\pm 6\%$ rel, $\pm 10\%$ abs)
Pulse width	0.75 μ sec
Pulse energy	4 mJ/p (nom)
Center wavelength	521.4 nm
Bandwidth	4.65 nm
Beamwidth (in water)	21.4 mrad (FWHM)

The lasing medium is a solution of a fluorescent organic dye in ethanol that circulates through a 7.6-cm-long quartz capillary tube. Curved mirrors at either end of the tube satisfy the feedback requirements for multimode laser action, and a linear xenon flashlamp acts as the laser pump. The flashlamp and parallel capillary lie along the foci of a cylindrical elliptical reflector built into the laser head.

The laser output level is stabilized by a feedback loop that includes a beamsplitter and fiber optic probe, detector, filter, and relay circuits within the control unit, and a motor-driven Variac in the high-voltage supply. The loop compensates for decreases in output caused by flashlamp and dye solution aging processes. Some 8 hours of operation could be expected between lamp and dye changes.

UNDERWATER RADIANCE RECEIVER

The underwater radiance receiver is shown mounted on the horizontal optical bench in figure 4.

The receiver is an underwater synchronous, optical pulse amplitude reading radiometer. It is positioned relative to the optical axis of a pulsed dye laser either on the axis or at some angle relative to it, and measures that component of the initially collimated laser

output that is scattered into the receiver's field-of-view.

The receiver is composed of two major subsystems, the sensor assembly and the receiver-control panel, connected by 46 meters of multiconductor underwater cable.

Incident light pulses of 0.75- μ sec width from the dye laser are received through a spectral filter at a rate of 20 per second and are brought to a focus on the faceplate of a photomultiplier by an $f/1.3$, 7.6-cm diameter objective lens. A neutral density filter is normally in the optical path to prevent photo multiplier tube damage and to provide over-range protection. This filter, which has a transmission of 0.1% (density 3), may be switched out of the optical path remotely via the filter position control unit located on the receiver-control panel.

From the photomultiplier, the output pulse passes through a line driver that feeds the shielded coaxial cable connecting the sensor assembly and the receiver control panel. The pulse is amplified and supplied to an oscilloscope for direct measurement of instantaneous pulse amplitude.

The same signal is routed to the sample-and-hold circuit, which outputs a DC voltage proportional to the instantaneous peak value of the input. Following the sample-and-hold, a statistical averaging circuit smooths the pulse-to-pulse fluctuations for monitoring by a digital voltmeter.

The relatively long pulse length of the dye laser avoids pulse width dispersion problems in the water medium so that peak detection is a valid measure of signal strength. To enhance the signal-to-noise ratio, a clock pulse is initiated in the laser circuitry whose leading edge is synchronized with the transmission of the dye laser pulse. The receiver is thus informed as to the temporal location of a pulse prior to its arrival. Thus, with the proper delay, the receiver may be switched into the sample mode to receive a signal and suppress much of the ambient noise. The clock output is also used as an oscilloscope sync for viewing the output of the video amplifier. The inherent uncertainty of the receiver radiance data derives from calibration standards, laser pulse-to-pulse variation, and human imprecision in reading the signal at $\pm 15\%$.

Some of the equipment features and specifications are shown in table 2.

Table 2. Underwater Radiance Receiver.

Aperture	7.6 cm diameter. $f/1.3$
Field-of-view	46 milliradians (in water)
Minimum detectable signal	$2 \times 10^{-7} \text{ Wcm}^{-2} \text{ - ster}^{-1}$
Maximum detectable signal (attenuator in optical path)	$5 \text{ Wcm}^{-2} \text{ - ster}^{-1}$
Optical bandwidth	100 Å centered at 5240 Å
Detector	RCA PF1023 2 inch diameter, 10 state photomultiplier
Detector electrical bandwidth	10 MHz
Output	0 - 10 V pulse to oscilloscope 0 - 10 Vdc time averaged peak value to DVM

EXPERIMENTAL PROCEDURE

OCEAN OPTICAL PROPERTIES

Optical properties of the waters at the test site were monitored by the Scripps Institution of Oceanography Visibility Laboratory. The principal instruments utilized were the ALSCAT (Alpha and volume scattering) and the GASM (General Angle Scatter Meter).²¹

The ALSCAT measured simultaneously the volume attenuation coefficient, k_{ext} , and the volume scattering function at three small angles 3, 6, and 12 milliradians.²² While data were obtained in 10 spectral bands, only the 520-nanometer band applies to this experiment.

The GASM measured the volume scattering function between 10 degrees and 170 degrees. It was only usable during the night, however, because of interference from ambient light. The procedure in monitoring ocean optical properties required extensive nighttime observations by both ALSCAT and GASM before and immediately after an experimental procedure. During the conduct of a day-light experimental event the ALSCAT was deployed hourly to sample the water volume.

By regression of the ALSCAT and GASM data using 48 nighttime data sets acquired over a 2-month period, it was possible to derive the volume scattering coefficient, k_{sca} , and the mean square scattering angle, γ_0^2 , from ALSCAT observations alone with correlation coefficients of 0.980 and 0.946, respectively. In this fashion detailed tabulations of all inherent ocean properties could be provided hourly. Figure 5 is a plot of ALSCAT monitored data showing k_{ext} , k_{sca} , and k_{abs} during one drop. The volume absorption coefficient, k_{abs} , is obtained from

$$k_{\text{abs}} = k_{\text{ext}} - k_{\text{sca}}$$

Table 3 shows excerpted tabular values of k_{abs} and k_{sca} for 5-meter depth intervals for the 5 ALSCAT drops made during the off-axis laser radiance measurements. An important climatological feature was the solar insolation provided by a heavy overcast on 23 July 1975. Consequently, no substantial thermal layers developed in the upper 25 meters of the water mass, and the optical characteristics remained relatively uniform. The means and standard deviations of each parameter are shown in table 3 for the times of the experimental procedure. At each depth the deviations were usually less than 10%, the largest, due to a short-lived thin scattering layer near 15 meters depth at 1130 hours, was 18%.

Table 3. Summary of Daylight Measurements - 23 July 1975.

Depth (meters)	Parameter	Time (PDT)					Mean	Standard Deviation
		0935	1024	1131	1227	1330		
5	k_{abs}	.171	.171	.170	.173	.170	.171	.001
	k_{sca}	.291	.271	.288	.304	.288	.288	.012
10	k_{abs}	.171	.173	.173	.172	.168	.172	.002
	k_{sca}	.296	.306	.306	.300	.273	.296	.014
15	k_{abs}	.177	.169	.172	.150	.169	.167	.010
	k_{sca}	.333	.277	.296	.198	.280	.277	.049
20	k_{abs}	.157	.164	.155	.145	.152	.155	.007
	k_{sca}	.224	.256	.215	.181	.204	.216	.028
25	k_{abs}	.143	.151	.148	.138	.139	.144	.006
	k_{sca}	.174	.202	.191	.159	.163	.178	.018
30	k_{abs}	.138	.137	.134	.130	.127	.133	.005
	k_{sca}	.161	.157	.151	.139	.132	.148	.022
35	k_{abs}	.133	.133	.125	.126	.129	.129	.004
	k_{sca}	.148	.146	.127	.129	.138	.138	.010
40	k_{abs}	.132	.127	.122	.105	.110	.119	.011
	k_{sca}	.143	.32	.122	.089	.099	.117	.023

If the mean values for the upper 20 meters of water are used, we have

$$\begin{aligned}\bar{k}_{abs} &= 0.166 & \text{std dev} &= 0.008; 5\% \\ \bar{k}_{sca} &= 0.269 & \text{std dev} &= 0.036; 13\%\end{aligned}$$

Such uniformity provides a medium in which measured off-axis radiance values can be compared to results predicted by various modeling techniques.

If the uniformity of the upper 25 meters is similarly examined, we have

$$\begin{aligned}\bar{k}_{abs} &= 0.162 & \text{std dev} &= 0.012; 7\% \\ \bar{k}_{sca} &= 0.251 & \text{std dev} &= 0.050; 20\%\end{aligned}$$

Unfortunately, the uniformity of the upper 50 meters is not as good as the above. However, to facilitate data comparison to come, we have averaged the absorption and scattering coefficients to yield

$$\begin{aligned}k_{abs} &= 0.1428 \text{ m}^{-1} \\ k_{sca} &= 0.1892 \text{ m}^{-1}\end{aligned}$$

The volume scattering function which most nearly corresponds to these upper 20-25 m values was acquired at 30 meters depth at 2106 hours and is shown in figure 6. This should not be significantly different from that throughout the total volume.

DATA ACQUISITION

The radiance measurements recorded the spatial impulse response of the dye laser about an off-axis point. In order to make this measurement, the optical receiver was transited beneath the water surface along the beam attached to the side of the barge (see figure 1). This receiver was mounted so that it could be stopped at any position along the optical bench and pivoted through $160^\circ (\pm 80^\circ)$ about the nadir in the plane which contained the underwater platform suspension pipe and the optical receiver.

Data were gathered as follows:

- (1) The dye laser was placed in a preselected angular orientation with respect to the zenith and was lowered to a predetermined depth, D , so that it transmitted in the plane that contained the laser, the pipe, and the optical receiver. D was known to ± 0.2 meter.
- (2) The optical receiver was positioned at a known horizontal position, d , away from the laser. The uncertainty in d was ± 0.1 meter.
- (3) The angular position, ϕ , of the optical radiance receiver was set, the dye laser was activated, and the signal level was received and recorded.
- (4) After the angular position of the optical receiver had been exercised through its range, the horizontal position, d , was changed, and the sequence was repeated.
- (5) When a complete sequence of measurements had been made that sufficiently exhausted the receiver angular and horizontal position possibilities, either the laser depth, its angular orientation, or both were changed. This different configuration then formed a new set of experimental knowns, and steps (2) through (4) were repeated.

Data were recorded as notebook entries of carriage position, d , laser depth D , laser tilt, w , and the received signal level. To reduce these quantities to the axial distance between laser and receiver, Z , the distance off the axis, r , and the angle with the optic axis, θ , we can relate

$$\begin{aligned} Z &= (d - D \tan \phi) \sin \phi + D \sec \phi \\ r &= (d - D \tan \phi) \cos \phi \\ \theta &= w - \phi \end{aligned} \quad (1)$$

For all data taken $w = 12.5$ degrees, r is always positive and the component of θ out of the plane of measurement is either 0 or π depending upon the side of the axis on which the receiver is located.

DATA

The radiance distributions found various distances off the optic axis of the laser are reported for three depth locations of the laser - 22.9, 38.1, and 45.7 meters. Because of the geometry (figure 1), the physical length of the optical path was always greater than the depth and varied with the location of the optical receiver on the horizontal optical bench.

The measured radiances are plotted in figures 7 through 9. To determine the path radiance transfer function, the ordinate may be normalized for transmitter power by multiplying by 2×10^{-4} .

DISCUSSION OF DATA

Examination of the data in figures 7, 8, and 9 shows the expected behavior in terms of the general trend of the data. The greater the distance off the optical axis, r , the lower the recorded radiance and the larger the angle of the peak radiance to the optic axis.

The 3 dB laser beam divergence being 0.0214 radian (in water), only one of the data sets contains an on-axis measurement, "on-axis" interpreted as the receiver located within the laser beam. This is the curve in figure 9 with a physical optical path of 46.9 meters and a receiver 0.526 meter from the axis. With absorption and scattering ignored, the laser spot diameter would be slightly more than a meter at the receiver (3 dB diameter), or 1.06 meters (1/e diameter).

One measure of the reasonableness of the data is made by considering the laser and the receiver as constituting a beam transmissometer.²³ Using the radiance from the 46.9-meter path and ignoring the losses in the medium, we can calculate the average power density over the 1/e diameter from the laser at the receiver to be

$$\frac{4 \times 5 \times 10^3}{\pi (0.0226 \times 46.9)^2} = 5.67 \times 10^3 \text{ W M}^{-2} = 0.567 \text{ W cm}^{-2} \quad (2)$$

The measured radiance at $\theta = 0$ was $1.82 \times 10^{-3} \text{ W cm}^{-2} \text{ sterad}^{-1}$. Multiplying by the solid angle of the receiver gives an on axis flux of $3.02 \times 10^{-6} \text{ W cm}^{-2}$; the loss is then

$$\frac{3.02 \times 10^{-6}}{0.567} = \exp(-12.1). \quad (3)$$

This can be interpreted in terms of the volume attenuation coefficient, k_{ext} , as

$$k_{\text{ext}} = k_{\text{abs}} + k_{\text{sca}} = 12.1/46.9 = 0.259 \text{ m}^{-1} \quad (4)$$

averaged over the path. Comparing this value with table 3 shows reasonable agreement. Better agreement would have been obtained with a smaller field on the receiver to eliminate more of the scattered photons.

The quality of the data can be judged from the curves in figures 7 through 9. The curves were plotted without benefit of a curve fitting routine by simply connecting data points by line segments. The resulting shapes show only minor dispersion in some of the data points, generally less than $\pm 1\frac{1}{2}$ dB from points at which a fair curve would have resulted.

Another observation, though not immediately obvious, is that the radiance distributions do not appear to be symmetrical about the maxima. The slope of the radiance distributions appears greater on the side toward negative observation angles. That is, the radiance decreases more rapidly in directions away from the source than in directions looking toward the optical axis.

MATHEMATICAL MODELS

For brevity, we will limit our discussion here to those models which yield closed-form, analytical solutions. The fundamental equation of interest is the equation of radiative transfer for a plane-parallel scattering medium.²⁴⁻²⁶

$$\left(\mu \frac{d}{dr} + 1 \right) I(\tau, r, \mu, \phi, t) = I_0(\tau, r, \mu, \phi, t) - \omega_0 \int_{-1}^{+1} \int_0^{2\pi} p(\theta, \phi; \theta', \phi') I(\tau, r, \mu', \phi', t) d\mu' d\phi', \quad (5)$$

where

- I \equiv scattered radiance,
- I_0 \equiv source radiance within the scattering medium,
- μ \equiv $\cos \theta$,
- τ $= k_{\text{ext}} Z \equiv$ optical thickness of the medium,
- Z \equiv physical thickness of the medium,
- r \equiv planar spatial coordinates,
- (θ, ϕ) \equiv angular coordinates,

- ω_0 = $k_{\text{sca}}/k_{\text{ext}}$ \equiv single scatter albedo,
 p \equiv scalar phase function of the medium,
 k_{sca} \equiv volume scattering coefficient,
 k_{ext} \equiv volume extinction coefficient,
 t \equiv time.

Figure 10 depicts the spatial and angular coordinates pictorially. Following Arnush,⁴ it can be shown that Eq. (5) reduces to

$$\left(\frac{\delta}{\delta z} + \gamma \cdot \frac{\delta}{\delta r} + k_{\text{ext}}\right) I(z, r, \gamma) \approx k_{\text{ext}} I_0(z, r, \gamma) + \omega_0 \iint_{-\infty}^{+\infty} p(|\gamma - \gamma'|) I(z, r, \gamma') d^2 \gamma' \quad (6)$$

for time-independent radiation transfer under the small-angle-scattering approximation.

Several authors^{4,5,8} have attempted closed-form solutions of equation (6). Arnush used Fourier analysis and a highly peaked scalar phase function,

$$p(\theta) = \frac{\gamma}{2\pi\theta} \exp\{-\gamma\theta\} \quad (7)$$

to yield a solution of the form

$$N(z, \xi, \zeta) = N_0 \exp\{-a^2 \gamma^2 + b \zeta \cdot \xi - r^2/r_1^2\} \quad (8)$$

with

$$N_0 = \frac{P_T \exp\{-(1 - \omega_0)\tau\}}{\pi^2 [\gamma_T^2 + 2\omega_0 \tau/\gamma^2] r_1^2} \quad (8a)$$

$$a^2 = \frac{1}{[\gamma_T^2 + 2\omega_0 \tau/\gamma^2]} + \frac{Z^2 [\gamma_T^2 + \omega_0 \tau/\gamma^2]^2}{r_1^2 [\gamma_T^2 + 2\omega_0 \tau/\gamma^2]^2} \quad (8b)$$

$$b = \frac{2Z [\gamma_0^2 + \omega_0 \tau/\gamma^2]}{r_1^2 [\gamma_T^2 + 2\omega_0 \tau/\gamma^2]} \quad (8c)$$

$$r_1^2 = r_0^2 + Z^2 \gamma_T^2 + \frac{2\omega_0 \tau}{3\gamma^2} Z^2 - \frac{[\gamma_T^2 + \omega_0 \tau/\gamma^2]^2}{[\gamma_T^2 + 2\omega_0 \tau/\gamma^2]} Z^2 \quad (8d)$$

r_0 \equiv radius of the initial laser beam,

γ_T \equiv beamwidth of the initial laser beam,

using only the low frequency Fourier components of the scattered radiance. Stotts,⁸ on the other hand, solved equation (2) using Fourier analysis and a distributed source to produce a solution of the form

$$N'(z, \xi, \zeta) = N_0 \exp\{-a^2 \gamma^2 + b \zeta \cdot \xi - r^2/r_1^2\} \quad (9)$$

with

$$N_0 = \frac{P_T \exp\{-(1 - \omega_0)\tau\}}{\pi [\omega_0 \tau \gamma_0^2] [r_0^2 + \frac{1}{12} \omega_0 \tau Z^2 \gamma_0^2]} \quad (9a)$$

$$a^2 = \frac{1}{\omega_0 \tau \gamma_0^2} + \frac{Z^2}{4(r_0^2 + \frac{1}{12} \omega_0 \tau Z^2 \gamma_0^2)} \quad (9b)$$

$$d = \frac{Z}{(r_0^2 + \frac{1}{12} \omega_0 \tau Z^2 \gamma_0^2)} \quad (9c)$$

$$r_1^2 = r_0^2 + \frac{1}{12} \omega_0 \tau Z^2 \gamma_0^2 \quad (9d)$$

assuming $\gamma_T = 0$ and a gaussian scalar phase function. Fante⁵ approached the solution to equation (6) by expanding the integral on the right-hand side in Taylor series. In particular, he transformed equation (6) into the following form

$$\frac{\delta N}{\delta Z} + \gamma \cdot \frac{\delta N}{\delta r} - \frac{\omega_0 k_{\text{ext}} \gamma_0^2}{4} \nabla^2 N + (1 - \omega_0) k_{\text{ext}} N \approx k_{\text{ext}} N_0 \quad (10)$$

neglecting terms of order $\omega_0 k_{\text{ext}} (\gamma_0^{-2})^2 \nabla^4 N$ and higher. Unfortunately, his solution to equation (10) could only be evaluated numerically for the scattered radiance. However, if one assumes

$$N_0(r, z, \chi) = \frac{\delta(r) \exp\left\{-r^2/r_0^2 - \gamma^2/\gamma_T^2\right\}}{\pi^2 r_0^2 \gamma_T^2} \quad (11)$$

then we find that

$$N(Z, z, \chi) = N_0 \exp\left\{-a^2 \gamma^2 + b \chi \cdot z - r^2/r_1^2\right\} \quad (12)$$

$$N_0 = P_T \frac{\exp\left\{-(1 - \omega_0) \tau\right\}}{\pi^2 [\gamma_T^2 + \omega_0 \tau \gamma_0^2] r_1^2} \quad (12a)$$

$$r_1^2 = r_0^2 + \frac{\omega_0 \tau \gamma_0^2 Z^2}{3} - \frac{\omega_0^2 \tau^2 \gamma_0^4 Z^2}{4 [\gamma_T^2 + \omega_0 \tau \gamma_0^2]} \quad (12b)$$

$$b = \frac{\omega_0 \tau \gamma_0^2 Z}{r_1^2 [\gamma_T^2 + \omega_0 \tau \gamma_0^2]} \quad (12c)$$

$$a^2 = \frac{1}{[\gamma_T^2 + \omega_0 \tau \gamma_0^2]} + \frac{\omega_0^2 \tau^2 \gamma_0^4 Z^4}{4 [\gamma_T^2 + \omega_0 \tau \gamma_0^2]^2 r_1^2} \quad (12d)$$

following Stotts.⁸ It is interesting to note that for $\gamma_T = r_0 = 0$, all the above solutions reduce to the following form:

$$N(Z, z, \chi) = N_0 \exp\left\{-a^2 \gamma^2 + b \chi \cdot z - r^2/r_1^2\right\} \quad (13)$$

with

$$N_0 = \frac{12 P_T \exp\left\{-(1 - \omega_0) \tau\right\}}{\pi^2 (\omega_0 \tau \gamma_0^2)^2 Z^2} \quad (13a)$$

$$a = \frac{1}{\omega_0 \tau \gamma_0^2} + \frac{3}{\omega_0 \tau \gamma_0^2} = \frac{4}{\omega_0 \tau \gamma_0^2} \quad (13b)$$

$$b = \frac{12}{\omega_0 \tau \gamma_0^2 Z} \quad (13c)$$

$$r_1^2 = \omega_0 \tau \gamma_0^2 Z^2 / 12 \quad (13d)$$

This can be found by noting that

$$\langle \theta^2 \rangle \equiv \gamma_0^2 = \int_0^{2\pi} \gamma \int_0^\infty \frac{\exp\{-\gamma \theta\}}{2\pi \theta} d^2 \theta = \frac{2}{\gamma^2} \quad (14)$$

Because of the small values of r_0 and γ_T used in the experiment, we will use equations (13) for the rest of our discussion.

In Arnush's formulation, the parameter γ was assumed to be on the order of 10. Figure 6 shows plotted values of equation (7) using $\gamma = 10$ against the experimentally measured form of $p(\theta)$. These appear to be in reasonable agreement; thus, we will assume this value for the rest of this analysis. This implies

$$\gamma_0^2 = (0.1414)^2 \text{ rad}^2,$$

which is in good agreement with earlier measurements of mean scatter angles in these same waters.²⁷

COMPARISON OF EXPERIMENT AND THEORY

Figures 11 and 12 compare experimental data with equation (13) for $r = (2.48 \text{ m}, \pi)$ and $Z = 24 \text{ m}$, and $r = (6.9 \text{ m}, \pi)$ and $Z = 25 \text{ m}$, respectively. The values assumed for k_{abs} and k_{sca} were 0.166 m^{-1} and 0.269 m^{-1} , respectively. It is apparent that the model does not predict as peaked a radiance distribution as measured "near" the optic axis, and as broad a radiance distribution as

measured "far" from the axis. In addition, the peaking angle of the radiance is different between theory and model, the theory's peak always being less. This is illustrated in more detail in table 4 as a function of the apparent source location for the 20-25 m depth range (the smaller y , the smaller the peak angle, and vice versa).

Table 4. Location of Apparent Source - ($z - y$) meters.

	Predicted y	Observed y
$Z = 23.3; r = 0.46$	7.77	19.8
$Z = 23.7; r = 0.99$	7.88	20.6
$Z = 24.0; r = 2.48$	7.99	17.2
$Z = 25.0; r = 6.90$	8.32	14.2

In light of the work of Stotts,²⁸ and Tam and Zardecki,²⁹ this is not too surprising. The former showed that the use of the lower frequency Fourier components yields only the diffusive radiance distribution and not the multiple forward-scattered radiation. This was contained in the higher order components. Tam and Zardecki²⁹ verified this peaking nature of the complete numerical solution of equation (6) but did not indicate why the Arnush/Stotts approximation²⁹ worked only in the large scattering limit.

Another indicator that the above models yield only the diffusive radiance distribution is that the first two formalisms give the same distribution, for $\gamma_r = 0 = r_0$, independent of the scalar phase function used. This type of performance was shown by Bucher¹⁴ to be true only when one was in the diffusion regime of scattering. Thus, for greater scattering depths and/or further off-axis, the models should agree more with theory. To test this, compare equation (13) with data gathered from the 45.7 source depth. The structure of the water will be ignored to first order (since the models assume homogeneity) by averaging k_{abs} and k_{sca} over a 50-meter path. This yields

$$\begin{aligned} \bar{k}_{abs} &= 0.1428 \text{ m}^{-1} \\ \bar{k}_{sca} &= 0.1892 \text{ m}^{-1} \end{aligned}$$

Figure 13 compares equation (13) and experimental data for $r = (3.9 \text{ m}, 0)$ and $Z = 42.8$, i.e., ~ 8 scattering lengths. It is apparent that the broadening and peaking of theory and experiment are more in agreement. A similar trend is illustrated in figure 14 for $r = (3.9 \text{ m}, \pi)$ and $Z = 47.6 \text{ m}$ (i.e., ~ 9 scattering lengths). Unfortunately, their magnitudes are not very close. This is probably because we still have not fully transitioned to the diffusion domain. This hypothesis is somewhat supported by figure 15, where we have moved farther off-axis from the previous two figures and observe better correlation. The point to be made is that current proposed closed-form analytical models have validity range limitations, and hence must be used with care in order to accurately predict experimental or overall system performance.

CONCLUSIONS

Several closed-form solutions of the equation of radiative transfer using small angle approximations have been examined. It has been shown that the solutions are equivalent and insensitive to the specific phase function used with a collimated pencil beam. The predicted radiance values are generally underestimated at less than 10 scattering lengths. The low frequency approximation made in Fourier space to facilitate the closed-form solution of the equations obscures details in the radiance distributions attributable to multiple small angle forward scatter. Thus, these models provide reasonable answers only where $k_{sca}Z \geq 10$.

It should be noted that the water characteristics used in analysis of the deeper data (9 scattering lengths) required an averaging of the inherent propagation parameters over the column. In general, this water column was composed of two distinct layers with a well defined transition. To first order, this analysis is sufficient to show the limitations of current models. Further work with these experimental results using Monte Carlo techniques or numerical solutions of the Fante⁵ model, equation (10), is indicated to account for this structure.

The sensitivity of any modeling effort to the precise propagation parameters of the medium should always be carefully treated. In the experimental portion of this work, the water column was sampled once an hour in 1 meter depth intervals. Comparing consecutive data results, such as figure 6, reveals little correlation between small scale details of the water properties over a one-hour period. The data were clearly undersampled, although the gross features were adequately sampled. Future work should incorporate sampling every 10 minutes to insure that the propagation parameters are well documented. Such a routine requires new and more versatile instruments for monitoring inherent water properties.

REFERENCES

1. R. A. Dell-Imagine, "A study of multiple scattering of optical radiation with applications to laser communications," in *Advances in Communication Systems*, edited by V. A. Balakrishnar (Academic, New York, 1966) Vol. II, p. 1.
2. H. M. Heggstad, "Multiple Scattering Model For Light Transmission Through Optically Thick Clouds," *J. Opt. Soc. Am.* **61**, 1293-1300 (1971).
3. D. M. Bravo-Zhivotovskiy, I. S. Dolin, A. G. Luchmin, and V. A. Sarelyev, "Structure of a narrow light beam in sea water," *Atmos. Oceanic Phys.* **5**, (2), 160-167 (1969) [translated by P. A. Kaehn].
4. D. Arnush, "Underwater light-beam propagation in the small-angle-scattering approximation," *J. Opt. Soc. Am.* **62**, 1109-1111 (1972).
5. R. L. Fante, "Propagation of electromagnetic waves through turbulent plasma using transport theory," *IEEE Trans. Antennas Propag.* **AP-21**, 750-755 (1973).

6. A. Ishimaru and S. T. Hong, "Multiple scattering effects on coherent bandwidth and pulse distortion of a wave propagating in a random distribution of particles," *Radio Sci.* **10**, 637-644 (1975).
7. S. T. Hong and A. Ishimaru, "Two frequency mutual coherence function, coherence bandwidth, and coherence time of millimeter and optical waves in rain, fog, and turbulence," *Radio Sci.* **11** (6), 551-559 (1976).
8. L. B. Stotts, "The radiance produced by laser radiation traversing a particulate multiple-scattering medium," *J. Opt. Soc. Am.* **67** 815-819 (1977).
9. A. Ishimaru, "Theory and application of wave propagation and scattering in random media," *Proc. IEEE* **65**, 1030-1061 (1977).
10. D. L. Fried, "Propagation of the mutual coherence function for an infinite plane wave through a turbid medium," *Opt. Lett.* **1**, 104-106 (1977).
11. R. F. Lutomirski, "Atmospheric degradation of electro-optical system performance," *Appl. Opt.* **17**, 3915-3921 (1978).
12. G. N. Plass and G. W. Kattawar, "Monte Carlo calculations of light scattering from clouds," *Appl. Opt.* **7**, 415-419 (1968).
13. E. A. Bucher, "Computer simulation of light pulse propagation for communication through thick clouds," *Appl. Opt.* **12**, 2391-2400 (1973).
14. E. A. Bucher, "Propagation models for optical communications through fog and clouds," *Proc. Nat. Electron. Conf.* **29**, 180-185 (1974).
15. E. A. Bucher and R. M. Lerner, "Experiments on light pulse communication through atmospheric clouds," *Appl. Opt.* **12**, 2401-2414 (1973).
16. W. H. Paik, M. Tebyani, D. J. Epstein, R. S. Kennedy, and J. H. Shapiro, "Propagation experiments in low-visibility atmospheres," *Appl. Opt.* **17**, 899-905 (1978).
17. J. S. Ryan and A. I. Carswell, "Laser beam broadening and depolarization in dense fogs," *J. Opt. Soc. Am.* **68**, 900-908 (1978).
18. G. C. Mooradian, M. Geller, L. B. Stotts, D. H. Stephens, and R. A. Krautwald, "B/G Pulse Propagation through Maritime Fogs," *Appl. Opt.* **18**, 429-448 (1979).
19. S. Q. Duntley, "Underwater lighting by submerged lasers," *Visibility Lab., SIO. Ref 71-1*, June 1971.
20. Naval Electronics Laboratory Center TD 490, "OPSATCOM Field Measurements," 1 June 1976.
21. Visibility Laboratory Scripps Institution of Oceanography UCSD Technical Memorandum ML-76-005t Rev "Ocean Optical Properties - 520 nanometers Santa Catalina Island, Lat: 33° 27.2'N, Long: 118° 29.0'W," 23 June 1976.
22. R. W. Austin and T. J. Petzold, "An Instrument for the Measurement of Spectral Attenuation Coefficient and Narrow Angle Volume Scattering Function of Ocean Waters," *Proc. SPIE* **64**, p. 50, 1975.
23. N. G. Jerlov, "Marine Optics," Elsevier, 1976.
24. S. Chandrasekhar, *Radiative Transfer* (Clarendon, Oxford, 1960) (reprinted by Dover, New York, 1960).
25. V. Kourganoff, *Basic Methods in Transfer Problems* (Dover, New York, 1963).
26. R. Preisendorfer, *Radiative Transfer on Discrete Spaces* (Pergamon, New York, 1965).
27. G. R. Allgaier, "Spreading of Light Beams Passing Through Substantial Air-Water Paths," *Proc. SPIE* **64**, p. 23 (1975).
28. L. B. Stotts, "Limitations of Approximate Fourier Techniques in Solving Radiative-Transfer Problems," *J. O. S. A.* **69**, p. 1719 (1979).
29. W. G. Tam and A. Zardecki, "Laser Beam Propagation in Particulate Media," *J. O. S. A.* **69**, p. 68 (1977).

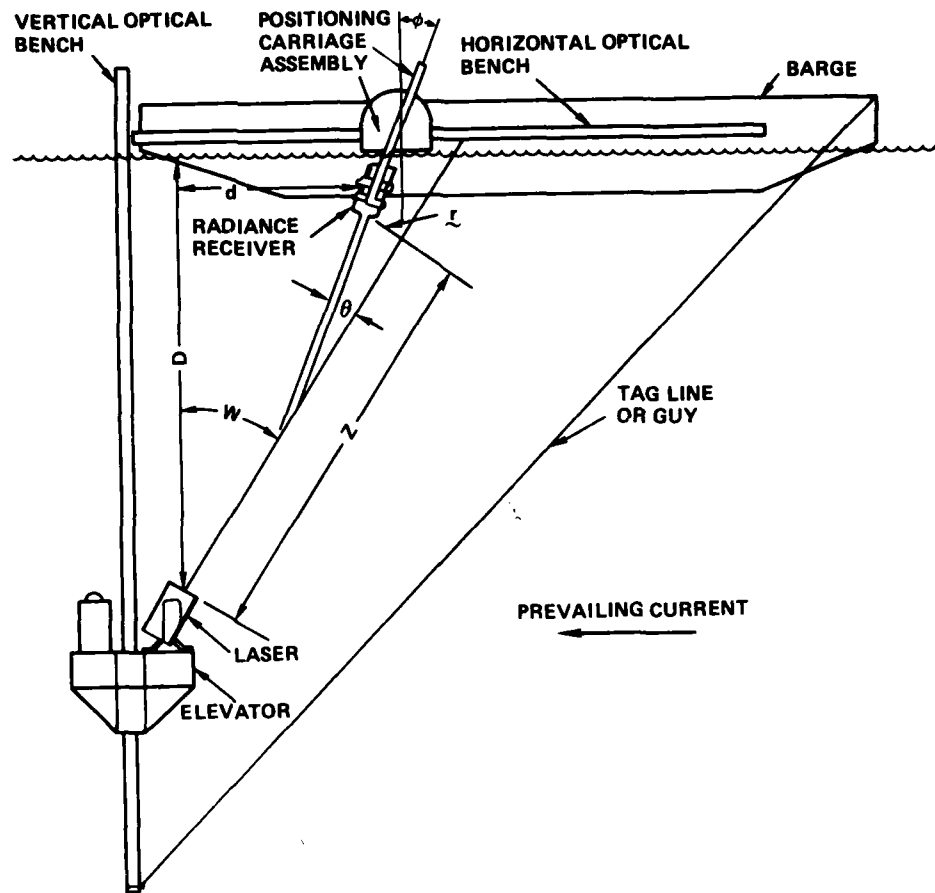


Figure 1. Experiment configuration.



Figure 2. Positioning carriage subassembly (side view).



Figure 3. Submerged instrument platform.



Figure 4. Underwater radiance receiver.

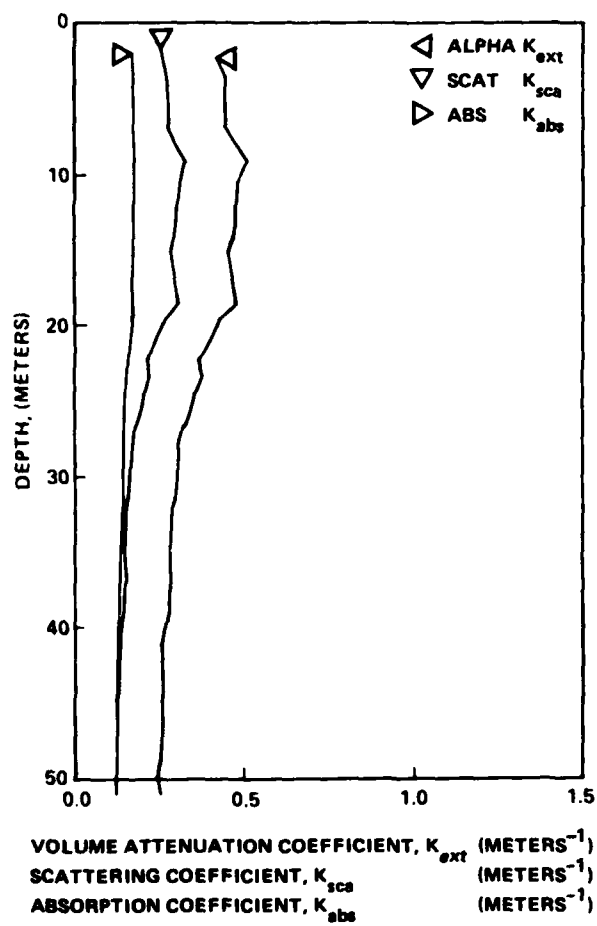


Figure 5. Ocean optical properties - 520 nm. Santa Catalina Is.
 Lat: 33-27.2 N; Long: 116-29.0 W. 23JUL1975.
 1024PDT.

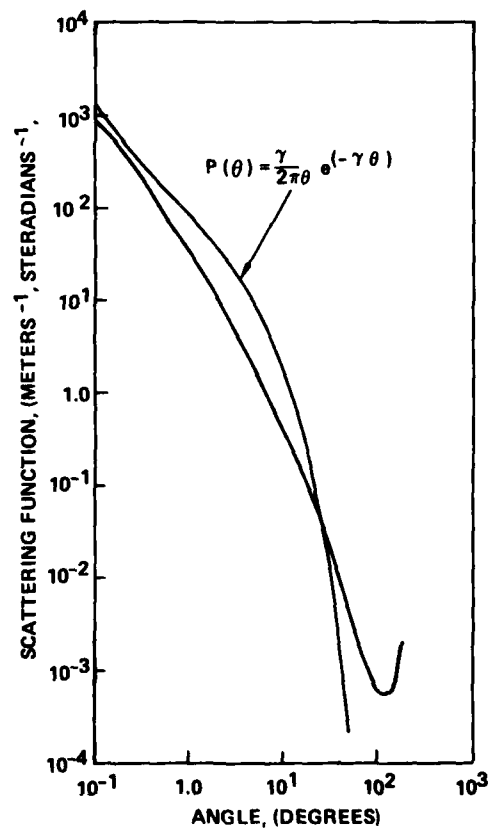


Figure 6. Volume scattering function. 520 23JUL75
 2106 STA.CAT/21 - SEA

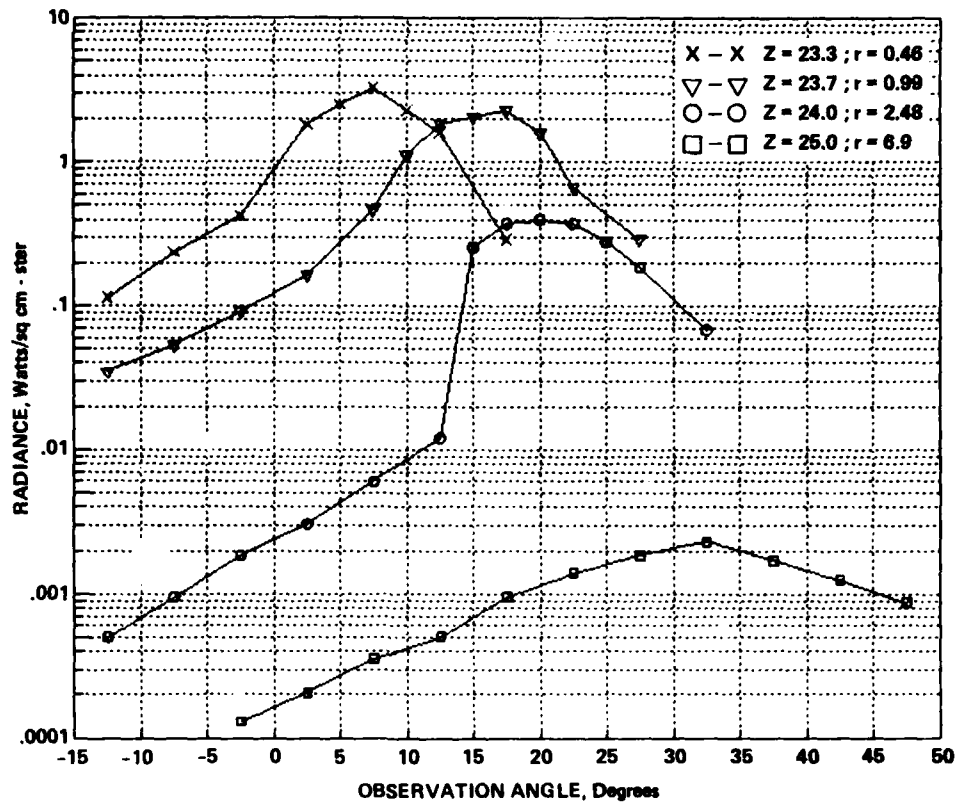


Figure 7. Source depth 22.9 meters.

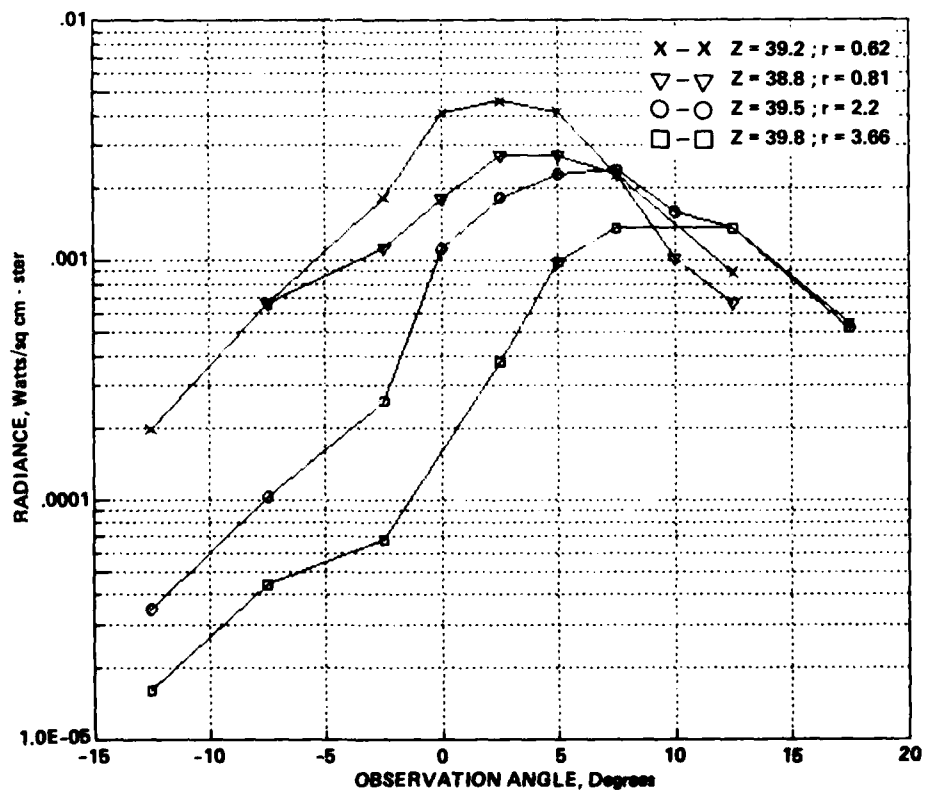


Figure 8. Source depth 38.1 meters.

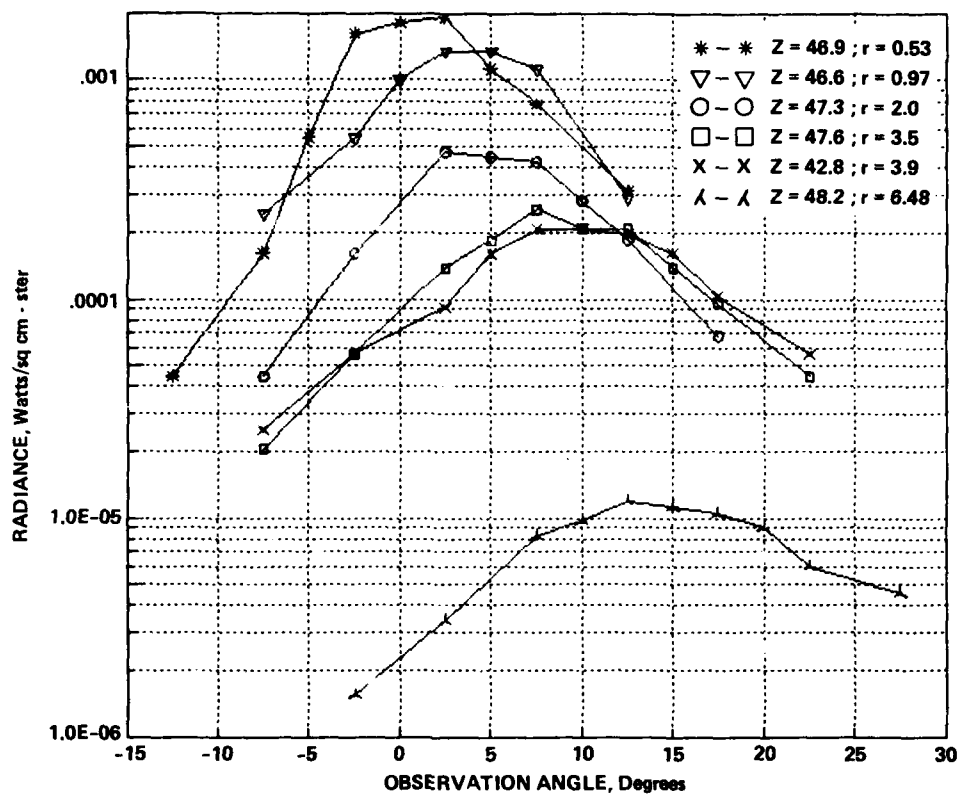


Figure 9. Source depth 45.7 meters.

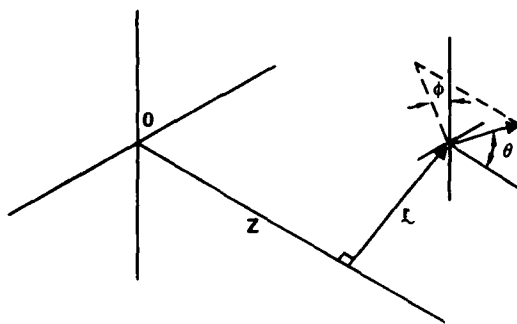


Figure 10. Spatial and angular coordinate system used in this problem.

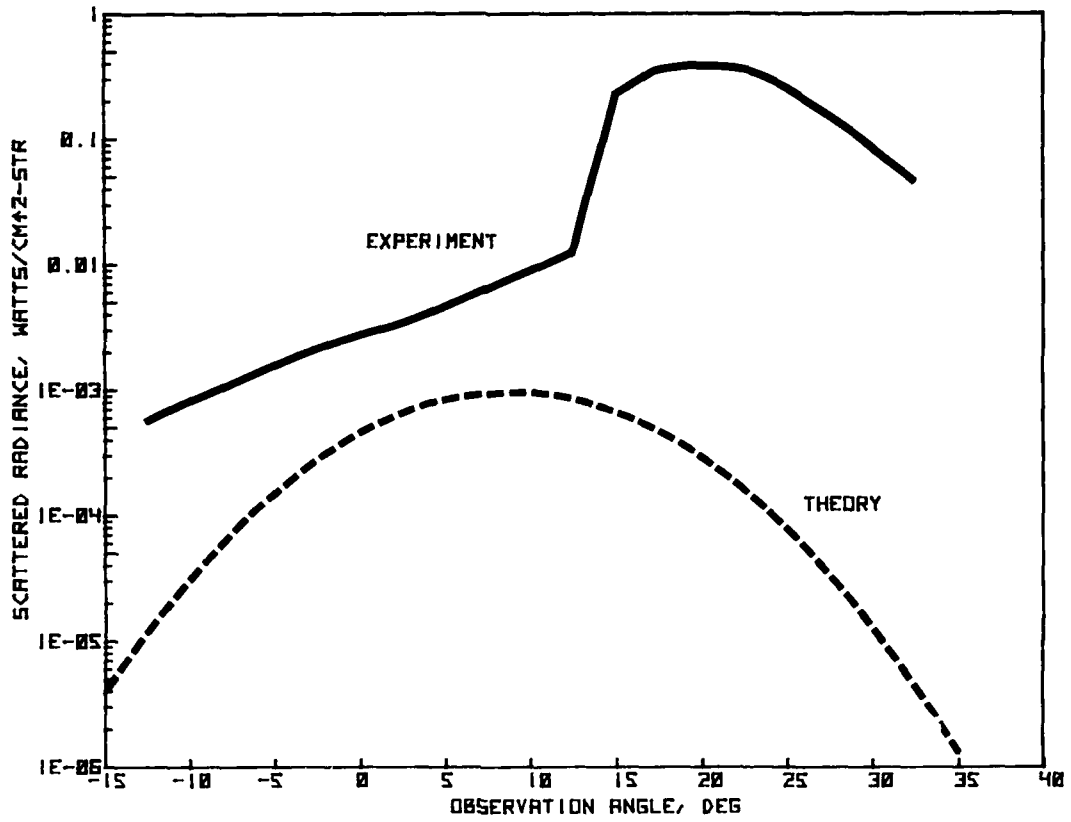


Figure 11. Comparison of equation (13) with measured data for $L = (2.48\text{m}, \pi)$ and $Z = 24\text{m}$.

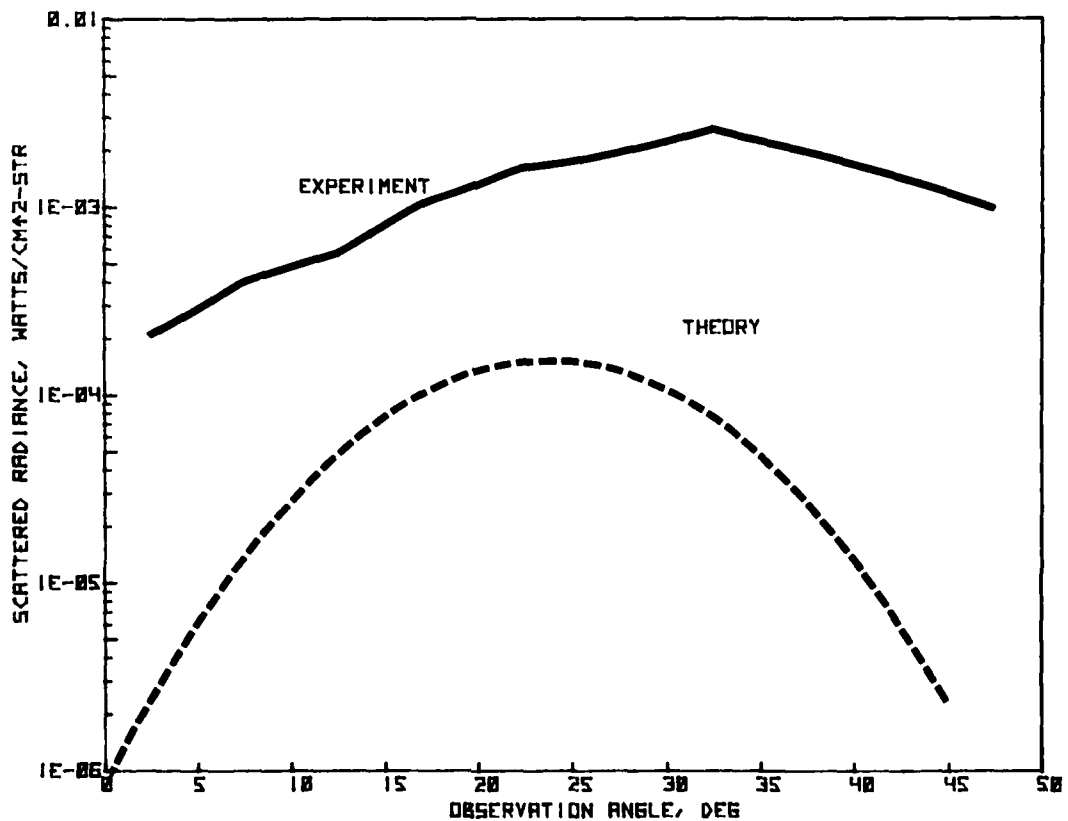


Figure 12. Comparison of equation (13) with measured data for $L = (6.9\text{m}, \pi)$ and $Z = 25\text{m}$.

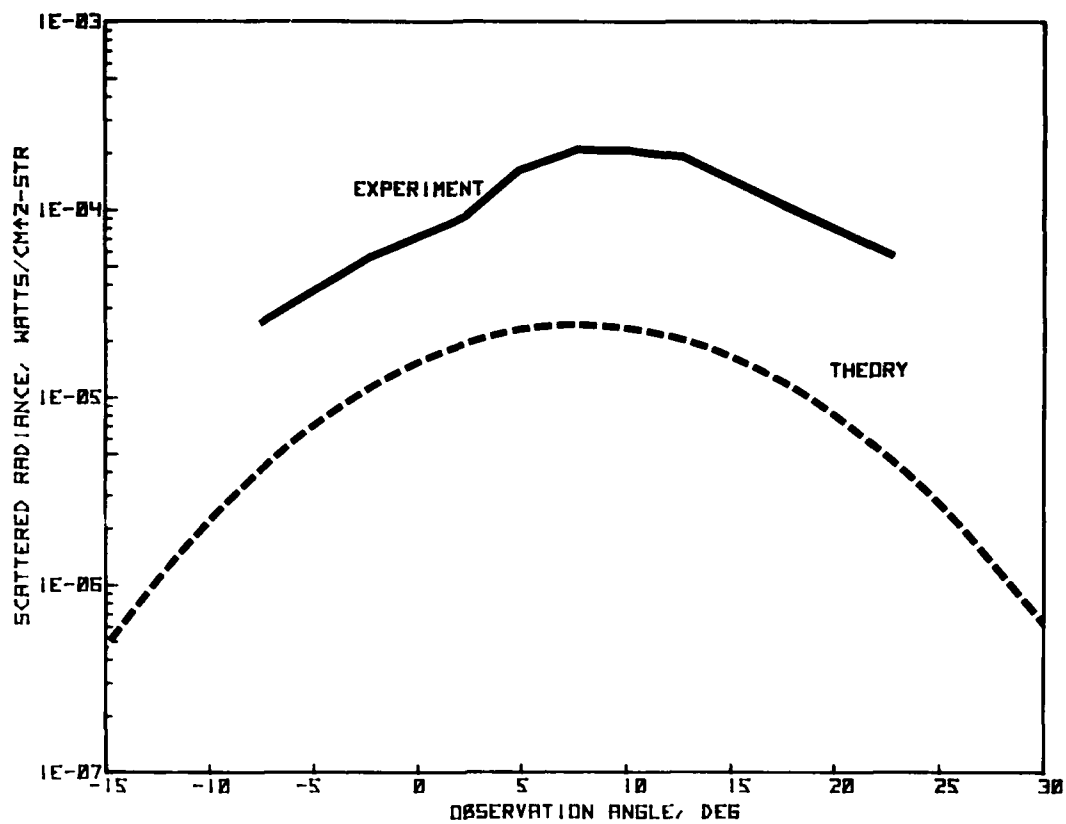


Figure 13. Comparison of theory and experiment at $r = (3.9m, 0)$ and $Z = 42.8m$.

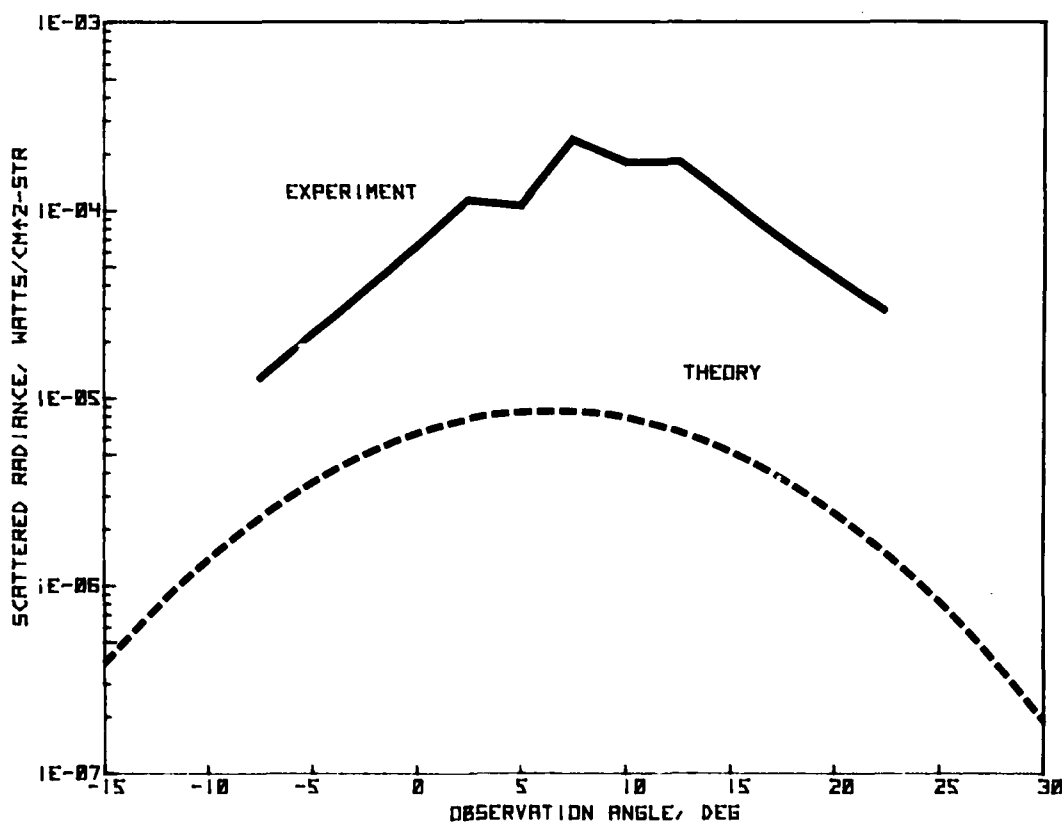


Figure 14. Comparison of theory and experiment at $r = (3.5m, \pi)$ and $Z = 47.6m$.

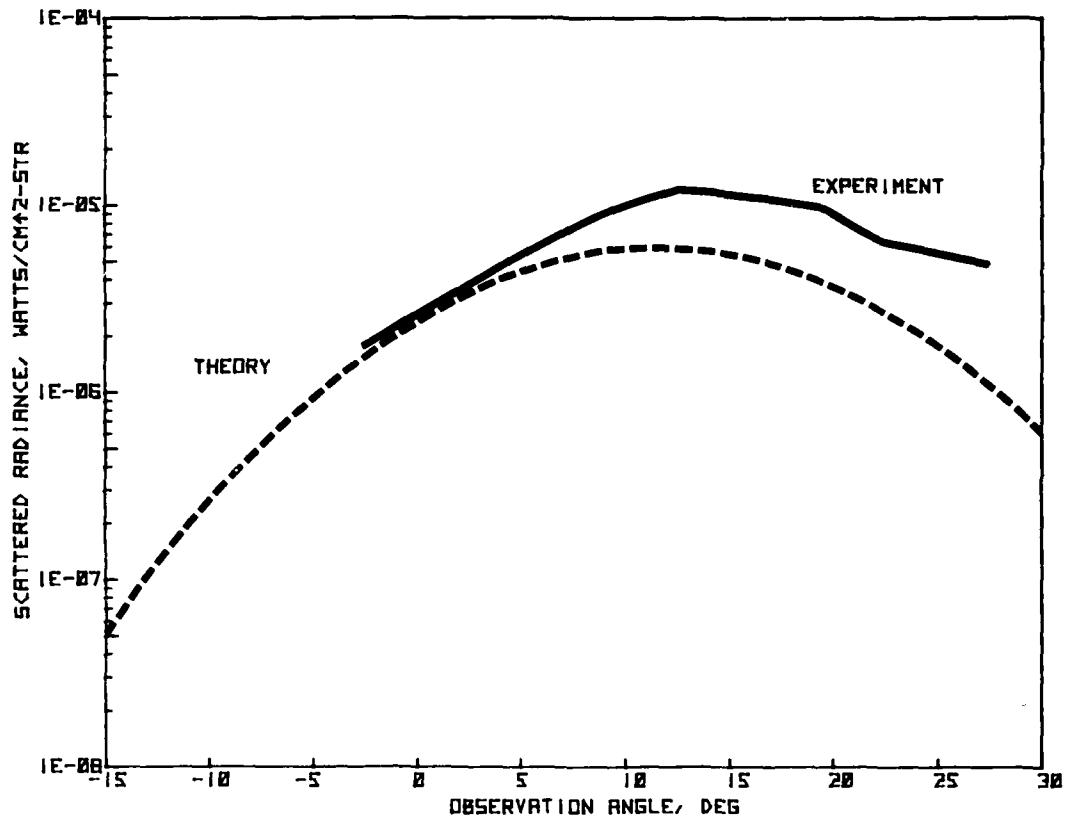


Figure 15. Comparison of theory and experiment at $r = (6.48m, \pi)$ and $Z = 48.2m$.

DOWNLINK LASER CLOUD PROPAGATION EXPERIMENT

G.R. Hostetter and P.J. Titterton
GTE Products Corporation
Sylvania Systems Group-Western Division
PO Box 188
Mountain View, California 94042

SUMMARY

During August and September 1979, GTE conducted the Downlink Laser Cloud Experiment on the island of Kauai, Hawaii. The experiment was designed to obtain the first measurements of laser pulse stretching resulting from downward vertical propagation through a cloud. For the nonuniform clouds that were present over Kauai, pulse stretching was found to be less than was expected from propagation theory.

The clouds were characterized by an aircraft-borne Knollenberg particle counter and by attenuation of moonlight passing through the cloud layer. For cloud geometric thicknesses of 4,000 to 8,600 feet and optical thicknesses of 19 to 86, the received pulsewidths ranged from 1 to 7 microseconds. These received pulsewidths were from 0.05 to 0.2 of the theoretically predicted values. Typically, the received pulses were composed of a fast and a slow component, indicating at least two different propagation modes through the clouds. The widths of the slow components were approximately equal to the theoretical values predicted for the entire pulse.

1. INTRODUCTION

During August and September 1979, GTE conducted the Downlink Laser Cloud Experiment. This experiment was designed to obtain the first data on the laser pulse stretching resulting from vertical propagation through a cloud layer. Previous measurements of cloud-induced pulse stretching had been between adjacent mountaintops. (Bucher, E. A., 1970 and 1973.)

The key elements of the experiment are illustrated in Figure 1 and include (a) the laser; (b) the ground-based receiver equipment; (c) the laser being fired as part of the routine preflight check; (d) the aircraft used to measure and characterize the clouds; (e) the layout of the experiment conducted at Kauai, Hawaii; and (f) an aerial view of the Kauai test site where the ground receiver was located.

The experiment was designed so that the laser pulse was transmitted from a high altitude aircraft and propagated through cloud layers to the optical receiver equipment on the ground. To improve the signal-to-noise ratio, the experiment was conducted at night. The data from the received laser pulse were digitized, stored on magnetic tapes, and have since been analyzed both manually and through the use of computer analysis techniques. The clouds through which the pulses propagated were characterized as to their geometric and optical thicknesses.

2. EXPERIMENT DESCRIPTION

The test site, test equipment, and data-taking procedures are discussed in the following paragraphs. Test-site selection involved choosing the general area as well as the specific location of the receiver equipment in the test area. The test equipment description covers the equipment used and its specific characteristics. The description of measurement operations provides a monthly schedule and includes details of the duties of the participants.

2.1 Test Site

Test site selection was based on four major requirements. The first requirement was that there be a high probability that a solid layer of clouds would consistently form above the site. The second requirement was to ensure the safety of the aircraft that would fly into the cloud layer above the selected site. The third requirement, a relatively unpopulated site, was imposed by the inclusion of an alternative experiment that operated simultaneously with the downlink laser cloud experiment. The fourth was the quality of access to the site and the presence of a flat area large enough to accommodate the generator and two trailers.

The east side of the island of Kauai, Hawaii, was chosen as the primary location because it best met the four site selection requirements. The site is located at longitude 159° 26'W and latitude 22° 3'16"N. It satisfies the first and fourth requirements for selection because it lies in a long, flat valley that leads up to the nearby mountain peaks 4.5 miles away. It is against these mountains that clouds are driven almost daily by the summer trade winds, thus consistently providing a solid layer of clouds over an easily accessible site.

The second requirement, the safety of the aircraft, was assured by three factors. The site was at a safe distance from the nearby mountains, the Lihue Airport provided navigation aids and lights to orient the pilot, and strobe lights were set up in the middle of the valley to add additional visual references for the pilot.

The third requirement, involving the alternative experiment, was satisfied because most of the length of the valley is unpopulated. This was an important factor because the alternative equipment, designed and manufactured by HSS, Incorporated, measured characteristics of the moonlight emerging from the bottom of the cloud. Since the moonlight coming through the cloud is indistinguishable from scattered city lights, the test site had to be located far from a large population center.

The test setup for the experiment is shown in Figure 1e. The facilities and services supplied by the Pacific Missile Range Facility (PMRF) at Barking Sands included the radar which tracked the high altitude aircraft with an accuracy of approximately 10 feet. The radar controller could, therefore, direct the aircraft carrying the laser transmitter directly over the receiver on the ground. The airspace in and around the island was controlled by the Barking Sands test range and the FAA. Hence, the second aircraft, which was flying through and characterizing the cloud layers, could fly the

pattern most suited to this purpose without posing a danger to other aircraft in the area. The Barking Sands test range also supplied miscellaneous support equipment such as generators, mobile shelters, and communication facilities.

2.2 Test Equipment

The test equipment included the laser transmitter, platform, receiver, and cloud characterization equipment. The laser source was carried to an altitude of 40,000 feet in a T-39 aircraft, which was leased specifically for this experiment. (See Figure 1c.) The outgoing beam was expanded to an angle of ± 15 degrees so that it formed a spot 3.7 miles (6 kilometers) in diameter on the tops of the clouds 35,000 feet below. The laser transmitter, shown in Figure 1a, has four key components. The large white object is a cooler. The water lines are connected to the laser head located just below the cooler. The green laser beam exits through the small window on the right side of the unit, and the power supply and control electronics are at the right of the laser head and cooler.

The laser pulses contained an average of 0.12 joules of energy and had a duration of approximately 15 nanoseconds at a wavelength of 0.532 micrometer. The laser was operated at a rate of 10 pulses per second. The firing time of these pulses was controlled from an oven-stabilized crystal oscillator time reference, the accuracy of which enabled synchronization of the transmitting and receiving equipment once an initial pulse was detected.

The laser was mounted in the aircraft's cabin as shown in Figure 2a. The beam coming out of the laser was expanded and deflected down into the final expansion optics in the escape hatch just below the laser. The beam exited from the aircraft through a window in that escape hatch. (See Figure 2b.) The path of the beam was enclosed in tubing both for safety and for reduction of glare, which would interfere with the pilot's vision during night operation. The laser was designed to operate over air-pressure changes encountered as the aircraft flew to and from 40,000 feet during each test flight. A photograph of the laser being test fired before takeoff is shown in Figure 1c. The transmitter characteristics are summarized in Table 1.

Table 1. Transmitter Characteristics

Type	Frequency-Doubled Nd:YAG Laser
Wavelength	0.532 Micrometer
Energy	0.12 Joules Per Pulse
Pulsewidth	15 Nanoseconds
Pulse Rate	10 Per Second
Average Power	1.2 Watts
Beam Divergence	$\sim 30^\circ$ Full Angle
Eye-Safe Range	164 Feet

The receiving equipment was designed to detect the transmitted laser pulse with an adequate signal-to-noise ratio. The Navy downlink propagation model (Stotts, L.B. 1979) can be used to predict the attenuation experienced by the laser pulse as well as the pulsewidth after propagating through a cloud layer. For clouds 1,600 to 6,500 feet thick, the estimated half-power pulsewidth varies from 5 to 50 microseconds. Therefore, the receiver equipment was designed to have a time resolution of 200 nanoseconds and to cover a window of 100 microseconds.

The receiver signal level can also be predicted from the model. The receiver had an optical power signal-to-noise ratio ranging from 1360 to 7.4 for clouds 1,000 to 6,000 feet thick. This signal-to-noise ratio is for a single pulse and was improved during the data analysis phase by averaging the signal from several pulses.

The receiver, shown in Figure 1b, uses a large area (6.8 inches in diameter) photomultiplier detector. Because of the detector's large surface area and wide field of view, a Wratten filter with a half-power optical bandwidth of 300 angstroms was employed. The signal from the photomultiplier was amplified in broadband amplifiers, compressed by a logarithmic amplifier, and applied to a transient digitizer capable of digitizing one sample every 200 nanoseconds. This data-handling system had an instantaneous dynamic range of three orders of magnitude in voltage and a 3-percent resolution. The digital output of the transient digitizer, combined with digital identification information, was stored on a digital tape recorder that is compatible with IBM computers. The identification information that was added to the data included 15 characters and 4 coded characters, the former indicating run number, day, hours, minutes, and seconds, and the latter indicating system gain, system bandwidth, special test conditions, etc. The system also had playback capability so that data could be reviewed and studied in the field. Just as the transmitter was operated from a stable time reference, the ground receiver also employed an oven-stabilized crystal oscillator so that it began digitizing data just before the laser pulse arrived. These oscillators were accurate enough that their center frequency drift rates were less than 2×10^{-8} , and synchronization of the units was required only once each day.

The receiver equipment as set up in one trailer is shown in Figure 3a. The detector was placed outside where it had an unobstructed view of the sky over its ± 45 degree field of view. (See Figure 3b.) A 75-kilowatt diesel generator and three radio links to the other participants in the experimental program also supported the receiver ground base. The receiver characteristics are summarized in Table 2.

Table 2. Receiver Characteristics

Aperture Diameter	6.7 Inches
Field of View	$\pm 45^\circ$
Optical Bandwidth	300 Å (30 nm)
Electronic Bandwidth	2.5 MHz
Sample Period	0.200 Microsecond
Dynamic Range (Voltage)	1000:1
Data Format	IBM Compatible

In order to attempt to compare the experimental results with analytical models, the clouds through which the laser pulses propagated were characterized. This aspect of the test program used the equipment and expertise of the Navy Ocean Systems Center, San Diego, and was conducted by Dr. Douglas Jensen. The equipment was installed in a twin-engine light aircraft as shown in Figure 1d. The cloud probe aircraft sampled the size and number density of the particles in the clouds and recorded temperature, dew point, and altitude. The cloud's particle density was measured by two Knollenberg probes in ranges of 0.5 to 29.5 micrometers and 14.7 to 320 micrometers. During the data reduction phase, test personnel used data reduction equipment to process the raw cloud data into cloud extinction coefficients, geometric thicknesses, and integrated optical thicknesses.

The cloud optical thickness was also inferred from measurements of moonlight irradiance at the surface by using the Navy propagation model (Stotts, L.B., 1979). The measurements were taken separately by NOSC and HSS.

2.3 Equipment Test and Calibration

The calibration of the receiver and transmitter equipment, which can be traced to the National Bureau of Standards, was done before the equipment was taken to the test site. After calibration, the equipment was subjected to various combinations of temperature, vibration, and altitude stress, with no measurable degradation.

2.4 Kauai Test Program Outline

During the test program 2 checkout flights and 17 test flights were conducted, resulting in 360 pulse profile runs averaging 60 seconds each and producing over 200,000 pulse shape profile records. The measurement flights were conducted between August 20 and September 21, 1979. HSS operated their equipment from August 31 through September 12 in parallel with the pulse shape recording equipment for possible correlation of their moonlight data with the laser pulsewidth.

These measurements were obtained in spite of the fact that the tests were conducted during an unusually dry period. The random fluctuations in the weather were unpredictable, but the fact that the tests were conducted at a spot 4.5 miles from the wettest place on Earth resulted in useful data. The test schedule is shown in Figure 4a.

As seen in Figure 4b, the daily schedule used at the beginning of the tests began with GTE personnel analyzing the weather to make a go versus no-go decision. (For this description, assume that sunset is at 7:30 p.m.) At 8:00 p.m. all personnel were prepared for the tests and the FSI (Flight Systems, Incorporated) laser transmitter aircraft took off from Barking Sands. By 8:30 p.m. all personnel were at their test stations and testing began. After 2 hours of testing, at 10:30 p.m., the test was over and the aircraft returned to their base of operations.

The daily schedule was changed on the days when HSS was operating. Since HSS used moonlight, the operation was scheduled to coordinate with the time when the Moon was at a high elevation angle. This meant operating at 3:00 a.m. in some cases.

2.5 Test Operations

The high altitude aircraft and the air controller at Barking Sands worked as a team to position the laser-transmitter aircraft directly over the ground receiver with an accuracy of approximately 650 feet. (See Figure 5.) The turn portion of the dogbone flight pattern (determined by the minimum turning radius at 40,000 feet) required approximately 150 seconds. The resulting dogbone required 18 minutes to complete. This meant that the aircraft would pass over the test site approximately every 9 minutes. As the program continued, a figure-eight pattern was adopted because it required less turning to reverse course and head back over the site. With this pattern, the aircraft passed over the site every 6 minutes, which significantly increased the data rate. Plots as well as computer printouts of aircraft position for every second were available for each pass of the test program.

The cloud probe aircraft operated on a more independent basis. Using strobe lights set up by GTE personnel, the pilot oriented himself to the receiver site location and began entering the clouds directly above the receiver site. He climbed at a slow rate, enabling characterization of the clouds, until he arrived above the cloud layer. He then proceeded to the east side of the island over the water, where he could safely descend. Returning over Lihue Airport he would begin another run toward the receiver location. Since each cycle of the cloud probe aircraft typically required 20 minutes compared with the 6 minutes per pass of the laser platform, there was no need to synchronize the flight paths of the two aircraft.

3. DATA REDUCTION AND ANALYSIS

The experiment consisted of 19 flights: 17 for measurements and 2 for test flights. Thirteen of the flights resulted in good data and three produced only marginal data. During these 19 flights, 360 data runs were made, producing over 200,000 separate pulse shape records.

The following paragraphs discuss the data reduction procedure, the systematic error correction techniques, the measured cloud data, and the analysis of the relationship between the pulse and cloud data.

3.1 Data Reduction Procedure

The data come from three main sources. Data such as flight time, run number, weather description, and test equipment parameters were recorded at the test site on both audio and cassette tape and in two separate logbooks. Aircraft position and miss-distance calculations were obtained from the Pacific Missile Range Facility tracking radars. These outputs were in the form of two independent printouts, with data for every second of the 40 hours of the aircraft flight time. The weather data from the probe aircraft came in the form of audio cassette recordings and logbook summaries. All of the data were thoroughly studied and scrutinized for errors and inconsistencies, and the inconsistencies were resolved.

The first task in the data analysis effort was to use time to generate tables of cross-references between the run numbering systems used by PMRF, GTE, and the NOSC cloud probe aircraft. The computer printouts from PMRF, listing aircraft position as a function of time, were used as the primary time reference for the experiment. With this foundation of aircraft position versus time, all of the data tapes were reviewed and cataloged. To aid in this survey, strip-chart

recordings of pulse peak value versus time were made for all of the data tapes. The portion of each data run during which the equipment was saturated can be determined from these charts. (Such saturation implies that there were very few clouds between the high altitude aircraft and the ground.)

These recordings allowed prioritizing of the many data runs. Those runs during which no beam saturation occurred were given a high priority in the succeeding data reduction procedures. Only the 80 high priority runs have so far been examined in detail, and they are the basis of the data analysis presented in the following paragraphs.

With the data correlated, cross-referenced, checked for errors, and cataloged, more detailed data analysis could proceed. The first step in the data analysis was to reduce the pulse shape data from 19 reels of tape to 2 reels. A special-purpose tape-reading program was developed to read the tapes, throw out incorrect records, and average every 10 pulses to form a single average pulse. The averaging was done by reading the data from the tape, choosing an appropriate voltage value from a table (which described the transfer function of the logarithmic amplifier), and then averaging these voltages into a single average pulse shape. The average pulse shape was then processed back through the same logarithmic table and stored on new digital recording tapes.

The next stage in the data analysis procedure was to operate on the 80 high priority runs and deduce several pulse shape parameters. This analysis was done separately for each 1 second of data, and the results were averaged over each 5-second interval centered around the time at which the aircraft was directly overhead. The data that resulted from the central 5 seconds were chosen to be the basis of further data analysis. It was these data which were compared with the cloud characteristics.

3.2 Data System Characteristics

The pulse shape recorded by the data system would be accurate only if the impulse response of the data system had a time constant much shorter than the time constant of the data. Figure 6a shows some photographs of the system response to the laser energy when propagated through relatively clear air. When there was no cloud attenuation, these laser pulses in most cases saturated the detector and the data system.

The impulse response shown in Figure 6a, therefore, shows that, in the worst case, the distortion caused by the detector and the recording system is negligible. The detector and amplifying system are a series of gain elements with individual bandwidths of more than 10 MHz. Together they form a system with a 3 dB bandwidth of approximately 2.5 MHz. This implies a 10- to 90-percent rise time on the order of 140 nanoseconds. This bandwidth and the corresponding time constant are commensurate with the data sampling interval of 200 nanoseconds. Since the time constant shown in Figure 6a is less than 150 nanoseconds, the time estimates of pulse shapes of 1 to 2 microseconds can be attributed to propagation characteristics rather than to recording system characteristics.

The data records were averaged to form composite pulse shapes. It is important to determine whether such averaging would hide pulse shape characteristics, thereby producing distorted pulse shapes and data analysis. In Figures 6b and Figure 6c, consecutive individual data pulses and consecutive 1-second averages are shown. It can be seen that there is very little variation from pulse to pulse and from second to second.

The logarithmic amplifier used in the system had a three-decade calibrated dynamic range. By exactly calibrating its transfer function and using this function in the data analysis, this source of systematic error was eliminated.

3.3 Cloud Characteristics

The test program began to operate on the first day of a 1-month period that was characterized by the weather bureau at Lihue as being an unusually dry period. The one advantage to operating 4.5 miles from the wettest spot on Earth, Mt. Waialeale, is that even during such a relatively dry period, clouds and rain will occur. The clouds experienced during the test program were cumulus and striated both vertically and horizontally. Typical comments from Dr. Douglas Jensen (NOSC) were "pockets of thick clouds separated by thin haze from a level of 2,000 feet to typically 6,000 or 7,000 feet." The tops in general were very nonuniform, and clouds varied typically from 6,000 to 10,000 feet.

Sunset was at approximately 7:30 p.m. during much of the test program, and after many days of observation the cyclic nature of the cloud pattern became apparent. One hour after sunset the clouds covered much of the valley, and a light rain shower would be observed. This rain shower would occur typically between 8:00 and 8:30 p.m. By 10:00 p.m. a second cloud condition would occur. Between these two cloudy conditions the cloud pattern would become more scattered and in some cases almost clear. After 12:30 or 1:00 a.m. a third period of cloudiness would occur. This pattern was not always observed, and in some cases a single cloudy period would occur at approximately 11:30 p.m.

Many of the data obtained by the cloud probe aircraft have been analyzed by Dr. Jensen. The optical thicknesses predicted by the analysis of these data are much less than the optical thicknesses inferred from a moonlight attenuation technique. In previous experiments, where the Knollenberg data were used in conjunction with an attenuation measurement in which the cloud pattern was a more uniform stratus layer, the measured and predicted data agreed within a factor of two. Therefore, the unusually low predicted value is attributed to the broken nature of the cloud pattern experienced during the program. One conclusion is that more modeling should be done to understand optical transmission through broken clouds.

As indicated above, optical thickness was also predicted by making measurements of the attenuation of moonlight through the cloud pattern. This information was recorded separately by HSS and also by NOSC. Their data roughly agree and correlate with a value estimated by observers at the test site.

3.4 Analysis and Results

The first step in this phase of data analysis and interpretation was to compare the value of pulsewidth predicted from theory and the value of the measured pulsewidth. The next step was to take into consideration the unusual, but consistent, shape of the pulse that has been described as being made up of two components, one with a short and one with a

long time constant. Using the long time constant as a pulse shape parameter, we again compared the shape with the theoretical prediction. This comparison showed a reasonable agreement. A detailed discussion of this process of analysis is presented in the following paragraphs.

The theory that is used here to describe the relationship between pulse shape and cloud geometric and optical thicknesses is contained in the Navy propagation model (Stotts, L.B., 1979). The optical thickness data from HSS, together with the geometric thickness estimated by the observers in the cloud probe aircraft, were applied to the theoretical relationship and resulted in predicted values of half-power pulsewidths. These values and the corresponding measured values are compared in Figure 7a. The vertical axis is the measured value for each pulse shape. The horizontal axis is the theoretical value. The solid line on the graph represents the position of data points if the measured and theoretical values were in perfect agreement. All of the runs during which HSS had estimated the optical thickness are plotted as points on this graph.

The general conclusion from this graph is that the measured pulsewidth values are much less than expected. The ratio (theoretical to measured) of values ranges from 3 to over 16. The average is approximately 8. This is the primary conclusion from the experimental program. For the measured clouds, the pulsewidth was much less than expected.

In order to understand the results better, an additional analytical step was taken. As shown in Figure 7b for the raw data and in Figure 7c for the reduced data, the pulse shape could be considered as the summation of two pulses with different characteristic exponential time constants. Since the pulse parameters (time to peak and half width) characterize time dependence near the peak of the pulse, they are influenced mainly by the short time constant component of the pulse. The lack of correlation of these values with predicted values, therefore, indicates a lack of correlation between the short time constant component and our present theory.

This disagreement leads to the idea of comparing the long time constant characteristic with the theoretical prediction. The Navy propagation model description of the pulse shape gives a relationship between the slope of a pulse (the time it takes for the pulse to fall to $1/e$ of its peak value) and the half-power pulsewidth. The pulsewidth is approximately 2.45 times the value of the slope. Using this relationship, we drew a graph of the theoretical pulsewidth, predicted from cloud characteristics, compared with the pulsewidth inferred from the long time constant value obtained from the semilog plots. This graph, Figure 7d, shows much better agreement between theory and measurement.

The exact implications of this agreement are not clear. One can certainly say that if the short time constant component were not in the pulse shape, this experiment would provide good agreement between theory and measurement. However, the measured pulse shapes were dominated by a short rise and fall time characteristic, and the pulsewidths were much less than expected.

4. CONCLUSIONS

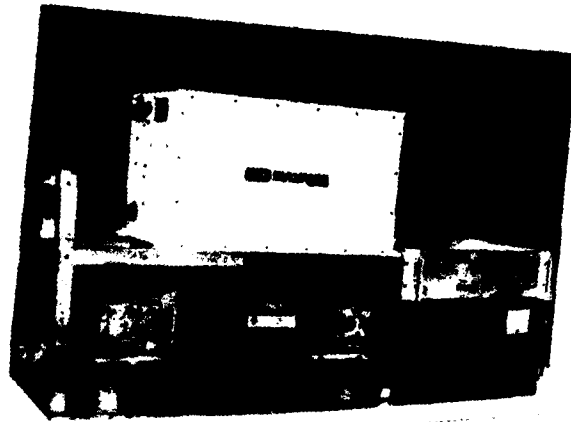
The principal conclusion that resulted from the data analysis is that for the clouds that were tested in Kauai, the stretching of a laser pulse (as measured by its time-to-peak and half-power width) is less than was expected from propagation theory. The mechanism responsible for these shorter pulsewidths is not completely understood at this time. It does appear that the nonuniform cloud layers experienced at Kauai do not stretch the laser pulses to the extent that a single uniform layer of clouds with the same thickness would stretch the pulses. The nonuniform clouds experienced during the tests at Kauai were very difficult to characterize independently and accurately. However, the laser pulsewidth measurements were direct and accurate measurements of the pulse stretching that resulted from multiple scattering in the clouds.

The measured pulsewidth (full width, half maximum (FWHM)) ranged from 1 to 7 microseconds for clouds ranging from 4,000 to 8,600 feet thick and having an optical thickness estimated to range from 19 to 86. The measured pulsewidth values are from 0.05 to 0.2 of the theoretically predicted pulsewidths. The data pulses typically appear to be composed of a fast and a slow propagation mode. The narrow pulsewidths are caused by the short time constant component, the existence of which was unknown before this experimental program.

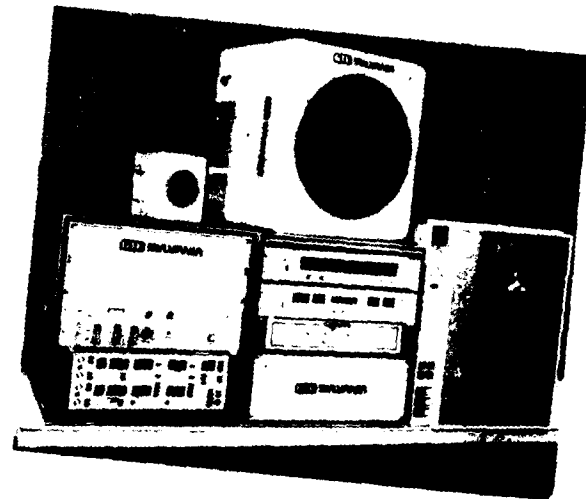
The analysis of the observed laser pulse shapes in relation to the cloud thickness leads to three major conclusions. First, for a cloud of a certain geometric thickness, the laser pulsewidth was less than predicted by the theory. Second, the analytical cloud models should be improved to include real-world cloud geometries (e.g., nonuniform clouds). Third, more field experimentation should be done to determine if the lesser amount of pulse stretching is observed with other types of cloud patterns found at other locations in the world.

References

- Bucher, E.A. and Lerner, R.M., 1973, "Experiments on Light Pulse Communication and Propagation Through Atmospheric Clouds," *Applied Optics*, Vol. 12 (10), pp. 2401-2414.
- Bucher, E.A., Lerner, R.M., and Niessen, C.W., 1970, "Some Experiments on the Propagation of Light Pulses Through Clouds," *Proc. IEEE*, Vol. 58 (10), pp. 1564-1567.
- Stotts, L.B. and other members of the Technical Advisory Group to the Blue-Green Optical Communication Program Joint Coordinating Committee, 1979, "Naval Blue-Green Single-Pulse Downlink Propagation Model," NOSC TR 387.



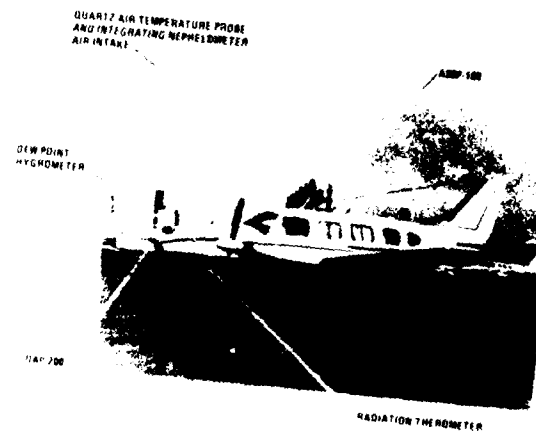
(a) Laser Transmitter



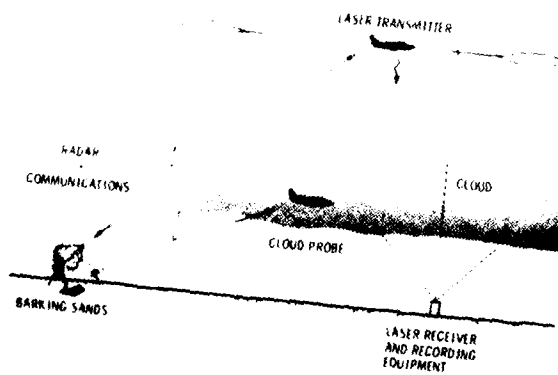
(b) Receiver



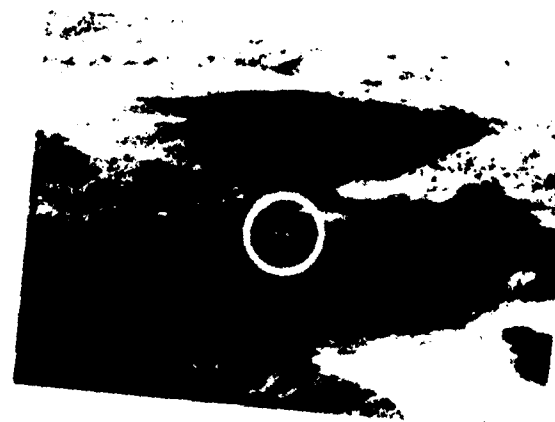
(c) Laser Aircraft



(d) Cloud Probe Aircraft



(e) Experiment Layout



(f) Test Site

Figure 1. Experiment Program Elements

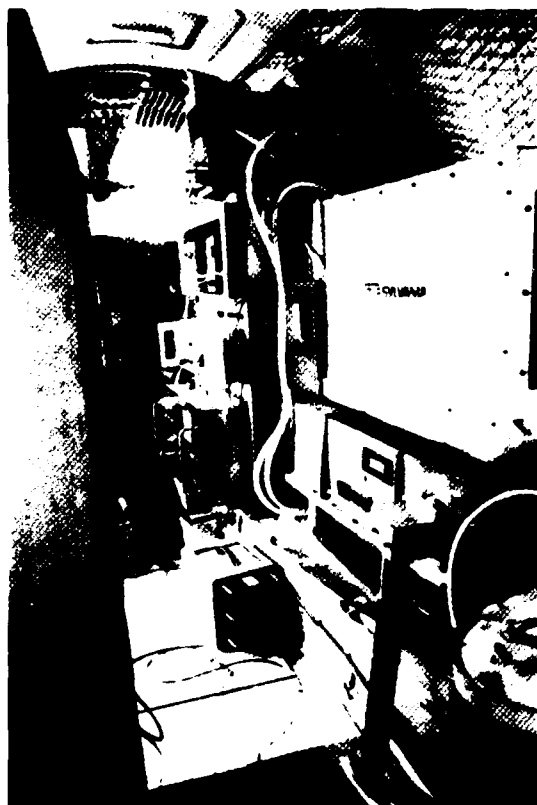


Figure 2a. Laser Mounted in Aircraft



Figure 2b. Aircraft Window For Laser Output



Figure 3a. Trailer-Mounted Receiver Equipment



Figure 3b. Test Site Layout

AUGUST 1979						
SUN	MON	TUES	WED	THURS	FRI	SAT
			1	2	3	4
5	6	7	8	9 FLIGHT TEST	10	11
12 GTE/HSS ARRIVE	13	14 PMRF INTERFACE	15	16	17	18
19 AIRCRAFT ARRIVE	20 BEGIN EXPERIMENT	21	22	23	24	25
26	27	28	29	30	31	

SEPTEMBER 1979						
SUN	MON	TUES	WED	THURS	FRI	SAT
						1
2	3	4	5 (BEST TWO NIGHTS FOR HSS)	6	7	8
9	10	11	12	13	14	15
16	17	18	19	20	21 LAST NIGHT	22
23 RETURN TO CONUS	24	25	26	27	28	29

Figure 4a. Monthly Schedule

- 1:00 PM ANALYZE WEATHER
- 2:00 PM DECIDE GO/NO GO; INFORM PARTICIPANTS
- 3:00 PM HOLD COORDINATION MEETING
- 6:00 PM DRIVE TO TEST SITE(S)
- 7:30 PM FINAL CHECKOUT EQUIPMENT/COMM SYSTEMS
- 8:00 PM BEGIN AIRCRAFT FLIGHT
- 8:30 PM BEGIN EXPERIMENT
- 10:30 PM END EXPERIMENT
- 11:30 PM AIRCRAFT LANDING/DEBRIEFING

Figure 4b. Typical Daily Schedule

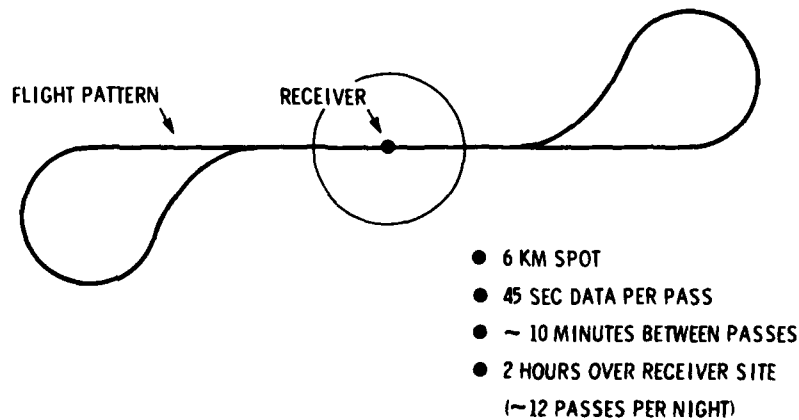


Figure 5. Typical Flight Path for Laser Aircraft

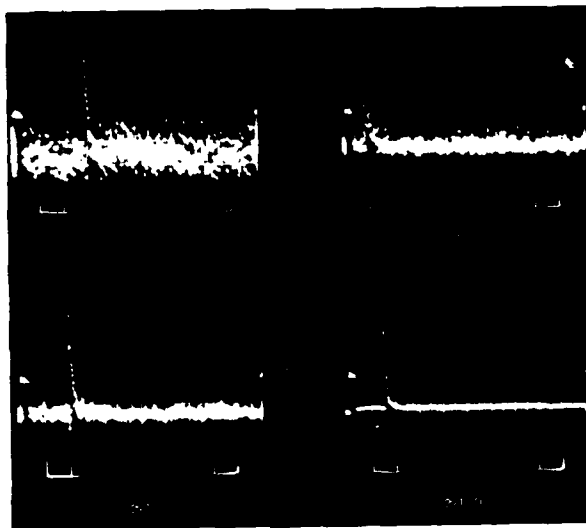


Figure 6a. Impulse Response

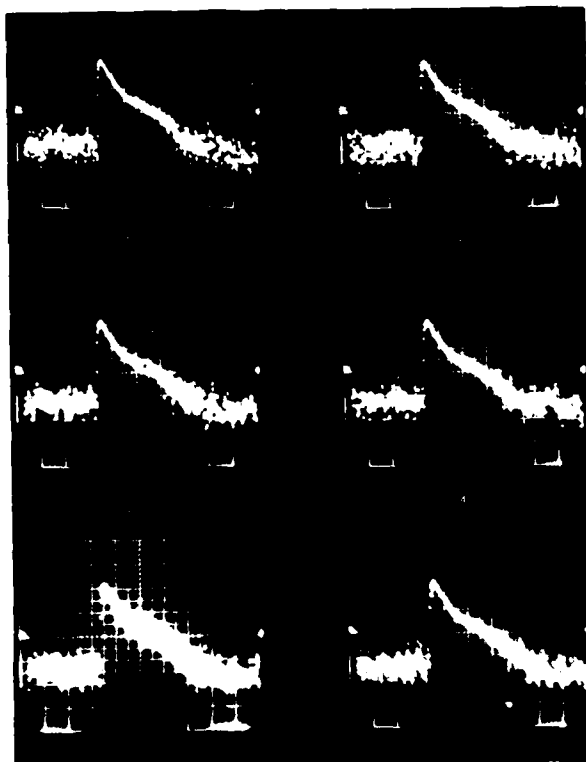


Figure 6b. Consecutive Data Samples, 0.1 Second Apart—Run 181

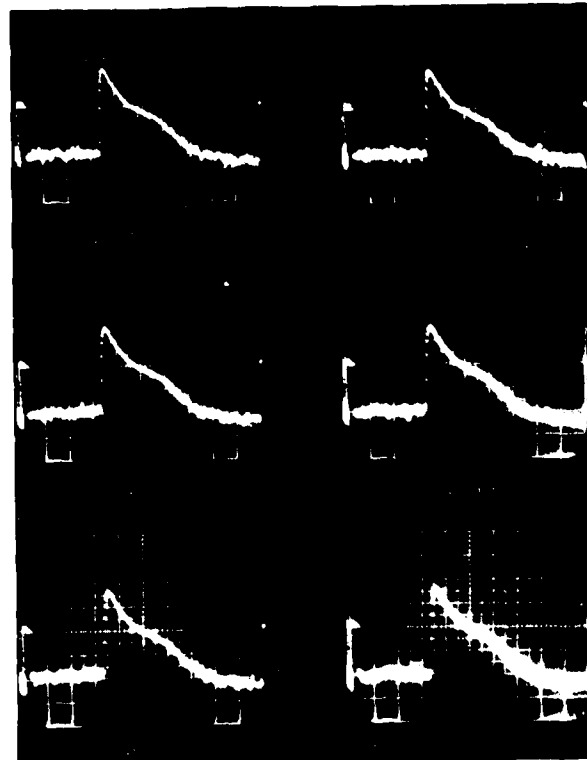


Figure 6c. Consecutive 1-Second Averages—Run 181

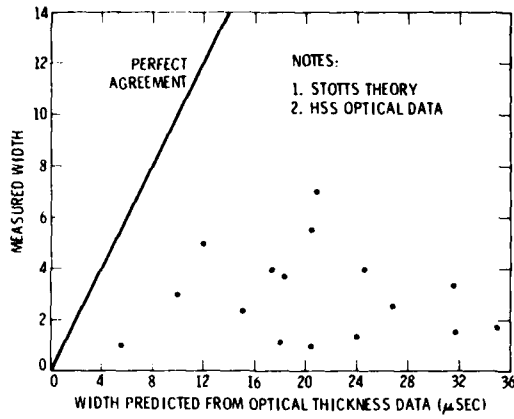


Figure 7a. Data Analysis: Pulsewidth-Predicted versus Measured

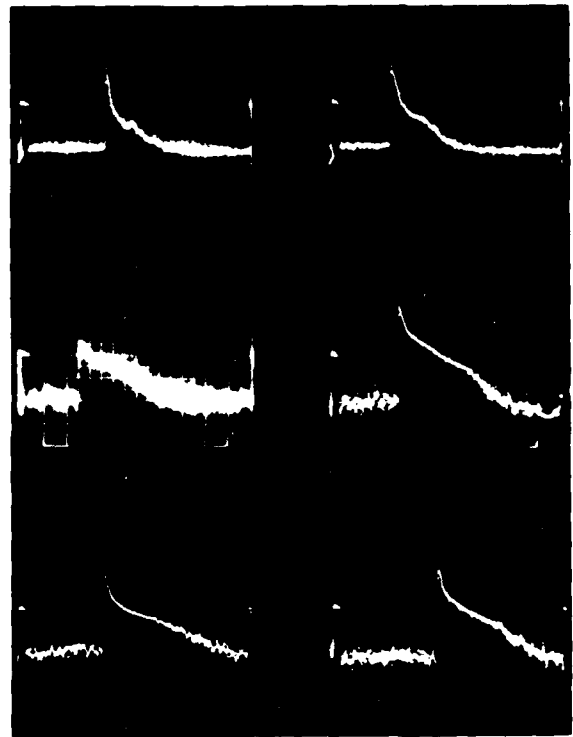


Figure 7b. Typical Raw Data From Six Runs

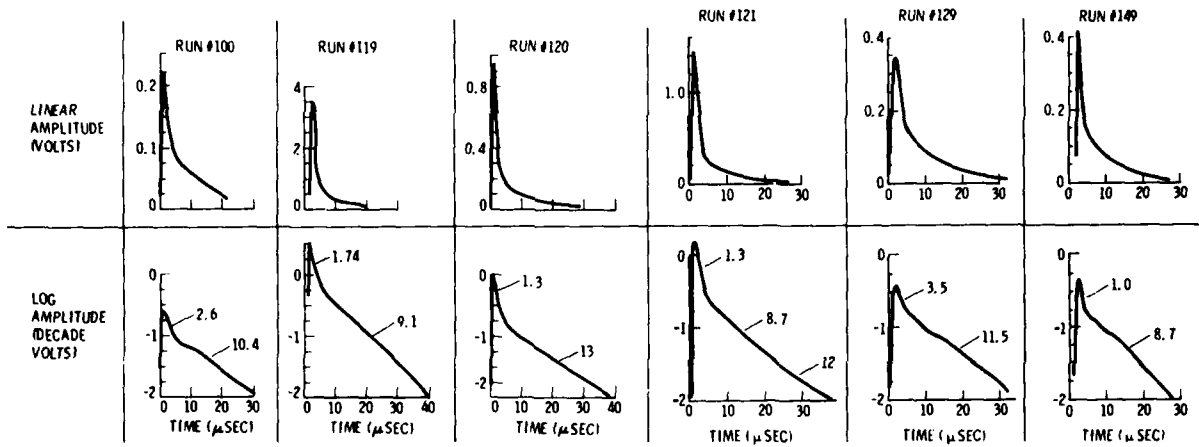


Figure 7c. Typical Reduced Data Plots

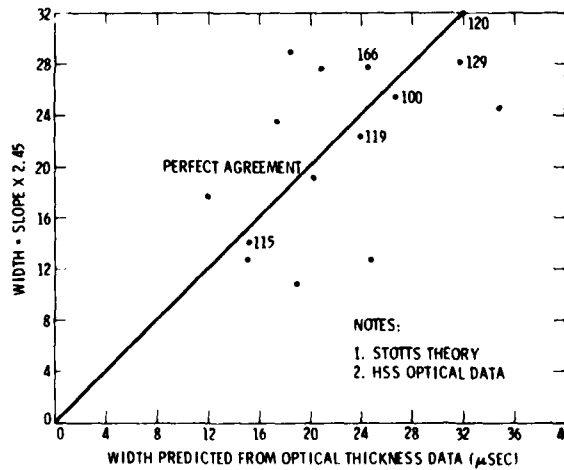


Figure 7d. Data Analysis: Pulsewidth-Predicted versus Inferred From Slope

LABORATORY MEASUREMENTS OF LIGHT PROPAGATION IN TURBID MEDIA

Allan I. Carswell
Dept. of Physics and CRESS
York University, 4700 Keele St., Downsview, Ont. Canada

SUMMARY

The propagation and scattering of laser beams in turbid media have been investigated experimentally. Water droplet clouds and liquid water suspensions of scatterers have been studied. A major area of interest has been the use of polarization information to measure multiple scattering. In the forward direction the effects of multiple scattering on the extinction coefficient and on the beam shape have been measured. It has been found that the incident beam characteristics (width, polarization, coherence) are strongly preserved in the forward direction even at extinction coefficients as high as 5 m^{-1} . In the backward direction measurements of cloud reflectance have been made. The polarization of the reflected signal is found to be spatially anisotropic and to depend strongly on the size parameter of the scatterers. Applications of the findings for diagnostics of turbid situations in the atmosphere are discussed.

1. INTRODUCTION

The propagation of laser beams in the atmosphere and in the ocean is of great current interest. Such beams can be used for a variety of remote sensing and communications applications. An area of particular importance is the interaction of the laser beams with conditions of higher turbidity because in these situations many of the desirable properties of the laser beam are significantly degraded. In such turbid media the optical propagation is complicated by the presence of strong multiple scattering. As a result, the quantitative description of the radiation transport of laser beams in turbid media is not well developed.

It is possible however, by using the characteristics of the laser beams themselves to experimentally investigate the effects of such high turbidity on the beam propagation. The laser source provides an incident beam whose properties (such as irradiance, wavelength, polarization state, degree of coherence etc.) can be carefully controlled. In addition, the beam can be accurately defined in both space and time. As a result it is possible to launch into a turbid medium a well-defined probe signal and to watch the evolution of its characteristics arising from interactions with the turbid medium. We have been investigating the value of such measurements recently as part of our program on lidar diagnostics of the atmosphere. (Pal, S.R. and Carswell, A.I., 1976). We have studied lidar returns from atmospheric clouds and fogs. As well, we have conducted a number of complementary laboratory measurements on laser propagation and scattering in dense water droplet clouds and liquid water suspensions of known scatterers. In this work an area of particular interest has been the utilization of polarization information and spatial filtering for quantitative measurements of multiple scattering. In this paper I summarize briefly some of our recent findings.

The polarization state of a laser probe beam can be carefully controlled and accurately measured. As the beam interacts with the turbid medium, the polarization state of the transmitted and scattered radiation will be altered and the changes can be used as a diagnostic of the properties of the turbid medium. The scattering of a linearly-polarized incident beam from spherical particles is particularly interesting. In this case, in the backward direction, the scattering from perfect spheres preserves the linear polarization. Thus any cross-polarized component observed in the backscatter direction is a direct measurement of the multiple scattering taking place. (Pal, S.R. and Carswell, A.I., 1973).

With spatial filtering we make use of the fact that the incident laser beam geometry can be employed to accurately define the single scattering volume. By using a combination of receiver fields of view and spatial filters, such as aperture stops, it is possible to investigate various regions in and around the single-scattering volume. For example, it is possible to arrange an optical system such that the receiver cannot see the incident laser beam via single scattering. In such a situation, the only radiation reaching the receiver will come via multiple scattering. Thus it is possible to measure quantitatively the properties of "pure" multiply-scattered radiation. (Ryan, J.S. Pal, S.R. and Carswell, A.I., 1979)

The laboratory apparatus used for the water droplet cloud measurements is shown in Fig. 1. (Ryan, J.S. and Carswell, 1978). An argon laser (wavelength 514 nm), a 1 m³ cloud chamber and two photometer systems are used. The photometers are arranged to collect scattered light in the forward and backward directions. The photometers are equipped for absolute intensity and polarization measurements and have variable entrance aperture and focal-plane field stops. An ultrasonic nebulizer is used for generating the water-droplet clouds. The experimentally measured cloud size distribution is described by a modified gamma function having a modal radius at 2.5 μm and exhibiting droplet radii in the range 1-10 μm . Very stable and reproducible drop size distributions can be generated and this is an important factor in making the scattering measurements. With the system, attenuation coefficients of up to 5 m^{-1} can be readily obtained. For this value of attenuation the droplet number density is of the order of $5 \times 10^4 \text{ cm}^{-3}$.

MEASUREMENTS

a) Forward Scattering

Using the system of Fig. 1 we have conducted a number of measurements of the optical transfer in both the forward and backward directions. For all of these measurements a parameter of importance in the characterization of the cloud is the attenuation coefficient, α . This coefficient is measured by monitoring the transmitted signal as a function of the droplet number density over a known path length in the cloud. At high cloud densities it is necessary to ascertain the effect of multiple scattering on the measured attenuation coefficient. Since the phase function of the water droplet clouds is highly peaked in the forward direction, the beam scanning photometer measuring the transmitted signal will record not only the unscattered radiation but also the light which is scattered at small angles in the direction of the incident beam. This, along with an additional contribution arising from multiple scattering would cause a reduction in the effective attenuation coefficient of the cloud as the particle density increases. This reduction would depend on the receiver aperture and the field of view.

In Fig. 2 we show sample data obtained on the dependence of the measured attenuation on the field of view of the forward receiver. In this measurement the receiver aperture was slightly larger than the diameter of the unattenuated laser beam. From Fig. 2 it is seen for the lower cloud densities, the α value obtained through the application of the simple Beers law relation is independent of the field of view. For the highest value of attenuation (5 m^{-1}) it is seen that the α value tends to decrease with increasing receiver field of view. This behaviour shows the effects of the increasing contribution of multiple scattering leading to a reduction in the measured value of the attenuation coefficient. This is an aspect which can be studied quantitatively in some detail by using a range of the appropriate parameters in the experiments. For most of our measurements however, we reduced the receiver aperture and field of view to insure that the multiple scattering effects were minimal.

Using the scanning capability of the forward-scatter receiver it is possible to measure the beam profile of the transmitted radiation as a function of the cloud properties. In Fig. 3 we show a sample data set for the receiver with a 1mm aperture and a 4° field of view. Five profiles are shown for cloud attenuation coefficients, ranging from zero (no cloud) to 5.3 m^{-1} . In this figure the irradiance of the five profiles is normalized to unity on the beam axis so that the behaviour of the off-axis radiation can be more clearly observed. The curves show that at all attenuation levels a narrow Gaussian core is retained in the beam down to at least the 10% signal level even in the densest fogs. This is attributable to the fact that near the beam axis the received signal is dominated by direct and singly-scattered light which has a very narrow angular distribution and thus preserves the incident Gaussian beam shape near the axis. Careful analysis of the beam wings at higher α values is possible and the transition from singly-scattered to multiply-scattered radiation can explain the behaviour observed. (Ryan, J.S. and Carswell, A.I., 1978). Comparison with theoretical modelling of the appropriate geometries is possible.

Using curves such as those of Fig. 3 it is possible to plot the beam width as a function of the attenuation coefficient. In defining the beam width it is necessary to stipulate the level of irradiance chosen. In Fig. 4 we show the beam width corresponding to Fig. 3 for the irradiance levels of $1/e^2$, 1%, 0.1% and 0.01%. The plots of Fig. 4 show clearly that the core of the beam undergoes relatively little broadening even at the highest values of attenuation. The quantitative variations of such curves, of course, depend strongly on the optical parameters employed. When narrow fields are utilized the effects of multiple scattering are greatly reduced as would be expected. From such measurements it is possible to obtain information not only on the multiple scattering process but also on the angular scattering dependence (phase function) of the scattering droplets.

We have also investigated the polarization properties of the transmitted beam and have found that the incident polarization is strongly preserved in the forward direction even at rather large values of α . Figure 5 shows sample results of the measured beam polarization (Ryan, J.S. and Carswell, A.I., 1978). In this case the polarization of the beam is described in terms of the two polarization components P_{\parallel} and P_{\perp} where P_{\parallel} is the power measured with the scanner polarizer aligned parallel to the polarization direction of the incident beam and P_{\perp} is the power measured with the polarizer perpendicular to this direction. From these two components, one can obtain the linear depolarization ratio $\delta = P_{\perp}/P_{\parallel}$. In Fig. 5 are shown plots of the measured δ values as a function of distance off-axis distance from the beam. It is found that the linear polarization of the beam is very strongly preserved even in the densest clouds. The on-axis value is essentially that of the incident beam. Although the off-axis value of δ increases it is by only a very small amount (a few parts in 10^3). Such measurements in the water-droplet fogs have consistently shown that the incident linear polarization is preserved in the multiply-scattered field even at rather significant off-axis scattering angles. This preservation of transmitted beam polarization is very important in the analysis of backscatter polarization measurements. Since the beam stays linearly polarized, any backscatter polarization changes are a result of backscattering only and not a mixture of forward and backward effects.

In some recent work we have also been investigating the change of spatial coherence in the transmitted beam. It has been found that in the forward direction the transmitted field displays a very strong speckle pattern characteristic of coherent scattering processes. In Fig. 6 we show a sample of the speckle pattern obtained in the forward direction. This photograph shows a small region of the forward scattered field approximately 5° off the beam axis. The speckle pattern is observed to vary in time as the cloud droplets move through the laser beam. The detailed spatial and temporal structure of the speckle pattern depends on the particular geometry of the system. Our measurements indicate that a considerable amount of useful information may be derivable from such measurements.

(b) Backscattering

In our measurements, the primary interest has been in the backscattered signal because of our application of these measurements to the interpretation of lidar data. (Pal, S.R. and Carswell, A.I., 1976). We have investigated in some detail the dependence of the total backscattered signal on the cloud density and the optical properties of the transmitting and receiving system. We have been especially interested in the information content of the polarization signal and the use of this to investigate multiple-scattering properties.

A complete specification of the polarization of any light beam can be provided by its Stokes parameters. These parameters of the backscattered light are determined in our experiments through four power measurements with a linear polarizer and quarter wave retarder in the receiver system. The Stokes parameters are obtained through the following linear combinations of measured signals. (Ryan, J.S., Pal, S.R. and Carswell, A.I., 1979).

$$\begin{aligned} I &= P_{||} + P_{\perp} , \\ Q &= P_{||} - P_{\perp} \\ U &= 2P_{45,45} - I \\ V &= I - 2P_{45,0} \end{aligned}$$

Where $P_{||}$ and P_{\perp} are the quantities introduced previously. $P_{45,45}$ is the power measured with reference axes of both polarizing elements at 45° with respect to the incident polarization direction, $P_{45,0}$ the power measured with the polarizer axis at 45° and the quarter wave retarder axis parallel to this direction. The ellipticity, ϵ and rotation angle χ of the polarization ellipse are calculated from the Stokes parameters as

$$\begin{aligned} \epsilon &= 1 - [I \pm (I^2 - V^2)^{1/2} / |V|] \\ \chi &= 1/2 \tan^{-1}(U/Q) \end{aligned}$$

The linear depolarization ratio introduced previously can also be written as:

$$\delta = (I-Q)/(I+Q)$$

As already mentioned the perpendicular component of the backscattered signal can be used as a quantitative measurement of the multiple scattering taking place when linearly polarized light is incident on spherical scatterers. It is clear that the perpendicular component arising from multiple scattering could originate in several ways. The multiple scattering could (a) rotate the polarization direction of the incident wave (i.e. χ would change,) (b) change the state of the polarized wave (i.e. convert linear to elliptical polarization and ϵ would change) or (c) depolarize the incident wave converting some of the linearly polarized light to unpolarized light. By careful measurements of the Stokes parameters it is possible to distinguish among these several mechanisms. In Fig. 7 we show sample results for the dependence of the rotation angle and the ellipticity of the backscattered signal from the water droplet cloud at different densities. Such results have shown that the values of the rotation and ellipticity do not differ consistently from their initial values (with no cloud). It may be concluded therefore, that the polarized component of the backscatter is linearly polarized in the direction of the polarization of the incident beam. Thus the increase in the perpendicular component would appear to arise solely from the presence of unpolarized light. This would indicate that the backscattering from such clouds at all α values has a Stokes vector of the form $[I, Q, 0, 0]$. This would then lead to the conclusion that the backscattered radiation is a superposition of linearly polarized light and unpolarized light. (We will see below that this conclusion is not necessarily valid.)

If this is the case however, the backscattered signal depends only on the two components $P_{||}$ and P_{\perp} and it is possible to utilize the polarization information to separate the contributions of singly and multiply scattered radiation. This can be achieved as follows. If we denote the total backscatter power as P_T we see that

$$\begin{aligned} P_T &= P_{||} + P_{\perp} \text{ and} \\ P_{||} &= p_{||}^s + p_{||}^m + p_u^m = p_{||}^{s,m} + p_u^m \\ P_{\perp} &= p_u^m \end{aligned}$$

where $P_{||}^s$ and $P_{||}^m$ are the single- and multiple-scatter components which preserve the incident polarization and P_u^m is the multiple-scatter component which is unpolarized. (This unpolarized signal also contributes an equal amount to the $P_{||}$ signal).

Using appropriate polarization measurements it is possible to separate the various components in the above equations and to determine their individual contributions to the backscattered signal. We can measure P_u^m directly since it is just $P_{||}$. We can also measure the linear depolarization ratio of the pure multiple scattering, δ_m by using spatial filters to prevent any of the singly-scattered radiation from reaching the receiver. We note that

$$\delta_m = \frac{P_u^m}{P_{||}^m + P_u^m}$$

By rearranging we have $P_{||}^m = P_u^m(1 - \delta_m)/\delta_m$. Thus we can write for the backscatter power from single scattering

$$P_{||}^s = P_T - (P_{||}^m + 2P_u^m) = P_{||} - P_u^m/\delta_m.$$

All of the quantities on the right side of this equation are measured to determine $P_{||}^s$. This quantity can then be compared with single-scatter calculations for the system. (Ryan, J.S. Pal, S.R. and Carswell, A.I., 1979).

In Fig 8. we show the results of such an analysis and it is apparent that quite good agreement is obtained. It is also obvious from such measurements that in dense clouds, the backscatter contribution from multiple scattering can be quite large even for rather small receiver fields of view.

In the foregoing analysis the measurements were based on the total backscattered return integrated over the entire field of view of the receiver. Implicit in the analysis was the assumption that the polarization state of the wave was uniform over this field. In recent work we have discovered that the polarization of the multiply-scattered radiation field is far from uniform. In fact, the multiply-backscattered radiation has been found to be anisotropic with preferred polarization directions which depend on the position of the scattering volume within the field of view of the receiver. Examples of this distribution are shown in Figs. 9 and 10. These show photographs of the signal backscattered from the water droplet cloud for an incident beam linearly polarized in the vertical direction in the figures. Figure 9 is the result obtained with the camera polarizer perpendicular to the incident polarization direction, and Fig 10 is for the camera polarizer parallel.

It is apparent in both of these photographs that the entire multiply-backscattered field is highly polarized. In both instances, we see an intensity distribution in the general shape of a cross. When the polarization axes of the transmitter and receiver are parallel this cross is oriented with its maxima vertical and horizontal as in Fig 10. When the viewing polarizer is perpendicular we see that the vertical and horizontal directions have now effectively zero intensity and the arms of the cross have rotated 45° to the intermediate position. Because of the symmetry of these polarization fields, when the resultant polarization over the whole field of view is averaged in Stokes parameter measurements, the presence of this anisotropy is not detected. We can see this for example if we consider a receiver field of view which has one half receiving parallel polarized radiation and one half receiving perpendicular polarized radiation of equal intensity. In this case the receiver would measure a resultant Stokes vector $[1,0,0,0] = [1,0,0,0] + [1,-0,0,0]$ which would indicate unpolarized radiation over the entire field of view. A similar conclusion would be reached if the two halves were illuminated by linearly polarized radiation at 45° to the parallel axis (since again $[1,0,U,0] + [1,0,-U,0] = [1,0,0,0]$) or by opposite handed circularly polarized light ($[1,0,0,V] + [1,0,0,-V] = [1,0,0,0]$). This shows the great limitation of applying a Stokes vector measurement to any region of spatially non-uniform polarization.

We have undertaken an investigation of the observed anisotropy in greater detail by making backscattering measurements of water suspensions of monodisperse polystyrene spheres. Sample photographs of the backscattering from these liquid suspensions are shown in Fig. 11 (Carswell, A.I. and Pal, S.R., 1980). For these measurements a small cylindrical cell 7 cm in diameter and 7 cm in length was employed. In this case the source was a linearly polarized helium neon laser. A range of sphere diameters, d , from about 0.08 μm to 6.8 μm was employed. With the 0.633 μm wavelength, λ , this represented a variation in the scattering size parameter, $\pi d/\lambda$ from 0.4 to 34. The measurements have shown that with particles of larger sizes (6.8 μm) the intensity distributions are very similar to those obtained in the cloud chamber. That is, when viewed with the unaided eye the multiply-backscattered field appears quite homogeneous, but when viewed through a linear polarizer, the cross-shaped pattern is clearly evident. As the size parameter decreases however, a significant change in the multiply-scattered field is observed. This behaviour is easily seen in Fig. 11.

These observations can be explained qualitatively in terms of the single scattering characteristics of the spherical particles. For very small size parameters we have primarily a Rayleigh scattering process. With linearly polarized incident radiation

it is well known that in this case there is no radiation scattered in the direction of the electric vector (vertical in Fig. 11). Our observations of the multiple scattering for the smallest particles reflect this single-scattering characteristic. For these small particles the multiply-scattered field shows the lack of scattering in the direction of the electric vector. It is however quite surprising how well the multiple scattering preserves the intensity and polarization dependence of the single scattering even though the radiation field has undergone a large number of scattering events.

For the larger particles the more general Mie theory applies and in this case also the observations qualitatively reflect the characteristics of the single-scattering properties. We are at present undertaking comparisons of our measurements with Mie scattering calculations. Although the general correspondence of the multiply-scattered field to the singly-scattered polarization distribution can be made, it is clear that one would not expect a complete correspondence in view of the fact that a large number of scattering events are involved.

From the observations it is evident that the spatial distribution of the backscattered polarization field is strongly dependent on the size parameter of the scattering. This means that with application of appropriate spatial filters to sample different regions of the backscattered field it should be possible to obtain some quantitative information about the size regime of the scattering particles from the backscattering at a single wavelength.

We have recently undertaken such measurements with our atmospheric lidar system and in Fig. 12 we show the type of spatial filters used for these measurements. This figure shows the sector geometry of the series of spatial filters employed. These filters were photographically reduced to the appropriate dimensions and sequentially introduced into the focal plane of the lidar receivers. Multiple channels equipped with similar filters were simultaneously employed to allow appropriate signal normalizations. In all of the spatial filters the central portion is blocked to eliminate the singly-scattered return. Thus by sequentially using the filters it is possible to observe the spatial distribution of the multiply scattered radiation in the focal plane of the lidar in a fashion similar to that shown in the photographs of Fig. 11. The end results of such a measurement are shown in Fig. 13 for the lidar return from the base of a low level cloud. In this figure the backscattered signal levels from the various angular regions are displayed in a polar plot. The solid and dotted arrows indicate that for all of the spatial filter orientations the receiver and transmitter polarization directions were vertical in the figures. Comparison of the lidar data of Fig. 13 with the lower right hand photographs of Fig. 11 indicates that for the particular cloud layer sampled, the particle sizes were in the Rayleigh regime since the pattern has the very definite anisotropy associated with the patterns of Fig. 11 for very small size parameter. Further work in this direction is in process and we feel that substantial useful new information can be obtained.

The backscattering data described above is all obtained from the total return signal integrated over the full length of the laser beam in the turbid media. In addition to such data it is also desirable to observe the spatial dependence of the backscattered signal properties as the beam progresses through the scattering chamber. Such data could then be directly related to lidar return signals which have range-resolved scattering information. One approach to such measurements would be the use of short laser pulses and time-resolved backscatter measurements similar to those obtained with the lidar system. For laboratory systems having dimensions of only a few meters however, useful range resolutions would require extremely short pulses, probably in the sub-nanosecond region, and would involve the use of very high-speed electronic systems since the entire interaction would be over in a few tens of nanoseconds.

An alternate method would be to employ selective chopping of the light signal within the cloud along with phase-sensitive detection of the scattered radiation. This method requires only a pair of rotating chopper blades at different depths in the cloud to interrupt the beam, and a lock-in amplifier to extract the desired scattered signal. Recently we have investigated this second method and found that it works extremely well providing excellent range-resolved backscattered data from the laboratory system.

The apparatus consisted of a chopper assembly with semi-circular blades mounted on a shaft so that they could be positioned at various depths in the cloud. The apparatus was designed to ensure that the blades filled the entire field of view of the backscatter photometer. Each blade was coated with a non-reflective layer to minimize signals. The blades were off-set so that as the shaft rotated the backscattering from two different thicknesses of fog were alternately viewed. This signal when fed into a lock-in system provided an output signal that depended directly on the magnitude of the scattering from the layer between the two chopper blades.

A sample of the range-resolved data obtained with this system is shown in Fig. 14. In this figure the backscattered return signal magnitude is shown for a series of values of the attenuation coefficient, α , for five layers at different depths in the cloud. These measurements were made in the cloud chamber with the chopper blades having a fixed separation of 15 cm. They were located at sequentially increasing depths in the fog so that the returns from the five different layers (0 to 15 cm, 15 to 30, 30 to 45, 45 to 60, 55 to 70.) The slight overlap in the bottom two layers was caused by the distance limitation in the apparatus. The data are plotted in the form of histograms showing the backscatter signal level as a function of beam penetration. The

parallel and perpendicular components of the return signal are shown in the histograms by the clear and shaded portions respectively.

The data of Fig. 14 show the excellent potential of this approach for range-resolved backscattering measurements. The increase of signal with increasing α is clearly evident. The measurements also show how the scattering process changes from being an essentially volumetric return at low α values to a more surface-like return at high α values where the first layer of the cloud contributes the majority of the backscattered signal and the returns from deeper layers are very heavily attenuated. Based on the signal-to-noise values of these measurements it is felt that range resolutions of the order of a few centimeters can be readily obtained in the laboratory using this technique.

By taking the ratio of the perpendicular to the parallel polarized return it is also possible to derive the variation of the linear depolarization ratio, δ , as a function of depth in the cloud. This has been done and results are shown in Fig. 15 where the data are again illustrated in histogram form. This time the δ values are shown as a function of penetration depth for several different values of the attenuation coefficient, α . Although there is a somewhat larger scatter in the data the results do show clearly the range dependence of δ . For $\alpha = 1\text{m}^{-1}$ the cloud is relatively transparent and the value of delta is rather uniform throughout the depth of the cloud at a value of the order of 0.12. At $\alpha = 2\text{m}^{-1}$ the dependence of δ on penetration into the cloud is beginning to appear quite clearly. This reflects the fact that the density of the cloud is high enough that a photon scattered forward from near the surface of the cloud has a reasonable probability of being scattered back towards the backscattered photometer from greater depths in the cloud. With further increases in α , this effect becomes increasingly prominent. The increase of δ with penetration depth becomes quite large at the highest values of α . For $\alpha = 4\text{m}^{-1}$, δ from the deepest layer reaches 0.55. This behaviour is similar to that observed in lidar measurements on atmospheric clouds.

Based on our measurements thus far we are confident that this technique can add substantially to our understanding of the multiple scattering processes taking place in such turbid situations.

CONCLUSION

In this paper we have reviewed briefly a number of our measurements on laser interactions with turbid media. The results indicate the potential of the measuring techniques for adding to our understanding of beam propagation in the presence of strong multiple scattering. They also indicate that there are many new aspects of this problem which remain to be investigated.

REFERENCES

- Carswell, A.I. and Pal, S.R., 1980. "Polarization Anisotropy in Lidar Multiple Scattering from Clouds" *Appl. Opt.* 19, 4123-4126.
- Pal, S.R. and Carswell, A.I., 1973. "Polarization Properties of Lidar Backscattering from Clouds", *Appl. Opt.* 12, 1530-1535.
- Pal, S.R. and Carswell, A.I., 1976. "Multiple Scattering in Atmospheric Clouds: Lidar Observations". *Appl. Opt.* 15, 1990-1995.
- Pal, S.R., Ryan, J.S. and Carswell, A.I., 1978. "Cloud Reflectance with Laser Beam Illumination" *Appl. Opt.* 17, 2257-2259.
- Ryan, J.S. and Carswell, A.I., 1978. "Laser Beam Broadening and Depolarization in Dense Fogs". *J. Opt. Soc. Amer.*, 68, 900-908.
- Ryan, J.S., Pal, S.R. and Carswell, A.I., 1979. "Laser Backscattering from Dense Water-Droplet Clouds" *J. Opt. Soc. Amer.* 69, 60-67.

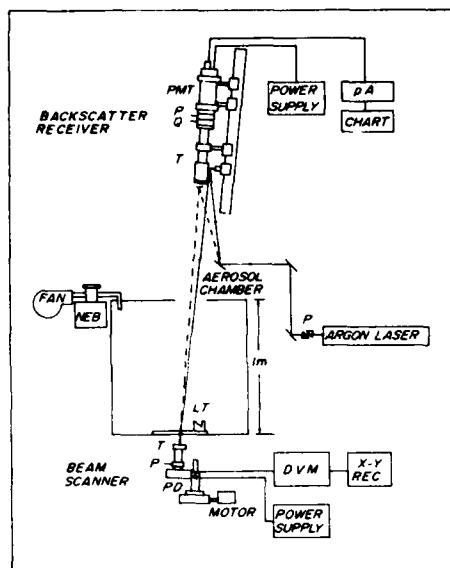


Fig. 1. Laboratory system used for cloud measurements.

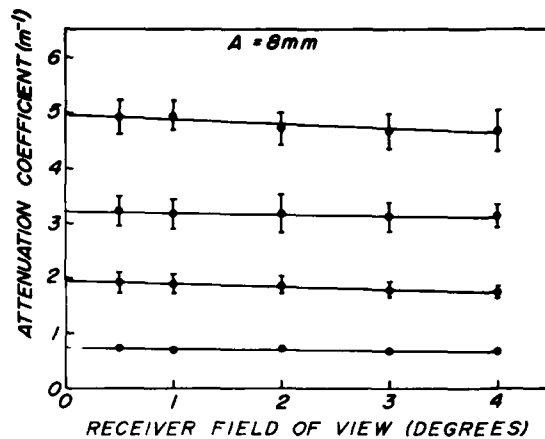


Fig. 2. Dependence of the measured attenuation coefficient on the receiver field of view for various cloud densities.

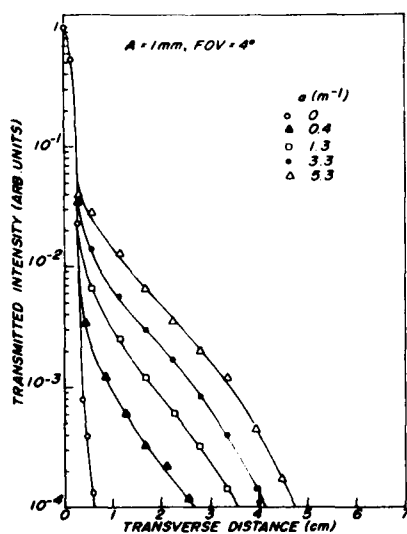


Fig. 3. Typical transmitted beam profiles. Path length in cloud was 1 m, the receiver aperture was 1 mm and the field of view was 4° .

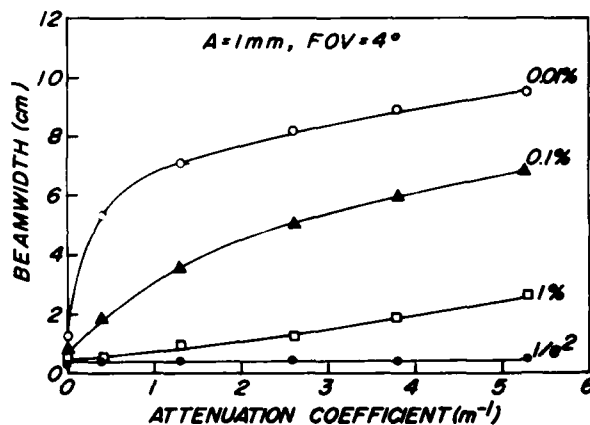


Fig. 4. Transmitted beam width at various intensity levels for the data of Fig. 3

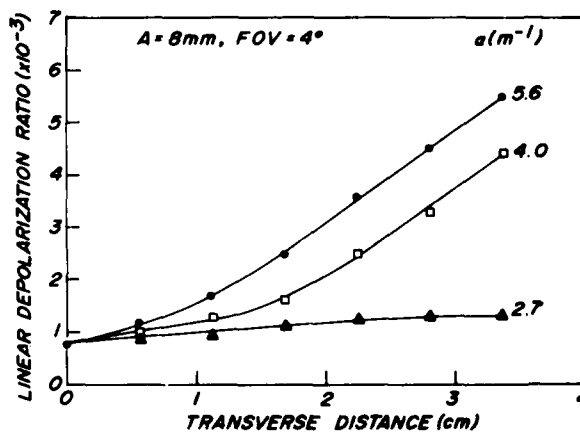


Fig. 5. Typical dependence of the linear depolarization ratio on off-axis distance for the transmitted beam.

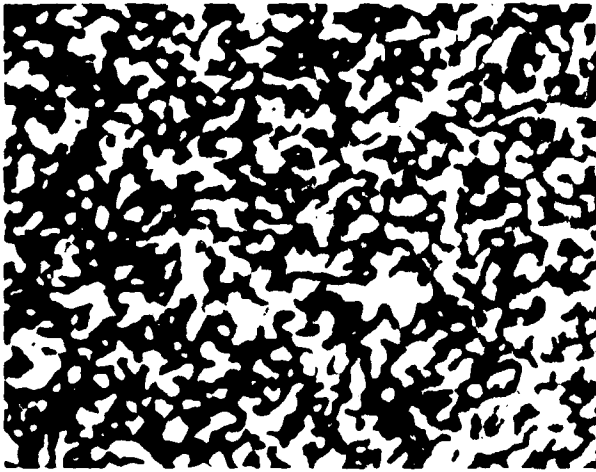


Fig. 6. Speckle pattern about 5° off axis from the forward direction after beam traverses the cloud.

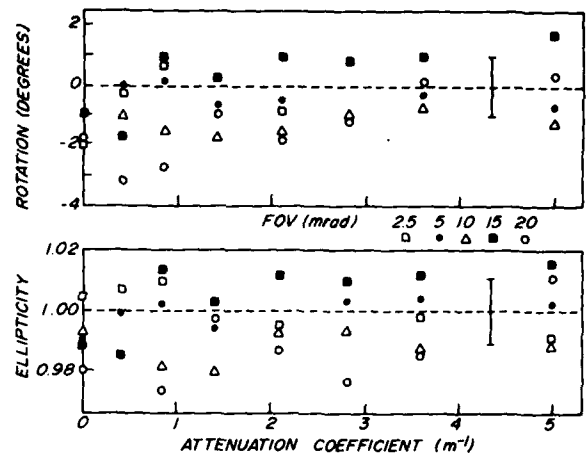


Fig. 7. Measured dependence of rotation angle, χ , and ellipticity, ϵ of the backscattered signal.

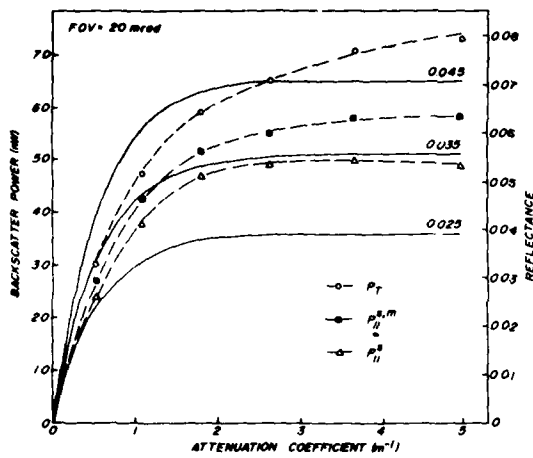


Fig. 8. Backscattered signal for the various polarization components as a function of cloud attenuation. Continuous curves are calculated for single scattering with values of the backscattering function indicated.

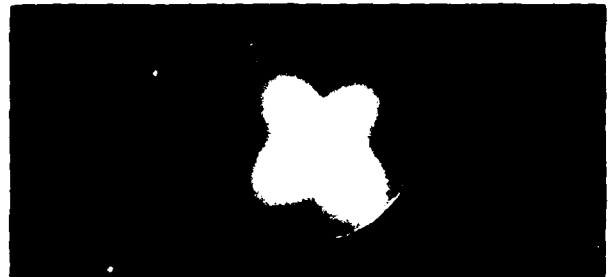


Fig. 9. Backscattering from cloud illuminated with linearly polarized light (incident polarization direction vertical). Camera polarizer perpendicular (i.e. horizontal).



Fig. 10. As in Fig. 9 but with camera polarizer parallel (i.e. vertical).

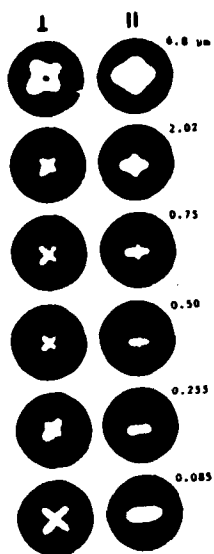


Fig. 11. Backscattering from water suspensions of monodisperse polystyrene spheres (diameters as shown). Left column was photographed through a perpendicular polarizer, right through a parallel polarizer. Black dot in upper left shows incident laser spot size for all cases.



Fig. 12. Sector geometry of lidar spatial filters for studying anisotropy of multiple scattering.

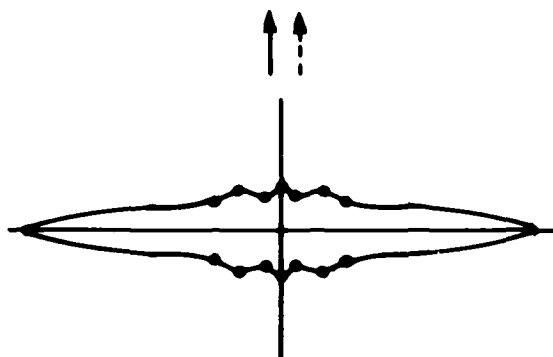


Fig. 13. Sample lidar data showing spatial variation of multiple scattering in the return from the base of a cloud layer.

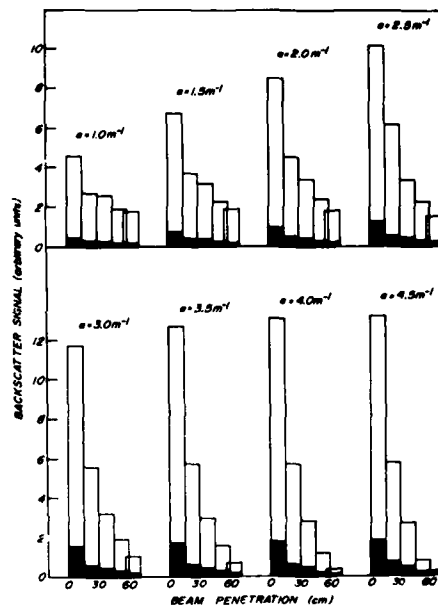


Fig. 14. Sample range resolved measurements of the backscatter signal. Parallel component is unshaded, perpendicular is shaded.

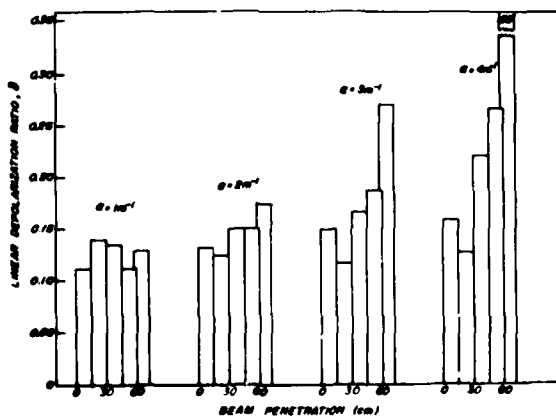


Fig. 15. Sample range resolved measurements of δ .

REMOTE SENSING OF THE DIFFUSE ATTENUATION COEFFICIENT OF OCEAN WATER

R. W. Austin
Visibility Laboratory
Scripps Institution of Oceanography
La Jolla, California, U.S.A.

ABSTRACT

A technique has been devised which uses remotely sensed spectral radiances from the sea to assess the optical diffuse attenuation coefficient, $K(\lambda)$, of near-surface ocean water. With spectral image data from a sensor such as the Coastal Zone Color Scanner (CZCS) carried on NIMBUS-7, it is possible to rapidly compute the $K(\lambda)$ fields for large ocean areas and obtain K "images" which show synoptic, spatial distribution of this attenuation coefficient. As a result of the frequent repeated coverage of which the satellite is capable, the potential exists for developing an extensive data base of both the regional distribution and seasonal variations of this optical property of sea water over the world's oceans. Such a data base would be impossible to compile by conventional sampling techniques.

A knowledge of the distribution of K is of obvious importance to optical communication and surveillance systems design and operational planning. Presently available data is very limited and suffers from grossly inadequate sampling both in space and time.

The technique described utilizes a relationship that has been determined between the value of K and the ratio of the upwelling radiances leaving the sea surface at two wavelengths. The relationship was developed to provide an algorithm for inferring K from the radiance images obtained by the CZCS, thus the wavelengths were selected from those used by this sensor, viz., 443, 520, 550 and 670 nm. The majority of the radiance arriving at the spacecraft is the result of scattering in the atmosphere and is unrelated to the radiance signal generated by the water. A necessary step in the processing of the data received by the sensor is, therefore, the effective removal of these atmospheric path radiance signals before the K algorithm is applied. Examples of the efficacy of these removal techniques are given together with examples of the spatial distributions of K in several ocean areas.

1. INTRODUCTION

The existing body of knowledge regarding the distribution of ocean properties has in large measure been restricted by the classical ocean data sampling techniques. Data are usually obtained at ocean stations whose separation have been determined by a preconceived notion of the nature of the horizontal variability of the phenomena under study or, more usually, by the economics of ship operating costs or the amount of available survey time and the ocean area to be examined. The result is the equivalent of viewing the ocean through a two-dimensional, low pass spatial filter. All knowledge of the high spatial frequency variations of the phenomena are lost. Remote sensing of surface properties from aircraft or spacecraft provides the investigator with a means of economically sampling at high spatial frequency, thereby obtaining a synoptic view of the properties at high resolution. Furthermore, by revisiting the region, the temporal as well as the spatial variations may be assessed.

Our knowledge of the worldwide distribution of the optical properties of sea water is indeed limited. Only a few major cruises have taken place where optical properties have been measured. The sampling, both in space and in time, have, therefore, been very restricted. Fortunately, except for the immediate coastal regions and for some limited regions affected by a few major rivers, most of the world's ocean water seems to behave in a predictable manner with regard to the near surface optical properties. The departure from pure water properties seems to be due almost entirely to the presence of various species of phytoplankton and their products of degradation. While the species distribution and concentration changes from location to location, the pigments involved are ubiquitous. The optical properties, then, are primarily the result of the absorption of the chlorophyll and related accessory pigments and of the scattering properties of these algal organisms or of their detrital products.

2. GENERAL OCEAN COLOR RELATIONSHIPS

The color of the ocean as perceived from above by an observer or remote sensor is determined by the upwelling spectral radiance, L_u , leaving the water surface. This radiance is the product of the downwelling irradiance, E_d , and the radiance reflectance, ρ_L . Thus,

$$L_u(\lambda) = \rho_L(\lambda) E_d(\lambda) \quad (1)$$

The irradiance reflectance, ρ_E , is

$$\rho_E = E_u/E_d \quad (2)$$

Morel and Prieur (1977) have shown that ρ_E can be closely approximated by the relationship

$$\rho_E = 0.33 b_b/a \quad (3)$$

where b_b is the backscatter coefficient and a is the absorption coefficient for the water and its dissolved and suspended matter. A coupling between L_u and E_u is needed to utilize this relationship between the inherent optical properties a and b_b and the upwelling radiance. Austin (1980) has pointed out that the ratio $Q = E_u/L_u$, where L_u is now the radiance from the nadir, departs significantly from the value of π which has frequently been assumed for the ocean* and is, in fact, close to 5 for a number of cases that have been examined. Thus

$$L_u = \frac{0.33}{Q} \cdot \frac{b_b}{a} \cdot E_d \quad (4)$$

and the upwelling ocean radiance will depend on the spectral nature of a , b_b , E_d , and Q .

Figure 1 shows the spectral reflectance factors, $R_L = \pi \rho_L$, for a variety of stations in the Gulf of Mexico. With the exception of Stations 3 and 4, which were in shallow water (10m and 14m respectively) and show effects of bottom reflectance and/or resuspension of bottom sediments, the remaining spectral reflectances show systematic changes in the blue and green portions of the spectrum. In fact, this change in the shape of the curves as indicated by the blue-green ratio is related to the concentration of chlorophyll- a and associated pigments. Their shapes and the existence of a "hinge point" around 500 nm was predicted by Duntley, *et al.* (1974) from laboratory

*The value of π applies to uniform or lambertian reflectors.

measurements of a and b , and the modeling of the spectral reflectance from radiative transfer theory.

As might be expected, a similar behavior is found in the shape of the spectral radiances which are observed at the water surface. Figure 2a shows that the ratio of upwelling radiances at 443 and 520 nm is highly correlated with the radiance ratio of 443 and 550 nm. The data used to form this regression were obtained by a variety of investigators working in widely different water types. Figure 2b shows a similar regression between $L_u(443)/L_u(670)$ and $L_u(443)/L_u(550)$. A least squares power law curve was fitted to the data for each set of ratios. The resulting expressions are

$$\frac{L_u(443)}{L_u(520)} = 0.900 \left(\frac{L_u(443)}{L_u(550)} \right)^{0.742} \quad (5)$$

156 data points, $r^2 = 0.985$

and

$$\frac{L_u(443)}{L_u(670)} = 12.06 \left(\frac{L_u(443)}{L_u(550)} \right)^{1.661} \quad (6)$$

101 data points, $r^2 = 0.943$

The implication that may be derived from the excellence of these regressions is that if one such ratio is known, the others may be inferred and the shape of the spectral radiance curve specified. Further, if the absolute value of the radiance is known at one wavelength, together with a radiance ratio, the absolute spectral radiance at other wavelengths may be specified. Figure 3 depicts the manner in which the radiances at 443, 550 and 670 nm depend on the ratio of the radiances at 443 and 550 nm if $L_u(520)$ is assumed fixed. Similarly, Fig. 4 displays the same information plotted against wavelength showing the hinge-point-like behavior of spectral radiances that results were $L_u(520)$ fixed.

3. THE DIFFUSE ATTENUATION COEFFICIENT

The diffuse attenuation coefficient of ocean water is a property that may be inferred from the ocean color. It has been used by Jerlov (1951), Smith and Baker (1978) and others as a means of classifying ocean waters. It is a property that is of significance to a variety of problems associated with the penetration of natural daylight into the ocean and is also an important variable in evaluating the propagation of artificial light in sea water for various optical and communications and surveillance systems.

An attenuation coefficient may be defined for the upwelling and downwelling radiance and irradiance light fields. For example, K may be defined operationally as

$$K_E = - \frac{1}{E} \frac{dE}{dz} \quad (7a)$$

or

$$K_L = - \frac{1}{L} \frac{dL}{dz} \quad (7b)$$

The solution of Eqs. (7) is of the form

$$E(z_2) = E(z_1) e^{-K(z_2-z_1)} \quad (8)$$

hence

$$K = - \frac{1}{z_2-z_1} \ln \frac{E(z_2)}{E(z_1)} \quad (9)$$

K is most frequently determined from measurements of the vertical profile of the downwelling irradiance. However, in the development of the technique for the remote sensing of K , the values of K associated with the upwelling radiance or irradiance were used for two reasons, both related to the presence of the sun in the downwelling light field. First, the upwelling K 's are less affected by solar position and depth of measurement and may be, therefore, more nearly associated with the inherent optical properties. Second, because of the more gradual change in upwelling radiance with angle and because the upwelling light field is less subject to rapid fluctuations caused by the refraction of sunlight at the moving ocean surface, the measurement of the upwelling light field and, therefore, the resulting K 's tends to be more precise.

3.1 The K Algorithm

The use of remote sensing techniques for the determination of K implies the existence of a relationship between the sensible upwelling radiances available at the remote sensor and the derived K . The method developed by Austin and Petzold (1980) uses a relationship between K and $L_u(443)/L_u(550)$ which was derived from spectral data from a variety of investigators and locations. The relationship is

$$K(490) = 0.0883 \left(\frac{L_u(443)}{L_u(550)} \right)^{-1.490} + 0.022 \quad (10)$$

where $K(490)$ is the value of K at a wavelength of 490 nm. Figure 5 shows the data used in the empirical derivation of the relationship and compares the reported or measured values, K_m , with the $L_u(443)/L_u(550)$ ratio and with K_c , the values calculated using Eq. (10). The table in Fig. 5 lists the various sources and shows the means (\bar{x}) and the standard deviations (s) for the ratio of the calculated to the measured K 's, i.e., K_c/K_m , and for their differences, $K_c - K_m$.

4. THE REMOTE SENSING OF K

All of the above is based on in-water measurements. The remote sensing of K requires an instrument designed specifically for over water measurements. LANDSAT, or other imaging sensors designed for land or meteorological applications, do not have appropriate

sensitivities or spectral characteristics for the task. An instrument suitable for this purpose is the Coastal Zone Color Scanner (CZCS) carried on NIMBUS-7, launched in October 1978. The CZCS has six spectral bands, four of which were optimized specifically for sensing water properties. These four bands are at wavelengths of 443, 520, 550 and 670 nm and each have a bandwidth of 20 nm. The spatial resolution at the nadir is 800 meters and the cross-track scan is 1968 picture elements wide. The total swath width is 1660 km and successive scans form a raster of slightly overlapping lines as a result of the along-track motion of the spacecraft. The data are arbitrarily packaged into two-minute scenes containing 970 scan lines. Each scene contains 1.9×10^6 picture elements and covers a region 1660×770 km, or 1.275×10^6 km² in area.

The signal arriving at the remote sensor, L_r , is comprised of a large component due to the path radiance, L_p , resulting from the scattering of ambient light by the intervening atmosphere; a small component due to sky radiance reflected from the water surface and transmitted back up through the atmosphere; and the residual of the water radiance, L_w , after it has been attenuated by passage through the water surface and through the atmosphere (Austin, 1974). Figure 6 depicts these components schematically. Table I shows the magnitude of the components of the signal received from individual resolution elements in three CZCS scenes. In the table, L_r is the portion of the path radiance due to molecular (Rayleigh) scattering in the atmosphere, and L_A is the component of path radiance contributed by scattering from the larger particulates (aerosols) in the atmosphere. The radiance due to skylight reflected from the water surface has been included as a part of L_R and L_A in computations from which the table was derived.

It can be seen from Table I that that portion of the received signal containing information related to the water color is a small fraction of the total signal. It is necessary, therefore, to remove the effects of the intervening atmosphere in a most accurate manner if the algorithms for inferring water properties from emerging radiances are to be effective. The NASA Experiment Team for the CZCS is developing and validating atmospheric correction algorithms for this purpose (Gordon, 1978). One version of this algorithm developed at the Visibility Laboratory (Smith & Wilson, 1980) invokes the relationship between $L_u(443)/L_u(670)$ and $L_u(443)/L_u(550)$ given in Eq. (6) in an iterative technique which solves for the surface radiances and requires fewer measured or stipulated parameters. This technique "forces" the resulting upwelling water radiances to conform with the relationship of Eq. (6) and, therefore, assumes the relationship is truly universal. The radiances in Table I were computed using this technique.

Table I
Typical CZCS Signal Components

		Band 1 443 μ m	Band 2 520 μ m	Band 3 550 μ m	Band 4 670 μ m
Orbit 350 18 Nov 1978 NW Atlantic $L_u(443)/L_u(550)=1.28$ $K(490)=0.083\text{m}^{-1}$	L_R	3.272	1.663	1.264	0.478
	L_A	0.304	0.279	0.269	0.178
	L_w	0.759	0.732	0.594	0.042
	T_A	0.729	0.816	0.828	0.901
	$T_A L_w$	0.553	0.597	0.492	0.038
	L_r	4.129	2.539	2.025	0.694
Orbit 660 11 Dec 1978 Mid Pacific $L_u(443)/L_u(550)=3.51$ $K(490)=0.036\text{m}^{-1}$	L_R	4.144	2.107	1.601	0.606
	L_A	0.217	0.199	0.192	0.127
	L_w	0.854	0.305	0.243	0.0087
	T_A	0.753	0.835	0.846	0.914
	$T_A L_w$	0.643	0.255	0.206	0.008
	L_r	5.004	2.561	1.999	0.741
Orbit 3226 14 Jun 1979 $L_u(413)/L_u(550)=0.821$ $K(490)=0.140\text{m}^{-1}$	L_R	5.116	2.601	1.977	0.748
	L_A	0.657	0.603	0.582	0.386
	L_w	0.676	0.900	0.823	0.078
	T_A	0.690	0.783	0.800	0.876
	$T_A L_w$	0.466	0.705	0.658	0.068
	L_r	6.239	3.909	3.217	1.202

Radiances in $\mu\text{w}\cdot\text{cm}^{-2}\cdot\text{nm}^{-1}\cdot\text{sr}^{-1}$

$$L_r = L_R + L_A + T_A L_w \quad L_w = \frac{1}{n_w^2} L_u$$

5. RESULTS

A variety of surface validation cruises have been conducted in the Gulf of Mexico, and the Atlantic and Pacific oceans. These campaigns were thoroughly instrumented with equipment for the measurement of the optical, physical and biological conditions of the ocean and the pertinent optical properties of the atmosphere (Austin, 1980). Oceanographic stations were selected to provide data beneath the NIMBUS-7 in the footprint of the CZCS. Figure 7 compares the values of K measured on these cruises with the values obtained from the CZCS images for the station's locations using the iterative atmospheric and the in-water K algorithms. The measured values of K were determined for the surface waters to the first optical depth, i.e., $1/K$ meters. It can be shown that 87% of the emerging signal results from a weighted interaction between the downwelling light field and the water in the first $1/K$ meters. This thickness of water may be considered the effective remote sensing depth. The excellent agreement between the measured and calculated K 's as shown in Fig. 7 provides strong evidence that the in-water and atmospheric algorithms are satisfactory.

Many applications, however, require a knowledge of the attenuation coefficient to depths significantly in excess of the first optical depth and the value of remotely sensed K 's would be abridged if the attenuation properties below this surface layer were completely independent of the surface values. Figure 8 shows a regression of data obtained on twelve stations on a cruise from Japan to Seattle, Washington in July 1980. The average or effective K over the upper 100 meters have been plotted against the average K over the first attenuation length (*i.e.*, first optical depth). There appears from the results to be a reasonable presumption that the remotely sensed K 's can be used to infer the average value of the diffuse attenuation coefficient over depths significantly greater than the effective remote sensing depth.

Figures 9, 10 and 11 are images of the distribution of $K(490)$ for three ocean areas. The images represent subsets of the larger 2 minute CZCS scenes that were processed using the iterative algorithm for the removal of the atmospheric effects and Eq. (10) for the calculation of K . Each image consists of 512 lines of 512 picture elements (pixels) and covers approximately 175,000 km^2 of ocean. Pixels containing clouds or land areas are flagged and are set to zero (black). Bright areas near the edge of clouds result from an imperfect thresholding criteria for setting this flag.

Figure 9 was obtained from a scene on Orbit #350 on November 18, 1978. The location is south of Newfoundland in the western Atlantic. The indicated values of $K(490)$ at the right side of the image are about $0.05 m^{-1}$, increasing to about $0.09 m^{-1}$ in the left side of the image.

Figure 10 was processed from a portion of Orbit #660 on December 11, 1978. The location is northwest of Wake Island in the western Pacific. The water is quite clear in this region with much of the area showing values of $K(490)$ below $0.035 m^{-1}$. The water near the top center appears to have K 's approaching $0.05 m^{-1}$ and the region at the upper left corner of the scene has values above $0.055 m^{-1}$.

Figure 11 represents an area just east of Cape Cod showing the eastern portion of Georges Bank in the upper left and the meanders of the north wall of the Gulf Stream showing at the bottom. The scene was obtained on Orbit #3226 on June 14, 1979. The clearest water in the scene occurs at the bottom where the K in Gulf Stream is less than $0.05 m^{-1}$. The majority of the water falls between $K = 0.05$ and $0.10 m^{-1}$. On Georges Bank the K exceeds $0.126 m^{-1}$ with some areas reaching indicated values as high as $0.25 m^{-1}$.

6. SUMMARY

Validation experiments conducted in conjunction with Coastal Zone Color Scanner operations appear to verify remote sensing techniques developed to assess the diffuse attenuation coefficient of ocean water. Further, the surface values of this coefficient which may be determined by remote sensing, appear to be sufficiently well correlated with the average coefficient over the upper 100 meters to permit the use of remote sensing for estimating the diffuse light transmittance of ocean water to these depths. The sensor and the techniques are available, and a significant data base of CZCS scenes has already been acquired. The global distribution of these attenuation properties together with a knowledge of the scale of their spatial and temporal variability can now be determined.

7. ACKNOWLEDGEMENTS

This work has been supported by the Office of Naval Research under Contract N00014-78-C-0566, by the National Earth Satellite Service of the National Oceanic and Atmospheric Administration under DOC Grants 04-6-158-44033 and NA80AA-D-00007 and the National Aeronautics and Space Administration under Contract NAS-5-26249. This support is gratefully acknowledged.

8. REFERENCES

- Austin, R. W. (1978), "The Remote Sensing of Spectral Radiance from Below the Ocean Surface", Chapt. 14 in *Optical Aspects of Oceanography*, Jerlov, N. J. & E. Steeman Nielsen, Eds. Academic Press, London & New York, 1974.
- Austin, R. W. (1980), "Gulf of Mexico, Ocean-Color Surface-Trust Measurements", *Boundary Layer Meteorology*, Vol. 18 (1980) pp. 269-285.
- Austin, R. W. & T. J. Petzold (1980), "The determination of the Diffuse Attenuation Coefficient of Sea Water Using the Coastal Zone Color Scanner", Presented at COSPAR/SCOR/IUCRM Symposium "Oceanography from Space" May 1980, Venice, Italy (in press).
- Gordon, H. R. (1978), "Removal of Atmospheric Effects from Satellite Imagery of the Oceans", *Applied Optics*, Vol. 17, No. 10, pp. 1631-1636.
- Jerlov, N. G. (1951), "Optical Studies of Ocean Water", Swedish Deep-Sea Expedition, 3:1-59.
- Morel, A. and Prieur, L. (1977), "Analysis of Variations in Ocean Color", *Lim. and Oceanog.* Vol. 22(4) pp. 709-722 (Jul. 1977)
- Smith, R. C. & K. S. Baker (1978a), "Optical Classification of Ocean Waters", *Lim. and Oceanog.* Vol. 23, No. 2, pp. 260-267 (Mar. 1978), also as SIO Ref. 77-4 (Mar. 1977).
- Smith, R. C. & W. H. Wilson (1980), "Ship and Satellite Bio-Optical Research in the California Bight", Presented at COSPAR/SCOR/IUCRM Symposium "Oceanography from Space" May 1980, Venice, Italy (in press).

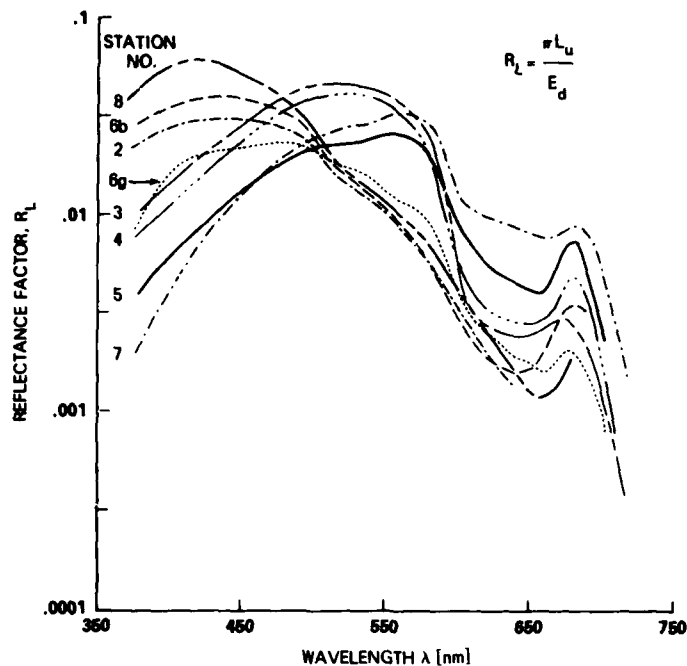


Fig. 1. Spectral reflectance factors for selected stations on the 1977 cruise of the R/V Researcher in the Gulf of Mexico. Curves for Stations 6b and 6g were obtained in blue and green water. Respectively, that occurred with changing tidal cycle. Stations 3 and 4 were in shallow water and show increased reflectance, possibly caused by the proximity of the reflective bottom or by backscatter from resuspended bottom sediments. Surface chlorophyll-related pigment concentrations varied from 0.02 mg/m³ for Station 8 to 9.3 mg/m³ for Station 7.

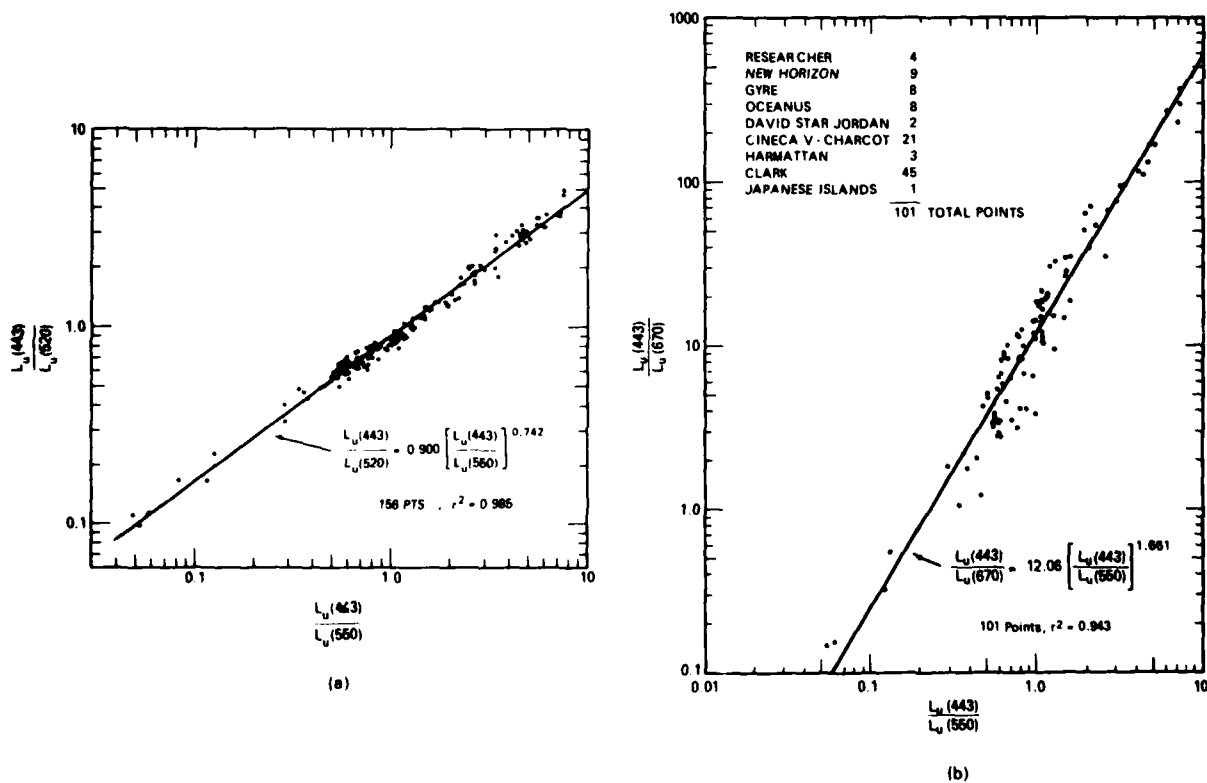


Fig. 2. Regression of the ratios of upwelling in-water radiances, $L_u(443)/L_u(520)$, (a), and $L_u(443)/L_u(670)$, (b), against the ratio $L_u(443)/L_u(550)$ obtained from a wide range of ocean spectral measurements.

SURFACE RADIANCE IN CZCS BANDS
 $L_u(520) = 1$

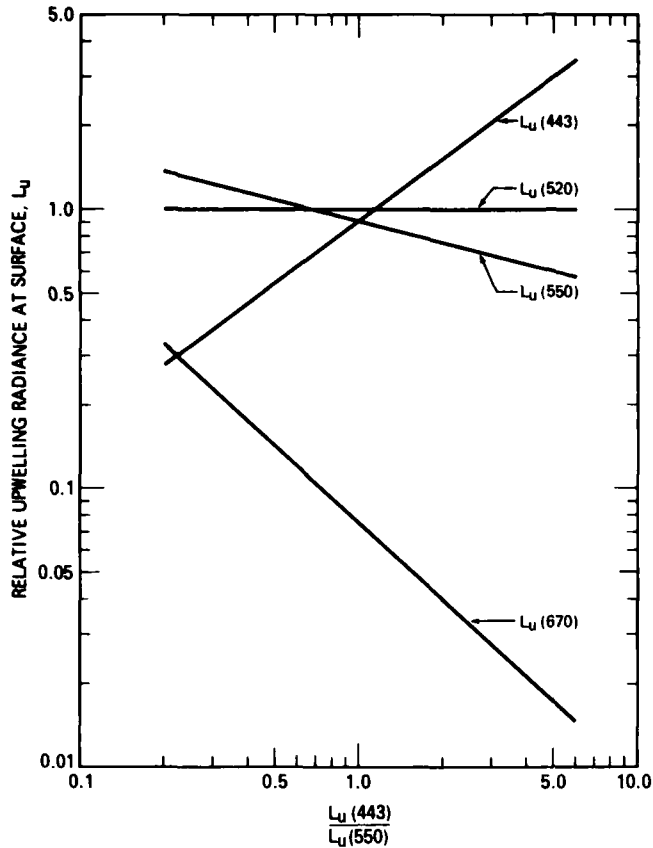
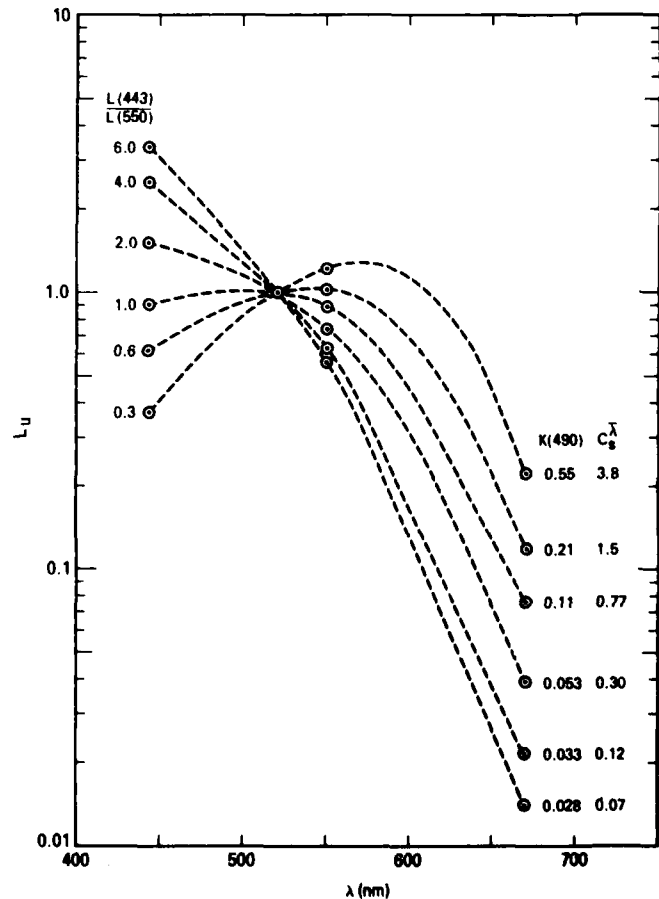
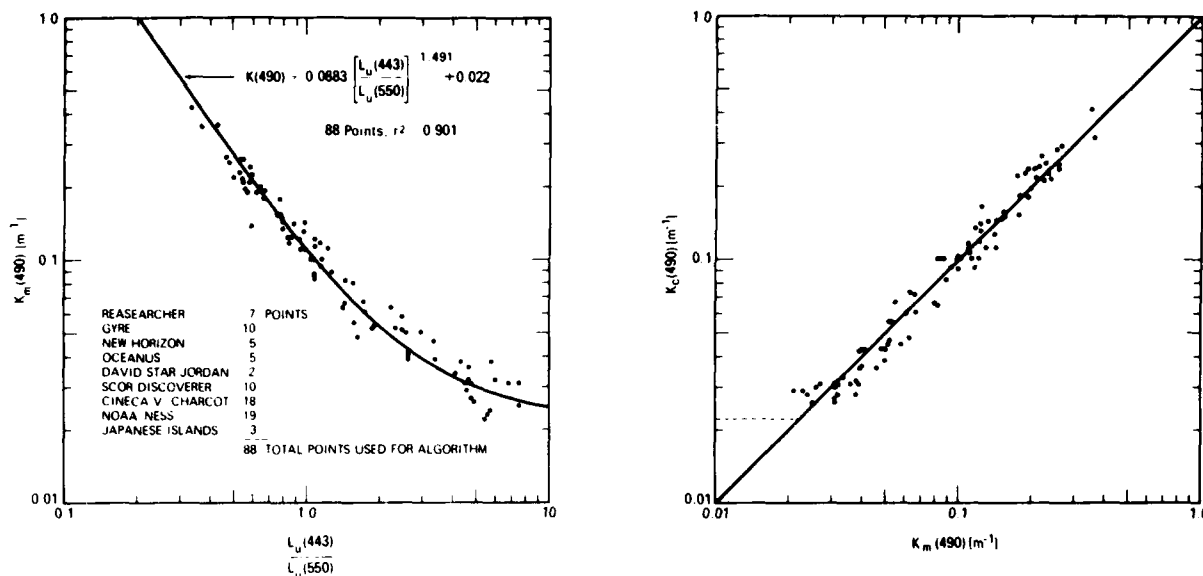


Fig. 3. Plots of the variations in $L_u(443)$, $L_u(550)$ and $L_u(670)$ with $L_u(520)$ fixed at unity and the ratio $L_u(443)/L_u(550)$ as the independent variable. Based on Equations (5) and (6).

Fig. 4. Plots of the upwelling radiances, L_u , at 443, 550 and 670 against wavelength with $L_u(520) = 1$ and the ratio $L_u(443)/L_u(550)$ as a parameter. The interconnecting lines are primarily to aid in identifying the points with the appropriate ratio but also serve to crudely indicate the manner in which the spectral signature varies with this ratio. The labels at the right are the diffuse attenuation coefficient values ($K(490)$ in m^{-1}) and the chlorophyll pigment concentrations (C_s^λ in mg/m^2) applicable to the radiance ratio for that curve.





SUMMARY K_c VS K_m
 $\lambda = 490 \text{ nm}$

DATA SOURCE	NO. POINTS	① 490nm	
		$\bar{x} = K_c / K_m$	$\bar{s} = K_c - K_m$
RESEARCHER (VIS LAB) OCT. 77	7	$\bar{x} = 1.002$ $\bar{s} = .138$	$.003$ $.025$
GYRE (VIS LAB) NOV. 78	10	$\bar{x} = .976$ $\bar{s} = .155$	$-.004$ $.013$
NEW HORIZON (VIS LAB) FEB. - MAR. 79	5	$\bar{x} = .971$ $\bar{s} = .134$	$-.003$ $.016$
OCEANUS (VIS LAB) AUG. 79	5	$\bar{x} = 1.052$ $\bar{s} = .118$	$.010$ $.014$
DAVID STAR JORDAN (VIS LAB) NOV. 79	2	$\bar{x} = .885$ $\bar{s} = -$	$-.006$ $-$
	29	$\bar{x} = .988$ $\bar{s} = .134$	$.000$ $.017$
SCOR - DISCOVERER (MOREL) MAY 70	10	$\bar{x} = 1.031$ $\bar{s} = .167$	$.001$ $.006$
CINECA V - CHARCOT (MOREL) MAR. - APR. 74	18	$\bar{x} = 1.015$ $\bar{s} = .119$	$.006$ $.024$
HARMATTAN (MOREL) MAY 71	9	$\bar{x} = .854$ $\bar{s} = .076$	$-.009$ $.007$
	37	$\bar{x} = .980$ $\bar{s} = .142$	$.001$ $.018$
NOAA NESS POST LAUNCH (CLARK) NOV. 78 - JUN. 79	19	$\bar{x} = 1.047$ $\bar{s} = .101$	$.004$ $.013$
JAPANESE ISLANDS (NOBORU & OKAMI)	3	$\bar{x} = .876$ $\bar{s} = .077$	$-.012$ $.006$
TOTAL DATASET USED TO FORM ALGORITHM	88	$\bar{x} = .994$ $\bar{s} = .133$	$.001$ $.016$
20 ADDITIONAL POINTS FROM ABOVE SOURCES	108	$\bar{x} = .983$ $\bar{s} = .201$	$-.002$ $.025$
		$\bar{x} = .961$ $\bar{s} = .145$	$-.003$ $.007$
		$\bar{x} = 1.025$ $\bar{s} = .113$	$.004$ $.021$

K_m values obtained from measured L_u or E_u in upper attenuation length.

Fig. 5. Data base, algorithm, and resulting fits for technique of Austin and Petzold (1980) for the determination of diffuse attenuation coefficient at 490nm from the ratio of the upwelling emerging radiances at 443 and 550nm. K_m values obtained from measured L_u (or E_u) in upper attenuation length.

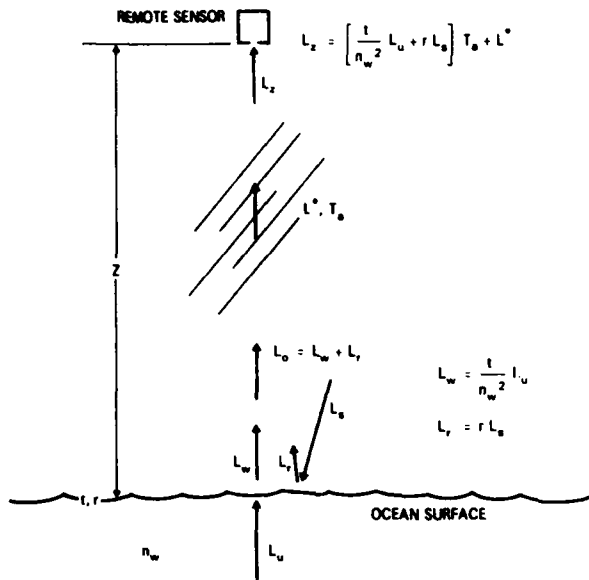


Fig. 6. Component parts of the Apparent Radiance Signal at Altitude z.

Fig. 7. Comparison of K's derived from CZCS observations with K's determined from surface station measurements. Solid points (●, ▲, ■,) overpass coincident with surface measurements. Open points (○, △, □,) overpass on different date than surface measurement.

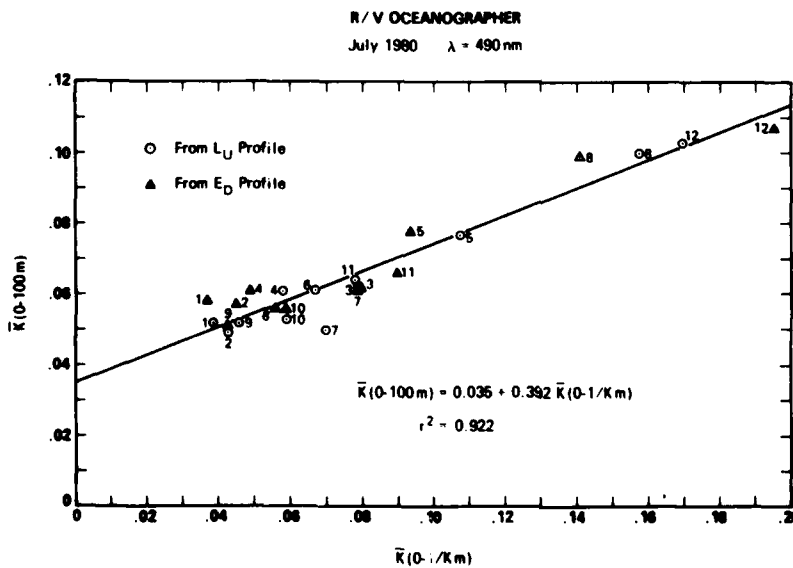
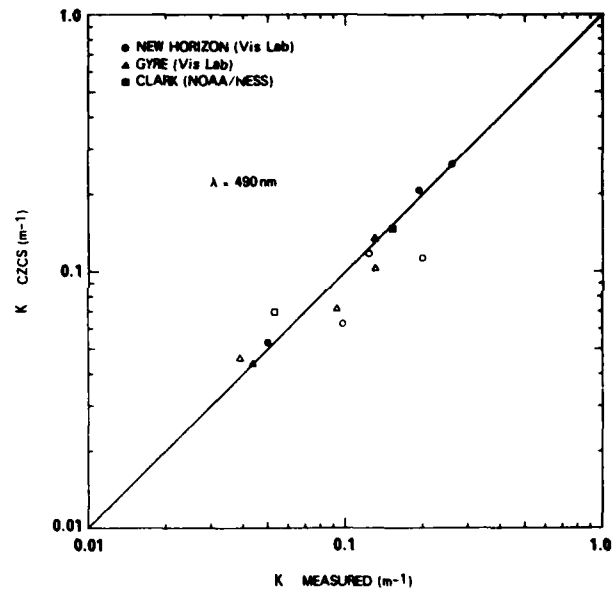


Fig. 8. Regression of $\bar{K}(0 - 100\text{m})$, the average diffuse attenuation coefficient to a depth of 100 meters, against $\bar{K}(0 - 1/\text{Km})$, the average K over the first attenuation length. Data derived from radiance (○) and irradiance (▲) profiles at 490nm obtained on the July 1980 cruise of the R/V OCEANOGRAPHER. Station numbers shown beside the data points.

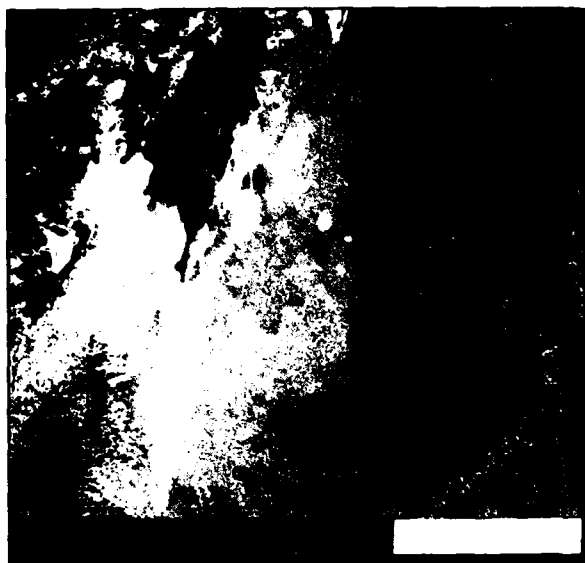


Fig. 9. Mapping of the diffuse attenuation coefficient at 490nm. Location is south and east of the Grand Banks of Newfoundland. From CZCS Orbit #350, November 18, 1978.

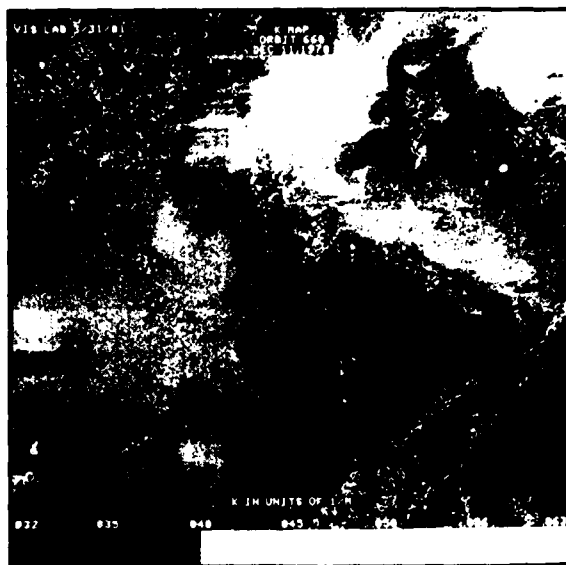


Fig. 10. Mapping of the diffuse attenuation coefficient at 490 nm. Location is in the open Pacific Ocean northwest of Wake Island. From CZCS Orbit #660, December 11, 1978.

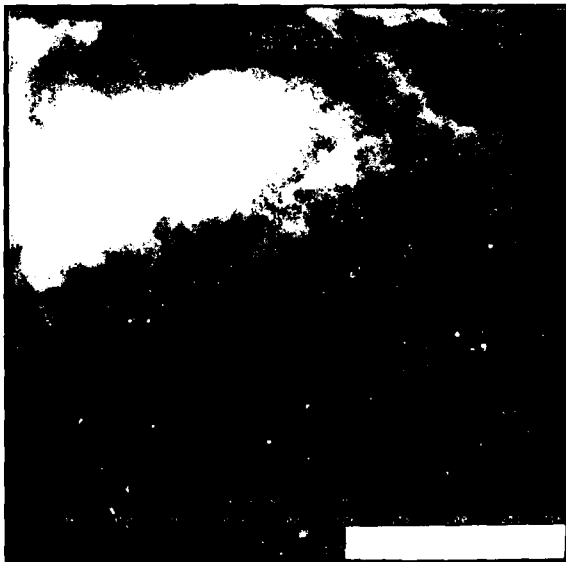


Fig. 11. Mapping of the diffuse attenuation coefficient at 490nm. Location is east of Cape Cod. Georges Bank visible in upper left. North wall of Gulf Stream appears at bottom of image. From CZCS Orbit #3226, June 14, 1979.

SUMMARY OF SESSION II

RECENT ATMOSPHERIC AND SEA WATER MEASUREMENTS

by

Dr. A. Kohnle, Chairman

Atmospheric optical and IR-data collected recently and during the last years at the ground as well as aloft, together with meteorological data, are being used for model development e.g. prediction of transmission, directional path radiance and contrast transmittance of any slant atmospheric path as a function of wavelength, model validation and improvement e.g. transmission codes and aerosol models and probability of occurrence studies of the individual parameters. These data should also be used for E/O system performance and feasibility studies as well as for the development of forecasting methods for optical and IR-atmospheric quantities.

In the area of remote measurements of atmospheric quantities, the LIDAR backscatter signal seems to be an effective tool for multiscatter analysis when analyzed with respect to polarization. The spatially anisotropic polarized backscatter signal is related to the size parameters of the scatterers and thus may provide a new tool for aerosol sizing purposes.

Experiments showed, that laser pulse stretching through inhomogeneous clouds is much less than expected following propagation theory for homogeneous turbid media.

Remote trace gas determination can be performed very accurately using a Raman LIDAR. Work should go on including artificial (battlefield created) gases.

Observation experiments on turbulent intensities and aerosol distributions as well as transmission measurements in the maritime atmospheric boundary layer have been performed over years near the Monterey - San Diego coast in the Pacific Ocean. Whereas the optical turbulence seems to be very accurately estimated by bulk meteorological quantities this is not yet so for the aerosol size distribution, where a reformulation of the existing models seems to be necessary, taking additionally into account the height of the inversion layer, stability of transport and air mass type, etc.

Such intensive measurements lack up till now for European coastal areas and for high seas.

Laser (520 nm) underwater propagation experimental results, compared with predictions provided by popular models derived from radiative theory, show that the predicted values underestimate the experimental ones at less than 10 scattering lengths.

Remote sensing techniques from satellites seem capable to assess the diffuse attenuation coefficient of ocean water for the upper 100 m.

QUESTIONS AND COMMENTS
ON SESSION II

RECENT ATMOSPHERIC AND SEA WATER MEASUREMENTS

- Paper 9 : Atmospheric measurements in a coastal environment.

Dr. M. Carnevale : Referring to the "laser link project" how much homogeneous was the link in order to ensure that meteorological measurements taken in just one point be representative of all the link ?

Dr. T. Bakker : As is mentioned in the paper meteorological measurements were done at the receiver as well at the transmitter sides of the link. We used only those measurements where the conditions at both locations were identical within certain limits. We planned to apply lidar measurements in parallel, which would give an immediate answer to the homogeneity problem. Unfortunately either the lidar or the laser link was inoperative.

- Paper 12 : Use of resonant Raman scattering for remote sensing of atmospheric gases.

Dr. C. Werner : Do you think that 10 % accuracy in your absolute humidity measurement is sufficient enough also for the relative humidity ?

Mr. J. C. Pourny : A comparable accuracy is obtained with the radiosoundings at an altitude of 2 000 m. The improvement of the precision will come from the increase of the laser power and rate. The reduction of the time of acquisition of data is important, as meteorological parameters may vary quickly.

- Paper 13 : Multiwavelength extinction and index fluctuation measurements.

Dr. J. Vernin : Have you done any measurements of the probability density function in the case of saturation regime ?

Dr. E. C. Crittenden : We have encountered probability density curves under saturation conditions that approach the exponential distribution. This has occurred for data taken in a hot desert location on sunny days. The curve shape is qualitatively rather like the Gaussian except that the tail of the curve on the side toward the origin rises above the horizontal axis. In the field this is possibly a useful warning of the existence of saturation, although one would usually already be alerted to saturation because of the high value of sigma, unless saturation is so heavy as to cause sigma to have risen to the maximum and then fallen off again. We have not attempted to measure C_n^2 by means of scintillation under saturation conditions. In the data discussed in this paper and also reported in paper 06, saturation never occurred on the paths over water during the periods reported.

- Paper 15 : Comparison of underwater radiance measurements with various analytical treatments of the radiative transfer equations.

Mr. R. C. Honey : Did your laser attract any marine life ?

Mr. R. Anderson : No fish or other marine life was noted directly by divers or inferred from signal level dropouts. The laser was operated on several occasions at night and provided a brilliant display in the water and on overhead clouds. Even then, no interference was noted from macroscopic animals in the beam.

- Paper 16 : Downlink laser cloud propagation experiments.

Pr. A. Ishimaru : Was the angular spectrum measured ?
Was the transmitted light diffused ?

Dr. P. J. Titterton : We did not measure the angular spectrum.
The light was diverged to $\pm 15^\circ$.

RECENT AURORAL AND AIRGLOW MEASUREMENTS IN THE INFRARED

A. T. Stair, Jr. and R. Nadile
Optical Physics Division
Air Force Geophysics Laboratory
Hanscom AFB, MA 01731

J. C. Ulwick, K. D. Baker and D. J. Baker
Electrical Engineering Department
Utah State University
Logan, UT 84322

Abstract

AFGL has developed specialized cryogenic infrared instrumentation for measuring the aurora, airglow, and upper atmospheric emissions from aircraft, rockets, and satellite platforms. Starting in 1972, a series of some 30 rockets have been launched from Poker Flat, Alaska. The highlights of these measurements, the first auroral enhancements at wavelengths longer than 2 micrometers and the first upper atmospheric radiation observed from 70 to 150 km in the wavelength region 2 - 20 μm , will be reviewed. In addition, more recent data obtained by a rocketborne cryogenic telescoped spectrometer which scanned the earthlimb and observed infrared (1.5 - 17 μm) emissions from 20 km to 200 km tangent altitudes, will be discussed.

Introduction

From the viewpoint of IR processes, the atmosphere can be divided into two altitude regimes. We consider a lower atmosphere from the surface to roughly 30 km, where collisions between molecules are rapid enough to maintain a Boltzmann distribution of the vibrational-rotational states. For this region of the atmosphere, the important radiative mechanisms are simply absorption and thermal emission. Above 60 km, on the other hand, collisions between molecules are considerably less effective in maintaining excited vibrational states, and radiative equilibrium becomes important. For this upper atmospheric region, there is additionally a large number of competing processes associated with IR airglow and auroral radiation.

We distinguish the aurora from airglow. The airglow results primarily from reactions among solar-generated labile species and from the excitation of atmospheric constituents by solar radiation. Consequently, the airglow is global in extent, with significant diurnal variability. There is also an empirically observed relationship between airglow intensity and structure related to geomagnetic disturbances. The aurora, on the other hand, comes primarily through excitation, ionization and reactions among atmospheric species by energetic charged particles, electrons, and protons.

Because of the interaction of the charged particles with the geomagnetic field, auroral radiation is concentrated in an oval centered on the geomagnetic latitude of 67°. The auroral events occur most often in the local geomagnetic evening and midnight sectors and are routine daily occurrences.

Viewing Geometry For Rocket Probe Measurements

Carrying out measurements of the radiation occurring in the upper atmosphere is difficult. The radiation levels are extremely low, and in fact, measurements are presently dependent on development and improvement of existing techniques. Further, these measurements often must be made with the lower atmospheric thermal emission as an interfering background. The thermal emission in the vertical direction is essentially the 300°K blackbody radiation with radiance levels between 10^{-4} and 10^{-3} $\text{w/cm}^2\text{-sterad-}\mu\text{m}$, many orders of magnitude greater than the upper atmosphere levels.

The availability of rocket probe instrumentation utilizing cryogenic sensors has opened the atmospheric regions to infrared studies. In particular, by operating above the lower atmosphere, they allow us to study the vertical distribution of infrared radiation, which constitutes the basic data required to understand the physical mechanisms underlying the infrared emissions.

There are two modes of operation available. We can record the change in zenith radiance as the rocket changes altitude. The derivative of the signal with respect to altitude then gives the height profile of the emission. The alternate procedure is to carry out a vertical scan through the limb and view the atmosphere tangentially. These are illustrated in Figure 1. Vertical probe measurements are referenced to the altitude of the sensor. For the limb scanning geometry, the tangent height, H , is used. This is the height of the sensor line of sight's closest approach to the earth's surface.

Vertical viewing probes have the advantage of catching and measuring a localized transient phenomenon such as an aurora. In addition, for improving model/

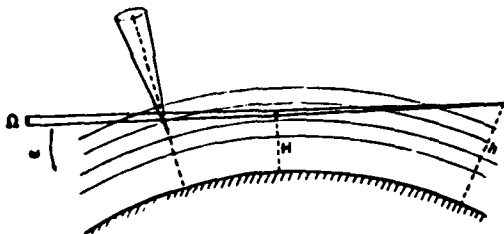


Figure 1. Rocket experiment measurement modes.

experiment comparisons, the vertical data are consistent with localized measurements of temperature, concentration, and density, parameters which are vital to calculations of radiation whether in equilibrium or not.

Experimental Data

Project ICECAP

The first infrared spectral radiance measurements of the aurora and the upper atmosphere were carried out by the Air Force Geophysics Laboratory (Baker et al., 1974; Stair et al., 1974-1978; Rogers et al., 1976-1977) under the program name ICECAP (Infrared Chemistry Experiments--Coordinated Auroral Program) which was supported by the Defense Nuclear Agency. Measurements were made from rocket probes utilizing cryogenically cooled instrumentation with a series of launches during the 1972-1976 period from Poker Flat, Alaska. Infrared spectra from 1.5 to 24 micrometers were measured under a variety of auroral conditions, ranging from aurorally quiet to an intense auroral breakup. The main infrared emission originating from NO, OH, CO₂, and O₃ showed varying degrees of enhancement associated with the aurora.

Five of the probe flights carried SWIR low-resolution spectral instrumentation (1.6 to 5.3 micrometers), while two of the flights took low-resolution spectra in the LWIR (7 to 24 micrometers) region. Data were taken primarily at night in the zenith direction with approximately 2 deg fields of view.

The sensors utilized circular variable interference filters (CVF) to obtain the spectral data. The CVF spectrometers were built by the Electro-Dynamics Laboratories of Utah State University. The resolution of the filters and, therefore, most of the spectral data were in the 3 to 4 percent range ($\Delta\lambda = 0.04\lambda$). For the LWIR measurements, arsenic-doped silicon detectors were used with liquid helium cooled sensors, while the SWIR instrumentation used In:Sb

detectors, with the entire sensor operating at liquid nitrogen temperatures. In addition to the CVF spectrometer, the rocket payloads were instrumented with diagnostic sensors including a 3914-angstrom photometer, which provided a measure of auroral activity.

Additionally, in 1976, a rocket probe experiment carried out measurements at significantly higher resolution, using a helium-cooled interferometer spectrometer (HIRIS). The sensor was built by the Honeywell Radiation Center in conjunction with AFGL and was based on a specially developed interferometer by Idealab, Inc. Data were obtained over the wavelength region from 4 to 16 micrometers (2500 to 600 cm⁻¹) with a spectral resolution better than 2 cm⁻¹. The payload rotated (not planned), vertical to downlooking to vertical, at 10.5 deg/sec and took a spectrum every 1.4 sec. The auroral conditions during flight were highly variable; consequently, the data assessment is still in progress.

Spectra were obtained of the CO₂ v₃ band, the NO fundamental and first overtone. In each of the above wavelength regions, distinct auroral enhancements were observed. Figure 2 is a spectrum obtained by a nitrogen-cooled CVF spectrometer at 86 km during a bright auroral breakup. Figure 3 indicates the peak radiance values observed for different auroral intensities, including the data obtained during the IBC III⁺ auroral breakup. For the 5.3 micrometer band, the weaker auroral profiles show radiance levels essentially equivalent to those for the quiet background, except that there are slight auroral enhancements in the 90 to 110 km region.

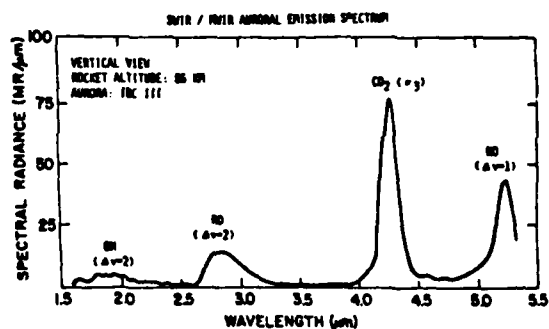


Figure 2. Auroral emission spectrum (vertical view).

The high altitude layer of emission at 5.3 micrometers observed under quiet auroral conditions has also been reported by the Russians (Markov et al., 1976) from a limb-viewing satellite experiment.

Figure 4 is a plot of two selected

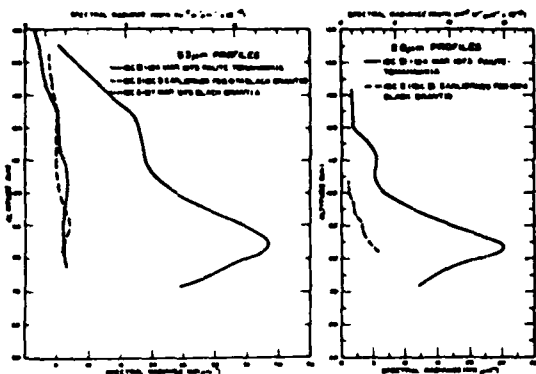


Figure 3. Zenith peak spectral radiance of an aurora measured with SWIR spectrometer.

spectra obtained by HIRIS. The lower dotted curve, obtained on the upleg of the flight at 98 km while oriented at a 15-deg elevation angle, observed a weakly disturbed (auroral) condition. The upper spectrum, also obtained at 98 km at a 15-deg elevation angle, but during the downleg, was viewing a bright class II/III auroral arc. The auroral activity was documented by all sky cameras and scanning photometers. The auroral spectrum is interpreted as NO produced in a highly excited vibrational distribution due to the chemiluminescent reaction $N(2D) + O_2 \rightarrow NO + O$ (Rawlins et al., 1980). Laboratory measurements obtained in the AFGL/OPR cryogenic facility COCHISE (Kennealy et al., 1978) support this conclusion.

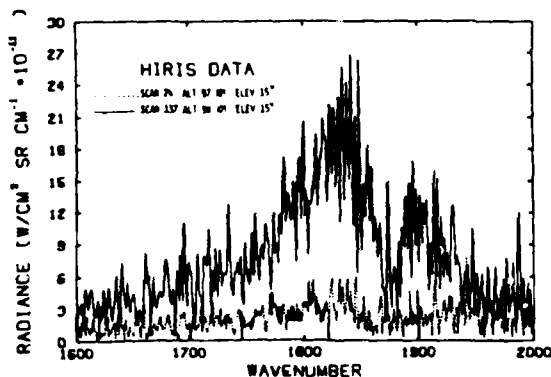


Figure 4. Aurorally enhanced and quiescent nitric oxide spectra at high resolution.

The Spectral Limb-Scanning Experiment

A limb-scanning infrared spectral probe designated SPIRE (Spectral Infrared

Rocket Experiment) was launched on September 28, 1977 (Nadile et al., 1977; Stair et al., 1978). This payload had three coaligned primary sensors: (1) a telescoped 2-channel photometer, (2) a cryogenic (77°K) telescoped SWIR CVP spectrometer, and (3) a cryogenic (10°K) telescoped LWIR CVP spectrometer. The spectrometers covered the 1.4 to 16 micrometer region. The telescopes had 1/4-deg fields of view with high off-axis rejection (point source rejection of 10^{-9} at 1 deg off-axis) and were coaligned to better than 0.1 deg. The payload reached an altitude of 285 km and the earth limb was spatially scanned from hard earth to local horizontal at 0.5 deg/sec while taking a spectrum at 2 scans/sec. The spectrometers were built at Utah State University and the telescopes at the Honeywell Radiation Center.

A spectrum of the dark atmosphere from 4 to 16 μ m at a tangent height of approximately 124 km is shown in Figure 5. This data, obtained with the liquid helium cooled spectrometer, is shown in two spectral intervals to match the split coverage of that instrument's two element circular variable filter. Emission from the NO fundamental ($\Delta v = 1$) at 5.3 μ m with clearly resolved P and R branches of the 1-0 transition dominates at this altitude. The long wavelength feature is the strong CO_2 v_2 emission showing the intense Q branch at 15 μ m.

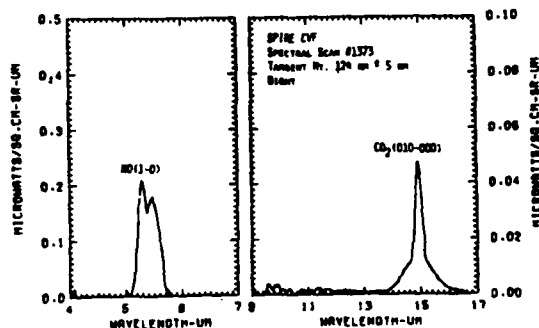


Figure 5. Night spectrum at 124 km (limb view).

As the tangent altitude is decreased to approximately 110 km (not shown), the 5.4 μ m NO emission increases, peaking at 6.5×10^{-7} watts $cm^{-2} sr^{-1} m^{-1}$. At about this same altitude, O_3 (v_3) emission at 9.6 μ m is first detected above sensor threshold and increases rapidly to the level shown in Figure 6, a spectrum of the dark atmosphere at 81 km. The CO_2 band at 15 μ m has also increased markedly allowing the spectrometer to just resolve the Q branches of some of the weaker transitions, such as $100 \rightarrow 010$, 13.8 μ m and $020 \rightarrow 010$, 16.2 μ m. NO(1-0) emission has dropped off slightly from its peak and is shown here riding on an instrument induced background.

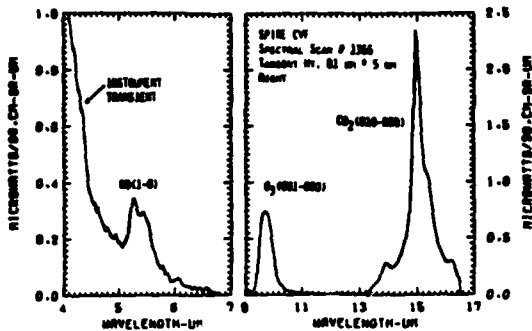


Figure 6. Night spectrum at 81 km (limb view).

Figure 7 is a spectrum at approximately the same altitude (81 km) measured during one of the sunlit limb scans. Significant differences from the night spectra are: (1) intense emission from the 4.3 μm CO_2 band due to solar pumped fluorescence (7.5×10^{-6} watt $\text{cm}^{-2}\text{sr}^{-1}\text{m}^{-1}$ compared to a night value of 2.5×10^{-7} watt $\text{cm}^{-2}\text{sr}^{-1}\text{m}^{-1}$), (2) reduced ozone emission at 9.6 μm , and (3) appearance of a band at $\sim 10.5 \mu\text{m}$ which is due either to CO_2 (101 + 120) and (021 + 120) solar pumped fluorescence (James and Kumer, 1973) and/or O_3 (010, 020, 030, ...) chemiluminescence due to the exothermic $\text{O} + \text{O}_2 + \text{M} \rightarrow \text{O}_3^* + \text{M}$ recombination reaction.

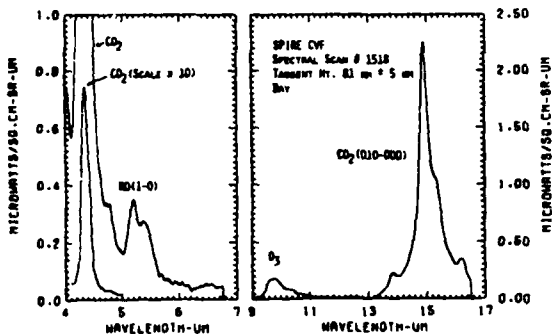


Figure 7. Sunlit spectrum at 81 km (limb view).

Substantial day-night differences are also evident in the data from the liquid nitrogen cooled spectrometer. Figure 8 shows a night spectrum at $\sim 80 \text{ km}$ tangent height with emission features interpreted as follows: hydroxyl airglow due to the $\text{H} + \text{O}_2 \rightarrow \text{OH}^* + \text{O}_2$ reaction, $\text{OH}(\Delta v = 2)$ from 1.4 to 2.3 μm and $\text{OH}(\Delta v = 1)$ from 2.5 to 3.5 μm with a peak at 2.94 μm corresponding to the 2-1 transition; and CO_2 (ν_3) at 4.26 μm .

The sunlit spectra show much weaker hydroxyl intensities, both in the 80 km

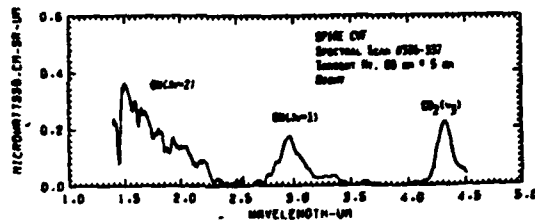


Figure 8. Night spectrum at 80 km (limb view).

region and at lower tangent altitudes. Several features unique to the day spectra are shown in Figure 9 ($\sim 56 \text{ km}$): appearance of a sharp spike at 1.58 μm , due to fluorescence of O_2 ${}^1\Delta(0-1)$; a band peaked at 2.7 μm , probably due to fluorescence of CO_2 and/or H_2O ; and the solar pumped fluorescence of the CO_2 emission at 4.3 μm . At still lower altitudes ($\sim 40 \text{ km}$), we return to a spectrum of the night atmosphere obtained by the long wavelength spectrometer (Figure 10). New features are 4.8 μm due to O_3 ($\nu_1 + \nu_3$) and CO_2 ($\nu_1 + \nu_2 + \nu_3$); 6.3 μm due to H_2O (ν_2) combined with NO_2 (ν_3) and 11.3 μm due to HNO_3 .

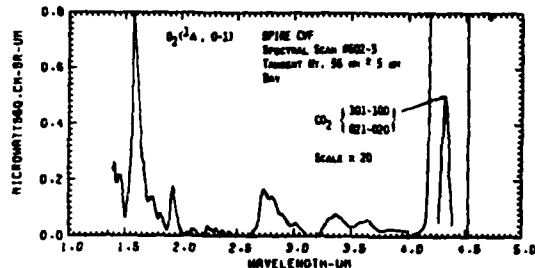


Figure 9. Sunlit spectrum at 56 km (limb view).

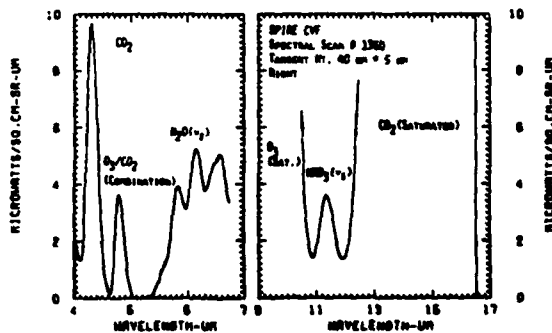


Figure 10. Night spectrum at 40 km (limb view).

Figure 11 is a summary plot of night peak radiance values versus approximate tangent altitudes for some of the observed species. The emission at $5.3 \mu\text{m}$ due to the $1-0$ transition of NO can be seen as a broad layer peaked around 110 km . For a non-auroral case, which this is, the populating mechanism for the high altitude radiation is due to O atom interchange $\text{NO} + \text{O}' \rightarrow \text{NO}' + \text{O}$. This layer was also observed during the ICECAP vertical sounding and has been reported by Russian investigators from a limb viewing satellite (Markov et al., 1976). A recent paper by Kockarts (1980) has demonstrated the importance of this feature in the radiative cooling of the upper atmosphere. The $9.6 \mu\text{m}$ emission due to the ν_3 band of O_3 is observed from 25 km to 120 km . The layer around 90 km is very marked in this data. There is an increase in ozone concentration at these altitudes which accounts for this effect. More unexpected is a "layer" in the limb radiance of the $15 \mu\text{m}$ $\text{CO}_2 \nu_2$ emission. An effect like this was observed in a 1974 vertical viewing CVF flight but was not evident in the 1973 data (Stair et al., 1974). Ongoing analysis of this data (Sharma and Nadile, 1980) indicate an unexpectedly high cross section for $\text{O} + \text{CO}_2(000) \rightarrow \text{O} + \text{CO}_2(0^110)$. The $4.26 \mu\text{m}$ $\text{CO}_2 \nu_3$ band becomes completely optically thick below 50 km as seen by the knee in the data. As mentioned previously, this wavelength region is significantly enhanced in the sunlit data by solar fluorescence ($2.7 \mu\text{m}$ and $2.77 \mu\text{m}$ absorption) and transitions at $4.3 \mu\text{m}$ which are not resolved from the $4.26 \mu\text{m}$ ν_3 band. The radiance level versus altitude of both $6.3 \mu\text{m}$, H_2O and $11.3 \mu\text{m}$, HNO_3 , do not appear to have any significant day/night variation in agreement with earlier balloon-borne measurements (Murcray, 1978).

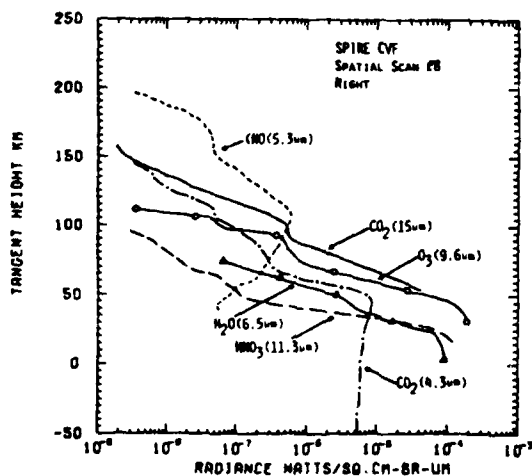


Figure 11. Night tangent altitude radiance profiles of several atmospheric species (limb view).

Future Programs

IR rocket probe studies of the upper atmosphere and the aurora will continue through the 1980's. As an example, we will carry out rocket probe studies with cryogenic field-widened interferometers. The instruments will view in the zenith direction, will have 1 cm^{-1} spectral resolutions, will cover the 2 to 7 micron region, and will obtain data under day, night and auroral conditions. A major effort is underway to couple the recovered HIRIS interferometer to a high spatial resolution telescope for a limb-scanning experiment to study upper atmospheric physics and chemistry from the Space Shuttle (CIRRIS).

References

- Baker, D. J. et al. 1974. "Rocket Launch of a SWIR Spectrometer into an Aurora (ICECAP 72)," TR-74-0077, Air Force Geophysics Laboratory, Hanscom Air Force Base, MA.
- James, F. C. and Kumer, J. B. 1973. *J. Geophys. Res.*, 78.
- Kennealy, J. P. et al. 1978. "Nitric Oxide Chemi-Excitation Occurring in the Reaction Between Metastable Nitrogen Atoms and Oxygen Molecules," *J. Chem. Phys.*
- Kockarts, G. 1980. "Nitric Oxide Cooling in the Terrestrial Thermosphere," *Geophysics Research Letters*, 7(2):137; February 1980.
- Markov, M. N. et al. 1976. "Infrared Radiation of Nitric Oxide in the Upper Atmosphere According to Measurements From Salyut 4," Preprint No. 8, Lebedev Physical Institute of the USSR Academy of Science, Moscow, pp. 1 - 18.
- Murcray, D. G. 1978. Private communication.
- Nadile, R. M. et al. 1977. "SPIRE-- Spectral Infrared Experiment," SPIE, Vol. 124, Modern Utilization of Infrared Technology.
- Rawlins, W. T. et al. 1980. "Infrared Emission From $\text{NO}(\Delta v=1)$ in an Aurora: Spectral Analysis and Kinetic Interpretation of HIRIS Measurements," Accepted for publication in the *Journal of Geophysical Research*.
- Rogers, J. W. et al. 1976. "LWIR (7-24 μm) Measurements from the Launch of a Rocketborne Spectrometer into an Aurora (1973)," TR-76-0274, Air Force Geophysics Laboratory, Hanscom Air Force Base, MA.

Rogers, J. W. et al. 1977. "LWIR (7-24 Micron) Measurements From the Launch of a Rocket-Borne Spectrometer into a Quiet Atmosphere (1974)," TR-77-0133, Air Force Geophysics Laboratory, Hanscom Air Force Base, MA.

Sharma, R. D. and Nadile, R. M. 1980. "Carbon Dioxide (v_2) Radiance Results Using a New Nonequilibrium Model," EOS, Transactions, American Geophysical Union, 61(17):322; April 1980.

Stair, A. T., Jr. et al. 1974. "Altitude Profiles of Infrared Radiance of O_3 (9.6 Microns) and CO_2 (15 Microns)," Geophysical Research Letters, 1, 117.

Stair, A. T., Jr. et al. 1975. "Rocket-Borne Observations of Atmospheric Infrared Emissions in the Auroral Region," in Atmospheres of Earth and the Planets, edited by B. M. McCormac, Dordrecht, Holland: D. Reidel Publishing.

Stair, A. T., Jr. 1976. "Cryogenic Spectrometry for the Measurement of Air Glow and Aurora," SPIE Proceedings, 91, 71.

Stair, A. T., Jr. et al. 1978. "A Rocket-Borne Cryogenic (100°K) High-Resolution Interferometer Spectrometer HIRIS," Submitted to Journal of Applied Optics.

BACKGROUND MEASUREMENTS FROM A BALLOON-BORNE STARING SENSOR

R. E. Murphy, F. H. Cook
Air Force Geophysics Laboratory
Hanscom AFB
Bedford, Massachusetts 01731

B. K. Yap
Yap Analytics, Inc.
365 Waltham Street
Lexington, Massachusetts 02173

ABSTRACT

Several hours of data were gathered on three successful data flights conducted as part of the Balloon Altitude Mosaic Measurements (BAMM) program which was designed to collect spectral, spatial, and temporal statistics on the infrared earth/atmospheric backgrounds. The program was conducted by the Air Force Geophysics Laboratory (AFGL) under the sponsorship of the Space Division (SD), formerly the Space and Missile Systems Organization (SAMSO). Two of these flights were out of Holloman AFB, NM and data were collected on a wide range of infrared backgrounds characteristic of the Southwestern United States. A third mission was flown from Keesler AFB, MS and provided statistics of the Gulf Coast region as well as solar specular reflections off land, water, and clouds. Measurements were made with a two-color SWIR radiometer and with a Michelson interferometer-spectrometer covering the 2.5 to 5.5 micron region from float altitudes of 70,000 to 100,000 ft. Both instruments were spatially co-aligned such that their 4x4 mosaic focal planes projected over-lapping footprints on the ground simultaneously. Data collected on these flights were reduced and relevant statistics were compiled. Samples of the data and results are presented in this paper.

1. INTRODUCTION

The BAMM program objective was to gather earth/atmosphere background infrared data, relevant to the staring mosaic sensor concept utilizing balloon-borne instrumentation. Characteristics of the infrared background essential to the staring concept are the spectral, spatial, and temporal statistics of the various categories of background. Such information is essential to surveillance sensor system designers in the evaluation, trade-off, and design of systems based on the staring concept.

The passive staring surveillance system concept derives its potential advantage from the invariability of the background during the operation of the sensor. If this premise could be substantiated by actual measurement, then the staring concept would unequivocally be superior to the scanning concept. Background clutter problems could be alleviated by the implementation of a simple scheme of signal change detection since such a change could occur only when a target traversed the sensor field-of-view (FOV). However, there are numerous natural phenomena which contribute to the variations in the background as observed by the staring sensor. Such phenomena include atmospheric turbulence, cloud motion, weatherfronts, temporally modulated solar specular reflections, and spatial background clutter induced by sensor platform instabilities. The BAMM program was therefore designed for the collection of the temporal background data from these natural phenomena. As a part of the BAMM measurement series, three successful data gathering flights were conducted during 1978-1979. Two flights were from Holloman AFB, NM resulting in a wide variety of infrared background information characteristic of the Southwestern United States. The third flight from Keesler AFB, MS added further statistics of infrared background variability caused by solar specular reflections off land, water, and clouds.

The spatial, spectral, and temporal data of the earth/atmosphere infrared background were measured with two co-aligned instruments mounted on a balloon platform capable of providing scan, dither, and stare functions. The radiometer, with a 4 x 4 mosaic element focal plane, provided high sensitivity measurements in the SWIR while the interferometer, equipped with a physically identical 4 x 4 mosaic element focal plane, provided spectral coverage from 2.5 to 5.5 micron. The infrared instrumentation developed for the BAMM program were guided by such system parameters as spectral bandwidth and band location, sensitivity, FOV, and observation time pertinent to future surveillance sensors monitoring points sources with radiant intensities of one kilowatt/sr or higher.

A description of the BAMM infrared instrumentation is given in the following section and samples of the reduced data of the variety of background are included.

2. INSTRUMENTATION2.1 Infrared Mosaic Radiometer

A schematic of the BAMM radiometer is shown in Figure 1. The instrument provides SWIR radiometric data in both a wide band and narrow band filters, R1 and R2, respectively. Three filter positions are selectable, and a fourth position is used to block off all incoming radiation. In position 1 the wider filter (R1) is inserted into the optical system. In position 2 the narrow filter (R2) is optically inserted into the system and in position 3, (R3), an aperture is used in tandem with R2 to reduce extremely bright backgrounds. A dust shutter which protects the internal assembly from foreign matter contamination is opened by command when operations commence. The focal plane of the instrument is shown in Figure 2. Both the focal plane and the spectral filters are operated at cryogenic temperatures. Table 1 summarizes some of the more important specifications of the radiometer. Details

of the BMM radiometer design has been given by Murphy. Specifications of the optical filters have been reported by Ransom.

The background radiation entering the radiometer is interrupted by means of a rotary mechanical chopper. This permits bandpass filtering of the signal at the chopper carrier frequency, retaining DC scene response while eliminating low-frequency noise of the detectors and electronics. To achieve the required radiometer dynamic range of 10^6 , the following scheme was devised.

TABLE 1 BMM RADIOMETER SPECIFICATIONS

- A. Electrical Bandwidth: 20 Hz
- B. Dynamic Range: 1.00×10^6
- C. Optics Entrance Aperture: 1.6" diameter (clear aperture), 2" focal length; optics anti-reflection coated.
- D. Detectors: PbS (16 element array, each element approx. 0.050" x 0.050" with 0.008" spacing between elements); $D^*(2.8, 200, 1) \geq 1 \times 10^{12}$. Element No. 13 is 0.025" x 0.025".
- E. Overall FOV: Approx. $6.0^\circ \times 6.0^\circ$ full-angle square.
- F. IFOV (each detector): $1.5^\circ \times 1.5^\circ$ full-angle square (0.8 Km x 0.8 Km at a distance of 31 Km). Element No. 13 is $0.72^\circ \times 0.72^\circ$ square (0.39 Km x 0.39 Km at 31 Km range.)
- G. Detector Operating Temperatures: 163°K
- H. Spectral Bandwidth: Defined by optical interference filters cooled to 77°K.
- I. Cryogenic Hold Time: 10 hrs. (3.6 liters of LN₂ or about 6.4 lb.)
- J. Optical Chopping Frequency: 200 Hz synchronously demodulated in-flight and sampled at 137 Hz for formatting PCM telemetry.

The chopper-modulated signal from each radiometer (each detector element) is preamplified and fed to three other amplifiers of different gains. All three of these signals are synchronously demodulated, filtered to 20-Hz bandwidth and fed to the pulse code modulation (PCM) encoder where all 48 signals (three gains, 16 detection channels) are formatted for telemetry using a sample rate of 137 Hz. The radiometer sensitivity is limited to 5.0×10^{-10} w/cm²-sr-band at low background levels and to 5.0×10^{-9} w/cm²-sr-bands at higher background levels.

2.2 Interferometer

The BMM interferometer provides spectral coverage from 2.5-5.5 micron and contains internal hot and cold reference sources. A 4 x 4 array of Indium Antimonide (InSb) detectors is cooled to operational temperature with liquid nitrogen. Two scan rates and four gain selections of X1, X4, X16 and X64 are provided and can be selected by ground command. The calibration modes and the optical alignment can also be controlled from the ground. The important characteristics are summarized in Table 2.

The optical layout of the interferometer system is shown in Figure 3. The basic building block of the unit is a Michelson type modulator which provides a method of coding the spectral elements of the incoming optical energy from a source. The components of the Michelson modulator include the beamsplitter-compensator, the translating mirror, and the adjustable fixed mirror. Background scenes are focused on the detector array by the three element lens system.

The Michelson interferometer cube is capable of achieving ± 0.05 cm of optical path difference (10cm^{-1} resolution) at scan rates of approximately 5 and 20 double-sided scans per second. The movable mirror is driven linearly one way through the full stroke length, stopped, and driven linearly in reverse through the full stroke length. This allows spectral data to be obtained while the movable mirror is being driven in either direction.

The interferometer field of view is defined by the active detectors in the InSb focal plane (same basic layout as radiometer array). Each 0.0475 in. square detector provides an IFOV of 23.75 mrad square with a 4 mrad gap between IFOV's. A total FOV coverage of 6.0 degree square is achieved with the mosaic focal plane. At a range of 31 km, the footprint of each detector is 0.73 km limiting the spatial resolution to 1.37 cycles/Km. Lower spatial resolution may, of course, be achieved by grouping the detectors to project larger effective footprints on the ground. In addition, one of the detectors in the array of 16 is 0.025 in. square, which provides a high spatial resolution of 2.58 cycles/Km.

2.3 TV Camera

Located on the platform is a TV camera which is used primarily for visual real-time background target-scene acquisition before the data taking sequence. This is a standard TV camera modified optically to provide a ground resolution of 1 Kft at an altitude of 100 Kft (0.01 radians [IFOV]). The total ground coverage is 50 Kft x 37.5 Kft ($28^\circ \times 21.1^\circ$) with this coarse resolution. This is achieved with a lens system with an effective F/5.6 and a focal length of 30 mm.

A motorized zoom feature, controlled from the ground support, permits the operator to increase the spatial resolution by a factor of 10 to 100 ft. footprint. At this full zoom, the effective focal length is 300 mm decreasing total field coverage to 4.2 kft x 3.2 kft ($2.4^\circ \times 1.8^\circ$).

TABLE 2

BAMM INTERFEROMETER SPECIFICATIONS

- A. Spectral Range: 2.5-5.5 μm ($4000 - 1818 \text{ cm}^{-1}$)
- B. NESR: $4.5 \times 10^{-10} \text{ watt/cm}^2\text{-sr-cm}^{-1}$ @ 4.3 μm
- C. Spectral Resolution: 10 cm^{-1} , OPD $\pm .05 \text{ cm}$
- D. Scan Rate: 5 Scans/sec or 20 scans/sec (4 detectors)
- E. Signal Passband: 500 - 2000 Hz in normal mode, 500 - 8000 Hz in fast mode
- F. Detector System: InSb 16-element array, each .0475 x .0475 inch, .008 inch spacing. D*
(4.3 μm) = $1 \times 10^{11} \text{ cm Hz}^{1/2}/\text{W}$ at 77°K
- G. Dynamic Range: 10^5
- H. Overall FOV: $6^\circ \times 6^\circ$ square, one element FOV $1.35^\circ \times 1.35^\circ$ square (.73 x .73 Km @ 31 Km distance)
- I. Optical Alignment: 50 sec of arc
- J. Optical Entrance Size: 1.8 inches diameter clear
- K. Optical Components: Triplet lens Ge and Si coated (F/1, 0.002 inch blur circle), beamsplitter and compensator Ca F1 coated, end mirrors gold coated.
- L. Cryogenic Hold Time: 10 hours
- M. Calibration: Internal hot and cold (77°K) sources

2.4 Pointing Platform

The pointing platform was a gyro compass stabilized system which provides 1 arc min/sec drift stability with a true pointing accuracy of 0.1° North in azimuth. After lock on the platform, system was capable of stare stabilities of the order of 0.01 Km/sec (nominally 0.1 Km drift in 10 seconds). This stability was achieved by the use of a three axis servo controlled system which accommodated for balloon velocity, rotation and pendulosity. This corresponds to 1 arc min/sec at balloon altitude, which equates of 0.05 arc sec/sec stability from synchronous altitude.

2.5 Data Processing

Processing of the data field tapes was accomplished in its entirety by AFGL, from decommutation of the data tapes to the generation of final data statistical formats. The computer codes used in processing the IR instruments, i.e., radiometer and interferometer, were documented in the BAMM series reports.

The final products in the data processing are preserved in microfiche. Included in the final products are:

1. Radiance Time Profile
2. Histogram
3. Exceedance
4. Biased Power Spectral Density (PSD)
5. Biased Truncated (or smoothed) PSD
6. Autocovariance
7. Unbiased Truncated PSD

3. Results

The critical parameter in the staring and dither scenes is drift velocity. This was obtained from the video recordings by direct measurement of movement of ground reference points on the display. A typical value for a stare scene instability referenced to a synchronous satellite is approximately 0.1 seconds of arc per second. There are periods of essentially zero velocity determined from the video data by observing a well-distinguished landmark. The dither scenes are representative of a drift rate 0.25 to 0.6 seconds of arc per second at synchronous altitude. Certain scenes also exhibited a well-defined jitter rate of 0.2 Km/sec. Noise level for the medium gain amplifier network of the SWIR radiometer is in the range of 5.0×10^{-10} to $1.0 \times 10^{-9} \text{ watt/cm}^2\text{-sr-band}$ for all three filters R1, R2 and R3. This can be converted to noise in the power spectrum.

$$N = 1 \times 10^{-7} (\text{uw/cm}^2/\text{sr}/\text{band})^2/\text{Hz}$$

The NESR of the interferometer is

$$\text{NESR} = 5 \times 10^{-10} \text{ watt/cm}^2\text{-sr-cm}^{-1}$$

The spectral bands of I1, I2 and I3 are 108, 100 and 134 cm^{-1} wide respectively; hence, the noise level for these bands is on the order of

$$\text{NER} = 5 \times 10^{-8} \text{ watt/cm}^2 \text{ sr band}$$

which is sufficient for BAMB objectives. For benign scenes, the atmospheric absorption from the CO_2 (γ 3) bands is sufficient to attenuate the background fluctuation in the I1 and I2 spectral bands to a level below the instrument NER. This is evident in the generally predominantly flat PSD's for I1 and I2. For scenes with specular points present, data taken with I1 and I2 filters provided useful information despite the background fluctuation attenuation due to the atmospheric absorption. Wide band interferometer filter I3 provided fluctuation data for all scenes analyzed in flights 2 and 3. Comparison of interferometer filters I1, I2, and I3 data with corresponding SWIR radiometer data in the scan scenes showed point correlations in amplitude which were also correlated to ground features in the video data.

In general, correlation of the radiance-time traces with ground features and/or clouds identified in the video data is qualitatively quite good. The results of a quantitative correlation of the IR data with the video data in terms of spatial extent of the specular regions is very favorable. A wide variety of earth/atmosphere infrared background data were gathered on the three BAMB data flights exhibiting statistics which range from being benign to most operational systems, to being adverse to staring systems even in the best operational environment. A sample spectrum of a benign scene, reduced from the data gathered with the interferometer, is shown in Figure 4. Characteristics of a blackbody spectral distribution, attenuated in the 2200-2400 cm^{-1} region by the intervening atmospheric, are quite apparent. The spectrum of an active scene, where solar specular scatter is present, is shown in Figure 5. The increased magnitude of the spectrum throughout most of the spectral range provides an indication of the severity the solar specular scatter has on the background data statistics.

Three platform modes were used to gather background spatial, temporal, and spectral data. The reduced data statistics for the three modes (stare, dither, and scan) indicated strong similarity of statistical behavior for the different classes of background. As an example, the histograms of the background data showed both uni-mode and multi-mode distributions for scenes observed in all three platform modes. An uni-mode histogram, as that shown in Figure 6 from radiometer data of sand background, is typical of very benign scenes which also visually (from video recordings) appear to be structurally uniform. Such probability distribution is reminiscent of the system Gaussian noise.

Multi-mode histograms are to be expected from data of scans across scenes which contain high spatial structures. However, such histograms were also obtained from dither and stare modes data of high structured background. These multi-mode histograms in the dither and stare modes are the results of platform instabilities causing the sensors FOV to drift over the background, resulting in false signal changes. Figure 7 is a sample of a multi-mode histogram reduced from stare mode data of mountains.

The Power Spectral Density (PSD) distributions reduced from the data exhibited no definite characteristics. Benign scenes for example had PSD which were essentially uniform with frequency. An example of a stare mode PSD of a benign scene is shown in Figure 8. An important conclusion to be drawn from such data statistics is that the atmospheric turbulence produces temporal changes below the sensitivity designed into the instruments.

PSDs of the reduced data generally have peaks at low frequencies and the PSD curves roll off to the system noise floor at high frequencies. Such low frequency PSD peaks of the stare data are attributed to the background spatial structure induced by platform motion into temporal signals. Natural temporal PSD, however, was observed in one instance when a cloud drifted into the instruments field during a stare data take. Figure 9 shows the increase in the low frequency PSD peak of a particular detector (#7), in which the cloud did appear, over that of a detector (#5), in which the cloud was absent. Detector #5, however, has a PSD low frequency peak attributed to the platform drift effects.

Active scenes tend to produce PSDs with steeper roll-offs. Figure 10 is the PSD reduced for a stare scene which contained solar specular point. The -2 power roll-off in the PSD curve is again the induced result of platform motion during the stare period. The impact of solar specular reflection is demonstrated in Figure 11 which is the PSD reduced from a scan across the solar specular point. The increase in PSD level and the steeper slope (higher than -2) indicates the potential problem that solar specular reflections may pose to infrared surveillance systems.

4 Background Data Conclusions

The three BAMB data flights produced results which were very consistent from flight to flight. BAMB data were gathered with the instruments (SWIR radiometer with 2 bands, and interferometer covering 2.5 - 5.5 μm) in three modes, i.e. stare, dither, and scan. Scans were made in azimuth, cross-elevation, and elevation directions.

BAMB data represent the first temporal information on earth/ atmospheric background in the SWIR and MWIR. Platform stabilities of better than 0.01 Km/sec permitted the instruments to gather temporal background from 0.01 to 10 Hz.

The following are highlights of BAMB data results:

Stare scenes where platform stability were excellent indicated that atmospheric scintillations in the SWIR and MWIR were below the sensitivities of the instruments. The conclusion is: atmospheric scintillations are below 5 watt/sr in equivalent target intensities in the SWIR.

PSDs obtained from stare data showed no distinct characteristic roll-off with frequency. Analysis of video data, taken simultaneous to the IR data, led to the conclusion that these stare mode PSDs were the results of the low platform drifts inducing background spatial structure into false temporal information. The resulting PSDs generally have peak values at low frequency and rolloff to system noise floor at high frequencies. The slopes of the curves were dependent on the PSD peaks in relation to the system noise floor, a higher peak will generate a steeper slope. The peaks were governed by the background features and the drift characteristics. Solar specular scatter, for example, would induce very high PSD peaks leading to PSD slopes approaching f^{-2} .

BAMM scan data of benign scenes produced PSDs that were apparently lower in roll-off rate than the familiar f^{-2} . An envelope characteristic of the footprint transfer function was evident in azimuth scan data. Elevation scan PSDs exhibit spatial frequency limitations in the data, caused by geometrical enlargement of the instrument footprint at high viewing angles. Solar specular scatter introduce large transient signals at the detector outputs which, when processed, produced PSDs of higher magnitude than those of benign scenes, and demonstrated PSD slopes steeper than f^{-2} .

The variability of reduced data, from detectors within an array, of the same scene indicates the important role of local background statistics. Platform motion sweeping the instruments field across these variable local background features induces variable detector outputs. When extreme features are sensed by neighboring detectors, especially in the presence of solar specular scatter, large differences in detector data are observed. These potential problems must therefore be considered in the design of future IR staring and scanning surveillance systems.

The importance of solar scatter must be stressed since BAMM data show the dominance of solar effects in active scenes. Two other observations intensify the role of solar scatter. One, the solar specular point extent appears to be wavelength dependent being larger in the R1 band and I3 band, where energy transmission is higher, than the I1 and I2 bands. Second, the view angle dependence of the specular point necessitates the consideration of the background geometry in dealing with solar scatter suppression. The specular point extent therefore could depend on both the observation wavelength as well as where the solar energy is impinging, (i.e. water, clouds, mountains, etc.) The results introduced by a cloud traversing an instruments field also indicate the importance, to a lesser extent than solar scatter, the importance of temporal clutter from clouds and therefore weather fronts, etc.

The voluminous data gathered on the three BAMM flights represent a significant step in the effort to generate a complete and useful data base of temporal earth/atmosphere backgrounds. Background information in the SWIR and MWIR were collected on terrain typical of the Gulf coast and Southwest United States. Various classes of benign and active scenes were observed from which the above conclusions were drawn.

REFERENCES

- R.E. Murphy et al, Balloon Altitude Mosaic Measurements Data Report No. 1 AFGL-TR-79-0020
- Ransom, M., 1/Lt and Siani, Robyn 2/Lt (1979) BAMM Radiometer Filter Characteristics, BAMM Report 6, AFGL-TR-6157

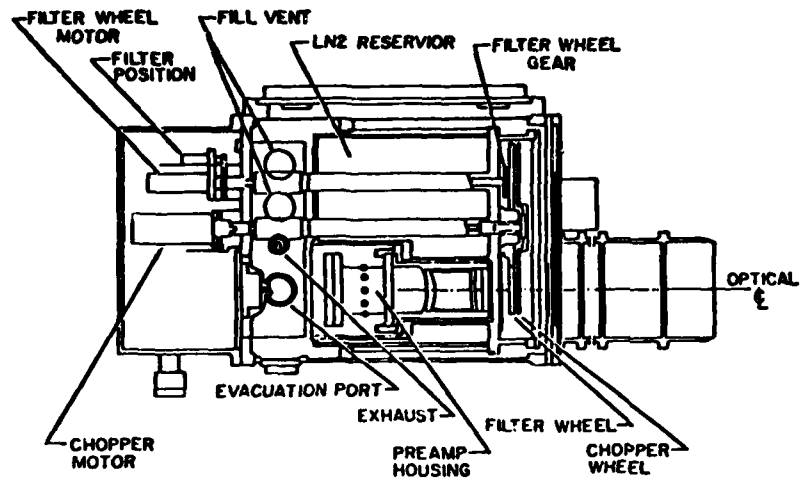
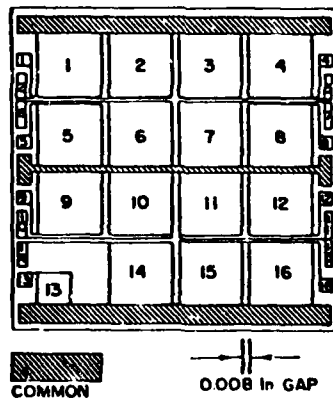


FIGURE 1 Bamm 16 DETECTOR COLD MOSAIC RADIOMETER



Viewed from in front of the instrument

FIGURE 2 LEAD SULPHIDE (PbS) MOSAIC RADIOMETER FOCAL PLANE

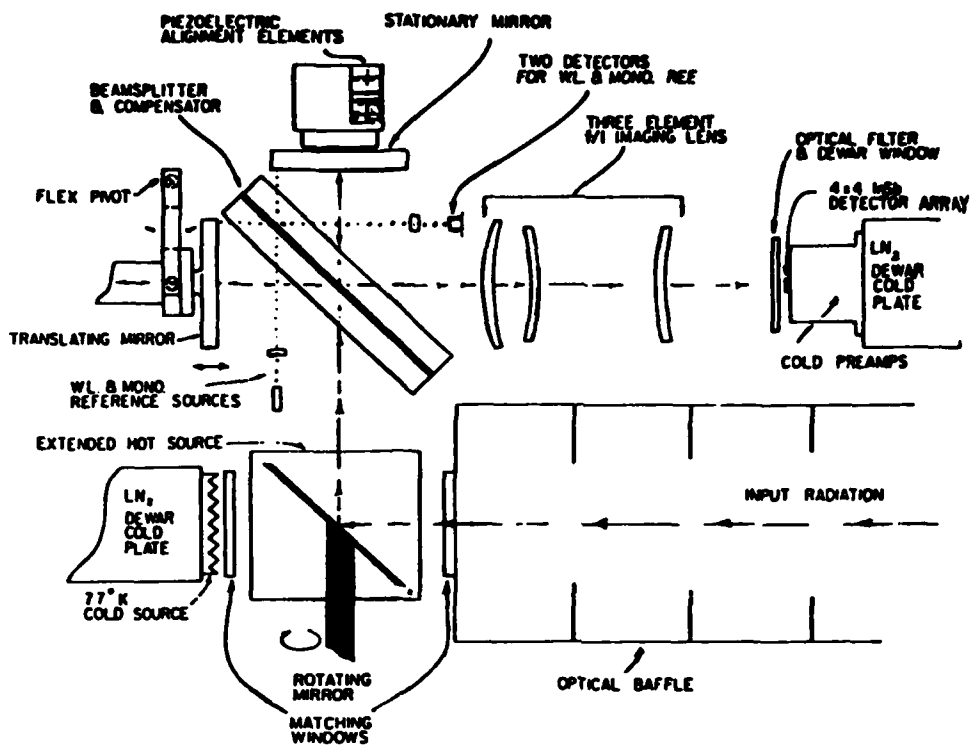


FIGURE 3 OPTICAL LAYOUT OF INTERFEROMETER SYSTEM

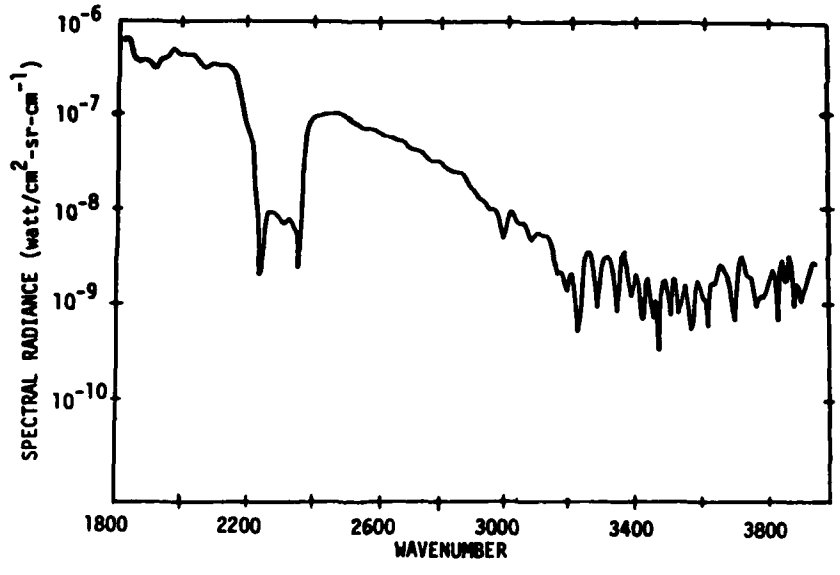


FIGURE 4 REDUCED SPECTRA OF LAND

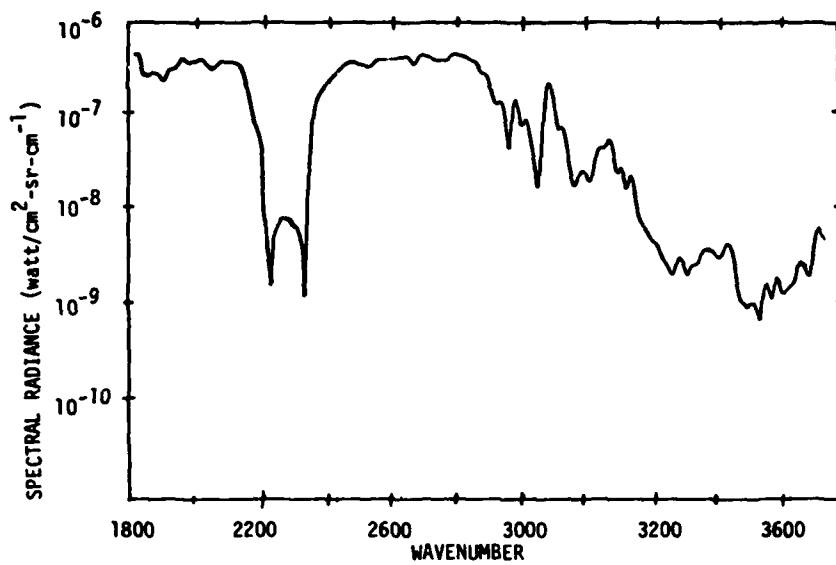


FIGURE 5 REDUCED SPECTRA OF SOLAR SPECULAR SCATTER

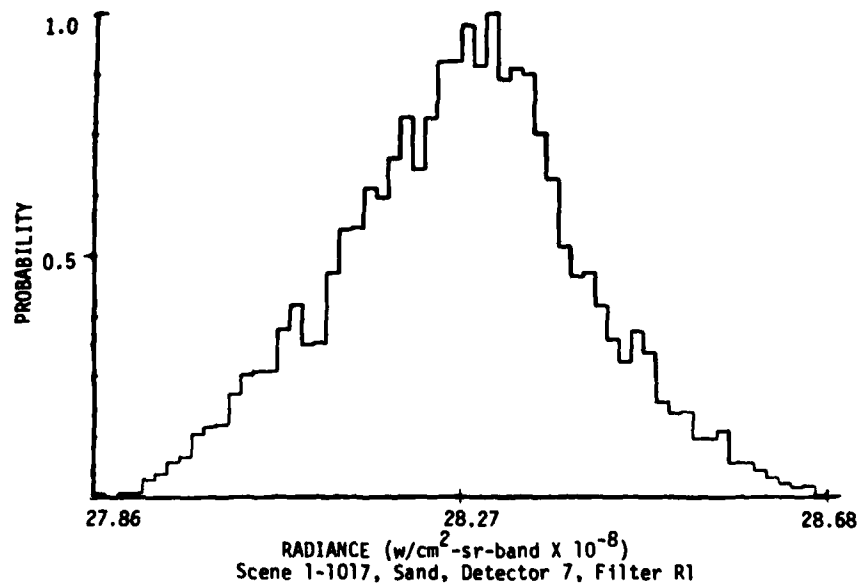


FIGURE 6 PDF OF BENIGN STARE SCENE

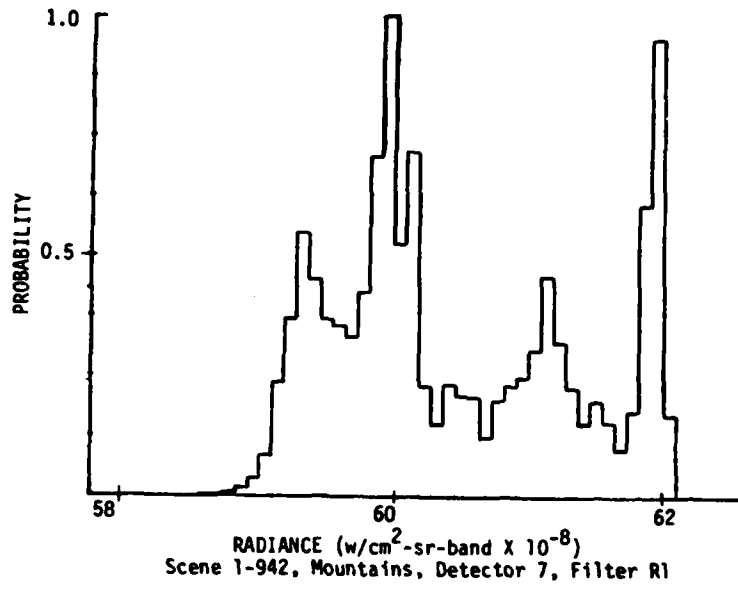


FIGURE 7 MULTI-MODE PDF OF STARE SCENE

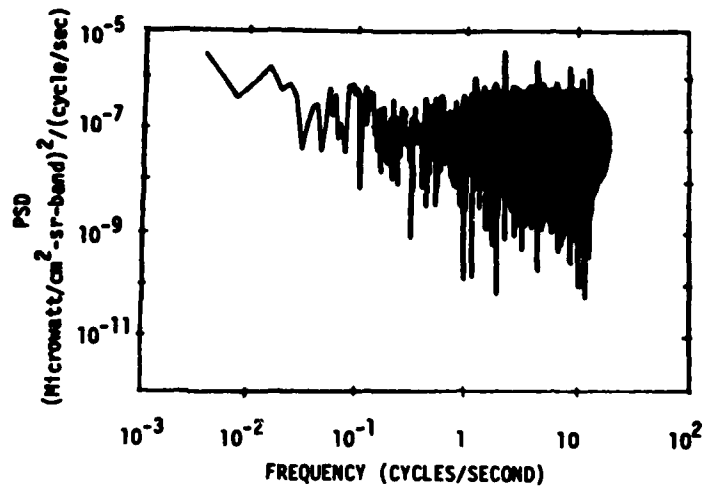


FIGURE 8 PSD OF BENIGN SCENE 2-1314 (STARE)

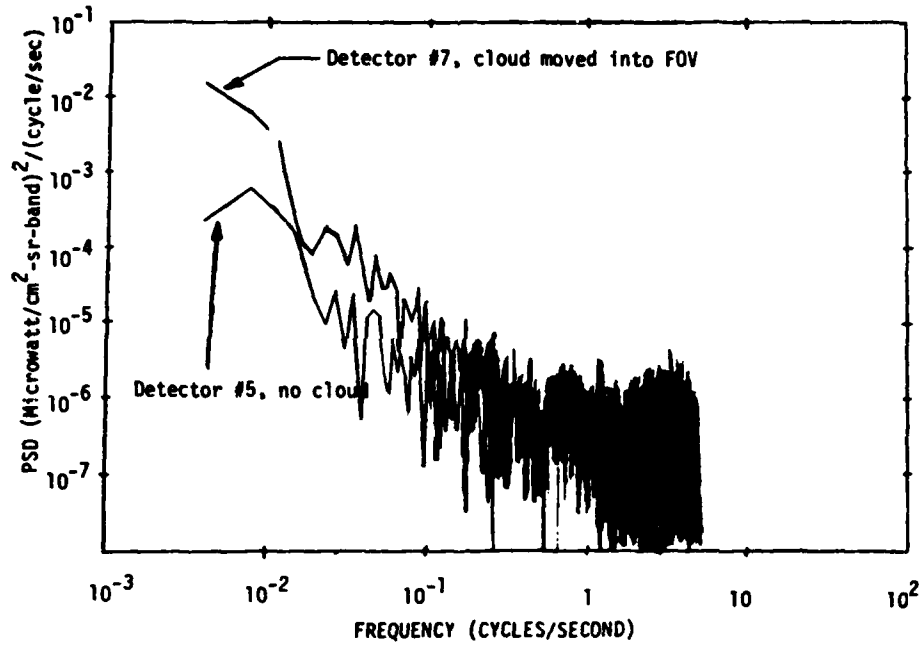


FIGURE 9 ILLUSTRATION OF TEMPORAL PSD IN SCENE 2-1317

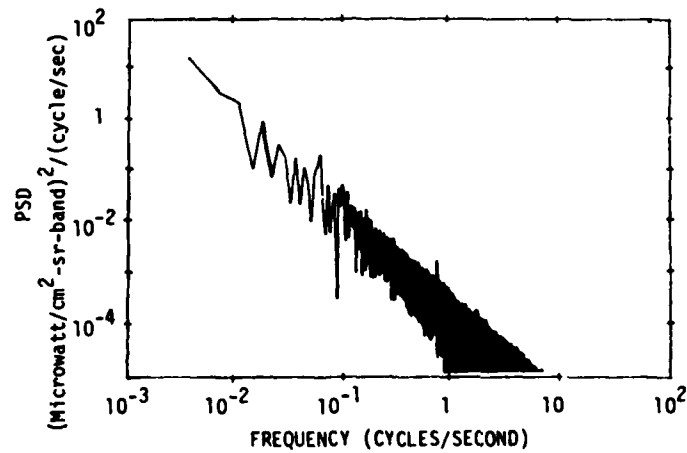


FIGURE 10 RADIOMETER PSD OF SCENE 3-1254 WITH SOLAR GLINTS

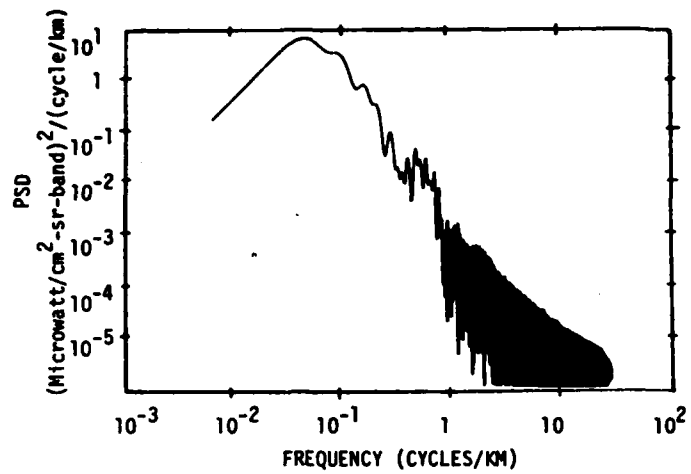


FIGURE 11 RADIOMETER PSD OF SCENE 3-1212
(SCAN ACROSS SOLAR SPECULAR POINT)

OPTICAL C_N^2 REMOTE SENSING IN THE UPPER ATMOSPHERE

BY MULTIDIMENSIONAL ANALYSIS OF STELLAR SCINTILLATION

VERNIN Jean, AZOUIT Max
 Département d'Astrophysique de l'I.M.S.P.
 Université de Nice - Parc Valrose
 E.R.A. 669 du C.N.R.S. - 06034 NICE CEDEX
 FRANCE

SUMMARY

Several geophysical parameters can be deduced from multidimensional statistical analysis of stellar scintillation. In particular, the motion of the various atmospheric turbulent layers can be determined both in magnitude and direction, in addition to their turbulent strength (as measured by C_N^2 or C_T^2) as a function of altitude.

Until now, the sequential analysis method took ~ 20 min, during which time stationarity could not be guaranteed because of intermittency. Here we present a system which is faster as a result of better use of available information. It consists of a very light-sensitive image receiver (television camera), followed by a specialized numerical computer (two-dimensional correlator) which utilizes in real time the spatial distribution of the irradiance of a large telescope entrance pupil.

This apparatus allows us to identify fast temporal variations of the vertical profiles of turbulence strength, using sounding only 10 sec apart. By tracking the double star γ Virginis, we achieve a vertical resolution of about 1.7 km. Temporal evolution of C_N^2 at a given altitude shows that the turbulence remains for several hours but it concentrates in small patches of a few kilometers length. A statistical study of these variations shows that it is possible to modelize the intermittency of the atmospheric turbulence by a time lag power law such as $\tau^{-0.31}$.

1. INTRODUCTION

Great attention has been given to atmospheric turbulence in recent years, under the increasing pressure of aviation requirements. Furthermore, improvement of meteorological forecasting, vertical transport of pollutants and problems of optical observation and communication require thorough knowledge of thermal non-homogeneities in the atmosphere.

Several measurements have been made in situ, using aircraft (Lilly and Lester, 1974) and balloons (Lawrence et al., 1970; Bufton et al., 1972; Coulman, 1973; Bartetti et al., 1974). Nevertheless, it soon became obvious that the measurements were not sufficiently continuous in time with respect to the intermittency of the turbulence. There is urgent need for an improved remote ground-based apparatus capable of ensuring continuous measurement of turbulence in space and time. In this field, the best results have been obtained through the use of radar (Atlas and Metcalf, 1970; Browning and Watkins, 1970; Konrad, 1970). Nevertheless, this method is restricted by the difficulty of achieving an absolute calibration of the temperature fluctuations, and by its poor sensitivity to turbulence. Recently, many investigations have been made on VHF doppler radars (T.E. Vanzandt et al. 1978; W.L. Ecklund et al., 1979; K.S. Gage and B.B. Balsley, 1980).

Another method is to use the effect of turbulence on the propagation of a beam coming from a source above the atmosphere. A recent theory of propagation in random media has been extensively developed (Tatarski, 1961; Lawrence and Strohbehn, 1970). Its application to stellar scintillation was begun by uni-dimensional analysis: either temporal or spatial correlation and power spectrum (Mikesell et al., 1951; Protheroe, 1961). But it is difficult to obtain vertical profiles because of the lack of precision in inverting an integral relationship. But a multi-dimensional analysis of scintillation leads to more complete and easier-to-process information. For some year, this approach has allowed us to detect turbulent layers, to determine their speed and their respective altitude (Vernin and Roddier, 1973; Rocca et al., 1974) and to use (Vernin and Roddier, 1975) spatiotemporal power spectrum or correlation techniques involving spatio-angular correlation.

More recently we constructed a fast optical ground-based apparatus (Azouit and Vernin, 1980) which processes in real time the spatial distribution of irradiance of a double star. Comparison with simultaneous in situ measurement of turbulence (Azouit et al., 1980) was satisfactory. Thus, we conclude that our apparatus in a very powerful system to monitor the turbulence between 2 and 30 km. Supplying a vertical profile every ten seconds, it may be useful for studying the intermittency of turbulent phenomena in the atmosphere.

2. PRINCIPLE

Stellar scintillation is a random function of five dimensions $I(x, \alpha, t)$ where the observer's position is x , the star coordinate α and the time t . In this paper, we will focus our attention on spatio-angular correlation to obtain vertical profiles of turbulence. But for one who is interested in achieving wind speeds, we refer to our article (Azouit and Vernin, 1980).

We have demonstrated (Vernin and Roddier, 1975) that the spatial correlation of the scintillation of a double star, measured in the direction ρ which is parallel to the component separation θ , gives a spatio-angular correlation

$$C(\rho, \theta) = \langle I(x, \alpha) I(x + \rho, \alpha + \theta) \rangle / \langle I \rangle^2 \quad (1)$$

where θ is the angular separation of the two stars. The altitudes h_i of the turbulent layers are connected to the positions ρ_i of the maxima of the function $C(\rho, \theta)$ by

$$\rho_i = \theta h_i \quad (2)$$

This is a triangulation method. The intensity of the maxima shows us the strength of the refractive index structure constant $C_N^2(h_i)$ integrated over an atmospheric thickness Δh , which is dependent on the correlation width $\Delta \rho$ by

$$\Delta h = \Delta \rho / \theta \quad (3)$$

Thus Δh is the thickness above which it is impossible to separate two layers.

Our apparatus is shown on Fig. 1. A field lens is put at the focus of a large entrance pupil making an image of the telescope pupil on the television target. We have opted for a T.V. camera for its electrical readout to ensure a real-time analysis. The faintness of observed light sources leads us to use a very sensitive tube (ISOCON tube) equipped with a one-stage image intensifier. The camera gives us 50 images per second of the 1.93 m. entrance pupil of the great telescope of the Haute-Provence Observatory (France).

On Fig. 2, we present the electronic apparatus for signal processing.

3. TWO OBSERVATIONS OF SPATIO-TEMPORAL EVOLUTION OF ATMOSPHERIC TURBULENCE

Here we present the results of two nights of observation on April 24 and 25, 1980. We used the great telescope of Haute-Provence Observatory. We tracked the double star γ Virginis whose component separation is 3.92 arcsecond allowing a vertical resolution, taking in account relation (3), of 2-5 km. The useful part of the telescope where we make our calculus is 0.52 m, thus permitting an exploration of the atmosphere up to 28 km. But during the observations, γ Virginis did not pass through the zenith and its sec z was 1.5. Instead of ranging the layers along a slanted line, we choose to project them on a vertical line dividing both the altitudes and turbulence strength by 1.5. So we explored the atmosphere up to 18 km with a vertical resolution of 1.7 km. In fact, the first few kms of atmosphere are not accessible since such low layers do not produce any scintillation.

Each night we track the double star during 3 hours. The computer was programmed to give us a vertical profile every 20 sec. So it computed and stocked on disk about 540 successive profiles. On Fig. 3, we have shown the temporal evolution of the turbulence strength C_N^2 versus altitude (Y axis) and time (X axis), for April 24, 1980. Fig. 4 refers to the night of April 25, 1980. The plot uses 16 grey levels for C_N^2 ranging from 0 to $10^{-16} \text{ m}^{-2/3}$.

On the first night, one can see three main layers at a mean altitude of 2.2, 7.2 and 12.5 kms above the observer. The lower the layer, the stronger the turbulence. The two lower layers seem to be stabler than the upper one, which shows some spottiness. One can see that the height of the layers drifts between certain limits. The middle layer varies between 6.5 and 7.9 kms, while the upper one lies between 11.5 and 13.5 kms. It is interesting to compare these altitudes with the tropopause deduced from meteorological soundings made at the Nîmes station, 110 km from the observatory. On this night there were two temperature profile inversions at 9.5 and 14.2 kms respectively. Noting that the telescope is 650 m above sea level, the two tropopauses are very close to the upper boundary of the two observed layers. Furthermore, the middle layer corresponds to a strong shear.

On the second night, one can notice a simpler situation, with only two layers at an altitude of 2.5 kms and 8.7 ± 0.9 km respectively. The turbulence strength is roughly twice that of the night before and the upper layer corresponds fairly well with the unique tropopause at 11.7 kms associated with a shear of 23 m s^{-1} between 10.3 and 12.4 kms.

On Fig. 5 for comparison, we have plotted two experimental models derived from Hufnagel (1974) and Barletti (1976). For the last one, the two curves correspond respectively to the average of many soundings and to the weaker C_N^2 . The other curves correspond to our observations averaged on 3 hours each night, showing a layered structure of the atmosphere with a permanent lack of turbulence near 5 km.

4. STATISTICAL ANALYSIS OF TEMPORAL EVOLUTION OF C_N^2

Because it is evident that the turbulence in a given layer is persistent but intermittent, we have tried to characterize it by some temporal parameter or law.

For example, on Fig 6(a), we have plotted the time evolution of C_N^2 on April 24, at an altitude of 12 km right within a turbulent layer. Each point is the estimation of C_N^2 over 20 sec. Measurements begin at 21 H T.U. and end at 0 H. On the bottom (b) we plot the same curve but smoothed by a 200 sec. sliding window.

It is obvious that the phenomenon is highly intermittent for all scales ranging between 20 sec. and 3 hours, and thus it appears to be a random process. In order to study its property, we have computed the structure function of the temporal variations of $C_N^2(t)$ for altitudes chosen inside turbulent layers :

$$D_{C_N^2}(\tau) = \langle (C_N^2(h_t, t) - C_N^2(h_t, t+\tau))^2 \rangle / 2 \langle C_N^2 \rangle^2$$

where h_t is the height of the turbulent layer, $\langle \rangle$ denotes an ensemble average and τ is a time lag. The means were calculated by averaging along the time t for each realization $C_N^2(h_t, t)$ and further by averaging on 8 turbulent layers distributed over 6 nights, representing 12 hours of observations.

Fig. 7 shows the computed curve $D_{C_N^2}(\tau)$ versus the lag τ in a log-log plane. The dots represent the experimental points while the straight line is the best fit if we neglect the last two points. On the horizontal scale, the upper graduation is the time lag and the lower is an approximate length deduced from the mean velocity of the 8 layers, if we assume a frozen turbulence structure.

We can thus infer that $D_{C_N^2}(\tau)$ follows a power law such as :

$$D_{C_N^2}(\tau) = 0.018 \tau^{0.31}$$

with $10 \text{ s} < \tau < 10 \text{ min}$

We must compare our power law with the time variability of winds over lags τ ranging from a few minutes to several hours. Gage and Clark, (1978), found a power of $1/3$ very close to our 0.31 . They conclude that since the $\tau^{1/3}$ power law for lag variability is consistent with a $k^{-5/3}$ inertial range, their observations provide evidence for a mesoscale inertial range.

5. CONCLUSION

We have extended our study of stellar scintillation to a two-dimensional analysis through the use of a large telescope, a surface photoelectric image receiver and a specialized two-dimensional correlator. This improved method allows us to investigate the turbulence strength C_N^2 both in altitude and in time with a resolution of 1.7 km and 10 sec. respectively.

All our observations show a layered atmospheric turbulence as already proved by many other techniques and authors. Our ground-based optical apparatus is, in many respects, comparable to the radars. For example, it is possible to follow the time variations of turbulence strength over periods ranging from 10 sec. to 3 hours simultaneously for several altitudes. If we average our profiles over a whole night, we are very close to experimental models.

At a given altitude, the time variations of C_N^2 appear to be a random process with energy at all scales. A statistical study shows that the structure function of $C_N^2(t)$ follows a power law for time lag. The best fit gives a time lag dependence satisfying $\tau^{0.31}$, for τ ranging from 10 sec to 10 min . We have thus a powerful tool to study the intermittency over the outer scale (mesoscale).

Since our technique uses a narrow light beam passing through the atmosphere without volume integration it seems that we should be able to begin a study of intermittency in the inner scale. For instance, the scatter of adjacent points in Fig. 4 is not due to a lack of precision, but probably to the spotiness of the small scales of order of 10 cm . This hypothesis is under investigation.

ACKNOWLEDGMENTS

We are indebted to the Observatory of Haute-Provence for the use of the 1.93 m telescope. We wish to thank S. Niquet for her help to correct our English translation.

REFERENCES

- ATLAS D. and METCALF J.I., 1970, "The birth of CAT and microscale turbulence", *J. Atmos. Sci.*, **27**, p. 903-913
- AZOUIT M. and VERNIN J., 1980, "Remote investigation of tropospheric turbulence by two-dimensional analysis of stellar scintillation", *J. Atmos. Sci.*, **37**, p. 1550-1557.
- AZOUIT M., VERNIN J., BARLETTI R., CEPPATELLI G., RIGHINI A. and SPERONI N., 1980, "Remote sensing of atmospheric turbulence by means of a fast optical method : A comparison with simultaneous in situ measurements" *J. Appl. Meteorol.*, **19**, p. 834-838.
- BARLETTI R., CEPPATELLI G., MORODER E., PATERNO L. and RIGHINI A., 1974, "A vertical profile of turbulence in the Atlantic air mass, measured by balloon-borne radiosondes", *J. Geophys. Res.*, **79**, p. 4545-4549.
- BARLETTI R., CEPPATELLI G., PATERNO L., RIGHINI A. and SPERONI N., 1976, "Mean vertical profile of atmospheric turbulence relevant for astronomical seeing", *J. Opt. Soc. Am.*, **66**, p. 1380-1383.
- BROWNING K.A. and WATKINS C.D., 1970, "Observations of clear air turbulence by high-power radar", *Nature*, **227**, p. 260-263.
- BUFTON J.L., MINOTT P.O., FITZMAURICE M.W. and TITTERTON P.J., 1972, "Measurements of turbulence profiles in the troposphere", *J. Opt. Soc. Am.*, **62**, p. 1068.
- COULMAN C.E., 1973, "Vertical profiles of small-scale temperature structure in the atmosphere", *Bound.-Layer Meteorol.*, **4**, p. 169.
- ECKLUND W.L., CARTER D.A. and BALSLEY B.B., 1979, "Continuous measurement of upper atmospheric winds and turbulence using a VHF Doppler radar : preliminary results", *J. Atmos. and Terrest. Physics*, **41**, p. 983-994.
- GAGE K.S. and CLARKE W.L., 1978, "Mesoscale variability of jet stream winds observed by the Sunset VHF doppler radar", *J. Appl. Meteorol.*, **17**, p. 1412-1416.
- GAGE K.S. and BALSLEY B.B., 1980, "On the scattering and reflection mechanisms contributing to clear air radar echoes from the troposphere, stratosphere and mesosphere", *Radio science*, **15**, p. 243-257.
- HUFNAGEL R.E., 1974, "Variations of atmospheric turbulence" in Digest of topical meeting on optical propagation through turbulence, Optical Society of America, Washington D.C.
- KONRAD T.G., 1970, "The dynamics of the convective process in clear air as seen by radar", *J. Atmos. Sci.*, **27**, p. 1138-1147.
- LAWRENCE R.S. and STROHBEHN J.W., 1970, "A survey of clear air propagation effects relevant to optical communications", *Proc. I.E.E.E.*, **58**, p. 1523-1545.
- LAWRENCE R.S., OCHS G.R. and CLIFFORD S.F., 1970, "Measurements of atmospheric turbulence relevant to optical propagation", *J. Opt. Soc. Am.*, **60**, p. 826.
- LEE R.W. and HARP J.C., 1969, "Weak scattering in random media, with applications to remote probing", *Proc. I.E.E.E.*, **57**, p. 375-405.
- LILLY D.K. and LESTER P.F., 1974, "Waves and turbulence in the stratosphere", *J. Atmos. Sci.*, **31**, p. 800-812.
- MIKESSELL A.H., HOAG A.A. and HALL J.S., 1951, "The scintillation of starlight", *J. Opt. Soc. Am.*, **41**, p. 689-695.
- PROTHEROE W.M., 1961 : "Stellar scintillation", *Science*, **134**, p. 1593-1599.
- ROCCA A., RODDIER F. and VERNIN J., 1974, "Detection of atmospheric turbulent layers by spatio-temporal and spatio-angular correlation measurements of stellar-light scintillation", *J. Opt. Soc. Am.*, **64**, p. 1000-1004

- TATARSKI V.I., 1961, "Wave propagation in a turbulent medium. Dover
- VANZANDT T.E., GREEN J.L., GAGE K.S. and CLARK W.L., 1978, "Vertical profiles of refractivity turbulence structure constant : Comparison of observations by the Sunset Radar with a new theoretical model", Radio Science, 13, p. 819-829.
- VERNIN J. and RODDIER F., 1973, "Experimental determination of two-dimensional spatio-temporal power spectra of stellar light scintillation. Evidence for a multilayer structure of the air turbulence in the upper troposphere", J. Opt. Soc. Am., 63, p. 270-273.
- VERNIN J. and RODDIER F., 1975, "Détection au sol de la turbulence stratosphérique, par intercorrélation spatio-angulaire de la scintillation stellaire", C.R. Acad. Sci. Paris, 280, p. 463-465.

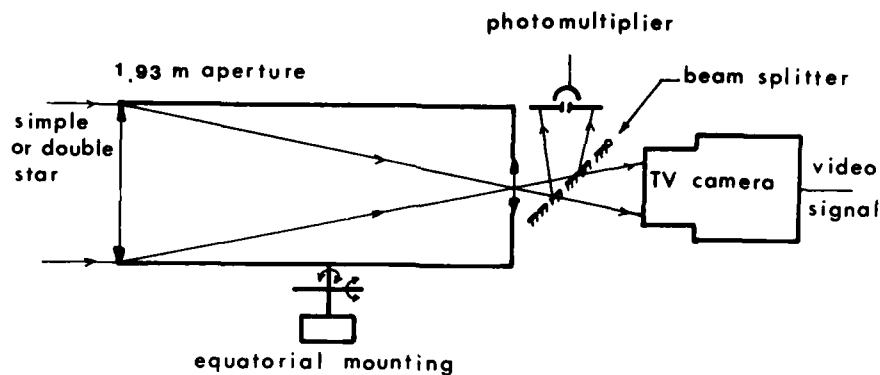


Fig. 1 - Optical system

The 1.93 meter entrance pupil of the large telescope of the Haute Provence Observatory is imaged onto the target of a very light-sensitive T.V. Camera

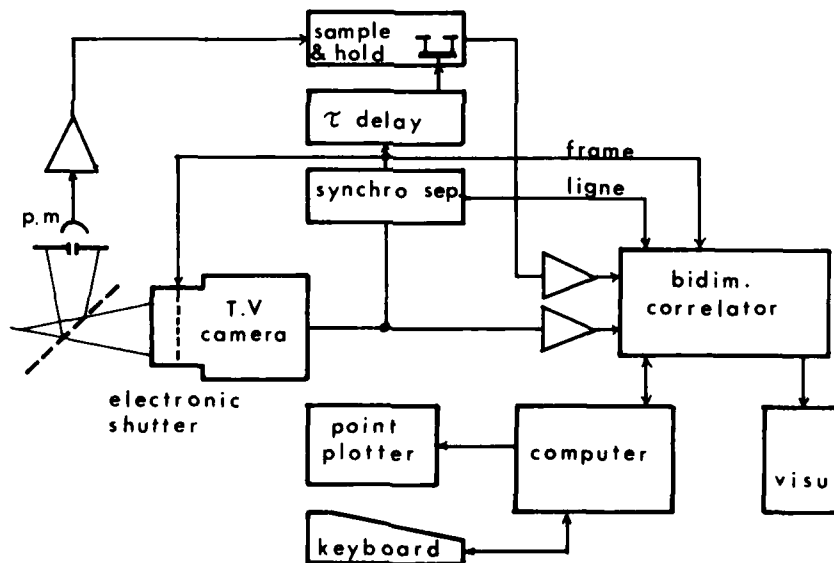


Fig. 2 - Schematic diagram of the electronic apparatus

The two-dimensional correlator calculates, in real time, the correlation function of the irradiance pattern scanned on the T.V. screen. After 500 images are processed, the correlation is fed into the computer which translates the correlation into a vertical profile of C_N^2 . Every 10 or 20 sec. a new sounding is added on a video output screen.



Fig. 3 - Photograph of the temporal evolution of vertical profiles of $C_N^2(h,t)$. Time is along the x-axis, each profile is computed 20 sec. apart and the whole observation takes 3 hours. The grey scale ranges from 0 to $10^{-16} \text{ m}^{-2/3}$ sampled on 16 levels. This picture evolves in real-time at each sounding. One can see three main turbulent layers at an altitude of 2.2, 7.2 and 12.5 kms. All "scales" are present in each layer. (Night of April 24, 1980).

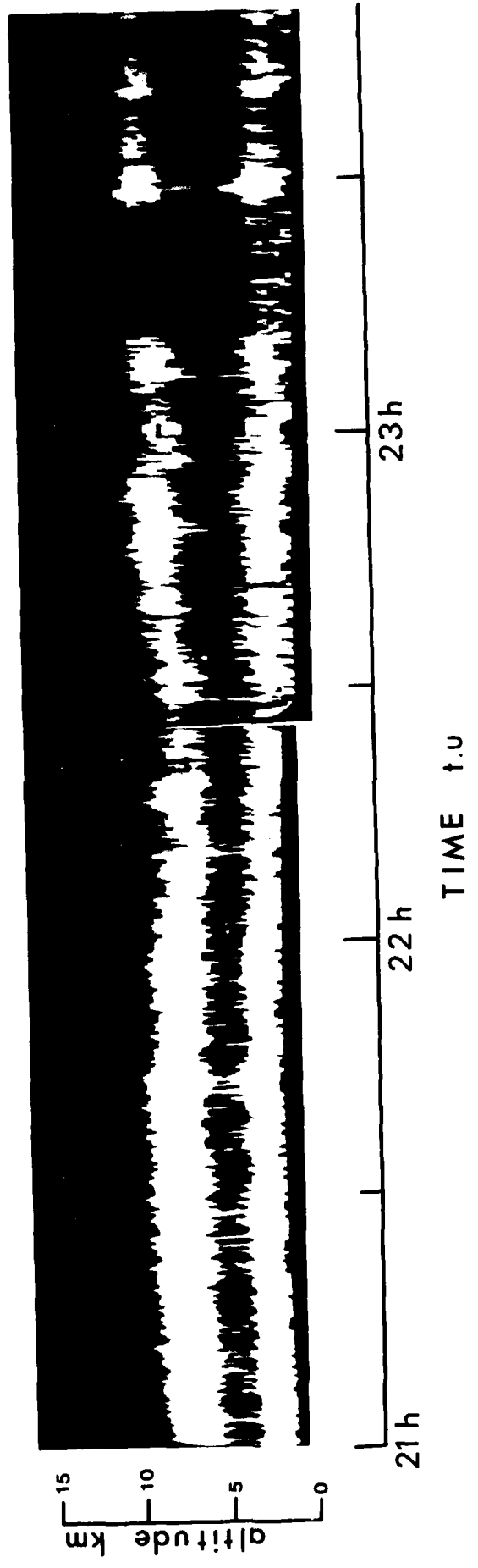


Fig. 4 - Same as Fig. 3 for the night of April 25, 1980. On this picture only two well-defined structures are recognizable near 2.5 and 8.7 kms.

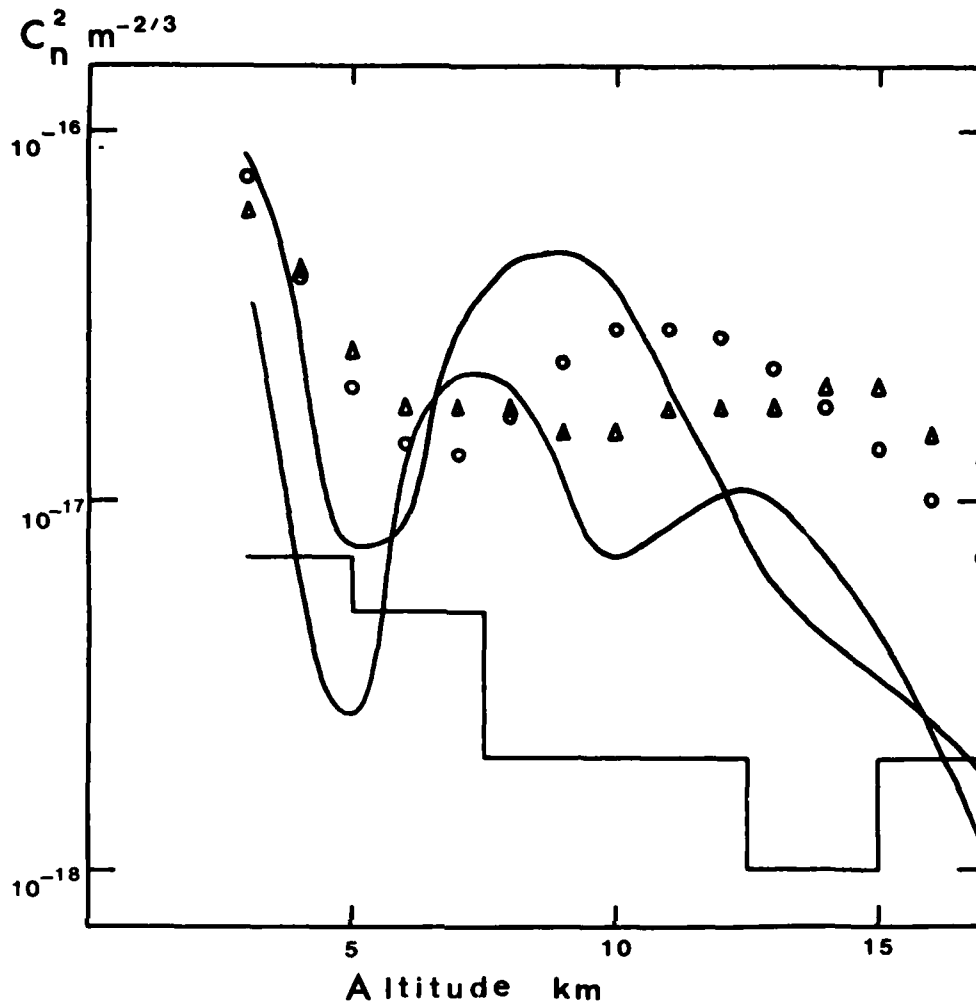


Fig. 5 - Plot on a semi-log plane of averaged C_N^2 profile VS altitude. The two curves, circles and triangles are the experimental models of Hufnagel and Barletti respectively. The broken line represents the weakest turbulence ever detected by Barletti. The two smooth lines refer to our observations averaged over a night for April 24 and 25, 1980.

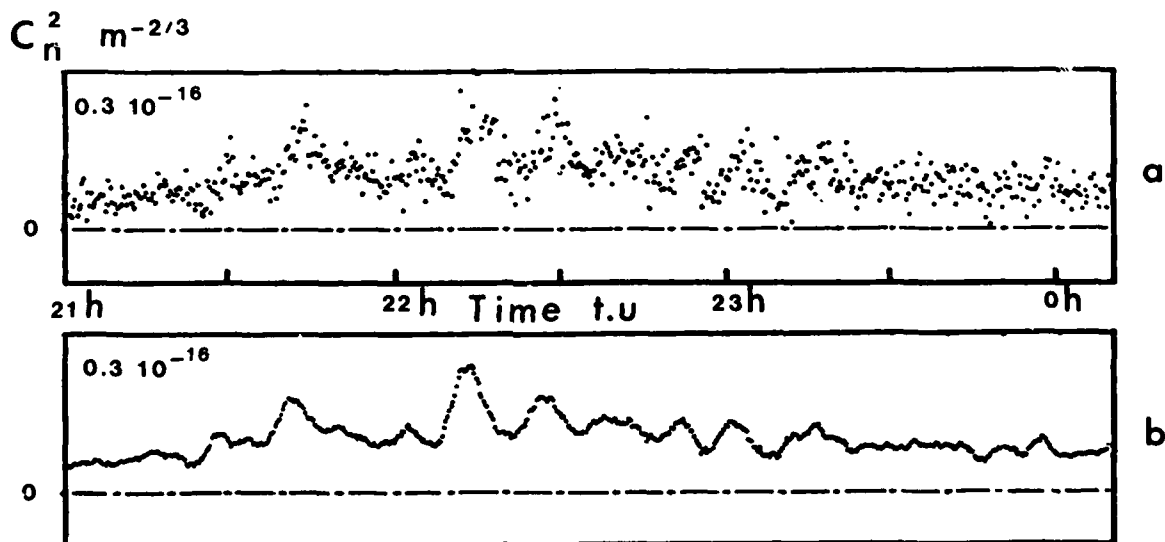


Fig. 6 - (a) Temporal evolution of C_N^2 within the 12 km high turbulent layer on April 24, 1980. Each point is the estimation of C_N^2 for 20 sec.
(b) Same curve as (a) but smoothed by a 200 sec. sliding window.

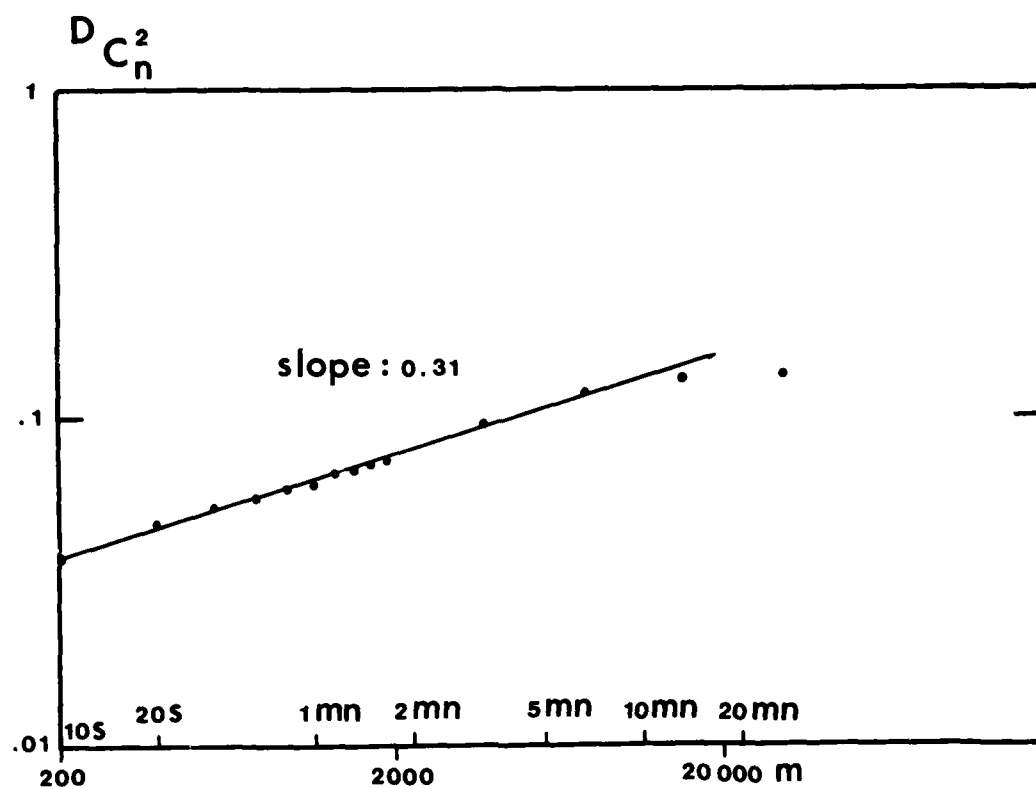


Fig. 7 -Time lag variability of C_N^2 at many altitudes within which we detect turbulence. The X-axis refers either to time lag τ or to horizontal scale if we assume a frozen turbulent structure. On Y-axis is the structure function $D_{C_N^2}(\tau)$ normalized by the averaged quantity $\langle C_N^2 \rangle^2$. Dots are the experimental results while the straight line is the best fit with a slope of 0.31.

INFRARED RADIANCE MODEL OF THE UPPER ATMOSPHERE

T.C. Degges
H.J.P. Smith

Visidyne, Inc.
5 Corporate Place
South Bedford Street
Burlington, MA 01803

A knowledge of the natural infrared radiance originating in the earth's upper atmosphere is of interest for systems design, military surveillance and the advancement of knowledge about physical processes in the upper atmosphere. A physical model to predict infrared emission has been implemented in a computer program that computes infrared radiances for an earth's limb viewing geometry. The nominal spectral region covered lies between 2.5 and 25 micrometers and emphasis is placed on radiation originating at altitudes between 50 and 300 km. The basic result from the model is the calculation of the populations of vibrational states of the important infrared emitters such as carbon dioxide, water vapor, ozone and nitric oxide. In the troposphere and lower stratosphere, molecular collisions are rapid enough to maintain vibrational populations in kinetic equilibrium. At higher altitudes, radiative de-excitation may be faster than collisional or radiative excitation, and a non-equilibrium vibrational population results. The model uses collisional excitation and de-excitation rates obtained from published data when possible and balances collisional processes with absorption and emission of infrared radiation. The equations of radiative transfer are solved at each level to include absorption of radiation from the earth's surface, all other atmospheric levels and the sun. Some collisional rates have not yet been measured. Some of these have been estimated by comparison with known rates and some have been approximated by comparing model calculations with rocket probe measurements.

Observations of the infrared limb have been made from a rocket platform in the Air Force Geophysics Laboratory Spectral Infrared Rocket Experiment (SPIRE experiment). We have inverted some of this data using a statistical method. First a model for the emission process must be assumed. We also assume that the emitting species has a uniform vertical profile in the region of the limb scans. With these assumptions, a best fit statistical analysis of the observed limb radiance profile is made to derive a profile of the radiating species. We use both a non-linear least squares and a non-linear minimum chi-square best fit criterion. We will present examples of profiles obtained from the SPIRE data by this method, and discuss the accuracy and sources of uncertainty in the analysis.

1.0 Introduction

The research reported here has had as its major objective the continued development and improvement of an infrared radiance model of the atmosphere. Such models are designed to simulate the radiative properties of the atmosphere

to provide predictions for Air Force and other Department of Defense design and surveillance programs. Comparison with available experimental measurements provides greater understanding of the atmosphere and serves to check the adequacy of the models. This paper summarizes work done since the report of Degges and Smith (Reference 1).

The goal of this effort has been the further development of a computer program to simulate the natural infrared radiance background of the earth's upper atmosphere. The nominal spectral region under study lies between 2.5 and 25 micrometers and emphasis is placed on radiation originating at altitudes between 60 and 500 kilometers. The general problem area is of interest for systems design, military surveillance and the advancement of knowledge about physical processes in the upper atmosphere. The immediate application of this work is to aid in developing optimum infrared background measurements programs and in interpreting the results of such measurements.

In the troposphere and lower stratosphere, collisional processes are rapid enough to control the population of vibrational levels. Above 30 to 50 km, however, collisional excitation becomes less efficient and radiative processes become important. The combined effects of collisional and radiative processes must therefore be considered. Below an altitude of about 90 km molecular nitrogen and oxygen are the most important collision partners. Above that altitude, atomic oxygen becomes important, both in exciting nitric oxide and in determining molecular oxygen and nitrogen vibrational temperatures.

2.0 Physical Processes and Modeling

The physical processes and assumptions used in developing a model for transport of infrared radiation in the upper atmosphere are sketched below, beginning with a general overview.

Figure 1 illustrates the geometry employed in the current modeling study. A molecule at Point P absorbs radiation from three sources; (1) a collimated beam from the sun, (2) a lower boundary which radiates as a black body, and (3) other molecules between the lower and upper boundaries. Radiative transfer functions have been derived to compute the effects of absorption of radiation by other molecules between each of the sources and the molecule at Point P. At the same time, each molecule is colliding with other molecules. These collisions excite and de-excite vibrational and rotational levels of the molecule and supplement or compete with radiational excitation and de-excitation.

In the absence of collisional excitation and de-excitation, the simplest integral equation that may be written to describe radiative transport in a finite plane parallel atmosphere is

$$J(\tau) = \frac{1}{2} \int_0^{\tau} \max k_1(|\tau - t|) J(t) dt + S(\tau) \quad (1)$$

This equation assumes that there is only one radiative transition involved and that the radiation emitted by a molecule after absorption is independent of the direction of incidence. Here τ is a measure of the optical path length in the vertical direction. $J(\tau)$ is a dimensionless measure of the population of the upper, emitting molecular state. $K_1(\tau)$ is the radiative transfer function which accounts for absorption of radiation emitted by molecules at a vertical path length τ distant from the absorbing molecule. $S(\tau)$ is an auxiliary function which includes the effects of radiation originating outside the atmosphere. If there is only a black body source located at the lower boundary from which optical path length is measured ($\tau = 0$ at the lower boundary) then

$$S(\tau) = -N_0 K_2(\tau) \quad (2)$$

Here N_0 is the radiance of the lower boundary in arbitrary units such as watts $\text{cm}^{-2}\text{-ster}^{-1}$ or the spectral radiance in units such as watts $\text{cm}^{-2} \text{cm}^{-2}\text{-ster}^{-1}$ (wavelength interval) $^{-1}$.

In the gray or spectrally independent case, when Equation (2) holds, the kernel function $K_1(\tau)$ is the first exponential integral $E_1(\tau)$ and the function $K_2(\tau)$ describing absorption from the black body source is the second exponential integral $E_2(\tau)$. These functions are described in detail in such works as Kourganoff (Reference 2).

When a collimated beam of light is incident on the top of the atmosphere, another term must be added to the function $S(\tau)$ in Equations (1) and (2) to account for this. If the flux is incident at a zenith angle with cosine μ and has an intensity in arbitrary units such as πF watts cm^{-2} normal to its direction, the term added to $S(t)$ has the form $FM_1[\tau_{\max} - \tau]/\mu$. In the gray case, $M_1(\tau)$ is simply $\exp(-\tau)$. The corresponding functions for individual spectral lines and bands will be described after a closer look at the interaction of electromagnetic radiation with a single molecule.

In developing a realistic model of the interaction of radiation with matter, it is necessary to take into account the details of absorption. Line shape must be considered because it determines the amount of radiation escaping from an optically thick layer of gas. Thus, for a large optical thickness (greater than a magnitude of about 10), the total emission from an isolated spectral line with Lorentz shape is proportional to the square root of the optical thickness, while that from a line with Doppler shape is proportional to the square root of the logarithm of the optical thickness. In addition, absorption of radiation emitted at one place in the gas by a molecule at another location cannot be computed without knowledge of the line shape.

At high altitudes, the profile of the spectral absorption curve of an individual line in a variation-rotation band is predominantly due to velocity or Doppler broadening. Kuhn and London (Reference 3), who investigated the heat budget of the atmosphere between 30 and 110 km, reported that radiative transfer calculations require the use of the Voigt profile (including both collisional and Doppler broadening) at altitudes between 20 and 70 km. However, the Doppler profile is adequate at higher altitudes where the Doppler shape is the largest contributor to line broadening.

The radiative transfer functions required to treat transfer of resonance radiation in a single line are well known for the Voigt profile and its two limiting cases, the Doppler and Lorentz profiles. Avrett and Hummer (Reference 4) review the properties of these functions, giving series expansions for small values of optical thickness.

For a single line with Voigt profile, the radiative transfer functions for use in Equation (1) are

$$K_1(a, \tau) = \frac{1}{\pi} \int_{-\infty}^{\infty} [f(a, x)]^2 E_1[\tau f(a, x)] dx \quad (3)$$

$$K_2(a, \tau) = \frac{1}{\pi} \int_{-\infty}^{\infty} f(a, x) E_2[\tau f(a, x)] dx \quad (4a)$$

$$= \tau \int_{\tau}^{\infty} M_1(t) \frac{dt}{t^2} \quad (4b)$$

and

$$M_1(a, \tau) = \frac{1}{\pi} \int_{-\infty}^{\infty} f(a, x) e^{-\tau f(a, x)} dx \quad (5)$$

In extending this treatment of radiative transfer to a vibration-rotation band, in addition to assuming that each line has the same Voigt profile shape, the following assumptions are made:

1. Rotational levels within a vibrational level remain in equilibrium with the translational temperature.
2. There is a complete redistribution of frequency within a single line following absorption of radiation.
3. There is complete redistribution of absorbed energy among all rotational levels.
4. Line strengths are used as if each line were at the band center, neglecting wavelength variation across a band.
5. There is no overlap of adjacent lines.
6. Temperature variations at different levels do not affect the radiative transfer.

If g_j is the fraction of total band strength associated with a single line, so that $\sum_J g_j = 1$ (6)

and the sum over J may involve complete summation over rotational quantum number for two or more branches. The optical thickness at the center of a single line will be given by τg_j , where τ is the optical thickness that would result if the entire band strength were in a single line. Then the radiative transfer functions for a band may be defined as functions of radiative transfer functions for a single line, as follows:

$$K_1^b(a, \tau) = \sum_J g_j^2 K_1(a, \tau g_j) \quad (7)$$

$$K_2^b(a, \tau) = \sum_J g_j K_2(a, \tau g_j) \quad (8)$$

$$M_1^b(a, \tau) = \sum_J g_j M_1(a, \tau g_j) \quad (9)$$

In practice, rather than formally integrate a modified Equation (1) including a τ dependent λ to account for collisional de-excitation, and an additional source term to account for collisional excitation, the computer program sets an initial vibrational population at each altitude and computes the total radiative excitation at each level which results from the sum of radiation from the earth and lower atmosphere, the sun and other levels in the atmosphere.

The band functions are used to determine the effects of absorption between a molecule at a given altitude and the various sources of radiation affecting a given band in the following way. The vertical optical paths to the lower boundary and to each level in the atmosphere are computed and, for daytime conditions, the optical path to the assumed top of the atmosphere in the direction of the sun using the secant of the solar zenith angle as a multiple. The effective radiation from the lower boundary is determined by multiplying the surface radiancy by the appropriate K_2^b function. The effective radiation from the other levels of the atmosphere may be obtained by integrating the produce of emission at each level and the band function K_1 ,

$$S_{atm}(t_p) = \int_0^{\tau_p} J(t_p - t) K_1^b(a, \tau_p - t) dt + \int_{\tau_p}^{\tau} J(t - \tau_p) K_1^b(a, t - \tau_p) dt \quad (10)$$

Numerical integration is avoided for contributions from nearby atmospheric layers by assuming that the relative vibrational population between two points varies linearly with optical thickness. The integral relations between the band are used in the form

$$\begin{aligned}
 \int_{\tau_1}^{\tau_2} J(t) k_1^b(a, t) dt &= \int_{\tau_1}^{\tau_2} (A + Bt) k_1^b(a, t) dt \\
 &= J(\tau_1) k_2^b(a, \tau_1) - J(\tau_2) k_2^b(a, \tau_2) \\
 &\quad + \frac{J(\tau_2) - J(\tau_1)}{\tau_2 - \tau_1} k_2^b(a, \tau_1)
 \end{aligned} \tag{11}$$

where

$$k_3^b(a, \tau) = \int_0^{\tau} k_2^b(a, t) dt \tag{12}$$

At large optical thicknesses, where the contribution to excitation is small, the radiative transfer functions used in the programs are not accurate enough for the subtractions in Equation (11) to yield meaningful results and Equation (10) is evaluated by the trapezoidal rule.

Vibrational populations are determined by balancing collisional and radiative excitation and de-excitation rates. The new vibrational populations are used to compute a second approximation to the radiation field. The iterative process is repeated between two and ten times, depending on the molecular vibration-rotation transition involved.

Total band intensities at an observation point inside or outside the atmosphere are computed by determining the optical path from each level to the observation point and integrating the product of local emission rate and the band function $M_1^b(a, \tau)$. This integration also uses a semi-analytical form for atmospheric layers close to the assumed detector location with the relation

$$\begin{aligned}
 \int_{\tau_1}^{\tau_2} J(t) M_1^b(a, t) dt &= \int_{\tau_1}^{\tau_2} (A + Bt) M_1^b(a, t) dt \\
 &= J(\tau_1) L^b(a, \tau_1) - J(\tau_2) L^b(a, \tau_2) \\
 &\quad + \frac{J(\tau_2) - J(\tau_1)}{\tau_2 - \tau_1} \left[L_1^b(a, \tau_1) - L_1^b(a, \tau_2) \right]
 \end{aligned} \tag{13}$$

where

$$L^b(a, \tau) = \int_0^{\tau} M_1^b(a, t) dt \tag{14}$$

and

$$L_1^b(a, \tau) = \int_0^{\tau} L^b(a, t) dt \tag{15}$$

Again, trapezoidal integration is used for layers far away from the detector.

The spectral distribution of radiation is determined by finding a mean effective temperature and line-of-sight column density for the radiating molecules, computing intensity for each line in the band with the line function $L(a, \tau)$, summing the line emission rates and scaling each line emission rate so that the total band intensity is obtained.

The above analysis has been presented for the general Voigt profile. Actual use of the radiative transfer functions in the programs has been restricted to the Doppler profile. This restriction is adequate for the water vapor and ozone bands which in the concentrations used in the program have a maximum vertical optical thickness at line center less than three. For limb viewing of carbon dioxide bands the Voigt profile should be used. Efforts to find a general way of setting up the radiative transfer functions to use a Voigt profile that varies with altitude have not been successful. Exploratory calculations show that the computed radiance values for strongest bands at a tangent height of 60 kilometers may be in error by 20 - 50 percent. In view of the uncertainties in chemical abundances, this error is not felt to be serious.

The same radiative transfer functions have been used for the non-linear molecules as were used for the linear molecules. The match between radiative transfer functions has been made by determining a single "effective" rotational constant for the non-linear tri-atomic molecules. This was done by computing actual radiative transfer functions for a limited range of optical thicknesses adequate to cover that need in the model. The computed functions were compared with those for the linear molecules and the effective rotational constant need to produce an approximate match at optical thickness at line center of about two was used.

3.0 Results From Computational Model

The high altitude spectral radiance program can produce spectral radiance profiles for wavelengths between 2.5 and 25 micrometers or between 400 and 4000 wave numbers. Results are presented here based on estimated abundance profiles of the four species CO_2 , H_2O , O_3 and NO . The temperature and pressure profiles used were taken from the U.S. Atmosphere, 1976 (Reference 5). Upwelling terrestrial radiances are assumed to be those corresponding to a black body source at the ground level temperature.

Representative limb viewing radiance profiles are shown in Figures 2 and 3. These results are based on the concentration profiles of Reference 1, with number densities of N_2 , O_2 and O from Reference 5. Comparison of day and night profiles for a given tangent height shows that the low energy (small wave number and long wavelength) band radiances do not vary appreciably during the day. The high altitude high energy bands, however, do vary in intensity by as much as two orders of magnitude as a result of resonant and fluorescent emission following absorption of solar radiation. This is shown clearly in the CO_2 4.3 micrometer bands and in the water vapor complex at 2.7 micrometers.

For some purposes, it may be more convenient to have available the total radiance of an individual band rather than the spectrum of the region where the band is located. This may aid in making allowances for species abundances different from those assumed in a computation or in assigning an experimentally observed radiance value to one species rather than another.

Figures 4 and 5 show night and day limb radiance values for CO₂ bands. Note particularly the seven bands of the CO₂ 15 micrometer band complex, the 4.3 micrometer ν_3 band and the two fluorescent bands originating from the ν_3 state, the 10.42 micrometer 000-10001 band and the 9.60 micrometer 00011. The 15 micrometer band radiances vary little between day and night. During the day, however, the radiance of the 4.3 micrometer band rises from its night value of between 10^{-9} and 10^{-8} watts/cm²-ster to a value of between 10^{-8} and 2×10^{-7} watts/cm²-ster. This band is thick in the limb viewing geometry, and most of the increase is due to increased vibrational temperatures at altitudes above 90 km. The 10.41 and 9.60 micrometer bands, which have much lower optical thickness, gives a better indication of the altitudes at which the solar excitation is important. The 60 km value is about 4×10^{-8} watts/cm²-ster day or night.

A limited amount of data from the ICECAP Program is available for comparison with the results of the radiance computer program. Figure 6 compares peak spectral radiance values for the 15 micrometer band measured by Rogers, et al. (Reference 6) with those computed by the present model and concentrations of Reference 1 (Model I), and (Model II) using the U.S. Standard Atmosphere, 1962 (Reference 7) temperature profile with 180 K mesopause temperature and uniform mixing of CO₂. The differences are due principally to differing temperature profiles and assumed CO₂ mixing ratios.

Figure 7 compares the radiance model prediction with the data of Rogers, et al. (Reference 6), this time for the ozone ν_3 band. The amount of ozone used for the calculation is optically thin in the upward direction, and doubling the amount would double the computed radiance. The plotted experimental data agrees with the measurement to within a factor of two. The shape of the observed radiance curve supports the accuracy of the ozone measurements of Hays and Roble (Reference 8) and their interpretation that their observed ultraviolet absorption is due to ozone and not a mesospheric aerosol layer. Figure 7, as well as Figure 6, shows that at least some results of the radiance program are in agreement with measured radiances, and suggests that with more accurate data on atmospheric temperature and composition, observations will either confirm model predictions or show how modeling algorithms must be modified. Rogers, et al. (Reference 0) have used this model to determine mesospheric water vapor composition.

Limb viewing geometry from a rocket or satellite offers advantages for inversion techniques. A principal advantage arises in the narrowing of the individual rotational linewidths as the altitude increases. This decrease in linewidth together with temperature variations causes the band structures to narrow as well and thus provides for gaps in the IR spectra of the major species in which the spectra of minor species may be observed. A case in point is provided by the AFGL SPIRE experiment in which a rocket instrumented with CVF spectrometers was launched at local dawn from Poker Flat, Alaska. Although the 6 μ m band of H₂O predominates at lower altitudes, the ν_3 band of NO₂ is observed

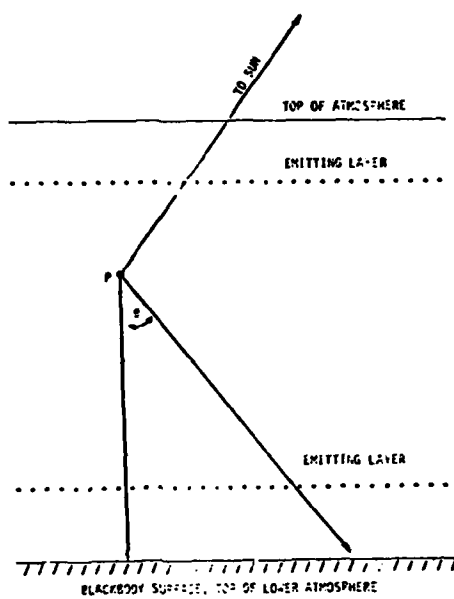
on the nightside between the P and R branches of water as the tangent height increases through the stratosphere. This has been used to estimate the concentrations of NO_2 (Reference 10) using the AFGL line-by-line radiance-transmission program, FASCODE (Reference 11).

The line-by-line method of inversion is clearly not efficient for inverting to such broad-band measurements. Another method was devised applying the non-linear least squares technique (References 12, 13) using Marguardt's maximum neighborhood technique (Reference 14). The heart of this technique lies in the approximation of the radiative mechanism of the molecule of interest. To illustrate the use of the least-squares method a simple band model was selected for the P branch of the $6 \mu\text{m}$ water band. The results of the inversion are shown in Figure HS $\Delta 1$ where we have plotted some of the RMS variance data from Harries (Reference 14). The agreement is satisfactory considering the known variability of water vapor and the fact that the SPIRE measurement is at sub-arctic latitudes and Harries' results are heavily weighted by the more humid mid-latitude observations.

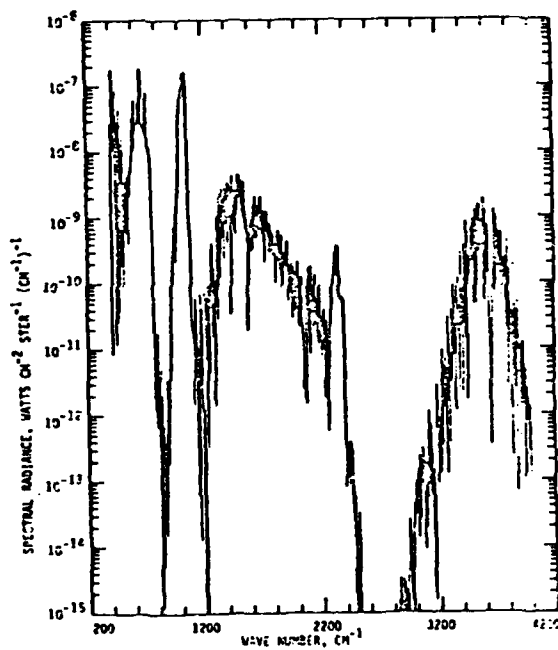
In summary, a number of inversion methods have been applied with success to IR limb scanning measurements. Further development of the statistical method is expected for use in the forthcoming CIRRIS experiment aboard the space shuttle.

REFERENCES

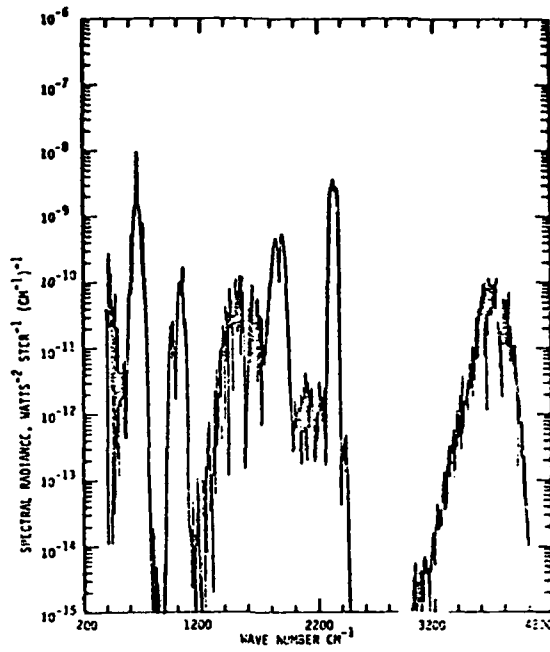
1. T.C. Degges and H.J.P. Smith, "A High Altitude Infrared Radiance Model" Visidyne, Inc., Burlington, Massachusetts, Report No. VI-395, AFGL-TR-77-0271, November 1977. UNCLASSIFIED The model was developed in the following reports:
 - V.L. Corbin, A. Dalgarno, T.C. Degges, F.B. House, P. Lilienfeld, G. Ohring and G.E. Opper, "Atmospheric Radiance Model for Limb-Viewing Geometry in the Five - to Twenty-five Micron Spectral Regions", Honeywell, Inc., Minneapolis, Minnesota, AFCRL-69-0552, March 1970. UNCLASSIFIED
 - T.C. Degges, "A High Altitude Radiance Model", Visidyne, Inc., Woburn, Massachusetts, Report No. VI-91, AFCRL-72-0273, May 1972. UNCLASSIFIED
 - T.C. Degges, "A High Altitude Infrared Radiance Model", Visidyne, Inc., Burlington, Massachusetts, Report No. VI-236, AFCRL-TR-74-0606, December 1974. UNCLASSIFIED
2. V. Kourganoff, Basic Methods in Transfer Problems, Dover Publications, Inc., New York, 1963.
3. W.R. Kuhn and J. London, "Infrared Radiative Cooling in the Middle Atmosphere", J. Atmos. Sci. 26, 189-204, 1969.
4. E.H. Avrett and D.G. Hummer, "Non-Coherent Scattering; II, Line Formation With A Frequency Independent Source Function", Mon. Not. Roy. Astron. Soc. 130, 295 - , 1965.
5. U.S. Committee on Extension to the Standard Atmosphere, U.S. Standard Atmosphere, 1976, NOAA-S/T 76-1562, U.S. Government Printing Office, Washington, D.C., 1976.
6. J.W. Rogers, A.T. Stair, Jr., N.B. Wheeler, C.L. Wyatt and D.J. Baker, "LWIR (7-24 μ m) Measurements From the Launch of A Rocketborne Spectrometer into A Quiet Atmosphere (1974)", Air Force Geophysics Laboratory, Bedford, Massachusetts, HAES Report No. 64, 1977.
7. U.S. Committee on Extension to the Standard Atmosphere, U.S. Standard Atmosphere, 1962, U.S. Government Printing Office, Washington, D.C., 1962.
8. P.B. Hays and R.G. Roble, "Observations of Mesospheric Ozone at Low Latitudes", Planet. Space Sci. 21, 273-279, 1973.
9. J.W. Rogers, A.T. Stair, T.C. Degges, C.L. Wyatt and D.J. Baker, "Rocketborne Measurement of H₂O in the Auroral Zone", Geophys. Res. Lett. 4, 366-368, 1977. UNCLASSIFIED
10. H.J.P. Smith, R.M. Nadile, A.T. Stair, D.G. Frodsham and D.J. Baker, "Interpretation of NO₂, Σ_{1+0+} Spectral Data Using the AFGL FASCODE Computer Model", in A. Deepole (Ed.) "Remote Sensing of Atmospheres and Ocean Academic Press (1980)
11. H.J.P. Smith, D.J. Dube, M.E. Gardner, S.A. Clough, FX Kneizys and L.S. Rothman, "FASCODE-Fast Atmospheric Signature Code (Spectral Transmittance and Radiance)", AFGL-TR-78-0081, U.S. Air Force (1978).
12. P.R. Bevington, "Data Reduction and Error Analysis for the Physical Sciences", McGraw-Hill (1969).
13. C. Daniel and F.S. Wood, "Fitting Equations to Data", 2nd Edition, John Wiley & Sons (1980).
14. D.W. Marquardt, "An Algorithm for Least-Squares Estimation of Non-Linear Parameters", J. Soc. Ind. App. Math, 11, 2 (1963) p 431.
15. J.E. Harris, "The Distribution of Water Vapor in the Stratosphere", Rev. Geophys. Space Phys. 14 (1976) p 565.



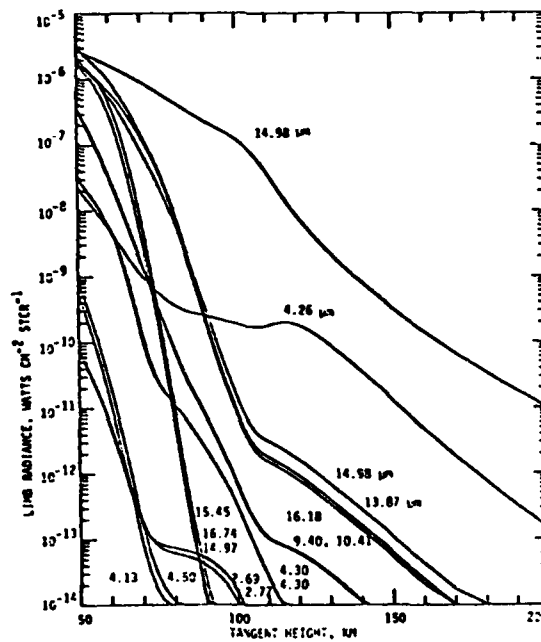
1. PLANE PARALLEL GEOMETRY USED IN RADIANCE MODEL



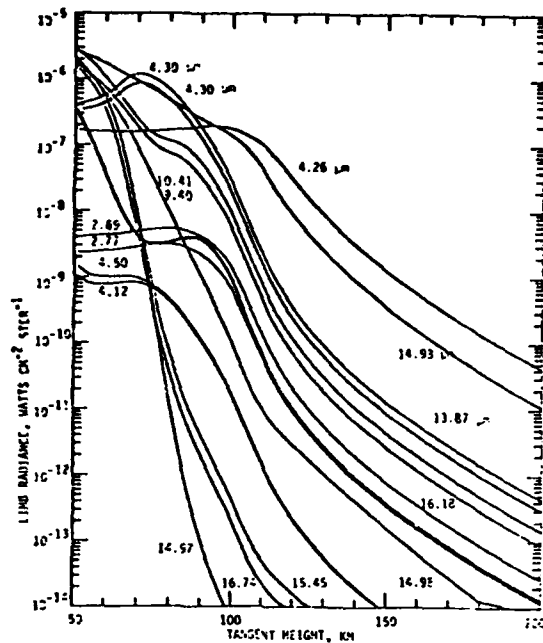
2. NIGHT LIMB VIEWING SPECTRAL RADIANCE, 400 TO 400 CM⁻¹, 60 KM TANGENT HEIGHT



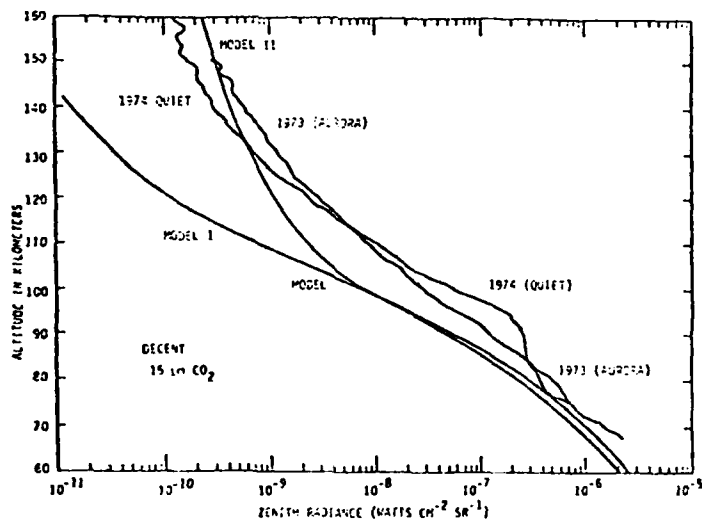
3. DAY LIMB VIEWING SPECTRAL RADIANCE, 400 TO 4000 cm^{-1} , 100 KM TANGENT HEIGHT



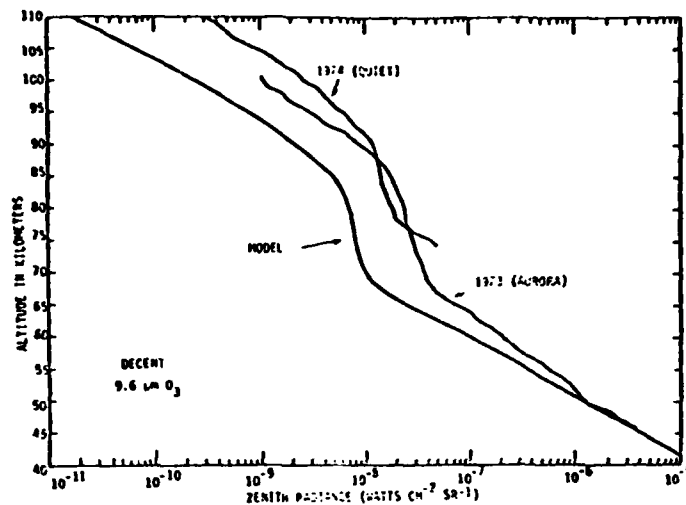
4. NIGHT LIMB VIEWING TOTAL RADIANCE VALUES FOR CARBON DIOXIDE BANDS



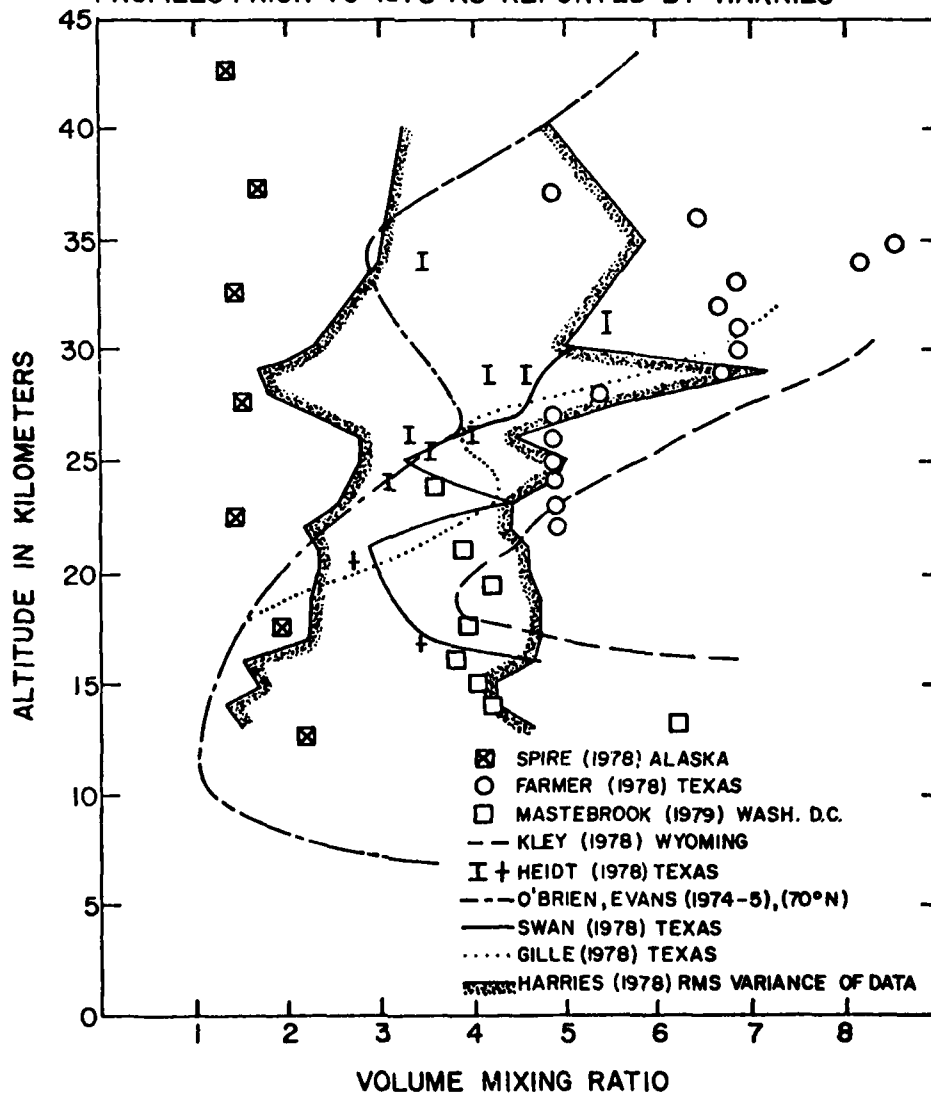
5. DAY LIMB VIEWING TOTAL RADIANCE VALUES FOR CARBON DIOXIDE BANDS



6. COMPARISON OF ZENITH RADIANCE ALTITUDE PROFILES AT 15 μM

7. COMPARISON OF ZENITH RADIANCE ALTITUDE PROFILES AT 9.6 μM

STRATOSPHERIC WATER VAPOR PROFILES FROM SPIRE AND UNPUBLISHED REPORTS COMPARED TO THE RMS VARIANCE IN PROFILES PRIOR TO 1978 AS REPORTED BY HARRIES

8. INVERSION OF SPIRE 6.3 μM WATER VAPOR RADIANCES

MINIMUM DETECTABLE QUANTITIES OF TRACE GASES

USING HIGH RESOLUTION SPECTROSCOPY

A. S. Zachor
Atmospheric Radiation Consultants, Inc.
59 High Street
Acton, Massachusetts 01720

B. Bartchi
Utah State University
Logan, Utah 84322

and

F. P. DelGreco
Air Force Geophysics Laboratory
Hanscom AFB
Bedford, Massachusetts 01731

ABSTRACT

We will summarize studies that define the capability of a Fourier spectrometer (FTS) system to remotely detect and characterize particular gaseous emissions by ground-level stationary sources. The principal result of the studies is a tabulation of predicted minimum detectable quantities (MDQ's) for 14 trace gases including DF, HF and N₂O. The detectable (observable) quantity of the target gas is essentially the product of the molecular column thickness of the gas in the line-of-sight and the Planck spectral radiance difference between the target gas and background averaged over the detection band. The MDQ's are the values of this quantity which correspond to approximately 95 percent probability of detection and one percent probability of false detection. Although derived for a particular baseline system and measurement geometry, the results can be scaled to other conditions.

The baseline FTS systems modelled in the studies employ mosaic focal planes together with optical designs or data processing techniques that perform background subtraction to obtain the target-background spectral radiance contrast. Detection and quantification of the target gases are based on the degree of correlation of the observed target spectral contrast with predicted target spectral contrast signatures. The predicted signatures for some of the target molecules are based on radiance/transmittance spectra generated by the computer code FASCOD1 developed by the U.S. Air Force Geophysics Laboratory. It is shown that this type of spectral correlation provides unambiguous detection and accurate quantification at spectrum signal-to-noise levels significantly less than unity.

1. INTRODUCTION

A localized cloud of particular gases that have IR absorption bands, eg, the chemical effluent of a stationary source or the exhaust plume of an aircraft engine, can be detected on the basis of the contrast it produces in an infrared scene image. Obvious requirements in this method of remote detection are that the cloud temperature is different from the background brightness temperature and that the resultant spatial radiance contrast is distinguishable from background clutter.

Resolution of the IR image into many spectral elements will enhance the ability of the system to distinguish between different target species having overlapping spectral bands and to suppress the effects of interferences, particularly those resulting from spatial and temporal variations in atmospheric absorption and background emission.

The detection problem that was studied is pictured in Fig. 1. A scene that includes a chemical effluent cloud is viewed by an airborne spectrometer having a mosaic of detectors, some of which see the target cloud-plus-background and others that see only the background. A related study performed by the Space Systems Group (ANAPOL, *et al*, 1979) compared both FTS and grating spectrometer concepts as candidates for this application. The study showed that when the relative throughputs and efficiencies and detector array requirements are compared (for the particular instantaneous fields of view and telescope sizes represented in our baseline sensor models), the FTS system is clearly superior, assuming the detector arrays were representative of then-current (1979) technology.

The basic radiometric design requirements and tradeoffs for this type of FTS application were established in an earlier study that was summarized yesterday by Mr. Coleman (Paper No. 22).

The FTS baseline configuration that was selected uses a four-port Michelson interferometer with a single dichroic and two detector mosaics in each of the two output ports (see Fig. 2). This arrangement allows the simultaneous detection of up to four different target species. The fourth port (a second input port) provides for illumination of the back side of the interferometer beamsplitter by an internal blackbody reference or by a different (background) portion of the external scene than is viewed by the primary input port. Utilization of the fourth port in this manner effects an optical subtraction of

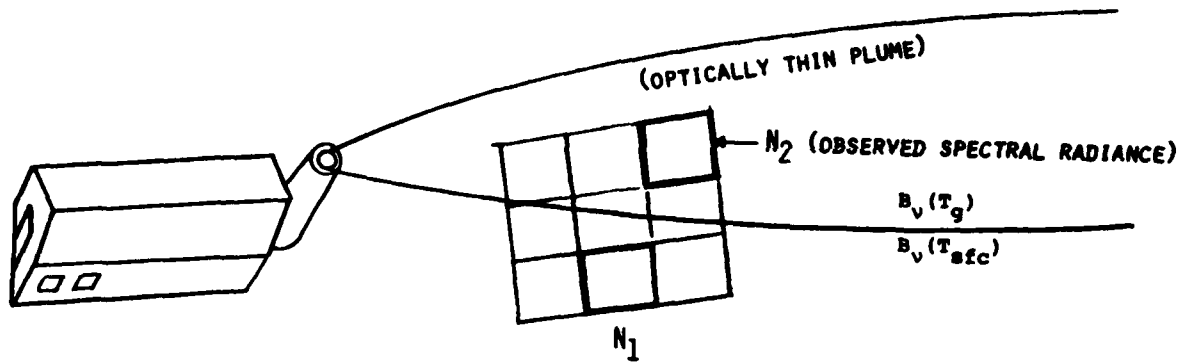


Figure 1. Detection Scenario

the scene and reference blackbody spectra or of the displaced scene spectra, and, more important, results in a potentially large reduction in the interferogram dynamic range (see VANASSE, *et al*, 1977). If the reference blackbody and background have the same brightness temperature, the resultant target-background spectral contrast obtained by this optical scheme is the same as would be obtained using a conventional single-port interferometer and merely subtracting the outputs of two different mosaic elements. The details of the selected baseline configuration are given in a technical report to be published by the Air Force Geophysics Laboratory (ZACHOR, 1980).

The computed system noise-equivalent spectral radiances (NESR's) and corresponding MDO's given in this paper apply to the baseline configuration defined in ZACHOR, 1980. However, many of the results are applicable, with suitable scaling and/or redefinition of parameters, to other sensor configurations including non-multiplexing spectrometers. Also, the results assume that the sensor views the target in the nadir direction from an altitude above most of the atmosphere. A Midlatitude Summer model atmosphere is assumed.

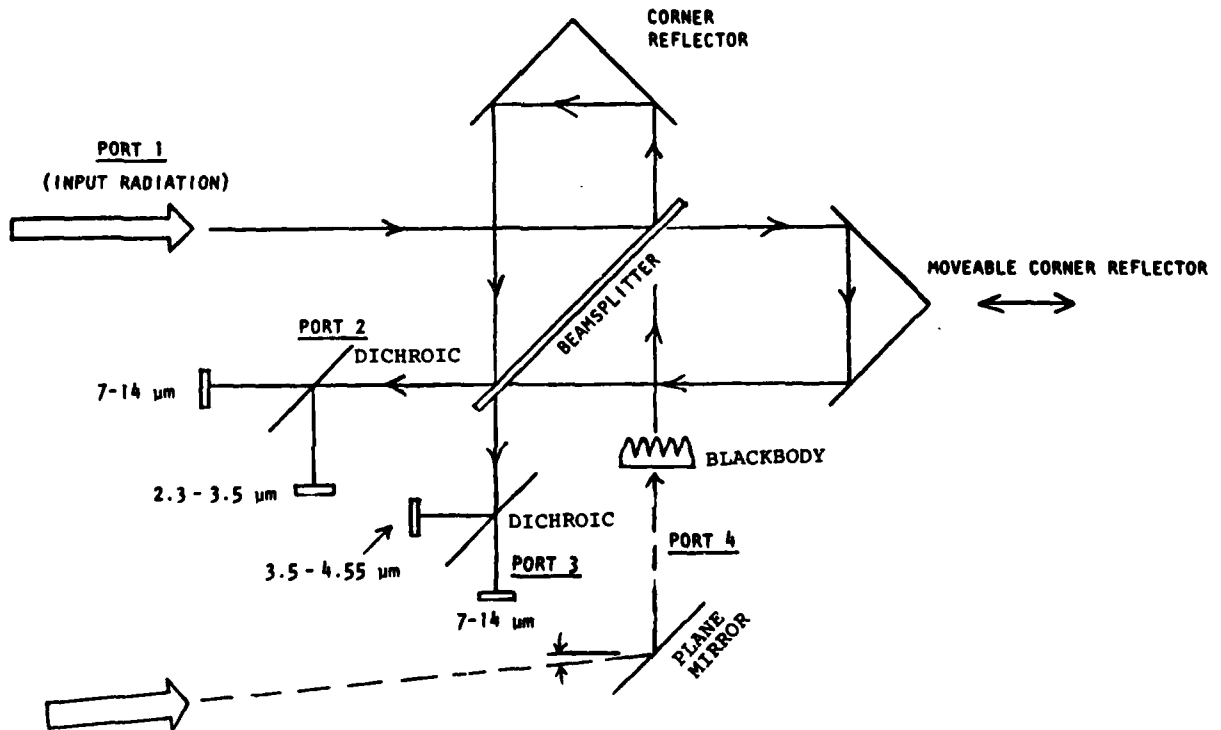


Figure 2. Optical Layout for Selected Baseline Configuration

2. THEORETICAL BASIS

The idea of a "minimum detectable quantity" (MDQ) implies that the target gas concentrations are very low. It also implies a benign background, since background (and atmospheric) interferences would generally require using a higher detection threshold, which would allow detection only at higher concentration levels. Specifically, it will be assumed that the target cloud is optically thin in the spectral bands used for detection, and that the background and atmosphere in the two fields of view (IFOV's) used to obtain the spectral contrast are identical. We will discuss in Section 4 how the effects of background and atmospheric interferences can affect the computed MDQ's. The only type of interference included is system (detector) noise.

It can be shown that under the stated assumptions the spectral radiance contrast for the two IFOV's indicated in Fig. 1 is given by

$$\begin{aligned}\Delta N_v &\equiv N_2 - N_1 \approx D \tau_v \alpha_{gv} + \text{NOISE}, \\ D &= u \overline{\Delta B}_v (T_g, T_{\text{sfc}})\end{aligned}\quad (1)$$

where

τ_v = atmospheric spectral transmittance between the target and sensor,
 α_{gv} = spectral absorption coefficient of the (single) target gas,
 u = molecular column thickness of the target gas (number of molecules per unit area),

and $\overline{\Delta B}_v$ = difference between the radiance of a blackbody at the gas temperature T_g and the actual radiance of the background at temperature T_{sfc} , averaged over the detection spectral band.

The detectable quantity, denoted by D , is essentially a scale factor in the measured contrast spectrum. Equation (1) is an approximation only because we have replaced the actual spectral variation ΔB_v by its average value. However, the variation is slow compared to that of τ_v and α_{gv} and is nearly linear over narrow spectral bands, so that the approximation is a good one, especially if $\tau_v \approx 1$ and α_{gv} is more-or-less symmetrical about the center of the detection band.

A reasonably accurate theoretical estimate of $\tau_v \alpha_{gv}$ can be obtained using a line-by-line computer code such as AFGL's FASCOD1. Then an estimate D' of D can be obtained by finding the value that minimizes the mean square difference between the measured spectrum ΔN_v and $D' \tau_v \alpha_{gv}$. Of course, α_{gv} is a function of the gas temperature, but $\frac{\partial \alpha_{gv}}{\partial T_g} \ll \frac{\partial \Delta B_v}{\partial T_g}$. Hence the use of some guess temperature in computing α_{gv} will not result in a large error in D' .

Some simple types of background and atmospheric interferences can be suppressed by subtracting the means of ΔN_v and $\tau_v \alpha_{gv}$ from these spectra before they are used to estimate D . Assuming this operation has been performed on Eq. (1), the least-squares estimator of D is

$$D' = \frac{\sum (a - \bar{a})(b - \bar{b})}{\sum (b - \bar{b})^2} \equiv \frac{\sigma_{ab}}{\sigma_b^2} \quad (2)$$

where $a \equiv \Delta N_v + \text{NOISE}$, $b \equiv \tau_v \alpha_{gv}$, and the summations are over the digitized spectrum values. Equation (2) is the prescription for computing the estimate D' given the measurement a and reference contrast spectrum b . By combining Eqs. (1) and (2), we find that D' can also be expressed by

$$D' = D + \frac{\sigma_{bn}}{\sigma_b^2} \quad (3)$$

where σ_{bn} is the covariance of the digitized reference spectrum and the spectrum noise, and σ_b^2 is the variance of the digitized reference spectrum.

The spectrum noise samples will be Gaussian with zero mean, and the samples will also be independent provided the sample spacing is equal to the resolution Δv of the FTS system. It can be shown that if the spacing is Δv the second term of Eq. (3) is simply

$$\frac{\sigma_{bn}}{\sigma_b^2} = \frac{x \sigma_n}{\sqrt{M} \sigma_b} = x \frac{\sqrt{2} \text{NESR}}{\sqrt{M} \sigma_b} \equiv x \sigma_{D'} \quad (4)$$

where x is a unit normal random variate, M is the total number of resolved spectral elements in the spectra a and b , and $\overline{\text{NESR}}$ is the average system noise-equivalent spectral radiance over the detection band. Note that the effective rms noise σ_n equals $\sqrt{2} \overline{\text{NESR}}$ because ΔN_v is the difference of two measurements with independent noise, or the result of an optical subtraction (interference) of two modulated interferometer signals with equal photometric (dc) components. Thus, the rms uncertainty in D' is $\sigma_{D'} = \sqrt{2} \overline{\text{NESR}} (\sqrt{M} \sigma_b)$.

The quantity

$$\frac{\sigma_{bD'}}{\sqrt{2} \overline{\text{NESR}}} \equiv \frac{S}{N} \quad (5)$$

is the rms signal variation over the rms spectral noise or the spectral *detection signal-to-noise*. Since $D'/\sigma_{D'}$ is this quantity times \sqrt{M} , it is evident that for sufficiently large M , the detectable quantity can be estimated accurately even if local spectrum features are well below the noise level ($S/N \ll 1$).

D will be negative if the target gas is observed in absorption (is cooler than the background) and positive if it is observed in emission. Hence, detection of the target gas can be based on the test

$$|D'| \stackrel{?}{>} R_D \quad (6)$$

where R_D is some predetermined threshold. Knowing the statistics of D' (Eqs. 3 and 4) we can work out the statistics for $|D'|$ for both target present ($D \neq 0$) and target not present ($D = 0$), and finally determine a threshold R_D that yields satisfactory detection and false detection probabilities. It can be shown that the value

$$R_D = 2.58 \sigma_{D'} = 2.58 \frac{\sqrt{2} \overline{\text{NESR}}}{\sqrt{M} \sigma_b} \quad (7)$$

results in approximately 95 percent detection probability and approximately one percent false detection probability when D equals

$$4.23 \sigma_{D'} = 4.23 \frac{\sqrt{2} \overline{\text{NESR}}}{\sqrt{M} \sigma_b} \equiv \text{MDQ} \quad (8)$$

This, by definition, is the minimum detectable quantity.

The $\overline{\text{NESR}}$, M and σ_b all vary with Δv . One can argue that a near-optimum value for Δv is the halfwidth of the target gas spectral lines, which is $\sim 0.1 \text{ cm}^{-1}$ for targets near sea-level. That is, $\Delta v \approx 0.1 \text{ cm}^{-1}$ will give the smallest MDQ from Eq. (8). The single parameter in Eq. (8) that depends on the target gas and detection geometry is σ_b , the standard deviation of the reference spectrum $\tau_{v\alpha_{GV}}$ degraded to 0.1 cm^{-1} resolution.

Figure 3 is an example of a radiance spectrum N_2 , transmission spectrum τ_v and reference spectrum $\tau_{v\alpha_{GV}}$ computed using FASCOD1. The spectrum N_2 ($\sim N_1$) determines the system $\overline{\text{NESR}}$ since the detectors in the baseline system are background limited.

3. MDQ RESULTS

The study determined the MDQ's for several candidate detection bands of each of 14 different molecular species. The "best" band for each species was selected on the basis of the corresponding minimum detectable column thicknesses (MIN u's) for a given temperature difference between target cloud and background. The relationship between MIN u and MDQ is, of course, strongly dependent on the spectral location of the detection band through the Planck function temperature derivative. Table 1 lists the best bands, the $\overline{\text{NESR}}$'s for a 10-second spectrum scan time, the corresponding MDQ and the MIN v. The last quantity is the minimum detectable concentration in ppmV for the conditions noted in the table footnote.

4. DISCUSSION

The computed MDQ's can be used to determine the combinations of localized trace gas column thickness and gas-background temperature difference that can be detected from a high altitude platform. The method as we have presented it can also quantify the detectable quantity D , but not the column thickness or temperature difference. This

* One can use spectra having many points per Δv -- this would not appreciably affect the MDQ, but Eq. (8) would not be valid for calculating the MDQ unless M is redefined.

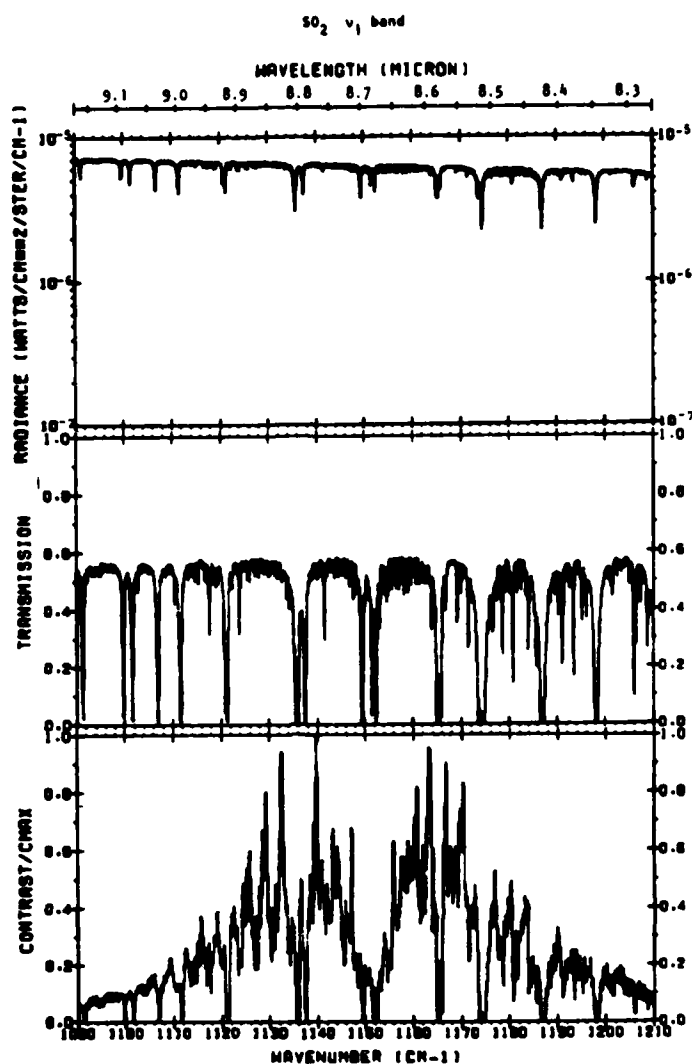


Figure 3. Examples of Computed N_1 , τ_v and $\tau_v \alpha_{gv}$ Spectra

deficiency might not be important in some applications. For example, the method might be useful as a screening technique to limit the number of targets or events that will require *in-situ* measurements or more sophisticated remote detection techniques.

We have examined the possibility of inferring u , T_g and T_{sfc} by a more detailed analysis of the measured spectra and have concluded that these quantities can be determined with reasonable accuracy when the detectable quantity is much greater than the MDQ. However, if the target cloud contains another species (such as CO_2) that may not be of particular interest but is present in sufficiently large quantity, the cloud temperature can be determined with high accuracy by a detailed analysis of its spectrum, and then the target gas column thickness can be inferred with high accuracy, even if the target gas is present at the MDQ level. The capabilities of the method to infer target gas column thickness and temperature requires a detailed specification of the expected total composition of the cloud.

We examined the effects of errors in the estimate of atmospheric transmittance τ_v arising from normal variations in the vertical column thickness and distribution of atmospheric species. These uncertainties result in MDQ and D' estimates that vary by less than a factor of two for most of the 14 species.

Atmospheric spatial variations on a scale equal to the displacement of the two IFOV's will not significantly alter the detection and false detection probabilities if spectral elements with strong atmospheric lines are excluded from the correlation processing. For most of the 14 selected detection bands the number of spectral elements that must be excluded to ensure high performance is not large enough to increase the MDQ significantly. The study also showed that serious degradation of system performance will result from spatial variations in background temperature unless the spectra measured in the two IFOV's are "prewhitened"; i.e., the Planck spectral radiance difference in the measured contrast spectrum must be removed before it is correlated with the reference spectrum.

Table 1. MDQ and MIN v Results

Gas	Band (cm ⁻¹)	*NESR (W/cm ² -sr-cm ⁻¹)	*MDQ (molec/cm ²) (W/cm ² -sr-cm ⁻¹)	**MIN v (ppmV)
HF	3240-3440	8.6 x 10 ⁻¹⁰	6.7 x 10 ¹³	(2.1 x 10 ⁶)
HCl	2900-3000	1.3 x 10 ⁻⁹	2.5 x 10 ⁹	20
NO ₂	2850-2935	1.4 x 10 ⁻⁹	1.3 x 10 ¹⁰	92
DF	2700-2900	2.6 x 10 ⁻⁹	3.5 x 10 ⁹	17
HBr	2450-2650	3.9 x 10 ⁻⁹	2.4 x 10 ¹⁰	51
N ₂ O	2160-2210	3.1 x 10 ⁻⁹	3.1 x 10 ¹⁰	22
CO	2130-2185	3.6 x 10 ⁻⁹	7.2 x 10 ¹⁰	16
HI	2100-2200	4.8 x 10 ⁻⁹	8.7 x 10 ¹²	5310
CH ₄	1295-1310	3.9 x 10 ⁻⁹	2.1 x 10 ¹²	163
SO ₂	1090-1210	1.5 x 10 ⁻⁸	2.7 x 10 ¹¹	16
NH ₃	915-970	1.1 x 10 ⁻⁸	2.0 x 10 ¹⁰	1.0
HNO ₃	887.5-902.5	6.0 x 10 ⁻⁹	3.4 x 10 ¹⁰	1.6
C ₂ H ₄ O ₂	880-1000	2.0 x 10 ⁻⁹	5.7 x 10 ¹⁰	2.8
CH ₃ I	790-990	2.4 x 10 ⁻⁸	6.7 x 10 ¹¹	32
NO ₂	710-795	1.3 x 10 ⁻⁸	4.0 x 10 ¹¹	19

* For baseline system and dwell time = 10 secs.

** MIN v = minimum detectable volume concentration for $t_d = 10$ secs., cloud thickness = 10 m, $\Delta T = 5^\circ\text{C}$., $T_{\text{sfc}} = 300\text{K}$.

5. ACKNOWLEDGEMENT

This work was supported by Utah State University under Subcontract No. SC-79-012 and funded under U.S. Air Force prime Contract No. F19628-77-C-0203.

REFERENCES

- ANAPOL, M., TITUS, J., CORKER, W. and GUNN, K., 1979, "System Design Study", Space Systems Group, Inc., Final Report on Utah State University Subcontract No. SC-79-080 (U.S. Air Force prime Contract No. F19628-77-C-0203).
- VANASSE, G.A., STAIR, A.T. Jr., SHEPHERD, O. and REIDY, W. P., 1977, "Background Optical Suppression Scheme (BOSS)", AFGL-TR-77-0135.
- ZACHOR, A.S., 1980, "Down-Looking Interferometer Study", Vols. I & II, AFGL-TR-80-XXXX (To be published).

SUMMARY OF SESSION III

UPPER ATMOSPHERE EFFECTS : THEORY AND EXPERIMENTS

by

Prof. A. M. Scheggi, Chairwoman

This session previously planned for including 9 papers was reduced to 5 papers, due to withdrawing or lack of clearance for 4 of them. Interesting experimental results [SPIRE, RAMON experiments] were shown (19, 20, 23) on infrared earth's upper atmosphere emission ($\sim 1.5 - 20 \mu\text{m}$) obtained from data measured by rocket or balloon borne sophisticated instrumentation (such as for instance specialized cryogenic i.r. instrumentations, cryogenic telescope spectrometer, SWIR spectrometer, MICHELSON interferometer spectrometer etc.) and the comparison with theoretical models were also discussed. Remote sensing of the structure function of the atmosphere by means of stellar scintillation measurements was described (21), performed with a new fast optical ground based apparatus (including a large telescope, a surface photo electric image receiver and a specialized two-dimensional correlator). Comparison with other technique measurements was quite satisfactory. The method appears to be a powerful tool for studying the phenomena of intermittency in the inner and outer scale and thus allowing to model the turbulence temporal variation.

Other reported studies (25) were aimed to define the capability and design requirements of a remote Fourier spectrometer system to detect and characterize gaseous emissions by ground level stationary sources. Further field tests will be useful to demonstrate the effectiveness of the developed method.

In conclusion the researches described in the cited papers have a twofolded interest : there is the aspect of the basic knowledge of the physical and chemical processes occurring in the upper atmosphere for which the remarkable amount and quality of data already collected or which will be obtained with designed experiments are of fundamental help. But there is also the practical interest of having an improved modeling of the atmosphere and related propagation effects in connection with problems such as sensing systems design or military surveillance.

QUESTIONS AND COMMENTS
ON SESSION III

UPPER ATMOSPHERE EFFECTS : THEORY AND EXPERIMENTS

- Paper 21 : Optical C_N^2 remote sensing in the upper atmosphere by multidimensional analysis of stellar scintillation.

Mr. D. W. Hanson : Have you compared the whole aperture scintillation calculated from a measured profile with the whole aperture scintillation directly measured with your instrument ?

Mr. J. Vernin : We have compared the scintillation on a small aperture and the scintillation deduced from a measured profile with the whole aperture scintillation. The agreement is very good.

(When you have the C_N^2 profile it is possible to make the integration over the whole atmosphere. If you have only one photomultiplier, you put on the entrance a pupil. You can reach the rate of scintillation and you know that there is a connection between the integral of C_N^2 over the whole atmosphere and the rate of scintillation on the pupil).

Dr. A. Consortini : Do you think that it will be possible to do measurement with time lag τ large in order to have informations on long period variations ?

Mr. J. Vernin : We are restricted to the period of the star passing near from the meridian (about 3 hours). For longer time lag (a day), we are restricted by the weather and the time we can use the telescope. I think it would be very difficult to make a daily statistical analysis.

Mr. J. C. Pourny : Faites-vous les mesures de nuit ?

Mr. J. Vernin : Oui uniquement. Toutefois les mesures de vitesses de couches turbulentes, dont je n'ai pas parlé ici, qui se font sur des étoiles excessivement brillantes, peuvent se faire de jour.

Mr. J. C. Pourny : Lorsque vous poursuivez une étoile avec le télescope vous êtes obligé de changer la direction de visée. Quelle compte en tenez-vous ?

Mr. J. Vernin : Le problème est d'effectuer la correction par sécante z au fur et à mesure que l'on suit l'étoile.

Le changement de direction de visée n'est pas autrement gênant, car la vitesse angulaire du télescope est petite devant la vitesse angulaire de déplacement des couches.

Mr. J. C. Pourny : Pouvez-vous décrire l'autocorrélateur sur les images de caméra ?

Mr. J. Vernin : Notre corrélateur a été conçu pour utiliser le maximum de l'information bidimensionnelle contenue dans nos images. Dans le cas d'une corrélation bidimensionnelle nous effectuons le produit d'un point particulier de l'image par tous les autres points. Pour une corrélation à une dimension, nous faisons le produit du premier point d'une ligne TV par tous les autres points de la même ligne et nous accumulons toutes les lignes. Dans les deux cas on peut montrer que la fonction calculée converge vers la corrélation recherchée.

Mr. P. Halley : Vous avez fait allusion aux ondes de gravité. Avez-vous tenté le rapprochement entre les scintillations optiques observées et des mesures de pression barométriques effectuées au sol, c'est-à-dire le rapprochement avec des ondes acoustico-gravitationnelles ?

Mr. J. Vernin : Non, nous n'avons jamais fait de mesures simultanées avec des microbarographes au niveau du sol, par contre nous avons fait beaucoup de mesures avec des sondes embarquées par des ballons pour mesurer la pression, la température, très rapidement, c'est-à-dire les fluctuations du C_T^2 et des sondes qui mesuraient aussi la vitesse pour essayer de retrouver le gradient de vent à l'intérieur des couches (équipe de J. BARAT du service d'aéronomie du CNRS). Disons que les résultats sont en cours d'élaboration et qu'il y a une très bonne concordance entre le C_T^2 qu'on trouve avec les sondes de température et nos mesures et qu'il y a aussi une bonne concordance entre la turbulence trouvée par les capteurs de vitesse et la turbulence de température mesurée par une autre méthode.

Dr. C.R. Giuliano : In looking at the color-coded sounding data there appeared to be a few occasions when the turbulence almost disappeared. Would you comment on these observations.

Dr. J. Vernin : It appears actually that in some circumstances several layers show simultaneously a low level of turbulence. In that cases the astronomers will have a very good "Seeing".

LINE-OF-SIGHT OPTICAL COMMUNICATION THROUGH LOW-VISIBILITY WEATHER

Jeffrey H. Shapiro
Department of Electrical Engineering and Computer Science
and Research Laboratory of Electronics
Massachusetts Institute of Technology
Cambridge, Massachusetts 02139

SUMMARY

There exists the possibility of improved atmospheric optical communication through low-visibility weather by exploitation of the scattered light. This paper summarizes the multiple forward-scatter propagation model for a line-of-sight optical link operating in low-visibility weather. Using this model, digital communication performance for diffraction-limited and wide field-of-view receivers are compared. It is shown that background-light suppression is the key to extended link operability in the daytime. Three techniques for achieving this suppression are: use of a wide-angle narrowband optical filter at the receiver, operation at mid-ultraviolet wavelengths, and use of adaptive phase compensation at the receiver. The promise and drawbacks of these approaches are briefly discussed.

1. INTRODUCTION

The apparent limitations imposed by low-visibility weather conditions (haze, rain, snow, fog, etc.) on atmospheric optical communication systems are self evident. Consider a conventional line-of-sight link, whose receiver responds only to the unscattered light arriving along the boresight from the transmitter. The principal effect of low-visibility atmospheric propagation on this link is to increase the path loss incurred by a factor of $\exp(-\beta L)$, where β is the atmospheric extinction coefficient at the operating wavelength, and L is the path length. A commonly accepted approximation holds that $\exp(-\beta L)$, at visible wavelengths, will be on the order of 10^{-2} when L equals the visibility (Middleton, W.E.K., 1958; McCartney, E.J., 1976). At these wavelengths, therefore, a conventional system must withstand a 40dB extinction loss to operate reliably when the visibility is half the path length; an 80dB power margin is needed when the visibility is a quarter of the path length.

The severity of the preceding extinction levels justifies the use of fiber optics for reliable, high-bandwidth, terrestrial optical-communication networks. Even so, there are circumstances in which atmospheric links may be preferable. For example, where cable rights-of-way are unobtainable, or where frequent link and network reconfiguration is necessary, or where optical-broadcast operation is desired.

To some extent, the atmospheric-link outage time caused by low-visibility weather can be reduced by operation at a wavelength, such as the 10.6 μm CO_2 -laser wavelength, for which the extinction coefficient is smaller than that for visible wavelengths (Chu, T.S., and Hogg, D.C., 1968; Kopeika, N.S., and Bordogna, J., 1970). This approach, however, merely postpones the inevitable. In particular, although a smaller β value enables operation at a higher L value for the same extinction, the conventional system is still limited to small optical thickness, $\tau = \beta L$, operation because of the $e^{-\tau}$ extinction loss. On the other hand, the extinction coefficient at most visible and many infrared wavelengths is due primarily to scattering rather than absorption. There exists, therefore, the potential for improved line-of-sight optical link operability through exploitation of the scattered light in addition to the unscattered light (Heggstad, H.M., 1968; Kennedy, R.S., 1970; Clark, J.R., and Baird, J.R., 1975; Robinson, S.R., 1977; Shapiro, J.H., and Warde, C., 1981).

For several years, the Optical Propagation and Communication Research Group at M.I.T. has been concerned with the problem of line-of-sight optical communications under low-visibility weather conditions. Drawing upon the talents of device physicists and communication engineers this group has been addressing the issues of optical propagation in turbid atmospheres (Paik, W.H., et al., 1978; Reilly, D.M., and Warde, C., 1979; Nakai, J., 1980; Ross, W.S., 1980; Nguyen, T.T., 1980; Ross, W.S., et al., 1981), communication through optical scattering channels (Kennedy, R.S., 1970; Robinson, S.R., 1977; Paik, W.H., 1978; Shapiro, J.H., 1980; Shapiro, J.H., and Warde, C., 1981), and devices and techniques for space distributed optical phase compensation (Warde, C., et al., 1978; Fisher, A.D., and Warde, C., 1979; Fisher, A.D., 1981).

This paper summarizes some of our recent communication analysis work. The development here is partly tutorial in order to emphasize the close interrelationships between propagation effects, communication system design, and device technology in approaching the fundamental performance limits for atmospheric optical communication.

2. COMMUNICATION ANALYSIS

This section comprises an abbreviated communication analysis for line-of-sight optical scattering channels based upon the multiple forward-scatter (MFS) propagation model (Shapiro, J.H., 1980; Ross, W.S., et al., 1981).

2.1 Propagation Model

In the MFS propagation model, the single-scatter atmospheric phase function is assumed to have a sharp forward-scattering peak plus significant amounts of wide-angle scatter and backscatter. It is assumed that the receiver does not collect any light that has undergone wide-angle scatter or backscatter so that these portions of the scattering function may be lumped into the absorption term (Mooradian, G.C., et al., 1979). The resulting truncated phase function, which consists solely of the forward-scattering peak permits the multiple-scattering equations to be solved via the small-angle approximation. Although the validity of this theory is not fully established, experiments (Mooradian, G.C., et al.,

1979; Russo, C.R., 1979; Ross, W.S., et al., 1981) indicate that it is consistent with observed power transfer and angular spread characteristics. Multipath predictions are less well validated (Nakai, J., 1980) and no confirmation is available as yet for the coherence time prediction. Nevertheless, lacking a better model at this time, we shall employ the MFS approach. Its principal results are as follows.

Power Transfer

Consider a continuous-wave laser transmitter of power P_T , wavelength λ , and initial beam divergence θ_T (half cone angle). Suppose the beam from this source is directed towards a receiver L meters away with entrance pupil radius ρ_R and field-of-view half cone angle θ_R . Let the intervening propagation medium be a turbid atmosphere of absorption coefficient β_a , scattering coefficient β_s , forward-scattering efficiency ϕ , and root-mean-square forward scatter angle θ_F . Under far-field propagation conditions, with $\beta_s L \gg 1$, the average detected power obeys (Shapiro, J.H., 1980)

$$\langle P_D \rangle = \frac{[P_T (\rho_R / \theta_T L)^2] \exp[-\beta_a L]}{[1 + (\theta_O / \theta_T)^2][1 + (\theta_O / \theta_R)^2]} \quad (1)$$

In Eq. (1): $P_T (\rho_R / \theta_T L)^2$ is the free-space propagation detected power; $\exp[-\beta_a L]$ is the effective absorption loss, where $\beta_a = \beta + \beta (1 - \phi)$; $[1 + (\theta_O / \theta_T)^2]^{-1}$ is the beam spread loss; and $[1 + (\theta_O / \theta_R)^2]^{-1}$ is the angular spread loss. Here $\theta_O = 21/2 / k \rho_O$, for $k = 2\pi/\lambda$, gives the beam spread/angular spread angle in terms of the channel coherence length $\rho_O = (3/\beta_s \phi L k^2 \theta_F^2)^{1/2}$. As will be seen below, $\langle P_D \rangle$ greatly exceeds the unscattered detected power,

$$(P_D)_{\text{uns}} = [P_T (\rho_R / \theta_T L)^2] \exp[-\beta L], \quad (2)$$

where $\beta = \beta_a + \beta_s$, under low-visibility conditions ($\beta_s L \gg 1$).

Multipath Spread

Suppose, in the system just described, that the field envelope at the source is modulated to a bandwidth W Hz. This modulation will undergo flat fading, i.e., all the frequency components of the beam suffer the same scattering-induced fading, when W is less than the coherence bandwidth of the channel, W_C , given by (Nakai, J., 1980)

$$W_C = 14c/\pi \beta_s \phi (L \theta_F)^2 \quad (3)$$

In Eq. (3), c is the speed of light, and far-field propagation with $\beta_s L \gg 1$ and $\theta_O / \theta_T \gg 1$ has been assumed. It follows from this result that multipath spread can be neglected for (transform-limited) pulses whose duration exceeds W_C^{-1} . Conversely, intersymbol interference will occur in a digital communication link that employs a pulse modulation format with pulse rate in excess of W_C^{-1} .

Coherence Time

Suppose that in the system being considered, a pulse of duration T is transmitted by the source. This pulse will undergo time-independent fading if T is less than the channel coherence time, T_C . Via the frozen-flow hypothesis, we have (Ishimaru, A., 1978)

$$T_C = \rho_O / v, \quad (4)$$

where v is the transverse wind velocity. If the channel is underspread, i.e., if $T_C W_C > 1$, then a pulse of duration $T < T_C$ and bandwidth $W \approx T^{-1} < W_C$ will propagate without suffering multipath spread or time-dependent fading.

2.2 Receiver Analysis

Consider the transmission of a single bit of information over the preceding propagation channel via binary pulse-position modulation with transmitter peak power P_T , pulse duration T , and bit interval $T_b \geq 2T$. In a real communication system a sequence of bits will be transmitted by repeated use of a basic signalling scheme. We have chosen binary pulse-position modulation for analysis because its symmetry obviates the need for channel parameter knowledge in designing optimum post-detection processing electronics.

We shall assume an underspread channel (see below), with $T_C < T_b$ and $T^{-1} < W_C$, so that the pulses arrive undistorted except for a random fading level. For the sake of brevity, only shot-noise-limited direct detection will be considered. Heterodyne-detection receivers for the low-visibility channel have been studied as well (Kennedy, R.S., 1970; Robinson, S.R., 1977). The direct-detection systems are simpler to build, and when they are quantum limited they outperform heterodyne systems.

Direct-Detection Receiver

A direct detection receiver for the preceding communication problem is shown schematically in Fig. 1. Optics are employed to focus the light collected within a θ_R half cone angle field of view over the entrance pupil through an interference filter onto a photomultiplier tube. The resulting output current is supplied to a discriminator/counter gated by the receiver clock. We assume that the receiver clock is synchronized to the pulse arrival times for the two possible message bit values. In the real sequential communication system, this synchronization information must be obtained with a tracking loop, or via a synchronization preamble attached to the data stream.

The electronics counts photon detections occurring in the two time intervals corresponding to the message 0 and the message 1 pulses, and chooses the bit value associated with the larger count as its output. Because of the symmetry of the pulse-position modulation signal set, the foregoing photocurrent processor is the minimum error probability decision rule. However, two general receivers may still be distinguished within the

framework of Fig. 1 according to whether θ_R is matched to the diffraction limit $1/k\theta_R$ of the entrance-pupil optics, or to the angular-spread limit θ_0 of the channel. The former receiver is the conventional "unscattered-light-only" system alluded to in the Introduction. The latter system is a wide field-of-view ("photon bucket") receiver which responds to the scattered light plus the unscattered light illuminating the entrance pupil. By employing the low-photon coherence condition (Kennedy, R.S., 1970) the following simple error probability results can be derived for these receivers.

Diffraction-Limited Performance

The diffraction-limited receiver uses the optimum field of view for communication through free space. In low-visibility weather, however, it is a very inefficient collector of signal light, although it is far less susceptible to background-light shot noise than is wide field-of-view reception. The error probability for the diffraction-limited receiver obeys (Kennedy, R.S., 1970; Robinson, S.R., 1977; Shapiro, J.H., 1980)

$$\Pr(e) \leq \begin{cases} 2^{-1} \exp(-n_{SDL}), & \mu_{DL} \gg 1 \\ 2^{-1} \exp(-n_{SDL} \mu_{DL}/4), & \mu_{DL} \gg 1 \end{cases} \quad (5)$$

where $n_{SDL} = n_S^0 \exp(-\beta L)$,

$$n_S^0 = \eta P_T T (\rho_R / \theta_T L)^2 / 2h\nu,$$

$$\mu_{DL} = n_{SDL} / n_B,$$

$$n_B = \eta \lambda^2 \Delta \lambda N_\lambda T / h\nu$$

for η the detector quantum efficiency, $h\nu$ the photon energy, $\Delta \lambda$ the optical filter bandwidth, and N_λ the background light spectral radiance.

Equation (5) exhibits the well known background light threshold effect. That is, when the signal-to-background ratio $\mu_{DL} \gg 1$, performance is signal shot-noise (quantum) limited; when $\mu_{DL} \ll 1$, performance is background shot-noise limited. For the same average number of detected signal photons, n_{SDL} , it is greatly disadvantageous to be background shot-noise limited. Equation (5) also shows the exponential extinction of n_{SDL} from its free-space value n_S^0 as the optical thickness increases.

Wide Field-of-View Performance

When there are significant amounts of scattering in the channel, better signal energy extraction results from matching the receiver field of view to the angular spread of the scattered light, i.e., $\theta_R = \theta_0$. This added signal energy is accompanied by increased background-light collection. The resulting error probability satisfies (Kennedy, R.S., 1970; Robinson, S.R., 1977; Shapiro, J.H., 1980)

$$\Pr(e) \leq \begin{cases} 2^{-1} \exp(-n_S), & \mu \gg 1 \\ 2^{-1} \exp(n_S \mu / 4), & \mu \ll 1 \end{cases} \quad (6)$$

where $n_S = n_S^0 \exp[-\beta_a L / (1 + (\theta_0 / \theta_T)^2)]$,

$$\text{and } \mu = n_S^0 \rho_0^2 / 2 \rho_R^2 n_B.$$

Comparison of Eqs. (5) and (6) reveals that indeed the wide field-of-view receiver has better signal energy collection than the diffraction-limited receiver but its signal-to-background ratio may be considerably worse than that for diffraction-limited reception. Thus, the wide field-of-view receiver yields a lower error probability than diffraction-limited reception does when the former is signal shot-noise limited, but the reverse may be true when the wide-field system is background limited.

2.3 Example

In order to assess the degree to which scattered-light utilization can extend the operability of a line-of-sight link, we must substitute transmitter, receiver, and channel parameters into the foregoing performance results. A sample calculation follows. The transmitter is assumed to be a frequency-doubled Nd:YAG laser with $P_T = 10W$, $\lambda = 0.53 \mu m$, $T = 100 \mu s$, and $\theta_T = 10 \text{ mr}$. The receiver is assumed to have $\rho_R = 5 \text{ cm}$, $\eta = 0.1$, and $\Delta \lambda = 10^{-3} \mu m$. The channel is assumed to have $\beta_a = 0 \text{ km}^{-1}$, $\beta_s = 4 \text{ km}^{-1}$, $\phi = 0.57$, $\theta_F = 11.3 \text{ mr}$, $v = 2.5 \text{ m/s}$, daytime $N_\lambda = 10W/m^2 \text{ Sr} \mu m$, and nighttime $N_\lambda = 10^{-3} W/m^2 \text{ Sr} \mu m$. These values are merely representative; our intent is not to provide an exhaustive assessment of system performance.

Propagation Effects

Figure 2 shows plots of n_S/n_S^0 and n_{SDL}/n_S^0 vs. path length L (using a dB scale, i.e., $10 \log n_S/n_S^0$, etc.). Notice that at $L = 1 \text{ km}$, which corresponds roughly to the visibility, the scattered light dominates the unscattered light by about 5 dB; at $L = 4 \text{ km}$ the scattered light is 30 dB stronger than the unscattered light. In Fig. 3 are plots of the beam-spread/angular-spread angle θ vs. path length; over the range shown θ varies from about one to three times the forward scatter angle θ_F . The coherence bandwidth result Eq. (3), has not been plotted because at worst ($L = 5.5 \text{ km}$) $W_C = 152 \text{ MHz}$ so that $TW_C \gg 1$ prevails under all conditions considered below. Finally, Fig. 4 shows the coherence time T_C predicted from the frozen-flow formula (Eq. (4)). This result must be regarded with some skepticism because of the absence of experimental data. Note that $T_C W_C > 1$ (the channel is underspread) for all path lengths between 1 and 5.5 km.

Communication Performance

In Fig. 5, curve a is a plot of the n_g value that is achieved with the given transmitter and receiver parameters. Curve b shows the n_g value that is required to yield $\text{Pr}(e) = 10^{-3}$ under daytime or nighttime background conditions for diffraction-limited reception. (The daytime and nighttime n_g requirements coincide because the diffraction-limited receiver is signal shot-noise limited in either case; the $\text{Pr}(e) = 10^{-3}$ value has been selected as a reasonable starting point from which reliable information transmission can be obtained via error-correcting codes.) Curves c and d show the n_g values that are needed for a wide field-of-view receiver to yield $\text{Pr}(e) = 10^{-3}$ under daytime and nighttime background conditions, respectively. Whenever curve a lies above the appropriate receiver curve, that receiver will have an error probability of less than 10^{-3} . We see, therefore, that the diffraction-limited receiver outperforms the wide field-of-view receiver out to $L = 2.8$ km in the daytime. This is because of the former's superior background light discrimination (cf. Fig. 2). At longer path lengths, the daytime wide field-of-view receiver is superior because of its better signal light collection. For the given transmitter/receiver parameters both approaches yield $\text{Pr}(e) < 10^{-3}$ out to about $L = 2.7$ km, which is almost three times the visibility. At night, however, the reduced background spectral radiance permits successful wide field-of-view reception out to about $L = 4.5$ km, which is more than four times the visibility. Moreover, nighttime wide field-of-view reception outperforms diffraction-limited reception over the entire path range considered.

3. BACKGROUND-LIGHT SUPPRESSION

The moral of the communication example in Section 2 is as follows. For the low background levels anticipated in nighttime operation, line-of-sight link operability can be maintained over path lengths substantially beyond the visibility by means of wide field-of-view reception. Unfortunately, the high background levels expected in the daytime may make daytime scattered-light utilization no more effective than the conventional (diffraction-limited) receiver. It behooves us, therefore, to seek techniques for reducing background-light collection in wide field-of-view (daytime) receivers. Three options are available: a) reducing the optical filter bandwidth by means of new or improved filter technology, b) reducing the background spectral radiance through operation at mid-ultraviolet wavelengths, and c) reducing the effective receiver field-of-view (with minimal signal energy loss) via adaptive phase compensation.

3.1 Wide Field-of-View Narrowband Filters

The best developed technology, at present, for narrowband optical filters is that of interference filters. However, this technology is fundamentally ill-suited to the needs of wide field-of-view scattered light reception because of the inherent coupling between the angular and spectral characteristics of interference filters. In particular, a filter made of material with refractive index n whose peak-transmission wavelength is λ_p for normally-incident illumination has a peak-transmission wavelength

$$\lambda_p' = \lambda_p [1 - n^{-2} \sin^2 \theta]^{1/2} \quad (7)$$

for illumination at angle θ (Lerner, R.M., 1971). Accordingly, interference-filter technology is incapable of the $\Delta\lambda \lesssim 10^{-5} \mu\text{m}$, $\theta_R \lesssim 30$ mr specifications necessary to significantly improve the daytime performance calculated in the previous section.

Absorption-type filters afford a decoupling between spectral and angular transmission characteristics, but materials for which very narrow optical bandwidths can be achieved with high peak-wavelength transmission are not known. On the other hand, extremely narrowband wide-angle filters can be made, in principle, by exploiting the zero-crossing of birefringence at the band edge in a uniaxial semiconductor (Lotspeich, J.F., 1979); the technology of these devices may be the solution to the wide field-of-view receiver problem. Another promising alternative is the use of nearly degenerate four-wave mixing (Pepper, D.M., and Abrams, R.L., 1978). This approach suffers the disadvantage that an auxiliary high-power laser is required at the receiver, and its narrowband response is achieved by an active process which creates additional noise. (The analyses in (Yuen, H.P., and Shapiro, J.H., 1979) can be adapted to show that this additional noise must be equivalent to at least one noise photon per detected spatio-temporal mode.)

3.2 Mid-Ultraviolet Communication

Most of the daytime background noise at visible wavelengths is due to scattered sunlight. In the spectral region below $0.29 \mu\text{m}$, no solar radiation reaches the earth because of absorption in the ozone layer of the earth's upper atmosphere (Simon, R.E., 1974). As there is relatively little ozone near the ground, operation in the $0.2 \mu\text{m} - 0.3 \mu\text{m}$ mid-ultraviolet region affords a region for "solar blind" wide field-of-view reception (Reilly, D.M., 1976; Ross, W.S., 1980). (The restriction to wavelengths longer than $0.2 \mu\text{m}$ is imposed by the high molecular oxygen absorption below $0.2 \mu\text{m}$ (Ditchburn, R.W., and Young, P.A., 1962).) The principal difficulty facing the potential user of this waveband is the relative dearth of suitable source and modulator technology as compared with that available at visible and near-infrared wavelengths.

3.3 Adaptive Phase Compensation

Adaptive phase compensation of the received signal wavefront enables the receiver to detect essentially all the signal light arriving over a wide field-of-view while accepting background light over what amounts to a diffraction-limited field-of-view.

The operating principles of a direct-detection phase compensated receiver for the

low-visibility channel are illustrated in Fig. 6. The received optical field first passes through a phase modulator that adds the appropriate control phase $\phi_m(\vec{r}, t)$ to "straighten out" the wavefront of the signal light. The compensated beam is then optically filtered, part of it is fed back to a phase estimator whose output is used to provide the control signal to the modulator, and the remaining compensated light is supplied to a diffraction-limited direct-detection communication receiver. Assuming that perfect phase estimation and correction have been performed (with a miniscule fraction of the signal light being split off for the feedback loop) the receiver error probability for pulse-position modulation signals is given by (Robinson, S.R., 1977; Shapiro, J.H., 1980)

$$\Pr(e) \leq \begin{cases} 2^{-1} \exp(-n_{\text{SPC}}), & \mu_{\text{PC}} \gg 1 \\ 2^{-1} \exp(-n_{\text{SPC}} \mu_{\text{PC}}/4), & \mu_{\text{PC}} \ll 1 \end{cases} \quad (8)$$

where

$$n_{\text{SPC}} = n_s \pi/4, \\ \mu_{\text{PC}} = n_{\text{SPC}}/n_B.$$

Equation (8) confirms our earlier statement: when compensation can be accomplished, we have a receiver whose signal light collection is comparable to that of wide field-of-view reception and whose background-light discrimination is comparable to that of diffraction-limited reception.

Unfortunately, achieving perfect compensation is no mean task. The phase estimation loop requires about four detected photons per coherence area per coherence time to maintain adequate lock (Robinson, S.R., 1976). When all the signal light is diverted to the estimation system, this condition becomes

$$n_{\text{S}0} \rho_{\text{T}}^2 / 4 \rho_{\text{R}}^2 \geq 4. \quad (9)$$

Figure 7 shows the n_B value required for the system in Section 2.3 to maintain good phase tracking in daytime background light. Comparison with the available n_B values (curve a of Fig. 5) shows that in our sample calculation phase tracking cannot be accomplished in the daytime. Even if this were not so, there would still be substantial difficulty in realizing the phase modulator necessary for perfect compensation, since this element would have to control

$$M = 2 \rho_{\text{R}}^2 / \rho_{\text{O}}^2 \quad (10)$$

spatial modes at T_C^{-1} Hz bandwidth (Robinson, S.R., 1977). Figure 8 shows $\log M$ vs. L for the parameter values in Section 2.3. Notice that M must vary from 6.8×10^7 to 3.7×10^8 as L goes from 1 km to 5.5 km for this example.

4. CONCLUSIONS

It appears that the MFS propagation model is well-suited to providing parameter values needed for the design of low-visibility optical communication systems. The power transfer and angular spread predictions of this model are reasonably well grounded in experiment, but more work needs to be done on the multipath and coherence time behavior. The coherence time is especially important since this parameter is crucial in determining the applicability of adaptive phase compensation to the low-visibility channel.

The communication theory of the low-visibility channel is fairly complete for single-bit transmission. Thus, in conjunction with the propagation model, it is now possible to obtain a preliminary assessment of link operability for a particular propagation geometry if the atmospheric scattering parameters are known. It is clear from our sample calculation that the principal conclusion to be drawn from such an analysis is the necessity of background-light suppression to realize useful scattered-light reception.

There are three generic approaches to the problem of background-light suppression, viz. the use of a wide-angle narrowband filter at the receiver, mid-ultraviolet operation, and adaptive phase compensation at the receiver. All of these approaches require significant device development.

ACKNOWLEDGEMENTS

The work reported here is the fruit of collaboration with many colleagues and students. In particular, we must acknowledge the contributions of D.J. Epstein, R.S. Kennedy, C. Warde, A.D. Fisher, W.H. Paik, S.R. Robinson, and W.S. Ross. This research was supported by National Science Foundation Grant ENG-78-7821603.

REFERENCES

- Chu, T.S., and Hogg, D.C., 1968, "Effects of Precipitation on Propagation at 0.63, 3.5, and 10.6 Microns," *Bell Syst. Tech. J.* 47, 723-761.
- Clark, J.R., and Baird, J.R., 1975, "Optical Communication under Low-Visibility Conditions: Recent Experimental Results," *1975 National Telecommun. Conf. Record*, IEEE, New York, pp 6.1-6.3
- Ditchburn, R.W., and Young, R.A., 1962, "The Absorption of Molecular Oxygen between 1850 and 2500 Å," *J. Atmos. Terrest. Phys.* 24, 127-139.

- Fisher, A.D., and Warde, C., 1979, "Simple Closed-Loop System for Real-Time Optical Phase Measurement," *Opt. Lett.* 4, 131-133.
- Fisher, A.D., 1981, "Techniques and Devices for High-Resolution Adaptive Optics," Ph.D. Thesis, Dept. of Elect. Engrg. and Computer Sci., M.I.T.
- Heggestad, H.M., 1968, "Optical Communication Through Multiple-Scattering Media," Tech. Rept. 472, Res. Lab. of Elect., M.I.T.
- Ishimaru, A., 1978, Wave Propagation and Scattering in Random Media, Vol. 2, Academic, New York, pp. 296-301.
- Kennedy, R.S., 1970, "Communication through Optical Scattering Channels: An Introduction," *Proc. IEEE* 58, 1651-1665.
- Kopeika, N.S., and Bordogna, J., 1970, "Background Noise in Optical Communication Systems," *Proc. IEEE* 58, 1571-1577.
- Lerner, R.M., 1971, "Limitations Imposed in the Use of Interference Filters in Wide Angle Optical Receivers," *Appl. Opt.* 10, 1914-1918.
- Lotspeich, J.F., 1979, "Iso-Index Coupled-Wave Electro-Optic Filter," 1979 CLEA Digest, IEEE, New York, p.7.
- McCartney, E.J., 1976, Optics of the Atmosphere, Wiley, New York.
- Middleton, W.E.K., 1958, Vision Through the Atmosphere, Univ. of Toronto Press, Toronto.
- Mooradian, G.C., Geller, M., Stotts, L.B., Stephens, D.H., and Krautwald, R.A., 1979, "Blue-Green Pulsed Propagation through Fog," *Appl. Opt.* 18, 429-441.
- Nakai, J., 1980, "A Spatio-Temporal Channel Model of Low-Visibility Optical Wave Propagation," S.M. Thesis, Dept. of Elec. Engrg. and Computer Sci., M.I.T.
- Nguyen, T.T., 1980, "A Combined Forward-Scatter and Diffusion Analysis of Low-Visibility Optical Propagation," S.M. Thesis, Dept. of Elec. Engrg. and Comp. Sci., M.I.T.
- Paik, W.H., Tebyani, M., Epstein, D.J., Kennedy, R.S., and Shapiro, J.H., 1978, "Propagation Experiments in Low-Visibility Atmospheres," *Appl. Opt.* 17, 899-905.
- Paik, W.H., 1978, "Optical Frequency Hopping for High Data Rate Optical Communication through Scattering Channels," Ph.D. Thesis, Dept. of Elect. Engrg. and Comput. Sci., M.I.T.
- Pepper, D.M., and Abrams, R.L., 1978, "Narrow Optical Bandpass Filter via Nearly Degenerate Four-Wave Mixing," *Opt. Lett.* 3, 212-214.
- Reilly, D.M., 1976, "Atmospheric Optical Communications in the Middle Ultraviolet," S.M. Thesis, Dept. of Elect. Engrg. and Comput. Sci., M.I.T.
- Reilly, D.M., and Warde, C., 1979, "Temporal Characteristics of Single Scatter Radiation," *J. Opt. Soc. Am.* 69, 464-470.
- Robinson, S.R., 1976, "Phase Estimates with Pre-detection Feedback for Optical Communication," *IEEE Trans. Commun.* COM-24, 1231-1237.
- Robinson, S.R., 1977, "Phase Compensation Receivers for Optical Communication," *IEEE Trans. Commun.* COM-25, 900-909.
- Ross, W.S., 1980, "Point-Source Optical Propagation in a Multiple Scattering Medium," Ph.D. Thesis, Dept. of Elec. Engrg. and Comput. Sci., M.I.T.
- Ross, W.S., Jaeger, W.P., Nakai, J., Nguyen, T.T., and Shapiro, J.H., 1981, "Atmospheric Optical Propagation: An Integrated Approach," *Opt. Engr.* 20, to appear.
- Russo, C.R., 1979, "Angular Spectrum Characteristics of Low-Visibility Optical Propagation," S.B. Thesis, Dept. of Elect. Engrg. and Comput. Sci., M.I.T.
- Shapiro, J.H., 1980, "Optical Communications through Low-Visibility Weather Conditions," 1980 National Telecommun. Conf. Record, IEEE, New York, pp. 27.6.1-27.6.6.
- Shapiro, J.H., and Warde, C., 1981, "Optical Communication through Low-Visibility Weather," *Opt. Engr.* 20, to appear.
- Simon, R.E., ed., 1974, RCA Electro. Optics Handbook, RCA, Harrison, p.62.
- Warde, C., Fisher, A.D., Cocco, D.M., and Burmawi, M.Y., 1978, "Microchannel Spatial Light Modulator," *Opt. Lett.* 3, 196-198.
- Yuen, H.P., and Shapiro, J.H., 1979, "Generation and Detection of Two-Photon Coherent States in Degenerate Four-Wave Mixing," *Opt. Lett.* 4, 334-336.

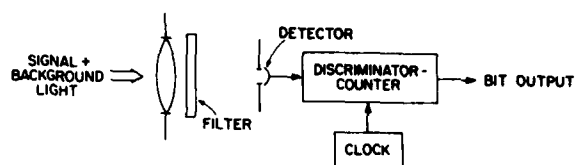


Figure 1 Direct-detection receiver for pulse-position modulation signals.

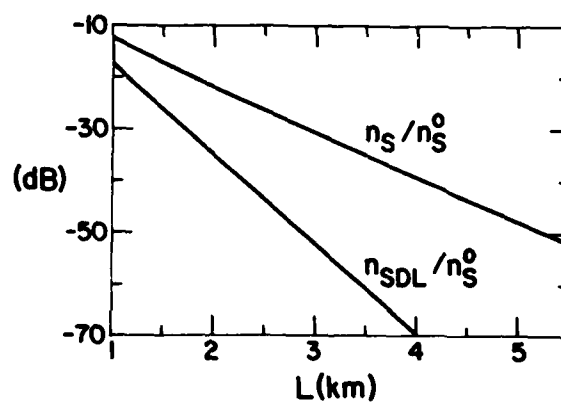


Figure 2 Energy collection comparison between diffraction-limited and wide field-of-view reception.

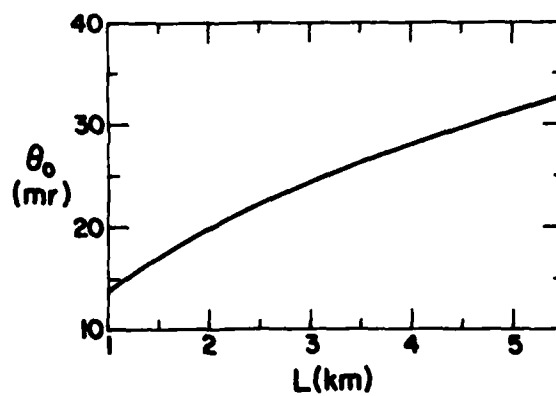


Figure 3 Half cone angle for wide field-of-view reception.

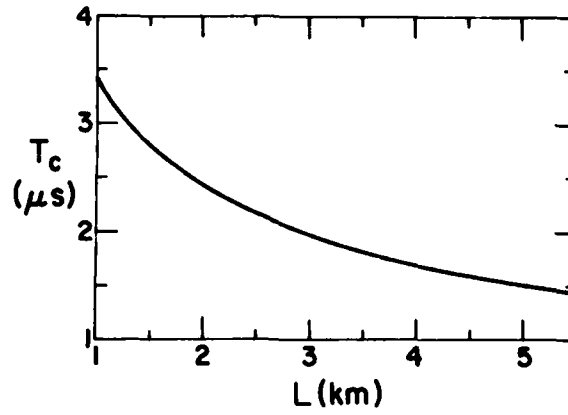


Figure 4 Coherence time predicted by the frozen-flow hypothesis.

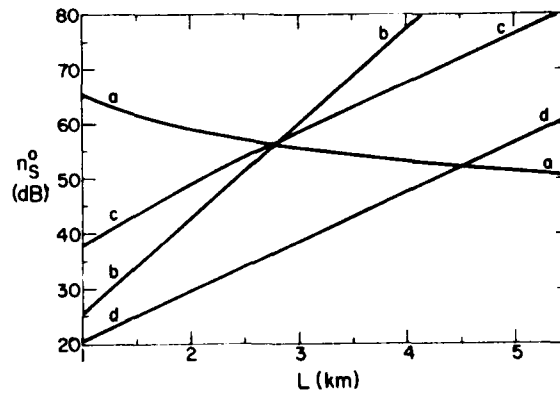


Figure 5 Low-visibility weather communication performance.

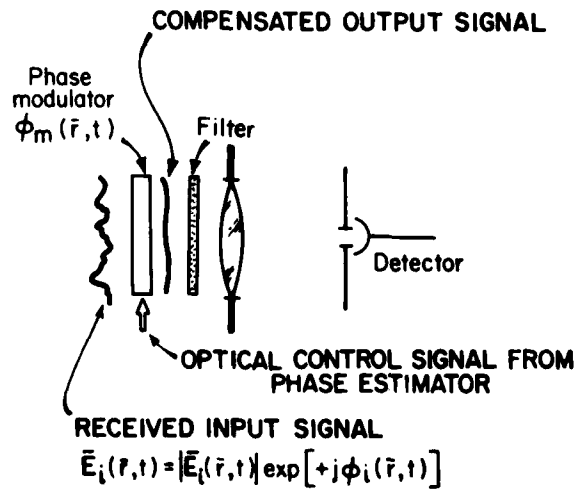


Figure 6 Direct-detection phase-compensated receiver.

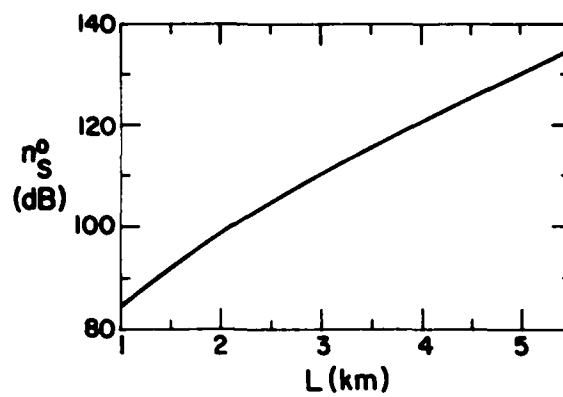


Figure 7 Signal energy needed for phase tracking using the frozen-flow coherence time.

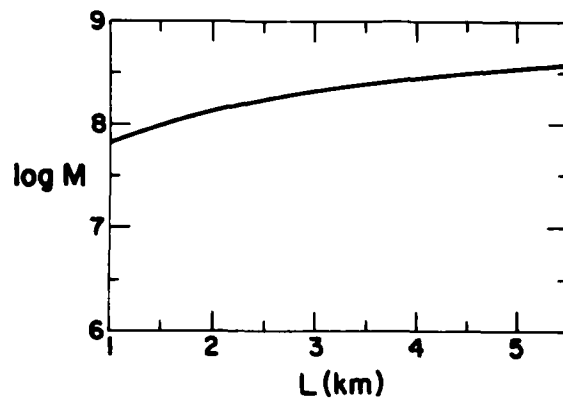


Figure 8 Number of spatial modes needed for phase tracking.

MERCURIC BROMIDE DISSOCIATION LASERS

E. Schimitschek
 Naval Ocean Systems Center
 San Diego, CA 92152

SUMMARY

HgBr₂/HgBr dissociation lasers, excited by electric discharge, have recently been shown to be efficient, scalable and wavelength-tunable sources in the blue-green spectral region. This paper will review the principal features of these lasers, their performance status and potential applications for underwater communication systems.

1. INTRODUCTION

Successful implementation of several advanced Navy system concepts, e.g., air-submarine communication (both tactical and strategic), optical detection of submarines at missile-launching depths and underwater surveillance, critically depends on the availability of powerful, pulsed lasers operating in the "blue-green window" of ocean water. The projected performance of those lasers varies somewhat with the specific application; however, for most cases the performance will be within the following baseline boundaries:

Table I
 Baseline Laser Performance for Blue-Green Systems

Wavelength	480 ± 20 nm
Pulse energy	0.1 - 10 Joules
Pulse width	20 - 1,000 nsec
Repetition rate	100 - 1,000 Hz
Efficiency	> 1% (overall)
Operating lifetime (MTBF)	10 - 40,000 hrs

Short pulsewidth is required for ranging and detection systems, but is not necessary for communication systems operating through heavy cloud layers (pulse stretching through multiple scattering). Required operating lifetime strongly depends on mission and platform accessibility. For laser communication, where the laser might be placed on a satellite, extremely long operation times would be required to make the system viable and cost-effective.

The HgBr₂/HgBr dissociation laser is one among several laser technologies now being explored for their potential usefulness in B/G systems. In this paper, work on that laser will be described which was performed at the Naval Ocean Systems Center.

2. THE HgBr₂/HgBr DISSOCIATION LASER

At room temperature, HgBr₂ is a white, crystalline powder with fairly low vapor pressure (~10⁻⁴ torr). On heating, the pressure rises quickly and reaches several torr at 155°C (Fig. 1). UV light around 200 nm is strongly absorbed by HgBr₂ vapor ($\epsilon_{200 \text{ nm}} \sim 1.6 \times 10^4$ liter mole⁻¹cm⁻¹) and causes photo-dissociation with simultaneous fluorescence in the blue-green spectral region:



Three features in process (I) are important:

(a) The quantum efficiency to produce the upper laser level is very high.

(b) The B-state of the HgBr is predominantly ionic, whereas the X-state is mostly covalent. This results in a strong Franck-Condon shift of the two electronic states. Together with fast relaxation within the vibrational manifolds in the presence of high buffer gas concentrations, the result is that the terminal levels will be essentially empty (Fig. 2).

(c) If container materials are chosen so that no side reaction can occur, the dissociation process is cyclic and the parent molecule HgBr₂ is reconstituted.

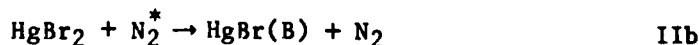
Using an ArF laser as pump source, we were able to demonstrate lasing by process (I) (SCHIMITSCHEK, E.J., CELTO, J.E., and TRIAS, J.A., 1977). Lasing occurred at several lines simultaneously centered around the strongest one at 502 nm. Although the HgBr₂/HgBr photodissociation laser works quite well and should be scalable to high pulse energies, the limited efficiency and lifetime of the ArF pump reduces the practicality of this approach.

Dissociative excitation of HgBr₂ can also be accomplished by collisions of the first and second kind rather than by photons. These considerations led us to experiments with direct discharge excitation and resulted in demonstrating lasing of HgBr₂/HgBr in a UV-preionized discharge (SCHIMITSCHEK, E. J. and CELTO, J.E., 1978). In the meantime, this laser has undergone considerable developments, some of which are discussed here.

2.1 UV-Preionized Discharge Excitation

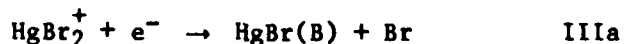
Dissociative excitation of HgBr₂ into HgBr(B) only requires between 6-7 eV. Therefore, limiting the electron temperature as well as providing for fast vibrational relaxation, calls for operating the discharge at fairly high buffer gas pressures. Also, the short radiative lifetime of the HgBr(B)- state (~27 nsec), which is further shortened by collisional deactivation, requires fast, high-rate pumping, conveniently obtained in a transverse discharge. At low rep. rates, external heat has to be provided to maintain the HgBr₂ partial pressure at several torr. A typical discharge configuration is shown in Fig. 3. All metal parts are 316 stainless steel, although tungsten and molybdenum were used by us with good results. In our UV-preionized discharge, the number density of the laser mixture is typically 1.2 Amagat, consisting mainly of Ne with 2.5% N₂ and 0.25% HgBr₂ (~155°C).

The formation of the HgBr B-state in a self-sustained discharge seems mainly to occur via two channels:



Process IIa probably occurs in all buffer gas mixtures, whereas IIb becomes more important with increasing N₂ concentrations.

Two additional formation pathways can be postulated, but, most likely, will be less significant



Quantitative data on the formation kinetics from modelling are becoming available now, as some of the previously unknown basic cross-sections are measured. $\text{HgBr}(X)$ is a radical and is not stable in the vapor phase. The recombination channels are not known in detail, but assuming no material is lost in side-reactions, several two- and three-body reactions can be postulated which reform HgBr_2 from the reaction products. To get accurate data on the reconstitution processes of HgBr_2 and the time scales involved, will be very important for a better understanding of this laser.

3. LASER PERFORMANCE

3.1 Single Shot Experiments

Most of our single shot experiments were performed with relatively small discharge volumes of about 120cm^3 . A Pyrex glass tube of 7 cm i.d. and 75 cm length was equipped with O-ring sealed brewster windows. The electrodes were two half-sections of a 2.5 cm o.d. 316 stainless steel tube, crimped at the ends to avoid arcing. The discharge length was 50 cm and the electrode spacing 3 cm. Each electrode was connected to the power supply with 6 adjustable glass-metal feedthroughs. A series of single line spark gaps above the electrodes provided the UV-preionization. The main discharge was driven by a Blumlein-type capacitor bank switched by a grounded grid thyatron. The laser tube was loaded with a small amount of HgBr_2 powder, evacuated and back-filled with the buffer gas. The valved-off tube was placed in an oven, which kept the center temperature regulated at 155°C (~ 2.3 torr HgBr_2). The window ends were slightly warmer to prevent condensation.

Measured output energies as a function of buffer gas composition and energy stored in the capacitors are shown in Fig. 4. Lasing efficiency of 1% could be achieved, although not at maximum output.

By monitoring voltage, current and side-light fluorescence intensities during the discharge at different N_2 concentrations, we conclude that the effect of added N_2 is most likely threefold: as expressed in IIb, N_2 helps in the formation of $\text{HgBr}(B)$; it also improves the extraction efficiency, possibly by reducing bottlenecking of the lower laser levels; also, it cools the electron temperature thereby allowing the discharge to run for a longer time at higher impedance, resulting in better power transfer.

More recently, using the same construction principle, we built a larger tube with a discharge volume of about 720cm^3 . We were able to extract 360 mJ out of this device. So far, discharge instabilities limited the efficiency to about 0.3%. Efficient, large volume operation of this laser with conventional UV-Preionization methods could be difficult. On the other hand, X-ray and E-beam preionization should readily allow scaling to several liters and corresponding energy levels.

3.2 Repetition Rate Scaling

In stationary gas mixtures of dimensions and pressures considered here, the time it takes to smooth out density gradients from the previous discharge, limits the rep rate to about 1 pps. Otherwise, severe arcing occurs. To avoid this problem, the gas has to be circulated.

We have obtained stable laser operation at 100 pps by recirculating the buffer gas and HgBr_2 vapor mixture inside the laser tube with a tangential (or cross-flow) blower. Fig. 5 shows the arrangement of the different parts inside the tube in cross-section. The container is a 75 cm long Pyrex tube with 15 cm i.d. The cathode (C) is located at the bottom of the tube and the anode (A) is held

in place by spiderweb-like supports. Both electrodes are connected with metal-glass feedthroughs to a folded Blumlein-type driver. The heater (H) provides additional heat to the tube, apart from the one coming from the discharge. The blower (B) recirculates the HgBr_2 /buffer gas mixture continuously inside the tube, clearing the discharge region between the electrodes of hot gases. When operating temperature is reached, the thermocouple (T) shuts off the heater (H) and from then on the laser is self-heating, a balance having been established between discharge heat input and heat loss through the glass walls.

We have run this laser at 100 pps and 30 mJ/pulse for 1-2 hours at a time. The output is quite steady with a slow decrease after about 10^6 shots.

3.3 Lifetime Issues

The present lifetime limitation is caused by side-reactions with the stainless steel parts, particularly the electrodes. What seems to happen is that reactive dissociation products like Br and Br_2 , form metal bromides with Fe, Ni, Cr and others. Their vapor pressure is probably too low at 155°C to detrimentally affect the lasing. However, their formation results in an excess of Hg. Hg then reacts with HgBr_2 and forms Hg_2Br_2 , a material which is yellow at elevated temperature and fluoresces pinkish under a black-light lamp. Both effects can be seen after prolonged lasing. Hg_2Br_2 is supposed to disproportionate in the vapor phase into HgBr_2 and Hg, but enough Hg_2Br_2 probably accumulates to interfere with efficient lasing, either by absorption, quenching or scattering.

Although stainless steel is a convenient material to use for initial experiments, it has been recognized from the beginning that long term corrosion is a problem. Recent results obtained at Westinghouse (LIU, C.S., FELDMAN, D.W., and HIRAYAMA, C., 1980) indicate that certain noble metals are much more compatible with the lasing species and long operation times might be achievable.

3.4 Narrow-bandwidth Operation

The HgBr B \rightarrow X fluorescence band is quite broad and structured, being made up of many vibrational and rotational lines with added complexity from the Br and Hg isotopes (Fig. 6a). The laser spectrum from a free running oscillator consists of several peaks, distributed around 502 and 504 nm (Fig. 6b). For application in communication systems, it is important for the laser to emit at a very narrow, single line for effective background noise rejection. In the main gain region, it is possible to operate HgBr with narrow-bandwidth by injection-locking.

Using a tunable dye laser as source, we effectively locked the HgBr laser wavelength between 495 and 505 nm with a bandwidth of less than 0.05 nm (Fig. 6c). The pulse energy obtained with injection-locking is (at least in the main gain region) somewhat higher than free-running, because of the shorter turn-on time for lasing in the resonator.

4. CONCLUSIONS

The UV-preionized $\text{HgBr}_2/\text{HgBr}$ dissociation laser, excited by electric discharge, has been operated at $\sim 0.4\text{J}$ energy/pulse, 1% efficiency, 100 pps and 0.05 nm bandwidth. Although so far, those performance data have not been obtained simultaneously, there is little doubt that that could be done. Experiments performed at other laboratories indicate that with X-ray or e-beam preionization, larger pulse energies can be extracted. In the near future, the technology will be available to build 100-1,000 watt average power, efficient and compact HgBr lasers. The most critical issue still to be resolved is material compatibility to achieve exceedingly long lifetimes.

If the lifetime problems can be solved - and there are indications that they will be - the HgBr₂/HgBr laser should have far-reaching impact on blue-green Naval systems in the area of tactical and strategic communication as well as in surveillance.

5. ACKNOWLEDGEMENTS

The author is grateful for helpful discussions with D. E. Altman, J. E. Celto, F. E. Hanson, and T. M. Shay. This work was supported in part by the Naval Electronics Systems Command Code 304 and by NOSC Independent Research Funds.

6. REFERENCES

Liu, C. S., D. W. Feldman, and C. Hirayama, "Electrode and Laser Tube Materials Considerations for Discharge Excited HgBr Lasers", Int. Conf. on Lasers '80, New Orleans, Dec. 15-19, 1980.

Schimitschek, E. J., J. E. Celto, and J. A. Trias, "Mercuric Bromide Photodissociation Laser", Appl. Phys. Lett. 31, 608 (1977).

Schimitschek, E. J. and J. E. Celto, "Mercuric Bromide Dissociation Laser in an Electric Discharge", Optics Lett., 2, 64 (1978).

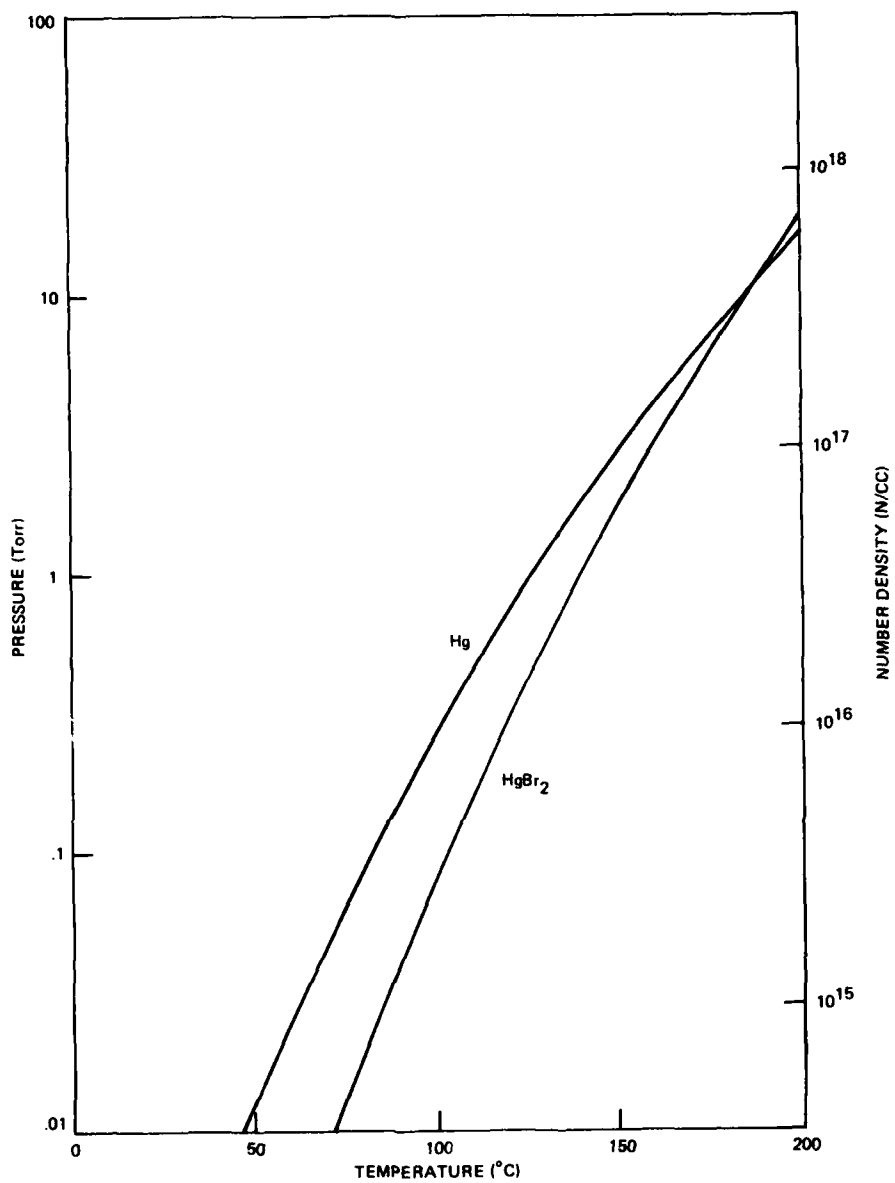


Fig. 1 HgBr₂ vapor pressure versus temperature.
Hg vapor pressure added for comparison.

HgBr₂/HgBr DISSOCIATION LASER ENERGY LEVELS (SCHEMATIC)

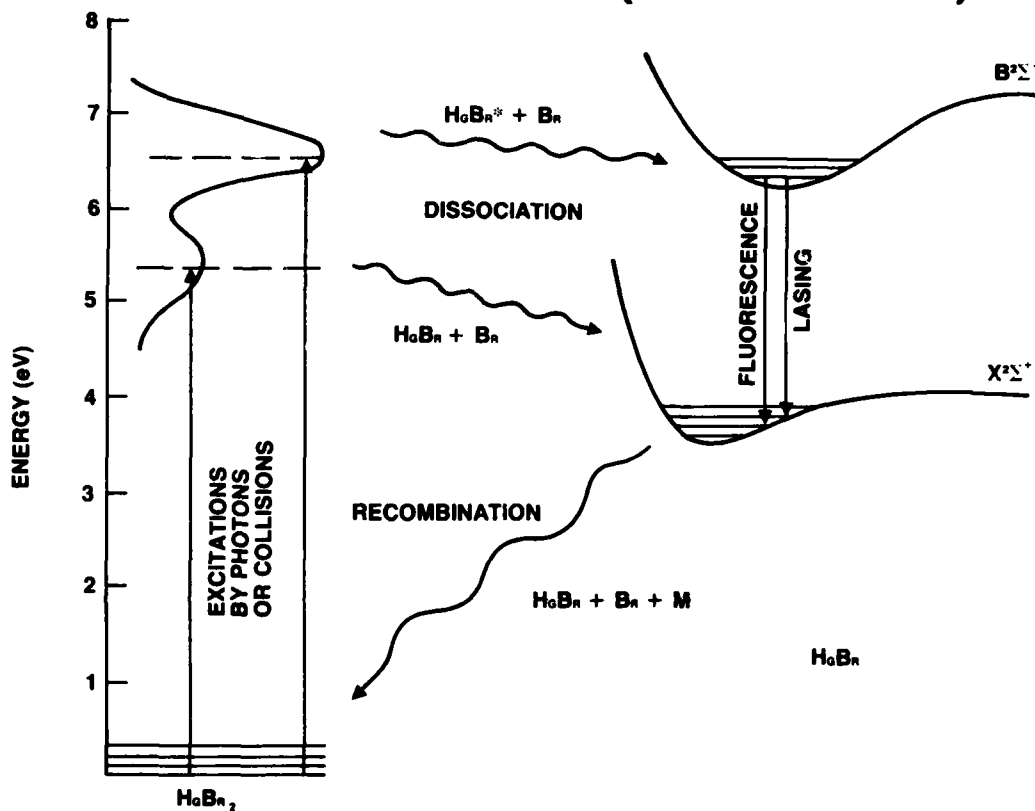


Fig.2 HgBr₂/HgBr dissociation, fluorescence (lasing) and recombination cycle (schematic)

UV-PREIONIZING DISCHARGE CIRCUIT FOR HgX₂ EXCITATION

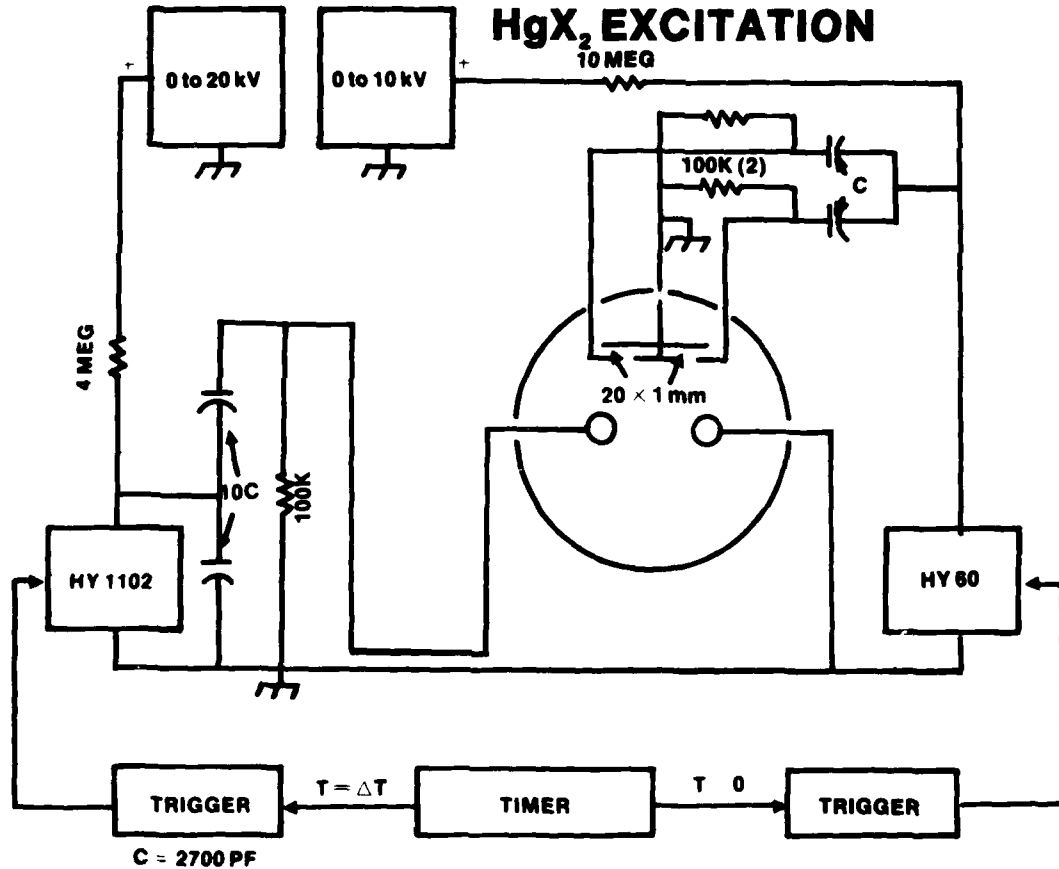


Fig. 3 UV-preionized, transverse, Blumlein-type discharge arrangement for HgBr₂/HgBr excitation. The laser tube is located in an oven (not shown).

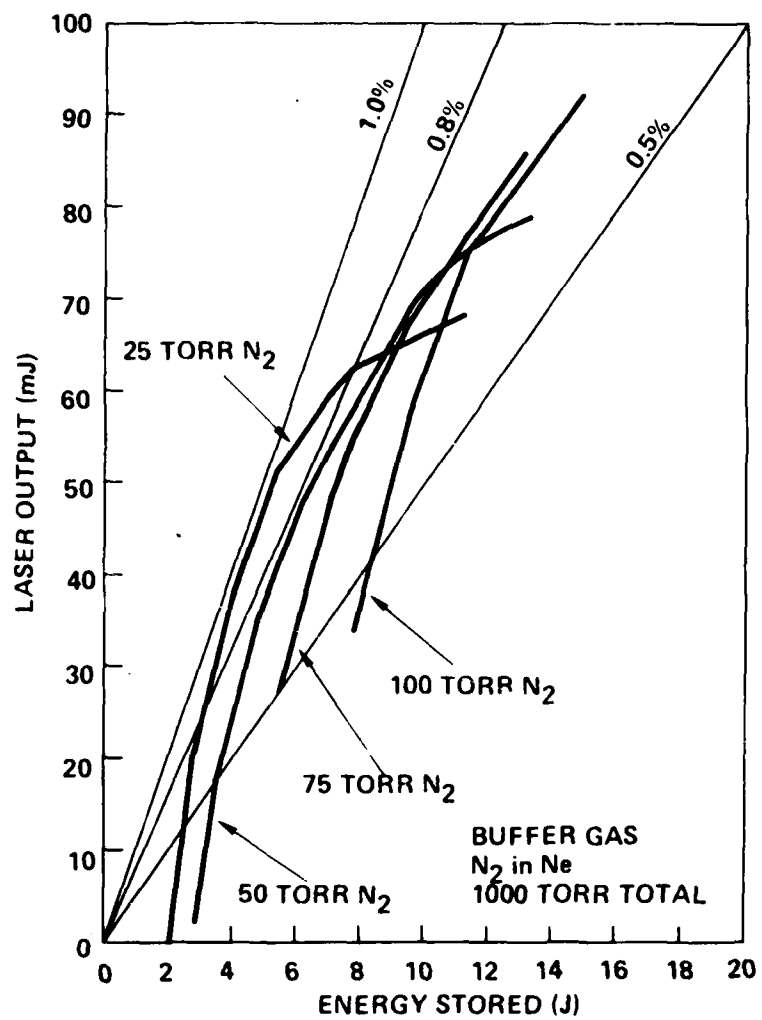


Fig. 4 Laser energy output versus stored energy in capacitor bank. The discharge volume was about 120 cm³.

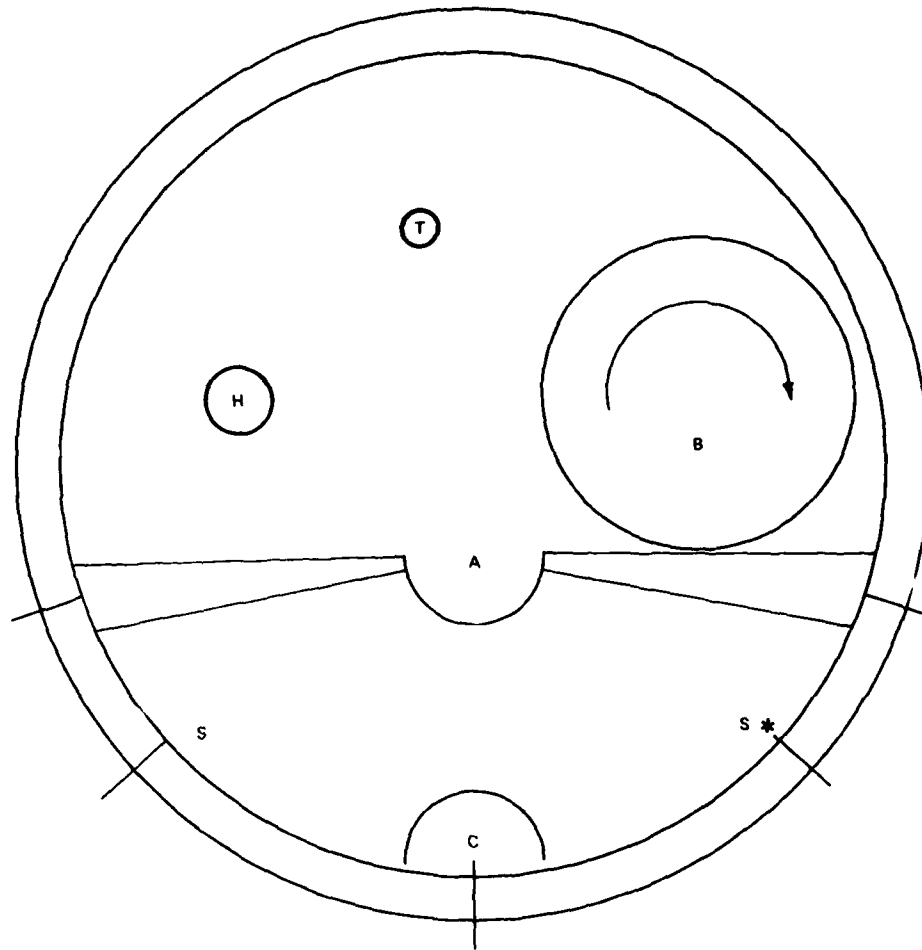


Fig. 5 Cross-section of 100 Hz $\text{HgBr}_2/\text{HgBr}$ laser. Anode (A) and cathode (C) are connected to driver. (S) are two rows of preionization spark gaps. (H) is an auxiliary heater in a quartz tube, shut off when the thermo-couple (T) senses operating temperature. (B) is a cross-flow blower, circulating the gas mixture in the laser tube.

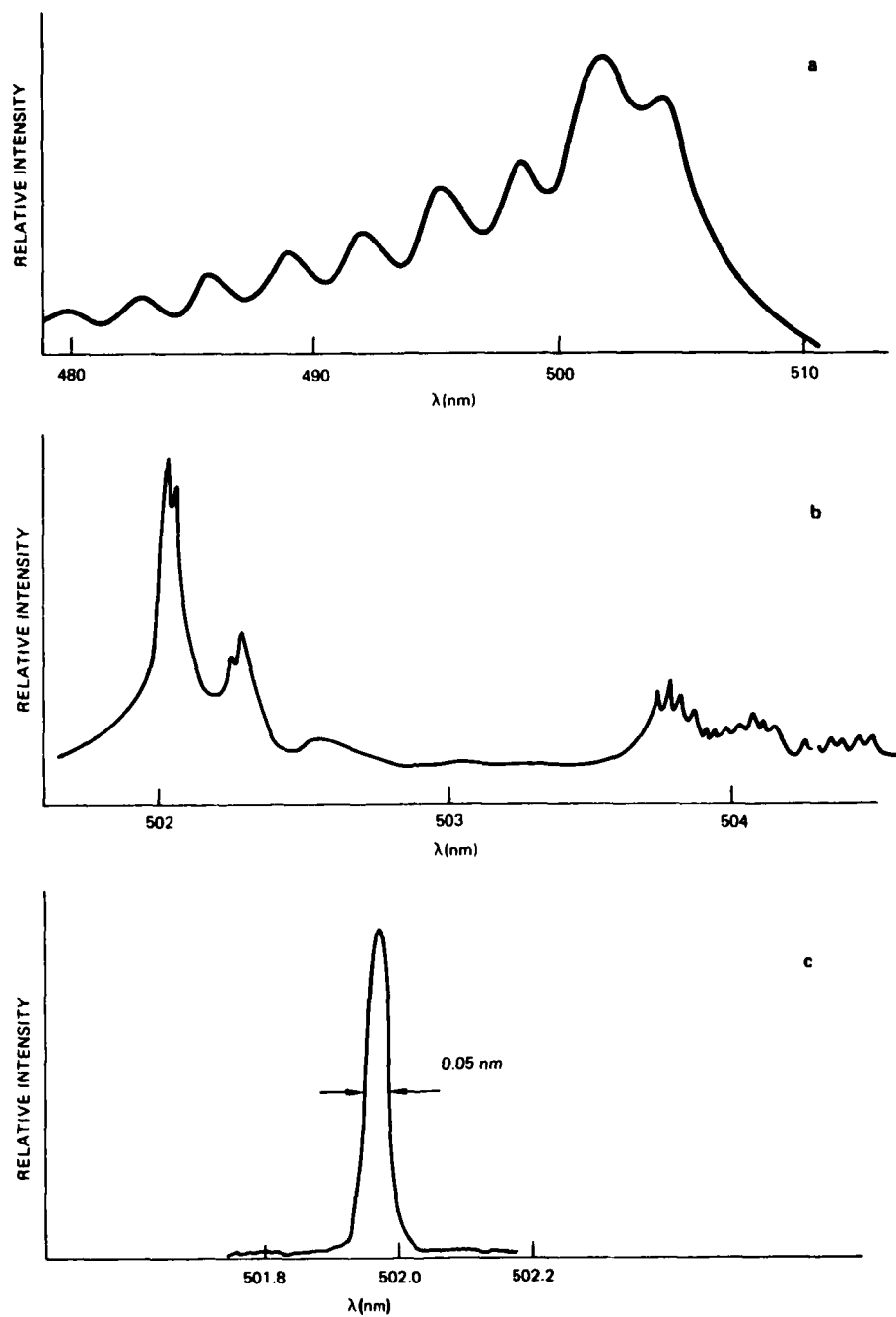


Fig. 6 HgBr (B \rightarrow X) fluorescence spectrum (a); free-running laser oscillator (b); injection-locked output (c). Note the change and shift in wavelength scale.

COPPER VAPOR LASERS: A REVIEW

T. W. Karras
 General Electric Company
 King of Prussia, PA, U.S.A.

ABSTRACT

The pulsed copper vapor laser is a practical useful source for emission in the blue-green. It can be operated as a high temperature sealed-off device with no moving mechanical parts and therefore is well suited to long life applications. Furthermore, its efficiency is among the highest of lasers emitting in the visible, making its operation at moderate to high average powers practicable.

Typical operation for two discharge configurations will be discussed: an immature transverse discharge mode and a more developed longitudinal discharge mode. Both have been demonstrated at average powers exceeding 50 watts. Master oscillator power amplifier operation has been used to extend the power of nominal 15-watt modules to over 100 watts.

This device also shows great flexibility in its various output parameters. Repetition rate can be varied from a single pulse to over 100 kilohertz. Pulse width can be changed from 5 to 185 nanoseconds. Its volume can be greatly increased while maintaining constant specific output.

Computer modeling studies will be discussed which can be used to project power scaling and these other output characteristics.

A. INTRODUCTION

The copper vapor laser is one of a class of pulsed self-terminating systems which emit in a wavelength band centered upon the visible (Walter, W.T., 1966). The gold laser line at 312.2 nm (Markova, S.V., 1978) and the strontium laser line at 6.45 μ (Platonov, A.V., 1978) represent the extremes in this range. While even at these extremes over 1 watt has been reported, the neutral atom copper laser, with its dominant line at 510.5 nm and a secondary line at 578.2 nm, is the most highly developed.

This wavelength is appropriate for water transmission (White, M., 1980), dye laser pumping (Hargrove, R.S., 1980), silicon annealing (Pivirotto, T.J., 1980), and many other applications requiring moderate to high average power. As a result of this interest the copper vapor laser has been demonstrated at higher power levels and over a wider range of operating parameters than any other laser of this class.

The following paper will discuss the physics and technology involved, the current state-of-the-art, and new computer simulation programs.

B. BACKGROUND1) Physics

Laser operation in neutral copper vapor, as in other media of this class, is inherently pulsed or self-terminated because the lower laser state is metastable. No mechanism for depopulating this state concurrently with excitation of the upper laser state has yet been found. Thus, the basic process has a cyclic pattern. A fast electrical discharge pulse produces an inversion, and this is followed sequentially by laser oscillation and an extended period during which the metastable lower state must relax before the cycle can be repeated (Walter, W.T., 1966).

The nature of this operation can be easily seen by referring to the energy level diagram of the copper atom shown in Figure 1. The upper laser states (4^2P) are excited from the ground state by direct electron collisions. These levels are resonant states which are strongly coupled to the ground state. Therefore, the cross section for collisional excitation is large and a significant percentage of the available copper atoms will be excited into these levels.

The resonance radiation will, at low copper densities, quickly deplete this excitation before an inversion can be established. However, with sufficient copper vapor density the resonance transitions are radiatively trapped. This is equivalent to a lengthening of the natural lifetime of the resonance lines and changes the branching ratio to favor the (laser) transitions into the 4^2D levels. Thus, a population inversion of the 4^2P states relative to the 4^2D states can be obtained. Laser oscillation in the 510.5 nm and 578.2 nm lines results when optical feedback from mirrors is provided.

2) Technology

Laser oscillation in atomic copper vapor was first reported by Walter in 1966. That work used a furnace and pure copper metal to produce the vapor pressure desired. A major improvement was made when Petrash and co-workers in the Soviet Union developed a discharge heated device during 1972 (Isaev, A.A., 1972). The required discharge tube temperature (copper vapor density) was achieved by a proper balance of input power to the electrical discharge and thermal insulation of the discharge tube. Thus, because the waste heat from

the discharge which excited the copper atoms also heated the laser tube, no additional source of energy was required. The overall system efficiency of the laser was thus improved.

A fundamental change in vapor source was developed by Russell and co-workers in response to the high temperatures required to vaporize pure copper (Chen, C.J., 1975). This technique used copper halides to provide the required vapor pressure at much lower temperatures. The compounds could then be dissociated, producing free copper, with the same discharge pulses that produced the inversion. Discharge heating was of course ultimately used in this sort of device as well. While many of the laboratory demonstrations obtained with the copper halide technology were generally equivalent to those obtained with a pure metal vapor source (Kazaryan, M.A., 1980), the best performance that now represents the state-of-the-art was obtained with pure metal. The following discussions will thus be limited to that technology.

Other major additions to the technology followed quickly. Transverse discharge operation was shown to have higher specific output than the longitudinal mode most commonly used (Isakov, I.M., 1976). Master oscillator power amplifier techniques were also shown to be practicable for increasing beam power and quality (Anderson, R.S., 1975). Unstable resonators produced nearly diffraction-limited output (Zemskov, K.I., 1974) and high pressure sealed-off operation extended laser lifetime to over 3,000 hours (Burmakin, V.A., 1978). Commercial sales also began (Laser Focus, 1976). The basic elements of a practical long life technology gradually came together.

Throughout this period of quickening development, advances in output power also took place at an increasing rate. Figure 2 shows how the maximum published output power increased during the last thirteen years, using both Soviet and American sources. As is often the case for such a plot, it follows an exponential trend. The reason for this dependence is not clear since different organizations and technologies were involved. However, it is interesting to note that there are two different trends for the two countries. Evidently the dynamics of these two interacting groups are different.

C. LASER CHARACTERISTICS

1) Longitudinal Discharge Lasers

The present state-of-the-art has been dominated by longitudinal discharge devices. This is in large part due to the relative simplicity of this design. Simple ceramic discharge tubes are used with electrodes at either end. The hot zone is confined to center regions of the tube with cylindrical insulators or heat shields. The device thus assumes a simple coaxial form. Testing of different discharge tubes under various operating conditions is quite straightforward and a large number of laboratories have been able to make contributions.

This has led to a wide variation in device characteristics. Table 1 lists the characteristics of several lasers with output of 10-20 watts average power. It can be seen that comparable output could be achieved with substantially different tube diameters, buffer pressure, and repetition rate. Each device was optimized differently producing this result.

Table 1. Characteristics of Several Experimental Longitudinal Discharge Copper Vapor Lasers

	Lebedev Institute (Ref. 7)	Institute of Atmospheric Physics (Ref. 15)	GE (Ref. 16)	Nuclear Research Center Negev (Ref. 17)
Discharge Tube Diameter	1.5 cm	2.0 cm	3.8 cm	4.0 cm
Active Length	70 cm	26.5 cm	60 cm	50 cm
Repetition Rate	15 kHz	8 kHz	1-3 kHz	2-5 kHz
Buffer Pressure	20 torr Ne	20 torr Ne	5 torr He	200 torr Ne
Average Power	16 W	9.75 W	12-18 W	15-20 W
Efficiency	1%	2.6%	0.5-1.0%	0.6-0.8%
Specific Energy	8.6 $\mu\text{J}/\text{cm}^3$	11.8 $\mu\text{J}/\text{cm}^3$	9-17 $\mu\text{J}/\text{cm}^3$	5.5-12.7 $\mu\text{J}/\text{cm}^3$

Table 2 gives a set of optimum characteristics, each generally obtained on a different device. For instance, the 55-watt average power figure was obtained with a 7.3 cm ID discharge tube (Warner, B.E., 1980) and the 150 kHz rate with one of 1.6 mm.

The wide range of capabilities covered by Tables 1 and 2 makes the copper vapor laser suitable for a wide range of applications. The dye pumping capability mentioned in the introduction coupled with high average power has made copper lasers useful as components in higher power systems used in photochemical studies (Grove, R.E., 1980). The short pulse length is useful in measurement of coastal water depths (White, R., 1980, and Karras, T.W., 1980). High data rate atmospheric probing has used the high repetition rate capability (Barber, T.R., 1979). Several copper lasers are offered commercially and the characteristics of a representative sample are shown on Table 3.

Table 2. Optimum Characteristics of Copper Vapor Lasers

	<u>Longitudinal Discharge</u>	<u>Transverse Discharge</u>
Maximum Average Power	55 W	75 W
Pulse Duration	5-185 nsec	5-30 nsec
Maximum Peak Power	800 kW	~1 MW
Maximum Efficiency	3%	2.5%
Repetition Rate	Single Pulse-150 kHz	Single Pulse-70 kHz
Maximum Lifetime-Sealed Off	3,000 hours	----
Maximum Specific Energy	75 $\mu\text{J}/\text{cm}^3$	650 $\mu\text{J}/\text{cm}^3$

Table 3. Commercially Available Copper Vapor Lasers

	<u>GE Model 6-15</u>	<u>USSR Milan 10</u>	<u>Laser Consultants Model CU-31</u>	<u>CJ Research Systems Model CU-1001</u>
Average Power	15 W	15 W	2 W	1 W
Pulse Duration	30 nsec	10 nsec	20 nsec	30 nsec
Beam Diameter	2.3 cm	2 cm	1.5 cm	2 cm
Maximum Laser Power Consumption	3 kW	4 kW	----	3 kW
Nominal Repetition Rate	6 kHz	15 kHz	2 kHz	10 kHz

2) Transverse Discharge Lasers

The transverse discharge configuration often used with gas lasers is more complex when applied to high temperature devices such as the copper laser. Most designs require that penetrations be made through thermal or electrical insulators (Bokhan, P.A., 1978). The long or multiple electrodes can thus lead to substantial thermal and vapor loss. The only alternative appears to involve electrical feed from the ends of a ceramic tube (Buzhinskii, O.I., 1979), giving an external appearance similar to that of a longitudinal discharge device.

The optimum characteristics thus far demonstrated with transverse discharge copper vapor lasers are also shown in Table 2. It is important to note that while many of these values are superior to those shown for longitudinal discharge devices they were not obtained during practical discharge heated operation. In fact, even the 75-watt value, far above any other previously reported with a transverse discharge, was obtained during experiments using auxiliary heating (Artem'ev, A.Yu., 1980).

This lack of development reflects the practical difficulties involved. Excellent results can be obtained in laboratory experiments, such as those reporting high specific energy (Bricks, B.G., 1975 and Fedorov, A.I., 1978), but their extension to practical large volume operation has not been accomplished (Bokhan, P.A., 1978).

Typical examples of the kind of results that have been obtained are given in Table 4.

Table 4. Characteristics of Several Experimental Transverse Discharge Copper Vapor Lasers

	<u>Bricks (Ref. 23)</u>	<u>Bokhan (Ref. 25)</u>	<u>Buzhinskii (Ref. 26)</u>	<u>Artem'ev (Ref. 22)</u>
Active Zone Dimensions	2x1x0.5 cm	6x0.6x0.8	42x5x2 cm	?
Average Power	1.8 W (Burst)	0.07 W	10 mJ Single Pulse	75 W
Efficiency	----	0.4%	2.5%	1.6%
Repetition Rate	18 kHz	1 kHz	----	3 kHz
Specific Energy	50 $\mu\text{J}/\text{cm}^3$	26 $\mu\text{J}/\text{cm}^3$	21.6 $\mu\text{J}/\text{cm}^3$?
Buffer Pressure	70 torr Ne	470 torr Ne	400 torr Ne	532 torr Ne

The large electrode area of a transverse discharge laser might be expected to lead a very large peak current requirement. This has been avoided by the use of large buffer gas pressure. Thus, even with high applied field strength the current density is low and specific input energy is maintained at required levels. At the extremes, then, are the high current density, low field strength, longitudinal discharge devices and, at the other, low

current density, high field strength, transverse discharge devices.

The ultimate trade off appears to be between the simplicity and lower specific energy of longitudinal devices and the complex structure but higher specific energy of the transverse discharge devices. Other factors, such as average power and efficiency, appear comparable. Of course, a simple reliable transverse discharge design could change the balance but at this time practical applications are still dominated by longitudinal discharge systems.

D. POWER SCALING

The most important of the laser characteristics covered in the previous section is that of output power. Most applications are critically dependent upon it. As pointed out earlier, master oscillator power amplifier (MOPA) techniques have been developed to use limited power modules as building blocks to produce high power output (Anderson, R.S., 1975; Grove, R.E., 1980 and Anderson, R.S., 1967). As the number of modules is increased the complexity of the control system mounts, eventually leading to practical limits to the attainable power. A high power module, however, can extend the total output without increase in complexity.

Increase in specific loading of the plasma is the most straightforward method of increasing specific, and therefore total, output of a single module. As noted above, this can be done at low pressure, low field strength across the discharge, and high discharge current, or at high pressure, high field strength across the discharge, and low discharge current. The controlling parameter is the energy (and power) deposited by the discharge per unit volume of active medium (specific input). Figure 3 shows this dependence for a wide variety of tubes of different diameter tested in our laboratory.

Since specific loading of the laser cannot be increased indefinitely, increase in active laser volume must also be turned to.

Some of the earliest experiments with the copper vapor laser, during the late 1960's, showed that increased average power and pulse energy could be obtained by such scaling of the laser volume. An increase of discharge tube ID from 1 cm to 5 cm, and consequently volume from 60 to 1600 cm³, produced a peak power increase from 2 kW to 40 kW (Walter, W.T., 1967). The average power also increased in roughly the same proportion from 0.02 W to 0.5 W (Walter, W.T., 1966 and 1968).

More detailed experiments at a later time and using higher specific loading energy also showed an increase of power with volume. Work in the U.S., at General Electric in 1975, showed a steady increase in average and peak power as discharge tube diameter was raised while maintaining the specific output energy at about 39 $\mu\text{J}/\text{cm}^3$ (Anderson, R.S., 1975 and Anderson, R.S., 1975). This work was extended to discharge tube diameters of 3.8 cm in work conducted a year later (Anderson, R.S., 1976). There it was shown that, for constant specific loading, the specific output grew linearly with active laser volume. Specific energy of 25 $\mu\text{J}/\text{cm}^3$ was maintained with a variety of tubes up to 3.2 cm ID and only fell off above this diameter because sufficient input was not supplied. Pulse energy of 12 mJ, the highest demonstrated to that date, was obtained.

This work was confirmed in Israel where output was also shown to rise linearly with laser volume using laser tubes with diameters up to 3.0 cm ID (Smilanski, I., 1978). A constant 8 $\mu\text{J}/\text{cm}^3$ specific output was maintained at 4 kHz. In a succeeding paper, data was presented that extended this to a 4 cm ID discharge tube (Smilanski, I., 1979).

There are modes of operation (e.g., those involving the use of a low pressure helium buffer) in which this scaling would be limited by metastable deactivation at the discharge tube walls (Miller, J.L., 1979). However, the presence of a volume active process which allowed laser operation when walls were remote had been previously reported by this laboratory in 1975 (Bricks, B.G., 1975). This took place in a high pressure (75-100 torr) neon buffer and it was suggested that collisions of the second kind between electrons and the copper metastable were responsible for the deexcitation. The transition from a wall dominated to a volume active deexcitation mechanism has since been confirmed (Bokhan, P.A., 1978) and the usefulness of high pressure neon, in particular, in the operation of large volume lasers has been noted (Warner, B.E., 1980 and Karras, T.W., 1980).

The importance of preionization in this volume active process had been mentioned (Bricks, B.G., 1975), but recent work has clarified it. Too little will shorten the pulse width, eventually at a cost of reduced pulse energy (Karras, T.W., 1980). Too much will limit or prevent operation in large diameter tubes. A proper balance, when repetition rate and recombination processes are taken into account, will lead to an optimum output (Smilanski, I., 1980 and Bokhan, P.A., 1980). Techniques for controlling this preionization, by using the current which charges the discharge capacitor, include command charging and bypass charging (Karras, T.W., 1980).

Recent analysis of data obtained with laser tubes varying from about 1 cm ID to over 7 cm ID, using optimum preionization (repetition rate), and loaded with approximately 0.2 mJ/cm³ input, showed that the specific output was uniformly in the range of 5-6 $\mu\text{J}/\text{cm}^3$. This is consistent with Figure 3 and indicates that the projections shown there can be extended to large diameter large volume devices. Experiments at lower specific energy have been conducted in tubes as much as 10 cm ID supporting this conclusion (Ludmirsky, A., 1979).

E. COMPUTER MODELING

As the physical size of laser modules increases, the incentive to design with computer simulation becomes greater. The empirical techniques previously used may have required less effort than the construction of an appropriate computer code but the development of large high power devices changes that trade off. The recent increase in the number and sophistication of computer codes applicable to copper vapor laser simulation attests to the general acceptance of this fact (Kusher, M.J. and Culick, F.E.C., 1980; Kushner, M.J. and Warner, B.E., 1980; Walter, W.T., 1980; and Arlantsev, S.V., 1980).

Computer models for simulation of longitudinal discharge copper laser operation were first attempted during early device development (Leonard, D.A., 1967). Succeeding work was used to estimate maximum performance that might be obtained (efficiency 7%, specific energy 3 mJ/cm^3) (Eletskii, A.V., 1975) but a model that was useful over a wide range of operating conditions was not developed.

Recent work has been quite successful in that regard. Work by Kushner (Kushner, M.J. and Warner, B.E., 1980) and Walter (Walter, W.T., 1980) have shown excellent agreement over a wide range of variables. Figure 4 shows such agreement between computer results obtained by Kushner (Kushner, M.J. and Warner, B.E., 1980) and experimental data obtained in this laboratory at a variety of repetition rates with a General Electric Model 6-15 laser. Walter has shown similar correspondence between his computer predictions and laser pulse energy obtained at different capacitor voltages (Walter, W.T., 1980). Possibly most significant is the agreement Walter obtained with the state populations measured by Smilanski (Walter, W.T., 1980, and Smilanski, I., 1980). Evidently microscopic variables are predicted as well as the laser output.

A computer model for a transverse discharge copper laser recently reported in the Soviet literature (Arlantsev, S. V., 1980), appears to be equally sophisticated. The results of this program are also found to agree with experiment but the principal purpose of the work is to determine an optimum operating condition for high buffer pressure operation. This result is summarized in Table 5. The principal limitation in volume scaling of these results was found to be heating of the gas and so wall or electrode dimensions are a major consideration. At these high buffer pressures the maximum electrode width was found to be 4.5 cm. In the single pulse regime of operation, where there is time for diffusion cooling, preliminary results showed operation to be only weakly dependent upon buffer density. Furthermore, they showed that the optimum copper density grows with the applied field strength reaching 10^{16} - 10^{17} cm^{-3} at 10-20 kV/cm. This is in rough agreement with early results obtained in our laboratory (Bricks, B.G., 1977).

Table 5. Optimum Transverse Discharge Laser Operating Conditions
(Arlantsev, S.V., 1980)

<u>Characteristic</u>	<u>Value</u>
Neon Density	$4-8 \times 10^{18} \text{ cm}^{-3}$
Copper Density	$0.5-1.0 \times 10^{16} \text{ cm}^{-3}$
Applied Field Strength	$\sim 1 \text{ kV/cm}$
Specific Loading of Stored Energy	3 mJ/cm^3
Repetition Rate	2.5 kHz
Specific Average Power	$36-55 \text{ mW/cm}^3$

We are now investigating operation in large diameter devices at low repetition rates. Preliminary results indicate that from several tenths to over 1 joule per pulse should be practicable.

F. SUMMARY

The copper vapor laser is an effective high power pulsed source with emission in the visible. It can operate over a wide range of parameters with efficiency of over 1%. Scaling to higher powers has progressed steadily and over 100 watts from a single oscillator module can be projected. This may be done with a large diameter longitudinal discharge configuration but transverse discharge devices are receiving increasing attention.

REFERENCES

1. Anderson, R.S., Bricks, B.G., Springer, L.W. and Karras, T.W., 1975, "A Discharge Heated Copper Vapor Master Oscillator Power Amplifier," *IEEE J. Quant. Elect.* QE-11, 56.
2. Anderson, R.S., Homsey, R.J. and Karras, T.W., 1976, "Low Repetition Rate Copper Vapor Laser," Final Report, Contract N00014-76-C-0975.
3. Anderson, R.S. and Karras, T.W., 1980, "A Three Amplifier Copper Laser MOPA Chain," *Proceedings of the International Conference Lasers '79*, Ed. by V.J. Corcoran, STS Press.
4. Anderson, R.S., Springer, L.W., Bricks, B.G. and Karras, T.W., 1975 "Discharge Heated Copper Vapor Laser," *IEEE J. Quant. Elect.* QE-11, 172.
5. Arlantsev, S.V., et al., 1980 "A Theoretical Study of a Repetitively Pulsed Copper Vapor Laser," *Kbantovaia Elektronika* 7, 2319.
6. Artem'ev, A.Yu., et al., 1980, "Energy Characteristics of a Transverse Discharge Copper Vapor Laser," *Kvatovaia Elektronika* 7, 1948.
7. Barber, T.R., 1979, "Short Time Mass Variation in Natural Atmospheric Dust," Thesis, New Mexico State University, Las Cruces, Mexico.
8. Bokhan, P.A. and Gerasimov, V.A., 1979, "Optimization of the Excitation Conditions in a Copper Vapor Laser," *Sov. J. Quant. Elect.* 9, 273.
9. Bokhan, P.A. and Schcheglov, V.B., 1978, "Investigation of a Transversely Excited Pulsed Copper Vapor Laser," *Sov. J. Quant. Elect.* 8, 219.
10. Bokhan, P.A., Gerasimov, V.A., Solomonov, V.I. and Shcheglov, V.B., 1978 "Stimulated Emission Mechanism of a Copper Vapor Laser," *Sov. J. Quant. Elect.* 8, 1220.
11. Bokhan, P.A., Silant'ev, V.I., and Solomonov, V.I., 1980, "Mechanism for Limiting the Repetition Frequency of Pulses from a Copper Vapor Laser," *Sov. J. Quant. Elect.* 10, 724.
12. Bricks, B.G., Karras, T.W., Anderson, R.S. and Anderson, C.E., 1977, "Results of a Parametric Study of a Flowing Copper Vapor Laser," *Bull. Amer. Phys. Soc.* 22, 190. Also 1975, "High Repetition Rate Flowing Copper Vapor Laser," *IEEE J. Quant. Elect.* QE-11, 57.
13. Burmakin, V.A., Evtyunin, A.N., Lesnoi, M.A. and Bylkin, V.I., 1978, "Long Life Sealed Copper Vapor Laser," *Sov. J. Quant. Elect.* 8, 574.
14. Buzhinskii, O.I., et al., 1979, "Copper Vapor Laser Excited by a Transverse Discharge," *Sov. J. Quant. Elect.* 9, 1201.
15. Chen, C.J. and Russell, G.R., 1978 "High Efficiency Multiple Pulsed Copper Vapor Laser Utilizing Copper Chloride as a Lasant," *Appl. Phys. Lett.* 26, 504.
16. Elets'kii, A.V., Zemtsov, Yu.K., Rodin, A.V. and Starostin, A.N., 1975, "Optimum Characteristics of a Laser with High Pressure Metal Vapors," *Sov. Phys. Dokl.* 20, 42.
17. Fedorov, A.I., Sergeenko, V.P. and Tarasenko, V.F., 1978, "Apparatus for Investigating Stimulated Emission from Explosively Formed Metal Vapors," *Sov. J. Quant. Elect.* 7, 1166.
18. General Electric Company, 1980, "Instruction and Service Manual, Discharge Heated Copper Vapor Laser Model 6-15," Space Division, King of Prussia, PA.
19. Grove, R.E., Coutts, G.W., Anderson, R.S., Homsey, R.J. and Karras, T.W., 1980, "100 Watt Copper Vapor Laser," Presented at CLEOS/ICF '80, San Diego, CA, Feb. 26-28.
20. Hargrove, R.S. and Kan, T., 1980, "High Power Efficient Dye Amplifier Pumped by Copper Vapor Lasers," *IEEE J. Quant. Elect.* QE-16, 1108.
21. Isaev, A.A., Kazaryan, M.A. and Petrash, G.G., 1972, "Effective Pulsed Copper Vapor Laser with High Average Generation Power," *JETP Lett.* 16, 27.
22. Isakov, I.M. and Leonov, A.G., 1976, "Atmospheric Pressure Copper Vapor Laser," *Sov. Phys. Tech. Phys. Lett.* 2, 339.
23. Karras, T.W., 1980, "High Repetition Rate Pure Metal Vapor Pulsed Lasers," *Proceedings of the International Conference Lasers '79*, Ed. by V.J. Corcoran, STS Press.
24. Karras, T.W., 1980, "Variation of Pulse Width in Copper Vapor Lasers," Presented at the International Conference Lasers '80, New Orleans, LA.

25. Kazaryan, M.A., Petrash, G.G. and Trofimov, A.N., 1980, "Comparison of the Characteristics of Copper, Copper Chloride, and Copper Bromide Vapor Lasers," Sov. J. Quant. Elect. 10, 328.
26. Kushner, M.J. and Culick, F.E.C., 1980, "A Model for the Dissociation Pulse, Afterglow, and Laser Pulse in the Cu/CuCl₂ Double Pulse Laser," J. Appl. Phys. 51, 3020.
27. Kushner, M.J. and Warner, B.E., 1980, "A Self-Consistent Model for High Repetition Rate Metal Vapor Lasers," Presented at the International Conference on Lasers '80, New Orleans, LA, December 15-19.
28. Laser Focus, 1976, "After Selling Three Copper Vapor Lasers a Developer Envisions a Rival to Argon," 12, 27.
29. Leonard, D.A., 1967, "A Theoretical Description of the 5106⁰A Pulsed Copper Vapor Laser," IEEE J. Quant. Elect. QE-3, 380.
30. Ludmirsky, A., Cohen, C.H. and Kagan, Y.U., 1979, Supplement to Journal de Physique FASC 7, C-7, Presented at the International Conference on Ionized Gases, Grenoble, France.
31. Markova, S.V., Petrash, G.G. and Cherezov, V.M., 1978, "Ultraviolet Emitting Gold Vapor Laser," Sov. J. Quant. Elect. 8, 904.
32. Miller, J.L. and Kan, T., 1979, "Metastable Decay Rates in a Cu-Metal Vapor Laser," J. Appl. Phys. 50, 3849.
33. Pivrotto, T.J., 1980, "Annealing Radiation Damaged Silicon Solar Cells with a Copper Halide Laser," Presented at the International Conference on Lasers '80, New Orleans, LA, USA.
34. Platonov, A.V., Soldatov, A.N. and Filonov, A.G., 1978, "Pulsed Strontium Vapor Laser," Sov. J. Quant. Elect. 8, 120.
35. Smilanski, I., 1980, "Effects of Preionization," IEEE J. Quant. Elect. QE-16, 598.
36. Smilanski, I., 1980, "Copper Hooks Investigation of the Copper Vapor Laser Kinetics," Proceedings of the International Conference on Lasers '79, Ed. by V.J. Corcoran, STS Press.
37. Smilanski, I., Erez, G., Kerman, A. and Levin, L.A., 1979, "High Power, High Pressure, Discharge Heated Copper Vapor Laser," Optics Comm. 30, 70.
38. Smilanski, I., Kerman, A., Levin, L.A. and Erez, G., 1978, "Scaling of the Discharge Heated Copper Vapor Laser," Optics Comm. 25, 79.
39. Walter, W.T., 1967, "40 KW Pulsed Copper Vapor Laser," Bull. Am. Phys. Soc. 12, 90.
40. Walter, W.T., 1968, "Metal Vapor Lasers," IEEE J. Quant. Elect. QE-4, 355.
41. Walter, W.T., 1980, "Computer Modeling to Direct Copper Vapor Laser Development," Presented at the International Conference on Lasers '80, New Orleans, LA.
42. Walter, W.T., Solimene, N., Piltch, M. and Gould, G., 1966, "Efficient Pulsed Gas Discharge Lasers," IEEE J. Quant. Elect. QE-2, 474.
43. Warner, B.E., Anderson, R.S. and Grove, R.E., 1980, "Large Bore Copper Vapor Laser," Presented at CLEOS/ICF '80, San Diego, CA, February 26-28.
44. White, M., 1980, "Future Hydrographic Lasers," Presented at Laser Hydrography Symposium, September 30-October 3, Defense Research Center, Salisbury, S. Australia.
45. Zemskov, K.I., Isaev, A.A., Kazaryan, M.A., Petrash, G.G. and Rautian, S.G., 1974, "Use of Unstable Resonators in Achieving the Diffraction Limited Divergence of the Radiation Emitted from High-Gain Pulsed Gas Lasers," Sov. J. Quant. Elect. 4, 474.

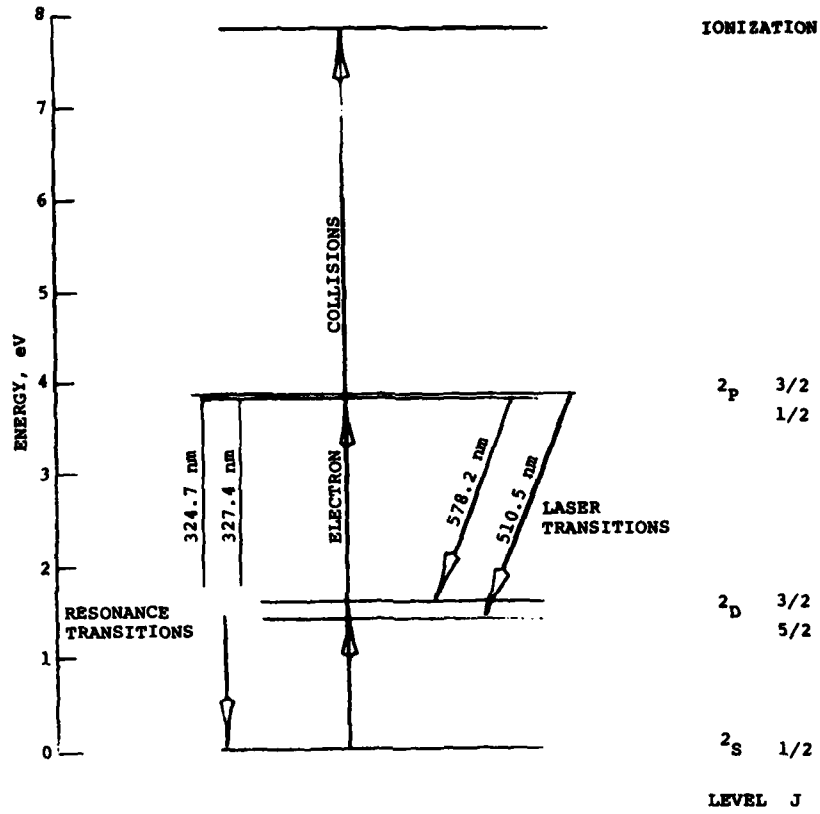


Figure 1. Simplified Copper Atom Energy Level Diagram

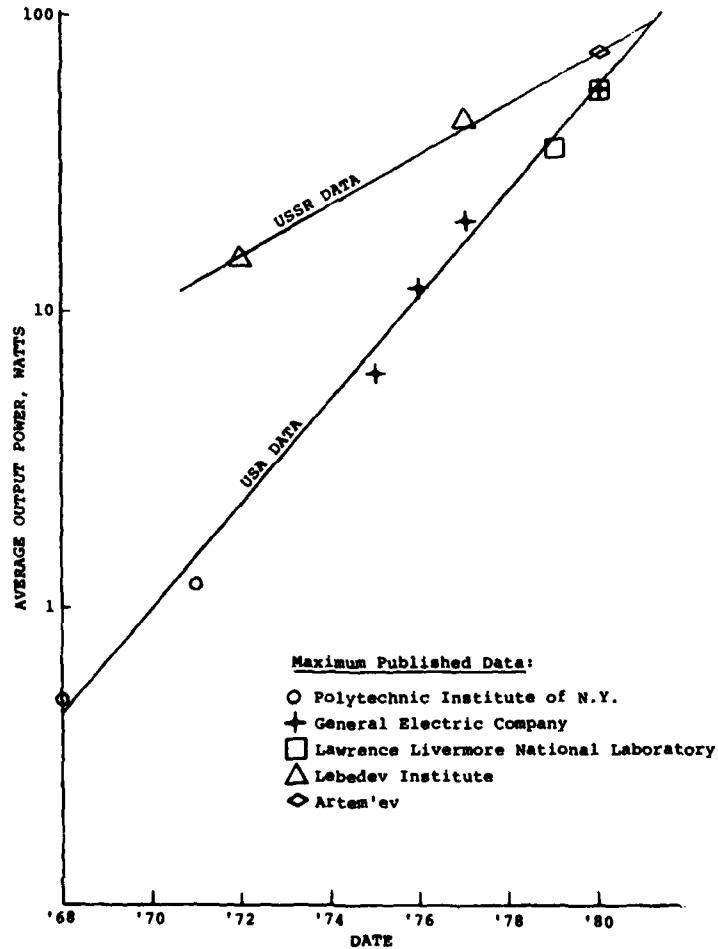


Figure 2. Progress in Average Output Power from Copper Vapor Lasers

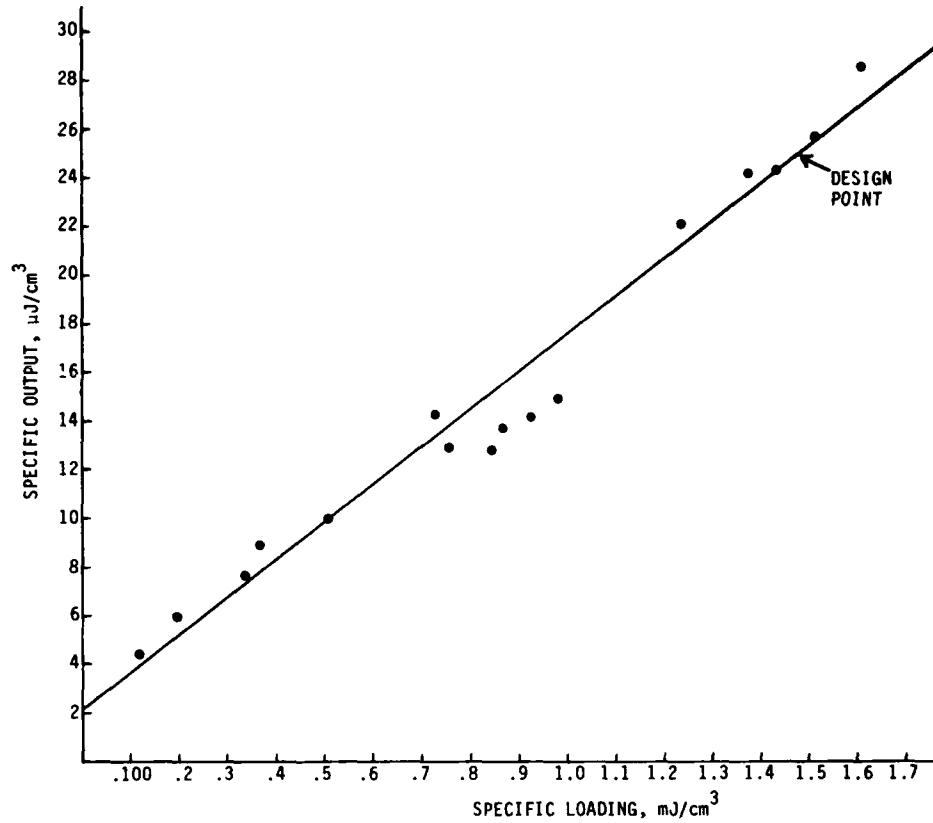


Figure 3. Specific Energy Scaling of Copper Vapor Laser Oscillators with Specific Loading (40"-50" Long Tubes)

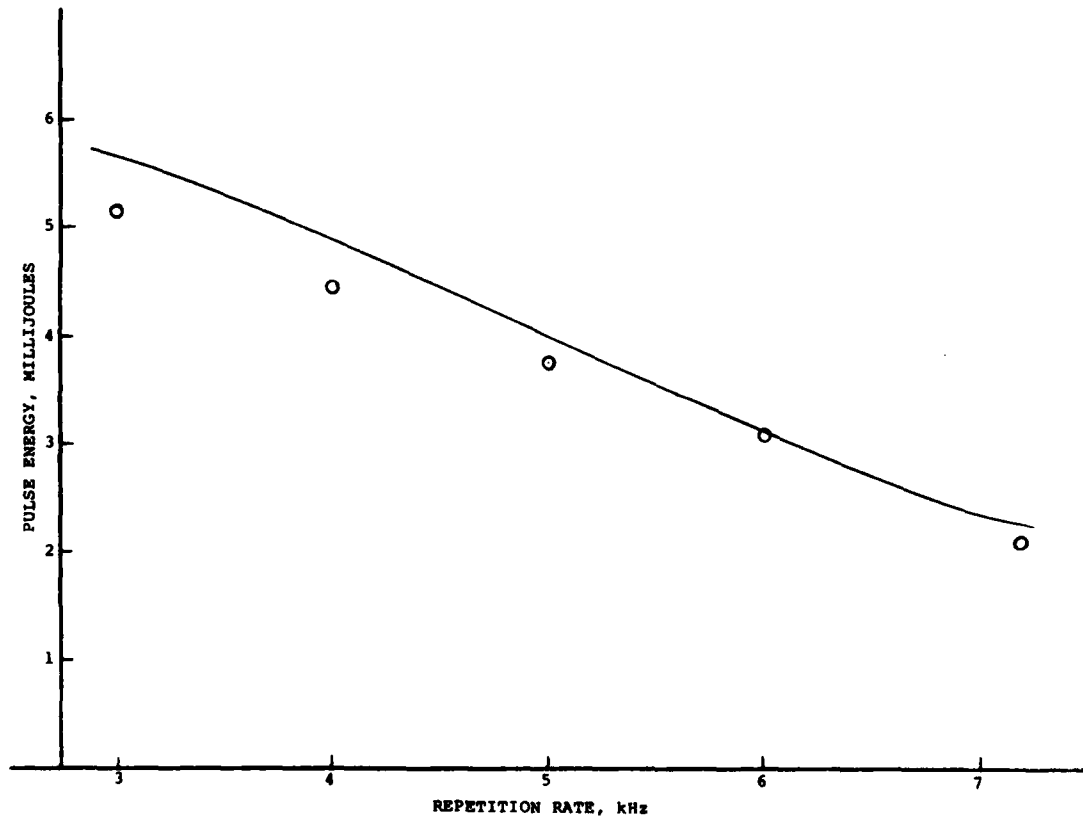


Figure 4. Comparison of Computer Code Results with Copper Laser Data

Computer predictions from Kushner and Warner, 1980, and experimental data from GE Model 6-15 Instruction Manual, 1980.

RECENT DEVELOPMENT OF HIGH-POWER VISIBLE LASER SOURCES EMPLOYING SOLID-STATE SLAB LASERS AND NONLINEAR HARMONIC CONVERSION TECHNIQUES

by

Yung S. Liu, W. B. Jones, and J. P. Chernoch
General Electric Company
Corporate Research and Development
Schenectady, New York 12301
U.S.A.

SUMMARY

Recent developments in high-power solid-state lasers (Nd:YAG, Nd:glass) have greatly improved both average power capability and beam brightness. This has been a result, to a large extent, of the development of the total-internal-reflection slab-type solid-state laser configuration, which provides a self-compensating mechanism to minimize the thermally induced distortion commonly observed in solid-state lasers.^(1, 2, 3) Near diffraction-limited, high peak-power, high average-power solid-state lasers are ideal pump sources for nonlinear frequency conversions using harmonic generation, stimulated Raman scattering and/or pumping dye lasers for ultraviolet (UV), visible, and infrared (IR) coherent light sources. Continuously tunable coherent sources covering a spectral range from 0.2 μm to beyond 3 μm , using these combined techniques, have been reported.⁽⁴⁾

In the present paper, we report recent developments of high-power solid-state slab laser technology in both Nd:YAG and Nd:glass. High-power nonlinear frequency conversion, employing second harmonic generation in various nonlinear crystals is discussed. Nonlinear phase-matching properties critical to efficient frequency conversion in LiIO_3 , LiNbO_3 , CDA, KDP, and recently developed KTP (KTiOPO_4) are presented. Efficient frequency conversion in the average power range exceeding 10 W imposes severe constraints in both fundamental beam properties and the nonlinear processes in various media.

1. INTRODUCTION

A slab-type solid-state laser which produces a high-brightness laser beam at high pump powers has been developed. The configuration is particularly useful for glass host material operated at high average power levels. Although laser glass is available in large volumes of good optical quality and glass lasers can produce high-energy pulses over a wide range of pulse durations, the use of the glass laser in the standard rod configuration has been limited in average power capability because the relatively low heat conductivity of glass leads to high thermal stress at high pump power and, thus, large optical distortion.

In the slab-type laser configuration, the solid host material (e.g., Nd:glass, Nd:YAG) is in the form of a rectangular cross-section slab with plane parallel surfaces or faces. The configuration is shown schematically in Figure 1a. The slab is face-pumped optically, i.e., illuminated through two opposing slab faces, to obtain the required inversion energy in the active material, and, simultaneously, the same faces are cooled to obtain a one-dimensional, steady, thermal state. Thermal stress results in the slab from the heating which is concomitant with optical pumping and cooling. The volume heating is symmetrical relative to the center plane of the slab, and, therefore, the thermal stress averaged from one slab surface to the other is zero. These conditions lead to a high degree of compensation for thermal-optic distortion for a beam passing from one slab face to the other. The laser beam is introduced into the slab through suitable entrance optics, usually through a surface at Brewster's angle, as shown in Figure 1b. With this arrangement, a relatively thin slab of solid host material can be used so that efficient cooling is possible, and at the same time, the active material is swept efficiently by the beam.

Near diffraction-limited, high peak power, and high average power solid-state slab lasers are ideal pump sources for nonlinear frequency conversion, using harmonic generation and stimulated Raman scattering for generating visible, UV, and IR coherent sources. The advances in this type of solid-state pump laser have led to the progress made in the development of high-power visible laser sources using harmonic conversion techniques. In this report, we review the recent development in solid-state slab lasers (Nd:glass, Nd:YAG) and discuss parameters relevant to the high-power second harmonic generation using nonlinear crystals. These discussions are applicable to other types of harmonic conversions, such as third and fourth harmonic generation.

2. SOLID-STATE SLAB-TYPE LASERS

The cross section of an arrangement of a slab laser, pump lamps, and lamp reflectors is shown in Figure 2. The intrinsic compensation for thermal-distortion effects occurs only for paraxial rays in a plane of reflection (p -plane). In the ideal case, the thermal gradients are parallel to a p -plane and, therefore, the principal thermal-optic distortion in the slab is compensated intrinsically. However, if the inversion pumping (strictly slab heating) is not uniform across the slab width, transverse thermal gradients will occur for which there is no intrinsic compensation. Consequently, care must be taken that the pumping distribution is uniform across the slab width to avoid distortion perpendicular to the p -plane. In practice, this has entailed a careful design of the reflectors for the pump lamps in order to achieve the required uniformity of pumping, as well as efficient coupling between the discharge lamps and the active material.

Slab cooling must be arranged so that the faces are cooled to equal temperatures and temperature gradients along the slab faces are minimized. In practice slab cooling has been accomplished either by convection cooling with a fluid (of sufficiently small refractive index) flowing across the slab faces or by conduction cooling through a thin layer of gas to the cooled windows used for the pump radiation. In either case the problem of minimizing surface temperature gradients occurs mainly at the lateral edges where the slab supports are located.

The slab configurations have been operated in a variety of modes for a number of applications. In all designs that have been implemented, the pump lamps employed have been linear discharge tubes Kr-filled for continuous wave (cw) operation and Xe-filled for pulsed operation. Two types of solid host materials have been used: Nd:YAG and Nd:glass. Nd:YAG is a crystalline material with relatively high heat conductivity available only in limited sizes of good optical quality. For these reasons, slab fracture due to thermal stress is of no concern in YAG designs, for pumping is limited by pump-lamp characteristics much below rates for which the slab heating can cause thermal fracture. Single-slab Nd:YAG laser designs have operated cw at 150 W beam power output, pulsed mode at 5 J/pulse, 20 pps, and Q-switched at 0.5 J/pulse, 20 pps, all with beam quality less than five times diffraction-limited. Designs with Nd:YAG have also been used as low-distortion amplifiers for Q-switched oscillators at repetition rates up to 20 pps.

In contrast to Nd:YAG, Nd:glass is available in essentially any desired size, with excellent optical quality. The low specific-gain coefficient of glass makes it useful only for pulse-pumped operation. The low heat conductivity is the key factor that sets a limit on glass slab thickness that can be used in a given design without exceeding the thermal fracture limit. In typical designs for operation in the range 3 to 10 pps, the inversion that can be obtained, which is compatible with useful pump-lamp operation, falls in the range 0.25 to 0.5 J/cm³ per pump pulse. For 10 pps operation, the heating associated with the desired inversion per pulse limits the slab thickness to approximately 6 mm. Since the thermal stress in a slab is proportional to the thickness squared for a given heat loading density, 12 mm is a suitable thickness for 3 pps operation.

The principal application of the Nd:glass slab laser has been as a Q-switched oscillator-amplifier in a single slab operating at a repetition rate of 3 to 10 pps, with an output beam energy greater than 2 J/pulse and of sufficiently good quality for efficient second harmonic generation in a KDP crystal. Unlike the traditional rod geometry, the slab laser with its large aperture aspect ratio lends itself to incorporation of both functions, oscillator and amplifier, in a single laser head. This provides a higher overall efficiency with a reduction in system complexity. Although the thermal self-compensating aspects of the slab geometry and the low gain necessary for the specific performance would permit the operation of an oscillator at high average powers, other system

components, such as the Pockels cell and cavity mirrors, are more limited in average power thermal capability and rule out use of a single multipass oscillator. Furthermore, efficient second harmonic generation using KD*P (Type II), requires power densities on the order of 100 to 150 MW/cm² with a beam divergence of less than 1 mrad. This requirement dictates TEM₀₀ mode operation for the oscillator. In an oscillator-amplifier configuration, TEM₀₀ mode operation is more easily maintained. In general, at the beam energy levels of interest here, the folded-beam amplifier is required in order to obtain sufficient beam intensity.

The limit on beam quality obtainable with the Nd:glass slab laser is determined by the spurious temperature gradients that result from nonuniformities in pumping and cooling of the slab. The low thermal conductivity of glass causes thermal gradients, and thus thermal distortion, to be very sensitive to nonuniformities in heating and cooling. In all practical cases, there is significant thermal distortion in the *s*-plane with maximum pumping power, but the intrinsic compensation in the *p*-plane results in negligible distortion in this plane.

In one laser design, a 6-mm thick, 46-mm wide, 280-mm long slab of LHG-5 phosphate glass is employed. The slab is pumped with two 10-mm bore, 20-cm long, Xe-filled flashlamps in the arrangement shown in Figure 2. The slab is convection-cooled by flowing an ethylene glycol and water mixture over the polished slab faces. Figure 3 shows the distortion measured with a shearing interferometer and plotted as the deflection (in the *s*-plane) of a ray passing through the slab at positions along the width of the slab. This distortion results from pumping at the maximum permissible power level (which produces 0.28 J/cm³ inversion, 10 pps). The central 10 mm of aperture width has very low distortion, and for a total aperture width of 33 mm the distortion is sufficiently low for a high-quality amplifier. Near the lateral edges of the slab aperture, the distortion increases due to the large temperature gradients near the edges. The laser oscillator-amplifier is configured with an electro-optic, Q-switched oscillator with one beam pass through the slab in a central part of the aperture area where the lowest distortion is measured. The oscillator produces a TEM₀₀ beam of 0.25 J/pulse. The remainder of the slab is used in a four-pass folded amplifier to yield a beam of 2 J/pulse. The beam suffers some distortion in the four-pass amplifier and emerges with a divergence of approximately three times the diffraction limit. The beam quality at this energy level is adequate for efficient (40%) second harmonic conversion in a Type II KD*P crystal.

3. HIGH-POWER NONLINEAR HARMONIC CONVERSION

In this section, techniques and design parameters for generating high average power visible radiation using harmonic conversion from a slab-type solid-state laser are discussed. Although the second, third, and fourth harmonic generation from a Nd solid-state laser, using various nonlinear crystals, has been well studied, efficient second harmonic conversion from a solid-state slab-laser in the average power range, exceeding 10 W and pulse energy over several joules, imposes some severe constraints with respects to both the fundamental beam properties (such as beam brightness, pulse shape, and transverse mode distribution) and the nonlinear media employed.

3.1 Phase Matching Properties

It is well known that efficient second harmonic generation in nonlinear crystals requires phase matching of the fundamental and second harmonic wave vectors. Dispersion and double refraction characteristics of a crystal determine its phase matching properties. The second harmonic conversion efficiency can be expressed as,

$$\eta = \eta_0 \text{sinc}(\Delta k \cdot L/2) = \eta_0 \text{sinc}\phi, \quad (1)$$

where η_0 is the power conversion efficiency under the perfect phase-match condition and η_0 is a function of the incident power density and the effective nonlinear coefficient of the crystal. Further,

$$\Delta k = k_2 - 2k_1,$$

$$\text{with } k_1 = 2\pi n_1/\lambda, \text{ and } k_2 = 2\pi n_2/\lambda_2,$$

where n_1 , n_2 , λ_1 , and λ_2 denote the refractive indices and the wavelengths for the fundamental and second harmonic waves, respectively. The function $\text{sinc}\phi = (\text{sinc}\phi)^2$ is the phase mismatch term, where $\phi = \Delta k \cdot L/2$ and L is the interaction length for the fundamental and second harmonic waves in the crystal.

The maximum conversion efficiency is obtained when $\phi = 0$, i.e., with no phase-mismatch. The quantity ϕ is a function of many parameters, and $\delta\phi$ can be expressed as

$$\delta\phi = \frac{\partial\phi}{\partial\lambda}\delta\lambda + \frac{\partial\phi}{\partial\theta}\delta\theta + \frac{\partial\phi}{\partial T}\delta T + \frac{\partial\phi}{\partial E}\delta E + \dots, \quad (2)$$

where $\delta\lambda$, $\delta\theta$, δT , and δE denote the deviations with the wavelength, angular displacement, temperature, and the applied electric field from the perfect phase-matching condition. For high-power applications, these quantities are interrelated and the maximum conversion efficiency is realized when the sum of the terms in Equation 2 is minimized.

The spectral phase-matching properties of several commonly used nonlinear crystals have been measured; the results are shown in Figure 4.^(5,6) In these measurements, the relative second harmonic conversion efficiency vs wavelength was measured using a line-narrowed, tunable Nd:glass laser, and scanning across its bandwidth. The spectral phase-matching conditions have been measured for the following materials:

1. LiNbO₃, 90° phase-matched, temperature-tuned.
2. Deuterated CsH₂AsO₄ (CD**A*), 90° phase-matched, temperature-tuned.
3. LiIO₃, Type I angle-tuned at 22 °C.
4. KH₂PO₄ (KDP), Type I angle-tuned at 22 °C.
5. Deuterated KH₂PO₄ (KD**P*), Type II angle-tuned at 22 °C.
6. KTiOPO₄ (KTP), Type II angle-tuned at 22 °C.

The phase-matching bandwidth is defined as $L \cdot \Delta\lambda$, where $\Delta\lambda$ is the full-spectral width of the fundamental wavelength at which the second harmonic conversion efficiency is reduced to one-half the maximum value (FWHM).

The spectral phase-matching bandwidth is of concern when a wideband source, such as a Nd:glass laser, is employed. The typical spectral bandwidth of a Q-switched Nd:glass oscillator is about 100 Å. Thus line narrowing is required in a Nd:glass laser for high-efficiency second harmonic conversion.

Among various tuning techniques, we have found that an intracavity Brewster-angle birefringent filter offers a simple and lossless tuning method particularly useful for a low-gain, high-power oscillator, such as a Nd:glass laser.⁽⁷⁾ Birefringent materials, such as LiNbO₃, can be used for low-power applications, while materials with a higher damage threshold, such as KDP and quartz, are required for high-power applications. The tuning and line-narrowing characteristics for a Q-switched Nd:glass oscillator, using an *x*-cut LiNbO₃ birefringent filter, are shown in Figure 5. For the higher power application, a 3-mm thick KD**P* has been employed at an intracavity power density exceeding 500 MW/cm² without damage. However, additional low-finesse solid etalons are required to reduce the line width to about 1 Å.

From measurements of the relative second harmonic conversion efficiency vs angle and vs crystal temperature, bandwidths for these parameters can be assigned to each crystal in a manner similar to the spectral phase-matching bandwidth. These and other properties for several materials useful for high average power second harmonic generation are summarized in Table 1. The angular bandwidth is important in determining requirements for the fundamental beam quality to achieve efficient second harmonic conversion. The temperature bandwidth is indicative of the required crystal temperature control for efficient second harmonic conversion and also indicative of the tolerance of a crystal for temperature gradients resulting from beam power absorption.

3.2 Nonlinear Materials with High-Power Capability

The selection of a nonlinear optical material for application at an average power exceeding 10 W is limited by the average power and peak power densities that a crystal can tolerate. Thermally induced phase mismatch, resulting from beam power absorption, limits the average power capability. The damage threshold limits the peak power density capability. There are only a few optical crystal materials available that satisfy these requirements. These are: KD*P, CD*A, and the most recently developed KTP crystals. Each of these crystals has properties which are unique for certain applications. Table 2 lists some of the special characteristics of these crystals. Some of the unique properties of these crystals and the results obtained with them are reviewed below.

3.2.1 KD*P (Deuterated KH_2PO_4)

KD*P is the most highly developed of the three nonlinear crystals discussed. The deuterated material is required to reduce absorption at $1.06 \mu\text{m}$ and thus minimize the thermally induced phase mismatch. Crystals are available in large sizes with excellent optical quality.

The KD*P crystal has a low absorption constant ($< 0.01 \text{ cm}^{-1}$) and a high power-density damage threshold at $1.06 \mu\text{m}$. Effects due to thermally induced phase mismatching are negligibly small at an incident average power level up to about 25 W, with peak power density of 250 MW/cm^2 and a 35 ns pulse duration. Nonlinear absorption due to two-photon processes is also insignificant under these conditions.

The effective nonlinear constant of a KD*P crystal depends upon the types of nonlinear interactions involved. It can be shown that the effective nonlinear constant for the Type II interaction, relative to that for Type I, is proportional to $(\sin 2\theta_{II})/(\sin \theta_I)$, where θ_I and θ_{II} are, respectively, the phase-matching angles for each type of phase matching. Given that $\theta_I = 41.5^\circ$ and $\theta_{II} = 53.5^\circ$, the ratio has a value of 1.44, and, consequently, enhancement of the second harmonic efficiency by a factor of about two can be obtained by using the Type II phase matching instead of the Type I.

A critical parameter in achieving a high conversion efficiency is the angular tolerance for phase matching. This is particularly important in the high-power application because of the difficulty in maintaining a low divergent beam. The angular tolerance for phase matching in Type II interaction for KD*P is greater by a factor of about two, as compared to that found in the Type I. The values of $L\Delta\theta$ were measured to be 5 mrad-cm for a KD*P (Type II) and 2.4 mrad-cm for KD*P in Type I interaction.

In Figure 6, the energy conversion efficiency as a function of the incident power density is shown for a KD*P crystal of 35 mm length.

3.2.2 CD*A (deuterated CsH_2AsO_4)

CD*A is isomorphous with KD*P and is usually found to be a more efficient harmonic converter than KD*P. The temperature-tuned, 90° phase-matched CD*A is a preferred configuration. However, the 90° phase-matching temperature of the crystal at $1.06 \mu\text{m}$ is $\sim 110^\circ\text{C}$. This temperature is sufficiently high that the crystal is susceptible to damage due to dehydration, which occurs at about 150°C .⁽⁸⁾ The damage level for a temperature-tuned CD*A was less than 10 W at an energy density of about 2 J-cm^{-2} (35 ns). This property has severely limited the usefulness of 90° phase-matched CD*A for high-power harmonic conversion.

The CD*A can also be used in higher-power applications with Type I angle-tuned phase matching at room temperature. This configuration is illustrated in Figure 7. The upper graph shows the crystal orientation and the incident $1.06\text{-}\mu\text{m}$ beam polarization. The lower curve shows the angular phase-matching tolerance in θ -direction; a value $\Delta\theta L = 9.0 \text{ mrad-cm}$ has been measured. The angular phase-matching tolerance in ϕ -direction has a value close to that of a 90° phase-matched crystal. Due to a larger angular tolerance, Type I CD*A is usually found to be more efficient in second harmonic generation than KD*P (Type II).

3.2.3 KTP (KTiOPO_4)

KTP is a new type of nonlinear crystal which is currently under development.^(6,9) The crystal exhibits several unique properties, including a high nonlinear coefficient comparable to that of $\text{Ba}_2\text{NaNb}_5\text{O}_{15}$, a high damage threshold, and a low degree of sensitivity to thermally induced phase mismatch. These combined properties make KTP the most attractive crystal for high-power frequency conversion.

The spectral, angular, and temperature phase-matching characteristics for second harmonic generation at $1.06 \mu\text{m}$ in KTP are shown in Table 1. The large temperature bandwidth observed is a unique characteristic of this nonlinear material. Because of its large nonlinear coefficient, this further reduces the length of crystal required for high conversion efficiency. As a result, a second harmonic generation efficiency near 50% can be readily obtained in a 3.5 mm crystal length at an incident power density of about 100 MW/cm^2 . The energy conversion efficiency of one KTP crystal (3.5-mm length) as a function of input power density is shown in Figure 8.

4. SUMMARY

The development of the high-power solid-state slab laser has greatly improved the beam brightness and average power capabilities obtainable from a solid-state laser. Previously, the average power from a solid-state laser has been limited by the thermal-optical distortion due to the relatively low thermal conductivity of the laser medium. In the slab-type solid-state laser, the optical beam inside the active medium undergoes total-internal reflection to provide a self-compensation of optical wavefront distortion due to thermally-induced index variation. Furthermore, because of the optical symmetry along a totally internally reflected zig-zag beam path, the net effect of the stress-induced birefringence disappears when integrated over the entire optical path inside the gain medium, and the depolarization effect is eliminated. This configuration makes possible a solid-state Nd:glass laser operable at a power level much exceeding that previously achieved, while maintaining a beam quality near the diffraction-limit. Nonlinear frequency conversion from a high-power slab-type solid-state laser offers the opportunity of developing high-power visible laser sources exceeding 10 W average power level.

5. REFERENCES

1. Martin, W.S. and Chernoch, J.P., 1972, Patent No. 3,633,126, "Multiple Internal Reflection Face Pumped Laser."
2. Liu, Y.S., Jones, W.B., Chernoch, J.P., and Hulme, G.J., 1977, "High Average Power Second Harmonic Generation Using Face-Pumped Slab-Typed Solid State Laser," *Proceedings of 7th DOD Conference on Laser Technology*.
3. Liu, Y.S., Jones, W.B., and Chernoch, J.P., 1976, "High-Efficiency, High Power Coherent UV Generation at 266 nm in 90° Phase-Matched Deuterated KDP," *Appl. Phys. Lett.* 29, 32.
4. Byer, R.L., 1980, "Tunable Laser Sources Based on Nd:YAG Laser" (Paper X-7), Proc. of the Third International Conference Lasers '80, New Orleans, LA, USA, December 16-19 (to be published).
5. Liu, Y.S., 1977, "Spectral Phase-Matching Properties for Second Harmonic Generation in Nonlinear Crystals," *Appl. Phys. Lett.* 31, 187.
6. Liu, Y.S., Drafall, L., Dentz, D., and Belt, R., 1980, "Properties in Second Harmonic Generation in KTP," *Proc. of the Third International Conference Lasers '80* (to be published).
7. Liu, Y.S., 1977, "Line Narrowing and Tuning of a High Power Nd:Glass Laser Using an Intracavity Brewster-Angle Birefringent Filter," *J. Appl. Phys.* 48, 647.
8. Liu, Y.S. and Shultz, A.R., 1975, "Specific Heat of Cesium Dideuterated Arsenate (CsD_2AsO_4)," *Appl. Phys. Lett.* 27, 585.
9. Zumsteg, F.C., Bierlein, J.D., and Gier, T.E., 1976, " $\text{KxRb}_{1-x}\text{TiOPO}_4$: A New Non-linear Optical Material," *J. Appl. Phys.*, 47, 4980.

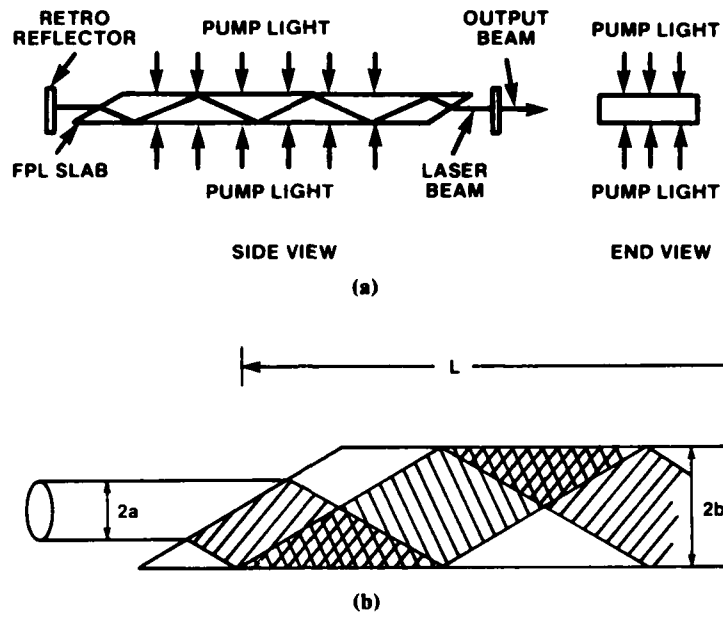


Figure 1. (a) Schematic of a total-internal-reflective slab laser.
 (b) Brewster-angle entrance face of a slab laser.

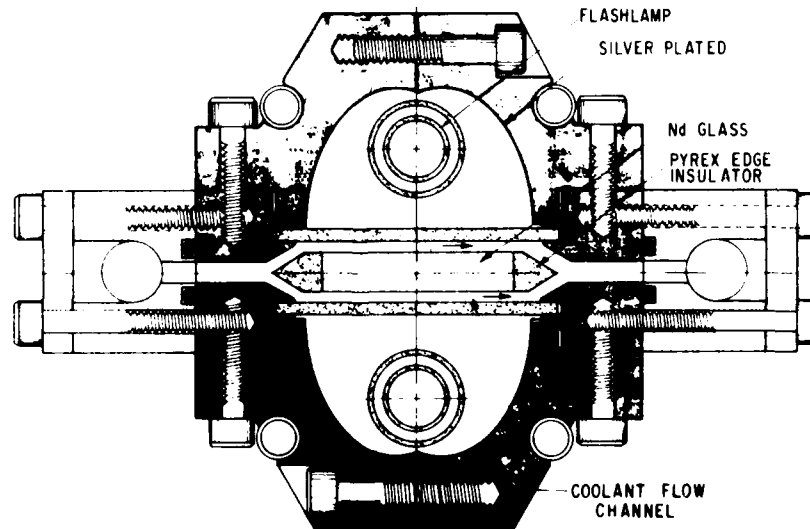


Figure 2. Cross section of a slab laser enclosure showing arrangement of slab, pump lamps, and lamp reflectors.

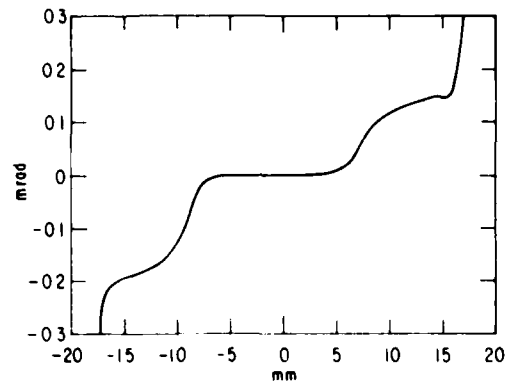


Figure 3. Thermal distortion measured as a probe ray deflection vs position in the Nd:glass slab aperture.

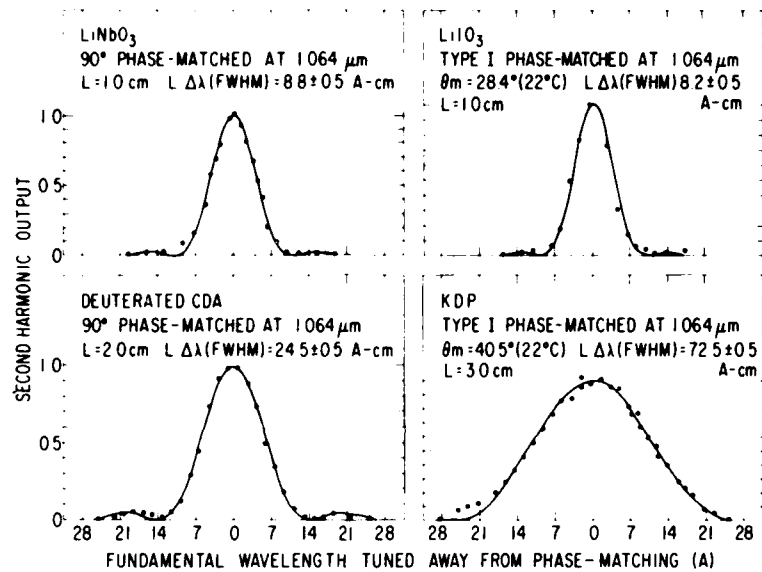


Figure 4. Spectral phase-matching characteristics in various nonlinear crystals at 1.06 μm .

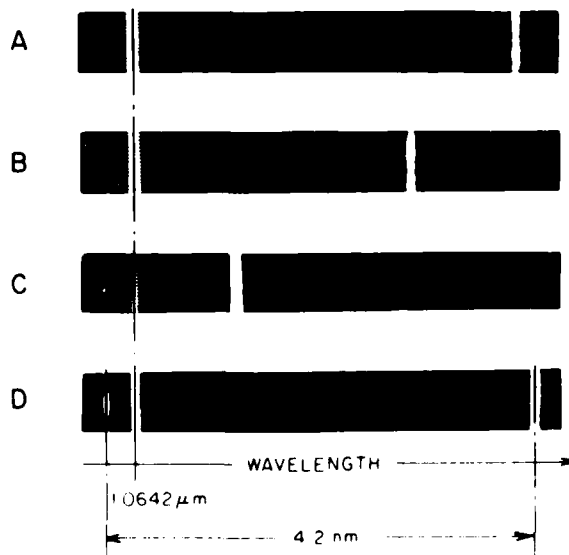


Figure 5. Spectral output of a line-narrowed Q-switched Nd:glass oscillator using a LiNbO₃ birefringent plate.

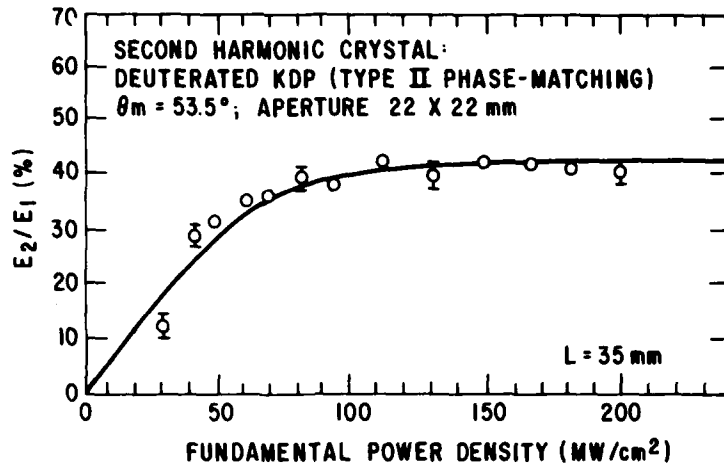


Figure 6. The energy conversion efficiency as a function of incident power density for a deuterated KD*P.

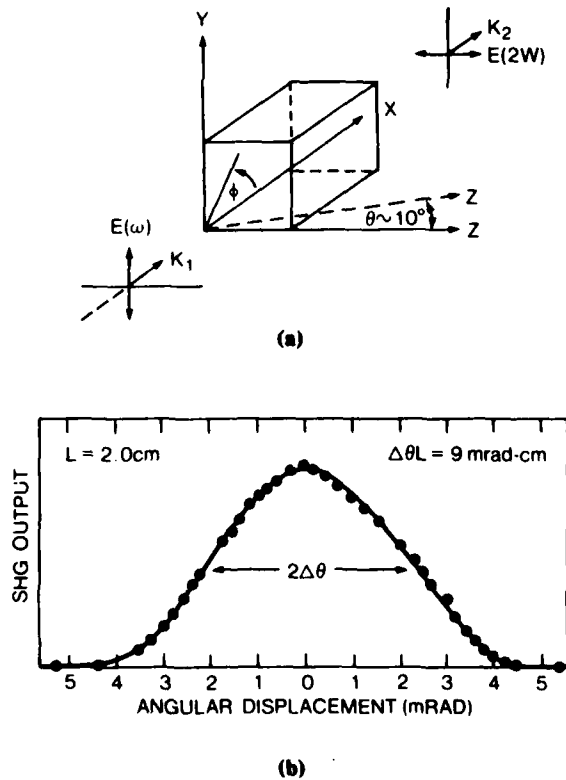


Figure 7. (a) CD*A crystal orientation in a Type I angle-tuned configuration.
(b) Angular phase-match bandwidth in θ -direction for a Type I CD*A angle-tuned at room temperature.

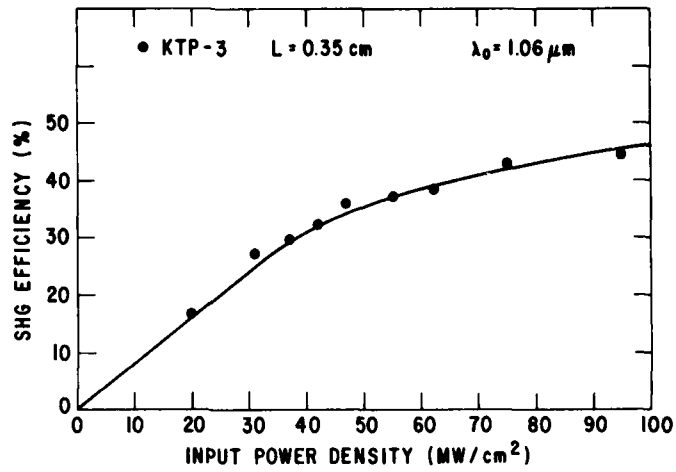


Figure 8. Conversion efficiency measured as a function of input power density at 1.06 μm.

Table 1

SUMMARY OF PHASE-MATCHING PROPERTIES FOR SECOND HARMONIC GENERATION IN KD*P, CD*A, AND KTP

Type of Phase Matching and Temperature	KD*P		CD*A		KTP
	Type I @ 22 °C	Type II @ 22 °C	Type I @ 22 °C	90° @ 105 °C	Type II @ 25 °C
Spectral Bandwidth $L \cdot \Delta\lambda$ (FWHM) (Å-cm)	72.5	55.7	22.5	22.5	5.7
Angular Bandwidth $L \cdot \Delta\theta$ (FWHM) (mrad-cm)	2.4	5	9	> 50	15
Temperature Bandwidth $L \cdot \Delta T$ (FWHM) (°C-cm)	6†	6	6†	6	15
Phase-matching angle @ 1.06 μm	41°	53.5°	82°	90°	26°
Walk-off angle (mrad)	27	18	3.1	0	1

† Values are estimated

Table 2
PROPERTIES OF KD*P, CD*A, AND KTP FOR DIFFERENT TYPES OF
OF PHASE-MATCH AT 1.06 μm

Crystal	Type of Phase Matching	Properties
KD*P	Type II @ 22 °C	<ul style="list-style-type: none"> • Effective nonlinear coefficient larger than Type I • Angular bandwidth larger than Type I • Large spectral bandwidth • High damage thresholds for both peak power and average power • Sensitive to temperature change • Larger-size material available
CD*A	90° @ 105 °C	<ul style="list-style-type: none"> • Noncritical phase match • Higher efficiency than that of KD*P • Lower damage threshold • Dehydration at ~ 150 °C causing permanent damage • Larger size crystal not available
	Type I @ 25 °C	<ul style="list-style-type: none"> • Room-temperature Operation • Improved damage threshold
KTP	Type II @ 25 °C	<ul style="list-style-type: none"> • Large nonlinear coefficient • High conversion efficiency • Relatively insensitive to temperature variation • Small walk-off angle • Nonhygroscopic • Crystal size limit

DOWN-CONVERSION OF RARE GAS HALIDE LASERS FOR BLUE-GREEN APPLICATIONS

R. Burnham, N. Djeu, B. L. Wexler
 Naval Research Laboratory
 Washington, D. C. 20375

SUMMARY

Rare-gas halide lasers, down-converted to the blue-green region, appear to be sufficiently scalable and efficient for applications in blue-green communications systems. Recent progress in Raman conversion of the XeCl laser output in atomic and molecular media are reviewed in this paper.

1. INTRODUCTION

The rare-gas halide lasers have the highest combined potential for overall efficiency and scalability of any visible-uv laser yet discovered. As such, they appear to be suitable as pump lasers for a high-average-power blue-green laser for space-based strategic communications. Of the rare-gas halides, the rare-gas fluorides were initially found to be greatly superior to the others in efficiency. Recently, the XeCl laser has been improved significantly and has shown overall efficiency and scalability comparable to KrF. In addition, the use of HCl as a halogen donor in this laser has been shown to prolong the running time of the laser in a rep. rated system significantly beyond that obtained in the rare-gas fluorides. This result is apparently attributable to the absence of buildup of deleterious contaminants in the laser gas, and to the tendency of the HCl to recombine following the XeCl laser pulse. XeCl, therefore, appears to be the most suitable rare-gas halide for long lived laser systems.

The XeCl laser operates at 308 nm and therefore must be down-converted to the blue-green region (450-510 nm). The most effective down-conversion technique to be demonstrated has been stimulated Raman scattering. Photon conversion efficiencies in excess of 70% have been observed in both electronic and vibrational (molecular) stimulated Raman scattering experiments using rare-gas halide lasers as pumps. Since the Raman medium is left unchanged in the conversion process (no irreversible photochemistry) this down-conversion technique is appropriate to long-lived blue-green laser systems.

2. XeCl LASER PERFORMANCE

Among the rare-gas halides the XeCl laser appears to be most suitable for blue-green applications. First, the XeCl laser has been excited in self-sustained discharges with overall efficiencies of 1-2%, (LIN, S. C. and LEVATTER, J. I., 1979), using both uv and x-ray preionization to obtain discharge uniformity in volumes greater than one liter. Specific output energies of 1 J/l-amagat have been obtained with a total output of five joules at 308 nm. A schematic diagram of a typical x-ray preionized XeCl laser is given in Fig. 1. Thus, the XeCl laser satisfies both the requirement for high efficiency (in the uv) and for high single pulse energy.

The second set of requirements on the blue-green laser is associated with the operating lifetime of the system. Here the XeCl laser has been shown to be significantly superior to the other rare-gas halides. In repetitively pulsed devices the XeCl laser has been operated for 3×10^6 shots to half power without gas treatment (McKee, et. al., 1981) and for greater than 10^7 shots with gas cleanup and replenishment of the halogen donor (TENNANT, R., 1980). These lifetimes are comparable to those of the external electrical components used to power the laser (i.e., capacitors and switches). The long operating life observed with the XeCl laser results from the use of HCl as the halogen donor. This is because the strong bond strength of HCl favors its reformation after each laser shot. In addition, most materials commonly used in construction of rare-gas halide lasers appear to be easily passivated against chemical attack by HCl.

3. RAMAN DOWNCONVERSION OF THE XeCl LASER

The requirement for high efficiency in blue-green applications dictates that frequency shifting of the 308 nm output from XeCl must itself be accomplished with very high efficiency. Fortunately, an efficient means for down-conversion has been found in stimulated Raman scattering in atomic and molecular gases. Conversion of the XeCl laser output to 459 nm has been demonstrated with an overall efficiency of 40-50% in a number of experiments using lead vapor as a Raman active medium (BURNHAM, R. and DJEU, N., 1978). Conversion is accomplished in a single Raman step since the Stokes shift in lead is approximately 1/3 of the initial 308 nm pump photon energy. An energy level diagram for Raman shifting in lead is shown in Fig. 2a. Temporal shapes for the pump (308 nm) and Stokes (459 nm) pulses are shown in Fig. 3. Raman shifting in atomic vapors has the advantage that competing non-linear effects such as second-Stokes generation and four-wave mixing have small transition probabilities compared to first Stokes generation which is enhanced by a strong near-resonance single-photon transition. Thus, beam quality requirements for efficient conversion are not severe.

An alternative approach to efficient down-conversion from the uv to the blue-green region is also under study (KOMINE, H. and STAPPAERTS, E. A., 1979). This approach involves multiple Raman scattering in hydrogen. Because the Raman shift in H_2 is only 4155 cm^{-1} , three successive scattering events are required to shift the output from the XeCl laser to the blue-green region. A diagram of third Stokes Raman generation in H_2 is shown in Fig. 2b. The requirement for high overall efficiency ($\sim 50\%$) in downconversion dictates that each step of the molecular Raman scattering process be accomplished with $\sim 80\%$ efficiency. To date, single step molecular Raman shifting in the uv has been accomplished with an efficiency of $\sim 50\%$ in H_2 (LORIE, T. R., et. al., 1979). A net efficiency of 30% for third Stokes generation has also been observed in experiments using a Raman oscillator-amplifier configuration pumped by a short-pulse ($\sim 10\text{ ns}$) XeCl laser (KOMINE, H. and STAPPAERTS, E. A., 1980). The experimental arrangement used in the latter experiment is shown in Fig. 4. Calculations indicate that, in principle, complete conversion of the uv pump laser pulse should be possible using such an oscillator-amplifier arrangement (NEWMAN, J. H. and SCHINDLER, G. M., 1981). Since Raman conversion in hydrogen is a non-resonant process, the Raman gains for practically all Stokes orders are of the same magnitude. The spatial and temporal shape of the pump beam must, therefore, be carefully controlled to prevent buildup of undesired Stokes orders. Four-wave mixing processes which convert the pump energy into Stokes and anti-Stokes orders are also probable in molecular Raman shifting. These higher-order parasitic processes are primarily responsible for the less-than-optimum efficiencies for conversion from the uv to the blue-green observed to date in molecular Raman experiments. However, down-conversion using multiple Stokes shifts in hydrogen is very attractive because the cell containing the Raman medium at pressures of ~ 10 atmospheres operates at room temperature. The issue of Raman cell life ceases to be a problem under the molecular approach to frequency shifting to the blue-green.

Raman down-conversion in both atomic and molecular vapors is an area of continuing research for blue-green laser systems.

4. NARROW BAND LASER OPERATION

The XeCl laser has been tuned between 307.6 and 308.8 nm using an injection locked amplifier such as shown in Fig. 4. (REINTJES, J., 1980). A laser linewidth of $\sim 0.01\text{ nm}$ was obtained by using a grating in the oscillator. The linewidth could be further narrowed to $< 0.001\text{ nm}$ by using etalons as frequency selective elements. This laser has been used to generate Raman-converted output in Pb vapor between 458 and 460 nm with linewidths of $< 0.015\text{ nm}$. The efficiency obtained in these experiments was somewhat higher than that obtained with a free running pump laser because extraction from both the XeCl laser and the Raman laser was improved by injection locking.

5. REFERENCES

- Burnham, R. and Djeu, N., "Efficient Raman Conversion of XeCl Laser Radiation in Metal Vapors", Opt. Lett. 3, 215 (1978).
- Komine, H. and Stappaerts, E. A., "Efficient High-Stokes-Order Raman Conversion in Molecular Gases", Opt. Lett. 4, 398 (1979), and unpublished work.
- Lin, S. C. and Levatter, J. I., "X-Ray Preionization of Electric Discharge Lasers", Appl. Phys. Lett. 34, 505 (1979).
- Loree, T. R., Sze, R. C., Barker, D. L. and Scott, P. B., "New Lines in the UV:SRS of Excimer Laser Wavelengths", IEEE J. Quant. Elect. QE-15, 337 (1979).
- McKee, T. J., James, D. J., Nip, W. S., Weeks, R. W. and Willis, C., "Lifetime Extension of XeCl and KrCl Lasers with Additives", Appl. Phys. Lett. 36, 943 (1980).
- Newman, J. H. and Schindler, G. M., "Numerical Model of Multiple-Raman-Shifting Excimer Lasers to the Blue-Green in H_2 ", Opt Lett. 6, 125 (1981).
- Tennant, R., LASL Report #LA-UR 80:1395 (unpublished).
- Reintjes, J. F., "Generation of Coherent Tunable VUV Radiation Near the Ly- β Transition of Atomic Hydrogen", Opt. Lett. 5, 342 (1980).

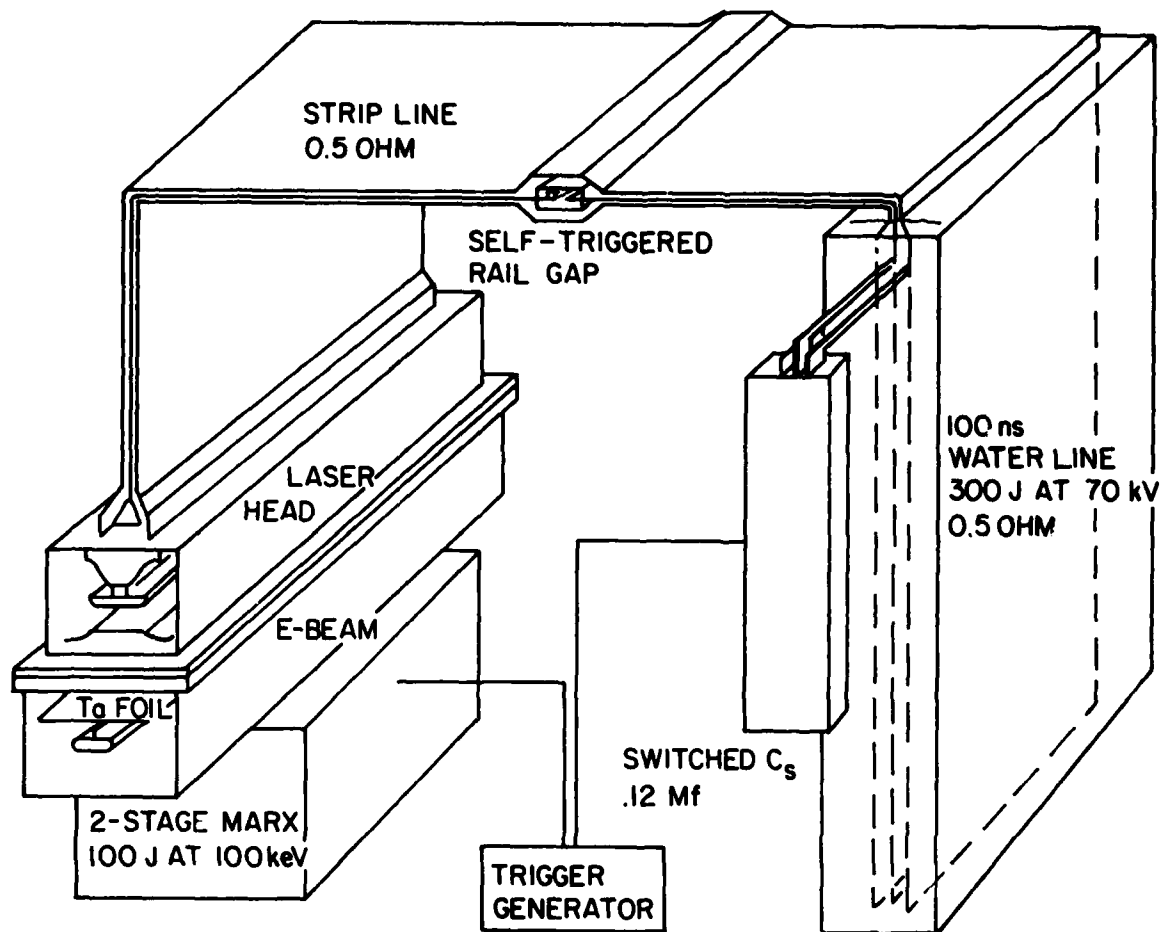


Fig. 1. Diagram of x-ray preionized XeCl discharge laser with > 1 J output at 308 nm in a 70 nsec pulse.

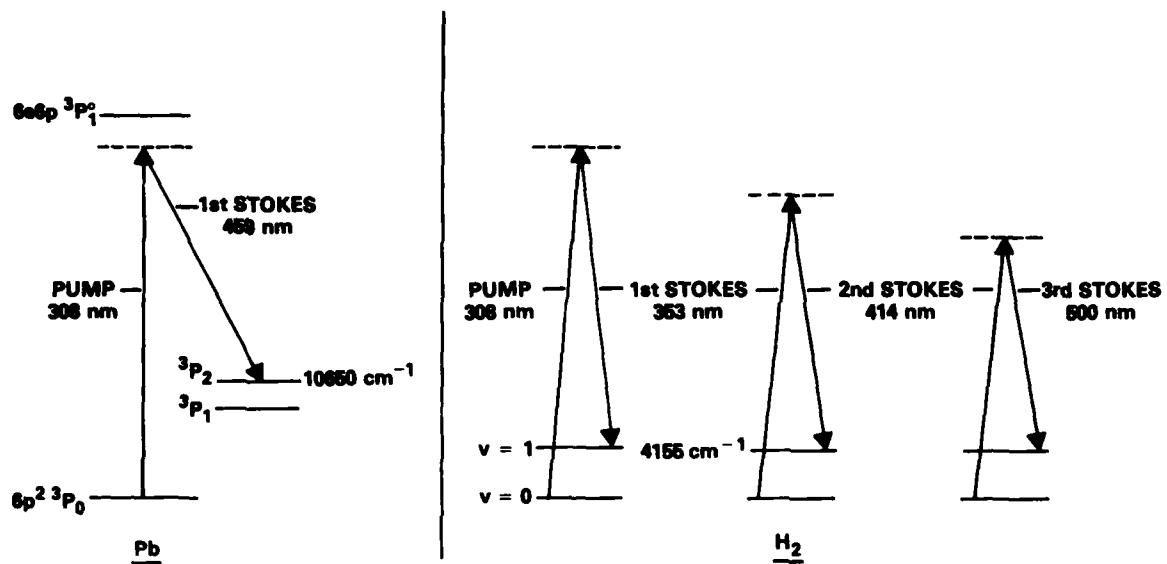
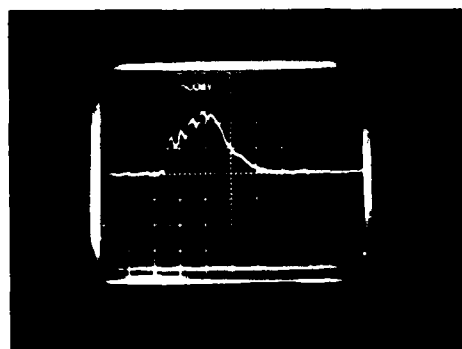


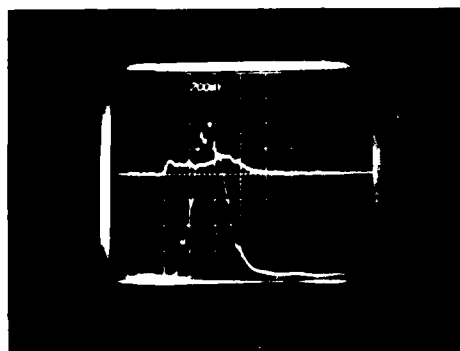
Fig. 2. a) Energy level diagram of Pb showing single-step Raman conversion; b) Vibrational energy levels of H_2 showing triple-step Raman conversion to the blue-green.



Pb CELL COLD
TRANSMITTED PUMP
(308nm)

RAMAN OUTPUT
(459nm)

20nsec/DIV



Pb CELL HOT
TRANSMITTED PUMP
(308nm)

RAMAN OUTPUT
(459nm)

Fig. 3. Initial and depleted XeCl pump laser pulses at 308 nm together with generated Raman pulse at 459 nm.

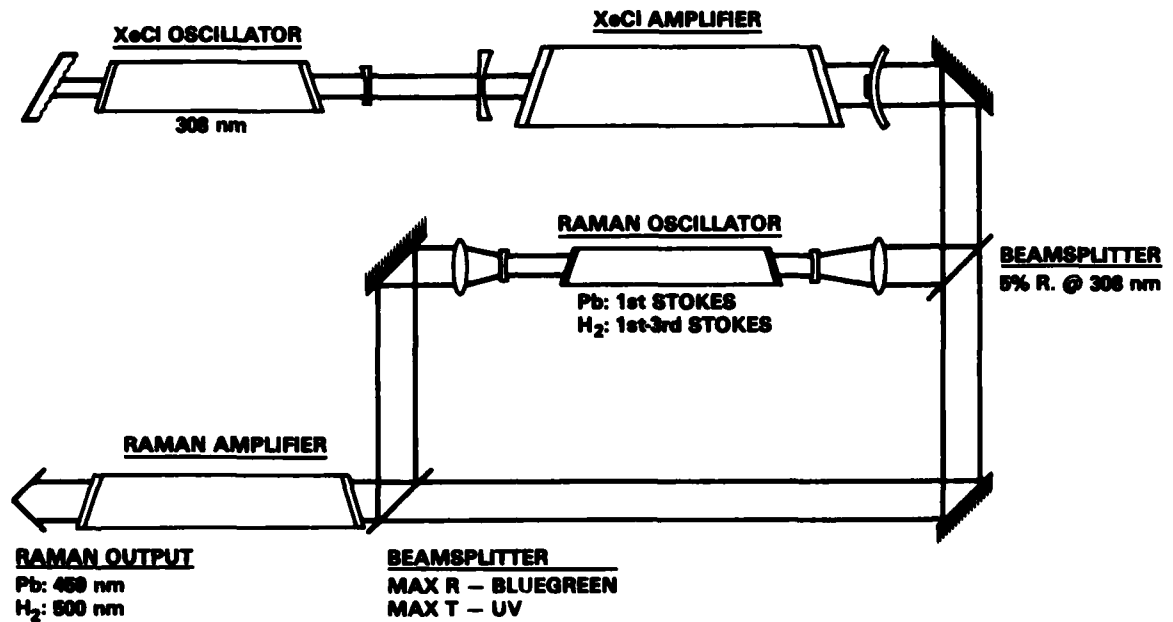


Fig. 4. Oscillator-amplifier configuration used for efficient Raman conversion to the blue-green using either Pb vapor or H₂ gas.

NARROW BANDPASS LARGE FIELD OF VIEW OPTICAL FILTERS

William J. Rosenberg and Alan M. Title
 Lockheed Palo Alto Research Laboratory
 3251 Hanover Street
 Palo Alto, California 94304

ABSTRACT

This article reviews the types and capabilities of birefringent filters. The general operating principles of Lyot (perfect polarizers), partial polarizing, and Solc (no internal polarizers) filters are introduced. Appropriate techniques for tuning each filter type are presented. Field of view of birefringent filters is discussed and is compared to Fabry-Perot and interference filters. The transmission and throughput advantage of birefringent filters are shown. Finally, the current state-of-the-art in practical filters is reviewed.

1. INTRODUCTION

The purpose of this paper is to introduce the reader to the principles and capabilities of birefringent filter systems. Although these filters have been used by solar physicists to study spectral lines in the solar atmosphere, their use in other disciplines has been limited. While commercial versions have been produced they have been expensive and have not achieved their full potential. Recent developments, however show that they can be practical optical devices. Their tunability and enormous throughput advantages, combined with new construction techniques, make them ideal for monochromatic collection.

We hope to provide a useful, though brief, introduction to birefringent filters in this presentation. In Section 2, the fundamental operation of a birefringent element is discussed. Since these are the building blocks of birefringent filters it is important to understand their effect on incident light. The time domain, impulse response, analytic technique is also introduced in Section 2.

The three main types of birefringent filters, Lyot, partial polarizing, and Solc, are presented in Section 3. Differences among these and the capabilities of each are discussed.

Tuning is introduced in Section 4. The emphasis is on waveplate tuning since that has proven to be the most practical at this time. Other mechanical and electrical techniques are presented briefly.

A major feature of birefringent filters is their large field of view. This gives them a significant throughput advantage over other filter techniques for both imaging and collection. The basic principles of wide field systems and the resulting capabilities are presented in Section 5.

A crucial issue in any optical system is transmission, or more precisely, throughput. Since polarizers are inherently lossy elements their use in birefringent filters limits the overall transmission. The capabilities and limitations are discussed in Section 6.

Finally, Section 7 contains a brief resume of the state of the art in birefringent filters. The current capabilities in spectral resolution and aperture size are discussed.

2. SIMPLE BIREFRINGENT ELEMENTS

The essential principle involved in birefringent filters is that light originating in a single polarization state can be made to interfere with itself. In a birefringent element this is accomplished by decomposing the input wave into two orthogonal polarization components, delaying one component relative to the other, and then recombining the components to effect interference. This process is illustrated in Figure 1. The light is forced into a single polarization state by the entrance polarizer. By placing this polarizer at 45° to the fast and slow axes of the birefringent crystal, two components of equal amplitude are created. A relative delay is introduced between these components by the difference in propagation velocity along these two axes. Finally, the exit polarizer forces the two waves, the ordinary and the extraordinary, to recombine and, hence, interfere.

An analogous situation occurs in a Michelson interferometer as shown in Figure 2. Here the two paths are created by a 50:50 beamsplitter and the relative delay is introduced by the path length difference between the two arms. Interference is effected by recombining the two beams with the beam splitter as shown. This analogy can be carried further by using polarizing beam splitters which create orthogonally polarized waves in the two paths just as in the birefringent element. Practical filter elements have been made this way and are very similar to birefringent elements (Title and Ramsey, 1980).

The effect of placing either a birefringent element or a Michelson interferometer in an optical path is to transmit at some wavelengths and to reject at others. In particular, the output due to white light input is a channel spectrum with alternating light and dark bands in the spectrum. Mathematically, the spectral transfer function of such an element is

$$T(\lambda) = \cos^2\left(\frac{\pi \Delta d}{\lambda}\right) \quad (1)$$

with Δ , the birefringence, d , the thickness of the element and λ , the wavelength. The birefringence is the difference between the ordinary and extraordinary indices of refraction, n_o and n_e , respectively. A thick plate produces a channel spectrum of many thin bands closely spaced while a thin plate produces a channel spectrum of fewer but wider bands.

An alternative perspective on birefringent systems is impulse response analysis borrowed from electrical engineering (Bracewell, 1965). Here, the Fourier transform duality between time and spectral domains is used to characterize birefringent filters. As in electrical filter theory the spectral transfer function of an optical filter is the square magnitude of the Fourier transform of its impulse response. For a birefringent element, or Michelson interferometer, the impulse response is especially easy to derive. As shown in Figure 3, an impulse passing through the entrance polarizer is split and travels along the fast and slow axes of the element. These two impulses are separated in time by the delay of the element. Finally, the exit polarizer creates two identically polarized impulses as the output. The orthogonally polarized impulses which are rejected by the exit polarizer represent the power which is lost in the dark bands of the channel spectrum. The impulse response of the element is thus a pair of impulses separated in time by

$$\Delta t = \frac{d}{c} (n_o - n_e) \quad (2)$$

in which c is the vacuum speed of light. Specifically this may be written as

$$h(t) = \frac{1}{2} \delta(t - \frac{n_o d}{c}) + \frac{1}{2} \delta(t - \frac{n_e d}{c}) \quad (3)$$

Since the absolute time of arrival of the impulses is not important in specifying the square magnitude of the transform, (3) is usually written as

$$h(t) = \frac{1}{2} \delta(t + \frac{\Delta t}{2}) + \frac{1}{2} \delta(t - \frac{\Delta t}{2}) \quad (4)$$

In equations (3) and (4), $\delta(t-a)$ is the Dirac delta function representing an impulse at time a . As is well known, equation (1) is the square magnitude of the Fourier transform of equation (3) or (4).

3. FILTER TYPES

The simple birefringent elements described in Section 2 can be combined in several different ways to produce useful optical filters. The three major classes, Lyot, partial polarizing, and Solc, differ in the use of polarizers between successive elements in a filter. In this section we will review these filter types, but will only reference the details and derivations of many of the properties of the filters.

Lyot filters are the simplest of the filter types (Lyot, 1933). In a Lyot filter, as shown in Figure 4, simple elements whose lengths are in the ratios 1:2:4:8:... 2^n are cascaded. Each element has an entrance and exit polarizer. The exit polarizer of each element serves as the entrance polarizer of the next. Each element, in effect, serves as a blocking filter for the next thickest element, doubling the spectral spacing between transmission maxima while changing the narrow pass band response only slightly. The overall effect of a four-element Lyot filter is shown in Figure 5. The transmission profile for each element is shown along with the overall profile for the entire filter. Since the elements are in series the overall profile is the product of the individual spectral responses. The impulse response for the entire filter is the convolution of the individual responses, a uniformly weighted impulse sequence.

The transmission profile for a Lyot filter with n elements is

$$T(\lambda) = \frac{1}{4^n} \frac{\sin^2(\frac{2^n \pi c \Delta t}{\lambda})}{\sin^2(\frac{\pi c \Delta t}{\lambda})} \quad (5)$$

in which Δt is the time delay of the shortest element. For a transmission maximum at λ_0 , the bandwidth (full width at half maximum) is approximately

$$FWHM = .88 \frac{\lambda_0^2}{2^n c \Delta t} \quad (6)$$

while the free spectral range is

$$FSR = \frac{\lambda_0^2}{c \Delta t} \quad (7)$$

Consequently the finesse, the ratio of free spectral range to bandwidth, of Lyot filters is

$$F = 1.13 2^n \quad (8)$$

Practical filters have been built with a FWHM of .05 Å at 15000 Å and a finesse of 290. The height of the first sidelobe, the largest secondary maximum, relative to the peak transmission, of a Lyot filter is approximately .045, or -13 db.

There are many possible variations of the basic Lyot filter. The most well known is the contrast element Lyot in which one additional element is added to the filter (Schoolman, 1973). This element,

instead of being twice the thickness of the longest element is, instead, approximately equal to the second longest element. Its purpose is to reduce the heights of the sidelobes and thereby increase the signal-to-noise, or contrast, in the filter transmission. Other variations include other modifications of the 1:2:4.... length ratios and deviations from having all the polarizers parallel.

By using contrast elements, the transmission spectral response may be varied somewhat from the pure Lyot response. Unfortunately, the freedom to specify spectral response is limited. Ammann and Chang (1965) describe a method for synthesizing arbitrary transmission functions but it is of more academic than practical interest. The theoretical transmission can be very low and the large number of polarizers limits the actual transmission even more.

By substituting partial polarizers in place of the perfect polarizers in a Lyot filter we can construct filters with arbitrary spectral transmission functions. In practice, since the partial polarizers are less lossy than perfect polarizers, this can also result in an increase in throughput for the filter. The details of how arbitrary partial polarizing filters are synthesized are too lengthy for this presentation, but a simple example will demonstrate the principles involved (Title, 1976).

Consider the configuration shown in Figure 6. As in a Lyot filter the crystals are in the ratios 1:2 and there are perfect polarizers at the entrance and exit planes of the filter. Between the two crystals, however, is a partial polarizer. It transmits 100% of vertically polarized light and some fraction, ρ , of the horizontally polarized component. Notice, also, that the crystals are oriented orthogonally. One has its fast axis at $+45^\circ$ while the other has its fast axis at -45° .

There is a simple way to visualize the operation of a partial polarizing module. As illustrated in Figure 7, the partial polarizing module may be considered to be a parallel combination of two optical paths. One contains a slightly attenuating perfect polarizer between the two birefringent plates while the other, accounting for the orthogonal transmittance of the partial polarizer, has just a neutral density filter between the two plates. The impulse response of such a combination is just the superposition of the impulse responses of the two components. The perfect polarizer section behaves just like a normal Lyot combination and has the impulse response:

$$\frac{(1-\rho)}{4} \left\{ \delta\left(t + 3 \frac{\Delta t}{2}\right) + \delta\left(t + \frac{\Delta t}{2}\right) + \delta\left(t - \frac{\Delta t}{2}\right) + \delta\left(t - 3 \frac{\Delta t}{2}\right) \right\} \quad (9)$$

The neutral density path, because the two crystals are crossed, acts like a single short element and has the impulse response:

$$\frac{\rho}{2} \left\{ \delta\left(t + \frac{\Delta t}{2}\right) + \delta\left(t - \frac{\Delta t}{2}\right) \right\} \quad (10)$$

In expressions (9) and (10), ρ is the orthogonal transmission of the partial polarizer. The superposition results in the overall impulse response:

$$\frac{1-\rho}{4} \delta\left(t + 3 \frac{\Delta t}{2}\right) + \frac{1+\rho}{4} \delta\left(t + \frac{\Delta t}{2}\right) + \frac{1+\rho}{4} \delta\left(t - \frac{\Delta t}{2}\right) + \frac{1-\rho}{4} \delta\left(t - 3 \frac{\Delta t}{2}\right) \quad (11)$$

Alternatively, the intermediate impulse responses of partial polarizing filters may be considered to be vector valued. That is, they have both vertically and horizontally polarized components. At the exit polarizer, when only one component is transmitted the orthogonal component disappears but until that time it must be considered. Following the partial polarizer there still remains a small horizontal component in each impulse. This causes the apodization (amplitude taper) of the responses following the second crystal and the exit polarizer.

As ρ varies between 0 (perfect polarizer) and 1 (no polarizer) the apodizations may be varied continuously. The corresponding spectral transmission is shown in Figure 8 for several values of ρ .

While this example has only shown a simple partial polarizing module the applicability of partial polarizers is considerably more general. Any symmetric apodized impulse response may be synthesized using partial polarizers between crystals. In fact, the two orthogonally polarized beams available at the exit aperture can have separately, almost independently, selectable impulse responses. This means that with a polarizing beam splitter as the exit polarizer, two separate transmission functions could be realized simultaneously.

Ivan Solc (1965) showed that it is even possible to construct birefringent filters without any intermediate polarizers. The original Solc filters were very simple to describe, but have been very difficult to understand. They came in two forms, as shown in Figure 9, the fan filter and the folded filter. In a fan filter, n identical, unit length, birefringent plates are stacked as in a fanned deck of playing cards. The orientations of the plates are:

$$\alpha, 3\alpha, 5\alpha, \dots, (2n-1)\alpha \quad (12)$$

where $\alpha = 45^\circ/n$. The orientations are symmetric around 45° and distributed regularly through the quadrant. Thus a four-plate filter would have its plates oriented at 11.25° , 33.75° , 56.25° , and 78.75° . For the fan filter the entrance and exit polarizers are oriented parallel at 0° .

The folded filter is simpler in design. Its plates are oriented, alternately, at $+ \alpha$ and $- \alpha$. A four-plate folded filter would have its plates oriented at 11.25° , -11.25° , 11.25° , and -11.25° . The entrance polarizer is at 0° , but the exit polarizer is at 90° .

The spectral transmissions of the fan and folded Solc filters are equivalent. They both have the same profile, although they are shifted from each other by half the free spectral range. In Figure 10, the transmission profiles of the four-plate fan and folded filters are shown. In general Evans (1958) has shown that the transmission profile of an n plate Solc filter is:

$$T(\lambda) = \left[\frac{\sin n\chi}{\sin \chi} \cos \chi \tan \alpha \right]^2$$

in which

$$\cos \chi = \cos \frac{\pi c \Delta t}{\lambda} \cos \alpha$$

and α , as before, is $45^\circ/n$.

In Figure 11 we compare Solc fan and Lyot filters. Notice that for filters using the same total crystal thickness the Lyot filter has slightly lower secondary maxima (side lobes) for comparable bandwidths. This was observed soon after Solc invented these filters and was thought to be a significant disadvantage. This objection, however, was due largely to a lack of understanding as to how the Solc filters really worked.

Harris, Ammann, and Chang (1964) made a significant contribution to the development of Solc filters by applying the impulse response concept to these filters. As in the analysis of partial polarizing filters the impulse response must be considered to be a vector quantity. Unlike the partial polarizing networks, however, in which the convenient coordinate system remains constant throughout the network, for Solc filters a better choice is one in which the coordinate system rotates with the crystal plates. In particular, at each intermediate stage the convenient coordinate axes are the fast and slow axes of the preceding crystal plate. By combining this idea with a mathematical technique developed by Pegis for the synthesis of multilayer dielectric interference filters, Harris *et al* demonstrated a general synthesis technique for Solc filters. That is, given any discrete time, finite impulse response, there is a set of crystal plate orientation angles which synthesizes such a filter. Thus, for example, with the plate orientation angles:

$$8.4^\circ, 18.9^\circ, 31.4^\circ, 45.0^\circ, 58.6^\circ, 71.1^\circ, 81.6^\circ$$

the corresponding filter would exactly duplicate the transmission profile of a Lyot filter. Schiffman and Young (1968) using the Harris procedure, demonstrated that more interesting filters could be built. They built a Dolph-Chebyshev minimum sidelobe filter. Figure 12 shows various seven-plate filter configurations and their spectral responses.

It is difficult to compare these filters directly since there are several attributes involved. The standard Lyot filter, or the Lyot filter with contrast element, while less general in its spectral characteristics requires far fewer elements than an equivalent Solc filter. The Solc filter, however, uses only two polarizers and therefore can achieve higher transmission in practice since even good polarizers have some losses. Partial polarizing filters or Lyot filters using some partial polarizing modules represent a compromise. They use more elements than a Lyot filter but have higher transmission and spectral versatility.

In order to reduce the complexity of Solc filters and make them more practical the present authors have developed procedures for synthesizing Solc filters with a combination of long and short plates. It was recognized that the Harris synthesis procedure specified several crystal orientation sets, each of which would synthesize the exact same transmission profile. By considering orientation sets in which several adjacent plates are parallel or nearly parallel, some filters have been developed which use far fewer plates than the usual Solc filters. Figure 13 shows a transmission profile and two crystal sets which synthesize it. Notice that while the total amount of crystal is the same for both filters, the second uses only about half as many elements. In general, these modified Solc filters use between one-third and one-half as many elements as a normal Solc filter.

It is possible to make hybrids in which two Solc filter sections separated by a polarizer are combined to make a higher finesse filter. Conceptually this is the same as thinking of the first half of a Lyot filter as the blocker for the second half. A combination of two of the modified Solc sections illustrated in Figure 13 is shown in Figure 14. The combined filter uses only ten elements but has a finesse of greater than 60. The price paid for this seven-fold increase in finesse with only twice the number of elements is the additional loss due to the extra polarizer. In practice, it is a matter of making appropriate compromises between number of elements and number of polarizers. More of one can always be traded for fewer of the other.

4. TUNING BIREFRINGENT FILTERS

One of the major advantages of birefringent filters over interference filters is the ease with which they can be tuned. There are, in fact, three basic tuning techniques which can be used in birefringent systems. The direct method, similar to air spaced Fabry-Perot tunable filters, is actually to change the birefringent optical path length. An indirect method which uses quarter wave plate analyzers as optical compensators for each retardation plate is more practical, however. Finally, electro-optical techniques which adjust the retardation of certain crystals can be used.

For the direct method some mechanism for adjusting the birefringent optical path length must be employed. Temperature control has often been used. The dominant effect of temperature change is a change in birefringence, although there is a physical length change also. For quartz the result is approximately a shift of $-.5 \text{ \AA}$ per degree Celsius while for calcite the shift is $-.3 \text{ \AA}$ per degree Celsius in the visible. The length can also be changed mechanically by using wedge shaped retardation plates in pairs. By sliding one plate in and out with respect to its mate, the physical thickness is changed. For imaging systems such a change in the optical path is undesirable, but for some applications it works well. A Solc filter with wedge tuning has been built and works well as an order separation filter for a spectrograph.

By far the best tuning method is to use quarter wave plate analyzers (Title and Rosenberg, 1979a). The basic configuration is shown in Figure 15. A quarter wave plate, achromatic over the wavelength range of interest, is mounted immediately following the retardation plate. Tuning is then accomplished by rotation of the exit polarizer. Mathematically this procedure can be shown to work, but intuitively it is difficult to understand. Briefly, the output of the retardation plate is elliptically polarized light, whose ellipticity is a function of wavelength,

$$\epsilon = \text{ellipticity} = \frac{\text{horizontal axis}}{\text{vertical axis}} = \tan \frac{\pi d}{\lambda} (n_e - n_o) \quad (14)$$

The quarter wave plate, as a polarization analyzer, transforms elliptically polarized light into a linearly polarized wave whose orientation is a function of the ellipticity,

$$\theta = \tan^{-1} \epsilon . \quad (15)$$

The orientation as a function of wavelength becomes

$$\theta = \frac{\pi d}{\lambda} (n_e - n_o) - n\pi . \quad (16)$$

At $\theta = 0$, vertical, the natural wavelength, λ_0 , is selected. The tuning relationship is, therefore,

$$\theta = \pi d (n_e - n_o) \left(\frac{1}{\lambda} - \frac{1}{\lambda_0} \right) \quad (17)$$

Rotation by half a revolution tunes through a free spectral range of the element. The sensitivity of the wavelength setting to angular orientation errors actually decreases for the longer, narrow bandwidth elements. This property makes tuning to within a small fraction of the filter bandwidth very practical.

For practical filters it is desirable to avoid rotating the polarizer as in Figure 15 since that would require rotating the following retardation plate and therefore all the subsequent elements. This may be avoided by introducing a rotatable half wave plate before the exit polarizer as shown in Figure 16. The polarizers and retardation plates remain fixed which improves the imaging performance and only the half wave plates rotate.

Partial polarizing filters and Solc filters retain both orthogonal polarization components from element to element. The tuning sections, therefore, must tune both polarization states simultaneously. The configurations shown in Figures 15 and 16 do not maintain the proper phase relationship between the orthogonal polarizations and must be modified in order to tune more general filters. In Figure 17 a general tuning configuration is shown. Notice that an additional, fixed, quarter wave plate has been added after the rotating half wave plate. The extra quarter wave is just the retardation needed to correct the phase difference between the orthogonal polarizations.

Electro-optic tuning is also possible, but has not yet been utilized in practical filter systems. There are two principles which can be used for electro-optic tuning. The first is to change the retardation of a birefringent element in response to an electric field. Materials such as ADP or KDP are used for this purpose and may either be used as the retardation element itself or as an additional tuning section following the main element. The other type of electro-optic tuning is a replacement for the rotating half wave plate in the tuning elements of Figures 16 and 17. Liquid crystal elements may be used as electrically controlled half wave plates, but have not yet been used in tunable birefringent filters.

The advantage of electrical tuning is that there are no moving parts in the optical path. Unfortunately, the electro-optic materials which have been used to date all require either transparent electrodes in the optical path or large electric voltages. The problems arise because transparent electrodes aren't really quite transparent enough. If several layers are included in a filter the losses combine to reduce the transmission significantly. If, alternatively, transverse electric fields are used for apertures of several centimeters the voltages required become excessive. Many liquid crystals, for example, require fields of about 1 volt/micron.

5. FIELD OF VIEW

Other than tunability, the great advantage of birefringent filters is the large field of view possible (Title and Rosenberg, 1979b). Unlike interference filters in which the off axis behavior is isotropic, uniaxial birefringent crystals have a strong azimuthal dependence. In particular, the fringe pattern of a uniaxial birefringent element is a series of hyperbolic isochromes rather than the circular pattern of an interference filter. Moreover, the change in retardation actually changes sign between consecutive quadrants of the fringe pattern. For rays at 0° azimuth, with respect to the optic axis, the

retardation decreases with incidence angle as:

$$\Delta(i, 0^\circ) = \Delta_o \left[1 - \frac{\sin^2 i}{2n_o^2} \right] \quad (18)$$

while in the next quadrant, at an azimuth of 90° , the retardation increases as

$$\Delta(i, 90^\circ) = \Delta_o \left[1 + \frac{\sin^2 i}{2n_o n_e} \right] \quad (19)$$

At arbitrary azimuth, θ , the retardation variation is

$$\Delta = \Delta_o \left[1 - \frac{\sin^2 i}{2n_o^2} \left(\cos^2 \theta - \frac{n_o}{n_e} \sin^2 \theta \right) \right] \quad (20)$$

The azimuthal behavior is the key to making widefield elements. If two plates are combined with their optic axes crossed then the positive increase in retardation of one plate will be offset by the negative change in retardation of the other plate. Lyot² has shown that there are two ways to exploit this behavior. The first is to use two identical plates of the same uniaxial material. Then, to avoid just having the plates cancel and produce a wide field zero retardation, a half wave plate must be placed between the two crossed elements. Such a configuration is shown in Figure 18. The spectral capability of the wide field element is limited by the half wave plate. If it is achromatic then so will be the wide field element (Title, 1975).

Another type of wide field element can be made by crossing two retardation plates, one being uniaxial positive and the other, uniaxial negative. Again the positive and negative azimuthal quadrants will cancel, but now the fast and slow axes will line up from one crystal to the next. Remember that for a uniaxial positive crystal the fast axis coincides with the optic axis while for a uniaxial negative crystal they are orthogonal. A wide field element may, therefore, be made from a combination such as quartz and calcite.

The negative and positive retardation changes, as given by equations (18) and (19), are not exactly equal. There is, therefore, still some limitation to the field of a wide field element. To second order the retardation of a wide field combination is:

$$\Delta(i) = \Delta_o \left[1 - \frac{\sin^2 i}{4n_o^2} \left(\frac{n_e - n_o}{n_e} \right) \right] \quad (21)$$

The variation of transmitted wavelength as a function of incident angle is, therefore,

$$\frac{\delta \lambda}{\lambda_o} = - \frac{\sin^2 i}{4n_o^2} \left(\frac{n_e - n_o}{n_e} \right) \quad (22)$$

This should be compared with the variation for interference filters, which is

$$\frac{\delta \lambda}{\lambda_o} = - \frac{\sin^2 i}{2n^2} \quad (23)$$

in which n is the index of the spacer layer. The field advantage of the wide field birefringent element results from the factor

$$\frac{n_e - n_o}{2n_e} \quad (24)$$

For quartz this factor is .003 and for calcite it is -.058 resulting in large field advantages for birefringent elements. For very small birefringences the second order approximations are not sufficient and more exact computations are necessary. The results of such exact computations are shown in Figure 19 for elements operating at $\lambda 5000 \text{ \AA}$. The incident angle corresponding to the relative wavelength tolerance, $\delta \lambda / \lambda$, is shown for quartz, calcite, and an air spaced Fabry-Perot interference filter.

6. THROUGHPUT

For any filter system the question always asked is, "How much light can be accepted?" This encompasses a variety of factors, but results in an objective basis for comparison between filter systems. The acceptance of any system can always be increased by using a larger aperture filter, so any comparison among types must assume similar apertures. Achievable aperture limitations may then be considered separately. What remains, therefore, is the solid acceptance angle over which the filter operates and the losses in the filter itself.

Birefringent filters operate over a large solid angle as implied by the field of view discussion in Section 5. The throughput advantage relative to Fabry-Perot interference filters is shown in Figure 20 for filters constructed of quartz and calcite. In practice this advantage is a factor of 50 to 200.

The throughput advantage of birefringent systems is somewhat diminished by internal losses in the polarizers. These need not be serious losses, however, if efficient polarizers are used. An unavoidable

loss is due to the entrance polarizer. This means that 50% of the incident light is lost immediately unless the source is polarized. A Lyot filter with a finesse of 250 requires nine polarizers. If their transmission, in polarized light, is 95%, the overall attenuation is a factor of 63%. The overall transmission of such a filter would then be 32% in unpolarized light. A modified Solc hybrid design using only three polarizers could transmit 43% in unpolarized light.

In the visible spectrum, where sheet polarizers are readily available, the Lyot designs are practical. Transmissions of about 30% are therefore realistic. For the infrared or ultraviolet the hybrid Solc filters become more attractive and will then yield transmissions of about 40%. The overall throughput advantage of birefringent filters, relative to ideal interference filters is therefore a factor of 15 to 80 in unpolarized light or 30 to 160 in polarized light.

7. STATE OF THE ART

Although birefringent filters have been in use for almost 50 years, relatively few have actually been constructed and used on a routine basis. Most have been delicate instruments requiring carefully controlled thermal environments. They failed, moreover, to exploit the tuning advantages described previously.

Recently, however, several filters have been built for space flight applications. They have been specifically designed to be rugged enough to be space qualifiable and to operate over a large temperature range. By using achromatic waveplates they are also fully tunable throughout the visible spectrum. In Figure 21, a 20Å quartz filter is shown. It has a 7.5 cm clear aperture and is fully blocked and tunable in the visible. A 0.1Å calcite filter is shown in Figure 22. While it is also tunable throughout the visible it has a free spectral range of only 12Å so that blocking filters are required. It operates under computer control and compensates for temperature variations by tuning. Operation from 5°C to 50°C is therefore possible with no thermal controller. A solid Michelson analog birefringent element has also been built and operated with this filter (Title and Ramsey, 1980). It has a bandwidth of 0.1Å and is insensitive to temperature variations because of the specific combination of glasses used in its construction.

Additionally, a fixed frequency Lyot filter for laser communications was recently finished and is shown in Figure 23. It has a 10 cm entrance aperture and tapers to 7.5 cm at the exit. The birefringent elements are quartz which gives it a $\pm 20^\circ$ field of view and a 2 Å bandwidth at $\lambda 5320 \text{ Å}$. Although it is fixed frequency its elements have tuning sections for initial spectral alignment and calibration.

At the present time we are constructing a 0.05Å calcite filter. Like its 0.1Å prototype it will be space qualified and fully tunable. A modified Solc filter with a 3.4Å bandwidth is being built with a 10 cm clear aperture. It will be tunable and have wide field elements like the Lyot filters.

8. ACKNOWLEDGEMENTS

It is a pleasure to acknowledge the assistance of Harry Ramsey, Larry Mertz, Ralph Reeves, Steve Schoolman, and the staff of the Lockheed Palo Alto Research Laboratory in the development of practical birefringent filters. This work has been generously supported by The Office of Naval Research under contract N00014-78-C-0526 and Lockheed Independent Research funds.

REFERENCES

1. Ammann, E. O. and I. C. Chang (1965), J. Opt. Soc. Am., 55, 835
2. Bracewell, R. (1965), The Fourier Transform and its Applications, (McGraw-Hill, New York)
3. Evans, J. W. (1958), J. Opt. Soc. Am., 48, 142 (1958) Harris, S. E., E. O. Ammann and I. C. Chang, J. Opt. Soc. Am., 54, 1267
4. Harris, S. E., E. O. Ammann and I. C. Chang (1964), J. Opt. Soc. Am., 54, 1267
5. Lyot, B. (1933), Compt. Rend., 197, 1593
6. Schiffman, B. M. and L. Young (1968), IEEE Trans. Microwave Theory, 6, 351
7. Schoolman, S. A. (1973), Solar Physics, 30, 255
8. Solc, I. (1965), J. Opt. Soc. Am, 55, 621
9. Title, A. M. (1975), Appl. Opt., 14, 229
10. Title, A. M. (1975), Appl. Opt., 15, 2871
11. Title, A. M. and H. E. Ramsey (1980), Appl. Opt., 19, 2046
12. Title, A. M. and W. J. Rosenberg (1979a), Proc. SPIE, 202, 47
13. Title, A. M. and W. J. Rosenberg (1979b), Appl. Opt., 18, 3443

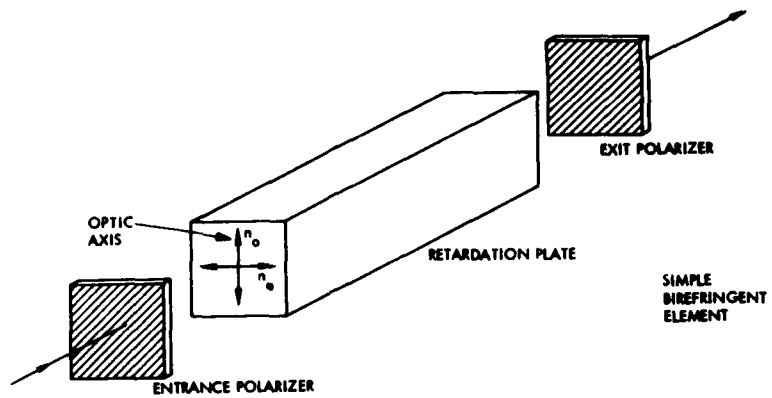


Figure 1. Simple birefringent element

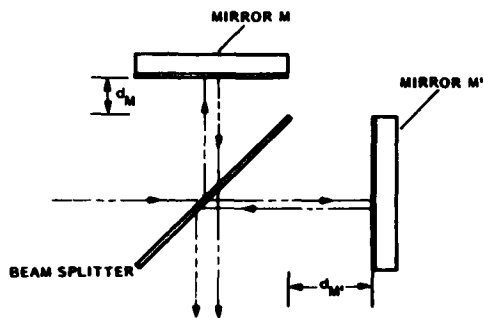


Figure 2. Michelson interferometer element

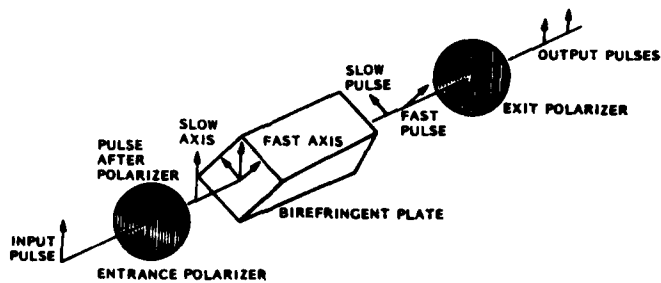


Figure 3. Pulse propagation through a simple element

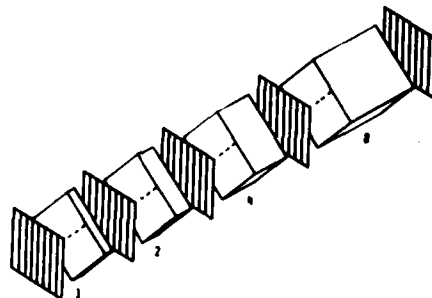


Figure 4. Lyot filter with four elements

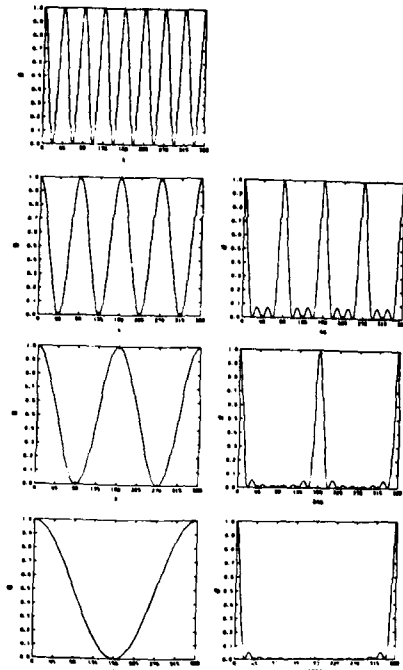


Figure 5. Transmission vs. frequency for the components of a Lyot filter (A,B,C,D) and the transmission through successive stages of the cascade (E,F,G)

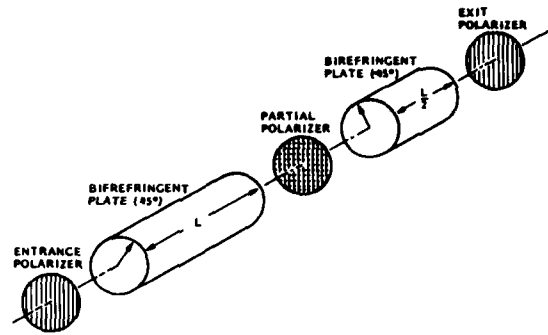


Figure 6. Partial polarizing module

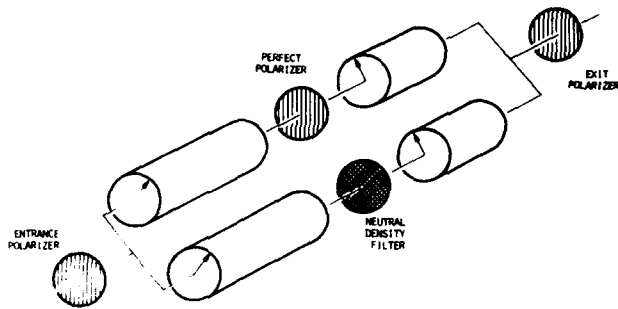


Figure 7. Conceptual decomposition of a partial polarizing module

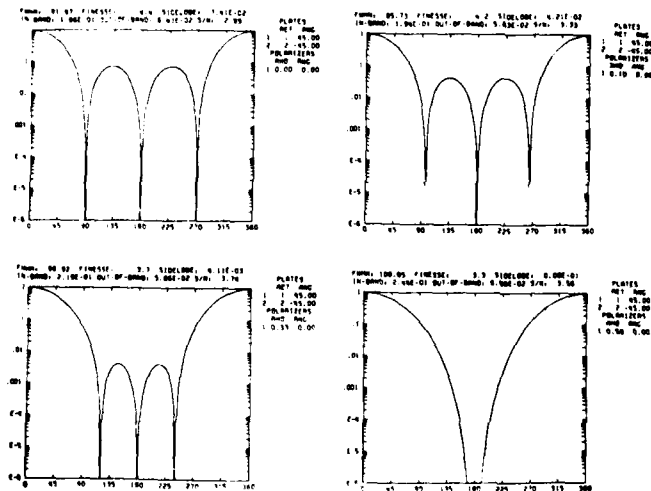


Figure 8. Transmission versus frequency of partial polarizing modules with orthogonal transmissions, ρ , of 0, .1, .33, and .5

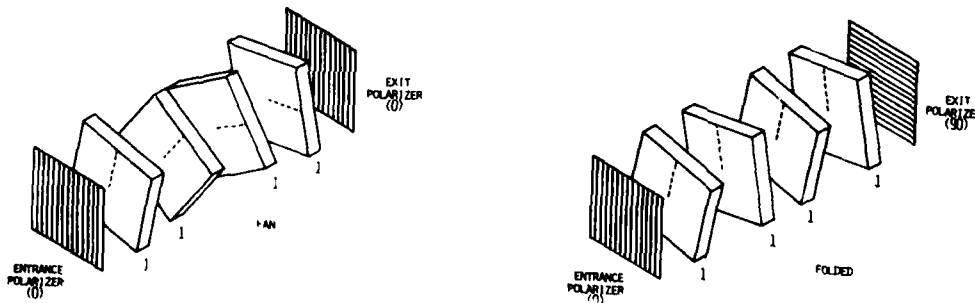


Figure 9. Solc fan and folded four-element filter configurations

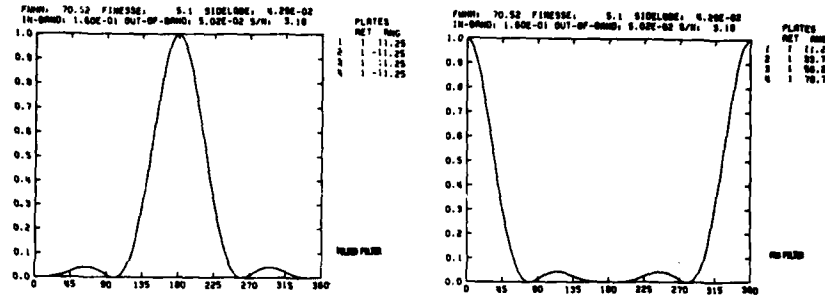


Figure 10. Transmission versus frequency of four-element fan and folded filters

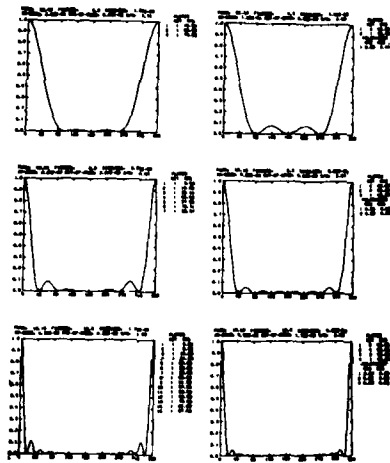


Figure 11. Transmission versus frequency of equal length Solc and Lyot filters

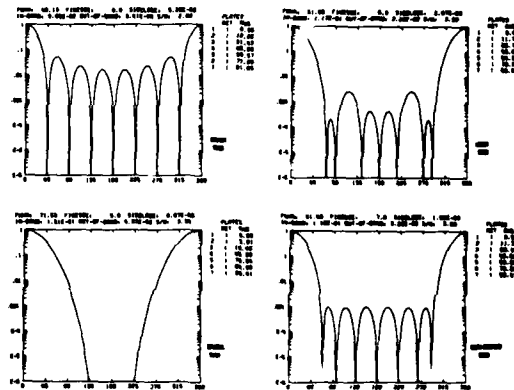


Figure 12. Transmission versus frequency for seven-element Solc filters with uniform linear taper, binomial, and Dolph-Chebyshev apodizations

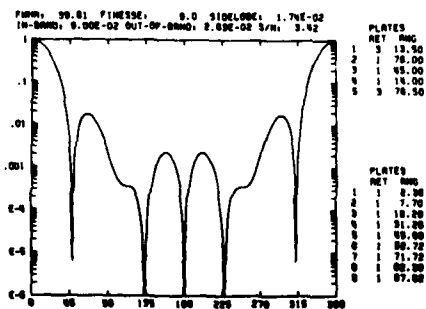


Figure 13. Transmission versus frequency of nine-element Solc filters and the five-element modified Solc equivalent

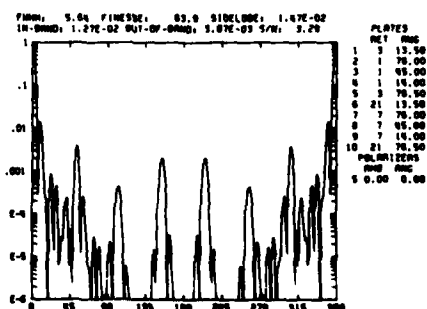


Figure 14. Transmission versus frequency of a ten-element hybrid modified Solc filter.

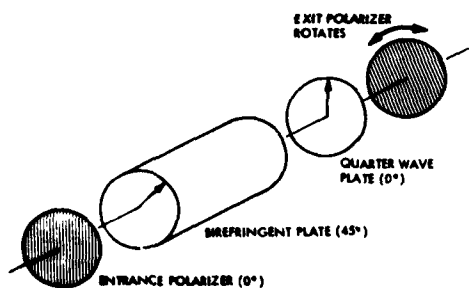


Figure 15. Simple quarter-wave tuning element

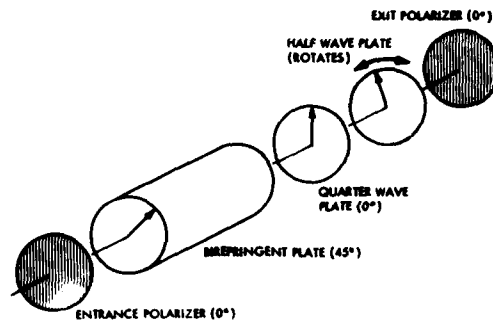


Figure 16. Practical quarter-wave : half-wave tuning element

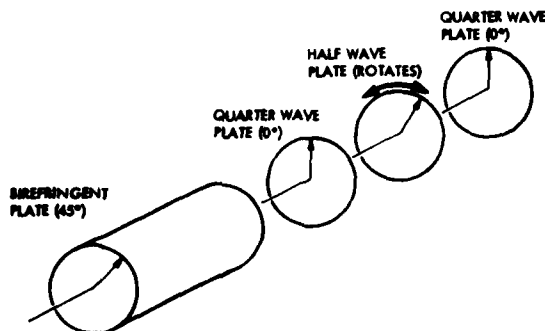


Figure 17. General tuning element suitable for Solc filters

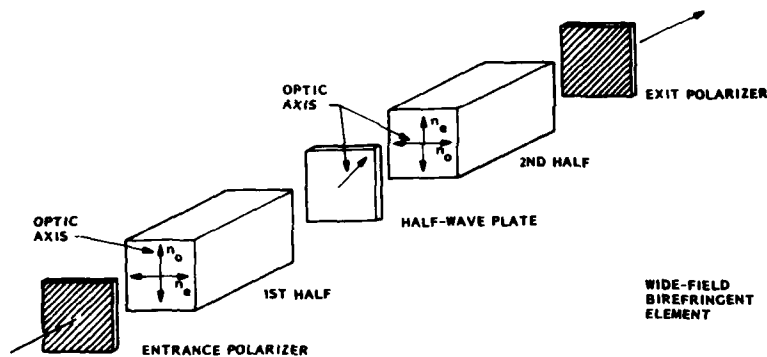


Figure 18. Wide field birefringent element

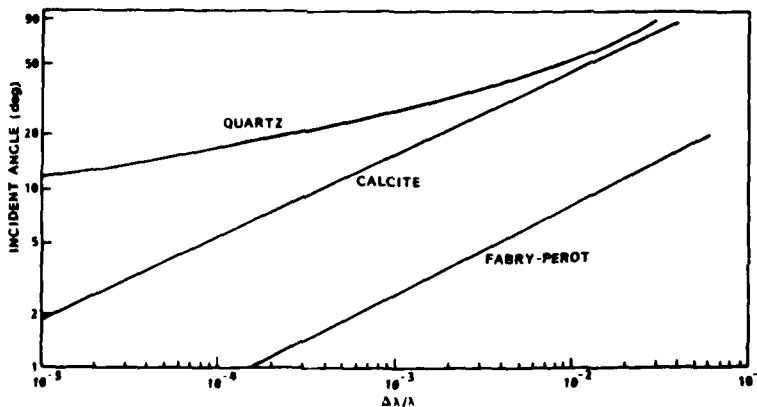


Figure 19. Off axis wavelength shift for wide field birefringent and interference filters

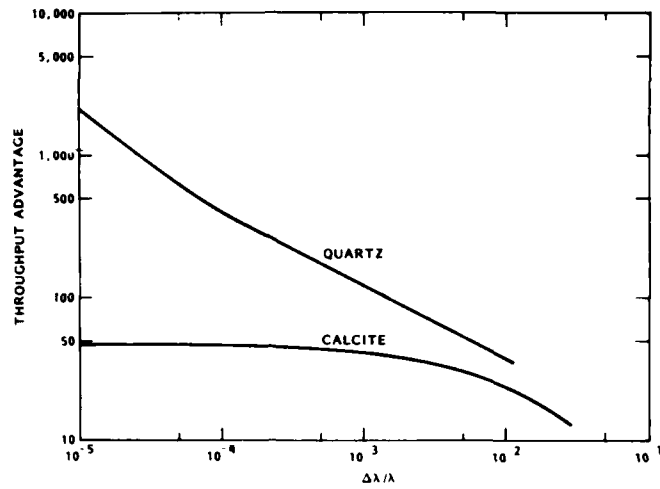


Figure 20. Throughput advantage of wide field birefringent filters



Figure 21. Tunable, wide field quartz filter with 7.5 cm clear aperture and 20 Å bandwidth



Figure 22. Tunable, wide field calcite filter with 3.5 cm clear aperture and 100 mÅ bandwidth

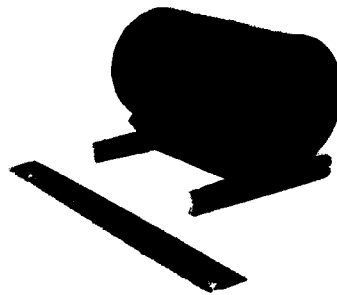


Figure 23. Laser communications receiver filter, 2 Å FWHM at $\lambda 5320 \text{ Å}$

OPTICAL RECEIVERS FOR UNDERWATER COMMUNICATION

AUTHORS:

John E. Jackson, Gary M. Lee, Charles M. Ciany

McDonnell Douglas Astronautics Company - St. Louis Division

ABSTRACT

Optical communications to submerged submarines requires an extremely sensitive receiver with a wide field of view and narrow optical bandwidth. The receiver requires a narrow optical bandwidth filter to discriminate against solar and bioluminescent background sources. The filter center wavelength should be selectable to match that of the most efficient laser transmitter. The receiver should have a large effective aperture (this may require multiple subapertures due to submarine space limitations). The field of view should be large ($>45^\circ$ full cone) to collect a significant fraction of the scattered signal. The transmission of all of the optical elements should be high. The detector must have a high quantum efficiency and be capable of operating with very large background variations from nighttime to full day light conditions (>150 dB variation). It is also desirable that the receiver be capable of efficient operation at varying depths.

This paper discusses the tradeoffs which must be considered to develop an optimum overall receiver design. The available choices for a receiver filter are discussed and an overall receiver configuration is developed.

GLOSSARY OF SYMBOLS AND ACRONYMS

SYMBOLS:

SNI	=	Current Signal to noise ratio
I_S	=	Total signal current at photocathode (amperes)
G	=	Gain of PMT
e	=	$1.602 \cdot 10^{-19}$ (coulomb) (electronic charge)
B_E	=	Electronic Bandwidth (Hz)
I_B	=	Total Background current at photocathode (amperes)
I_D	=	Total dark current at photocathode (amperes)
I_M	=	Total current at photocathode from miscellaneous sources (amperes)
F	=	Multiplication noise factor of PMT
N_D	=	Number of PMT's
k	=	$1.38054 \cdot 10^{-23}$ (J/ $^\circ$ K) (Boltzman's constant)
T	=	Resistive temperature -- ($^\circ$ K)
F_a	=	Noise factor of amplifier
R_L	=	Output Load resistor of PMT's (ohms)
E_p	=	Energy in Laser pulse (J)
R	=	PMT responsivity (amperes/watt)
t_s	=	Pulse width (sec)
A_r	=	Receiver aperture area (m^2)
d	=	Effective receiver diameter (m)
d_s	=	Diameter of laser spot at receiver (m)
T_a	=	Transmission due to atmosphere
T_{cl}	=	Transmission due to clouds
T_{aw}	=	Transmission due to air-water interface
T_w	=	Transmission due to water
R_S	=	Relative angular radiance distribution at receiver referenced to receiver zenith of signal (watts/steradian)
T_F	=	Transmission of narrow band filter
T_O	=	Transmission of all receiver components (including material absorption and coated interfaces) excluding narrow band filter
T_V	=	Transmission due to vignetting

θ_F	=	Receiver half angle FOV (deg)
θ	=	Zenith angle referenced to receiver zenith (deg)
ϕ	=	Azimuth angle (deg)
λ	=	Wavelength (angstroms = A)
H_B	=	Background irradiance (watts/(m ² • Angstrom))
B_O	=	Effective FWHM of optical filter
R_B	=	Relative angular radiance distribution at Receiver referenced to receiver zenith of Background (watts/steradian)

ACRONYMS:

FOV	=	Field of View
NBOF	=	Narrow Band Optical Filter
ELF	=	Extremely Low Frequency
VLF	=	Very Low Frequency
UV	=	Ultraviolet
BER	=	Bit Error Rate
PMT	=	Photomultiplier Tube
QE	=	Quantum Efficiency
FSR	=	Free Spectral Range
BNBF	=	Birefringent Narrow Band Filter
DBF	=	Dispersive Birefringent Filter
MCPC	=	Modified Compound Parabolic Concentrator
AGC	=	Automatic Gain Control
PPM	=	Pulse Position Modulation
DPIM	=	Differential Pulse Interval Modulation

1.0 INTRODUCTION

One of the most serious communication problems facing the Navy today is that of transferring information to submarines without affecting their operational capabilities. Ideally such a communications capability should be available at all operational speeds and depths and not require any external receivers which would compromise the submarine's strategic or tactical function. In addition, the communications system should be survivable in the face of a nuclear attack. Until recently, most attempts at solving this problem have focused on systems which utilize the lower end of the electromagnetic spectrum for transmission of the desired information (i.e., ELF, VLF, etc.) since the transmission in sea water is high as shown in Figure 1. The advent of the high power UV-visible laser has changed this emphasis to include optical techniques since this spectral region also has a high transmission.

In order for optical techniques to be effective, the submarine must be retrofitted with an optical receiver optimized for detection of short laser pulses in the presence of all the natural underwater background noise sources. Figure 2 illustrates the configuration of this communication link. The more important noise sources are the solar background and bioluminescence. Due to scattering in clouds and water, the signal and background irradiance typically have a very wide angular distribution at the operational submarine depth. The spectral content of the solar background is well known. The laser wavelength is yet to be determined but generally it is assumed that it will have a bandwidth of less than 1 A centered in the 450 nm to 550 nm blue-green window which is the region of the optical spectrum most highly transmitted by most ocean waters encountered operationally. Jerlov ⁽¹⁾ has characterized the sea water transmission for the spectral region of interest in much more detail according to water type. Figure 3 shows the types of water in various parts of the oceans. Figure 4 defines the spectral transmission of the most important water types at operational depth. As observed, a large amount of signal and background is absorbed in the water; consequently, the receiver must be designed to compensate for this large loss.

Since laser power is always a very precious and scarce commodity in optical communication systems, the natural inclination of the designer is to stress receiver technology to the limit in order to minimize required laser power. Although receivers usually seem simpler than lasers, the designer quickly discovers that there are fundamental theoretical and practical constraints that set limits to receiver performance that are just as unyielding as the more obvious limits on laser power.

In order to discriminate between the noise sources and the signal, optical receivers generally rely upon temporal, spectral, and spacial or angular discrimination. Because the clouds and water scatter the light to such a large degree, spacial or angular discrimination is not feasible at large depths leaving only temporal and spectral. The temporal discrimination is also complicated by the fact that clouds, and to a lesser extent water, cause pulse spreading. Most of the laser sources that are anticipated have output pulse widths of <200 ns but at the receiver, the pulse is spread from 1 to 50 μ sec depending primarily on the cloud thickness. An adaptive electronic bandwidth filter is used to optimally separate out the signal pulse from the low frequency background irradiance variations and the corresponding wideband shot noise.

Spectral discrimination is straight forward in principle. The practical implementation of a wide field of view (FOV) narrow band optical filter (NBOF) is the real challenge to the receiver designer. The NBOF should have an optical bandwidth that matches that of the signal source plus any wavelength shift due to Doppler effects. The NBOF should have a large aperture and a large FOV in order to accept as much signal as practical. The NBOF and other receiver optical components should also have as large a transmission as practical.

The detector is required to have a large quantum efficiency and low detector noise so that the receiver is signal shot noise limited for nighttime conditions and background noise limited for high background conditions of full sun. These requirements can most efficiently be achieved with an S-20 photomultiplier tube (PMT) with dynamic gain control of from 1 to 10^6 .

From the total communications system point of view, the total link loss is calculated (for each submarine location at its operational depth, cloud conditions, water type, background, angle of incidence, etc.) and the transmitter laser spot size is changed such that the link margin will be adequate to assure a communication performance of 10^{-6} bit error rate (BER).

If the submarine depth increases, then the received signal will be smaller and the number of bit errors will increase. If the submarine comes up to shallower depths or even out of the water, the attenuation due to the water is greatly decreased and the angular distribution of the signal and background sources are greatly changed especially for no cloud conditions. In the limit for the out of the water case, no signal would be collected for a laser signal source outside of the FOV of the receiver.

The receiver aperture area (A_r) is proportional to the amount of laser power required at the transmitter. How large should A_r be? The final answer to this question can only be arrived at from a cost trade off analysis of the minimum cost of delivered laser power plus cost of receiver area times the number of submarine receivers. This cost analysis can only be done after the laser and its scanning and delivery system have been defined. An estimate for A_r of $1m^2$ has been assumed.

2.0 ANALYTICAL RECEIVER MODEL

Assuming that the receiver response and the signal and background radiance profiles are time independent, the optimum receiver design requires the solution of a three dimensional detection problem. Let

$S(\phi, \theta, \lambda)$ = Underwater signal radiance profile at the receiver
(watts/(steradian \cdot $m^2 \cdot A$))

$N(\phi, \theta, \lambda)$ = Underwater background radiance profile at the receiver
(watts/(steradian \cdot $m^2 \cdot A$))

$F(\phi, \theta, \lambda)$ = Receiver response to a point source

where ϕ and θ are the spherical coordinate angles and λ is the wavelength. The mean signal and noise power at the detector output is given by

$$X_s = \int_0^{\infty} \int_0^{360^\circ} \int_0^{90^\circ} F(\phi, \theta, \lambda) S(\phi, \theta, \lambda) \sin\theta \, d\phi d\theta d\lambda \quad (1)$$

$$X_n = \int_0^{\infty} \int_0^{360^\circ} \int_0^{90^\circ} F(\phi, \theta, \lambda) N(\phi, \theta, \lambda) \sin\theta \, d\phi d\theta d\lambda \quad (2)$$

The receiver design problem is to choose $F(\phi, \theta, \lambda)$ to maximize the probability of detecting the signal which is roughly equivalent to maximizing signal-to-noise ratio (S/N). For optical detection, S/N is proportional to

$$S/N \propto \frac{X_s^2}{X_n} = \frac{\left[\int_0^\infty \int_{0^\circ}^{360^\circ} \int_{0^\circ}^{90^\circ} S(\phi, \theta, \lambda) F(\phi, \theta, \lambda) \sin \theta \, d\phi d\theta d\lambda \right]^2}{\int_0^\infty \int_{0^\circ}^{360^\circ} \int_{0^\circ}^{90^\circ} N(\phi, \theta, \lambda) F(\phi, \theta, \lambda) \sin \theta \, d\phi d\theta d\lambda} \quad (3)$$

In particular the receiver performance can be given by

$$SNI = \frac{I_S G}{\left[2eB_E G^2 (I_B + I_D + I_M + I_S) F N_D + \frac{4kT B_E F_a}{R_L} \right]^{1/2}} \quad (4)$$

The required value of SNI is dependent upon the modulation format (PPM or DPIM), the type of detection (greatest of or threshold), and the noise photoelectrons per slot width. For these variables, SNI is bounded by 5 to 10.6.

The signal and background currents are given by equations (5) and (6) respectively.

$$I_S = E_p \frac{R}{t_s} \left(\frac{d}{d_s} \right)^2 \left[T_a T_{cl} T_{aw} T_w \right] \frac{\int_{0^\circ}^{360^\circ} \int_{0^\circ}^{\theta_F} R_S T_F T_O T_V \cos \theta \sin \theta \, d\theta \, d\phi}{\int_{0^\circ}^{360^\circ} \int_{0^\circ}^{90^\circ} R_S \sin \theta \, d\theta \, d\phi} \quad (5)$$

$$I_B = H_B R \frac{\pi d^2}{4} \left[T_a T_{cl} T_{aw} T_w \right] B_O \frac{\int_{0^\circ}^{360^\circ} \int_{0^\circ}^{\theta_F} R_B T_O T_V \cos \theta \sin \theta \, d\theta \, d\phi}{\int_{0^\circ}^{360^\circ} \int_{0^\circ}^{90^\circ} R_B \sin \theta \, d\theta \, d\phi} \quad (6)$$

If the receiver is background limited where

$$I_B \gg I_S + I_M + I_D \text{ and } 2e B_E G^2 I_B F N_D \gg \frac{4 kT B_E F_a}{R_L}$$

then E_p can be solved for and is given by

$$E_p = \frac{t_s d_s^2 (SNI) (2eH_B \pi/4)^{1/2} (B_E F B_O)^{1/2} \left[\int_{0^\circ}^{360^\circ} \int_{0^\circ}^{\theta_F} R_B T_O T_V \cos \theta \sin \theta \, d\theta \, d\phi / \int_{0^\circ}^{360^\circ} \int_{0^\circ}^{90^\circ} R_B \sin \theta \, d\theta \, d\phi \right]^{1/2}}{\left[d^2 R (T_a T_{cl} T_{aw} T_w) \right]^{1/2} \int_{0^\circ}^{360^\circ} \int_{0^\circ}^{\theta_F} R_S T_F T_O T_V \cos \theta \sin \theta \, d\theta \, d\phi / \int_{0^\circ}^{360^\circ} \int_{0^\circ}^{90^\circ} R_S \sin \theta \, d\theta \, d\phi} \quad (7)$$

If the receiver is signal shot noise limited where

$$I_S \gg I_B + I_M + I_D \text{ and } 2e B_E G^2 I_S F N_D \gg \frac{4 kT B_E F_a}{R_L}$$

then E_p can be solved for and is given by

$$E_p = \frac{t_s d_s^2 (SNI)^2 (2e B_E F) \int_{0^\circ}^{360^\circ} \int_{0^\circ}^{90^\circ} R_S \sin \theta \, d\theta \, d\phi}{d^2 R (T_a T_{cl} T_{aw} T_w) \int_{0^\circ}^{360^\circ} \int_{0^\circ}^{\theta_F} R_S T_F T_O T_V \cos \theta \sin \theta \, d\theta \, d\phi} \quad (8)$$

Equations (7) and (8) set the upper and lower bounds of required laser energy for the extreme conditions of high background and no background respectively.

The receiver components selected will define many of the parameters of the given equations. Table 1 lists the major receiver components and the parameters they affect. The parameters that are affected by the various communication scenario conditions while maintaining a constant BER are given in Table 2.

3.0 TRANSMIT LASER CENTER WAVELENGTH

If one could choose the laser wavelength that was the most optimum from the receivers point of view, what would it be? Assuming that the transmission of the optics and NBOF are roughly independent of wavelength, only water transmission, solar irradiance, and detector quantum efficiency need be considered to determine the relative receiver responsivity versus wavelength. Figure 5 shows the maximum quantum efficiency (QE) that can be expected from head on PMT's. Figure 6 shows the relative required laser power in dB versus wavelength for 11.7 absorption lengths in Jerlov Type III sea water, full solar irradiance, and the best QE PMT's.

Superimposed on the continuous curve are spikes that represent the Fraunhofer absorption lines of the solar spectrum. Note that if a laser could be matched to one or these lines a savings of at least 5 dB in laser power could be gained. Ignoring the Fraunhofer lines for the 450 nm to 550 nm interval, only a 3 dB variation occurs.

4.0 NARROW BAND OPTICAL FILTER

The selection of the NBOF type and its design is the single most important design task. The selected NBOF will determine the requirements of the optical transfer system, the blocking filter, and the detector array configuration. The parameters of importance for the NBOF are the optical bandwidth (B_O), free spectral range (FSR), the acceptance FOV, transmission, aperture area, out of band rejection, and thermal stability or control required. Table 3 lists all of the conceived generic filter concepts that could be considered.

In order for a filter concept to be useful for this application, it must be wide angle; i.e., the filtering action should not be affected by the angle of incidence. Most common narrowband filters use interference and are affected by the angle of incidence.

Atomic/molecular basis filters⁽²⁾ are unaffected by the angle of incidence but only certain wavelengths are found to be passed by these filter types.

Self-filtering narrowband detectors are truly wide angle but their bandwidth is greater than 10 Å. Wide angle, very narrowband filters could be constructed using the concept of hole-burning in saturable absorbers⁽³⁾ but the effect only occurs stably at liquid helium temperatures and no research has been done to prove the feasibility of this approach.

Schineller⁽⁴⁾ developed a narrowband wide angle filter using single mode waveguides as the spacer in a Fabry-Perot filter; but the aperture sizes and transmission are not adequate for this application.

Christiansen scattering filters^(5, 6) employ particles in liquid suspension which have an index of refraction whose rate of change with wavelength is different from that of the liquid. If the index of refraction of the particles and liquid are equal at a particular wavelength, then the suspension will transmit perfectly at that wavelength and be unaffected by the angle of incidence. At all other wavelengths, scattering will occur and wavelength selection can be implemented. Because the angle parameter is required to discriminate against scattering, the Christiansen scattering filter cannot be wide angle. But the concept can be extended to the Christiansen-Bragg filter⁽⁷⁾ where a multilayer coating is constructed such that two materials composing the alternate layers have an index of refraction that is equal at some wavelength. At other wavelengths, the multilayer coating is designed to be a high reflection coating; thus filtering action should be observed. Although this approach shows theoretical promise, required materials do not seem to exist for implementation into a viable filter concept.

Both the dispersive birefringent filter⁽⁸⁾ (DBF) and the isotropic-index coupled-wave filter⁽⁹⁾ (ICF) have recently been undergoing research and development. Both use the fact that some materials exhibit zero birefringence at a wavelength of interest. At the wavelength where the birefringence is zero, the material is isotropic and no angle of incidence effects are exhibited. Although simple DBF and ICF filters have been demonstrated having very promising performance characteristics the type of filter required for the submarine receiver has not been demonstrated.

Of the concepts listed in Table 3, only the birefringent narrowband filter (10, 11, 12, 13) (BNBF) employing crystalline quartz is a viable candidate for near term implementation.

AD-A105 193

ADVISORY GROUP FOR AEROSPACE RESEARCH AND DEVELOPMENT--ETC F/G 17/2
SPECIAL TOPICS IN OPTICAL PROPAGATION.(U)

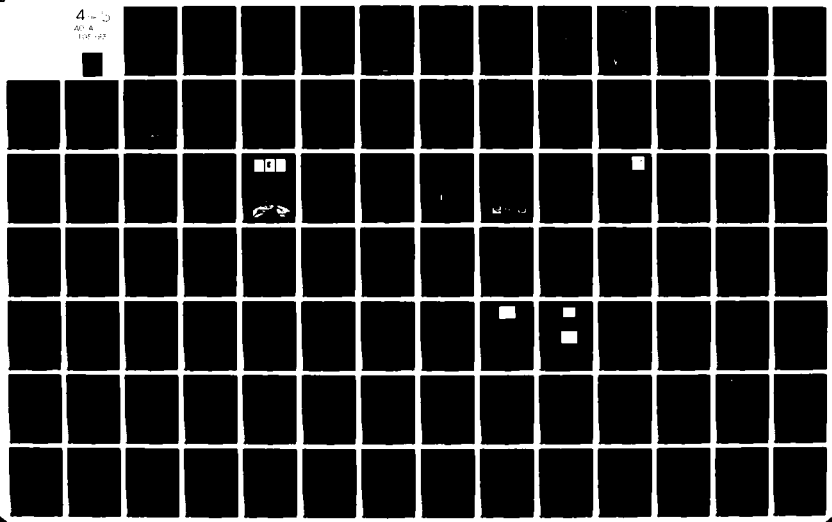
JUL 81 P HALLEY

AGARD-CP-300

NL

UNCLASSIFIED

4 - 10
AD-A
105-193



Typical BNB characteristics are given in Table 4. Figure 7 shows a schematic of a single stage of the two stage hybrid Solc filter. In actuality, the elements are not rotated with respect to one another but instead a waveplate is inserted between each element pair to control the effective polarization rotation from one element to the next. Figure 8 defines the transmission performance of the BNB versus angle of incidence; for an angle of incidence of 21° (in air), the transmission falls to 50% of the on axis value. Figure 9 and 10 defines the spectral transmission of the BNB on an expanded and struck wavelength scale respectively.

5.0 OPTICS

The requirements on the receiver optical system are to optimally transfer signal light through the NBOF onto the detector sensitive area while limiting the FOV to that most efficiently filtered by the NBOF. The limiting FOV is required to prevent background at large angles of incidence from being collected onto the detector. The transmission at the laser signal wavelength will decrease with angle of incidence to the NBOF due to the center wavelength shift with angle of incidence; but since the background is a continuum in wavelength, the total background transmission with angle of incidence is essentially constant except for the cosine of the incident angle aperture area loss effect.

Since no imaging capability is required, nonimaging concentrators⁽¹⁴⁾ which are most highly transmissive can be used to both limit the angular acceptance to the required FOV and transfer the light flux from the NBOF to the detector. As a side benefit, the nonimaging concentrator in the form of a modified compound parabolic concentrator (MCPC) is also used to limit the angles of incidence to the detector sensitive area to values where quantum efficiency is not degraded due to fresnel reflection losses.

Very simply the optics consists simply of four components shown in Figure 11. The entrance window is highly transmissive but structurally strong to support the required pressure difference. The NBOF is the limiting aperture of the total receiver.

6.0 OPTICAL DETECTOR

The operational submarine receiver will encounter a large range of incident background levels due to large changes in exoatmospheric background irradiation from daytime to nighttime, changes in atmospheric attenuation from cloudy to cloudfree conditions, and large changes in water attenuation from Jerlov Type IB (clean) to Jerlov Type III (dirty) water. Figure 12 illustrates the components of background dynamic range variations in the operational system and quantifies each. Note that a total dynamic range of 165 dB in receiver background is anticipated.

The first step in designing a receiver to meet the dynamic range requirement is the choice of an appropriate optical detector and associated gain control. The detector should also have:

- High QE in the blue-green spectrum
- Large photocathode area in comparison to tube area
- High maximum photocathode and anode current ratings
- Low dark current noise
- Large range of multiplier gain to limit anode power dissipation under high background conditions (low-gain operation) and provide insensitivity to electronics and dark current noise under low-background conditions (high gain operation)
- Response time less than the received laser signal pulse width

Solid state detectors have both high QE and high current capability but the required large area detectors have high thermal noise preventing shot noise limited operation in low background conditions since no gain is available. Conventional head on type photomultiplier tubes (PMT's) can be operated either shot noise limited (because of their high gains) or background noise limited. The S-20 photocathode sensitive surface has an order of magnitude greater cathode current (250 na/cm^2) capability than any other and has an adequate QE especially with the prismatic window photocathodes of EMI. PMT temperature should be held at less than 20°C where the dark current is less than $10^{-16} \text{ amp/cm}^2$ so that its responsivity is not degraded for low background conditions.

7.0 THERMAL CONTROL

Normal thermal control is required to maintain the detector at less than 20°C and control the processing and control electronics within their normal operating temperature of $20^\circ\text{C} \pm 20^\circ\text{C}$. But very sensitive temperature control is required to keep the NBOF at a specially uniform bias temperature of about 45°C with a control variation of about $\pm 0.5^\circ\text{C}$. The adequacy of this control to a large part will determine how narrow a band pass the NBOF should have.

8.0 ELECTRONICS

The electronics must provide optimal noise rejection to maximize the probability of detecting the laser pulses. The system uses a pulse position modulation format where the pulse can be in any one of a number of slots. The receiver electronics must first establish and maintain time synchronization with the transmitter and then detect the arrival time of each pulse. Synchronization can be provided either by the use of a message preamble or by using the arrival time of each pulse as the reference for the next pulse.

The electronics must also provide AGC signals to protect the detectors and must combine the output of the detectors prior to signal processing. Some decoding both for error correction and security may also be required.

REFERENCES

1. N. G. Jerlov, "Marine Optics", Elsevier (1976).
2. J. B. Marling, et. al., J. Appl. Phys. 50 (1979) 610.
3. B. M. Khazlamov, R. I. Personov, and L. A. Bykovskaya, Opt. Spectrosc. 39 (1975) 137.
4. E. R. Schineller, "Development of a Wide-Angle Narrowband Optical Filter", Report 1507 Wheeler Labs. (1968).
5. C. Christiansen, Ann. Phys. Chem. 23 (1884) 298.
6. R. H. Clark, Appl. Optics 7 (1968) 861.
7. P. Yeh, Optics Comm. 35 (1980) 9.
8. P. Yeh, Optics Comm. 35 (1980) 15.
9. J. F. Lotspeich, IEEE JOE 15 (1979) 904.
10. A. M. Title, Appl. Optics 14 (1975) 229.
11. A. M. Title, Appl. Optics 14 (1975) 445.
12. A. M. Title, Appl. Optics 15 (1976) 2871.
13. A. M. Title and W. J. Rosenberg, Appl. Optics 16 (1979).
14. W. T. Welford and R. Winston, "The Optics of Nonimaging Concentrators", Academic Press (1978).

TABLE 1. PARAMETERS DEFINED BY MAJOR RECEIVER COMPONENTS

MAJOR RECEIVER COMPONENT	RECEIVER PERFORMANCE PARAMETERS AFFECTED
PRESSURE WINDOW	T_0
DYNAMIC SCATTERER	R_S, R_B, T_0
BLOCKING FILTER	B_0, T_0
OPTICAL ATTENUATOR	T_0
NARROW BAND OPTICAL FILTER	B_0, T_F, T_V, d
COMPOUND PARABOLIC CONCENTRATOR	θ_F, T_0
PMT	N_D, R, G, F, I_D, T_0
PROCESSING ELECTRONICS	B_E, R_L, F_a
THERMAL CONTROL SYSTEM	
- FOR NARROW BAND FILTER	T_F
- FOR PMT	I_D, F
- FOR ELECTRONICS	F_a, T

TABLE 2. COMMUNICATION SCENARIO CONDITIONS AND PARAMETERS AFFECTED TO MAINTAIN CONSTANT BER

SCENARIO CONDITION	PARAMETERS
BACKGROUND LEVEL	$d_s, H_B, G, I_B, I_S, T_0$
BACKGROUND SOURCE POSITION (θ, ϕ)	$d_s, H_B, G, I_B, R_B, I_S, T_0, T_a, T_{aw}, T_w$
LASER SOURCE POSITION (θ, ϕ)	$d_s, T_a, T_a, T_{aw}, T_w, R_s$
RECEIVER DEPTH	$d_s, G, I_B, I_S, T_0, R_B, R_S$
JERLOV WATER TYPE	$d_s, G, I_B, I_S, T_0, R_B, R_S, T_w$
CLOUDS	$d_s, G, I_B, I_S, T_0, R_B, R_S, T_{cl}, T_{aw}, t_s$
SEA STATE	$d_s, G, I_B, I_S, T_0, R_B, R_S, T_{aw}$
RECEIVER ATTITUDE	$d_s, G, I_B, I_S, T_0, R_B, R_S$

TABLE 3. GENERIC FILTER CONCEPTS

<p style="text-align: center;">SOLID STATE FILTERS</p>	<ul style="list-style-type: none"> • BIREFRINGENT NARROWBAND FILTER • DISPERSIVE BIREFRINGENT FILTERS • ISOTROPIC-INDEX COUPLED-WAVE OPTICAL FILTERS • FABRY-PEROT INTERFEROMETER FILTERS • INTERFERENCE FILTERS • SELF-FILTERING NARROWBAND DETECTORS • ACOUSTICALLY TUNABLE OPTICAL FILTERS • IMPURITY INDUCED FLUORESCENCE OF RARE EARTH IONS • HOLE-BURNING IN SATURABLE ABSORBER • CHRISTIANSEN-BRAGG FILTERS • CHRISTIANSEN SCATTERING FILTERS • SINGLE MODE WAVEGUIDE FABRY-PEROT FILTERS
<p style="text-align: center;">ATOMIC/MOLECULAR BASIS</p>	<ul style="list-style-type: none"> • SPECULAR REFLECTION • ATOMIC RESONANCE ABSORPTION AND FLUORESCENCE FILTERS • ATOMIC RESONANCE ABSORPTION AND PHOTOIONIZATION DETECTORS • MOLECULAR BASED FILTERS

TABLE 4. SELECTED BIREFRINGENT NARROW-BAND FILTER CHARACTERISTICS

CHARACTERISTICS	VALUE
BIREFRINGENT MATERIAL	CRYSTALLINE QUARTZ (NATURAL OR SYNTHETIC)
DESIGN TYPE	2 STAGE HYBRID SOLC (3 POLARIZERS AND 16 FIELD WIDENED QUARTZ ELEMENTS)
APERTURE SIZE	15 CM X 15 CM
LENGTH	15 CM
OPTICAL BANDWIDTH, B_0	3 A
OPTIMUM FOV	$\pm 17^\circ$ (IN WATER)
ON-AXIS TRANSMISSION	35%
FREE SPECTRAL RANGE, FSR	750 A
SIDE LOBE TRANSMISSION	<1%
REFERENCE CENTER PASS WAVELENGTH	5320 A
THERMAL STABILITY	0.5 A/ $^\circ$ C
REQUIRED THERMAL CONTROL	$\pm .5^\circ$ C

ELECTROMAGNETIC PROPAGATION IN SEA WATER

10-1711

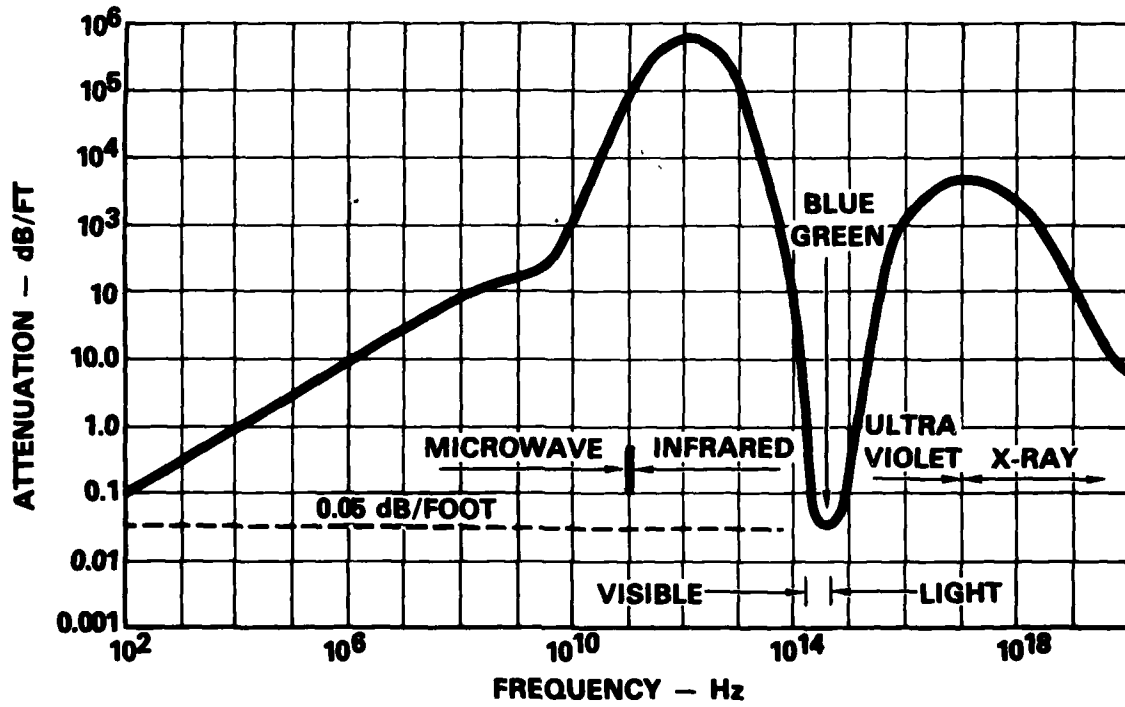


FIGURE 1

UNDERWATER COMMUNICATIONS SCENARIO

10-6817

OPTICAL DOWNLINK

- PULSE SPREADING/CLOUD
- SPATIALLY
 - ANGULARLY
 - TEMPORALLY

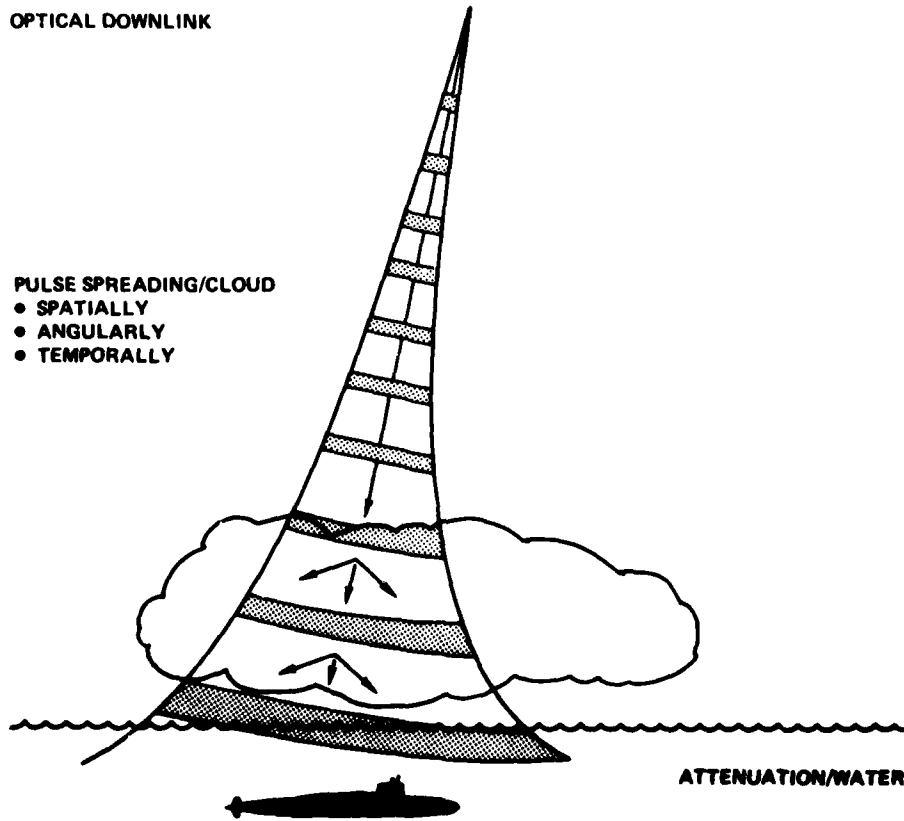


FIGURE 2

REGIONAL DISTRIBUTION OF OPTICAL WATER TYPES

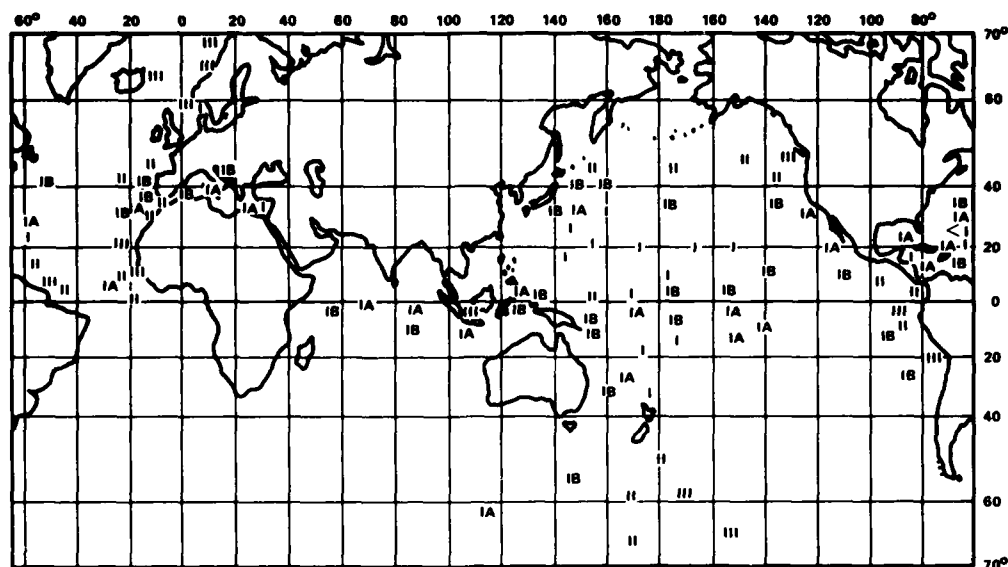


FIGURE 3

UNDERWATER SOLAR SPECTRUM AT OPERATIONAL DEPTH

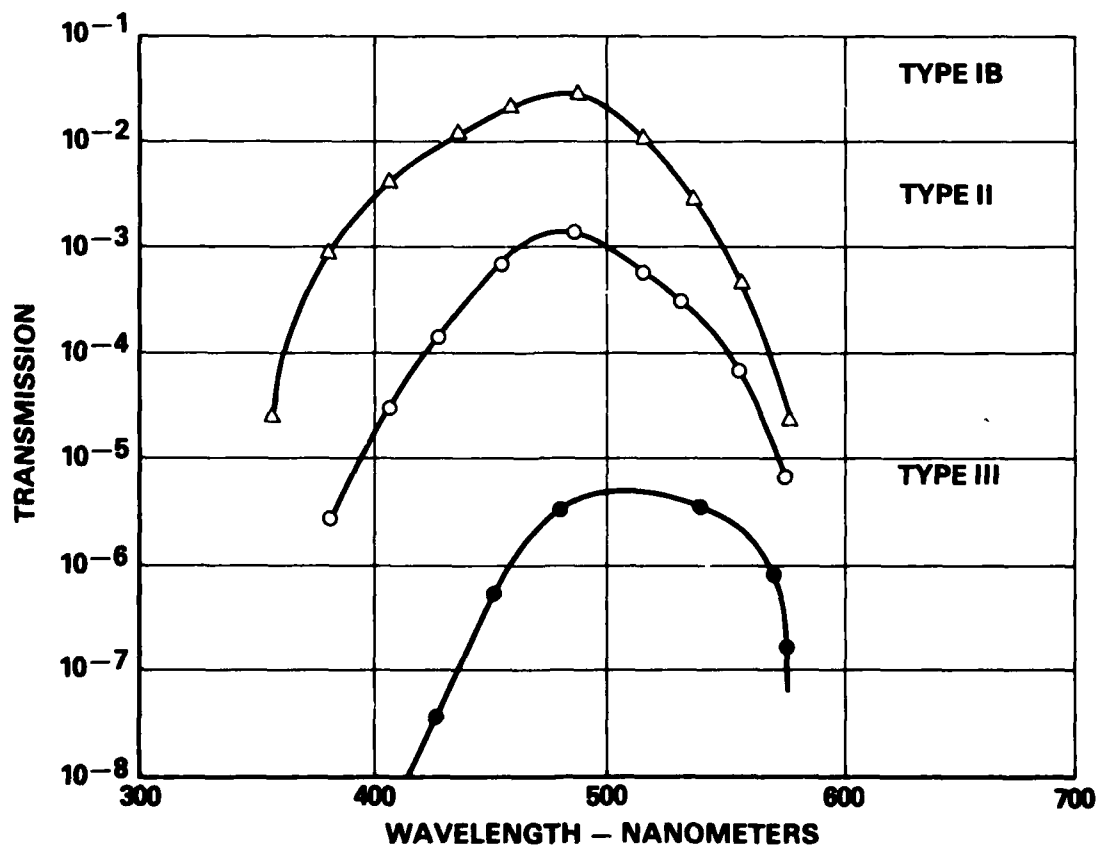


FIGURE 4

BEST QUANTUM EFFICIENCY FOR HEAD ON PMT'S

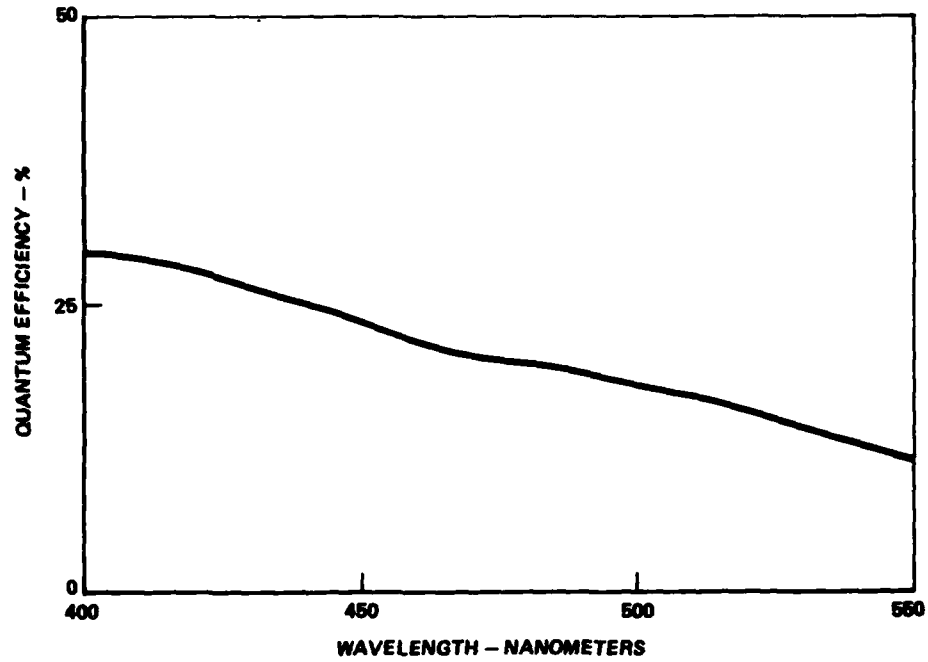


FIGURE 5

RELATIVE FIGURE OF MERIT FOR SUBMERGED RECEIVER CONSIDERING TYPE III WATER TRANSMISSION, SOLAR IRRADIANCE, AND PMT QE

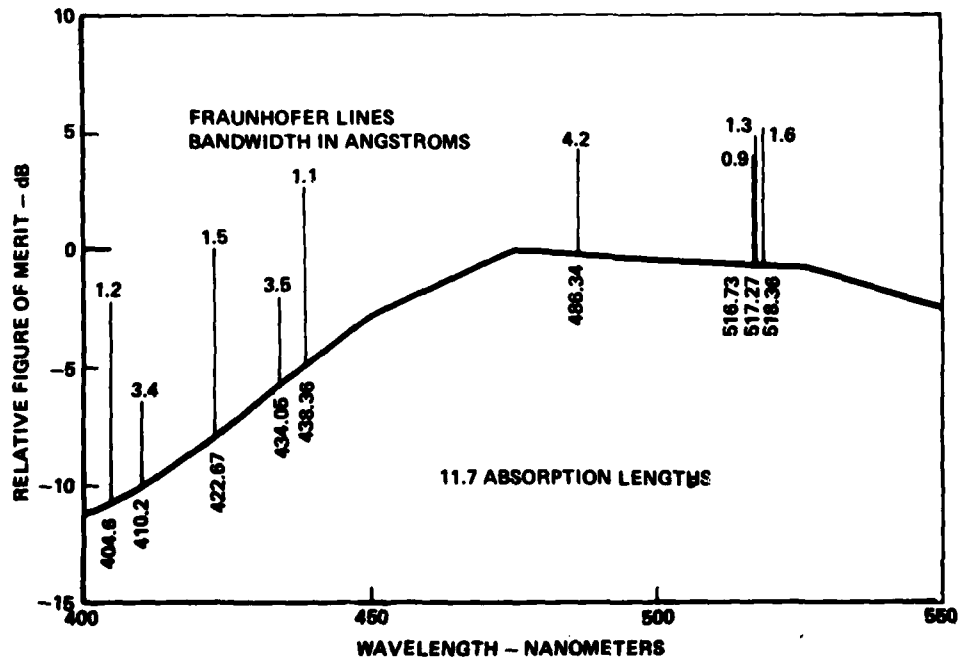


FIGURE 6

HYBRID SOLC FILTER STAGE (Two Stages Required)

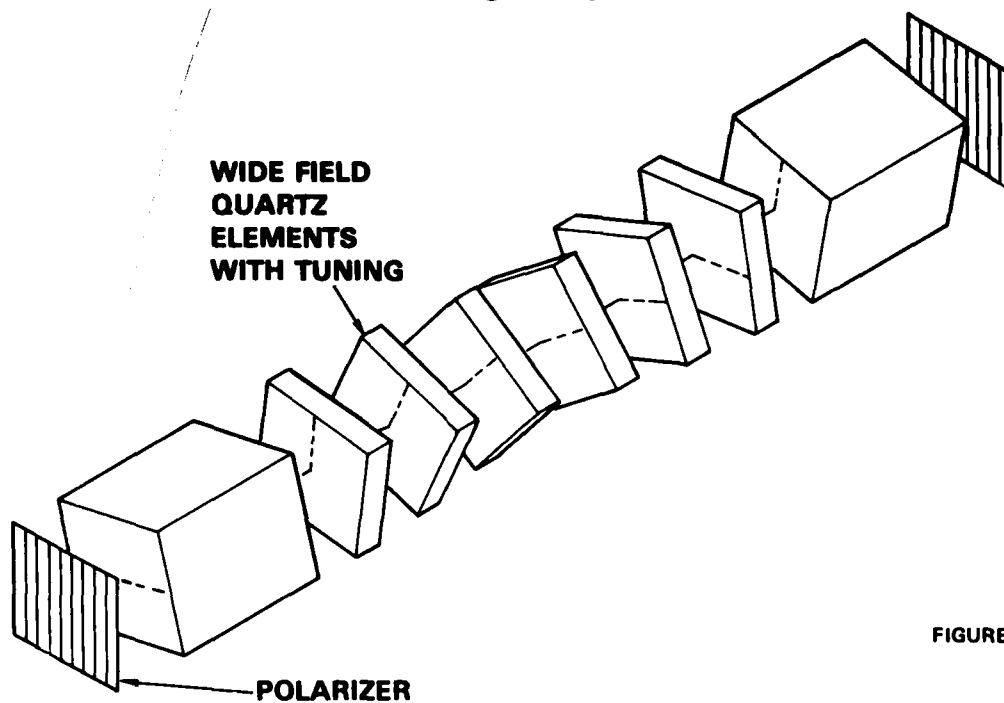


FIGURE 7

TRANSMISSION OF BNBFB AT CENTER WAVELENGTH VERSUS ANGLE OF INCIDENCE

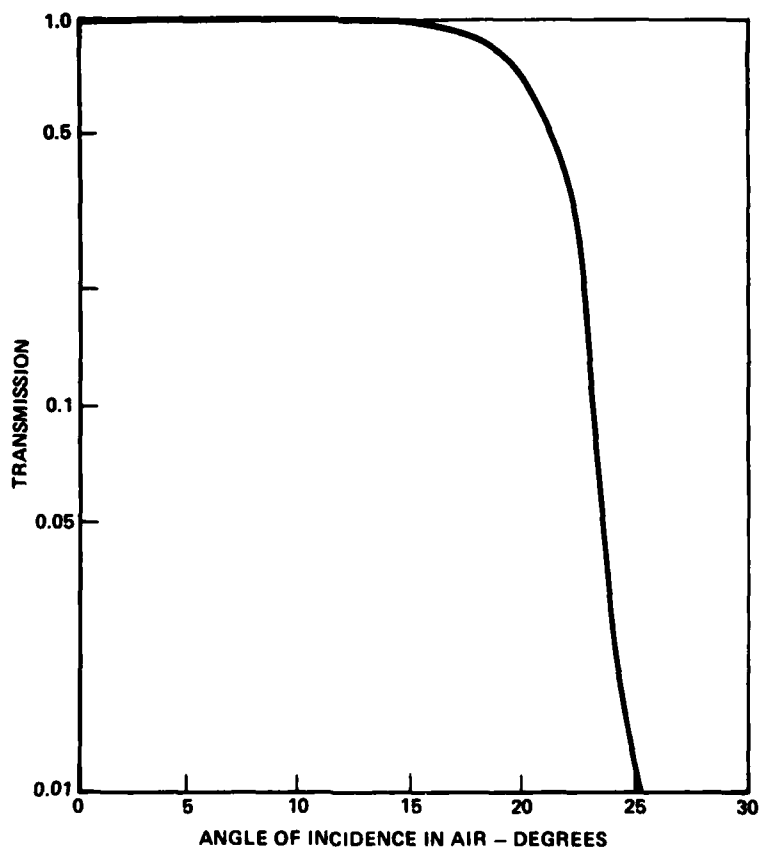
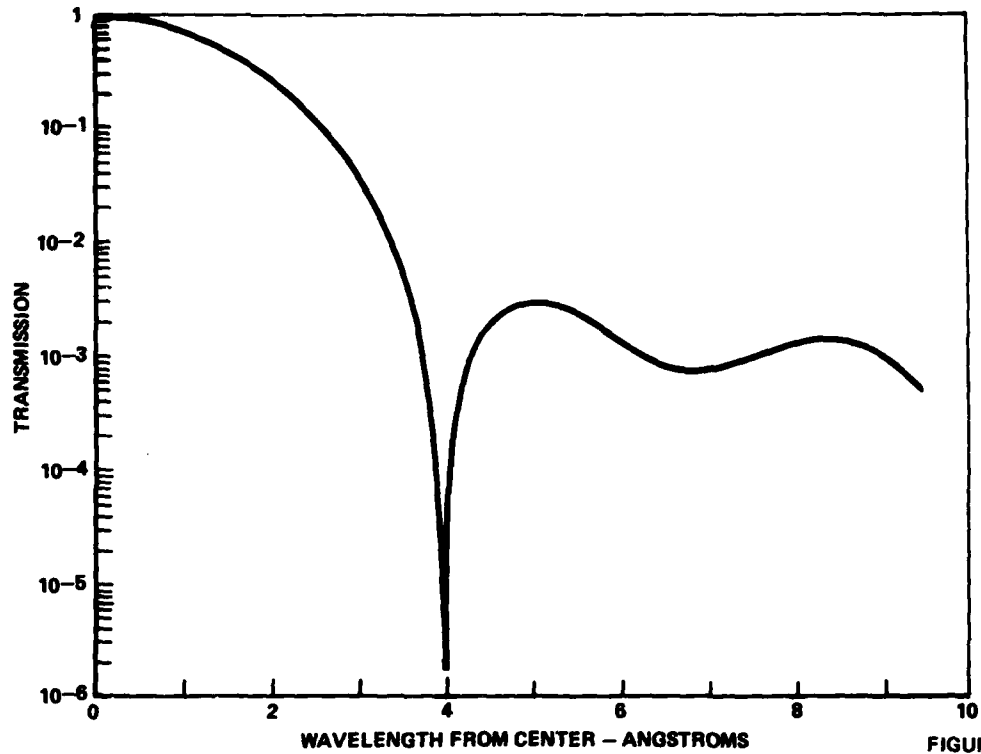
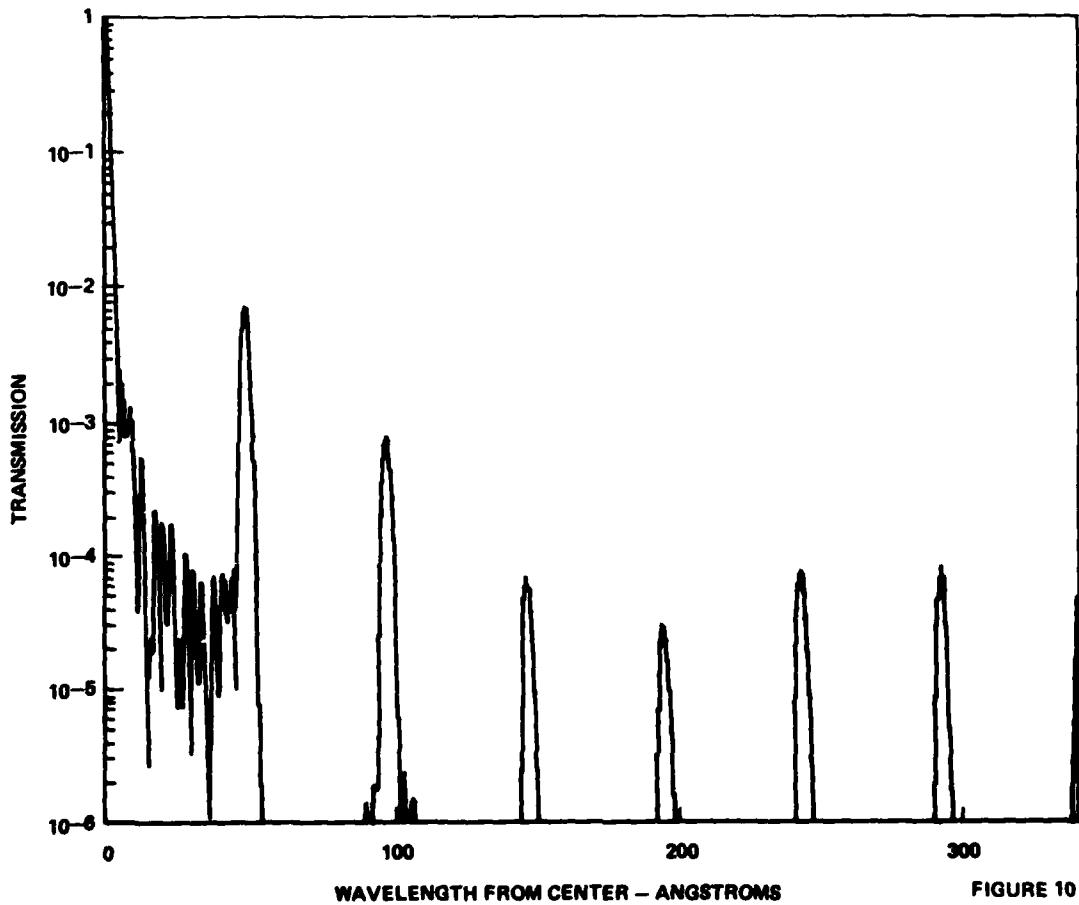


FIGURE 8

SPECTRAL TRANSMISSION PROFILE OF BNB (EXPANDED SCALE)



SPECTRAL TRANSMISSION PROFILE OF BNB



MAJOR COMPONENTS OF UNDERWATER COMMUNICATIONS OPTICAL RECEIVER

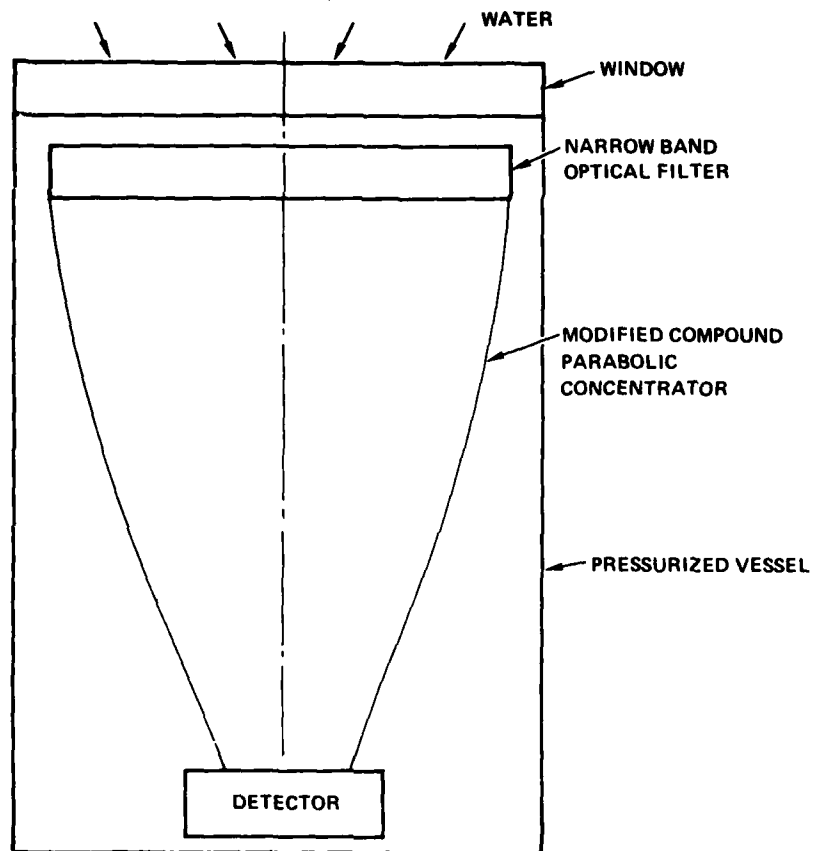


FIGURE 11

BLUE-GREEN BACKGROUND DYNAMIC RANGE COMPONENTS AT OPERATIONAL DEPTH

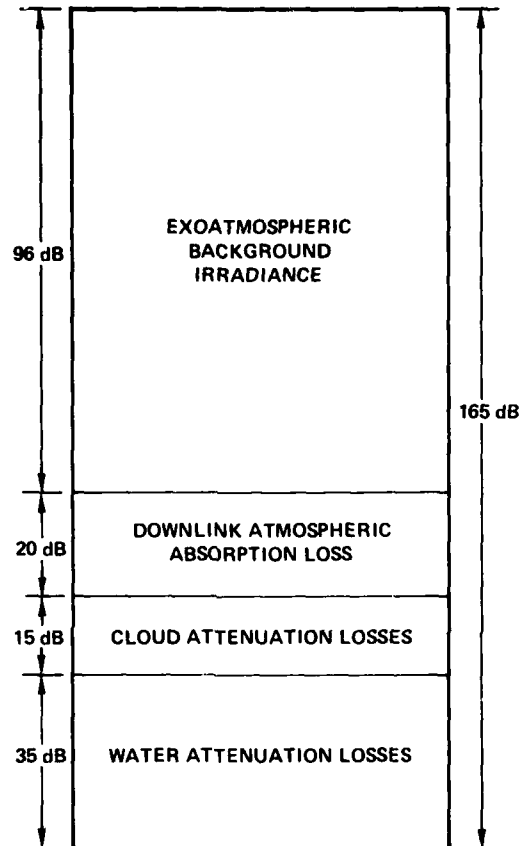


FIGURE 12

Optical Fiber Communication at different Transmission Wavelengths

K. Hess and H. Haupt

SEL Research Centre (ITT), Stuttgart, Germany

SUMMARY

34-Mbit/s optical transmission systems operated at 850 nm and 1200 nm and using graded-index multimode fibres are reported and compared. The results of a field trial with an 850 nm system which had been started in 1978 in the local telephone network of Berlin, prove that fibre optic transmission systems are well suited for real applications. The development of GaInAsP/InP-dh-laser and GaInAs/InP-pin-diode enable to take advantage of the superior fibre characteristics at 1200 nm. As a result a remarkable increase of repeater spacings has been achieved and a distance of 36 km has been bridged without repeater. This reduces drastically the number of repeaters in trunk lines and the required maintenance and makes most systems independent of power feeding, thus leading to the breakthrough in terms of reliability and economy.

1. INTRODUCTION

Optical communication systems are expected to be used widespread in the near future. Low-loss high-bandwidth optical fibres offer some fundamental advantages as compared with metallic conductors. Repeater spacings are significantly increased providing in addition a much wider bandwidth. The complete electrical isolation eliminates grounding and safety-related problems. Crosstalk between adjacent fibres is simply prevented by opaque coatings. Fibres are neither susceptible to nor do they emit electromagnetic radiation; they are immune to interference. Small size, light cables are further advantages.

Apart from the fibre cables the main components of an optical communication system are the light source in the transmitter and the photodetector in the receiver. Semiconductor devices are the components of choice because they are small, efficient, capable to operate at frequencies extending into the GHz range and also offer the possibility of being combined with couplers, switches and modulators to form singlechip integrated optical circuits.

2. FIBRE CHARACTERISTICS

The design of optical fibre systems is governed by two transmission parameters, namely attenuation and dispersion of fibre (Fig. 2). The losses in fibre waveguides are due to both material imperfections and to waveguide - related mechanisms. The losses of this fibre (core diameter 49 μm , numerical aperture 0.22) at 850 nm, 1200 nm and 1550 nm are 2.1 dB/km, 0.54 dB/km and 0.31 dB/km respectively (1). Fabrication of such extremely low-loss fibres in the long wavelength range has been enabled by reduction of hydroxyl ions in the fibre core and cladding. The material dispersion of doped silica fibres approaches zero near 1.3 μm . Low loss and minimum dispersion are highly important for long haul and wide bandwidth systems.

3. TRANSMISSION SYSTEMS AT 850 NM WAVELENGTH

Most of installed field trial systems operate at transmission wavelengths near 850 nm, utilizing GaAs/GaAlAs double-heterostructure lasers or light emitting diodes (LEDs) as sources and silicon avalanche photodiodes (APDs) or pin-diodes as detectors. This choice of wavelength regime was made primarily on the basis of the advanced development state and the commercial availability of these sources and detectors.

German PTT Administration has initiated field trials to test the potential of optical transmission systems in the telecommunication network. Sponsored by German PTT and German Ministry of Research and Technology, Standard Elektrik Lorenz has installed a 34 Mbit/s optical field trial system in the local telephone network of Berlin in 1978 (2). The link connects two local telephone exchanges and has a length of 4.3 km (in one direction) and 8.6 km (in a loop), respectively. The cable route between the exchange offices has been carefully selected in order to test the optical cable under severe environmental conditions such as sharp directional changes, vibrations caused by motorways and underground, tensional stress and interference from electrical railways.

This system comprises a GaAlAs/GaAs dh laser and a Si APD. The cable contains eight graded-index fibres with 4.7 dB/km attenuation and 1.95 ns/km dispersion (average values) for a numerical aperture of 0.25. The receiver sensitivity (mean optical power to achieve a bit error rate of 10^{-9}) is -53 dBm. The large margin of the system (20.5 dB) allows a link of double the length i.e. 8.6 km to be bridged without a repeater.

Tests and measurements carried out in the meantime by the German Bundespost indicate that system performance has not changed within the last three years and that optical transmission systems are well suited for real applications.

Two other communication systems carrying actual traffic with maximum repeater spacings above 9 km (1.: 34 Mbit/s system telephone traffic over a link of 14.5 km, installed in the Stuttgart area in 1980, 2.: 2 Mbit/s system along a power distribution line) work also satisfactorily.

4. TRANSMISSION SYSTEM AT 1200 NM WAVELENGTH

4.1 Optical Devices

In order to take advantage of the superior fibre characteristics at 1200 nm, it is necessary, of course, to have sources and detectors with high performance available for this wavelength. The emission of lasers and LEDs in the GaAs/GaAlAs system is restricted to wavelengths shorter than 900 nm and silicon photodetectors have essentially no response beyond 1100 nm. With respect to lasers, there is no elemental or binary III-V compound semiconductor with a direct bandgap correspon-

ponding to this wavelength region. With respect to photodiodes, Ge (bandgap energy 0.65 eV) and GaSb (bandgap energy 0.07 eV) are candidates for this spectral region. Ge is one of the semiconductor materials most widely investigated and has been used for fabrication of pin and avalanche detectors for several years (3,4). Ge APDs are the only commercially available avalanche detectors for wavelengths longer 1 μm at present. Due to the high dark current and to the almost identical ionization coefficients for electrons and holes, Ge photodiodes are not suitable for optical transmission in the low Mbit/s range. But, as the importance of the dark current decreases with increasing bandwidth, such detectors may be advantageous at high bitrates.

The most promising material system for both lasers and photodetectors in the wavelength range 1.0 to 1.6 μm is (Ga,In)(As,P) (5;6). Fig. 2 illustrates the dependence of the energy bandgap on alloy composition for this material system. The solid curves running approximately horizontally across the alloy system are constant-bandgap curves and the dashed lines are the iso-lattice-constant curves. Quaternary alloys have one degree of freedom more than ternary alloys, thus allowing the independent control of energy bandgap and lattice constant over rather wide ranges. For this reason, GaInAsP layers with a bandgap energy corresponding to wavelengths between 960 nm and 1660 nm can be deposited lattice-matched to InP substrates by proper choice of the alloy composition.

We have realized both GaInAsP/InP dh lasers, emitting at 1.2 μm and GaInAs/InP-pin-diodes efficient in the wavelength range 1.0 to 1.6 μm . Fig. 3 shows the lay-out of the laser. The four layer double-heterostructure is grown by liquid phase epitaxy (LPE) in a horizontal graphite slider boat, using super-cooling technique. The wafer consists of an n-type InP confining layer (Sn- or Te- doped, $n=4 \cdot 10^{18} \text{cm}^{-3}$), an undoped GaInAsP active layer ($n=2 \cdot 10^{16} \text{cm}^{-3}$), a p-type InP confining layer (Zn-doped, $p=2 \cdot 5 \cdot 10^{17} \text{cm}^{-3}$) and a p-type GaInAsP cap layer (Zn-doped, $p=2 \cdot 10^{18} \text{cm}^{-3}$) successively grown on an n-type InP substrate (Sn-doped, $n=2 \cdot 10^{18} \text{cm}^{-3}$). The bandgap of the quaternary layers corresponds to 1.2 μm and the lattice mismatch is smaller than .05 %. Close lattice matching between the active layer and the adjacent barrier layers is necessary for efficient device operation. Stripe-geometry lasers have been fabricated by depositing a 120 nm thick SiO_2 layer on the GaInAsP cap layer and etching 15 μm wide grooves into the SiO_2 by standard photolithographic techniques. Contacts have been formed by evaporation In-Zn-Ag-Au and Au/Sn onto the p- and n- type sides, respectively. The wafer is cleaved to a length of about 200 μm . The chip is soldered "up-side-down" with the epitaxial side to the heat sink.

The lasers operate continuously at room temperature at an emission wavelength close to 1.2 μm . Fig. 4 shows the light-current characteristic from one side of a cw-operated laser at three different temperatures (numerical aperture is .5). The laser threshold is 180 mA and the differential quantum efficiency is 22 % per face. For the emission of 4 mW optical power from one face an injection current of 200 mA is required. The lowest value of threshold current density obtained for room temperature pulsed operation of broad-contact GaInAsP/InP dh laser is 1.4 kA/cm². The cavity length of this laser is 280 μm , the stripe width 120 μm and the active layer thickness 0.3 μm . This means a reduced threshold current density of 4.6 kA/cm² μm , comparable to the value of GaAlAs/GaAs lasers.

An important factor of the semiconductor lasers for practical use is the temperature dependence of the lasing threshold current. The change in pulsed threshold of the GaInAsP/InP dh lasers with increasing temperature is shown in Fig. 5. Over the range 15 to 70° C the data are well fitted by the expression $I \sim \exp(T/T_0)$ with $T_0=50-70$ K. This value of T_0 is considerable smaller than that of GaInAsP/InP lasers, which means a high rate of threshold current increase with temperature, and which limits the range of cw operation at the high temperature side. This is so far the main difficulty of the GaInAsP/InP lasers. The steeper temperature sensitivity of these lasers may be compensated to some extent however, by the higher thermal conductivity of the InP layers, which is an important factor in cw or high-duty-cycle operation. From Fig. 6 it can be seen, that the laser operates in a number of longitudinal modes. The most intensive mode appears at 1 195 nm and the longitudinal mode separation is 0.6 nm. The far field emission patterns along and perpendicular to the junction plane are shown in Fig. 7. Typical emission beam divergences at half peak intensity are 6° parallel to the junction plane and 45° perpendicular to the junction plane and this beam divergence must be considered when the laser emission is coupled into an optical fibre.

A cross section of the GaInAs/InP pin-diode is shown in Fig. 8. The 5 to 10 μm thick ternary $\text{Ga}_{.47}\text{In}_{.53}\text{As}$ layer is undoped and has a background doping concentration as low as $3 \cdot 10^{15} \text{cm}^{-3}$. The pn-junction is formed later in a closed ampoule by diffusion of zinc. Au/Zn and Au/Sn contact layers are evaporated onto the p- and n- type sides, respectively. Inverse mesa-type structures with 150 μm diameter are fabricated by photolithographic processes. The light signal impinges onto the InP substrate, penetrates this without remarkable attenuation and is absorbed in GaInAs within the depletion region. The SiO_2 layer reduces the reflection losses, yet it is not optimized in this respect. The diodes have a high external quantum efficiency (Fig. 9), even at a low reverse bias voltage of -3 V. The quantum efficiency is higher 60 % in the whole spectral range from 960 to 1640 nm with a 1200 nm value of 65 %. Hence, this diode can also be used in optical receivers for wavelengths around 1300 and 1550 nm, comprising the whole low loss wavelength range of silica fibres. Capacitance and dark current of the diode in dependence of bias voltage are shown in Fig. 10. The capacitance decreases from 3 pF (at zero bias voltage) to 1.4 pF at -5 V; at this bias the dark current is 30 nA. From the response of a GaInAs/InP diode to a 1200 nm laser light signal (Fig. 11), measured at a bias voltage of -5 V and a load resistance of 50 Ω , rise and fall time of about .5 ns have been evaluated. These response times are RC-limited and they can be reduced further by smaller capacitance and/or series resistance.

4.2 System Characteristics

For a simple interface to usual PCM test equipment and to a standardized PCM-480 system the optical transmission system has to be terminated at both sides by an HDB3-to-binary code converter as shown in Fig. 12. The binary bit-stream at the transmit side is scrambled into a randomized bit sequence by a 7-stage shift register with fixed feedback, in order to reduce the loading of the laser diode by an all "ones" sequence and to facilitate the clock recovery at the receiver side. At the receiver side the bit stream is descrambled in the inverse shift register. Code conversion, scrambling and descrambling, as well as clock recovery are well known techniques and do not specifically apply to optical transmission.

The GaInAs/InP dh laser is return-to-zero operated at 34 Mbit/s with a duty cycle of 1:3. The optical output power is backlight controlled by a GaInAs/InP pin-photodiode. The fibres used are secondary

coated graded-index fibres with a core diameter of 50 μm . The total length of 36 km consists of seven arc-fused individual pieces. The fibre ends are joined to the transmitter and receiver by the double-eccentric ball cage connectors. Total link loss including splices and connectors is 35.3 dB. The optical receiver is a transimpedance amplifier with a GaInAs/InP pin-diode. A bit-error-rate (BER) of 10^{-9} is achieved with a minimum optical average power of -41.7 dBm. The signal power budget of the system is given in Table I.

For comparison the power budget of a 34 Mbit/s-system at 850 nm with comparable effort (except an APD instead of a pin-diode) is listed. Requiring the same system margin, the repeater spacing of the 1200 nm system is 2.5 times longer than for 850 nm, though using an APD. The pulse dispersion in the graded-index fibres of our system is very small (3.5 ns for the total fibre length). This allows to transmit also 140 Mbit/s over the distance of 30 km.

5. TRANSMISSION SYSTEM AT 1550 NM WAVELENGTH

Fiber systems with this wavelength may have a greater potential in terms of repeater spacings. However, at the moment the use of this wavelength range is restricted mainly by the following problems:

- i) development of required light sources is less advanced as in the case of 1200/1300 nm and wafer growth is more difficult
- ii) material dispersion of low loss fibres is zero at wavelengths around 1300 nm; so far shift of zero dispersion to 1550 nm is always coupled with an increase of fibre losses.

But as the problems appear to be solvable within the next years, this wavelength range seems to be very promising for optical links with extremely wide repeater spacings.

6. CONCLUSION

Optical transmission system, operating at 850 nm have already proven reliability in communication systems carrying actual traffic over repeater spacings of at least nine km. Experimental systems for 1200 nm transmission wavelength have demonstrated the even much bigger potential in terms of repeater spacings and bandwidth and will certainly dominate if the lasers and detectors have reached the expected high performance.

REFERENCES

- 1.) U. Zwick, W. Auer, I. Riegl, H. Haupt, W. Heitmann
Electr. Lett., Vol. 15, p. 159 (1979)
- 2.) E. Adler, H. Haupt, W. Zschunke
Fourth European Conf. on Optical Communication, Genova, Italy, Sept. 1978
- 3.) H. Melchior and W.T. Lynch
IEEE Trans. Electron Devices ED-13, 829 (1966)
- 4.) H. Ando, H. Kanbe, T. Kumura, T. Yamaoka, T. Kaneda
IEEE J. of Quantum Electronics QE-14, 804 (1978)
- 5.) J.J. Hsieh, J. A. Rossi, J.P. Donnelly
Appl. Phys. Lett. 28, 709 (1976)
- 6.) C.E. Hurwitz and J.J. Hsieh
Appl. Phys. Lett. 32, 487 (1978)

TABLE I: Signal power budget for 34 Mbit/s systems

- a) our 1200 nm experimental system (GaInAsP/InP laser and GaInAs/InP pin-diode)
- b) an 850 nm system (GaAlAs/GaAs laser and Si - APD)

Transmission Wavelength:	a) 1200 nm		b) 850 nm	
Optical Power of Laser (CW):	4 mW	6 dBm	5 mW	7 dBm
"0" and "1" Equally Occuring:	3 dB		3 dB	
Duty Cycle 1:3:	4.8 dB		4.8 dB	
Coupling Loss Laser-Fibre (measured with 2 km reference fibre):	2.7 dB		2.7 dB	
Mean Power Launched into Fibre		- 4.5 dBm		- 3.5 dBm
Fibre Cable Loss:				
36.1 km $\bar{\Delta}$ 0.89 dB/km:	32.2 dB		14.2 km $\bar{\Delta}$ 3.2 dB/km =	45.4 dB
Connector Loss: 2 x 0.75 dB:	1.5 dB		2 x 0.75 dB =	1.5 dB
Splice Losses: 8 x 0.2 dB:	1.6 dB		4 x 0.2 dB =	0.8 dB
Total Link Losses:	35.3 dB			47.7 dB
Coupling Loss Fibre-Detector:	1.0 dB			1.0 dB
Mean Power Incident upon Detector:		- 40.8 dBm		- 52.2 dBm
Minimum Power Receiver Sensitivity (BER= 10^{-9}):		- 41.7 dBm		- 53.0 dBm
System Margin:		0.9 dB		0.8 dB

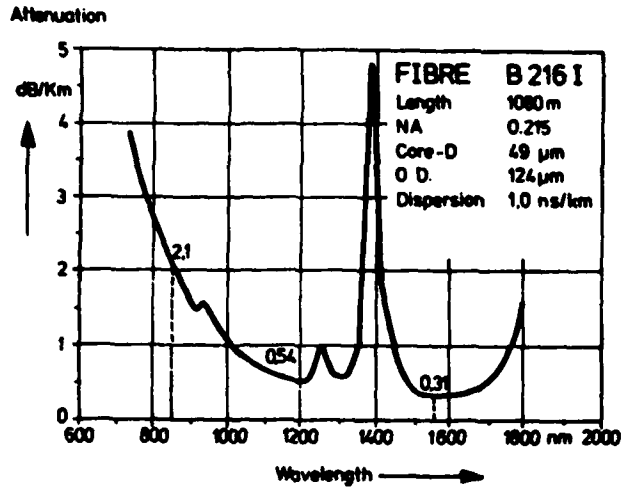


Fig. 1: Spectral attenuation curve of a graded-index fibre

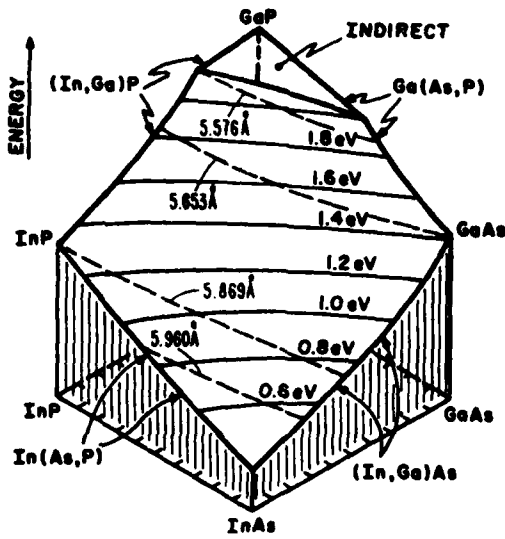


Fig. 2: Energy bandgap composition for (Ga,In)(As,P) system (after Nuese)

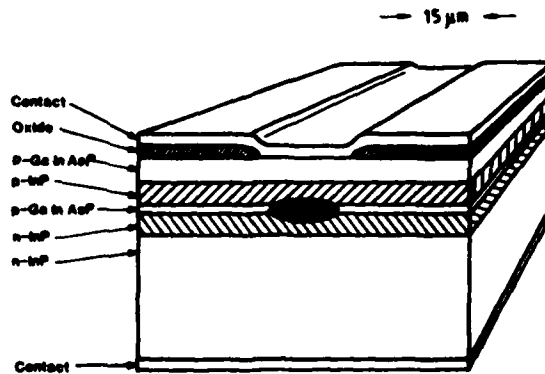


Fig. 3: GaInAsP/MP oxide-defined stripe geometry laser

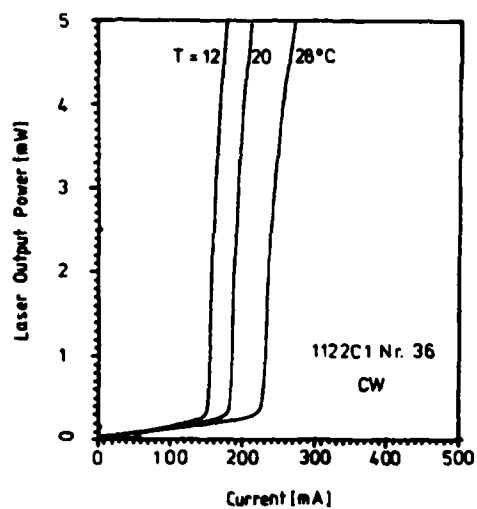


Fig. 4: Light-current characteristics for a GaInAsP/InP dh laser (cw operation) as a function of temperature

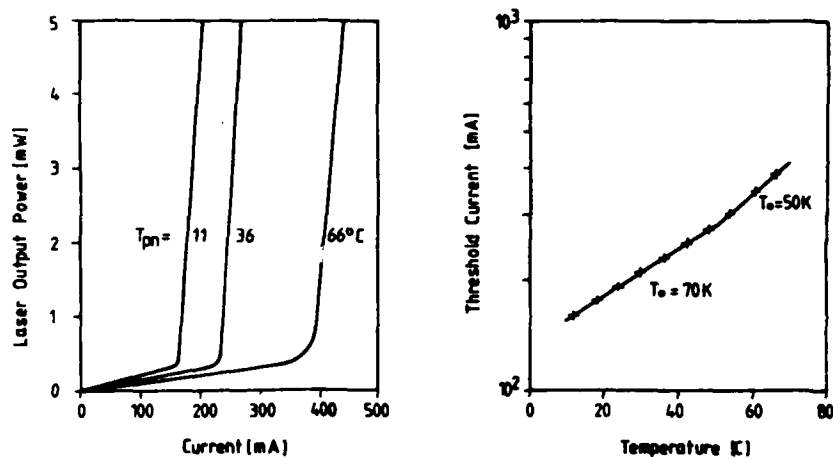


Fig. 5: Temperature dependence of threshold current for a GaInAsP/InP dh laser

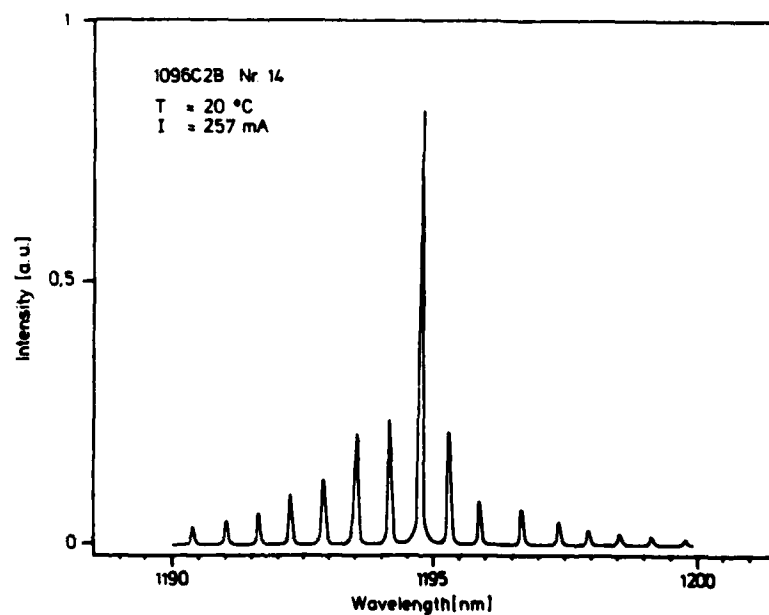


Fig. 6: Emission spectra for a GaInAsP/InP dh laser

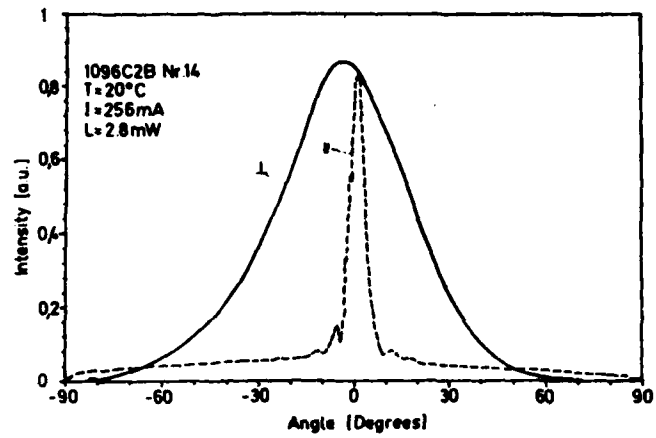


Fig. 7: Far-field patterns of a stripe-geometry GaInAsP/InP diode laser

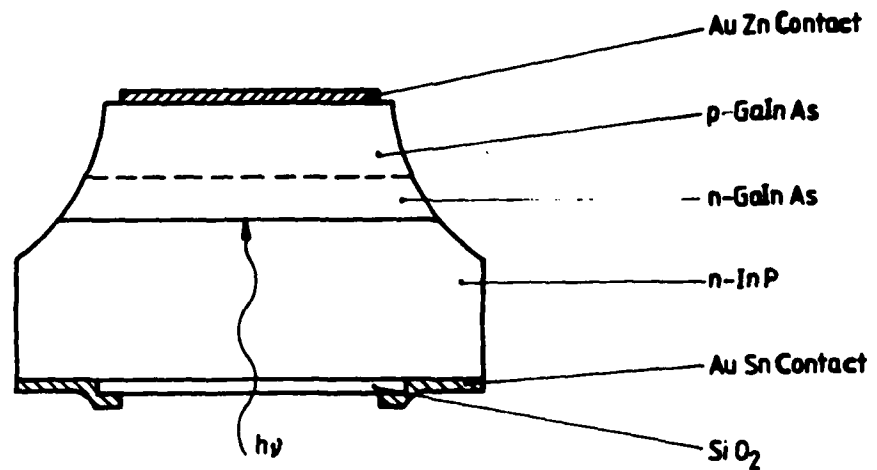


Fig. 8: Cross section of a GaInAs/InP mesa-diode

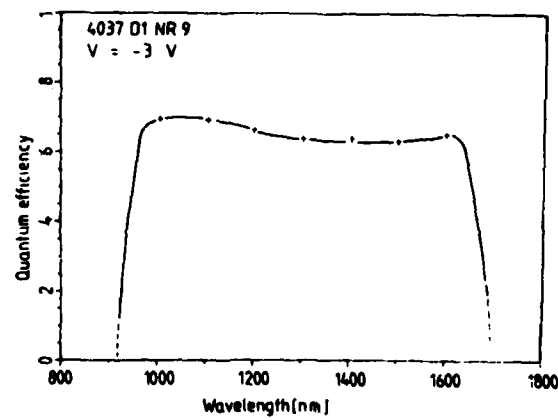


Fig. 9: Quantum efficiency of a GaInAs/InP mesa-diode

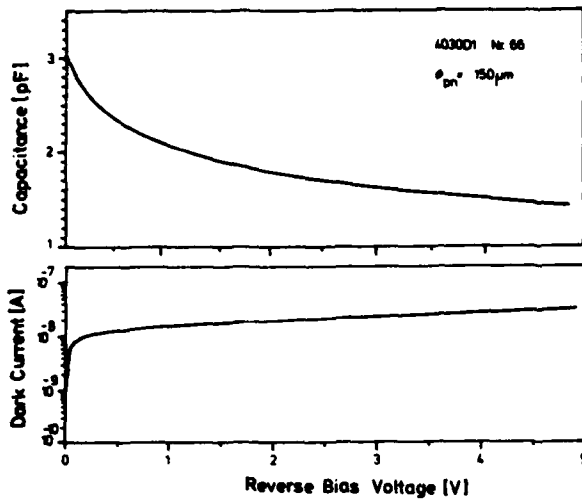


Fig. 10: Capacitance and dark current of a GaInAs/InP mesa-diode as a function of bias voltage

Fig. 11: Pulse response to a 1.2 μm laser beam

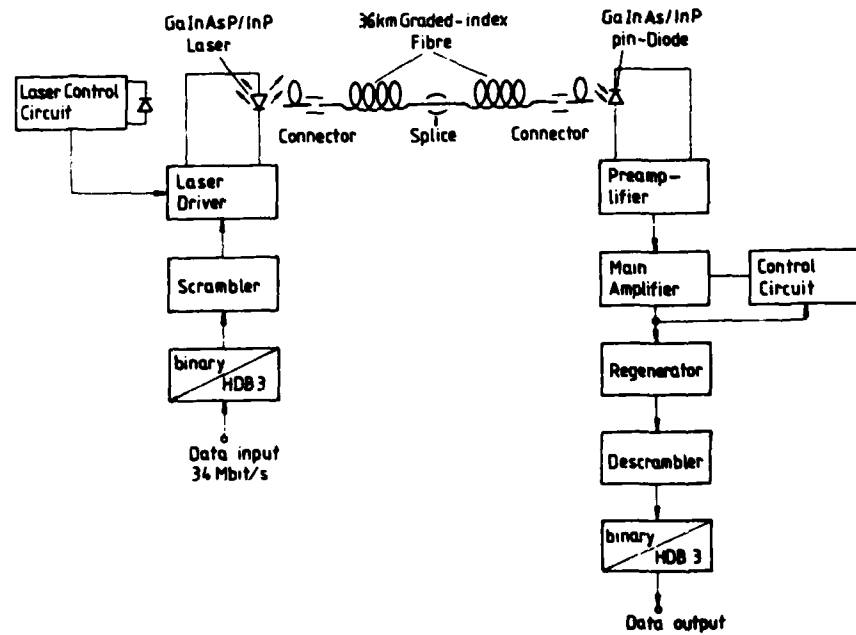
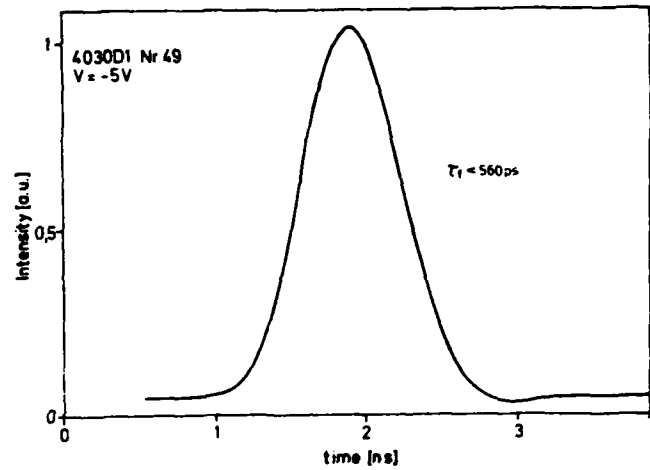


Fig. 12: 34 Mbit/s optical fibre transmission experiment with 36 km long repeater spacing

SUMMARY OF SESSION IV

NOVEL COMMUNICATION TECHNIQUES AND DEVICES

by
Matthew B. White, Ph.D., Chairman

There are essentially four distinct blue-green laser approaches that are presently being actively pursued in the US for various applications.

The frequency-doubled Nd:YAG laser is the only source of intense green radiation that is sufficiently well developed to be suitable for near term underwater systems applications that require highly reliable components. Present state-of-the-art frequency-doubled Nd:YAG lasers are capable of producing on the order of a joule per pulse of green output at a ten hertz pulse repetition rate. The average power that is achievable by these devices could perhaps be doubled by using clever thermal engineering in conjunction with oscillator-amplifier configurations. However, scaling the average output power per aperture to much above twenty watts will probably require major advances in both laser cavity design and doubling crystal technology.

The discharge pumped mercury bromide dissociation laser and the frequency downshifted xenon chloride excimer laser are, at present, the most vigorously pursued US blue-green laser options. The emphasis placed upon the development of these devices can be principally attributed to their perceived ultimate utility for satellite to underwater communications. There are sizable ongoing DARPA-funded programs in the US to scale both these laser to the one joule per pulse/one hundred hertz levels.

The mercury bromide laser operates directly in the green (near 5100Å) and is tunable over at least two hundred Angstroms with a bandwidth of less than one Angstrom. Overall efficiencies of over one percent have been achieved, and two percent appears possible.

The xenon chloride laser, on the other hand, operates in the ultra-violet (at 3510Å) and must therefore be frequency downshifted to the blue-green. This is most easily and efficiently achieved through use of Stimulated Raman Effect in either hot lead vapor or molecular hydrogen. Although the lead vapor approach is somewhat inconvenient from a hardware implementation standpoint, it requires only one Raman Stokes shift to reach the blue-green, and is therefore inherently capable of high efficiency. Over fifty percent UV-to-blue-green down-conversion efficiency has been reported, and sixty-five percent appears possible. The molecular gas approach, on the other hand, does not involve the use of a hot corrosive gas as the Raman medium, but requires three successive Stokes shifts to yield blue-green radiation. Over thirty percent down-conversion efficiency has been achieved using this approach.

The other blue-green radiation source that is being given significant attention in the US is the copper vapor laser (output wavelength = 5100Å). This device has been slowly developed over the last ten years, principally in the US, the Soviet Union, and Israel. A system that produces seventy-five watts of average power has recently been demonstrated in the laboratory, and devices with fifteen watts of average output power are now available commercially in both the US and the Soviet Union. Because highly allowed electronic transitions are involved in its operation, the copper vapor laser possesses a relatively poor energy storage capability, and is therefore not able to produce high output energy per pulse. However, for some applications, this deficiency is more than compensated for by the fact that the copper vapor laser is capable of high pulse repetition rate operation (10-20 kHz) at efficiencies exceeding one percent.

US military applications have been identified that require the unique features of all four of the blue-green laser sources mentioned above. It is therefore likely that US development of these lasers will continue at least at the present level for the next three to five years.

QUESTIONS AND COMMENTS
ON SESSION IV

NOVEL COMMUNICATION TECHNIQUES AND DEVICES

- Paper 27 : Line-of-sight optical communication through low-visibility weather

Dr. M. Carnevale : Is the multiple forward scatter propagation model a satisfactory one ? Which way could it be improved?

Prof. J. H. Shapiro : The multiple-forward-scatter (MFS) model is an ad hoc approach for which there is as yet no rigorous theoretical region of validity. Experiments performed at NOSC and by our group seem to indicate a reasonable agreement between data and MFS theory for the power transfer predictions. We have used a diffusion analysis for the wide-angle plus back-scattered light that the MFS approach treats as absorbed.

This analysis shows that the diffuse light is far weaker than the MFS light in our experiments and in the calculational example given in this paper. More work on validating and/or refining the MFS model would be worthwhile.

- Paper 28 : Mercuric bromide dissociation lasers

Dr. C. Werner : You mentioned in the introduction of your paper that coastal bottom profiling is one of the applications. Do you think that you can use the same kind of laser (Mercury bromide diss. laser) also for this application ? I think you need shorter pulse lengths.

Dr. E. Schimitschek : Coastal bottom profiling is one of the application areas for blue-green lasers, but not necessarily to be done with mercury bromide dissociation lasers. For that application, very short pulses (~ 2.5 nsec) of relatively low energy (~ 1 mJ) are best. Doubled Nd^{3+} : YAG and copper lasers are presently being developed and tested for this purpose.

- Paper 29 : Copper vapor lasers : a review

Mr. W. B. Jones : Would you comment on the beam quality that is obtained with this type laser.

Dr. T. W. Karras : In the far field you can obtain a gaussian spot of near diffraction limited performance by using an unstable resonator. Most experiments use stable resonators however with about 2 - 4 m r divergence.

- Paper 30 : Recent development of high power visible laser sources employing solid state slab - type lasers and non - linear harmonic conversion techniques.

Ir. T. Bakker : $\text{KD}^* \text{P}$, you mentioned to confine the spectrum at the fundamental frequency. How much of the laser output power at this fundamental frequency is lost by this confinement technique ?

Mr. W. B. Jones : Since there is some inhomogeneous broadening of the fluorescence line of Nd^{3+} glass, there is a reduction of oscillator output as the laser line is narrowed with an intracavity filter. Thus there is an optimum linewidth for maximum output of the 0.53 μm beam. Using a $\text{KD}^* \text{P}$ crystal for the second harmonic conversion, the optimum linewidth for the Nd glass laser is approximately 2 Å.

- Paper 32 : Narrow bandpass, large field-of-view optical filters

Mr. W. B. Jones : In the multiplate filters, are the elements AR coated or is there any problem with Fresnel reflections ?

Dr. W. J. Rosenberg : We either AR coat the elements or immerse them in an index matching fluid.

Mr. M. A. Blizard : In several of your viewgraphs the quantity representing the abscissa was missing. You said the curves were identical in nature to antennae patterns (which are of the form $\sum_n A_n \cos(n\phi)$ where $\phi = \pi \frac{d}{\lambda} \cos \theta$ and θ is the angle of incidence). Is ϕ your abscissa quantity ? Is there any ambiguity between λ and θ in your filters ?

Dr. W. J. Rosenberg : The curves are mathematically equivalent to antenna radiation patterns.

The abscissa is reciprocal wavelength $2 \pi \frac{\lambda_0}{\lambda}$ and the curves are on - axis transmission profiles .

Off - axis effects are more complicated than the simple geometric path length changes represented by $\sin \theta$. The actual off - axis effects are a combination of geometric path length changes and the change in aspect angle of the ellipsoidal wavefront of the extraordinary ray. The resulting off - axis effect is given by equations (20) and (21) for narrow field and wide field elements, respectively.

- Paper 33 : Optical receivers for underwater communication

Dr. M. Carnevale : At the present state-of-the-art of the technology is it possible to have to day an air-submarine communication system ? Or some of the components must still be improved.

Mr. J.E. Jackson : Yes it is possible to construct a system that would communicate to a designated submarine or submarines ; but technology does not exist to accomodate the required strategic requirements of scanning the total ocean surfaces every 15 minutes, with the required communication message length.

NONLINEAR ADAPTIVE OPTICS

Concetto R. Giuliano
Hughes Research Laboratories
Malibu, California 90265 USA

ABSTRACT

This paper presents a brief history of the activity in the new field of nonlinear optical phase conjugation. Besides interest in questions surrounding the physics of conjugate wave generation, there is a promise of applying this phenomenon to lasers and laser-related fields such as adaptive optics, laser fusion, laser communications, and power transmission. Several nonlinear optical phenomena are known to exhibit conjugate wave generation, two of the most promising of which are stimulated Brillouin scattering, SBS, and degenerate four-wave mixing, DFWM. The basic physics of these phenomena is discussed briefly and several examples are given of how they might be used for specific applications. A comparison is made of "nonlinear" adaptive optics and "conventional" adaptive optics, the principal advantage of the former being the promise of great simplicity over the latter.

Introduction

In recent years a considerable amount of interest has been generated in a new approach to adaptive optics, nonlinear optical phase conjugation. This approach, which exploits a recently discovered property of several nonlinear optical phenomena for generating conjugate waves, offers the promise of greatly simplifying the currently pursued adaptive optics technologies; the multichannel servos, wavefront sensors, and deformable mirrors employed in conventional systems would be replaced by a single nonlinear optical element.

This paper first discusses what is meant by optical phase conjugation. This is followed by a discussion of the principle for utilizing a nonlinear conjugator in an adaptive optics application. Next we discuss how to make nonlinear conjugators and describe briefly the physics of the two most promising nonlinear phenomena. Then we present several examples of potential applications for optical phase conjugation and finally summarize where we stand by tabulating the wide range of wavelengths and experimental conditions under which nonlinear phase conjugation has been observed.

What Is Phase Conjugation

Before launching into a discussion of the means of achieving optical phase conjugation it may be useful to describe the properties of conjugate fields. Consider for example an optical wave of frequency ω moving in the positive z direction

$$E = \text{Re} [\Psi(x,y,z) \exp(i\omega t)]$$

where $\Psi(x,y,z) = A(x,y) \exp i(-kz + \phi(x,y))$, A real. The phase conjugate of the wave E is defined as

$$\begin{aligned} E(\text{phase conjugate}) &= \text{Re} [\Psi^*(x,y,z) \exp(i\omega t)] \\ &= \text{Re} [A(x,y) \exp i(kz - \phi(x,y)) \exp(i\omega t)] \end{aligned}$$

Note that to get the phase conjugate wave we take the complex conjugate of only the spatial part of E leaving the temporal part unchanged. The conjugate wave corresponds to a wave moving in the $-z$ direction with the phase $\phi(x,y)$ reversed relative to the incident wave. This is equivalent to leaving the spatial part of E unchanged and reversing the sign of t , hence the term "time reversal". We can think of the conjugation process as a kind of reflection process combined with a phase reversal.

An intuitive appreciation of phase conjugation can be realized by comparing reflection from an ordinary mirror to reflection from a "conjugate mirror." This is illustrated in Fig. 1. Here we show a diverging spherical wave striking an ordinary mirror at an angle θ and leaving the mirror at an angle $-\theta$ while continuing to diverge. In contrast the same wave striking the conjugate mirror is converted to a converging wave that retraces the path of the incident wave.

To elaborate a bit further, suppose the wave incident on the conjugator were aberrated - if for example a uniform plane wave were passed through a distorting medium such as a piece of bottle glass or a turbulent atmosphere or a severely strained optical element. Such a wave incident on a conjugator would result in a new wave that would be as severely aberrated as the input wave. However when the output wave passes back through the aberrator it will emerge completely free of distortion instead of twice as distorted as would be the case if the conjugate mirror were replaced with an ordinary mirror. In fact it is this type of demonstration - passing a clean wave through an aberrator, into a conjugator, and back through the aberrator to recover the clean wave again - that is the subject of the first published observations in 1971 and 1972 of optical phase conjugation by researchers in the Soviet Union.

The Use Of Nonlinear Phase Conjugation In Adaptive Optics

The property of phase conjugators to restore severely aberrated waves to their original unaberrated state on double passing the distorting medium suggests a potential application to adaptive optics. However it wasn't until several years after the first observations of phase conjugation that a concept for application to adaptive optics was first described (Wang and Giuliano, 1978). This concept is illustrated in Fig. 2. The goal is to deliver energy from the laser system to the target or receiver while minimizing the deleterious effects of optical path distortions which spread the beam and reduce the energy density at the target. Here

we discuss the elements of the scheme in the context of a laser fusion application in which the energy is to be deposited onto a target pellet assumed to be a small sphere.

The first element is the generation of a reference. This is done, for example, by illuminating the target with a pulsed laser source whose wavelength is within the gain bandwidth of the system's amplifiers. Having been illuminated, the pellet now acts as a source that radiates in all directions. Some of the light from the pellet reference is captured in the aperture of the focusing element (shown in the figure as a lens) and enters the optical system. Note that in a real system that contains many optical elements and possibly a propagation medium the reference wave accumulates phase distortions which can cause its phase-front to deviate substantially from what it would be if it propagated in free space and encountered perfectly figured optics.

The second element of the scheme is amplification of the distorted reference wave followed by the third element, conjugation. After conjugation the wave undergoes further amplification and propagates back through the optical train; this time because of the conjugation process the phase distortions accumulated step-by-step on the first pass are eliminated in a reverse sequence as the wave makes the second pass through the system. The result of this process is the delivery to the target of an intense (if the gain is sufficiently high) pulse of light that is virtually diffraction limited or, more precisely, a pulse whose wavefront incident on the target is a replica of the reference wavefront that radiated from the target in the first place.

The beauty of this approach is that once the reference is created everything else follows automatically. Moreover, for laser fusion systems which consist of multiple arms that irradiate the target from several directions the problem of beam alignment, pointing, and focusing using conventional technology is extremely complex requiring that the target be precisely located within a narrowly defined field of view and requiring sophisticated sensor/servo systems to say nothing of the many tens of optical elements, turning mirrors, etc. within the optical train, each of which is a source of optical distortion. The use of phase conjugators in multiple arm systems has the potential for eliminating this complexity. A single reference pulse illuminating the target to initiate the process can result in precise delivery of energy from a multiple arm system. Pointing and focusing are automatically provided no matter where the pellet is located in the target chamber (within reason); simultaneity of arrival of the intense pulses is assured by making all arms the same length to fairly loose tolerances, i.e., a small fraction of the pulse length (~ 1 nsec or ~ 30 cm).

Similar considerations to those just described apply to the delivery of laser energy to a remote receiver or target through a turbulent atmospheric path. It is often of utmost importance to deliver the energy in a beam that has minimal distortion. "Conventional" adaptive optics approaches utilize schemes that somehow or other measure the atmospheric turbulence along the propagation path and then use deformable mirrors to predistort the outgoing laser beam in a manner to just compensate for the atmospheric distortions to be encountered along the propagation path to the target. Sensing the atmospheric path errors can be accomplished by measuring the phasefront of a reference wave that originates from a bright glint or a beacon at the target. The reference wave from the target glint is received at the aperture of the laser transmitter. This aperture is divided into a number of subapertures for each of which a local wavefront tilt is measured using for example, Hartmann sensors or shearing interferometers. The size of each subaperture is chosen to be consistent with the scale of atmospheric turbulence one expects to encounter for the particular operating conditions. The wavefront tilt information is used to drive actuators on a deformable mirror from which the outgoing laser beam reflects on its way out to the target. Through this sequence of wavefront measurement, error signal generation, and mirror deformation the outgoing wave is transmitted as the phase conjugate of the incoming reference wave.

Here we see the essential contrasting features between conventional adaptive optics and nonlinear adaptive optics. In the conventional case the reference wave is measured and discarded, the results of the measurement used to obtain the necessary settings on the deformable mirror actuators. This is followed by the transmission of a beam from a different source, i.e. the laser, (hopefully one relatively free of distortion) through the optical system. In the nonlinear case, the reference wave is not discarded, nor is it measured in the usual sense of the word. It is amplified, conjugated and retransmitted.

One distinct advantage of the nonlinear over the conventional approach to wavefront correction of laser beams is that compensation will still occur even if the reference wave has substantial transverse amplitude variation, as will be the case in the event of severe turbulence; the conventional approach does not compensate for amplitude variations - only phase variations.

In the conventional adaptive optics approach the reference wave, since it is measured and then discarded, need not be at the same wavelength as the wave that is ultimately transmitted. It can be derived from a completely different source in no way related to the laser. Of course if the reference wave and transmitted wave have vastly different wavelengths the compensation process may suffer because of dispersive effects. Nevertheless this fact represents a potential advantage over the nonlinear approach in which the reference wave must have a wavelength that is compatible with the amplification process and the conjugation process.

Key to the feasibility of nonlinear phase conjugation to adaptive optical systems are the combined amplifier gain and conjugator efficiency, especially for cases that involve weak references. Other critical issues are target range, reference optical cross section, illuminator power (or beacon power), and collecting aperture of the receiver/transmitter. As we will see below certain types of conjugators can have reflectivities well in excess of 100%, a factor that is of great importance from an applications point of view.

How Are Conjugators Made

Up to this point we have assigned the function of phase conjugation to a "black box" labeled ϕ^* . Several nonlinear optical effects have been reported that exhibit phase conjugation. Zel'dovich and coworkers (1972) and Nosach and coworkers (1972) observed wavefront conjugation resulting from the nonlinear

optical phenomenon, stimulated Brillouin scattering, SBS. Stepanov and coworkers (1971) observed conjugation via real-time holography, a phenomenon that is similar to degenerate four-wave mixing, DFWM, a nonlinear phenomenon recognized by Hellwarth (1977) as a conjugation process and subsequently demonstrated by Bloom and Bjorklund (1977). Other nonlinear optical processes that give rise to conjugate wave generation are backward stimulated Raman scattering, SRS, (Zel'dovich, et. al., 1977) and three-wave down conversion (Yariv, 1976, and Avizonis, et. al., 1977).

In the following two sections we will discuss briefly two of the most promising nonlinear phase conjugation phenomena and attempt to give some intuitive physical understanding of how they work.

Stimulated Brillouin Scattering

Stimulated Brillouin scattering, SBS, involves the generation of a coherent acoustic wave through the interaction of an intense optical wave with a nonlinear medium. The mechanism generally acts through electrostriction, that is the tendency of the medium to increase its density where the electric field is large relative to where it is small. Without going into details of the SBS mechanism it is observed that when an intense light wave is allowed to propagate in a nonlinear medium, there results above a certain threshold intensity an intense back-scattered optical wave that is frequency down-shifted by an amount equal to the acoustic frequency. The collinear process, that is, the one that corresponds to counterpropagating incident and scattered waves has the highest gain of all the possible scattering processes and is the only one observed in SBS. In this process the acoustic wave propagates in the same direction as the incident wave and can be thought of as a moving mirror or dielectric stack from which the incident wave reflects to give a Doppler-shifted scattered wave. In fact, the wavelength of the SBS-generated acoustic wave is 1/2 that of the optical wave in the medium and as such is a moving half-wave dielectric stack.

When thinking of SBS in terms of electrostriction we note that the two counterpropagating optical waves interfere to form a moving interference pattern whose speed $v_{\text{fringe pattern}} = (\omega_1 - \omega_2) / (k_1 + k_2)$ is equal to the speed of sound in the medium. In fact it is this condition that allows for the buildup of the acoustic wave and the scattered optical wave at the expense of the incident optical wave.

Analysis by Zel'dovich et. al. (1972) and by Hellwarth (1978) has indicated that under certain conditions the process for which the Brillouin gain is greatest is the one in which the scattered wave is the conjugate of the incident wave. Consequently, an aberrated input wave generates through SBS an equally aberrated acoustic wave with a phase surface that exactly matches (See fig. 3). The nonlinear process can be thought of as creating in the medium a deformable mirror whose surface is just right to reverse the phase of the reflected wave over that of the incident wave so that the reflected wave, when it retraces the original path, has removed from it whatever phase errors were accumulated in the first pass. The idea of time reversal comes from the notion that if one were able to take a moving picture of the incident wave, the complete behavior of the conjugate wave would be obtained by running the movie backwards.

SBS can be made to occur in a highly controlled manner and with efficiencies approaching unity especially under the conditions where it works best as a conjugator, i.e. in multimode optical waveguide configurations. It has been observed at a wide range of optical wavelengths and under both cw and pulsed conditions.

Degenerate Four Wave Mixing

Four-wave mixing is a nonlinear process in which three input waves mix to yield a fourth output wave. The geometry for degenerate four wave mixing DFWM is shown in Fig. 4. The three input waves consist of two counterpropagating pump waves, labeled E_f and E_b (f for forward and b for backward), taken to be plane waves and a probe wave E_p entering at an arbitrary angle to the pumps. Under these conditions the waves couple through the third-order susceptibility, $\chi^{(3)}$, to yield a fourth wave, E_s , which is proportional to the spatial complex conjugate of E_p . The third order polarization that yields the conjugate wave, $P_{NL} = \chi^{(3)} E_f E_b E_p^*$, is proportional to the product of the three input wave amplitudes. More specifically, in isotropic media the nonlinear polarization that yields the conjugate of E_p can be shown to arise from the contribution of three separate terms,

$$P_{NL} = A(\theta) (\vec{E}_f \cdot \vec{E}_p^*) \vec{E}_b + A(\pi - \theta) (\vec{E}_b \cdot \vec{E}_p^*) \vec{E}_f + B(\vec{E}_f \cdot \vec{E}_b) E_p^* \quad (1)$$

The first two terms in equation (1) are responsible for the analogy between DFWM and holography. Each contains a scalar product in parentheses corresponding to the interference between one of the pump waves and the probe wave which is then multiplied by the field of the other pump wave. Thus each term corresponds to the creation of a hologram using one of the pumps and the probe while simultaneously reading it out with the other pump. This is illustrated in a simple way in Fig. 5, where we show the holographic (or dual grating) picture of DFWM. In the figure the formation process and readout process are shown separated for simplicity whereas in fact they take place at the same time. The formation process is shown as the generation of two overlapping grating structures (also shown separately for simplicity) each one consisting of a series of planes whose normals are in the directions $\vec{k}_f - \vec{k}_p$ and $\vec{k}_b - \vec{k}_p$ respectively and whose separations are given by $D = \lambda / (2 \sin \theta / 2)$. We refer to the pattern arising from the interference between forward pump and probe as the large-spaced grating and the one between backward pump and probe as the small spaced grating. The readout process occurs when the backward pump scatters from the large-spaced grating and the forward pump scatters from the small-spaced grating yielding the conjugate wave. Thus one can view the phenomenon described by the first two terms in equation (1) as one in which the refractive index of the nonlinear material is spatially modulated by the interference between pump and probe followed by scattering by the other pump.

The third term in equation (1), $B(\vec{E}_f \cdot \vec{E}_b) E_p^*$, has no holographic analogy. Here the scalar product between \vec{E}_f and \vec{E}_b corresponds to a nonlinear index which has no spatial modulation but which oscillates at a frequency 2ω . The probe wave interacting with this driven coherent excitation at 2ω creates a polarization that results in conjugate wave generation.

The relative sizes of the coefficients A and B in (1) depend strongly on the properties of the nonlinear medium chosen for the four-wave interaction. In particular, if the nonlinear medium has an optical resonance for a single quantum transition at a frequency near ω , the frequency of the experiment, large enhancements (Abrams and Lind, 1978) of the four wave mixing signals arising from the first two terms in (1) are possible over that obtainable from a nonresonant system. For example, if the nonlinear medium consists of an ensemble of 2-level atoms, the near resonant contribution to the nonlinear index will manifest itself as a spatial modulation of the population of the lower state relative to the upper state. The gratings formed by interference between pumps and probe would be "population gratings" i.e., if one were to walk along the direction $\vec{k}_f - \vec{k}_p$ in the nonlinear medium one would notice that the population of atoms in the excited state relative to the ground state would vary sinusoidally with a period $D = \lambda / (2 \sin \theta/2)$. Alternatively, if the medium possesses a pair of energy levels of the same parity such that they may be coupled coherently through an interaction involving 2 quanta, then the third term in (1) may be dominant in contributing to the four wave signal.

Unlike SBS where the conjugate wave intensity cannot exceed the input intensity, DFWM allows for conjugate reflectivities (i.e., $I_{\text{signal}}/I_{\text{probe}}$) in excess of unity and in fact many such examples have been observed experimentally (see below). This fact has practical implications for DFWM.

Another characteristic of DFWM that can have practical impact involves its behavior for waves of different polarization. In fact, increased fundamental understanding of DFWM has been obtained through experiments in which the polarizations of pumps and probe waves have been manipulated to achieve the desired results. (Steel, et. al., 1979).

Note that each of the terms in equation (1) involves the scalar product between two fields multiplied by a third field. We see that a given term will contribute to the nonlinear polarization only if the scalar product term is non-zero, that is only if the fields in the scalar product have polarization components along a common direction. This fact can be exploited to explore the fundamental properties of DFWM. For example by performing an experiment in which E_f and E_p are linearly copolarized while E_b is cross polarized one is examining the contribution of only the first of the three terms in (1) i.e., the large spaced grating. Note that in this example the conjugate wave will emerge with the polarization of the backward pump, E_b , which is cross polarized to the probe wave E_p . Hence, by appropriate selection of co- and cross-polarized combinations one can examine separately the contributions of the different terms in (1) for various nonlinear materials.

Fidelity Of Aberration Correction

One of the questions that comes up in connection with the conjugation process is, how good is it? The answer is, perfect-within the measurement limits that have been employed so far. Qualitative evidence of the ability of a conjugator to correct for optical distortion is depicted in Fig. 6. Here we show far field photographs of a laser beam profile showing a) the unperturbed laser, b) the beam after having passed through a random aberrator (an etched glass plate), and c) the beam profile obtained after the aberrated beam was conjugated and passed back through the etched glass plate. When the detailed profile of the beam in a) is compared with that of c) using a multiple exposure photographic technique it is found that they are identical within experimental measurement error (Lind and Giuliano, 1979). These measurements extend from the center of the beam out into the wings where the intensity is as low as 10^{-5} of the on-axis peak intensity. The most severe random aberration employed in this work is one that degraded the unperturbed diffraction-limited beam to ~ 35 times the diffraction limit. Note, this degradation corresponds to a reduction of on-axis intensity by a factor of about 1000 from the unperturbed to the perturbed condition. These kinds of results have been demonstrated for both SBS and DFWM (Lind and Giuliano, 1979).

It appears that the only limitation to the fidelity of the conjugation process is the effective aperture of the conjugator itself. This is equivalent to saying that the laws of diffraction still hold. In other words if a conjugator having a finite aperture a is located a distance L away from a random phase plate the smallest transverse scale of aberration that will be compensated will be of order $\lambda L/a$ - smaller scale transverse bumps in the phase fronts emanating from the phase plate will not be compensated when the conjugate wave passes back through.

Another way of saying this is that light that comes from small scale regions, smaller than $\lambda L/a$, will diffract by the time it gets to the conjugator such that an appreciable fraction will spill over the collecting aperture. Hence, if you don't collect all the light, you can't conjugate it completely.

Optical Resonators With Conjugate Mirrors

An interesting and potentially valuable application for phase conjugate optics is the use of a phase conjugator as an element in an optical resonator. Fig. 7 shows schematically the essential features of a phase conjugate resonator, an optical resonator in which one (or both) of the conventional mirrors is replaced by a conjugate mirror. Several analytical papers (Lam and Brown, 1980, Bel'dyugin, et. al., 1979, AuYeung, et. al., 1979, Belanger, et. al., 1980) have been written predicting the properties of these devices and a few experimental demonstrations have taken place (Pepper, et. al., 1978, Feinberg and Hellwarth, 1980, Lind and Steel, 1980).

There are several unique properties that phase conjugate resonators are expected to exhibit. One of these is the curious property that such a resonator will not possess longitudinal modes that depend on the cavity length.

An ordinary optical resonator possesses longitudinal modes separated in frequency by $c/2L$, where L is the cavity length. This is a consequence of the boundary condition that after one round trip the wave that corresponds to a mode must constructively interfere with itself. Stated another way, the net accumulated phase after one round trip must be an integral times 2π , i.e. the only waves that "fit" in the resonator are those for which $n\lambda = 2L$, n an integer. In contrast, in a phase conjugate resonator the phase that is

accumulated as the wave propagates from the ordinary mirror to the conjugate mirror is subtracted by the same amount on the way back to the ordinary mirror so that in one round trip the net accumulated phase is always zero. Consequently, a phase conjugate resonator of length L can support any wavelength consistent with the bandwidth of the gain medium and the conjugator itself. Moreover a conjugate resonator oscillating at a particular wavelength will continue to oscillate at that wavelength independent of whether or not the cavity length is varied. This in contrast to an ordinary resonator whose spectral output will exhibit "mode hopping" and frequency drifting if the cavity length is allowed to vary.

Another property of a phase conjugate resonator, one which is highly attractive for application to high power oscillators, is that of compensation for intracavity optical distortion. It can be shown that if one extracts the light from the "ordinary" mirror end of the resonator the transverse phase of the wave will only depend on the figure of the output mirror itself and not on any other sources of distortion within the body of the resonator (Lam and Brown, 1980). This feature has been qualitatively demonstrated in laboratory experiments (Feinberg and Hellwarth, 1980, Lind and Steel, 1980).

Self-Steering Power Transmission Systems

One intriguing potential application of phase conjugation is in the transmission of high power electromagnetic radiation from a space-borne power generating station to a terrestrial site. Many concepts have appeared over the years that involve the conversion of solar energy to electrical energy in a space station followed by a beaming of the energy to earth via coherent optical or microwave power. NASA is also interested in the possibility of direct conversion of solar energy for pumping high power space-borne lasers. One of the concerns about this type of concept is the safety requirement to provide accurate pointing of the multi-megawatt beams from the space station to the earth station with high reliability.

Phase conjugation provides a unique approach to this potential problem as illustrated conceptually in Fig. 8. The space based power generating station consists of a power source, i.e. solar radiation, a coherent oscillator, e.g. a high energy laser, and a four-wave mixing medium. The space-borne high energy laser provides the counterpropagating pumps for the four wave mixing medium which could in one possible implementation be contained within the resonant cavity of the laser itself. Ideally the pump power and nonlinear medium would be chosen so that coupling from the laser resonator is provided through the nonlinear medium via a pilot beam that originates at the terrestrial receiving station. The conjugation process returns the earth-directed output beam along the same path that the input beam is received thus assuring that the only energy delivered to earth is along the pilot beam path. Moreover the energy circulating inside the space borne laser will only be coupled out when the pilot beam is present.

Image Transmission And Delivery Of Special Field Distributions

Optical phase conjugation has application in a number of areas in which one wishes to deliver a "special" field distribution from one point to another. An example of a special field distribution is an image. One of the first such potential applications suggested has to do with the transmission of images along optical fibers (Yariv, 1976). The problem with sending an image along an optical fiber and recovering it at the other end is that modal dispersion in the fiber causes a scrambling of spatial information which can seriously degrade the image. If one could send an image through a length of fiber, then into a conjugator, and finally through another fiber identical to the first it can be easily shown that the effects of modal dispersion would be undone by the insertion of the conjugator at the midpoint and the image could be recovered. The real question here is whether or not it would be possible to find lengths of fiber that are "identical" with respect to their modal dispersion characteristics, an issue yet to be addressed experimentally.

Another area involving imaging and optical phase conjugation is in photolithography. Projection of complex patterns onto photo resist layers is of great technological importance in the microelectronics industry. Projection systems using conventional optical techniques are very complex in their design due to the need for near diffraction-limited low f -number performance.

An approach to a lensless 1:1 projection system employing optical phase conjugation is shown in Fig. 9. The object, in this case a transparency, is illuminated from the back with a laser. The image is formed on the surface of the sample to be exposed after having reflected from the conjugator by way of the beam splitter. Advantages of this type of scheme are that diffraction-limited performance can be achieved without the need for expensive optical components. (The only element that needs to be of high optical quality is the beam-splitter). This approach accomplishes the same goal as in contact photolithography without the need (sometimes highly undesirable) of placing the mask in direct contact with the sample. Projection of high quality images via a scheme similar to that described in Fig. 9 has recently been demonstrated (Levenson, 1980).

A variation on the photolithography application is one in which it is important to deliver a special field distribution to a target plane at intensities that are substantially higher than could be used to illuminate a mask or transparency without causing damage. This scheme is shown in Fig. 10. Here the mask is illuminated using a low power beam. This is amplified, conjugated, reamplified, and delivered to the target as a high intensity beam having a special field distribution. An experiment demonstrating this sort of approach has been reported recently (Pilipetskii, et. al., 1978). This type of scheme would be applicable to situations such as laser annealing in which one wished to irradiate specific areas on the sample and not others. Another potential use would be in laser fusion if it were deemed important to illuminate the target pellet with other than a quasiuniform illumination function.

Pump Manipulation in DFWM

Till this point the applications we have discussed are essentially independent of the type of conjugator employed. We will now discuss examples of applications that are unique to DFWM. Four wave mixing

is more complicated experimentally than SBS because it requires the use of auxiliary pump waves. However for this reason it offers a greater flexibility in that the pump parameters can be purposely modified to yield an output wave which in addition to being the spatial conjugate of the input wave has some other desirable property that one may exploit for a specific application. We will give examples in the following.

Pointing Control by Pump "Misalignment"

Take the laser fusion example illustrated in Fig. 2. Suppose the target were moving transverse to the direction of the beam at a speed sufficiently large that it will have moved an appreciable fraction of a beam diameter in the time it takes light to travel from the target to the conjugator and back to the target again. In this case, the goal of delivering the laser energy to the target will not be met unless it is possible to override the tendency of a true conjugator to produce a retro beam. We can deviate from the precise retro behavior by intentionally misaligning the pumps from the counterpropagating geometry. The degree to which the direction of the conjugate wave deviates from the reference wave as the pumps are misaligned can be calculated in a straight-forward manner from the phase matching conditions and is a function of the pump misalignment angle and the pump-probe angle. The conjugate wave reflectivity drops off as the pumps are misaligned but only a few percent for misalignments of the order of a few milliradians (Lind and O'Meara, 1980).

Thus by controlling the precise propagation direction of the pump waves it is possible to control the direction of the conjugate wave. Of course it is important to remember that compensation for optical path errors begins to degrade if the conjugate wave is not allowed to exactly retrace the path taken by the reference wave. The extent to which this happens depends upon the detailed spatial structure of the propagation path errors and will ultimately limit the amount of point ahead that can be tolerated in an adaptive optical system.

Pump Polarization Manipulation

As discussed earlier it is possible to generate a conjugate wave whose polarization is orthogonal to that of the reference wave. This fact allows the physical separation of the two waves through the use of polarization splitters opening the door for a variety of applications. One such application is the re-pointing of the conjugate wave away from the retrodirection or possible refocusing to different a plane than that from which the reference originates. This concept is shown schematically in Fig. 11.

Another application that takes advantage of polarization separation is shown in Fig. 12. Here we illustrate a concept for a high power-high brightness laser (Hon, 1980) consisting of an oscillator whose output is spatially filtered, an amplifier or amplifier chain that is double passed, and a conjugator that rotates the optical polarization (i.e. a four wave mixer with cross polarized pumps as shown). Because the conjugation occurs between the first and second pass of the amplifier the optical distortions in the amplifier chain are compensated: the polarization rotation allows efficient coupling of the energy through the polarization splitter while minimizing feedback into the oscillator.

As in all the other applications described in this paper this concept requires that the optical distortions experienced on the first pass through the amplifier are the same as those on the second pass. To the extent that this is true the aberration compensation will be perfect.

Pump Temporal Modulation

Another application using four-wave mixing in a similar manner to that just described is in the area of covert optical communications. The application here is one in which it is necessary to impart information to one of a number of remotely located mobile receiver sites from an airborne or space-borne platform without broadcasting over a wide area. Here again the four wave mixer is situated in the transmitter location and the receiver sites are equipped with interrogating lasers. See Fig. 13. At prearranged times the interrogators illuminate the remotely located transmitter using their interrogating lasers tuned to a predetermined operating frequency. For the example considered here the interrogating beam and one of the pump beams is taken to be cw and the other pump is modulated in an appropriate fashion. The information is transmitted as a modulated conjugate wave back to the interrogation site. In this way the information is communicated only to those sites that possess the proper interrogation capability. There is the additional advantage that the total power required to operate the transmitter is potentially many orders of magnitude smaller than that required for a broadcasting system.

Several other pump parameters can be varied with potentially interesting results. The imposition of phase variations on the pump waves results in a transfer to the signal wave and has the potential for imposing focus or other phase information on the conjugate wave which could be important for certain adaptive optics applications.

Whats Been Done

Lets conclude this paper with a brief summary of where we stand after these relatively few years in this young field. Most of the fundamental physical understanding of the physics of optical phase conjugation is well in hand. Many predictions of the details of DFWM have been experimentally confirmed with good agreement; deviations from theoretical predictions are understood at least qualitatively. A large number of demonstrations have been made both under pulsed and cw conditions, over a wide range of wavelengths and for many different materials. Table I gives a feeling for this. Here we show wavelength, type of laser employed, laser operating conditions (pulsed or cw), type of nonlinear interaction, nonlinear material, and pertinent comments (percent reflectivities, power densities, conjugator longitudinal dimensions) along with references. Note that there have been a number of impressively high reflectivities observed at modest power densities in samples of modest dimensions.

Table I

9392-71A1

WAVELENGTH	LASER	PULSED OR CW	NONLINEAR INTERACTION	NONLINEAR MEDIUM	COMMENTS	REFERENCE
10 μm	CO ₂	PULSED	DFWM DFWM DFWM DFWM	SF ₆ HgCdTe CO ₂ (INVERTED) Ge KCl: R ₂ O ₄	37%, 200 kW/cm ² , 2 cm 10%, 100 kW/cm ² , 0.5 mm 0.5% 26%, 10 MW/cm ² , 15 cm NARROW BAND RESPONSE	(LIND, et al., 1979) (JAIN AND STEEL, 1980) (FISHER AND FELDMAN, 1979) (BERGMANN, et al., 1978) (WATKINS, et al., 1980)
3.8 μm	DF	PULSED	DFWM	Ge		(DE PATIE AND HAUEISEN, 1980)
1.06 μm	Nd: YAG	PULSED	DFWM SBS DFWM 3 WM DFWM	Si CS ₂ , CH ₄ Nd: YAG Li FORMATE BDN (DYE)	180%, 1 mm, 6 MW/cm ² 10 - 90% ~0.5% POOR CORRECTION 600%	(JAIN, et al., 1979) (HON, 1980) (TOMITA, 1979) (AVIZONIS, et al., 1977) (MOSES AND WU, 1980)
0.69 μm	RUBY	PULSED	SBS SBS DFWM DFWM DFWM	CS ₂ CH ₄ CRYPTOCYANINE CdS CdSe GLASS CS ₂	10 - 90% 30% (PRELIM) ~5% >100%, 40 cm	(NOSACH, et al., 1972) (ZEL DOVICH, et al., 1972) (LIND AND JAIN, 1979) (LIND AND JAIN, 1979) (PEPPER, et al., 1978)
5890Å	DYE	CW PULSED	DFWM DFWM	Na Na	40%, NARROW BAND 10%, NARROW BAND	(LIND AND STEEL, 1980) (BLOOM, et al., 1978)
5320Å	DOUBLED Nd: YAG	PULSED	DFWM DFWM DFWM DFWM	CdS, CdSe GLASSES IODINE VAPOR RHODAMINE 6G RHODAMINE B	~30% ~0.1% (PRELIM) >100%, 1 mm ~10% (PRELIM) (ALSO 5850Å)	(LIND AND JAIN, 1979) (LIND AND JAIN, 1979) (LIND, 1980) (LIND, 1980)
5100Å	DYE	PULSED	DFWM	CdS, CdSe GLASS	~1% (PRELIM)	(LIND AND JAIN, 1979)
4880Å, 5145Å	Ar ⁺	CW	DFWM DFWM DFWM DFWM	RUBY BSO BaTiO ₃ LIQUID CRYSTALS	~0.2% ~1% SLOW >100% SLOW ~0.1% SLOW	(LIAO AND BLOOM, 1978) (HUIGNARD, et al., 1979) (FEINBERG AND HELLWARTH, 1980) (LIND AND JAIN, 1979)

This is only the beginning; there's a lot yet to be done especially in finding new nonlinear materials tailored for specific applications. The only demonstrations carried out so far have been on a laboratory scale under controlled conditions using well behaved, low average power lasers. No demonstrations have yet been made at high average powers using conjugators that are larger than a centimeter or so in cross section (usually smaller). In addition, the issue of taking a weak input wave, amplifying it and conjugating it with sufficient overall gain that the output wave has adequate energy for practical applications is yet to be addressed experimentally. Other issues include the fidelity of conjugation via DFWM under very high reflectivity conditions, the extent to which other nonlinear phenomena might compete with the desired conjugation process, how a conjugator behaves under extremely weak signal conditions, and how the DFWM reflectivity degrades as the probe: pump ratio approaches unity.

Acknowledgement

This paper was inspired by the existence of an intensive activity in optical phase conjugation at Hughes Research Laboratories. This activity has been highly interactive involving the participation and key contributions of several highly competent scientists and engineers. The author wishes to acknowledge the influence of these individuals. They are R. L. Abrams, W. P. Brown, D. T. Hon, R. K. Jain, M. B. Klein, J. F. Lam, R. C. Lind, R. A. McFarlane, T. R. O'Meara, D. G. Steel, S. M. Wandzura, and V. Wang.

References

- Abrams, R.L. and Lind, R.C., "Degenerate Four-Wave Mixing in Absorbing Media", Opt. Lett. 2, 94 (1978), and Erratum, Opt. Lett. 3, 205 (1978).
- AuYeung, J., Fekete, D., Pepper, D.M. and Yariv, A., "A Theoretical and Experimental Investigation of the Modes of Optical Resonators with Phase Conjugate Mirrors", IEEE J. Quantum Electron. QE-15, 1180, (1979).
- Avizonis, P., Hopf, F.A., Bomberger, W.D., Jacobs, S.F., Tomita, A., and Womack, K.H., "Optical Phase Conjugation in a Lithium Formate Crystal", Appl. Phys. Lett. 31, 435 (1977).
- Belanger, P.A., Hardy, A., and Siegman, A.E., "Resonant Modes of Optical Cavities with Phase Conjugate Mirrors", Appl. Opt. 19, 602 (1980).
- Bel'dygin, I.M., Galushkin, M.G., and Zemskov, E.M., "Properties of Resonators with Wavefront-Reversing Mirrors", Sov. J. Quantum Electron. 9, 20 (1979).
- Bergmann, E.E., Bigio, I.J., Feldman, B.J., and Fisher, R.A., "High-Efficiency Pulsed 10.6 Micron Phase Conjugate Reflection via Degenerate Four-Wave Mixing", Opt. Lett. 3, 82 (1978).
- Bloom, D.M., and Bjorklund, G.C., "Conjugate Wave-Front Generation and Image Reconstruction by Four-Wave Mixing", Appl. Phys. Lett. 31 592 (1977).

- Bloom, D.M., Liao, P.F., and Economou, N.P., "Observation of Amplified Reflection by Degenerate Four-Wave Mixing in Atomic Sodium Vapor", *Opt. Lett.* 2, 58 (1978).
- DePatie, D., and Hauelsen, D., "Multiline Phase Conjugation at 4 Microns in Germanium", *Opt. Lett.* 5, 252 (1980).
- Feinberg, J. and Hellwarth, R.W., "Phase Conjugation Mirror with Continuous Wave Gain", *Opt. Lett.* 5, 519 (1980).
- Fisher, R.A. and Feldman, B.J., "On-Resonant Phase Conjugate Reflection and Amplification at 10.6 Microns in Inverted CO₂", *Opt. Lett.* 4, 140 (1979).
- Hellwarth, R.W., "Generation of Time-Reversed Wavefronts by Nonlinear Refraction", *J. Opt. Soc. Amer.*, 67, 1 (1977).
- Hellwarth, R.W., "Theory of Phase Conjugation by Stimulated Scattering in a Waveguide", *J. Opt. Soc. Amer.* 68, 1050 (1978).
- Hon, D.T., "High Brightness Nd:YAG Laser Using SBS Phase Conjugation", *J. Opt. Soc. Amer.* 70, 635 (1980).
- Huignard, J.P., Herriau, J.P., Aubourg, P., and Spitz, E., "Phase Conjugate Wavefront Generation via Real-Time Holography in Bismuth Silicate Crystals", *Opt. Lett.* 4, 21 (1979).
- Jain, R.K., Klein, M.B., and Lind, R.C., "High Efficiency Degenerate Four-Wave Mixing of 1.06 Micron Radiation in Silicon", *Opt. Lett.* 4, 328 (1979).
- Jain, R.K. and Steel, D.G., "Degenerate Four-Wave Mixing of 10.6 Micron Radiation in HgCdTe", *Appl. Phys. Lett.* 37, 1 (1980).
- Lam, J.F. and Brown, W.P., "Optical Resonators with Phase Conjugate Mirrors", *Opt. Lett.* 5, 61 (1980).
- Levenson, M.D., "High Resolution Imaging by Wavefront Conjugation", *Opt. Lett.* 5, 182 (1980).
- Liao, P.F. and Bloom, D.M., "Continuous-Wave Backward-Wave Generation by Degenerate Four-Wave Mixing in Ruby", *Opt. Lett.* 3, 4 (1978).
- Lind, R.C., Steel, D.G., Klein, M.B., Abrams, R.L., Giuliano, C.R., and Jain, R.K., "Phase Conjugation at 10.6 Microns by Resonantly Enhanced Degenerate Four-Wave Mixing", *Appl. Phys. Lett.* 34, 457 (1979).
- Lind, R.C. and Giuliano, C.R., "Detailed Measurements of the Degree of Phase Conjugation by SBS", Presented at the Conference on Laser Engineering and Applications, Wash. D.C., June, 1979, unpublished work.
- Lind, R.C. and Jain, R.K., "Materials for Phase Conjugation in the Visible", unpublished work, 1979.
- Lind, R.C. and O'Meara, T.R., "Angle Misalignments and Offsets in Four-Wave Mixers", 1980, submitted for publication.
- Lind, R.C. and Steel, D.G., "High Reflectivity Phase Conjugation in Sodium Vapor", 1980, unpublished work.
- Lind, R.C. and Steel, D.G., "Experimental Demonstration of a Phase Conjugate Resonator", 1980, unpublished work.
- Lind, R.C., "Phase Conjugation in Saturable Dyes", 1980, unpublished work.
- Moses, E.I., and Wu, F.Y., "Amplification and Phase Conjugation by Degenerate Four-Wave Mixing in a Saturable Absorber", *Opt. Lett.* 5, 300 (1980).
- Nosach, O.Yu., Popovichev, V.I., Ragul'skii, V.V., and Faizullov, F.S., "Cancellation of Phase Distortions in an Amplifying Medium with a Brillouin Mirror", *Sov. Phys. JETP* 16, 435 (1972).
- Pepper, D.M., Fekete, D., and Yariv, A., "Observation of Amplified Phase Conjugate Reflection and Optical Parametric Oscillation by Degenerate Four-Wave Mixing in a Transparent Medium", *Appl. Phys. Lett.* 33, 41 (1978).
- Pilipetskii, N.F., Popovichev, V.I., and Ragul'skii, "Concentration of Light by Phase-Conjugating Its Wavefront", *JETP Lett.* 27, 585 (1978).
- Steel, D.G., Lind, R.C., Lam, J.F., and Giuliano, C.R., "Polarization-Rotation and Thermal Motion Studies via Resonant Degenerate Four-Wave Mixing", *Appl. Phys. Lett.* 35, 376 (1979).
- Stepanov, B.I., Ivakin, E.V., and Rubanov, A.S., "Recording Two-Dimensional and Three-Dimensional Dynamic Holograms in Bleachable Substances", *Sov. Phys. Doklady* 16, 46 (1971).
- Tomita, A., "Phase Conjugation Using Gain Saturation of a Nd:YAG Laser", *Appl. Phys. Lett.* 34, 463 (1979).
- Wang, V., and Giuliano, C.R., "Correction of Phase Aberrations via Stimulated Brillouin Scattering", *Opt. Lett.* 2, 4 (1978).
- Watkins, D.E., Figueira, J.F., and Thomas, S.J., "Observation of Resonantly Enhanced Degenerate Four-Wave Mixing in Doped Alkali Halides", *Opt. Lett.* 5, 169 (1980).
- Yariv, A., "Three Dimensional Pictorial Transmission in Optical Fibers", *Appl. Phys. Lett.* 28, 88 (1976).
- Zel'dovich, B.Ya., Popovichev, V.I., Ragul'skii, V.V., and Faizullov, F.S., "Connection Between the Wavefronts of the Reflected and Exciting Light in Stimulated Mandel'shtam-Brillouin Scattering", *Sov. Phys. JETP* 15, 109 (1972).
- Zel'dovich, B.Ya., Mel'nikov, N.A., Pilipetskii, N.F., and Ragul'skii, V.V., "Observation of Wavefront Inversion in Stimulated Raman Scattering of Light", *JETP Lett.* 25, 36 (1977).

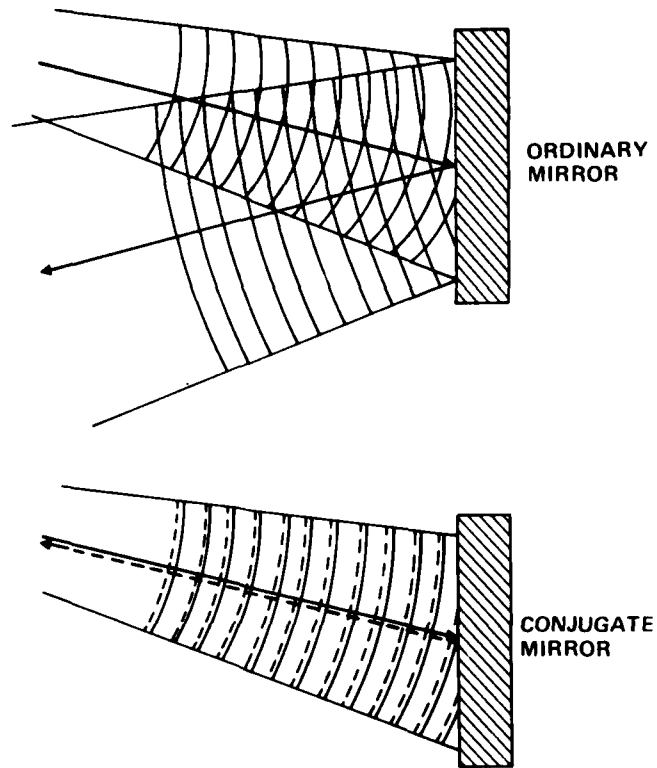


Figure 1. Comparison between an ordinary mirror and a "conjugate" mirror.

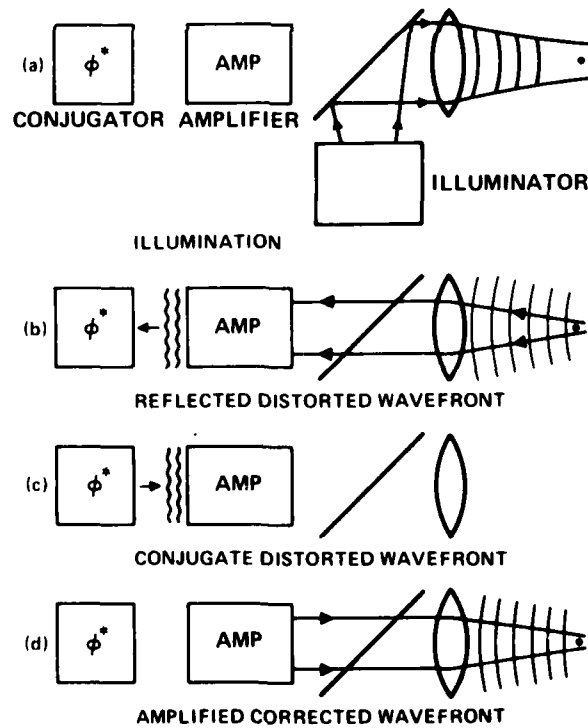


Figure 2. Conceptual scheme for application of optical phase conjugation to adaptive optics for laser fusion.

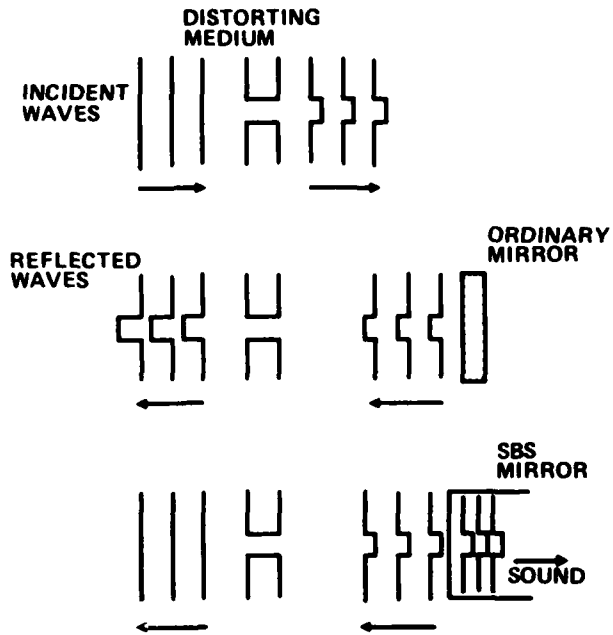


Figure 3. Phase conjugation via SBS. The aberrated optical wave generates an aberrated acoustic wave whose surfaces of constant phase exactly match those for the light.

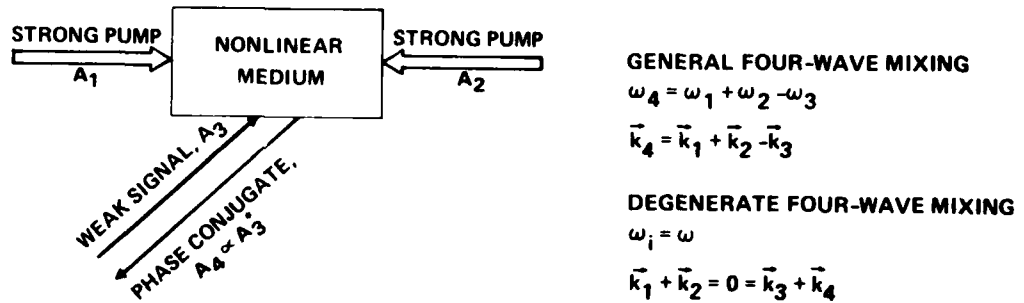


Figure 4. Geometry for degenerate four wave mixing.

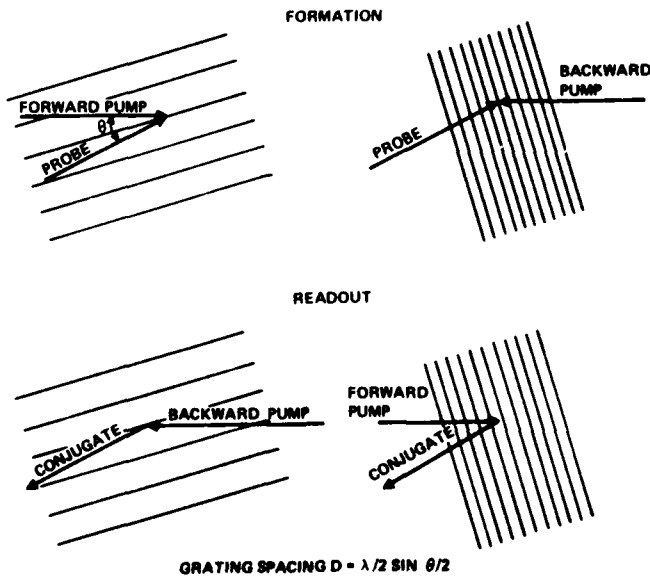


Figure 5. The dual grating picture for DFWM.

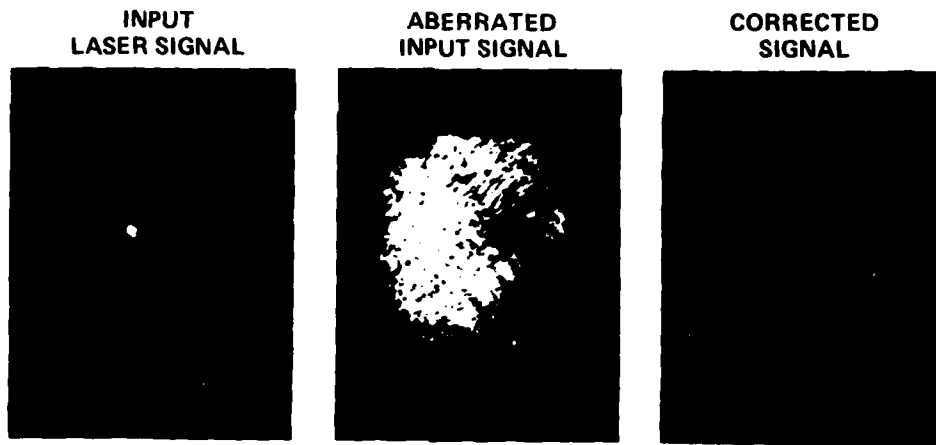


Figure 6. Far-field photographs of laser beam a) unperturbed, b) after passing through random aberrator plate, c) after phase conjugation.

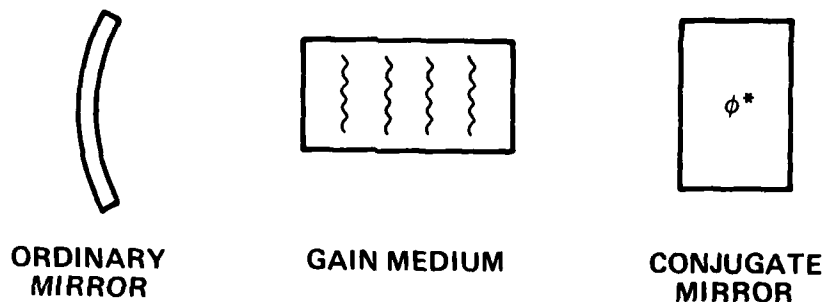


Figure 7. Phase conjugate optical resonator.

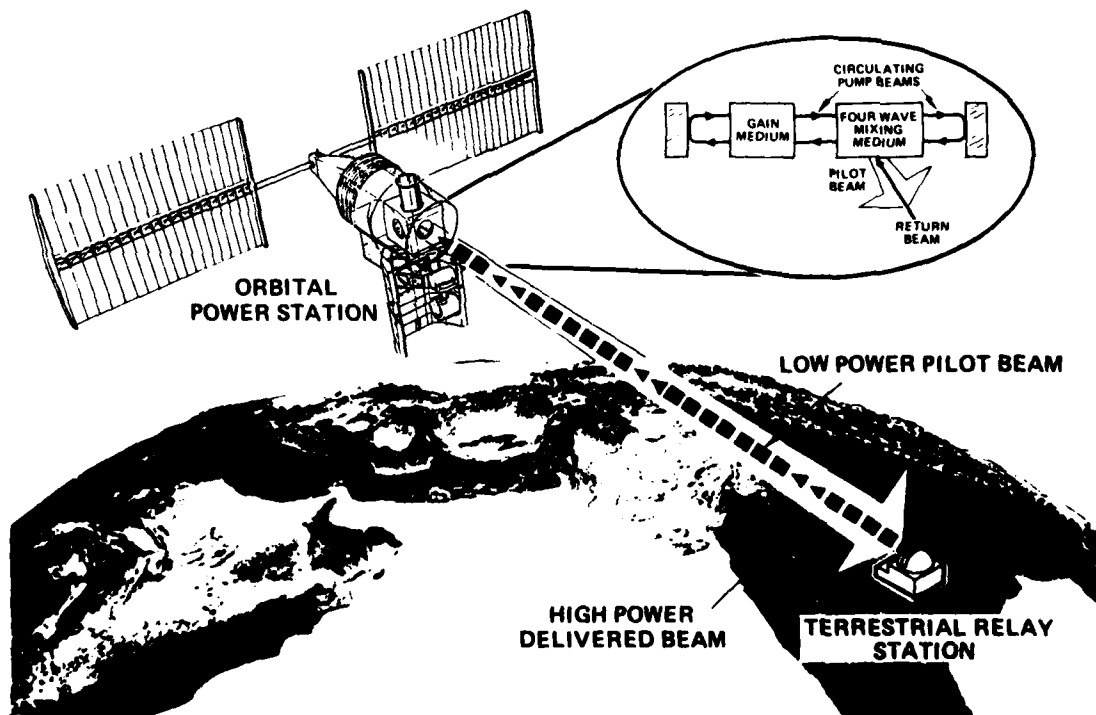


Figure 8. Self-pointing scheme for space-to-earth power transmission.

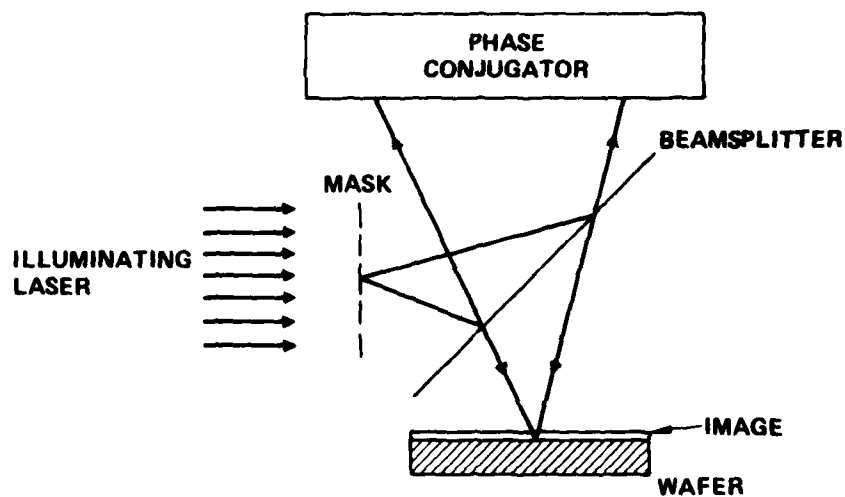


Figure 9. Application of phase conjugation to photolithography.

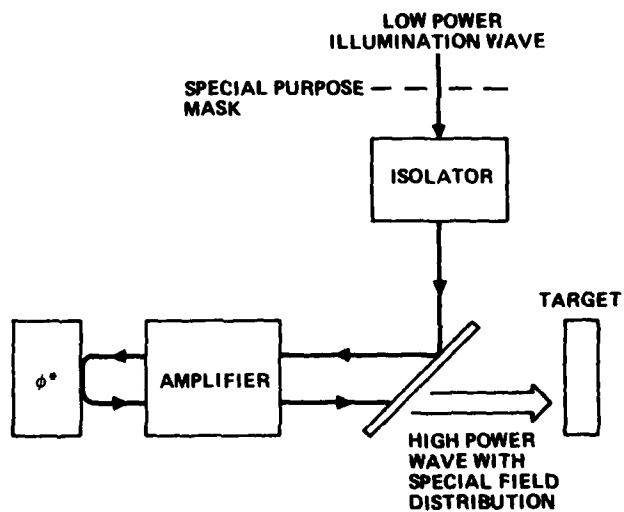


Figure 10. Scheme for delivery of a high power "special field" distribution.

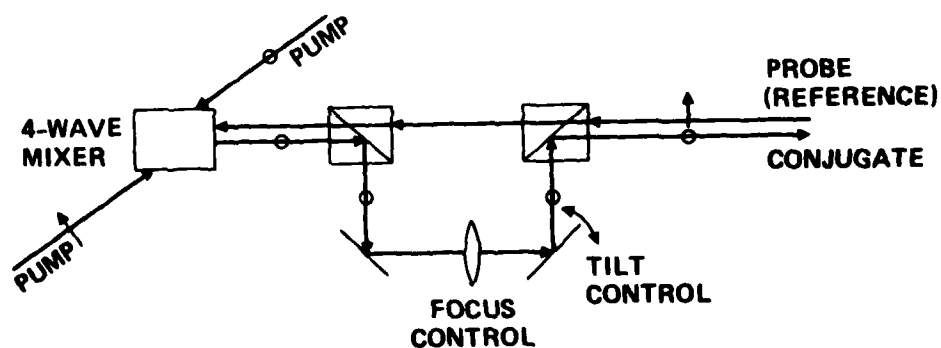


Figure 11. Four wave mixing pump manipulation to accomplish repointing of the conjugate wave.

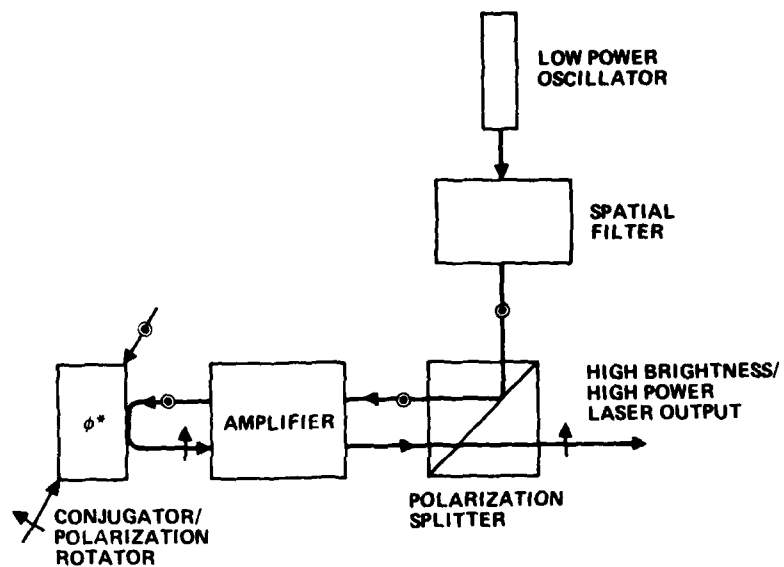


Figure 12. High brightness laser concept using polarization separation properties of DFWM.

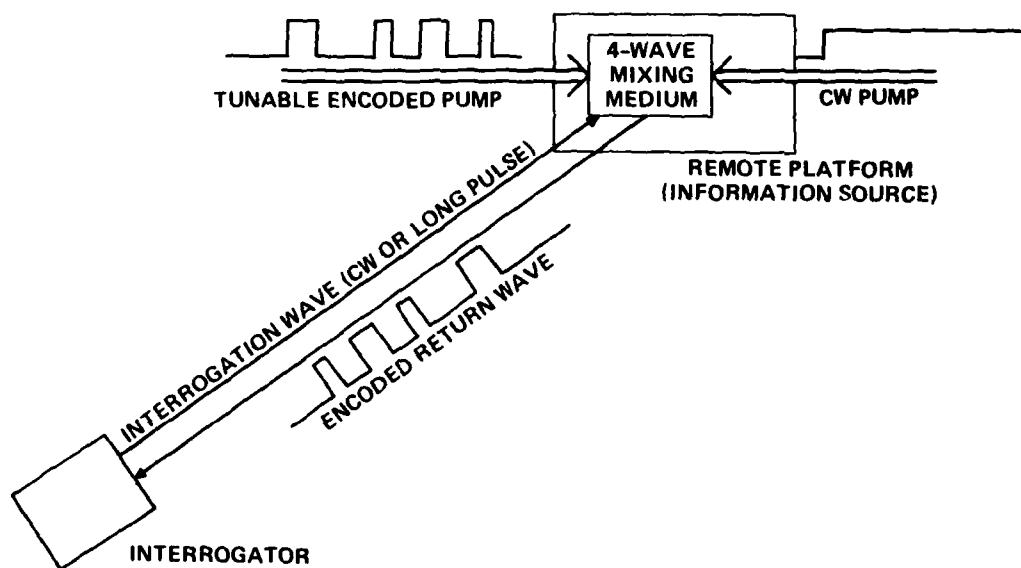


Figure 13. Covert communications concept using modulated pump wave to yield modulated conjugate wave.

PHASE CONJUGATION AND DEGENERATE FOUR WAVE MIXING
IN PHOTOREFRACTIVE $\text{Bi}_{12}\text{SiO}_{20}$ CRYSTAL

J.P. HUIGNARD, J.P. HERRIAU
Laboratoire Central de Recherches, THOMSON-CSF
Domaine de Corbeville-91401 ORSAY (France).

Abstract

Phase conjugate wavefront generation has recently received much attention because of its potential applications to real-time adaptive optics, information processing and imaging through phase disturbing media or optical fibres. The object of the lecture is to demonstrate an alternative approach to phase conjugation by using real-time holography and degenerate four wave mixing in photorefractive $\text{Bi}_{12}\text{SiO}_{20}$ crystals (B.S.O.) (See for a review : STEPANOV, B.I et al 1971 ; HELLWARTH, R.W. 1977 ; YARIV; Y. 1978 ; JAIN, R.K.-KLEIN, M.B. 1979 ; MARKOV et al, 1980 ; HUIGNARD, J.P. et al 1979).

Introduction

BSO crystals are now known to be very attractive materials for dynamic holographic experiments and phase conjugate wavefront generation. Main interesting characteristics result from a "photographic" sensitivity for hologram recording and erasure at Argon laser lines and good optical quality. Specific application of the crystal to real time interferometry, image processing, and imaging capabilities through phase disturbing media will be considered in this conference. The physical process involved for hologram recording are now well established. The crystal is biased with a transverse electric field E_0 in the $\bar{1}10$ crystallographic direction and illuminated with holographic fringes (Incident beams in the $\bar{1}10$ directions) (figure 1-a). The recording medium contains donors and trapping centers. The electrons released from donors centers are driven in the conduction band by a diffusion or external applied field. Trapping of these charges leads to a space charge field which modulates the birefringence through linear electro-optic effect (phase volume hologram recording). The specific properties of these crystals arise from the characteristic "drift" and "diffusion" lengths $\mu \tau E_0$ and $(D\tau)^{1/2}$, which are larger or comparable to usual holographic fringes where μ is charge mobility ; τ is lifetime before trapping, D is diffusion coefficient and E_0 is the applied electric field (GLASS, A.M. 1978 ; HUIGNARD, J.P. MICHERON, F. 1976).

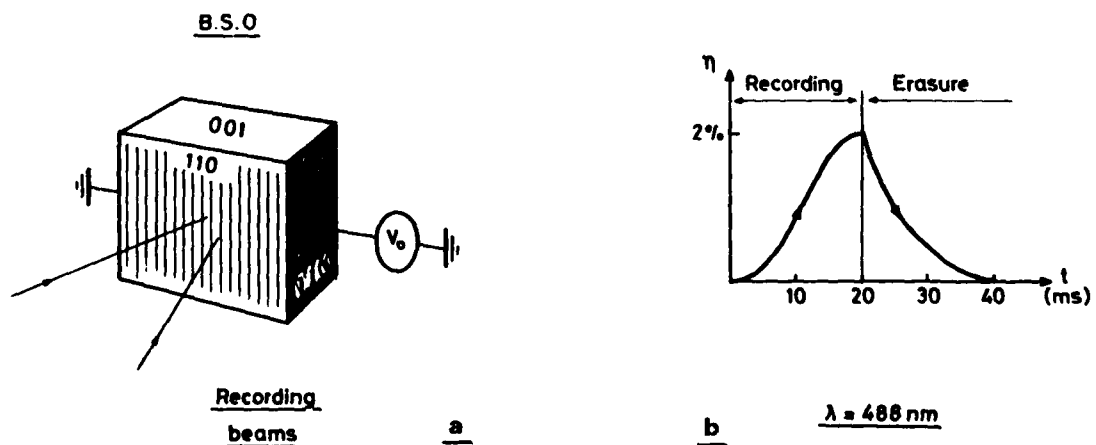


Figure 1 : Crystallographic orientation for holographic recording in BSO crystals. (See Figure 1-a). Typical recording - erasure cycle - Incident power 13 mW.cm^{-2} . $\lambda = 488 \text{ nm}$; Applied Voltage 6 kV.cm^{-1} . Crystal size $10 \times 10 \text{ mm}^2$ - thickness 3 mm (Fig. 1-b)

According to the theoretical models this efficient charge transport provides the ultimate photorefractive sensitivity. Typical incident energy required for elementary grating recording at beam ratio of one is between $100\text{-}300 \mu\text{J.cm}^{-2}$ $\lambda = 488 \text{ nm}$ - or $\lambda = 514 \text{ nm}$ $E_0 = 6 \text{ kV.cm}^{-1}$. BSO crystals actually provides the best known photorefractive sensitivity combined with crystal disponibility in large size area and required optical quality. A typical recording and erasure cycle in the BSO is given in Figure 1-b. Since uniform illumination with the reference beam relaxes the space charge field, a special optical configuration is required to permanently observe the diffracted wavefront. This is achieved by retroreflection of the plane wave reference beam. This mode of readout causes the crystal to diffract in real-time a phase conjugate wavefront of any complex incident object wavefront. (Figure 2).

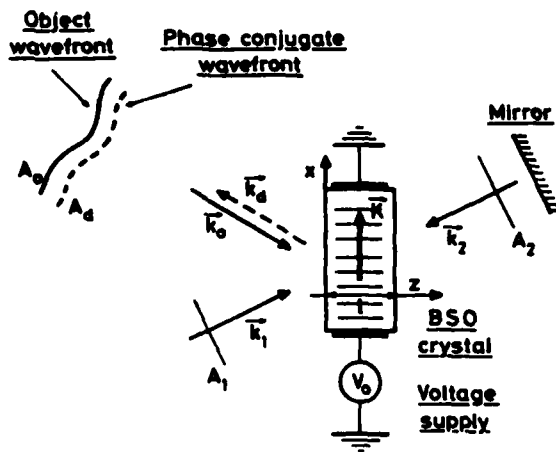


Figure 2 : Phase conjugation and degenerate four wave mixing in BSO crystals. The main properties and applications of the crystal will be reviewed while including numerous experimental results :

1) Imaging through a phase disturbing media

Real-time transposition of the KOEGLNIK imaging technique through a phase disturbing media will be experimentally demonstrated (HUIGNARD J.P. et al, 1979). The incident object-wavefront travels through a strongly inhomogeneous and phase disturbing media : Phase distortions can thus be removed by allowing the time reversed phase conjugate wavefront to travel back through the aberrating medium. Efficiency of the device will be analysed in terms of phase conjugate wavefront reflectivity. (figures 3-4).

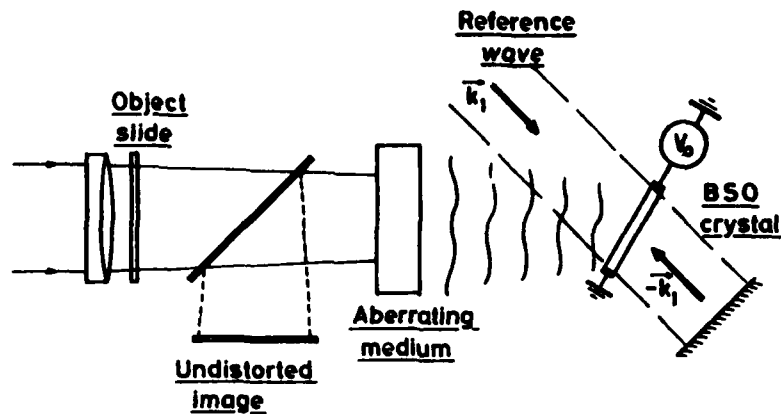


Figure 3 : Application of phase conjugation to imaging through phase disturbing media.

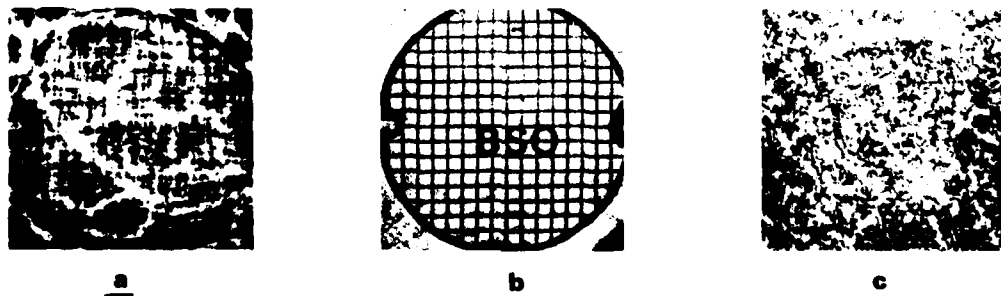


Figure 4 : Reconstructed image with aberrating glass plate : (a) direct imaging through aberrating glass, (b) imaging via real-time phase-conjugate wavefront generation, (c) imaging with a vertical misalignment of the mirror by 1.5 mrad.

2) Spatial frequency dependence of wavefront reflectivity :

Precise knowledge of the spatial frequency response of the recording parameters in BSO constitutes an important feature for imaging applications. (HUIGNARD J.P et al, 1980). According to the respective values of applied field E_0 and fringe spacing Λ "drift" or "diffusion" of the photocarriers affect differently the conjugate wavefront intensity. Experimental results are interpreted on the basis of the recent dynamic theory of Kuktarev et al. which applies to photorefractive crystals with long transport lengths of the photocarriers (KUKHTAREV N. et al, 1979 ; KUKHTAREV N, ODULOV, S, 1980). This theory describes in a dynamic way any possible changes of the fringe pattern along the crystal length due to the intensity distribution between the two writing beams (beam coupling) for both the initial and steady state stage of the hologram formation. From the results presented in Figure 5 it is demonstrated that BSO provides the interesting property that the modulation transfer function can be controlled with external applied field E_0 . Recording by "drift" with $E_0 = 6 \text{ kV.cm}^{-1}$ provides low pass spatial filtering. Through a pure "diffusion" process $E_0 = 0$ high pass filtering is achieved and $E_0 = 2 \text{ kV.cm}^{-1}$, allows a flat spatial frequency response. These specific properties should be important for application of the crystal to real-time image processing.

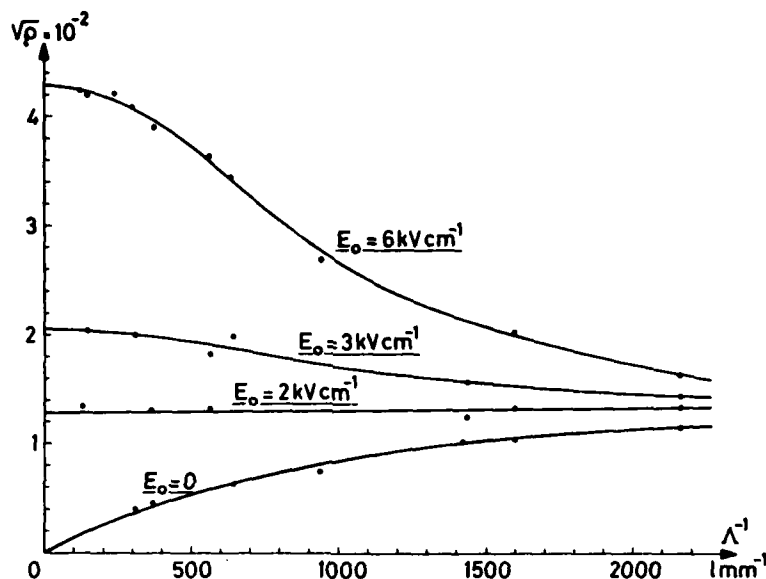


Figure 5 : Spatial frequency response of BSO versus applied electric field.

3) Real-time interferometry :

BSO appears to be particularly suitable for in situ interferometry without any displacement and processing of the recording medium. These experiments take advantages of the high quality reconstructed images and photographic sensitivity for recording and erasure at Argon laser lines. The material is continuously reusable without any fatigue effect and permanent applied field of about 6 kV.cm^{-1} (MARRAKCHI et al, 1980).

Application of degenerate four wave mixing in BSO to mode pattern visualization of a vibrating membrane can be explained as follows. when the object structure considered in Figure 6 is vibrating at frequency F we now obtain a diffracted image I_d on which are superimposed dark fringes corresponding to zero of Bessel function $J_0^2 \left| \frac{4\pi\delta}{\lambda} \right|$; δ = local vibration amplitude.

Following Powell and Stetson theory, this arises when the time constant to build-up the hologram at saturation time is long compared to the vibration period. $T = 1/F$ $t \gg T$ for time average intensity recording in the crystal volume.

For each excitation frequency of the membrane, the so described method permits in a dynamic way a mode pattern visualisation of the vibrating structure. These dynamic properties of the crystal should bring and important improvement for application of coherent optical techniques to industrial non destructive testing.

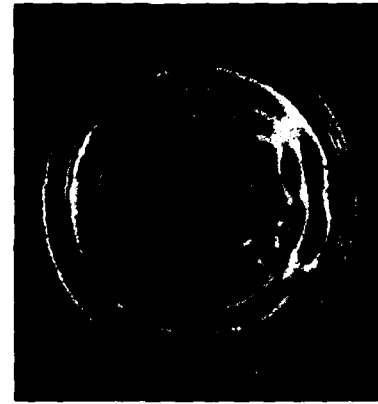
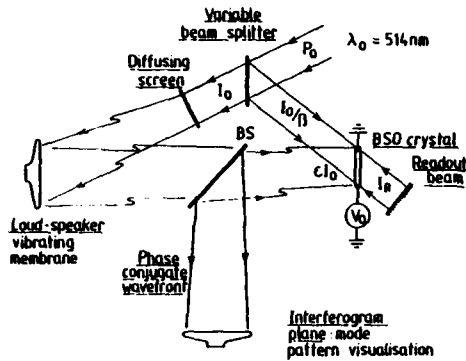


Figure 6 : Application of phase conjugation in BSO to mode pattern visualisation of a diffuse Vibrating Loudspeaker membrane.

4) Degenerate four wave mixing with a pulsed laser

The purpose of this paragraph is to demonstrate temporal response of the crystal on a nanosecond time scale using a frequency doubled Nd, YAG Laser ($\lambda = 532 \text{ nm}$; pulse width $\approx 30 \text{ ns}$) as a writing source. (HERMANN et al, 1981)

The optical configuration used for real-time grating recording and readout is given in Figure 7. The retro-mirror is placed just behind the BSO crystal in order to obtain a negligible optical delay of the readout pulse with respect to the incident writing laser pulse. The laser source is a high quality single transverse and longitudinal mode Nd-YAG Q switched by a dye cell and whose TEM₀₀ operation is obtained by use of a small aperture in the cavity. The output pulse is then frequency doubled in a KD P crystal. A total energy is so available in a 20 ns diffraction limited spot.

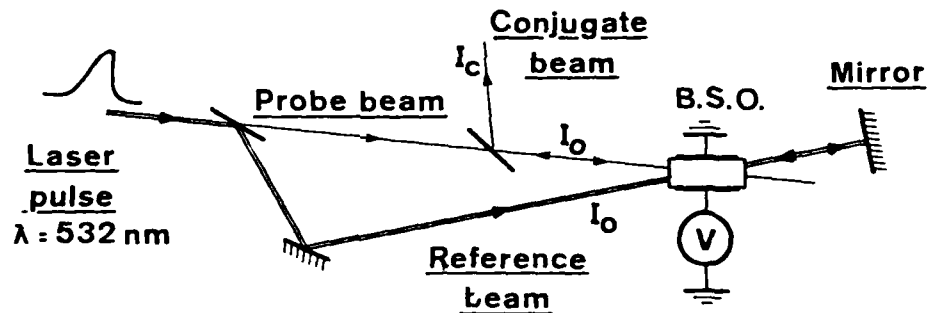


Figure 7 : Four wave mixing in photorefractive BSO crystals with a frequency doubled pulsed YAG laser as writing source. Crystal size : $4 \times 4 \text{ mm}$ - Thickness = 8 mm : fringe spacing $\Lambda = 7 \mu\text{m}$: Applied voltage in the $\parallel 110$ direction : $2,5 \text{ kV}$. Conjugate beam reflectivity $\rho = \frac{I_c}{I_0}$

The beam is expanded to a diameter of 6 mm in order to achieve a good uniformity of crystal illumination on the entrance face (distance between electrodes : 4 mm ; Interaction length of the recording beams : 8 mm). The single mode operation of the laser maintains an optimum fringe contrast inside the crystal volume. Typical experimental results re-drawn from oscilloscope trace of the incident writing beams are given in Fig. 8. Fig. 8a shows the oscilloscope trace of the incident writing pulse, and Fig. 8b is the conjugate image pulse generated by the fourwave mixing set up. As seen on this picture the wavefront reflectivity increases for subsequent shots showing an accumulation of trapped photo-carriers. The conjugate beam reflectivity $\rho = \frac{I_c}{I_0}$ reaches in this experiment a saturation value of the order of 0.1% . From these experiments, the following conclusions can be retained :

- The response time of the BSO can be fast ($< 5 \text{ ns}$) provided that the incident power density on the recording beams is high ($> 10 \text{ kW.cm}^{-2}$ at $\lambda = 532 \text{ nm}$). The corresponding diffraction efficiency is proportional to the square of incident laser intensity before saturation.

- The energy S^{-1} required for elementary grating recording is nearly equivalent for both CW or pulsed experiments $S^{-1} \approx 100-500 \mu\text{J}\cdot\text{m}^{-2}$. Comparable values of saturation efficiency or wave front reflectivity are also obtained for equivalent experimental conditions (fringe spacing $\Lambda = 5 \mu\text{m}$; Applied electric field $E_0 = 6-8 \text{ kV}\cdot\text{cm}^{-1}$; crystal thickness = 8 mm).



Figure 8 : (a) Incident laser pulse. Power density on the crystal : $I_0 = 50 \text{ kW}\cdot\text{cm}^{-2}$ at $\lambda = 532 \text{ nm}$ (Relative units).
(b) Evolution of conjugate beam reflectivity ρ as a function of the number of shots. Saturation occurs for $N = 5$

Conclusion

Real-time holography and degenerate four wave mixing in $\text{Bi}_{12}\text{SiO}_{20}$ crystals provides another way of generating a phase conjugate wavefront. Because of the low energy required to build-up the space charge field at Argon Laser lines and holographic spatial carrier frequencies, the crystal should provide new attractive developments and applications which include real-time interferometry, coherent image processing, optical computing and imaging through all kinds of stationary or moving phase disturbing media. The demonstrated capabilities of nanosecond writing and erasing time constants also suggest applications of the crystal to high speed adaptive optics and coherent optical processing.

References

- GLASS. A.M.
The photorefractive effect.
Opt. Eng. 17, 470, 1978
- HELLWARTH. R.W.
Generation of time reversed wavefronts by non linear refraction.
J. Opt. Soc. Am. 67, 1, 1977
- HERMANN. J.P., HERRIAU. J.P., HUIGNARD. J.P.
Nanosecond four wave mixing and holography in BSO crystals.
To be published
- HUIGNARD. J.P., MICHIRON. F.
High sensitivity read-write holographic storage in $\text{Bi}_{12}\text{SiO}_{20}$ - $\text{Bi}_{12}\text{GeO}_{20}$ crystals.
Appl. Phys. Lett. 29, 591, 1976
- HUIGNARD. J.P., HERRIAU. J.P., AUBOURG. P., SPITZ. E.
Phase conjugate wavefront generation via real-time holography in $\text{Bi}_{12}\text{SiO}_{20}$ crystals.
Opt. Lett. 1, 21, 1979
- HUIGNARD. J.P., HERRIAU. J.P., RIVET. G., GUNTER. P.
Phase conjugation and spatial frequency dependence of wavefront reflectivity in $\text{Bi}_{12}\text{SiO}_{20}$ crystals.
Opt. Lett. 5, 102, 1980
- JAIN. R.K., KLEIN. M.B.
Degenerate four wave mixing near the band-gap of semiconductors.
Appl. Phys. Lett. 35, 454, 1979
- KUKHTAREV. N., ODULOV. S.
Degenerate four wave mixing in LiNbO_3 and LiTaO_3 .
Opt. Comm. 32, 183, 1980
- MARKOV. V., ODULOV. S., SOSKIN. M.
Dynamic holography and optical image processing.
Opt. and Laser techn. 11, 95, 1979
- MARRAKCHI. A., HUIGNARD. J.P., HERRIAU. J.P.
Application of phase conjugation in $\text{Bi}_{12}\text{SiO}_{20}$ crystals to mode pattern visualisation of diffuse vibrating structures.
Opt. Comm. 34, 15, 1980

STEPANOV. B.I., IVAKIN. E.V., RUBANOV. A.S.

Recording two-dimensional and three dimensional dynamic holograms in transparent substances.

Sov. Phys. Dok. 16, 46, 1971.

YARIV. Y.

Phase conjugate optics and real-time holography.

IEEE. J. Q.E. 14, 650, 1978

THEORY OF NONLINEAR PROPAGATION IN MULTIMODE OPTICAL FIBERS

B. Crosignani and P. Di Porto
Fondazione Ugo Bordoni, Istituto Superiore P.T., Roma,
Italy

C.H. Papas
California Institute of Technology, Pasadena, Cal. 91125

SUMMARY

A set of equations which describes pulse propagation in multimode optical fibers in the presence of an intensity-dependent refractive index is derived by taking advantage of the coupled-mode theory usually employed for describing the influence of fiber imperfections on linear propagation. This approach takes into account in a natural way the role of the waveguide structure in terms of the propagation constants and the spatial configurations of the propagating modes and can be applied to the most general refractive index distribution. In particular, the conditions under which envelope soliton transmission in the presence of many modes can take place are discussed. The way in which these conditions are modified by the possible presence of carrier fluctuations is finally considered.

1. INTRODUCTION

The nonlinear response of a dielectric medium includes contributions to the polarization from quadratic, cubic and higher order terms in the electric field. The related nonlinear effects can be most conveniently observed at relatively low powers over the long interaction lengths provided by an optical fiber. This circumstance can also make these processes detrimental for telecommunication fibers, in that they increase signal attenuation and dispersion. Among the effects associated with third-order nonlinearity, stimulated Raman scattering, stimulated Brillouin scattering and self-phase modulation put a limit on the peak power transmissible on a fiber link. In particular, self-phase modulation directly influences dispersion and can become significant at power levels below the critical powers of stimulated Raman and Brillouin scattering, so that it may set the ultimate limit on the pulse power in high capacity single-mode fibers (STOLEN, R.H., 1979). This fact justifies a detailed investigation of pulse propagation in single-mode and multimode optical fibers in the presence of this mechanism alone.

Self-phase modulation is associated with the intensity-dependent self-induced changes of the refractive index resulting from the contribution to the third-order polarizability proportional to the field itself. These variations of the refractive index, proportional to the intensity of the field, give rise to self-focusing (CHIAO, R.Y., GARMIRE, E., and TOWNES, C.H., 1964), an effect usually negligible in fibers where an intrinsic radial confinement is already present, and to phase-modulation of the propagating pulse connected with the phase charges induced by the pulse itself. The corresponding frequency broadening (the leading edge of the pulse is downshifted in frequency and the trailing edge upshifted) gives rise in general to an increase of dispersion and pulse spreading (SHIMIZU, F., 1967), which may limit the information transmissible in a fiber. However, as first pointed out by HASEGAWA and TAPPERT (1973), it is possible, in the presence of anomalous dispersion, to choose the pulse intensity and shape in such a way as to balance exactly the effect of chromatic dispersion broadening the pulse with that of self-phase modulation which tends to shrink it. These stable solutions which propagate as distortion-free pulses are called "bright solitons" and have been recently experimentally observed by MOLLENAUER, STOLEN and GORDON (1980).

In general, self-phase modulation is studied in single-mode fibers (STOLEN, R.H., LIN, C., 1978). In this frame, the influence on soliton transmission of the radial dependence of the refractive index profile and of its eventual longitudinal inhomogeneity has been explicitly taken into account (BENDOW, B., GIANINU, P.D., TZOAR, N., and JAIN, M., 1980), and the effects of the fast intensity fluctuations of the exciting source placed into evidence (CROSIGNANI, B., DI PORTO, P., and PAPAS, C.H., 1980). The first attempt to include the effect of the presence of many modes has been made by HASEGAWA (1980), who addresses himself to the problem of longitudinal self-confinement of optical pulses without explicitly examining the possibility of propagating solitons over a multimode fiber. In a recent paper (CROSIGNANI, B., DI PORTO, P., and PAPAS, C.H., 1981), we have adopted a different method for investigating nonlinear propagation associated with intensity dependent refractive index, based on the extension of the coupled-mode formalism usually employed for describing linear propagation in optical fibers in the presence of irregularities (MARCUSE, D., 1975). This method, which in particular allows to recover in a simple way the results concerning single-mode fibers, furnishes the most natural approach for studying the effect of the presence of more than one mode on nonlinear propagation, as already shown for the case of the two orthogonally polarized states of a single-mode fiber (CROSIGNANI, B., DI PORTO, P., 1981).

In the present paper, we extend the results of ref. 12 to describe nonlinear pulse evolution in multimode fibers. We derive a set of nonlinear differential equations for the mode amplitudes which determine the behavior of the field, including the case where the different modes are excited at different frequencies. This last situation is relevant for obtaining the conditions under which multimode fibers can support solitons. Finally, we examine the influence on soliton transmission of the statistical fluctuations of the source and of the degree of correlation among the various modes.

2. COUPLED-MODE THEORY APPROACH

Let us briefly recall the formalism of coupled-mode theory developed for describing time-dependent propagation in the presence of fiber imperfections (MARCUSE, D., 1975; CROSIGNANI, B., DI PORTO, P., and PAPAS, C.H., 1977). Denoting by E_{ω} and H_{ω} the time-Fourier transforms at (angular) frequency ω of the electric and magnetic field and by $n(x, y, z, \omega)$ the refractive index distribution pertaining to the perturbed fiber, one has to find solutions of the Maxwell's equations

$$\begin{aligned}\nabla \times \underline{H} &= i\omega \epsilon_0 n^2 \underline{E} \\ \nabla \times \underline{E} &= -i\omega \mu_0 \underline{H}\end{aligned}\quad (1)$$

where ϵ_0 and μ_0 are the electric and magnetic permeabilities of vacuum. To this end, \underline{E} and \underline{H} are expressed as linear combinations of the modes $\underline{E}_m(\omega)\exp(-i\beta_m(\omega)z)$ and $\underline{H}_m(\omega)\exp(-i\beta_m(\omega)z)$ pertaining to the ideal (that is, without imperfections) waveguide characterized by a refractive index distribution $n_1(x,y,\omega)$, with z -dependent expansion coefficients. Following this procedure (normal mode expansion technique), one obtains a set of linear coupled differential equations for the expansion coefficients which are equivalent to Maxwell's equations and generate solutions automatically satisfying the boundary conditions. More specifically, if one writes the forward-traveling transverse part of the electric field in the form

$$\underline{E}_T(\underline{r}, z, t) = \sum_m \int_{-\infty}^{+\infty} \underline{E}_{mT}(\underline{r}; \omega) c_m(z; \omega) \exp[i\omega t - i\beta_m(\omega)z] d\omega \quad (2)$$

where $\underline{r}=(x,y)$ indicates the transverse coordinates and

$$\underline{E}_m(\underline{r}; \omega) = \underline{E}_{mT}(\underline{r}; \omega) + \underline{E}_{mz}(\underline{r}; \omega) \quad (3)$$

the expansion coefficients c_m can be shown to obey the set of equations (MARCUSE, D., 1975)

$$\frac{dc_m(z; \omega)}{dz} = \sum_n K_{mn}(z; \omega) \exp\{i[\beta_m(\omega) - \beta_n(\omega)]z\} c_n(z; \omega) \quad , \quad m=1, 2, \dots \quad (4)$$

with

$$K_{mn} = (\omega \epsilon_0 / 4iP) \iint_{-\infty}^{+\infty} (n_1^2 - n^2) \{ \underline{E}_{mT}(\underline{r}; \omega) \cdot \underline{E}_{nT}(\underline{r}; \omega) + (n_1^2/n^2) \underline{E}_{mz}^*(\underline{r}; \omega) \cdot \underline{E}_{nz}(\underline{r}; \omega) \} dx dy \quad (5)$$

and

$$P = (1/2) \iint_{-\infty}^{+\infty} \underline{e}_z \cdot \underline{E}_{mT}(\underline{r}; \omega) \times \underline{H}_{mT}(\underline{r}; \omega) dx dy \quad (6)$$

\underline{e}_z being a unit vector in the positive z -direction. The normalization constant P does not depend on the mode and the transverse parts of \underline{E}_m and \underline{H}_m are assumed to be real, the relative longitudinal parts being then purely imaginary quantities.

The above formalism can be as well applied to describe situations in which the departure of the fiber from ideality is associated with nonlinear effects giving rise to a variation of the refractive index. In our case, one has (CHIAO, R.J., GARMIRE, E., and TOWNES, C.H., 1964)

$$n(\underline{r}, z; \omega) = n_1(\underline{r}, z; \omega) + n_2 |\underline{E}(\underline{r}, z, t)|^2 \quad (7)$$

where \underline{E} is the analytic representation of the electric field and n_2 a nonlinear coefficient approximately independent from ω . The expression of n furnished by Eq.(7) can be inserted in Eq.(1), so that a derivation analogous to that leading to the set of Eqs.(4) still applies, provided that the bandwidth $\delta\omega$ and the average frequency ω_0 of the field verify the (generally satisfied) condition

$$\delta\omega/\omega_0 \ll 1 \quad (8)$$

In this way, one obtains the set of equations

$$\begin{aligned}\frac{dc_m(z; \omega)}{dz} &= -4i \sum_n c_n(z; \omega) \exp\{i[\beta_m(\omega) - \beta_n(\omega)]z\} \sum_{pq} \int_{-\infty}^{+\infty} R_{pq}^{m,n}(\omega, \omega', \omega'') c_p(z; \omega') c_q^*(z; \omega'') \exp\{i(\omega' - \omega'')t\} \\ &\quad \times \exp\{-i[\beta_p(\omega') - \beta_q(\omega'')]z\} d\omega' d\omega'' \quad , \quad m=1, 2, \dots \quad (9)\end{aligned}$$

where

$$R_{pq}^{m,n}(\omega, \omega', \omega'') = (\omega n_2 / c) \frac{\iint_{-\infty}^{+\infty} f(\underline{r}) \underline{E}_m^*(\underline{r}; \omega) \cdot \underline{E}_n(\underline{r}; \omega) \underline{E}_p(\underline{r}; \omega') \cdot \underline{E}_q^*(\underline{r}; \omega'') dx dy}{\iint_{-\infty}^{+\infty} f(\underline{r}) \underline{E}_m^2(\underline{r}; \omega) dx dy} \quad (10)$$

In deriving the set of Eqs.(9) and (10), we have assumed $n_1^2/n^2=1$ and the validity of the local approximation for the refractive index, that is

$$n_1(\underline{r}; \omega) = f(\underline{r}) n_1(\omega) \quad (11)$$

Besides, we have taken advantage of the relation

$$e_z \times H_{-mT}(r, \omega) = (\epsilon_0 / \mu_0)^{1/2} n_1(r, \omega) E_{-mT}(r, \omega) \quad (12)$$

approximately true for weakly-guiding fibers, for simplifying Eq.(6). If we now observe that the $E_{-mT}(r, \omega)$'s are smoothly varying functions of ω and recall Eq.(8), the set of Eqs.(9) can be recast in the simpler form

$$\frac{dc_m(z, \omega)}{dz} = -i \sum_n c_n(z, \omega) \exp\{i[\beta_m(\omega) - \beta_n(\omega)]z\} \sum_{pq} R_{pq}^{m,n}(\omega_n, \omega_p, \omega_q) \hat{\psi}_p(z, t) \hat{\psi}_q^*(z, t) \quad , m=1, 2, \dots \quad (13)$$

where

$$\hat{\psi}_m(z, t) = 2 \int_0^{+\infty} c_m(z, \omega) \exp\{i\omega t - i\beta_m(\omega)z\} d\omega \quad (14)$$

having assumed, in full generality, the amplitude $c_m(z, \omega)$ of each mode to be centered on a frequency ω_m . If we multiply both sides of Eq.(13) by $2\exp\{-i\beta_m(\omega)z + i\omega t\}$ and integrate over ω in the interval $(0, +\infty)$, after expanding $\beta_m(\omega)$ around ω_m up to the second-order derivative, we obtain a set of coupled equations in the time-domain, which reads

$$\begin{aligned} L_m \hat{\phi}_m(z, t) = & -i \hat{\phi}_m \sum_p R_{pp}^{m,n}(\omega_m, \omega_p, \omega_p) \hat{\phi}_p \hat{\phi}_p^* - i \sum_{n \neq m} \hat{\phi}_n (R_{mn}^{m,n}(\omega_n, \omega_m, \omega_n) \hat{\phi}_m \hat{\phi}_n^* \\ & + \sum_{l \neq m} \sum_{q \neq n} R_{pq}^{m,n}(\omega_n, \omega_p, \omega_q) \exp\{i(\omega_n - \omega_m + \omega_p - \omega_q)t - i[\beta_n(\omega_n) - \beta_m(\omega_m) + \beta_p(\omega_p) - \beta_q(\omega_q)]z\} \hat{\phi}_p \hat{\phi}_q^*) \quad , \\ & m=1, 2, \dots \quad (15) \end{aligned}$$

where

$$L_m = \partial/\partial z + (1/V_m) \partial/\partial t - (1/2A_m) \partial^2/\partial t^2 \quad (16)$$

with

$$V_m^{-1} = d\beta_m/d\omega \Big|_{\omega=\omega_m} \quad , \quad A_m^{-1} = d^2\beta_m/d\omega^2 \Big|_{\omega=\omega_m} \quad (17)$$

and the slowly varying amplitudes $\hat{\phi}_m$ are defined through the relation

$$\hat{\psi}_m = \exp\{i\omega_m t - i\beta_m(\omega_m)z\} \hat{\phi}_m = 2 \exp\{i\omega_m t - i\beta_m(\omega_m)z\} \int_0^{+\infty} c_m(z, \omega) \exp\{i(\omega - \omega_m)(t - z/V_m) - i(\omega - \omega_m)^2/2A_m\} d\omega \quad (18)$$

The choice of different frequencies ω_m for the different modes is suggested by the fact that, as we shall see in next Section, soliton propagation can occur only by suitably selecting the different frequencies at which the different modes are excited. Conversely, nonlinear propagation of a generical pulse is usually investigated through Eq.(15) by exciting all the modes at the same central frequency ω_0 .

The set of Eqs.(15) can be substantially simplified if $\beta_m(\omega) \neq \beta_n(\omega)$ for all $m \neq n$. In fact, one can in this case resort to the rotating wave approximation and neglect the fast oscillating terms of the kind $\exp\{i[\beta_m(\omega_m) - \beta_n(\omega_n)]z\}$, thus getting

$$L_m \hat{\phi}_m = -i \hat{\phi}_m \left\{ \sum_n R_{nn}^{m,m}(\omega_m, \omega_n, \omega_n) \hat{\phi}_n \hat{\phi}_n^* + \sum_{n \neq m} R_{mn}^{m,n}(\omega_n, \omega_m, \omega_n) \hat{\phi}_n \hat{\phi}_n^* \right\} \quad , m=1, 2, \dots \quad (19)$$

The set of Eqs.(15) refers to an ideal fiber, mode coupling being only due to the presence of nonlinear effects. Whenever the fiber possesses intrinsic departures from ideality associated with imperfections, Eqs.(15) are modified by adding on the right-hand side a linear contribution of the kind

$$\sum_n K_{mn}(z) \exp\{i(\omega_n - \omega_m)t - i[\beta_n(\omega_n) - \beta_m(\omega_m)]z\} \hat{\phi}_n \quad (20)$$

where the coupling coefficients K_{mn} depend on the fiber irregularities.

3. SOLITON PROPAGATION

The set of Eqs.(19) can admit particular solutions in the form of envelope solitons provided that all the modes are made to travel with a common group velocity, that is if their excitation frequencies $\omega_1, \omega_2, \dots$ are chosen in such a way that

$$d\beta_1/d\omega \Big|_{\omega=\omega_1} = d\beta_2/d\omega \Big|_{\omega=\omega_2} = \dots = 1/V \quad (21)$$

In fact, the structure of Eqs.(19) implies that nonlinear coupling does not modify the group velocity of the single modes, so that modal dispersion, obviously detrimental for soliton propagation, can only be avoided by imposing the coincidence of the group velocities assured by Eq.(21). Under this circumstance, it is immediate to verify that solutions of the set of Eqs.(19) in the form of bright solitons are given by

$$\hat{\phi}_m(z,t) = \hat{\phi}_{om} \exp(iz/2A_m \tau^2) \operatorname{sech}\{(t-z/V)/\tau\}, \quad m=1,2,\dots, \quad (22)$$

provided that the relations between the temporal width τ and the amplitudes of the pulses

$$-1/A_m \tau^2 = \sum_n R_{nn}^{m,m}(\omega_m, \omega_n, \omega_n) |\hat{\phi}_{on}|^2 + \sum_{n \neq m} R_{mn}^{m,n}(\omega_n, \omega_m, \omega_n) |\hat{\phi}_{on}|^2, \quad m=1,2,\dots, \quad (23)$$

are satisfied. Since all the $R_{mn}^{m,n}$'s are positive quantities, Eqs.(23) imply, as a necessary condition for the existence of solitons, all the A_m 's to be negative, that is

$$d^2 \beta_m / d\omega^2 \Big|_{\omega=\omega_m} < 0, \quad m=1,2,\dots, \quad (24)$$

The set of Eqs.(23) furnishes in a very natural way the existence condition for soliton propagation in terms of the superposition integrals $R_{mn}^{m,n}$ and the propagation constants β_m of the various modes. In particular, the influence of the waveguide on the existence region of bright solitons (in its absence, bright soliton propagation is possible only for anomalous material dispersion) is expressed by Eq.(24), where $c^2 \beta_m / d\omega^2$ contains both material and waveguide dispersion, and is valid for any refractive index profile.

In particular, if only one polarization state is excited, Eq.(23) furnishes

$$-(1/\tau^2) (d^2 \beta_1 / d\omega^2) \Big|_{\omega=\omega_1} = R_{11}^{1,1}(\omega_1, \omega_1, \omega_1) |\hat{\phi}_{10}|^2, \quad (25)$$

while for the two polarization-states of a single-mode fiber one has

$$\begin{aligned} -(1/\tau^2) (d^2 \beta_1 / d\omega^2) \Big|_{\omega=\omega_1} &= R_{11}^{1,1}(\omega_1, \omega_1, \omega_1) |\hat{\phi}_{10}|^2 + R_{22}^{1,1}(\omega_1, \omega_2, \omega_2) |\hat{\phi}_{20}|^2, \\ -(1/\tau^2) (d^2 \beta_2 / d\omega^2) \Big|_{\omega=\omega_2} &= R_{11}^{2,2}(\omega_2, \omega_1, \omega_1) |\hat{\phi}_{10}|^2 + R_{22}^{2,2}(\omega_2, \omega_2, \omega_2) |\hat{\phi}_{20}|^2. \end{aligned} \quad (26)$$

In writing Eq.(26), we have neglected the terms proportional to $R_{12}^{1,2}$ and $R_{21}^{2,1}$ since, due to the orthogonality of the transverse components of the two states, they contain only the longitudinal components which, for weakly-guiding fibers, are small compared to the transverse ones. The same argument allows us to verify, starting from Eq.(15), that Eq.(26) holds true for the two polarization-states of a perfectly circular single-mode fiber also if in this case their degeneracy ($\beta_1(\omega) = \beta_2(\omega)$) so that, according to Eq.(21), $\omega_1 = \omega_2$) prevents one from applying the rotating-wave approximation leading from Eq.(15) to Eq.(19). For this kind of fiber, all the R 's coincide so that the set of Eqs.(26) reduces to the single equation

$$-(1/\tau^2) (d^2 \beta_1 / d\omega^2) \Big|_{\omega=\omega_1} = R_{11}^{1,1}(\omega_1, \omega_1, \omega_1) (|\hat{\phi}_{10}|^2 + |\hat{\phi}_{20}|^2), \quad (27)$$

which shows that the peak intensity necessary for soliton transmission can be shared between the two polarization-states in an arbitrary way. The departure from degeneracy occurring in polarization-maintaining fibers (elliptical or stress-birefringent) is in most cases small enough to preserve the validity of Eq.(27), notwithstanding the small difference between ω_1 and ω_2 necessary to satisfy Eq.(21), and the associated difference between β_1 and β_2 justifies the neglect of the linear coupling (see Eq.(20)) always present in non-ideal fibers.

4. INTENSITY FLUCTUATIONS OF THE CARRIER AND SOLITON PROPAGATION

The results of the previous Sections concern a situation in which the pulse undergoing nonlinear propagation is obtained by suitably modulating a carrier free from fluctuations, which is true whenever the pulse duration τ fulfills the condition

$$\tau \ll t_c, \quad (28)$$

where t_c is the coherence time of the exciting source. In this Section, we wish to consider for sake of completeness the opposite situation in which

$$\tau \gg t_c. \quad (29)$$

To this end, we observe that Eq.(19) holds true for the single realization of the field, whose random nature is associated with the fluctuations of the exciting source. The hypothesis contained in Eq.(29) allows us to consider a situation in which the detector performs an average of the instantaneous intensity over time intervals much larger than t_c (and smaller than τ), which is equivalent to an ensemble averaging operation over the source fluctuations. Accordingly, we write

$$\hat{\phi}_m(z,t) = F_m(z,t) S_m(z,t) \exp(-ix_m z), \quad (30)$$

F_m representing the fast fluctuating part and S_m the deterministic (real) signal of duration τ which one wishes to propagate, the relevant quantity being

$$\langle \hat{\phi}_m^*(z,t) \hat{\phi}_m(z,t) \rangle = \langle F_m^*(z,t) F_m(z,t) \rangle S_m^2(z,t), \quad (31)$$

where the angularbrackets indicate the averaging operation. By multiplying both sides of Eq.(19) by $\hat{\phi}_m^*(z,t)$

and its complex conjugate by $\hat{\phi}_m(z,t)$, by adding and subtracting the resulting expressions and averaging, one obtains

$$\partial S_m^2 / \partial z + (1/V_m) \partial S_m^2 / \partial t = 0, \quad m=1,2,\dots \quad (32)$$

implying S_m to be a function of $t-z/V_m$, and

$$\frac{d^2 S_m}{dt^2} + f_m S_m = 2A_m S_m \left\{ \sum_n R_{nn}^{m,m}(\omega_m, \omega_n, \omega_n) \langle B_m^2 B_n^2 \rangle / \langle B_m^2 \rangle S_n^2 + \sum_{n \neq m} R_{mn}^{m,n}(\omega_n, \omega_m, \omega_n) \langle B_m^2 B_n^2 \rangle / \langle B_m^2 \rangle S_n^2 \right\} - 2\chi_m A_m S_m, \quad m=1,2,\dots \quad (33)$$

In deriving Eq.(32) and Eq.(33), we have assumed

$$F_m = B_m \exp(i\gamma_m) \quad (34)$$

where B_m and γ_m are real statistically independent stationary variables (e.g., $\langle A_m^2(z,t) \rangle$ is independent from z and t^m), and we have defined

$$f_m = \langle B_m \partial^2 B_m / \partial t^2 \rangle / \langle B_m^2 \rangle - \langle \partial \gamma_m^2 / \partial t^2 \rangle \quad (35)$$

The set of Eq.(33) admits, once that Eq.(21) is satisfied, a soliton-type solution of the kind

$$S_m(z,t) = S_{om} \operatorname{sech}[(t-z/V_m)/\tau] \quad (36)$$

provided that the two conditions

$$-(1/A_m \tau^2) = \sum_n R_{nn}^{m,m} S_{on}^2 \langle B_m^2 B_n^2 \rangle / \langle B_m^2 \rangle + \sum_{n \neq m} R_{mn}^{m,n} S_{on}^2 \langle B_m^2 B_n^2 \rangle / \langle B_m^2 \rangle, \quad m=1,2,\dots \quad (37)$$

and

$$\chi_m = -(1/2A_m \tau^2)(1 + f_m \tau^2), \quad m=1,2,\dots \quad (38)$$

are fulfilled.

The influence of the field fluctuations is essentially associated with the appearance of the coefficients $\langle B_m^2 B_n^2 \rangle / \langle B_m^2 \rangle$. In particular, for the single-mode case, Eq.(37) reduces to

$$-(1/A_1 \tau^2) = R_{11}^{1,1} \eta \langle B_1^2 \rangle S_{o1}^2 \quad (39)$$

with

$$\eta = \langle B_1^4 \rangle / \langle B_1^2 \rangle^2 \quad (40)$$

Equation (40) coincides with Eq.(23) (in the single-mode case) if $\eta=1$, that is for an amplitude-stabilized source. In general, η is greater than one and attains the value two for a chaotic source so that soliton propagation can be achieved in this case with half the power required with a laser source.

5. REFERENCES

1. STOLEN, R.H., 1979, "Nonlinear properties of optical fibers", in "Optical Fibers Telecommunications", edited by S.E. Miller and A.G. Chynoweth, Academic, New York.
2. CHIAO, R.Y., GARMIRE, E., and TOWNES, C.H., 1964, "Self-trapping of optical beams", Phys.Rev.Lett. 13, 479-482.
3. SHIMIZU, F., 1967, "Frequency broadening in liquids by a short light pulse", Phys.Rev.Lett. 19, 1097-1100.
4. HASEGAWA, A. and TAPPERT, F., 1973, "Transmission of stationary nonlinear optical pulses in dispersive dielectric fibers. I. Anomalous dispersion", Appl.Phys.Lett. 23, 147-149.
5. MOLLENAUER, L.F., STOLEN, R.H., and GORDON, J.P., 1980, "Experimental observation of picosecond pulse narrowing and solitons in optical fibers", Phys.Rev.Lett. 45, 1095-1098.
6. STOLEN, R.H. and LIN, C., 1978, "Self-phase modulation in silica optical fibers", Phys.Rev. A 17, 1448-1453.
7. BENDOW, B., GIANINO, P.D., TZOAR, N., and JAIN, M., 1980, "Theory of nonlinear pulse propagation in optical waveguides", J.Opt.Soc.Am. 70, 539-546.
8. CROSIGNANI, B., DI PORTO, P., and PAPAS, C.H., 1980, "Role of intensity fluctuations in nonlinear pulse propagation", Opt.Lett. 5, 467-468.

9. HASEGAWA, A., 1980, "Self-confinement of multimode optical pulses in a glass fiber", *Opt.lett.* 5, 416-417.
10. CROSIGNANI, B., DI PORTO, P., and PAPAS, C.H., 1981, "Coupled-mode theory approach to nonlinear pulse propagation in optical fibers", *Opt.Lett.* (in press).
11. MARCUSE, D., 1975, "Theory of Dielectric Optical Waveguides", *Academic, New York*, Ch.3.
12. CROSIGNANI, B. and DI PORTO, P., 1981, "Nonlinear pulse propagation over the two polarizations of a single-mode optical fiber" (submitted for publication).
13. CROSIGNANI, B., DI PORTO, P., and PAPAS, C.H., 1977, "Theory of time-dependent propagation in multimode lightguides", *J.Opt.Soc.Am.* 67, 1300-1307.

THEORY OF NONLINEAR PULSE PROPAGATION IN INHOMOGENEOUS DISPERSIVE MEDIA: APPLICATION TO OPTICAL WAVEGUIDES

N. Tzoar
Department of Physics, The City College of
The City University of New York
New York, New York 10031

B. Bendow and P.D. Gianino
Solid State Sciences Division
Rome Air Development Center
Hanscom AFB, Massachusetts 01731

SUMMARY

We analyze nonlinear pulse propagation in longitudinally uniform and nonuniform optical waveguides. The approximate analysis employed takes account of various physical effects associated with transverse confinement, dispersion and nonlinearity. One concludes that both bright and dark solitons may be supported in typical fiberguides under a variety of conditions. This is in marked contrast to the unbounded medium case, where bright solitons exist only under conditions of anomalous dispersion. In the presence of weak longitudinal inhomogeneity, one finds that solitons continue to propagate without a change of shape, but that their group velocity becomes time-dependent.

1. INTRODUCTION

The possibility of transmitting undistorted pulses with high peak powers could prove useful and find application in various fields. Intense, ultrashort light pulses guided by fibers could be used to achieve ultrahigh data rates in communications, to perform surgery in medicine, for cutting and welding in industrial processes, etc. The nonlinearity which governs the propagation characteristics arises from the real part of the guide refractive index, although dissipative nonlinear processes could in principle affect the pulse as well.

The theoretical problem of transmission of nonlinear pulses in optical waveguides is both interesting and challenging, since it involves the simultaneous interplay of transverse confinement, dispersion and nonlinearity. Solutions in many areas of physics have already been obtained (SCOTT, A.C., et al., 1973, for example) and considerable knowledge has been gained for the one-dimensional pulse propagation case, while two- or three-dimensional nonlinear propagation is still in its infancy stage (GERSTEN, J.I., et al., 1975; KAW, P.K., et al., 1975; WILCOX, J.Z., et al., 1975; ZAKHROV, V.E., et al., 1979).

A critical limitation in the realization of the full-bandwidth capability of optical transmission systems is pulse broadening resulting from dispersion effects (GLOGE, C., 1971; KECK, D., 1976, for example). Although dispersion can be minimized by an appropriate choice of guide materials, geometry and operating frequency, it is apparent that dispersion effects will be detrimental for sufficiently narrow pulsewidths. To overcome this problem the nonlinear dependence of the refractive index on pulse intensity may be used. Here the dispersion effects result in the broadening of the pulse, while nonlinearity tends to sharpen it. It is the appropriate interplay of these opposite effects which can lead to a stable soliton solution for the optical pulse. But nonlinearity can also introduce a host of other effects (CHIAO, R.Y., et al., 1964; HASEGAWA, A., et al., 1973; TZOAR, N., et al., 1976; SHIMIZU, F., 1967) such as self-focusing and self-phase modulation. However, each of these effects is dominant only in certain regimes characterized by the dispersion, peak intensity and nonlinear parameters.

Self-focusing, which occurs for finite-sized beams, requires a very high critical intensity. This phenomenon is an instability which causes a finite-sized beam to collapse to a point, due to an effective focusing lens induced by its own intensity. The condition for self-focusing is independent of the dispersion parameter and represents a competition between nonlinearity and diffraction effects. Indeed, for Gaussian beams the condition for self-focusing to occur is given by

$$k^2 \rho_0^2 \geq \frac{\epsilon_0}{\epsilon_{NL} E_0^2} \quad (1)$$

where $k = 2\pi/\lambda$, where λ is the free space wavelength; ϵ_0 (ϵ_{NL}) is the linear (nonlinear) dielectric function; and ρ_0 and E_0 are, respectively, the radius and on-axis field intensity of the beam. This condition is not affected by the guide's parameters. The guide, by balancing diffraction, provides stable trapping of the beam at a finite size even for fields below the critical field (the critical field is defined by Eq. (1) when the equal sign is taken). For glasses one finds the critical power for self focusing to be of the order of 10^7 - 10^8 W/cm², much greater than the power needed for soliton propagation.

Self-phase modulation is observed at high intensities when dispersion effects are negligible and no solitary solution can be sustained. In order to achieve solitary pulse propagation, we deliberately limit the pulse intensity so that the nonlinearity just balances the dispersion effects instead of dominating them (as would be the case for self-phase modulation).

The soliton problem in optical waveguides appears to have been considered first by HASEGAWA and TAPPERT (HT) (1973) but these authors did not take detailed account of the transverse inhomogeneity in their analysis. Subsequently, JAIN and TZOAR (JT) (1978) introduced an approach that accounted for the transverse inhomogeneity of the waveguide in an average fashion, and were thereby able to demonstrate that in fact typical fiberguides could indeed support "bright" solitons. This contrasts with the

results of HT who found that anomalous material dispersion or very large core-clad differences ($\Delta n \sim 0.5$) are required for "bright" solitons to exist. The approach of JT has been generalized by BENDOW, GIANINO, TZOAR and JAIN (BGTJ) (1980) to include variational analysis and to treat longitudinal inhomogeneities, and by CROIGNANI, PAPAS and DI PORTO (1980) to consider the role of intensity fluctuations on nonlinear soliton propagation in optical waveguides.

2. MATHEMATICAL FORMULATION

Consider an optical waveguide having a dispersive and nonlinear refractive index of the form

$$n(\vec{r}, \omega, \vec{E}) = n_1(\vec{r}, \omega) + n_2 |\vec{E}|^2 \quad (2)$$

where ω is the frequency, \vec{E} is the electric field and n_2 the nonlinear coefficient, taken to be independent of frequency. Moreover, n_1 is represented by its local approximation, i.e.

$$n_1(\vec{r}, \omega) = n_1(\omega) f(\vec{r}). \quad (3)$$

In what follows we consider propagation of pulses which are narrowly centered about a given frequency ω_0 and assume that $n_1(\omega)$ is a slowly varying function of ω in the vicinity of ω_0 . The electric field is taken to be

$$\vec{E}(\vec{r}, t) = \hat{e} A(\vec{r}, t) e^{i(qz - \omega_0 t)} \quad (4)$$

where \hat{e} is a unit vector in the transverse direction, $\vec{r} = (\rho, z)$, and z is the direction of propagation. We then obtain for A the wave equation:

$$\left[\frac{\partial^2}{\partial \rho^2} + \frac{\partial^2}{\partial z^2} - q^2 + 2iq \frac{\partial}{\partial z} + f(\vec{r}) k_0^2 + 2ik_0 k_0' f(\vec{r}) \frac{\partial}{\partial t} - (k_0 k_0'' + k_0'^2) f(\vec{r}) \frac{\partial^2}{\partial t^2} + 2 \frac{n_2 k_0^2}{n_0} |A(\vec{r}, t)|^2 \right] A(\vec{r}, t) = 0. \quad (5)$$

In Eq. (5) $k(\omega) = \omega/c n_1(\omega)$ and the primes indicate derivatives with respect to ω at $\omega = \omega_0$. The appearance of the time and frequency derivatives only to second order is a consequence of using the slowly varying envelope approximation in deriving Eq. (5).

For the waveguide problem f is always inhomogeneous in the transverse direction, i.e., $f(\vec{r}) = f(\rho)$. Under these conditions it is extremely difficult to obtain time-dependent solutions to Eq. (5), either analytically or numerically. We therefore seek an approximate solution to Eq. (5), based on the observation that the material dispersion in optical waveguides is generally very small. Our previous discussion regarding the balance between dispersion and nonlinearity suggests that the nonlinear effects will also be small in the guide case. We thus expect a negligible effect from the nonlinearity on the mode structure of the guide. Physically, the spatial trapping of the beam and its localization within the guide is dominated by the transverse inhomogeneity. If nonlinearity were absent, the pulse in the guide would experience broadening due to dispersion. The correspondingly small effect induced by the nonlinearity is capable of balancing this longitudinal dispersion. Moreover, it seems reasonable on general grounds to assume that transverse inhomogeneity has only a weak effect on the longitudinal propagation of a pulse along a narrow guide. Rather, the main effect of the transverse inhomogeneity is to determine the mode structure of the linear guide, with the longitudinal propagation characteristics of the modes subsequently being modified by the nonlinearity. This approach, which was first introduced by JT, leads to an approximate solution

$$A(\vec{r}, t) = \phi(\vec{\rho}) \theta(z, t) \quad (6)$$

where the longitudinal characteristics of the pulse are found by taking the transverse average of Eq. (5). Taking any of the linear mode solutions for $\phi(\rho)$, multiplying Eq. (5) by $\phi(\rho)$, using Eq. (6) for $A(\vec{r}, t)$ and integrating over the cross section of the guide, results in the following wave equation for $\theta(z, t)$:

$$\left[d_1 - q^2 + \bar{f}(z) k_0^2 + \frac{\partial^2}{\partial z^2} - (k_0 k_0'' + k_0'^2) \bar{f}(z) \frac{\partial^2}{\partial t^2} + d_2 |\theta|^2 + 2i \left(q \frac{\partial}{\partial z} + k_0 k_0' \bar{f}(z) \frac{\partial}{\partial t} \right) \right] \theta(z, t) = 0. \quad (7)$$

In eq. (7) we define the function $\bar{f}(z)$ as

$$\bar{f}(z) = \int d\vec{\rho} \phi(\vec{\rho}) f(\vec{\rho}, z) \phi(\vec{\rho}) \quad (8)$$

and

$$d_1 = \int d\vec{\rho} \phi(\vec{\rho}) \frac{\partial^2}{\partial \rho^2} \phi(\vec{\rho}) \quad (9)$$

$$d_2 = 2 \frac{n_2}{n_0} k_0^2 \int d\vec{\rho} |\phi(\vec{\rho})|^4. \quad (10)$$

The electric field can now be written as

$$\vec{E}(\vec{r}, t) = \hat{e} \phi(\vec{\rho}) \theta(z, t) e^{i(qz - \omega_0 t)}. \quad (11)$$

The effect of the waveguide is now included solely by means of the parameters d_1 , d_2 and $\bar{f}(z)$.

3. LONGITUDINALLY HOMOGENEOUS GUIDES

We now consider the longitudinally homogeneous guide. Here $\bar{f}(z) = \bar{f}$ and Eq. (7) supports a particular solitary solution for $\theta(z, t) = \theta(t-z/v)$, where

$$v = q/k_0 k_0' \bar{f} \quad (12)$$

and

$$\theta = \theta_0 \operatorname{sech}[\gamma(t-z/v)] \quad (13)$$

with the conditions:

$$q^2 = k_0^2 \bar{f} + d_1 + d_2 \theta_0^2/2, \quad (14a)$$

$$\left[\frac{(k_0 k_0' \bar{f})^2}{q^2} - (k_0 k_0'' + k_0'^2) \bar{f} \right] \gamma^2 = \frac{1}{2} d_2 \theta_0^2. \quad (14b)$$

The significant difference of our result (given in Eqs. (14)) from the homogeneous medium case, is the factor d_1 above, which is a direct consequence of the transverse inhomogeneity, i.e., the waveguiding mechanism. For example, we consider the condition for the "bright" soliton solution, given in Eq. (13) when the nonlinear factor d_2 is larger than zero. The requirement $\gamma > 0$ implies that

$$\frac{1}{1 + [d_1 + \frac{1}{2} d_2 \theta_0^2]/k_0 \bar{f}} \cdot \frac{1}{1 + \frac{k_0 k_0''}{k_0'^2}} > 1. \quad (15)$$

For the present case, in which d_1 will be negative, Eq. (15) may be satisfied even when $k_0'' > 0$. This contrasts with previous predictions and with the one dimensional soliton solutions which predict that "bright" solitons will exist only if $k_0'' < 0$.

We point out that Eq. (7) admits a "dark" soliton solution, first realized by HT. Here a solution of the form $\theta = \theta_0 [1 - \theta_1^2 \operatorname{sech}^2[\gamma(t-z/v)]]^{1/2}$ exists for $\theta_1 \leq 1$. We shall consider here only the particular case of dark solitons where θ_1 is taken to be unity. We thus obtain

$$\theta = \theta_0 \tanh[\gamma(t-z/v)] \quad (16)$$

and the corresponding conditions

$$q^2 = k_0^2 \bar{f} + d_1 + d_2 \theta_0^2, \quad (17a)$$

$$- \left[\frac{(k_0 k_0' \bar{f})^2}{q^2} - (k_0 k_0'' + k_0'^2) \bar{f} \right] \gamma^2 = \frac{1}{2} d_2 \theta_0^2. \quad (17b)$$

For the "dark" soliton we require the existence condition

$$\frac{1}{1 + [d_1 + d_2 \theta_0^2]/k_0^2 \bar{f}} \cdot \frac{1}{1 + \frac{k_0 k_0''}{k_0'^2}} < 1, \quad (18)$$

which may be satisfied for either $k_0'' \geq 0$, depending on the values of the remaining parameters. We also point out that as in the case of plane waves there exists a zero dispersion condition in our theory. For plane waves $k_0'' = 0$ indicates the zero dispersion condition which determines the frequency at which a pulse of "zero" amplitude will propagate without distortion. In our case the zero-dispersion condition becomes

$$\left(1 + \frac{d_1}{k_0^2 \bar{f}}\right) \left(1 + \frac{k_0 k_0''}{k_0'^2}\right) = 1 \quad (19)$$

for either type of soliton. Since $d_1 < 0$ we require $k_0'' > 0$ for the zero-dispersion condition to be realized. To illustrate these results we consider the truncated quadratic profile

$$f(\bar{\rho}) = \begin{cases} 1 - \rho^2/L^2 & ; \quad \rho < \rho_0 \\ 1 - \rho_0^2/L^2 & ; \quad \rho \geq \rho_0 \end{cases} \quad (20)$$

We approximate $\phi(\bar{\rho})$ by the transverse wave solution for the linear problem when $\rho_0 \rightarrow \infty$, in order to avoid numerical computations. This approximation is very good for the lowest modes. Following our procedures described above, we obtain for the bright soliton,

$$\theta = \theta_0 \operatorname{sech}[\gamma(t-z/v)],$$

$$q^2 = k_0^2 \left(\bar{f} - \frac{1}{k_0 L}\right) + \frac{1}{2} \frac{n_2}{n_0} k_0^2 \theta_0^2, \quad (21)$$

$$\gamma^2 = \left\{ [(k_0 k_0' \bar{f})^2 / q^2] - [k_0 k_0'' + k_0'^2 \bar{f}] \right\} = \frac{1}{2} \frac{n_2}{n_0} k_0^2 \theta_0^2,$$

$$\bar{f} = (k_0 L)^{-1} (e^{-k_0 \rho_0^2 / L} - 1) + 1.$$

The zero-dispersion condition becomes

$$\frac{k_0 k_0''}{k_0'^2} \approx \frac{1}{k_0 L \bar{f}}. \quad (22)$$

For 1 μm light in fused silica we then have $k_0 L \sim 2 \times 10^2$. If $\rho_0^2/L^2 = 2\%$, for example, $\rho_0 \sim 4.5 \mu\text{m}$, while if $\rho_0^2/L^2 = 1\%$, $\rho_0 \sim 3.2 \mu\text{m}$. These estimates become increasingly inaccurate as ρ_0/L decreases. JT have obtained similar results in a previous paper, where regimes of bright and dark solitons as a function of L and ω_0 are indicated graphically as well. These authors also present calculations for step-index fibers, utilizing the transverse function of the linear problem (i.e. the Bessel function). We may use their graphical results to estimate the soliton pulse power density for typical cases. We find, e.g., for the lowest-order mode in a silica fiber with core radius $\sim 5 \mu\text{m}$ and carrier wavelength 1 μm , that the power density $P \sim 10^5 \text{ W/cm}^2$ for a pulsewidth of $\tau \sim 1 \text{ ns}$.

Our theory was developed under the assumption that the electric field is coherent and can be written in terms of a well-defined, time-dependent deterministic function. CROSIGNANI, PAPAS and DI PORTO (1980) have generalized the above theory to include pulse propagation in optical waveguides when the source of the radiation has a finite coherence time arising from its statistical fluctuations. Here, $\theta(z,t)$ of Eq. (6), must be replaced by $A e^{i\epsilon} \theta(z,t)$ where A and ϵ represent a time-dependent fluctuating amplitude and phase for the source, respectively, with characteristic fluctuation time much smaller than the pulse width. The most important result of their work, in terms of our formalism, is that one must replace θ_0^2 , in Eq. (14b), by $\theta_0^2 \eta$, where η is given by

$$\eta = \langle A^4 \rangle / \langle A^2 \rangle^2. \quad (23)$$

Here, $\langle \rangle$ represents the time, or equivalently the ensemble, average of the fluctuating field. For a coherent source $\eta = 1$ and one obtains our previous results. However, for a chaotic source $\eta = 2$, and therefore, assuming all other parameters remain unchanged, one needs only half of the intensity to support the soliton solution.

4. LONGITUDINALLY INHOMOGENEOUS WAVEGUIDES

The nonlinear pulse propagation problem becomes further complicated when the guide refractive index varies as a function of z . Longitudinal inhomogeneity is, in fact, quite common, and stems from compositional and diametral variations, as well as microbending. Such variations can be modelled, at least approximately, by retaining a longitudinal dependence in the effective guide refractive index, $f=f(z)$, in Eq. (7). Unfortunately, there are no known methods of solving Eq. (7) in this instance. On the other hand, methods for treating slowly varying variations have been developed, within the adiabatic approximation, for one-dimensional nonlinear propagation in the absence of frequency dispersion (CHEN, H.H., et al., 1976 and 1978). We are thus led to consider an approximation in which dispersion and longitudinal inhomogeneity are assumed decoupled; specifically, we assume

$$\frac{\partial^2}{\partial t^2} = \frac{\partial^2}{\partial z^2} \Big|_{f(z)=\bar{f}(0)} \quad (24)$$

i.e., the dispersive terms are replaced by their values in the homogeneous limit. Thus, we retain interactions between transverse inhomogeneity, dispersion and nonlinearity, on the one hand, and between longitudinal inhomogeneity and nonlinearity on the other.

The solution of Eq. (7) in this instance is straightforward but tedious. The reader interested in details is directed to BENDOW, et al. (1979 and 1980); we will here just state the results. As in the longitudinally homogeneous case, E is given formally by Eq. (11), but θ now takes the form

$$\theta(z,t) = \theta_0 \operatorname{sech}[\tilde{\gamma}(z-v_e t)] e^{i(q_e - q)z} e^{-i(\omega_e - \omega_0)t} \quad (25)$$

where $\tilde{\gamma} = \gamma k_0' k_0'' \bar{f}/q$, and q_e , ω_e and v_e are the effective wave vector, frequency and soliton group velocity of the longitudinally inhomogeneous waveguide, respectively. These are given by (GIANINO, P.D., et al., 1980)

$$v_e = \bar{Z}(t)/t; \quad q_e = qR[\bar{Z}(t)]; \quad \omega_e = \omega_0 + q_e v_e - W[\bar{Z}(t)]/t$$

$$R(x) = (1 - 2k_0' k_0'' \bar{f} q^{-2} \Delta n(x))^{1/2} \quad W(x) = (2k_0' k_0'' \bar{f})^{-1/2} q \int_0^x R(s) ds \quad (26)$$

where

$$\begin{aligned} \bar{Z} &= (2k_0' k_0'' \bar{f})^{1/2} z \\ \Delta n &= - \frac{k_0 [f(z) - f(0)]}{2k_0' \bar{f} (1 - (k_0' k_0'' + k_0''^2) q^2 / k_0' k_0'')} \end{aligned} \quad (27)$$

and \bar{Z} is determined from the classical Hamiltonian relation

$$\int_0^{\bar{Z}(t)} \frac{dz}{2 \left(\frac{q^2}{2k_0' k_0'' \bar{f}} - \Delta n(\bar{Z}) \right)^{1/2}} = t. \quad (28)$$

The principal result of the above development is that, remarkably, the soliton retains its shape in the presence of weak longitudinal inhomogeneity, although its velocity changes according to Eqs. (26)-(28). The time-dependent velocity in this case contrasts markedly with that of the longitudinally homogeneous case where $v = q/k_0' k_0'' \bar{f}$ is a constant. For example, when the inhomogeneity is nearly linear, i.e., when $\Delta n = 2\alpha z$, then

$$v_e = \frac{q}{k_0' k_0'' \bar{f}} - \alpha \left(\frac{k_0' k_0'' \bar{f}}{2} \right)^{-1/2} t, \quad (29)$$

so that the soliton acquires a constant acceleration proportional to α . When the inhomogeneity varies quadratically, $\Delta n = \alpha^2 z^2$, then

$$v_e = \frac{q}{k_0' k_0'' \bar{f}} \left(2 - \frac{\sin 2\alpha t}{2\alpha t} \right), \quad (30)$$

i.e., the velocity varies sinusoidally as a function of t . Not surprisingly, the soliton executes oscillatory motion as a function of time, characteristic of a particle trapped in a harmonic well. Formal solutions may be written down for a variety of other cases as well, such as $\Delta n \sim \sin^2 \alpha z$, in which case v_e involves elliptic integrals (GIANINO, P.D., et al., 1980). In this instance, one again finds that the soliton executes a complicated oscillatory motion as a function of time.

5. REFERENCES

1. BENDOW, B. and GIANINO, P.D., 1979, "Theory of Nonlinear Pulse Propagation in Inhomogeneous Waveguides", *Opt. Lett.* 4, 164-166.
2. BENDOW, B., GIANINO, P.D., TZOAR, N. and JAIN, M. 1980, "Theory of Nonlinear Pulse Propagation in Optical Waveguides", *J. Opt. Soc. Am.* 70, 539-546.
3. CHEN, H.H. and LIU, C.S., 1976, "Solitons in Nonuniform Media", *Phys. Rev. Lett.* 37, 693-697.
4. CHEN, H.H. and LIU, C.S., 1978, "Nonlinear Wave and Soliton Propagation in Media with Arbitrary Inhomogeneities", *Phys. Fluids* 21, 377-380.
5. CHIAO, R.Y., GARMIRE, E., and TOWNES, C.H., 1964, "Self-Trapping of Optical Beams", *Phys. Rev. Lett.* 13, 479-482.
6. CRUSIGNANI, B., PAPAS, C.H. and DI PORTO, P., 1980, "Role of Intensity Fluctuations in Nonlinear Pulse Propagation", *Opt. Lett.* 5, 467-468.

7. GERSTEN, J.I. and TZOAR, N., 1975, "Propagation of Localized Electromagnetic Pulses in Plasma", *Phys. Rev. Lett.* 35, 934-937.
8. GIANINO, P.D. and BENDOW, B., 1980, "Simplified Formulae for Solitons in Media with Slowly Varying Inhomogeneity", *J. Phys. Fluids* 23, 220-221.
9. GLOGE, D., 1971, "Dispersion In Weakly Guided Fibers", *Appl. Opt.* 10, 2442-2445.
10. HASEGAWA, A. and TAPPERT, F., 1973, "Transmission of Stationary Nonlinear Optical Pulses in Dispersive Dielectric Fibers I. Anomalous Dispersion", *Appl. Phys. Lett.* 23, 142-144. "II. Normal Dispersion", *Appl. Phys. Lett.* 23, 171-172.
11. JAIN, M. and TZOAR, N., 1978, "Propagation of Nonlinear Optical Pulses in Inhomogeneous Media", *J. Appl. Phys.* 49, 4649-4654, and, "Nonlinear Pulse Propagation in Optical Fibers", *Opt. Lett.* 3, 202-204.
12. KAW, P.K., NISHIKAWA, K., YOSHIDA, Y. and HASEGAWA, A., 1975, "Two-Dimensional and Three-Dimensional Envelope Solitons", *Phys. Rev. Lett.* 35, 88-91.
13. KECK, D., 1976, in "Fundamentals of Optical Fiber Communications", edited by M. Barnoski, Academic Press.
14. SCOTT, A.C., CHU, F.Y.F. and MC LAUGHLIN, D.W., 1973, "The Soliton, A New Concept in Applied Science", *Proc. IEEE* 61, 1443-1483. An extensive list of references is contained in this review article.
15. SHIMIZU, F., 1967, "Frequency Broadening in Liquids by a Short Light Pulse", *Phys. Rev. Lett.* 19, 1097-1100.
16. TZOAR, N. and GERSTEN, J.I., 1976, in "Optical Properties of Highly Transparent Solids", edited by S.S. MITRA and B. Bendow, Plenum Press.
17. WILCOX, J.Z. and WILCOX, T.J., 1975, "Stability of Localized Plasma Model in Two and Three Dimensions", *Phys. Rev. Lett.* 34, 1160-1163.
18. ZAKHROV, V.E. and KUZNETSOV, E.A., 1979, "Three-Dimensional Solitons", *Sov. Phys. JETP* 39, 285-286.

HOW TO TAP A FIBER-OPTIC LINK AND ELUDE

DETECTION - WHAT'S NEW IN QUANTUM COMMUNICATION

Jeffrey H. Shapiro
 Department of Electrical Engineering and Computer Science
 and Research Laboratory of Electronics
 Massachusetts Institute of Technology
 Cambridge, Massachusetts 02139

SUMMARY

The cornerstone of semiclassical optical communication theory is the conditional Poisson process statistical model for direct detection, from which the signal plus additive white Gaussian noise statistical models for heterodyne and homodyne detection may be derived. This paper reviews the relationship between these results and recently derived quantum-mechanical photodetection formulas. It is shown that the two coincide only when the radiation field incident on the detector is in a Glauber coherent state or a random mixture of such states. The two-photon coherent states, which are not of this class, are described. They have novel quantum-noise characteristics that permit noise reduction to be realized in homodyne detection. In particular, use of two-photon coherent state light makes possible high signal-to-noise ratio detection from a directional coupler that is very weakly linked to an information-bearing optical waveguide. Accordingly, a low-loss waveguide tap may permit an unauthorized party to obtain information from an optical data bus in a virtually undetectable manner. This result as well as other mysteries and applications of two-photon coherent states are explained.

1. INTRODUCTION

The quantum-mechanical theory of optical communications seeks to delineate the ultimate physical constraints imposed on the transmission of information (Helstrom, C.W., et al., 1970; Holevo, A.S., 1973; Yuen, H.P., et al., 1975; Helstrom, C.W., 1976). In particular, by establishing the structure and performance of optimum optical communication systems within an abstract quantum-mechanical framework, this theory yields benchmarks against which the performance of conventional systems, i.e., those which employ laser transmitters and direct, heterodyne, or homodyne detection receivers, can be compared. Moreover, to the extent that there is a large difference between the performance of an optimum quantum system and that of conventional systems, there is a strong justification for undertaking the research necessary to produce the devices which realize (or approximate) the optimum quantum system.

Much of the work to date in quantum communication theory has focused on determining optimum quantum measurements when the radiation field in the vicinity of the receiver is in a Glauber coherent state or a classically random mixture of such states. This is a realistic assumption in that conventional light sources such as incandescent lamps, light-emitting diodes, and lasers produce radiation fields which satisfy the foregoing condition. Unfortunately, the performance obtained with optimum measurements of these states is not dramatically better than that of the best conventional receiver for the same signal field. It might appear, therefore, that there is little hope that quantum communication theory will open up new vistas for optical communication technology. However, to determine the ultimate performance limitations imposed by quantum effects it is essential to consider optimum quantum state generation in addition to optimum quantum state measurement. In this area, quantum communication theory does predict startlingly different communication possibilities, as described below.

For the past several years we have been engaged in quantum-transmitter theory research. We have found that certain "generalized" coherent states of the radiation field, called two-photon coherent states (TCS), offer the potential for greatly improved optical communications (Yuen, H. P., 1976; Yuen, H.P., and Shapiro, J.H., 1978; Shapiro, J.H., et al., 1979; Yuen, H.P., and Shapiro, J.H., 1980). The TCS are, in essence, minimum uncertainty states for the quadrature components of the electromagnetic field possessing an asymmetric noise division between the two quadratures. TCS light beams have yet to be observed experimentally; they can be generated, in principle, through interferometric combination of the two output beams from a degenerate four-wave mixer (Yuen, H.P., and Shapiro, J.H., 1979). As the technology of these mixers is rapidly advancing, due to their conjugate-wave applications in adaptive optics, the prospects for TCS generation are good.

Because of their novel quantum-fluctuation behavior, TCS light beams yield demonstrably different noise statistics from ordinary laser light in direct, homodyne, and heterodyne detection systems. The most promising configuration appears to be homodyning, for which a TCS source can give a signal-to-noise ratio (SNR) value ($N_S + 1$) times that of an ordinary laser when both produce N_S photons, on average, over the observation interval. This noise-reduction capability of TCS light makes possible high SNR detection from a directional coupler that is very weakly linked to an information-bearing optical waveguide (Shapiro, J.H., 1980a). Accordingly, a low-loss waveguide tap may permit an unauthorized party to obtain information from an optical data bus in a virtually undetectable manner (Shapiro, J.H., 1980b).

This paper is aimed at conveying the essential features of TCS communication theory without recourse to detailed analysis. We begin with a tutorial discussion of the quantum interpretation of photodetection.

2. QUANTUM-FIELD PHOTODETECTION

This section comprises an abbreviated survey of the quantum measurements realizable with photoemissive detectors (Shapiro, J.H., et al., 1979; Yuen, H.P., and Shapiro, J.H., 1980).

2.1 Quantum Fields

Consider the single-mode narrowband optical field of center frequency ω_0 whose complex envelope is

$$E(t) = (\hbar\omega_0/T)^{1/2} \underline{a} \exp(-j\omega_0 t), \quad (1)$$

for $0 \leq t \leq T$, where \hbar is Planck's constant in joules-sec/radian, and the polarization and spatial characteristics have been suppressed. In classical physics, \underline{a} is a complex-valued parameter whose real and imaginary parts, a_1 and a_2 , give the normalized quadrature components of $E(t)$, and whose squared modulus, $|\underline{a}|^2$, gives the normalized energy in $E(t)$. For a non-random field a_1 and a_2 will be constants α_1 and α_2 ; for a random field $a_1 = \alpha_1$ and $a_2 = \alpha_2$ will occur with some probability density $p(\alpha_1, \alpha_2)$.

In quantum physics, Eq.(1) is a field-operator representation in terms of \underline{a} , the photon-annihilation operator for the mode. The field quadratures a_1 and a_2 are now conjugate observables whose measurement uncertainties obey the Heisenberg inequality

$$\langle \Delta a_1^2 \rangle \langle \Delta a_2^2 \rangle \geq 1/16. \quad (2)$$

The quantum analog of the classical field with $\underline{a} = \alpha$ is the Glauber coherent state $|\alpha\rangle$, which could be produced as the output of a stabilized laser operating far above threshold. The state $|\alpha\rangle$ yields equality in (2) with equal fluctuation levels in the a_1 and a_2 quadratures. Conventional light sources produce a classically random mixture of coherent states $|\alpha\rangle$ with some probability density $p(\alpha_1, \alpha_2)$; this additional randomness leads to increased noise in both quadratures.

2.2 Direct Detection

In an idealized photon counting system, the field (1) illuminates a unity quantum efficiency photoemissive detector with no internal noise. The photocount output of this direct detection scheme, N , is the number of emissions that occur during the time interval $0 < t < T$. The semiclassical photodetection theory treats the field classically and the emissions as a conditional Poisson process (Gagliardi, R.M., and Karp, S., 1976), so that

$$\text{Pr}[N=n | \underline{a}=\alpha] = (|\alpha|^2)^n / n! \exp(-|\alpha|^2). \quad (3)$$

For a non-random field, this is the well-known "photon noise" whose mean count $\langle N \rangle$ and variance $\text{var}(N)$ both equal $|\alpha|^2$, which is the field energy in photon units. For a random field, Eq.(3) must be averaged over the probability density $p(\alpha_1, \alpha_2)$; this invariably leads "excess noise", viz. $\text{var}(N) > \langle N \rangle$.

The quantum theory of photodetection holds that N realizes the photon-number operator observable $\hat{a}^\dagger \hat{a}$ (Kelley, P.L., and Kleiner, W.H., 1964), so that for a coherent-state field $|\alpha\rangle$ there results the same Poisson distribution (3). It follows that the semiclassical formulation is correct only if the field is in a "classical" state, i.e., a Glauber coherent state or a classically random mixture of such states. For example, the photon number state $|n\rangle$, which is not of this class, yields the non-random count distribution $N=n$ with probability one. The two-photon coherent states are also non-classical.

2.3 Field Detection

In an idealized field detection system the field (1) illuminates a photoemissive detector in combination with the field from a strong local oscillator laser. In homodyne detection, the local oscillator frequency is ω_0 , and a baseband filter extracts a normalized output level y . In heterodyne detection, the local oscillator frequency is $\omega_0 + \omega_{IF}$, and a passband filter at the intermediate frequency ω_{IF} extracts a normalized output complex envelope $\underline{y} = y_1 + jy_2$. The semiclassical and quantum statistics for these measurements are as follows.

Homodyne Detection

Suppose the local oscillator is in phase with the signal field (1). The semiclassical theory holds that y has mean value α_1 , variance $1/4$, and a Gaussian probability density, when $\underline{a} = \alpha$. Moreover, the mean value is due to the signal field, and the noise is due to the local oscillator through the shot effect. The quantum theory tells us that y realizes the a_1 observable. Thus, for a coherent-state field $|\alpha\rangle$ the same y statistics obtain. However, the quantum theory correctly shows that the noise is not due to the local oscillator through the shot effect, but rather to the fundamental quantum fluctuations in the a_1 quadrature of the signal field.

Heterodyne Detection

The semiclassical theory predicts that \underline{y} equals α plus a zero-mean circulo-complex Gaussian random variable with variance one, when $\underline{a} = \alpha$. Once again the mean is ascribed to the signal field and fluctuations to local oscillator shot noise. The quantum theory has that \underline{y} realizes the \underline{a} measurement. For a coherent-state field $|\alpha\rangle$ this gives the same statistics for \underline{y} , but the noise turns out to be due to the quantum fluctuations in the signal field and an image-band field (frequency $\omega_0 + 2\omega_{IF}$).

3. TWO-PHOTON COHERENT STATES

Let μ and ν be complex numbers which satisfy

$$|\mu|^2 - |\nu|^2 = 1, \quad (4)$$

and let \underline{b} obey

$$\underline{b} = \underline{\mu a} + \underline{\nu a}^\dagger \quad (5)$$

where \underline{a} is the annihilation operator in (1). The TCS $|\beta; \mu, \nu\rangle$ is the eigenstate of \underline{b} with eigenvalue β . The relevant properties of TCS are summarized below (Yuen, H.P., 1976; Shapiro, J.H., et al., 1979; Yuen, H.P., and Shapiro, J.H., 1979; Yuen, H.P., and Shapiro, J.H., 1980).

3.1 State Properties and State Generation

When $\mu=1, \nu=0$ the TCS $|\beta; \mu, \nu\rangle$ is the Glauber coherent state $|\beta\rangle$; for $\nu \neq 0$ the TCS $|\beta; \mu, \nu\rangle$ is a non-classical state. When μ, ν are positive real the TCS $|\beta; \mu, \nu\rangle$ is a minimum uncertainty state for the Heisenberg inequality (2) with

$$\langle \Delta a_1^2 \rangle = (\mu - \nu)^2 / 4 < 1/4, \quad (6)$$

and

$$\langle \Delta a_2^2 \rangle = (\mu + \nu)^2 / 4 > 1/4.$$

Thus the TCS allow an interchange between the quantum fluctuations in the a_1 and a_2 quadrature at minimum uncertainty product.

Equation (5) implies that TCS generation may be achieved with active optical systems which mix the annihilation and creation operators for a single field mode. One attractive approach to TCS generation is degenerate four-wave mixing. The usual classical analysis of such mixers shows the output beams to be mixtures of one input beam and the complex conjugate of the other (Yariv, A., and Pepper, D.M., 1977). In a quantized theory, the conjugate amplitude becomes a creation operator and TCS generation should result from interferometric combination of the two output beams (Yuen, H.P., and Shapiro, J.H., 1979).

3.2 Photodetection Statistics

Suppose, in the photodetection systems of Section 2, that the field (1) is in the TCS $|\beta; \mu, \nu\rangle$, with $\beta, \mu, \nu > 0$. Using the quantum photodetection formulas we obtain the following results.

Direct Detection

The photocount N is Hermite distributed

$$\text{Pr}[N=n] = (\nu^n / 2^n n! \mu^{n+1}) |H_n(\beta / (2\mu\nu))^{1/2}|^2 \cdot \exp[-\beta^2 + \nu\beta/\mu], \quad (7)$$

and $\text{var}(N) < \langle N \rangle$ can occur.

Homodyne Detection

The baseband output y is Gaussian distributed with mean $(\mu - \nu)\beta$ and variance $(\mu - \nu)^2 / 4 < 1/4$. By appropriate choice of β, μ, ν , a signal-to-noise ratio of $4N_s(N_s + 1)$ can be achieved for homodyne detection of a TCS field as compared to an SNR of $4N_s$ for a coherent state field, both with average energy N_s photons.

Heterodyne Detection

The passband output complex envelope \underline{y} is Gaussian distributed with mean $(\mu - \nu)\beta$, independent real and imaginary parts, and

$$\text{var}(y_1) = [(\mu - \nu)^2 + 1] / 4, \quad (8)$$

$$\text{var}(y_2) = [(\mu + \nu)^2 + 1] / 4.$$

The first term in each variance is due to the TCS signal field; the second term in each variance is due to the zero-point fluctuations of the vacuum-state image-band field.

4. THE TCS WAVEGUIDE TAP

Consider an information-bearing single-mode optical waveguide. Suppose this waveguide is tapped by bringing an auxiliary waveguide into proximity to form a directional coupler of coupling constant $\kappa > 0$. With \underline{a}_s and \underline{a}_t being the annihilation operators for the signal and tap waveguide fields entering the coupler, and \underline{a}_s' and \underline{a}_t' the respective output field annihilation operators, the coupler equations are

$$\underline{a}_s' = (1 - \kappa)^{1/2} \underline{a}_s - \kappa^{1/2} \underline{a}_t, \quad (9)$$

$$\underline{a}_t' = \kappa^{1/2} \underline{a}_s + (1 - \kappa)^{1/2} \underline{a}_t.$$

We wish to show that TCS noise-reduction permits high SNR detection from \underline{a}_t' at very low coupling levels.

Suppose that the incoming signal field is the coherent state $|N_s^{1/2}\rangle$, which has N_s photons. An ordinary waveguide tap would not supply an input to the a_t -port, so that zero-point fluctuations prevail there. As a result a homodyne-detection measurement of a_{t1} yields signal-to-noise ratio

$$\begin{aligned} \text{SNR} &= \frac{\langle a_{t1}' \rangle^2}{\langle \Delta a_{t1}'^2 \rangle} \\ &= \frac{\kappa \langle a_{s1} \rangle^2}{\kappa \langle \Delta a_{s1}^2 \rangle + (1-\kappa) \langle \Delta a_{t1}^2 \rangle} \\ &= 4\kappa N_s. \end{aligned} \quad (10)$$

At low κ values, the predominant noise contribution comes from the vacuum-state fluctuations in a_{t1} . Thus, by supplying a TCS $|0; \mu, \nu\rangle$ at the a_t -port, with $\mu, \nu > 0$ chosen to make $\langle \Delta a_{t1}^2 \rangle = \kappa/4(1-\kappa)$ we get a signal-to-noise ratio

$$\text{SNR}_{\text{TCS}} = 2N_s \quad (11)$$

for all $\kappa > 0$. This shows that by means of TCS quantum-noise reduction a very low insertion loss tap can have the same signal-to-noise ratio as a 50% insertion loss ($\kappa=0.5$) conventional tap (Shapiro, J.H., 1980a).

5. DISCUSSION

The preceding result suggests that it may be possible for an unauthorized party to obtain information from an optical data bus in a virtually undetectable manner by employing a high SNR waveguide tap whose insertion loss is extremely small. In fact it may be considerably more difficult to achieve undetectable tapping of present-day fiber-optic networks in that we have omitted certain loss considerations as well as the effects of multiple spatial modes from our analysis. Nevertheless, the basic fact seems clear that quantum-noise reduction techniques permit very different communication possibilities than the usual semiclassical photodetection formulas would allow.

We foresee a TCS waveguide tap, in particular configured as a $\Delta\beta$ switch, as a new integrated-optics network element. With this device, the information waveguide can be tapped either at high insertion loss (in the conventional manner) or at low insertion loss (via TCS noise-reduction). In the former case new information can be loaded on the information waveguide through the a_t -port. In the latter, the original information remains, virtually unattenuated, on the main waveguide for other users farther downstream. An hierarchic data bus or a quasi-passive ring network are two network topologies which could benefit from the availability of such a switch/tap.

REFERENCES

- Gagliardi, R.M., and Karp, S., 1976, Optical Communications, Wiley, New York.
- Helstrom, C.W., Liu, J.W.S., and Gordon, J.P., 1970, "Quantum Mechanical Communication Theory," Proc. IEEE 58, 1578-1598.
- Helstrom, C.W., 1976, Quantum Detection Theory, Academic, New York.
- Holevo, A.S., 1973, "Statistical Decision Theory for Quantum Systems," J. Multivar. Anal. 3, 337-394.
- Kelley, P.L., and Kleiner, W.H., 1964, "Theory of Electromagnetic Field Measurement and Photoelectron Counting," Phys. Rev. 136, A316-A334.
- Shapiro, J.H., Machado Mata, J.A., and Yuen, H.P., 1979, "Optical Communication with Two-Photon Coherent States-Part II: Photoemissive Detection and Structural Receiver Performance," IEEE Trans. Inform. Theory IT-25, 179-192.
- Shapiro, J.H., 1980a, "Optical Waveguide Tap with Infinitesimal Insertion Loss," Opt. Lett. 5, 351-353.
- Shapiro, J.H., 1980b, "How to Tap a Fiber-Optic Link and Elude Detection," presented at the International Conf. on Quant. Electron., Boston, MA, J. Opt. Soc. Am. 70, 1401-1402A.
- Yariv, A., and Pepper, D.M., 1977, "Amplified Reflection, Phase Conjugation, and Oscillation in Degenerate Four-Wave Mixing," Opt. Lett. 1, 16-18.
- Yuen, H.P., Kennedy, R.S., and Lax, M., 1975, "Optimum Testing of Multiple Hypotheses in Quantum Detection Theory," IEEE Trans. Inform. Theory IT-21, 125-134.
- Yuen, H.P., 1976, "Two-Photon Coherent States of the Radiation Field," Phys. Rev. A 13, 2226-2243.

- Yuen, H.P., and Shapiro, J.H., 1978, "Optical Communication with Two-Photon Coherent States- Part I: Quantum State Propagation and Quantum Noise Reduction," *IEEE Trans. Inform. Theory* IT-24, 657-668.
- Yuen, H.P., and Shapiro, J.H., 1979, "Generation and Detection of Two-Photon Coherent States in Degenerate Four-Wave Mixing," *Opt. Lett.* 4, 334-336.
- Yuen, H.P., and Shapiro, J.H., 1980, "Optical Communication with Two-Photon Coherent States- Part III: Quantum Measurements Realizable with Photoemissive Detectors," *IEEE Trans. Inform. Theory* IT-26, 78-92.

USE OF A REMOTELY CONTROLLED INTEGRATED DIRECTIONAL COUPLER
SWITCH IN AN OPTICAL FIBER LINK

P. PAPUCHON, C. PUECH, and A. SCHNAPPER

THOMSON CSF Laboratoire Central de Recherches

B.P. n° 10

91401 ORSAY (FRANCE)

SUMMARY

For the past several years, there has been increasing interest shown in bistable optical devices. Optical bistability was first observed using Fabry Perot resonators filled with saturable absorbers or electrooptical materials to generate feedback and obtain bistable behaviour.

In fact a Fabry Perot cavity is not required and optical bistability has been observed with bulk or integrated modulators or switches.

In their output light intensity versus incident light intensity behaviour, such devices can exhibit hysteresis and can be used as optical limiters, pulse shapers, "optical transistors" and bistable switches.

In this paper experimental result concerning the remote control of a bistable directional coupler switch will be reported. It will be shown that the output light from the directional coupler can be switched from one channel to the other via switching informations contained in the incident light itself

INTRODUCTION

Since several years there has been increasing interest in bistable optical devices.

Optical bistability was first observed with Fabry Perot interferometer filled with saturable absorbers or electrooptical materials to generate the feedback and obtain the bistable behaviour (1-5).

In fact, to observe optical bistability it is sufficient to use a device the transmission of which is a non linear fonction of an external parameter. Then the effect can be observed using classical bulk or integrated modulators or switches (6-10).

In their output light intensity versus incident light intensity behaviour, such devices can exhibit hysteresis and can be used as optical limiters, pulse shapers, "optical transistors" and bistable devices.

In this paper we will report experimental results concerning the remote control of a bistable directional coupler switch.

DESCRIPTION OF THE DEVICE

Directional coupler switches in Ti : LiNbO₃ are now well known devices (11-13).

The operation of these devices is based on the evanescent coupling between two dielectric waveguides (in general single mode waveguides). Using the electrooptic effect, the properties of the coupler can be modified and an electrooptical switch can be realized.

The transmission characteristics of this kind of circuit depends on various important parameters which are : the coupling length l , the phase mismatch $\Delta\beta = \beta_1 - \beta_2$ between the two waveguides and the interaction length L which is the length along which the two waveguides are coupled.

A schematic of the basic directional coupler device is shown on Fig. 1.

If $E_1(z)$, and $E_2(z)$ are the amplitudes of the slowly varying electric fields of the guided light in the two waveguides, it can be shown easily that the light output intensities $I_1(L) \sim |E_1(L)|^2$ and $I_2(L) \sim |E_2(L)|^2$ can be expressed by

$$I_1(L) = (1 - 2A^2)^2 I_1(0)$$

$$I_2(L) = (1 - A^2)^2 4A^2 I_1(0)$$

when $I_2(0) = 0$ and where

$$A = \frac{L/\ell}{\sqrt{(L/\ell)^2 + (\frac{\Delta\beta L}{\pi})^2}} \sin \frac{\pi}{4} \sqrt{(L/\ell)^2 + (\frac{\Delta\beta L}{\pi})^2}$$

in the so call two section $\Delta\beta$ reversal configuration (12-13)

The switch is in the \otimes state

$$(I_1(0) = I_1(0), I_2(0) = 0; I_1(L) = 0, I_2(L) = I_1(0))$$

or in the \ominus state

$$(I_1(0) = I_1(0), I_2(0) = 0; I_1(L) = I_1(0), I_2(L) = 0)$$

when the following conditions are satisfied :

$$\otimes \text{ state : } A = \pm \frac{\sqrt{2}}{2}$$

$$\ominus \text{ state : } A = \{ \pm 1, 0 \}$$

These conditions are summarized on the switching diagram of Fig. 2 which is a plot of the loci of the \otimes and \ominus states as a function of L/ℓ and $\Delta\beta L/\pi$.

Experimentally the corresponding $\Delta\beta$ can be obtained using the electrooptical effect via electric fields applied with suitable electrodes (11-12-13).

To look at the properties of the switch as a bistable element, part of the light coming out from one of the waveguides is supposed to be detected and sent back to the drive electrodes. In the case where the light is detected at the output of waveguide 2, the induced $\Delta\beta$ can be written as :

$$\Delta\beta = 2G I_2(L) + (\Delta\beta_0)$$

Where $\Delta\beta_0$ is used to bias the switch to the desired operating point.

The switching characteristics $I_1(L) = f(I_1(0))$ can then be calculated and typical results are shown in Fig. 3 for a directional coupler in which $\frac{L}{\ell} \approx 2.05$ (corresponding to the coupler used in the experiments).

The type of response represented by the third curve in Fig. 3 can be used to realized a remotely controlled switch. Consider Fig. 4a where such a type of response has been redrawn for the two outputs of the switch (I_1 and I_2). Let us suppose that the input light intensity varies between $I_{inf.}$ and $I_{sup.}$. Thus, if the light emerges initially from the guide 1, by decreasing the input intensity below the value $I_{inf.}$, light will then come out from guide 2 and will stay in this state until the input light intensity becomes higher than $I_{sup.}$ in which case the light is switched back in waveguide 1. The corresponding outputs are shown on Fig. 4b and 4c.

EXPERIMENTS

Experiments have been performed to verify the previous conclusions. We use a two section stepped $\Delta\beta$ reversal directional coupler switch to obtain electrically the two states of the switch.

The waveguides are realized by titanium in diffusion technique in a C plate of LiNbO_3 -Gold electrodes are then realized and the edges of the crystal are polished to permit end fire coupling of the TE polarized light which is used all along the experiments.

The response of the switch when voltage is applied to the electrodes is shown on Fig. 5 (no feed-back)

For $\lambda = 5145 \text{ \AA}$ which is the wavelength used in our experiments, we have, for this particular coupler :

$$\ell = 4,97 \text{ mm}$$

$$\text{and } \frac{L}{\ell} \approx 2,05 \quad (L \approx 10 \text{ mm})$$

To observe the response of the device when inserted in a feedback loop the set up of Fig. 6 was used. The laser beam, amplitude modulated by an acoustooptic modulator (A.M.) is partly end-fire coupled in the device the other part being detected by PD_3 to give a signal proportional to the incident light. This signal is sent to the Y_3 (X) input of an oscilloscope.

The two output light intensities I_1 (I) and I_2 (L) are then detected by the photodetectors PD_1 and PD_2 and the corresponding signals sent to the Y_1 and Y_2 inputs of the oscilloscope. At the same time, a part of the detected signal coming from PD_2 is used to drive the electrodes A and D (feedback loop). The electrodes B and C receive a bias voltage inducing a Δp_0 which is adjusted to obtain a large bistability domain area.

By applying a triangular control signal the bistable behaviour of the switch can be observed (Fig. 7).

To achieve the remote control of the device, the CW level of the input light is adjusted to be slightly higher than I_{inf} . (in Fig. 4). A square wave voltage is superimposed and applied to the A.M. to simulate an information channel. At this point the maximum light intensity must be kept below I_{sup} . (in Fig. 4) to obtain the self switching of the device. By superposing an electrical pulse to the command voltage of the A.M. (input light intensity greater than I_{sup} .) the output is switched from guide 2 to guide 1.

By making the incident light suddenly lower than I_{inf} . the output is then switched back to waveguide 2.

The corresponding experimental results are shown on Fig. 8 where the top trace represents the command voltage of the A.M. (the switching pulse are not visible on this photograph). The two other traces show the outputs of guide 1 and 2 respectively switched on and off via periodical switching pulses contained in the incident light itself.

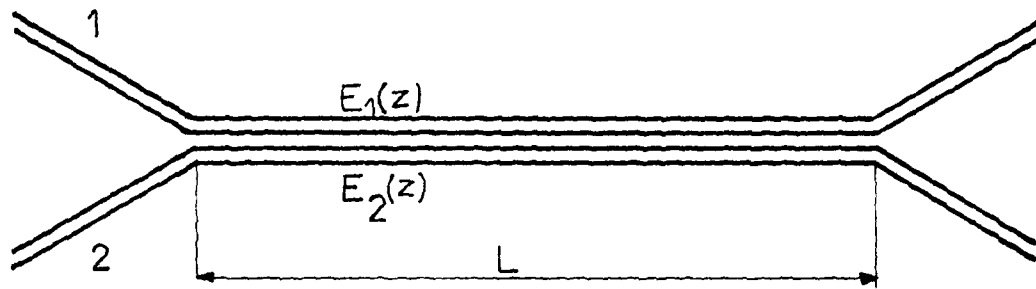
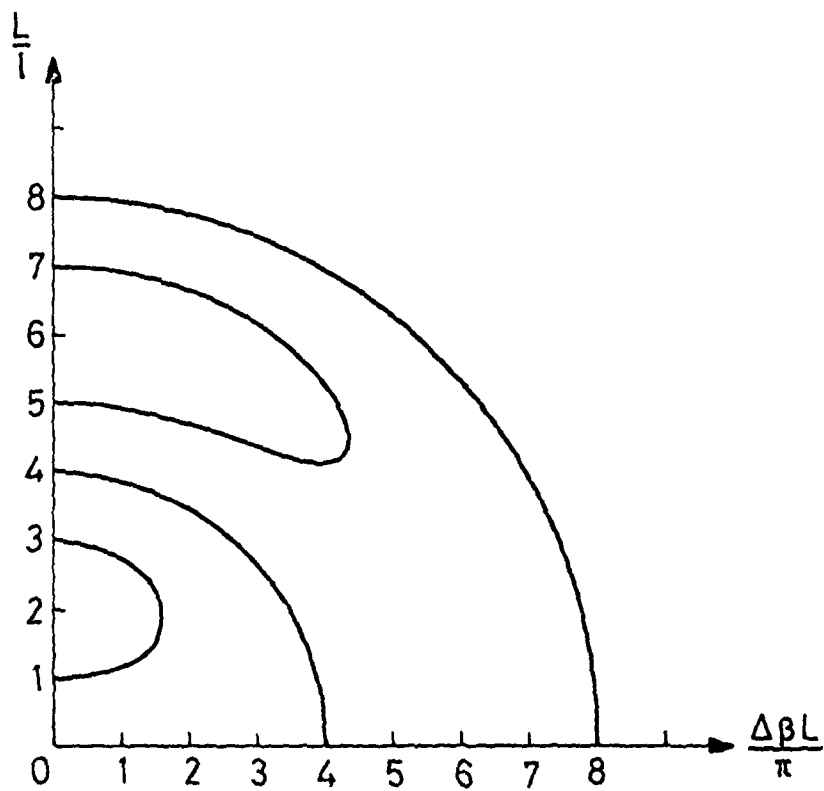
CONCLUSION

Experiments concerning the remote control of an integrated optical switch have been reported. In our case switching time of the order of 100 μ s has been obtained only limited by the electronic feedback loop. Much faster switching is expected since response time smaller than 500 ps has already been obtained for the switch itself.

Such remotely controlled switches can find important applications in high speed communication systems where the information train containing its own address can be self oriented to the desired output channel.

REFERENCES

- 1 - E. SPILLER "Saturable Optical Resonator"
J. Appl. Phys., vol. 43, pp. 1673-1681, 1972 -
- 2 - H.M. GIBBS, S.L. Mc CALL and T.N.C. VENKATESAN
"Differential Gain and Bistability Using a Sodium - Filled Fabry-Perot Interferometer" Phys. Rev. Lett., vol. 36, pp. 1135-1138, 1976 -
- 3 - P.W. SMITH and E.H. TURNER "A bistable Fabry-Perot resonator"
Appl. Phys. Lett., vol. 30, pp. 280-281, 1977 -
- 4 - P.W. SMITH, I.P. KAMINOW, P.I. MALONEY and L.W. STULZ
"Integrated Bistable Optical Devices" Appl. Phys. Lett., vol. 33, pp. 24-25, 1978 -
- 5 - P.W. SMITH, I.P. KAMINOW, P.J. MALONEY and L.W. STULZ
"Self- contained Integrated Bistable Optical Devices" Appl. Phys. Lett., vol. 34, pp. 62-65, 1979 -
- 6 - E. GARMIRE, J.H. MARBURGER and S.D. ALLEN "Incoherent Mirrorless Bistable Optical Devices" Appl. Phys. Lett., vol. 32, pp. 320-321, 1978 -
- 7 - E. GARMIRE, S.D. ALLEN, J. MARBURGER and C.M. VERBER
"Multimode Integrated Optical Bistable Switch" Opt. Lett., vol. 3, pp. 69-71, 1978 -
- 8 - A. SCHNAPPER, M. PAPUCHON and C. PUECH "Optical Bistability Using an Integrated two Arm Interferometer" Opt. Comm., vol. 29, pp. 364-368, 1979 -
- 9 - M. OKADA and K. TAKIZAWA "Optical Multistability in the Mirrorless Electrooptic Device with Feedback" IEEE J. Quantum Electron., vol. QE-15, pp. 82-85, 1979 -
- 10 - P.S. CROSS, R.V. SCHMIDT, R.L. THORNTON and P.W. SMITH "Optically Controlled Two Channel Integrated-Optical switch" IEEE J. Quantum Electron., vol. QE-14, pp. 577-580, 1978 -
- 11 - M. PAPUCHON, Y. COMBEMALE, X. MATHIEU, D.B. OSTROWSKY, L. REIBER, A.M. ROY, B. SEJOURNE and M. WERNER "Electrically switched Optical Directional Coupler : COBRA" Appl. Phys. Lett., vol. 27, pp. 289-291, 1975 -
- 12 - R.V. SCHMIDT and H. KOGELNIK "Electro Optically switched coupler with Stepped $\Delta\beta$ Reversal Using Ti-diffused LiNbO_3 Waveguides"
Appl. Phys. Lett., vol. 28, pp. 503-506, 1976 -
- 13 - H. KOGELNIK and R.V. SCHMIDT "Switched Directional Couplers with Alternating $\Delta\beta$ "
IEEE J. Quantum Electron., vol. QE-12, pp. 396-401, 1976 -

FIG. 1FIG. 2

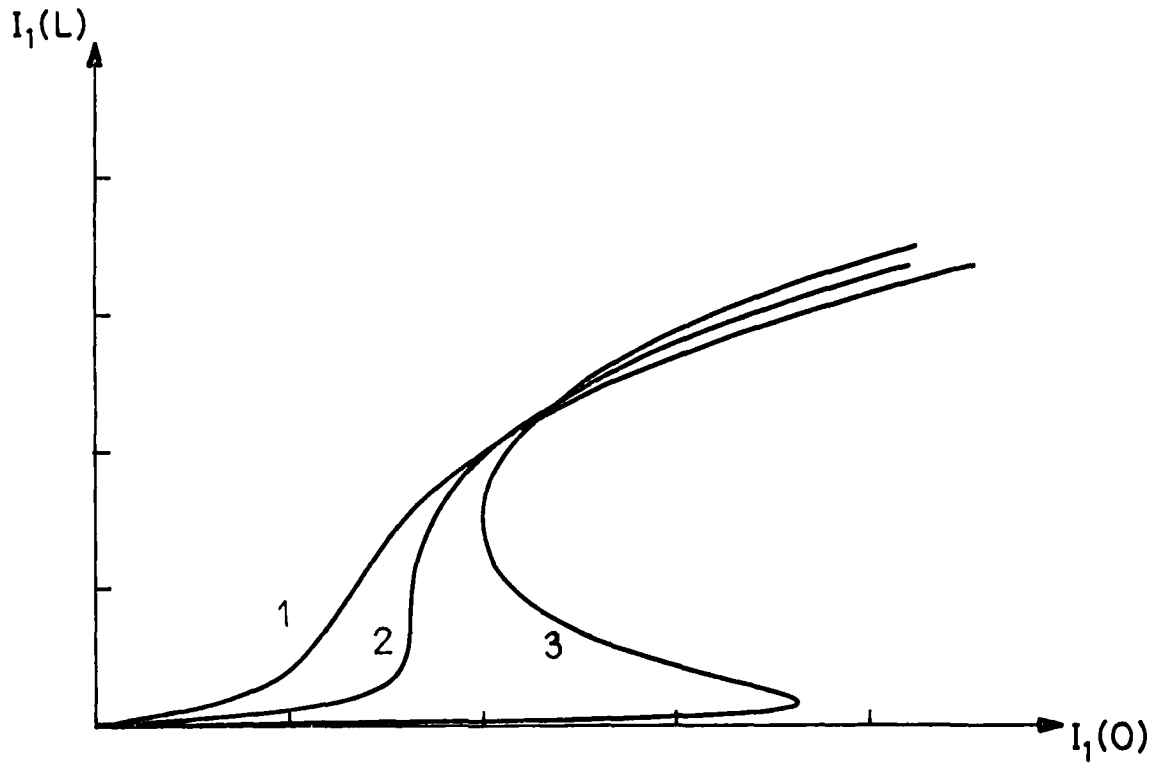


FIG. 3

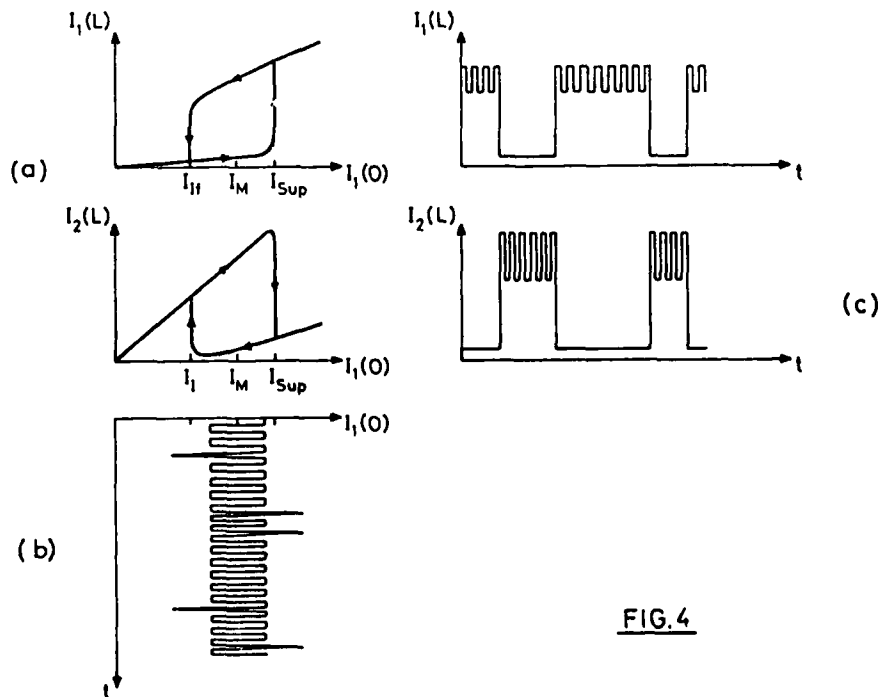


FIG. 4



Fig. 5

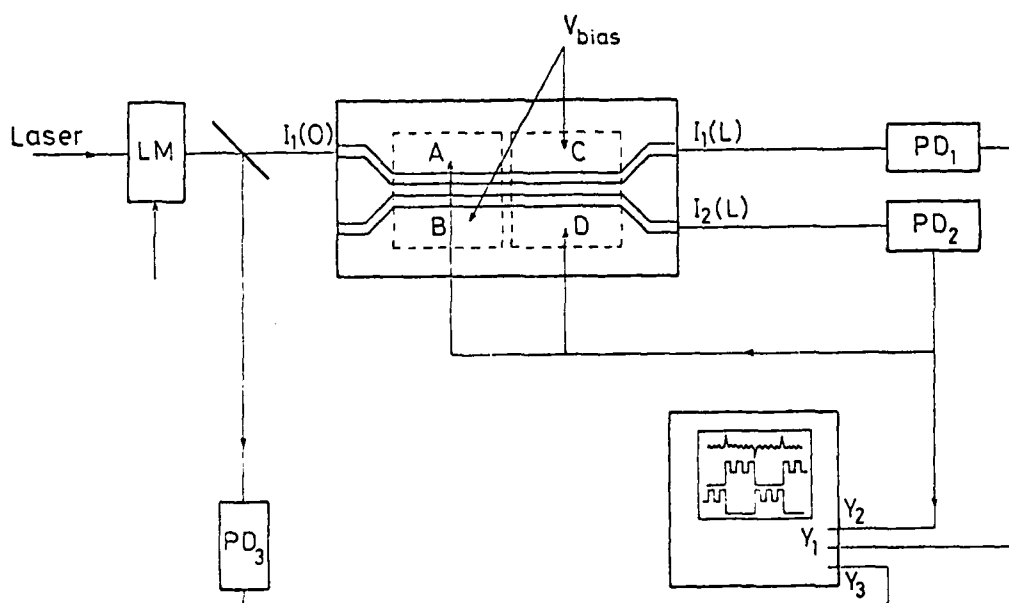


FIG.6

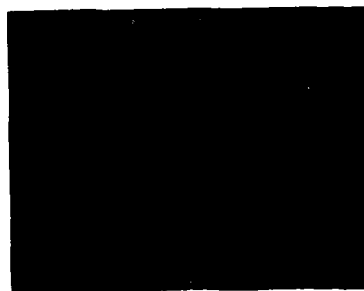


Fig. 7



Fig. 8

FIGURE CAPTIONS

- Fig. 1 - Directional coupler configuration
- Fig. 2 - Switching diagram of a two sections stepped $\Delta\beta$ reversal switch
- Fig. 3 - Theoretical response curves of a directional coupler switch inserted in a feedback loop (curves 1 to 3 coorespond to increasing values of which is used to bias the device).
- Fig. 4a) - Principle of the remotely controlled switch : output light intensities of guides 1 and 2 versus incident light intensity ($I_1(0)$)
- b) - typical incident light signal including the pulses for the remote control of the switch
- c) - output light intensities of guides 1 and 2 respectively when signal represented on fig. 4b is coupled in guide 1
- Fig. 5 - Response of the switch in the stepped $\Delta\beta$ reversal configuration (no feedback)
- Fig. 6 - Experimental set up used to test the properties of the switch when inserted in a feedback loop and to perform the remote switching experiments.
- Fig. 7 - Output light intensities in guides 1 and 2 when the switch is inserted in a feedback loop versus input light intensity. (upper trace : guide 2, lower trace : guide 1)
- Fig. 8 - Experimental results demonstrating the remote control of the switch :
 - top trace : input light intensity detected by PD 3 (the switching pulses are not visible on this photograph),
 - middle trace : output light intensity of guide 1 detected by PD 1,
 - bottom trace : output light intensity of guide 2 detected by PD 2.

QUESTIONS AND COMMENTS
ON SESSION V

NON-LINEAR OPTICS

Paper 35 : Non-linear adaptive optics

Mr. J. E. Jackson : How is the point ahead requirement accommodated for space applications ?

Dr. C. R. Giuliano : The point-ahead requirements are the same as for conventional adaptive optics and indicate the need for a beacon or retroreflector that leads the relay mirror by the required distance.

Paper 38 : Theory on non-linear propagation in multimode optical fibres

Pr. A. M. Scheggi : (1) Can you give practical values of power threshold beyond which these non-linear effects occur ?

(2) Did you consider solutions such as multimode graded index fibres ?

They should satisfy even better the assumption you make.

Dr. B. Crosignani : (1) Experimental soliton propagation has been obtained with powers of about 1 w (see Ref. 5).

(2) The present theory applies to any kind of index profile.

Paper 39 : Theory of non-linear pulse propagation in inhomogeneous dispersive media-application to optical waveguides.

Mr. J. Harris : Does the velocity of bright soliton propagation depend upon the soliton amplitude ?

Pr. N. Tzoar : In principle, if you use our equations (12) and (14a), the velocity of the bright soliton depends on the soliton amplitude. In practice however, for fibers, this dependence is very small. The main role of the soliton amplitude is to compensate between dispersion and non-linear effects to produce a steady state pulse.

Dr. G. R. Giuliano : When there is interest in propagating as solitons whole trains of pulses. Is there any concern about the possibility that a single pulse may propagate as a soliton. But once you consider many pulses the whole thing might fall apart. How far apart must they be in order not to perturb one another ?

Pr. N. Tzoar : I cannot give you a precise answer to your question. I do not know of a rigorous proof that a non-linear wave equation will support an undistorted train of pulses. Let us consider for a moment the case of a single pulse. If we look for the propagation of a truncated hyperbolic secant pulse, numerical solution indicates that the pulse propagates large distances without noticeable distortion provided the truncation is taken to be far in the tail of the pulse. It is therefore reasonable to assume that two well separated pulses will also propagate large distances without much distortion. However, quantitative information regarding your question can be only obtained either experimentally or by numerical solutions.

Paper 40 : How to tap a fiber-optic link and elude detection. What's new in quantum communication.

Dr. B. Crosignani : What happens to the entropy of the whole system ?

Pr. J. H. Shapiro : Quantum noise manipulation through TCS, generation does not violate fundamental physical laws. Consider the symmetric fluctuations of the Glauber coherent state : $\langle \Delta a_1^2 \rangle = \langle \Delta a_2^2 \rangle = 1/4$. The TCS with $\langle \Delta a_1^2 \rangle < 1/4$ and $\langle \Delta a_2^2 \rangle > 1/4$; $\langle \Delta a_1^2 \rangle \langle \Delta a_2^2 \rangle = 1/16$ will have more total noise $\langle \Delta a_1^2 \rangle + \langle \Delta a_2^2 \rangle$ than the value 1/2 found for Glauber states. Thus, by analogy with a refrigerator as pointed out by Willard Wells, we are "cooling" part of the universe and "heating" another part in such a way that total fluctuations (and hence entropy) are increased. Moreover, as with the refrigerator, TCS generation requires an expense of energy in order to drive the quadrature components away from their natural condition of symmetric noise content.

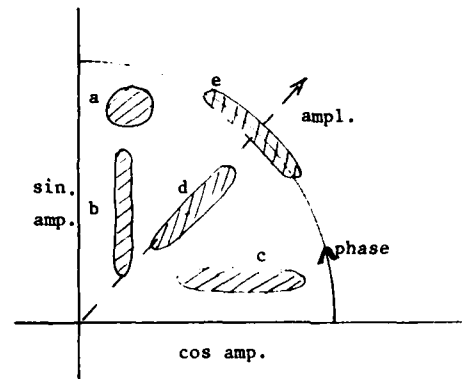
Dr. W. H. Wells : As I understand this, you take noise out of one quadrature, say $\cos \omega t$ at the expense of the other $\sin \omega t$, which is then very noisy. So you must be very careful of phase stability. In particular, a counter measure to tapping is simply to use unstable phase deliberately, as in conventional fiber-optic communications. Even in an advanced homodyne system, one could deliberately use a laser with very short coherence length and equal paths of signal and phase reference from the same laser. In this case it appears that a tapper must extract lots of power merely to make his phase-tracking loop work. Is this correct ?

Pr. J. H. Shapiro : In essence, what you say is true. My analysis for waveguide tapping has been presented for single-mode waveguides and monochromatic light sources. However the future direction of fiber-optic communications seems to be heading towards single-mode fibers with lasers whose frequency stability is compatible with heterodyne/homodyne detection. Moreover some groups are specifically working towards heterodyne reception fiber-links. In such links one can in principle adopt a spread-spectrum modulation format ; retain heterodyne detection at the intended receiver ; make tapping very difficult. This would then be a fiber-optic version of spread-spectrum low-probability of intercept radio communication.

Pr. W. H. Wells : I like to think of quantum noise by analogy to thermal noise. Then is it valid to think of your 4-wave system as a quantum refrigerator ? In this analogy, it cools one quadrature dumping heat in the other. As in the Carnot cycle, there is a fundamental limit on efficiency, so more heat is dumped in one quadrature than is extracted from the other. Then the problem of phase stability is one of insulating the heat sink from the quadrature that is cooled. Right ?

Pr. J. H. Shapiro : Indeed, by skewing the noise distribution between the quadratures one must supply energy to the system. As shown in my published works however, the energy in the TCS beam needed for waveguide tapping remains quite modest at 10-20 dB quantum noise reduction.

Dr. W. H. Wells : On a phasor diagram (see sketch) I understand that you change the usual circular uncertainty (a) to a vertical or horizontal ellipse (b or c). Is there a way to make the ellipse always radial (d) so that phase modulation is noiseless ? Or in the phase direction (e) so that AM is noiseless ? If not, is the limitation fundamental or state of the art ?



Pr. J. H. Shapiro : One can set up a TCS noise ellipse to have any angular orientation desired by choice of the state parameters. This will not however lead to noiseless reception for analog transmission using phase modulation. Low-noise reception of double-sideband suppressed carrier amplitude modulation, on the other hand is possible, as can be deduced from amplitude modulation results in my published work.

Dr. W. H. Wells : Will you do the experiment ?

Pr. J. H. Shapiro : Yes.

- Paper 41 : Use for remotely controlled integrated directional coupler switch in an optical fiber link.

Ir. T. Bakker : In order to determine the amplification of your optical transistor, it must be rather important to know the amplification in the reverse direction. The feed back from the output to the input. Did you measure that as well ?

Dr. J. P. Huignard : In the optical transistor mode a low modulation can be amplified, for example, we demonstrated a gain of about 50, using a characteristic with a very non-linear part. I do not think we have studied this problem in detail.

General comment (Round table discussion)

Dr. W. H. Wells : Nonlinear optics is not my specialty and my opinion may not be authoritative.

I was very intrigued with the phase conjugation discussion and the interesting way that those waves behave to take errors in the propagation medium and various other applications. We heard about two such techniques : One involving a simulated Brillouin scattering and the other involved four wave mixing. I guess that was sort of a subject to itself, the four wave mixing, and its applications and we went from there to optical fibers and non-linearities in these which is quite a different subject. These non-linearities are not in the sorts of time intervals, bandwidths and powerlevels used in optical telecommunications today, but I am looking forward to a time when we shall see this experimentally observed and pulses hanging together by virtue of non-linearity in the fiber medium itself.

I was quite intrigued with Dr. Shapiro's technique for getting rid of the quantum noise in one quadrature, cooling off the cosine while heating up the sine phase in a link. Most people accept this as being quite fundamental, until you look into it then it isn't quite so fundamental. Experiments have not been done, but are forthcoming I understand from him. I am not sure what the practical implications are there and will be intrigued to find out.

RESOLVING POWER EVALUATION OF OPTICAL ADAPTIVE SYSTEMS THROUGH THE ATMOSPHERE

Anna Consortini
 Istituto di Ricerca sulle Onde Elettromagnetiche of C.N.R.
 Via Panciatichi, 64
 50127 Firenze (Italy)

SUMMARY

The resolving power is evaluated of coherent optical adaptive systems in the turbulent atmosphere. General formulas are given for two systems which produce different kinds of partial corrections of phase and amplitude fluctuations. Numerical results are presented in the case of a modified Karman model of turbulence. The conclusion is that even a partial correction can allow one to overcome the limit of the aperture diameter imposed by the turbulence.

1. INTRODUCTION

In recent years adaptive optical systems have been developed, where suitable techniques allow one to compensate, at least partially, for the deformations of the incident wavefronts due to the medium in front of the optical instruments. Such a compensation may be obtained in real time. As a consequence an improvement of the image quality is obtained.

In the present paper we evaluate the resolving power of an adaptive optical system, operating in the atmosphere, which partially corrects a radiation, initially coherent, deteriorated by the atmospheric turbulence. The considered model of turbulence is of Karman type.

To correct, (partially) the field fluctuations means to reduce the structure function or the power spectrum of the fluctuations. Therefore in order to investigate the resolution of the system one needs to know what kind of correction the system introduces and what the residual fluctuations are. One problem is therefore to describe in a sufficiently simple and general way the behaviour of the correcting system. We have examined two different behaviours. In a case the power spectra of the fluctuations of phase and of amplitude respectively are cut at a given frequency κ_c , which corresponds to eliminate all the fluctuations having a spatial frequency less than κ_c and to maintain unaltered the fluctuations with frequencies higher than κ_c . This behaviour has been already used by other Authors (FANTE 1976, and WANG 1977) in connection with a Kolmogorov-Tatarski model of turbulence. In the other case the system is assumed to reduce the structure functions of amplitude and phase fluctuations by factors less than one. Both cases of short and long exposures have been also examined. Horizontal propagation has been considered.

2. POSITION OF THE PROBLEM

From the point of view of image formation the optical system can be skematized as a lens of diameter D and focal length F , illuminated by the corrected radiation. According to FRIED (1966) the resolving power of a system illuminated by a radiation having travelled a path in a random medium is described in terms of the quantity \mathcal{R} defined as

$$\mathcal{R} = 2\pi \int_0^{D/\lambda F} \langle \tau(f) \rangle f df \quad (1)$$

where f denotes the spatial frequency, λ the wavelength and $\langle \tau(f) \rangle$ the modulation transfer function of the "optical system" constituted by the lens and the turbulent medium. Brackets denote statistical averages. Recall that in the case of long exposures the resolving power is obtained with a sufficiently long exposure time (theoretically infinitely long), while in the case of short exposures the resolving power represents the mean value obtained by averaging an infinite number of instantaneous images. It is well known that in the case isoplanatism the transfer function $\langle \tau(f) \rangle$ can be written as a product of two transfer functions

$$\langle \tau(f) \rangle = \tau_0(f) \exp \left[-\frac{1}{2} G(\lambda F f) \right] \quad (2)$$

where $\tau_0(f)$ denotes the transfer function of the lens given by

$$\tau_0(f) = \frac{2}{\pi} \left[\arccos \frac{\lambda F f}{D} - \frac{\lambda F f}{D} \left\{ 1 - \left(\frac{\lambda F f}{D} \right)^2 \right\}^{1/2} \right] \quad \text{for } f < \frac{D}{\lambda F}$$

$$\tau_0(f) = 0 \quad \text{for } f > \frac{D}{\lambda F} \quad (3)$$

and the exponential term represents the modulation transfer function due to the atmosphere. Our unlimited confidence in the adaptive techniques leads us to the work hypothesis that the system corrects also the anisoplanatism due to the turbulence, so that we can apply eq. 2.

The expression of $G(\lambda Ff)$ is different in the two cases of short and long exposures. For long exposures one has

$$G(\rho) = D_w(\rho) = D_x(\rho) + D_s(\rho) \quad (4)$$

where D_w denotes the wave structure function of a spherical wave having travelled a path L in the atmosphere and having been corrected by the adaptive techniques. D_w is the sum of the corresponding structure functions of the log-amplitude D_x and of the phase D_s . In the case of short exposures

$$G(\rho) = D_w(\rho) - 32 \left(\frac{\lambda F f}{D} \right)^2 \int_0^D (F_c - F_L) D_s(r) r dr \quad (5)$$

where

$$F_c - F_L = \frac{4}{\pi} \left[-\arccos \frac{r}{D} + \left\{ 3 \frac{r}{D} - 2 \left(\frac{r}{D} \right)^3 \right\} \left\{ 1 - \left(\frac{r}{D} \right)^2 \right\}^{1/2} \right] \quad (6)$$

These are approximated expressions, as noted by WANG (1977), and care must be taken to use them within the limits of their validity.

The atmospheric turbulence, assumed to be homogeneous and isotropic, is described by means of a modified Karman model, according to which the spatial frequency spectrum of the refractive index fluctuations is given by

$$\phi_n(\kappa) = 0.033 C_n^2 \exp(-\kappa^2/\kappa_m^2) (\kappa^2 + \kappa_o^2)^{-11/6} \quad (7)$$

where C_n^2 represents the structure constant of the refractive index, $\kappa_m = 5.92/\lambda_o$ and $\kappa_o = 1/L_o$, λ_o and L_o denoting the inner and the outer scale of the turbulence, respectively. This expression of the spectrum allows one to take into account the effect of both the inner and the outer scale of the turbulence. For small fluctuations, the two-dimensional spectral density of phase fluctuations, F_s' , and that of log-amplitude fluctuations F_x' of a spherical wave, after a path L in the atmosphere, without any correction, are given by (ISHIMARU A., 1969).

$$F_s'(\kappa) = 2\pi k^2 \int_0^L \left(\frac{L-n}{n} \right)^2 \cos \left(\frac{L(L-n)\kappa^2}{2kn} \right) \phi_n \left(\frac{\kappa L}{n} \right) dn \quad (8)$$

$$F_x'(\kappa) = 2\pi k^2 \int_0^L \left(\frac{L-n}{n} \right)^2 \sin \left(\frac{L(L-n)\kappa^2}{2kn} \right) \phi_n \left(\frac{\kappa L}{n} \right) dn \quad (9)$$

respectively. The corresponding structure functions D_s' and D_x' result to be of the form

$$D_s'(\rho) = 8k^2\pi^2 \int_0^\infty [1 - J_0(k\rho)] k dk \int_0^L \left(\frac{L-n}{n} \right)^2 \cos^2 \left(\frac{L(L-n)\kappa^2}{2kn} \right) \phi_n \left(\frac{\kappa L}{n} \right) dn \quad (10)$$

$$D_x'(\rho) = 8k^2\pi^2 \int_0^\infty [1 - J_0(k\rho)] k dk \int_0^L \left(\frac{L-n}{n} \right)^2 \sin^2 \left(\frac{L(L-n)\kappa^2}{2kn} \right) \phi_n \left(\frac{\kappa L}{n} \right) dn \quad (11)$$

The "prime" on top denotes structure functions not corrected by the adaptive system. Correspondingly the function $G(\rho)$ given by Eq.(5) takes the form $G'(\rho)$ given by

$$G'(\rho) = D_x' + 0.264 k^2\pi^2 C_n^2 \int_0^L dn \left(\frac{L-n}{n} \right)^2 \cdot \int_0^\infty \cos^2 \left(\frac{L(L-n)\kappa^2}{2kn} \right) \frac{e^{-(\kappa L)^2 / (\eta \kappa_m)^2}}{\left[\kappa_o^2 + \left(\frac{\kappa L}{n} \right)^2 \right]^{11/6}} H k dk \quad (12)$$

where

$$H = 1 - J_0(k\rho) \quad \text{for long exposures} \quad (13)$$

$$H = 1 - J_0(k\rho) - 64 \frac{-Q^2}{\left(\frac{\kappa_o D}{2} \right)^2} J_2 \left(\frac{\kappa_o D}{2} \right) \quad \text{for short exposures}$$

3. RESOLVING POWER OF ADAPTIVE SYSTEMS

3.1. System acting on the spectra of fluctuations as a high pass filter

Let us assume that the partial correction introduced by the system is such that the spectra F_S and F_X of phase and amplitude fluctuations after correction be given by

$$\begin{aligned} F_S &= F_X = 0 & \text{for } \kappa < \kappa_C \\ F_S &= F'_S & \text{for } \kappa \geq \kappa_C \\ F_A &= F'_A & \end{aligned} \quad (12)$$

where κ_C depends on the considered system. This corresponds to evaluate the integrals in dk , appearing in Eqs. (10), (11), and (12), from κ_C to infinite, instead of from 0 to infinite.

In Fig. 1 the results are reported of the numerical evaluation for a system using a radiation operating at the wavenumber $k = 10^7 \text{ m}^{-1}$, after a path of 1 km through the atmosphere, in a particular case of atmospheric turbulence. Solid lines refer to long exposures, dashed lines to short exposures. The resolving power, suitably normalized, is represented versus aperture diameter, for a number of values of κ_C . The curve $\kappa_C = 0$ corresponds to the case of no correction, the line $\kappa = \infty$ to perfect correction. In abscissa is represented also the quantity $\kappa_0 D$.

3.2 System acting on the spectra of fluctuations as an attenuator

In this case the correction introduced by the system is assumed to be such that the spectra F_S and F_X , after correction, be given by:

$$F_S = \alpha F'_S \quad F_X = \beta F'_X$$

where α and β are constant factors not larger than 1. On the aperture the corrected structure functions are given by:

$$D_S(\rho) = \alpha D'_S(\rho) \quad C_X(\rho) = \beta D'_X(\rho)$$

Consequently Eq.12 becomes

$$G(\rho) = \alpha D'_X + 0.264 \beta k^2 \pi^2 C_n^2 \int_0^L dn \left(\frac{L}{n}\right)^2 \cdot \int_0^\infty \cos^2\left(\frac{L}{2} \left(\frac{L}{kn} - \rho\right) k\right) \frac{e^{-\frac{(\kappa L)^2 / (\kappa \kappa_m)^2}{\left[\kappa_0^2 + \left(\frac{\kappa L}{n}\right)^2\right]^{11/6}}}}{H} \kappa d\kappa$$

where H is still given by (13).

Numerical computations have been done for this type of correction in the case as Fig.1.

The resolving power versus the diameter aperture is represented in Fig.2 for different values of α and β . Solid lines refer to long exposures, dashed lines to short exposures. The asymptotic behaviour is represented by straight lines. Each line is labelled by the couple of values α and β . As it appears from these figure, amplitude fluctuations play a practically negligible role as expected. This result is in agreement with results that WANG (1977) and FANTE (1976) have obtained in the case of Kolmogorov-Tatarski turbulence and systems correcting the spectrum.

4. DISCUSSION AND CONCLUSION

As it appears from Figs 1 and 2, for both types of adaptive corrections examined the short exposures are favourable with respect to the long ones at low corrections and diameters of the order of L_0 . At larger diameters they coincide. At low corrections there is an optimum value of D where the resolving power presents a maximum. This behaviour can be qualitatively explained by noting that for values of D sufficiently small ($< L_0$) the aperture is smaller than a coherence area of the phase and the overall effect of the turbulence over the aperture is a tilt of the wavefront. If on the contrary the diameter becomes large and comprises a large number of coherence areas the averaging effect of the aperture is the same (ergodic theorem) as that of time.

The main result of the present work is that even partial corrections of the phase fluctuations give rise to large increases in the resolving power. If the corrections are sufficient ($\kappa_C = 3$ for systems of the first kind here considered, and $\alpha = .2$ for systems of the second type) the limitations imposed by the turbulence on the aperture diameter are overcome and the resolving power continuously increases with the aperture diameter.

REFERENCES

FANTE R.L., J.Opt.Soc.Am. 66, 730, 1976

FRIED D.L., J.Opt.Soc.Am., 56, 1372, 1966

ISHIMARU A., Radio Science 4, 295, 1969; see also CARLSON F.P. and ISHIMARU A., J.Opt.Soc.Am. 59, 319, 1969

WANG J.Y., J.Opt.Soc.Am., 67, 383, 1977.

* A discussion on the different results obtained for a conventional system when taking or not taking into account K is developed in: A.Consortini and L.Ronchi JOSA 63, 1246, 1973 and A.Consortini, P.Pandolfini, L. Ronchi and R.Vanni in Space Optics ISBN0-309-02144-8 National Academy of Sciences Washington D.C. 1974, P.490.

Note added in proofs: During the Conference, D.P.Greenwood pointed out the paper: D.P.Greenwood J.O.S.A. 69, 549, 1979 where he discusses the MTF of a wavefront corrected by segmented corrector with either piston only or piston with a local tilt fit.

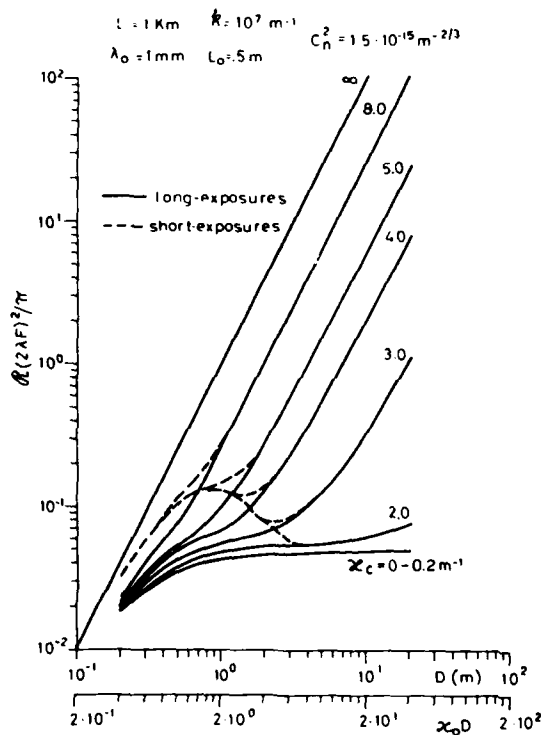


Fig. 1

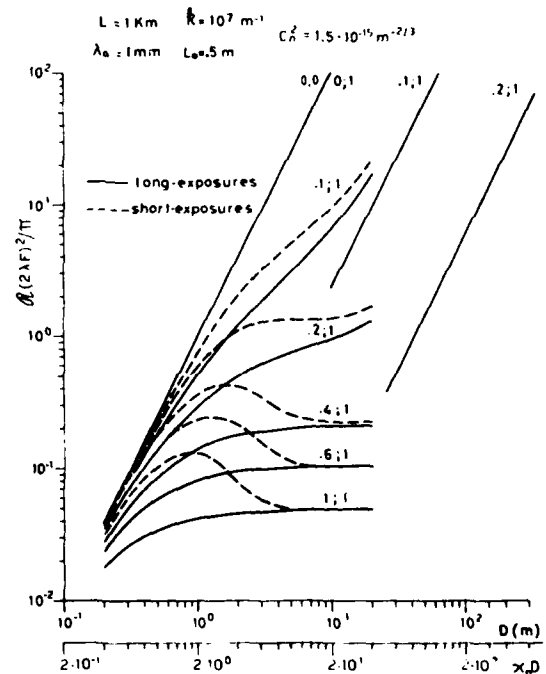


Fig. 2

ADAPTIVE OPTICS FOR THERMAL BLOOMING

by

Wilbur P. Brown
Hughes Research Laboratories
3011 Malibu Canyon Road
Malibu, California 90265

ABSTRACT

Fundamental limitations on the ability to correct for the effects of thermal blooming will be discussed. It will be shown that in contrast to the correction of linear propagation effects such as those caused by atmospheric turbulence, in which essentially full correction can be achieved given a suitable reference, the effects of thermal blooming cannot be completely compensated for in general. The degree to which thermal blooming can be compensated depends on the magnitude of the blooming effects, their distribution along the propagation path, and the type of correction algorithm. Optimum correction is obtained by adaptive algorithms that are based on sensing target plane irradiance with a time constant that is long compared to the thermal blooming time constant. In fact, systems that respond faster than the medium may cause the target irradiance to decrease rather than increase. Conventional return wave adaptive systems that sense the phase of the reference wave and outgoing wave multidither systems that employ fast phase dithers in conjunction with a target irradiance sensor suffer this defect. Adaptive systems based on a slow dithering of the transmitted wave in conjunction with a target irradiance sensor provide the best correction. Computer simulation results illustrating these considerations will be given. In addition, results from work in progress on the combined effects of thermal blooming and turbulence at visible wavelengths and the adaptive correction of these effects will also be discussed. We expect this work to show that amplitude scintillation associated with the turbulence will significantly affect the degree of correction obtained.

Anisoplanatism In Adaptive Optics

David L. Fried

the Optical Sciences Company
Placentia, Ca. 92670

ABSTRACT

In this paper we examine the consequences for an adaptive optics system of the fact that the turbulence induced wavefront distortion for two propagation paths with only very slightly different propagation directions can be significantly different. We consider the implications of this fact for a compensated imaging system and for an adaptive optics laser transmitter. Theory and numerical results are presented. The basic results are presented in terms of the average optical transfer function of a compensated imaging system in terms of the average antenna gain of an adaptive optics laser transmitter, each expressed as a function of the angular separation, θ , between the propagation path along which the reference signal arrives and the propagation path along which the adaptive optics system is to provide performance.

It is shown that for high spatial frequencies (for the compensated imaging system), and for large aperture diameters (for the adaptive laser transmitter), i. e., large compared to r_0/λ and to r_0 , respectively, the magnitude of the anisoplanatism effect can be characterized by an "isoplanatic patch" angular size which we denote by θ_0 . If the angular separation between the two propagation paths is θ , it is shown that the optical transfer function and the antenna gain are each reduced by a factor of $\exp[-(\theta/\theta_0)^{5/3}]$. This simply expressed performance reduction factor represents an asymptotic limit for very high spatial frequencies and for very large transmitter diameters. For lower spatial frequencies and smaller transmitter diameters the reduction factor is not as severe. Numerical results are presented to illustrate this.

1. Introduction

In this paper we shall present some results which we have obtained over the last several years in analyzing limitations in the performance of adaptive optics systems. We have been concerned with the performance of an adaptive optics imaging system as measured by the OTF, and the performance of an adaptive optics laser transmitter as measured by the antenna gain. We shall present results concerning two effects which can degrade system performance — which two effects we refer to here as "random apodization", and as "anisoplanatism".

While adaptive optics are normally thought of as providing only phase corrections, they could also adjust the transmission across the aperture. This can be thought of as representing a complex phase correction, where conventional adaptive optics only provide the real part of the complex phase correction. Provision of the ability to also provide the imaginary part of the complex phase correction can be thought of as representing an apodization capability. Since this would be used to compensate for the random effects of atmospheric turbulence we consider it to represent a random apodization capability — hence our choice of the term.

We shall present results defining system performances with and without random apodization. Rather surprisingly we have found that the form of the random apodization correction that optimizes performance of an adaptive optics imaging system is quite different from that which optimizes performance of an adaptive optics laser transmitter. It will be noted in examining these results that in general the magnitude of the effects associated with random apodization are quite small, nominally inconsequential.

The adaptive optics systems we are concerned with rely on a beacon to provide information on the instantaneous (random) phase correction required to produce compensation for the effects of atmospheric turbulence. It is normally assumed that the beacon is colocated with the target, the target being either the object being imaged or the aim-point to which the transmitted laser beam is directed. When this assumption is satisfied, and if there are no wavelength (dependent refraction effects) differences between the beacon and the imaging signal or laser beam, then there should be essentially perfect coincidence of the two propagation paths between the adaptive optics system and the beacon, and between the adaptive optics system and the target. When the two paths are exactly coincident then the wavefront distortion that is sensed by analyzing the beacon is exactly what the adaptive optics should be adjusted to correct for. In that case the adaptive optics system's imaging or laser transmitter performance will be exactly equal to the diffraction limited value. If the beacon is located in a position (or rather in a direction) that is slightly displaced from that of the target then the system performance can still be very nearly equal to the diffraction limited value, but only if the separation of the beacon and the target is sufficiently slight. In such a case we say that the beacon and the target are in the same isoplanatic patch.

If the separation between the positions of (or rather the directions to) the beacon and the target is more substantial, then the two propagation paths through the atmospheric turbulence will be significantly different. In such a case the wavefront distortion measured by observing the beacon does not accurately indicate what adaptive optics wavefront distortion correction is needed to compensate for the turbulence encountered on the target's propagation path. As a result the adaptive optics system performance will be significantly less than diffraction limited. For this case we say that the system is suffering from anisoplanatism effects.

In this paper we shall present results for the effects of anisoplanatism on system performance of an adaptive optics imaging system and of an adaptive optics laser transmitter. Results will be shown including random apodization effects, both with and without random apodization compensation in the adaptive optics, as well as results obtained with a very simple geometric optics propagation theory, in which random apodization considerations are manifestly absent. An examination of these results will show that in general, no matter how it is treated the random apodization effects are more-or-less inconsequential and that the geometric optics type results contain all of the interesting aspects of the results.

Starting from the geometric optics version of the anisoplanatism dependence results we shall show how the formulas giving the results can be cast into a quite generalized and numerically quite easy to use form. It will be shown that the propagation path can be characterized by a very few propagation parameters. Finally a set of graphs will be presented in normalized form allowing the effects of anisoplanatism on the performance of optics systems to be rapidly determined.

2. Diffraction Limited System Performance

We take the optical transfer function (OTF) as our basic measure of the performance of an imaging system. Working with a spatial frequency vector \vec{f} , whose magnitude, f , is measured in cycles per radian of field-of-view. For operation at a wavelength λ with a clear circular aperture of diameter D it is well known that the diffraction limited OTF can be written as

$$T_{DL}(\vec{f}) = K(\lambda f/D) \quad (1)$$

where

$$K(x) = \begin{cases} 2/\pi [\cos^{-1}(x) - x(1-x^2)^{1/2}] & , \quad \text{if } x \leq 1 \\ 0 & , \quad \text{if } x > 1 \end{cases} \quad (2)$$

For a laser transmitter it is convenient to define the antenna gain as the ratio of peak power density at the aim-point to the transmitted laser power, all times the square of the range from the transmitter to the target. This definition differs from the rf engineering definition of transmitter antenna gain relative to isotropic to the extent that it yields a value for antenna gain that is numerically smaller by a factor of $(4\pi)^{-1}$ than the gain defined relative to isotropic. Our definition has the convenience of having dimensions of inverse steradians, and thus being in a sense the inverse of the laser transmitter's beam spread. This antenna gain times the transmitted laser power gives the effective laser beam intensity in the far field in units of watts per steradian. It is easy to show that for a diffraction limited laser transmitter operating at a laser wavelength λ , and having a clear circular aperture of diameter D , the antenna gain is

$$G_{DL} = \frac{1}{4} \pi (D/\lambda)^2 \quad (3)$$

3. Random Apodization Effects

Atmospheric turbulence will produce a complex phase shift on the beacon signal. Measured at the position denoted by the two-dimensional vector \vec{r} on the aperture plane of our optical system, we write this random complex phase shift as $\phi(\vec{r}) - i\ell(\vec{r})$. The real part of this, $\phi(\vec{r})$, is the random function which we normally understand when we refer to the "turbulence induced phase shift". Conventional adaptive optics measure and compensate for this real phase shift, $\phi(\vec{r})$. The (negative of the) imaginary part of the complex phase shift, $\ell(\vec{r})$, is referred to as the "log-amplitude variation" and is a logarithmic measure of the variation (called scintillation) of beacon intensity across the aperture plane. It is this variation that gives rise to the random apodization effects, and for which adaptive optics with random apodization compensation capability must compensate.

Where ordinary adaptive optics applies a real phase correction equal to $-\phi(\vec{r})$, adaptive optics with random apodization correction would apply a complex phase shift correction equal to $-\phi(\vec{r}) + i\mu\ell(\vec{r})$. Here μ is some constant chosen to optimize system performance*. It is easy to see that for an adaptive optics imaging system with random apodization compensation, the performance of an imaging system will be optimized with $\mu = +1$. For an adaptive optics laser transmitter system with a capability of providing random apodization compensation we find that while the choice of the optimum value of μ is not nearly so sharply defined, it appears that for most situations choosing $\mu = -1$ gives very near optimum results.

To present our results for system performance considering random apodization effects, it is first necessary to define the statistics of log-amplitude variation. The statistical nature of the log-amplitude variation is given for our purposes by the log-amplitude covariance, $C_\ell(\rho)$. This function is defined by the expression

$$C_\ell(|\vec{r} - \vec{r}'|) = \langle [\ell(\vec{r}) - \bar{\ell}] [\ell(\vec{r}') - \bar{\ell}] \rangle \quad (4)$$

* There are some very real practical (possibly also fundamental) problems involved in trying to implement random apodization correction. Working with extreme values for μ will simply aggravate these problems. Here we shall ignore this matter of practicality.

where

$$\bar{l} = \langle l(\vec{r}) \rangle \quad (5)$$

The angle brackets, $\langle \dots \rangle$, used here and throughout this paper imply an ensemble average. Implicit in the fact that in Eq. (4) C_l is not written as a function of $\frac{1}{2}(r+r')$ [as well being a function of $(r-r')$] and that l in Eq. (5) is not written as a function of \vec{r} , is the assumption of stationarity of the log-amplitude statistics.

We have been able to show that for an adaptive optics imaging system (when the beacon and the target are coincident, so that there is no anisoplanatism) if the system does not provide for random apodization compensation, the optical transfer function can be written as

$$\langle T(\vec{f}) \rangle = T_{0L}(\vec{f}) \exp [-C_l(0) + C_l(\lambda f)] \quad (6)$$

It is appropriate to remark here that the nature of the propagation statistics is such that the log-amplitude variance, $C_l(0)$, is never significantly greater than 0.5, and that the log-amplitude covariance is a relatively short range function, i. e., $C_l(\vec{r})$ vanishes for large values of r . Since λf corresponds to the diameter of an aperture whose diameter is such that it just barely allows diffraction limited imaging of the spatial frequency, f , for the higher spatial frequencies which mostly are of interest to us, $C_l(\lambda f)$ can be considered to be very nearly zero. In this case we can write

$$\langle T(\vec{f}) \rangle \approx T_{0L}(\vec{f}) \exp [-C_l(0)] \quad (7)$$

When random apodization correction is provided by the adaptive optics, with $\mu = +1$, there is no residual turbulence induced degradation. In that case it can be shown that the imaging system's OTF is identical to the diffraction limited value, i. e.,

$$\langle T(\vec{f}) \rangle = T_{0L}(\vec{f}) \quad (8)$$

For an adaptive optics laser transmitter (when the beacon is coincident with the target, so that there is no anisoplanatism) if the system does not provide for random apodization compensation, then it can be shown that the antenna gain is given by the expression

$$\langle G \rangle = G_{0L} \exp [-C_l(0)] \left\{ \frac{\int d\vec{r} K(r/D) \exp [C_l(\vec{r})]}{\int d\vec{r} K(r/D)} \right\} \quad (9)$$

where D is the aperture diameter. In as much as the log-amplitude covariance function, $C_l(\vec{r})$, is a short range function relative to aperture diameters that are nominally of interest to us, it follows that the quantity in the curly brackets is nearly equal to unity. Accordingly we can write for this case

$$\langle G \rangle \approx G_{0L} \exp [-C_l(0)] \quad (10)$$

For an adaptive optics laser transmitter which is capable of providing random apodization compensation, evaluation of system performances is complicated by the fact that implementation of random apodization compensation implies a variation in the average laser power transmitted. Assuming that the log-amplitude variations are normally distributed, as theory and experimental evidence both seem to indicate, then it can be shown that introducing random apodization correction will result in a change in the average transmitted laser power by a factor of

$$M = \exp [2\mu(\mu+1)C_l(0)] \quad (11)$$

Obviously there is no change in the average laser power that is transmitted when $\mu = 0$, the case of no random apodization compensation, and when $\mu = 1$, the case which we find to generally give nearly optimum performance.

We have been able to show that the average antenna gain of an adaptive optics laser transmitter system with random apodization compensation varies with our choice of μ according to the expression

$$\langle G \rangle = G_{0L} \exp [-(1+\mu)^2 C_l(0)] \left\{ \frac{\int d\vec{r} K(\vec{r}/D) \exp [(1-\mu)^2 C_l(\vec{r})]}{\int d\vec{r} K(\vec{r}/D)} \right\} \quad (12)$$

Assuming that we are dealing with a laser transmitter with a larger aperture diameter, so that because of the fact that the log-amplitude covariance is a limited range function, the exponential in the integrand is equal to unity over most of the range of the r -integration, then it follows that the quantity in the curly brackets is a very weak function of μ . From this it follows that the average antenna gain is nearly optimized when we choose $\mu = -1$. In this case the average antenna gain of the adaptive optics laser transmitter with random apodization compensation is

$$\langle G \rangle = G_{0L} \frac{\int d\vec{r} K(\vec{r}/D) \exp[4 C_L(\vec{r})]}{\int d\vec{r} K(\vec{r}/D)} \quad (13)$$

It is perhaps interesting to note that in the rather unusual case of a very small laser transmitter diameter, when the diameter is much less than the very limited range of the log-amplitude covariance function, then it is a reasonable approximation to replace $C_L(\vec{r})$ by $C_L(0)$ in Eq. (12). When this is done our result for the average antenna gain reduces to

$$\langle G \rangle = G_{0L} \exp[-4\mu C_L(0)] \quad (14)$$

Clearly, for this tiny aperture case the laser transmitters average antenna gain is maximized by choosing a very large negative value for μ . This can be recognized as a form of "burst transmission", sending out most of the transmitted laser power in the instants when the random variable, $L(\vec{r})$, (which is well correlated over the entire tiny aperture) takes a large value. The concept, while not unphysical, is of limited value, and for the adaptive optics laser transmitters of general interest to us Eq. (13) applies when random apodization compensation is employed.

4. Anisoplanatism: Theoretical Results

To study anisoplanatism effects we consider the case in which the separation between the beacon position and the target position corresponds to the angle $\vec{\delta}$ as seen from the location of the adaptive optics system. In presenting our results for this problem it is convenient to make use of an extension of the definition of the log-amplitude covariance function, $C_L(\vec{r}, \vec{\delta})$. We consider two sources at angular positions $\vec{\theta}_1$ and $\vec{\theta}_2$ where

$$\vec{\delta} = \vec{\theta}_1 - \vec{\theta}_2 \quad (15)$$

(These can be thought of as sources collocated with the beacon and with the target.) Then the extended log-amplitude covariance function can be defined by the expression

$$C_L(\vec{r} - \vec{r}', \vec{\delta}) = \langle [L(\vec{r}, \vec{\theta}_1) - \bar{L}] [L(\vec{r}, \vec{\theta}_2) - \bar{L}] \rangle \quad (16)$$

In the case in which $\vec{\delta}$ is equal to zero the extended log-amplitude covariance function reduces to the ordinary log-amplitude covariance function, i. e.,

$$C_L(\vec{r}, 0) = C_L(\vec{r}) \quad (17)$$

We have been able to show that the value of the extended log-amplitude covariance function expressed as an integral over the propagation path can be written as

$$C_L(\vec{r}, \vec{\delta}) = \frac{8.16}{4\pi} k^2 \int_{\text{PATH}} dv C_N^2 \int_0^\infty d\sigma \sigma^{-5/3} [1 - \cos(\sigma^2 v/k)] \times J_0\{\sigma |\vec{r} [1 - (v/L)] - \vec{\delta} v|\} \quad (18)$$

where the propagation path has length L and runs from $v = 0$ at the plane where the log-amplitude variation is measured to $v = L$ at the point source. In Eq. (18) C_N^2 denotes the so called refractive-index structure constant (a measure of the optical strength of turbulence) and k is the optical wave number, equal to $2\pi/\lambda$.

We have found it convenient to define the function $S(\vec{r}, \vec{\delta})$ according to the equation

$$S(\vec{r}, \vec{\delta}) = 2.905 k^2 \int_{\text{PATH}} dv C_N^2 \left(\{r [1 - (v/L)]\}^{5/3} + \{\delta v\}^{5/3} - \frac{1}{2} \{ \{r [1 - (v/L)]\}^2 + 2r\delta [1 - (v/L)]vc + \{\delta v\}^2 \}^{5/3} - \frac{1}{2} \{ \{r [1 - (v/L)]\}^2 - 2r\delta [1 - (v/L)]vc + \{\delta v\}^2 \}^{5/3} \right) \quad (19)$$

where c corresponds to the cosine of the angle between the orientations of \vec{r} and $\vec{\delta}$, and has a value given by the expression

$$c = \vec{r} \cdot \vec{\delta} / (r\delta) \quad (20)$$

We have been able to show that for an adaptive optics imaging system that has no random apodization compensation capability, the optical transfer function can be written as

$$\langle T(\vec{f}) \rangle = T_{0L}(\vec{f}) \exp[-S(\lambda\vec{f}, \vec{\delta}) + C_L(0, 0) - C_L(\lambda\vec{f}, 0) - 2C_L(0, \vec{\delta}) + C_L(\lambda\vec{f}, \vec{\delta}) + C_L(\lambda\vec{f}, -\vec{\delta})] \quad (21)$$

Consideration of Eq. 's (17) and (19) makes it clear that this result reduces to the corresponding result, as given in Eq. (6), when there is no anisoplanatism, i. e., when $\vec{\delta}$ equals zero. Taking account of the limited range of the log-amplitude covariance function, a property not only of the ordinary covariance, $C_L(\lambda f)$, but also of the extended covariance, $C_L(\lambda \vec{f}, \vec{\delta})$, we argue that for all but the very lowest spatial frequencies, i. e., for all spatial frequencies of interest to us, we can drop the extended log-amplitude covariance functions which have $\lambda \vec{f}$ as an argument. Accordingly we can write in place of Eq. (21)

$$\langle T(\vec{f}) \rangle \approx T_{0L}(\vec{f}) \exp [-S(\lambda \vec{f}, \vec{\delta}) + C_L(0, 0) - 2 C_L(0, \vec{\delta})] \quad (22)$$

This quite obviously, in view of Eq. 's (17) and (19), reduces to the results given in Eq. (7) when there is no anisoplanatism.

Similarly, we have been able to show that for an adaptive optics imaging system with random apodization compensation capability, the optical transfer function can be written as

$$\langle T(\vec{f}) \rangle = T_{0L}(\vec{f}) \exp \{ -S(\lambda \vec{f}, \vec{\delta}) + 4 [C_L(0, 0) - C_L(0, \vec{\delta})] \}. \quad (23)$$

From consideration of Eq. 's (17) and (19) it is clear that this result reduces to the corresponding result given in Eq. (8) when there is no anisoplanatism, i. e., when $\vec{\delta}$ equals zero.

As a practical matter we can in general ignore the log-amplitude covariance functions in Eq. 's (22) and (23), in as much as these quantities make an almost negligible impact on the results, being independent of the spatial frequency, \vec{f} , and being quite limited in magnitude. Accordingly we suggest that we take as the appropriate expression for the anisoplanatism dependent optical transfer function for an adaptive optics imaging system, with or without the ability to compensate for random apodization,

$$\langle T(\vec{f}) \rangle \approx T_{0L}(\vec{f}) \exp [-S(\lambda \vec{f}, \vec{\delta})] \quad (24)$$

We believe it is interesting to remark that we obtain exactly this result when we utilize a very simple geometric optics type propagation theory with no allowance for diffraction effects. In such a geometric optics theory the ray from a source to a measurement point is assumed to run in a straight line (no bending), with no diffraction (interference) effects, with the ray simply accumulating phase shift contributions from the refractive-index variations along the path. The phase shift is only taken note of at the measurement, i. e., the aperture plane (or the aim point), where its system performance implication is determined. Correlation of the random phase shifts for two rays arises simply because whatever proximity there is between the two rays insures some correlation of the refractive-index variations encountered along the two ray paths. Obviously most all of our results for anisoplanatism effects on adaptive optics imaging systems are subsumed in this rather simple geometric optics propagation theory.

Our analysis of anisoplanatism effects in an adaptive optics laser transmitter without random apodization compensation leads to the result that antenna gain has the value

$$\langle G \rangle = G_{0L} \left\{ \frac{\int d\vec{r} K(r/D) \exp [-S(\vec{r}, \vec{\delta}) + C_L(0, 0) - C_L(\vec{r}, 0) - 2 C_L(0, \vec{\delta}) + C_L(\vec{r}, \vec{\delta}) + C_L(\vec{r}, -\vec{\delta})] }{\int d\vec{r} K(r/D)} \right\} \quad (25)$$

It is easy to see that when there is no anisoplanatism, i. e., when $\vec{\delta}$ equals zero, this reduces to the previously given result of Eq. (9). Taking account of the fact that the log-amplitude covariance function is a short ranged function of \vec{r} , then for large aperture diameters we can approximate Eq. (25) by the result that

$$\langle G \rangle \approx G_{0L} \exp [C_L(0, 0) - 2 C_L(0, \vec{\delta})] \left\{ \frac{\int d\vec{r} K(r/D) \exp [-S(\vec{r}, \vec{\delta})] }{\int d\vec{r} K(r/D)} \right\} \quad (26)$$

When there is no anisoplanatism, i. e., when $\vec{\delta}$ equals zero, this result reduces to the result previously given by Eq. (10).

For an adaptive optics laser transmitter with the ability to provide random apodization compensation, assuming that the random apodization compensation is set on the basis of $\mu = -1$ (which value we recall was shown to provide near optimum results for a large aperture diameter system in the absence of an anisoplanatism effects), we have been able to show that in general the antenna gain has the value

$$\langle G \rangle = G_{0L} \left\{ \frac{\int d\vec{r} K(r/D) \exp [-S(\vec{r}, \vec{\delta}) + 2 [C_L(\vec{r}, \vec{\delta}) + C_L(\vec{r}, -\vec{\delta})]] }{\int d\vec{r} K(r/D)} \right\} \quad (27)$$

It is obvious that in the absence of any anisoplanatism, i. e., when $\vec{\delta}$ equals zero, this result reduces to that previously given in Eq. (13).

Making use of the fact that the log-amplitude covariance function is a short ranged function of \vec{r} , and assuming that we are dealing with a fairly large diameter aperture laser transmitter, we can

replace our results for the adaptive optics without random apodization compensation, as given by Eq. (25), and with random apodization compensation, as given by Eq. (27) by the approximate one that

$$\langle G \rangle \approx G_{D,L} \left\{ \frac{\int d\vec{r} K(r/D) \exp[-S(\vec{r}, \vec{\vartheta})]}{\int d\vec{r} K(r/D)} \right\}. \quad (28)$$

This expression represents our basic result for the effect of anisoplanatism on the antenna gain of an adaptive optics laser transmitter, and is in a sense exactly parallel to the result we gave in Eq. (24) for the effect of anisoplanatism on an adaptive optics imaging system.

Just as we noted after Eq. (24) we remark again here that this result, i. e., Eq. (28), is exactly what we obtain when we utilize a very simple geometric optics type of propagation theory in our calculations of an antenna gain. This simple propagation theory makes no allowance for diffraction effects. It simply accumulates refractive-index variations along a straight line ray running between the point source (or target) and the aperture. It is only at the end of the ray that the accumulated variations in refractive-index are expressed as a phase shift to evaluate the implications for system performance.

Eq. 's (24) and (28), backed up by Eq. (19), represent the basic results for anisoplanatism. In the next section we examine these equations quantitatively, developing numerical and simplified approximate asymptotic results.

5. Anisoplanatism: Quantitative Results

It is convenient to start our development of quantitative results for anisoplanatism effects by considering Eq. (19) in the two limiting cases of r/ϑ going to infinity and of r/ϑ going to zero. When r/ϑ goes to infinity it is easy to see that the two five-sixths power terms in Eq. (19) each take on an approximate value of $-\frac{1}{2} \{ r [(v/L)] \}^{5/3}$, and accordingly we can write

$$\lim_{r/\vartheta \rightarrow \infty} S(\vec{r}, \vec{\vartheta}) = 2.905 k^2 \int_{\text{PATH}} dv C_N^2 (\vartheta v)^{5/3}. \quad (29)$$

Similarly when r/ϑ goes to zero it is easy to see that the two five-sixths power terms in Eq. (19) each take on an approximate value of $-\frac{1}{2} (\vartheta v)^{5/3}$, and accordingly we can write

$$\lim_{r/\vartheta \rightarrow 0} S(\vec{r}, \vec{\vartheta}) = 2.905 k^2 \int_{\text{PATH}} dv C_N^2 \{ r [1 - (v/L)] \}^{5/3}. \quad (30)$$

If we define the quantities r_0 and ϑ_0 by the expressions

$$r_0 = \{ (2.905/6.88) k^2 \int_{\text{PATH}} dv C_N^2 [1 - (v/R)]^{5/3} \}^{-3/5}, \quad (31)$$

and

$$\vartheta_0 = \{ 2.905 k^2 \int_{\text{PATH}} dv C_N^2 v^{5/3} \}^{-3/5}, \quad (32)$$

then we can rewrite Eq. 's (29) and (30) in rather compact form as

$$\lim_{r/\vartheta \rightarrow \infty} S(\vec{r}, \vec{\vartheta}) = (\vartheta/\vartheta_0)^{5/3}, \quad (33)$$

and

$$\lim_{r/\vartheta \rightarrow 0} S(\vec{r}, \vec{\vartheta}) = 6.88 (r/r_0)^{5/3}. \quad (34)$$

Making use of the quantities r_0 and ϑ_0 we can rewrite Eq. (19) as

$$S(\vec{r}, \vec{\vartheta}) = [(r/r_0) (\vartheta/\vartheta_0)]^{5/3} \mathcal{Q} [(r/r_0) / (\vartheta/\vartheta_0)] \quad (35)$$

where

$$\begin{aligned} \mathcal{Q}(Q) = A \int_{\text{PATH}} dv C_N^2 \{ & Q^{5/6} [1 - (v/L)]^{5/3} + Q^{-5/6} v^{5/3} \mathcal{L}_0^{-5/3} \\ & - \frac{1}{2} \{ Q [1 - (v/L)]^2 + 2 [1 - (v/L)] v \mathcal{L}_0^{-1} c + Q^{-1} v^3 \mathcal{L}_0^{-3} \}^{5/6} \\ & - \frac{1}{2} \{ Q [1 - (v/L)]^2 - 2 [1 - (v/L)] v \mathcal{L}_0^{-1} c + Q^{-1} v^3 \mathcal{L}_0^{-3} \}^{5/6} \}. \end{aligned} \quad (36)$$

where

$$\mathcal{L}_0 = r_0 / \vartheta_0 \quad (37)$$

and

$$A = 2.905 k^2 (r_0 \vartheta_0 \mathcal{L}_0)^{5/6} \quad (38)$$

From Eq. 's (31), (32), and (37) it follows that

$$A = 6.88 \left\{ \int_{\text{PATH}} dv C_N^2 [1 - (v/L)]^{5/3} \right\}^{-1} \quad (39)$$

and accordingly we can rewrite Eq. (36) as

$$\begin{aligned} \mathcal{J}(Q) = & 6.88 \left\{ \int_{\text{PATH}} dv C_N^2 [1 - (v/L)]^{5/3} \right\}^{-1} \int_{\text{PATH}} dv C_N^2 \\ & \times \left\{ Q^{5/6} [1 - (v/L)]^{5/3} + Q^{-5/6} v^{5/3} \mathcal{L}_0^{-5/3} \right. \\ & \left. - \frac{1}{2} \{ Q [1 - (v/L)]^2 + 2 [1 - (v/L)] v \mathcal{L}_0^{-1} c + Q^{-1} v^2 \mathcal{L}_0^{-2} \}^{5/6} \right. \\ & \left. - \frac{1}{2} \{ Q [1 - (v/L)]^2 - 2 [1 - (v/L)] v \mathcal{L}_0^{-1} c + Q^{-1} v^2 \mathcal{L}_0^{-2} \}^{5/6} \right\}. \quad (40) \end{aligned}$$

It is obvious from consideration of Eq. 's (24) and (35) that if we understand how $\mathcal{J}(Q)$ behaves as a function of Q , we understand the effects of anisoplanatism on the performance of an adaptive optics imaging system. To gain some insight into the asymptotic behavior of $\mathcal{J}(Q)$ for very large and for very small values of Q we have developed power series expansions for the five-sixth power curly bracket terms in Eq. (40). Making use of these expansions we have been able to recast Eq. (40) in the following two asymptotic forms;

$$\mathcal{J}(Q) \approx Q^{-5/6} \left[1 - \alpha \left(1 - \frac{1}{3} c^2 \right) Q^{-1/3} \right], \quad \text{for } Q \gg 1, \quad (41)$$

and

$$\mathcal{J}(Q) \approx 6.88 Q^{5/6} \left[1 - \beta \left(1 - \frac{1}{3} c^2 \right) Q^{1/3} \right], \quad \text{for } Q \ll 1, \quad (42)$$

where

$$\alpha = \frac{5}{8} \mathcal{L}_0^{-1/3} \left\{ \int_{\text{PATH}} dv C_N^2 [1 - (v/L)]^{1/3} v^2 \right\} \left\{ \int_{\text{PATH}} dv C_N^2 v^{5/3} \right\}^{-1}, \quad (43)$$

and

$$\beta = \frac{5}{8} \mathcal{L}_0^{1/3} \left\{ \int_{\text{PATH}} dv C_N^2 [1 - (v/L)]^2 v^{-1/3} \right\} \left\{ \int_{\text{PATH}} dv C_N^2 [1 - (v/L)]^{5/3} \right\}^{-1}, \quad (44)$$

Taking note of Eq. (35) it is easy to see that Eq. 's (41) and (42) are in agreement with Eq. 's (34) and (35), respectively.

To gain a more complete insight into the behavior of the function $\mathcal{J}(Q)$ we have developed numerical results for the case of a nominal horizontal propagation path, in particular the case in which the value of C_N^2 is the same along the entire propagation path. In this we note that not only are the values of α and β independent of the value of C_N^2 [as can be seen by studying Eq. 's (43) and (44)] but that the value of \mathcal{L}_0 is also independent of the value of C_N^2 [as can be seen from a consideration of Eq. 's (31), (32), and (37)]. In as much as \mathcal{L}_0 has a value independent of C_N^2 , then it follows from consideration of Eq. (40) that the function $\mathcal{J}(Q)$ is independent of the value of C_N^2 when C_N^2 has a constant value along the propagation path. In Fig. 1 we show $\mathcal{J}(Q)$ as a function of Q for $c = 0.00, 0.25, 0.50, 0.75$, and 1.00 . To test the limits of usefulness of the asymptotic results given by Eq. 's (41) and (42), in Fig. 2 we have reproduced the $\mathcal{J}(Q)$ curves for $c = 0.00$ and 1.00 , and superimposed on these we have plotted the asymptotic values as the dashed line curves. As can be seen the asymptotic results are not useful around the peaks of the $\mathcal{J}(Q)$ curves, which appear to occur at about $(6.88)^{-6/10} = 0.314$. However, about a factor of 3 (for $c = 1.00$) to 15 (for $c = 0.00$) away from the peak, and beyond, the asymptotic approximations appear to be quite accurate.

For this case of a constant value for C_N^2 we have found that the following expressions apply for the various parameters introduced above;

$$r_0 = 3.02 k^{-6/5} L^{-3/5} (C_N^2)^{-3/5} \quad (45)$$

$$\vartheta_0 = 0.950 k^{-6/5} L^{-4/5} (C_N^2)^{-3/5} \quad (46)$$

$$\mathcal{L}_0 = 3.18 L \quad (47)$$

$$\alpha = 1.020 \quad (48)$$

$$\beta = 2.206 \quad (49)$$

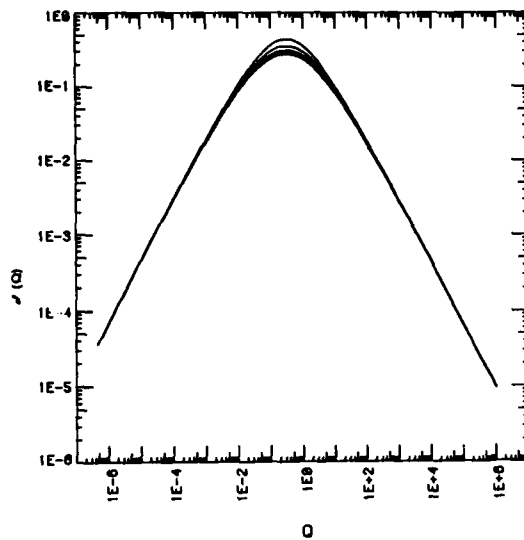


Figure 1. $\langle G \rangle / G_{0L}$ For Constant C_N^2 .

Results are shown for $c = 0.00, 0.25, 0.50, 0.75,$ and 1.00 . The lowest of the curves corresponds to $c = 0.00$ (with the $c = 0.25$ curve so nearly coincident with it as to be indistinguishable,) while the highest of the curves corresponds to $c = 1.00$.

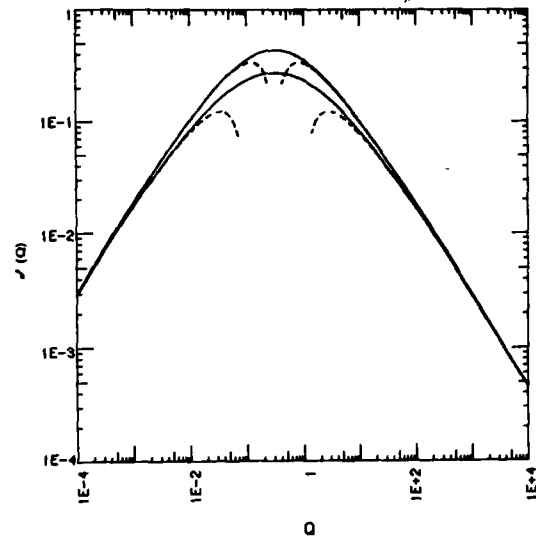


Figure 2. Asymptotic Approximations To $\langle G \rangle / G_{0L}$ For Constant C_N^2 .

The asymptotic approximations to $\langle G \rangle / G_{0L}$ given by Eq.'s (41) and (42) are shown here as the dash curves, for the two cases of $c = 0.00$ and 1.00 . The corresponding exact result, taken from Fig. 1, are shown as the solid curves. The upper curve corresponds to $c = 1.00$. As can be seen for $c = 1.00$ we may consider the asymptotic approximations to be quite useful for $Q < 0.1$ and $Q > 1.0$, while for $c = 0.00$ the corresponding limits are $Q < 0.02$ and $Q > 5.0$.

Making use of the numerical results for $\langle G \rangle / G_{0L}$ shown in Fig. 1 we have evaluated the anisoplanatism limited antenna gain of an adaptive optics laser transmitter for a propagation path along which the value of C_N^2 is constant. The calculations are based on use of Eq.'s (28) and (35) along with Eq.'s (31) and (32) [or Eq.'s (45) and (46)] for the values of the path length L and the value of the optical strength of turbulence, i. e., the refractive-index structure constant, C_N^2 . However, by evaluating the normalized antenna gain, $\langle G \rangle / G_{0L}$, considering this as a function of the normalized aperture diameter, D/r_0 , and expressing the parametric dependence of antenna gain on the angular separation in normalized form, i. e., as a dependence on the normalized angular separation parameter, ϑ/ϑ_0 , we have been able to develop a set of results with no explicit dependence on path length or strength of turbulence. (Any such dependence is implicit in the dependence of the normalization parameters, r_0 and ϑ_0 , on these propagation path parameters.) In Fig. 3 we show these results for the effect of anisoplanatism on the normalized adaptive optics laser transmitter antenna gain as a function of normalized aperture diameter, D/r_0 , for value of the normalized angular separation, ϑ/ϑ_0 ranging from 0.25 to 6.0. Table 1 shows the numerical values used in preparing Fig. 3.

We may generally characterize each of the curves shown in the following way. For very small and for very large values of D/r_0 , the value of $\langle G \rangle / G_{0L}$ is constant. For small values of D/r_0 , $\langle G \rangle / G_{0L}$ is about equal to unity, while for large values of D/r_0 its value is equal to $\exp[-(\vartheta/\vartheta_0)^{5/3}]$. The applicability of this expression may be tested (and verified) numerically from the data plotted, but its form is obtained analytically by consideration of Eq.'s (28) and (33) in the limiting case of very large aperture diameters. It will be observed in examination of Fig. 3 that the drop off of $\langle G \rangle / G_{0L}$ from its initial value of unity occurs at about D/r_0 equal unity. We have been unable to obtain an expression characterizing the dependence of $\langle G \rangle / G_{0L}$ on D/r_0 in the transition region, and simply note that the slope is greater, the greater the value of the normalized angular separation, ϑ/ϑ_0 . Similarly, we have been unable to obtain a convenient expression for the value of D/r_0 at which the large aperture asymptotic results region may be considered to have been reached.

The rather convenient and impressively complete normalization which we have been able to force upon our results suggests the possibility that we have captured most all of the dependence on the distribution of the strength of turbulence in the dependence of r_0 and ϑ_0 on these quantities. We have developed some evidence that suggests that for cases of practical interest this is very nearly true. Our evidence is based on results for propagation through the atmosphere, between ground and space—with the adaptive optics system on the ground and the beacon target in space, using the profile for the distribution of C_N^2 as a function of altitude shown in Fig. 4. (Two profiles are shown, one for daytime and the other for nighttime.)

For this ground/space propagation problem it is convenient to modify the various integrals given previously in the following ways. First we replace v/L by zero since for all values of v for which C_N^2 is not negligibly small, v/L is negligibly small. Second we change the variable of integration from v to the variable h , corresponding to altitude, replacing v by $h \sec(\Psi)$ where Ψ is the zenith angle

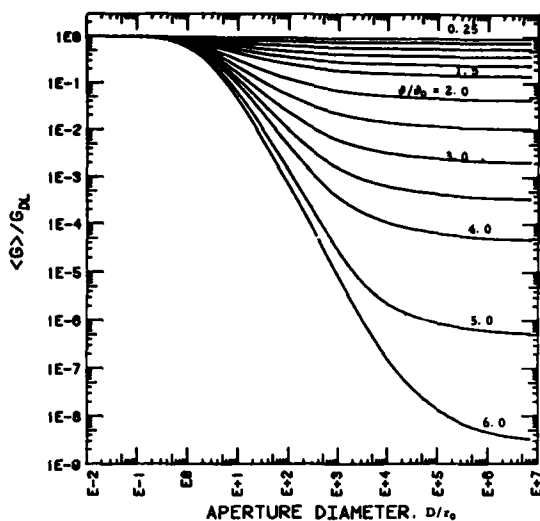


Figure 3. Effect of Anisoplanatism On The Normalized Antenna Gain of An Adaptive Optics Laser Transmitter For Constant C_N^2 .

The normalized antenna gain, $\langle G \rangle / G_{0L}$, (where G_{0L} is diffraction limited antenna gain) is shown as a function of the normalized transmitter aperture diameter, D/r_0 , for various values of the normalized angular separation, θ/θ_0 . Each curve corresponds to a value of θ/θ_0 running over the set of values 0.25, 0.50, 1.00, 1.25, 1.50, 2.0, 2.5, 3.0, 3.5, 4.0, 5.0, and 6.0.

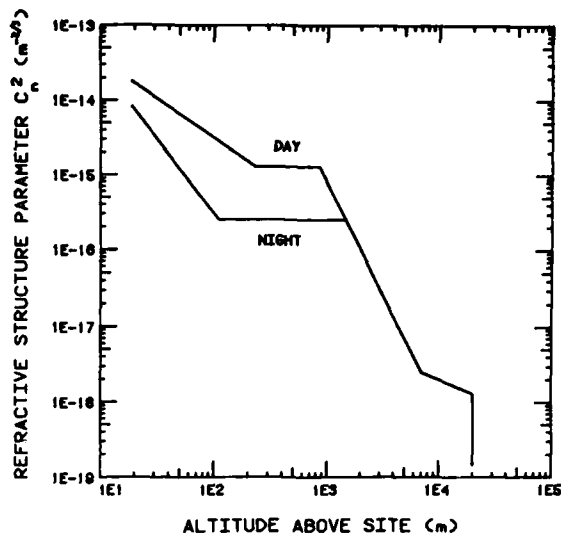


Figure 4. Vertical Distribution Of The Refractive-Index Structure Constant, C_N^2 .

Above one kilometer altitude the value of C_N^2 is independent of whether it is daytime or nighttime. Below one kilometer distinct values of C_N^2 are shown for daytime and nighttime.

associated with the propagation path. With these changes we get the new results, in place of Eq.'s (31), (32), (40), (43), and (44) that

$$r_0 = \left\{ (2.905/6.88) k^2 \sec(\Psi) \int_0^\infty dh C_N^2 \right\}^{-3/5} \quad (50)$$

$$\theta_0 = \left\{ 2.905 k^2 [\sec(\Psi)]^{8/3} \int_0^\infty dh C_N^2 h^{5/3} \right\}^{-3/5} \quad (51)$$

$$\begin{aligned} \mathcal{J}(Q) = & 6.88 \left\{ \int_0^\infty dh C_N^2 \right\}^{-1} \int_0^\infty dh C_N^2 \left\{ Q^{5/6} + Q^{-5/6} (h/H_0)^{5/3} \right. \\ & \left. - \frac{1}{2} [Q + 2(h/H_0)c + Q^{-1}(h/H_0)^2]^{5/6} \right. \\ & \left. - \frac{1}{2} [Q - 2(h/H_0)c + Q^{-1}(h/H_0)^2]^{5/6} \right\} \quad (52) \end{aligned}$$

$$\alpha = \frac{5}{8} H_0^{-1/3} \left\{ \int_0^\infty dh C_N^2 h^3 \right\} \left\{ \int_0^\infty dh C_N^2 h^{5/3} \right\}^{-1} \quad (53)$$

$$\beta = \frac{5}{8} H_0^{1/3} \left\{ \int_0^\infty dh C_N^2 h^{-1/3} \right\} \left\{ \int_0^\infty dh C_N^2 \right\}^{-1} \quad (54)$$

where

$$H_0 = (6.88)^{3/5} \left\{ \int_0^\infty dh C_N^2 h^{5/3} \right\}^{3/5} \left\{ \int_0^\infty dh C_N^2 \right\}^{-3/5} \quad (55)$$

Making use of these equations and with the values of C_N^2 given in Fig. 4 we obtain in place of Eq.'s (45) to (49) the results that

$$r_0 = \left\{ 1.666 \times 10^7 \mid 3.369 \times 10^7 \right\} k^{-6/5} [\sec(\Psi)]^{-3/5} \quad (56)$$

$$\theta_0 = \left\{ 4.188 \times 10^3 \mid 4.604 \times 10^3 \right\} k^{-6/5} [\sec(\Psi)]^{-8/5} \quad (57)$$

$$\mathcal{L}_0 = H_0 \sec(\Psi) \quad (58)$$

where

$$H_0 = \left\{ 3979 \mid 7319 \right\} \quad (59)$$

$$\alpha = \left\{ 0.955 \mid 0.846 \right\} \quad (60)$$

and

$$\beta = \{ 2.651 \mid 2.930 \}$$

(61)

In these equations we have used the notation $\{ \dots \mid \dots \}$ to allow us to show both the daytime and the nighttime results in one expression. The daytime value appears to the left of the vertical bar, i. e., we have $\{ \text{day value} \mid \text{night value} \}$.

By means of Eq. (52) used in conjunction with the C_N^2 data of Fig. 4 we have developed numerical results for $\mathcal{J}(Q)$. These results are shown in Fig. 's 5a and 5b for daytime and nighttime, respectively, for $c = 0.00, 0.25, 0.50, 0.75,$ and 1.00 . These two sets of results and the constant C_N^2 results of Fig. 1 are, generally speaking, quite similar. There are however, some noticeable differences in the values of the three sets of curves around $Q = 1$.

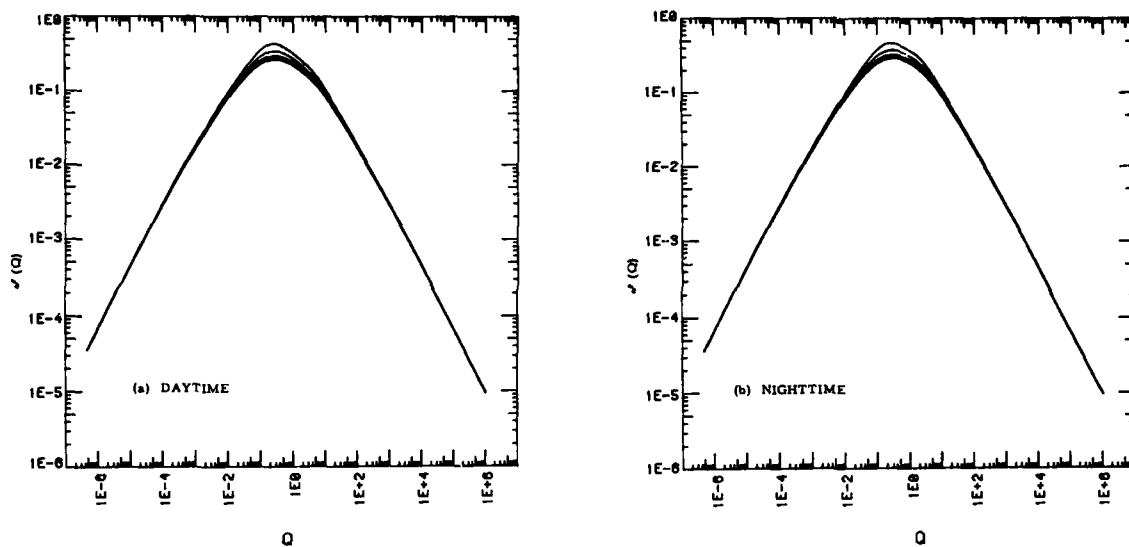


Figure 5. $\mathcal{J}(Q)$ For Vertical Propagation.

Results are calculated with Eq. (52) using the values of C_N^2 shown in Fig. 4, with Fig. 5a based on the daytime values of C_N^2 and Fig. 5b based on the nighttime values. Results are shown for $c = 0.00, 0.25, 0.50, 0.75,$ and 1.00 . The lowest of the curves in each figure corresponds to $c = 0.00$ while the highest is for $c = 1.00$. The curve for $c = 0.25$ is so close to that for $c = 0.00$ as to be just barely distinguishable near the peak.

The ability of the asymptotic approximations defined by Eq. 's (41) and (42), using the values of α and β given by Eq. 's (60) and (61), to match the numerical values of $\mathcal{J}(Q)$ in Fig. 's 5a and 5b may be judged by consideration of Fig. 's 6a and 6b. In Fig. 's 6a and 6b we have reproduced the $c = 0.00$ and $c = 1.00$ curves from Fig. 's 5a and 5b, respectively, and shown them as the solid curves. The asymptotic approximations are shown as the dashed curves. Though some of the details of the fit of the asymptotic approximations to the corresponding exact results are different than they were for the constant C_N^2 case shown in Fig. 2, we may consider the general quality of the fits and the remarks that we might offer about the utility of the asymptotic approximations to be the same.

Making use of the $\mathcal{J}(Q)$ values shown in Fig. 's 5a and 5b [as calculated from Eq. (52) with the C_N^2 data of Fig. 4], and using Eq. 's (28) and (35) we have calculated a set of normalized antenna gain results showing the effects of anisoplanatism on the performance of an adaptive optics laser transmitter for ground to space transmission. We have found that these results are so nearly identical for daytime and nighttime, and for various zenith angles, that we shall simply present here one graph (the daytime zero degree zenith angle case) for both times of day and all zenith angles. This is shown in Fig. 7. It is significant to note that these results, when overlaid on the constant C_N^2 results shown in Fig. 3, indicate a nearly perfect match. To the extent that differences exist they are less than a line width. Accordingly we suggest that the normalized antenna gain results shown in Fig. 3 may be considered to be a very nearly universal set of results.

Acknowledgement

I would like to take this opportunity to thank Mr. Don Hanson of the Rome Air Development Center, U. S. Air Force, for providing the C_N^2 data shown in Fig. 4, and to express my sincere appreciation to Dr. Stephen L. Browne, of this company for carrying out the computer work that generated all of the other figures and all of the other numerical results which we have utilized. This work was supported by

a DARPA funded contract F30602-80-C-0305, monitored at Rome Air Development Center.

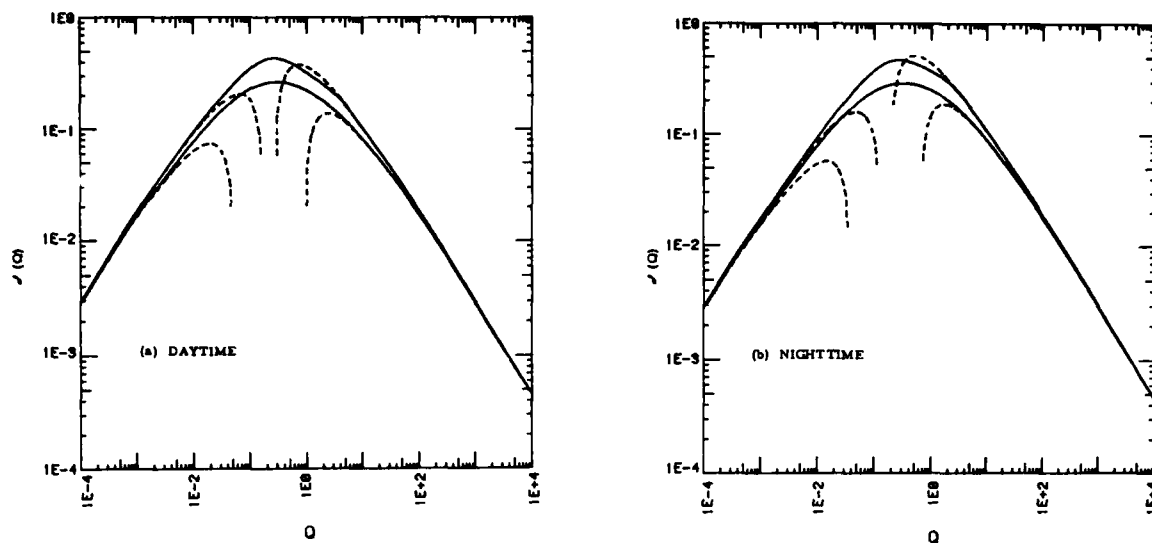


Figure 6. Asymptotic Approximation To $J(Q)$ For Vertical Propagation.

The asymptotic approximations to $J(Q)$ given by Eq.'s (41) and (42), with the values of α and β taken from Eq.'s (60) and (61) are shown here as the dash curves, for the two cases of $c = 0.00$ and 1.00 . The corresponding exact results, taken from Fig.'s 5a and 5b, are shown as the solid curves. The upper curve in each figure is for $c = 1.00$.

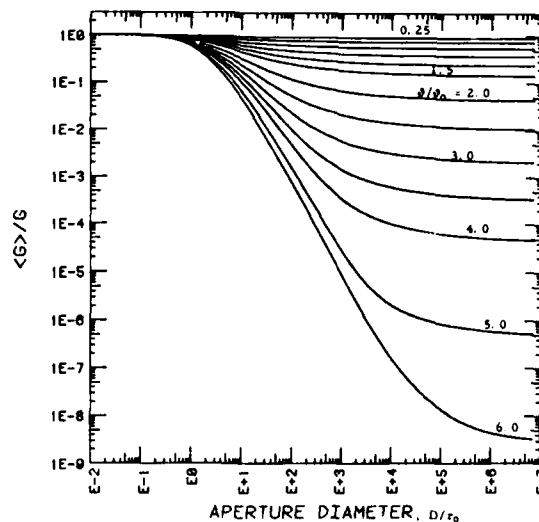


Figure 7. Effect Of Anisoplanatism On The Normalized Antenna Gain Of An Adaptive Optics Laser Transmitter For Vertical Propagation

The normalized antenna gain, $\langle G \rangle / G_0$, is shown as a function of the normalized aperture diameter, D/r_0 , for various values of the normalized angular separation, θ/θ_0 . Each curve corresponds to a value of θ/θ_0 running over the set of values 0.25, 0.50, 0.75, 1.00, 1.25, 1.50, 2.0, 2.5, 3.0, 3.5, 4.0, 5.0, 6.0. The results shown here are for daytime turbulence conditions and a zero degree zenith angle, but they are identical (to within line width type accuracy) to results obtained for other zenith angles and for nighttime conditions. Moreover, the results shown here appear to be identical to those obtained for propagation over a path along which C_n^2 is constant, which results are shown in Fig. 3.

REDUCTION OF ANISOPLANATIC ERRORS

Donald W. Hanson
Rome Air Development Center
Griffiss Air Force Base, N.Y. 13441

Nathan Schwartz
Syracuse University
Syracuse, N.Y. 13210

SUMMARY

An optimum linear estimator for the phase at the point ahead angle is developed for the case where the optical line of sight slews through the turbulent atmosphere faster than the turbulence is transported by the ambient winds. Difficulties encountered when using the standard approach to optimum linear estimation are discussed. The optimum linear estimate is developed in terms of the structure and hyperstructure functions, rather than the correlation function, since the correlation function for the phase aberrations is difficult to observe. The relaxation in station keeping requirements which can be achieved through the use of the optimum linear estimator is derived and found to be on the order of 15%.

1. INTRODUCTION

The performance of phase conjugate adaptive optical systems is limited by several sources of error, such as sampling error, photon error, amplitude scintillation error, and anisoplanatic error. When transmitting to a moving cooperative target, which has a bright beacon, the first three errors can in theory be reduced to negligible levels through the use of nonlinear optics. However, presently the anisoplanatic error can only be reduced through the use of a spatially separated beacon located at the point ahead angle. Since the anisoplanatic error increases rapidly with station keeping errors, it is necessary to maintain the station keeping between the beacon and the receiver with very high accuracy. A method for reducing the station keeping requirements between the receiver and the beacon is developed. The method estimates the future value of a random process based on observed data. Before developing the estimate we review the ill-behaved nature of random processes associated with optical propagation, and introduce the structure and hyperstructure functions.

1.1 Description of Random Processes

In the study of real physical systems the analyses can usually be greatly simplified if the processes which describe the systems can be assumed to be stationary in the wide sense (i.e., second order statistics are not a function of absolute time). However for many physical systems of interest the assumption of wide sense stationarity cannot be used since parameters of these systems have mean values which tend to be a function of absolute time. Meteorological processes such as wind speed, temperature, and pressure are examples of processes which tend to have mean values which are a function of absolute time. Since such processes are nonstationary, they are nonergodic. Therefore, time averages cannot be used in place of ensemble averages. However, since time averages are all that are available, attempts are made to use the time averages as ensemble averages to implement the powerful statistical analysis procedures which have been developed over the last several hundred years. When attempting to use the time averages, it is difficult to assess which fluctuations are associated with first order statistics and which are associated with higher order statistics. For example meteorological parameters such as wind speed, temperature, and pressure at a given location have variations with periods of less than 0.01 seconds and greater than days, years, and probably much longer. Thus when using the time averages of these processes it is difficult to determine the correlation function. Large variances can result when time averages are used to approximate ergodic averages for such processes. These large variances can lead to mathematical problems when analyzing such processes.

To avoid these types of problems a statistical description, called the structure function, related to the difference between the value of the process at two different times, has been developed (KOLMOGOROV, A.N., 1941). The differencing process tends to suppress slow fluctuations (i.e., those which have a period longer than the differencing time) and to suppress problems associated with large variances. Time averages of the difference function are thus more representative of ensemble averages than are time averages of the basic process.

1.2 The Structure Function

The temporal structure function of the random process $f(t)$, denoted as $D_f(t_1, t_2)$, is defined as follows:

$$D_f(t_1, t_2) = \langle [f(t_1) - f(t_2)]^2 \rangle \quad (1.1)$$

where the $\langle \rangle$ brackets indicate an ensemble average. Assuming that the differencing process in equation (1.1) eliminates any dependence on absolute time the structure

function can be written as follows:

$$D_f(t_1, t_2) = \{ [f(t_1) - f(t_2)]^2 \} \quad (1.2)$$

We note that D can be written as follows:

$$D_f(t_1, t_2) \equiv C_f(t_1, t_1) - 2C_f(t_1, t_2) + C_f(t_2, t_2) \quad (1.3)$$

where: $C_f(t_1, t_2)$ is the correlation function of the process f .

For processes with large variances, direct measurement of the structure function avoids the procedure of differencing large quantities, which can lead to mathematical difficulties.

Formulation of the spatial structure function follows in a straight forward manner from the above.

1.3 The Hyperstructure Function

The hyperstructure function is similar to the structure function, and is useful for describing processes which are a function of more than one variable (Fried D.L., 1974).

The hyperstructure function, F , of the random process $f(\vec{x}, \vec{\psi})$, where \vec{x} and $\vec{\psi}$ are two arbitrary variables (e.g., time, linear dimension, angle) is defined as:

$$F_f(\vec{x}_1, \vec{x}_2, \vec{\psi}_1, \vec{\psi}_2) = \{ [f(\vec{x}_1, \vec{\psi}_1) - f(\vec{x}_2, \vec{\psi}_1)] \times [f(\vec{x}_1, \vec{\psi}_2) - f(\vec{x}_2, \vec{\psi}_2)] \} \quad (1.4)$$

Note that for the case where $\vec{\psi}_1 = \vec{\psi}_2$ the hyperstructure function reduces to the structure function. The purpose of the differencing procedure in equation (1.4) is to reduce the dependence of F on the absolute value of the variables \vec{x} and $\vec{\psi}$. Thus, at least over a certain range of $\vec{x}_1 - \vec{x}_2$ and $\vec{\psi}_1 - \vec{\psi}_2$ F can be written as:

$$F_f(\vec{x}_1, -\vec{x}_2, \vec{\psi}_1, -\vec{\psi}_2) = \{ [f(\vec{x}_1, \vec{\psi}_1) - f(\vec{x}_2, \vec{\psi}_1)] \times [f(\vec{x}_1, \vec{\psi}_2) - f(\vec{x}_2, \vec{\psi}_2)] \} \quad (1.5)$$

In the next section we determine the optimum linear estimate for the prediction problem in terms of the structure and hyperstructure functions.

2.0 SOLUTION OF THE PREDICTION PROBLEM USING THE HYPERSTRUCTURE FUNCTION

2.1 Standard Procedure

We wish to form an estimate of the future value of the process f , i.e., $f(t+\Delta t)$, which we denote as $\hat{f}(t+\Delta t)$. The standard approach for the optimum estimate is developed as follows. We assume that we have the observed data set (f_i) where:

$$f_i = f(t_i) \quad (2.1)$$

We can represent the observed data as a vector \vec{f} where:

$$\vec{f}^T = [f_1, f_2, f_3, \dots, f_n] \quad (2.2)$$

The optimum linear estimate is given by:

$$\hat{f}(t+\Delta t) = \vec{a} \cdot \vec{f} \quad (2.3)$$

where: the vector multiplication is the standard inner product:

\vec{f}^T is the transpose of \vec{f} ; and

the vector \vec{a} is chosen such that the orthogonality principle is satisfied, i.e.,:

$$\{ [f(t+\Delta t) - \hat{f}(t+\Delta t)] \vec{f} \} = \vec{0} \quad (2.4)$$

Using equation (2.3) in equation (2.4) gives:

$$\{ [f(t+\Delta t) - \vec{a} \cdot \vec{f}] \vec{f} \} = \vec{0} \quad (2.5)$$

Carrying out the multiplications and the expectation gives the matrix equation:

$$\begin{bmatrix} C_f(t+\Delta t, t_1) - (a_1 C_f(t_1, t_1) + a_2 C_f(t_2, t_1) + \dots + a_n C_f(t_n, t_1)) \\ C_f(t+\Delta t, t_2) - (a_1 C_f(t_1, t_2) + a_2 C_f(t_2, t_2) + \dots + a_n C_f(t_n, t_2)) \\ \vdots \\ C_f(t+\Delta t, t_n) - (a_1 C_f(t_1, t_n) + a_2 C_f(t_2, t_n) + \dots + a_n C_f(t_n, t_n)) \end{bmatrix} = \vec{0} \quad (2.6)$$

Solution of this equation determines the vector \vec{a} which will provide the optimum linear estimate. If the process is stationary equation (2.6) can be written as follows:

$$\begin{bmatrix} C_f(t+\Delta t-t_1) - (a_1 C_f(0) + a_2 C_f(t_2-t_1) + \dots + a_n C_f(t_n-t_1)) \\ C_f(t+\Delta t-t_2) - (a_1 C_f(t_1-t_2) + a_2 C_f(0) + \dots + a_n C_f(t_n-t_2)) \\ \vdots \\ C_f(t+\Delta t-t_n) - (a_1 C_f(t_1-t_n) + a_2 C_f(t_2-t_n) + \dots + a_n C_f(0)) \end{bmatrix} = \vec{0} \quad (2.7)$$

Both equations (2.6) and (2.7) require knowledge of the correlation function. We also note that equations (2.6) and (2.7) involve the difference of the variance and the correlation function of the process for various times. Thus for processes with large variances, equations (2.6) and (2.7) pose a mathematical stability problem, since they involve the difference of large quantities in an attempt to observe small quantities.

2.2 Optimum Linear Estimate for the Future Value of the Difference Between Two Random Variables of a Process.

For many practical cases of interest the value of a process at some absolute time is not what is required. Many times the problem can instead be formulated such that it is the difference between the value of the random process at two different times that is of interest. Formulation of the problem in such a manner allows use of the hyperstructure function and the structure function, functions which can be observed, to describe the process. We now develop the optimum linear estimate for the future value of the difference between two random variables of the same process.

We desire an estimate, $\hat{h}(t+\Delta t)$, of $h(t+\Delta t)$ where:

$$h(t+\Delta t) = f(t) - f(t+\Delta t) \quad (2.8)$$

For many processes the differencing procedure in equation (2.8) will remove the nonstationary aspects of the process $f(t)$, at least for a certain range of Δt . For processes for which this is true, such as meteorological processes, we can use time averages to approximate ensemble averages.

Obviously one approach to forming the desired estimate would be to measure $f(t)$ and to form an estimate of $f(t+\Delta t)$ separately using the procedures discussed in section 2.1. We develop another approach which does not require the assumption of stationarity or knowledge of the correlation function of the process.

We will use the observed data set (h_i) where:

$$h_i(\Delta t) = f(t_i) - f(t_i+\Delta t) \quad (2.9)$$

We define the temporal hyperstructure function for a process, which is a function of a single variable, as follows:

$$F_f(t_i-t_j, \Delta t) = \{[h_i(\Delta t)][h_j(\Delta t)]\} \quad (2.10)$$

We note that for $t_i = t_j$, the temporal hyperstructure function reduces to the temporal structure function. We form a linear estimate of $h(t+\Delta t)$ as follows:

$$\hat{h}(t+\Delta t) = \vec{a} \cdot \vec{h} \quad (2.11)$$

and optimize the estimate by requiring that:

$$\{[h(t+\Delta t) - \vec{a} \cdot \vec{h}] \vec{h}\} = \vec{0} \quad (2.12)$$

Multiplying and taking the expectation gives:

$$\begin{bmatrix} F_f(t-t_1, \Delta t) - [a_1 D_f(\Delta t) + a_2 F_f(t_2-t_1, \Delta t) + \dots + a_n F_f(t_n-t_1, \Delta t)] \\ F_f(t-t_2, \Delta t) - [a_1 F_f(t_1-t_2, \Delta t) + a_2 D_f(\Delta t) + \dots + a_n F_f(t_n-t_2, \Delta t)] \\ \vdots \\ F_f(t-t_n, \Delta t) - [a_1 F_f(t_1-t_n, \Delta t) + a_2 F_f(t_2-t_n, \Delta t) + \dots + a_n D_f(\Delta t)] \end{bmatrix} = \vec{0} \quad (2.13)$$

where $D_f(\Delta t)$ is the temporal structure function of the process $f(t)$.

Comparing equations (2.13) and (2.7) we see that they are identical except that in equation (2.13) the hyperstructure function, F , and the structure function, D , have replaced the correlation function, C . It is important to emphasize that F and D can be determined through time domain averages since the differencing procedure creates a

process which is stationary, at least for some values of Δt . Thus equation (2.13) can be solved since the $F_f(t_1-t_1, \Delta t)$ and $D_f(\Delta t)$ can be determined, whereas neither equation (2.6) nor equation (2.7) can be solved since the C_f 's cannot be determined through time domain averages. Also the problems associated with large variances have been suppressed through the use of the hyperstructure function. Thus, equation (2.13) involves the difference of small quantities while attempting to observe small quantities.

2.3 Optimum Linear Estimate for the Difference Between Two Random Variables of a Process Which is a Function of Two Variables

The development in this section follows that in the previous section very closely. Here the problem of interest is to predict the future value of the difference between two random variables of a process which is a function of both space and time.

We desire to form an estimate, $g(p, t+\Delta t)$, of $g(p, t+\Delta t)$ where:

$$g(p, t) = [f(\vec{x}_1, t) - f(\vec{x}_2, t)] \quad (2.14)$$

and
$$p = \left[\vec{x}_1 - \vec{x}_2 \right] \quad (2.15)$$

We note that implicit in the definition of equation (2.14) is the assumption that the differencing procedure has removed any nonhomogeneous and nonisotropic characteristics of the process $f(t)$, thus making g a function of p and t only.

Obviously one approach to forming the desired estimate would be to form an estimate of $f(\vec{x}_1, t+\Delta t)$ and $f(\vec{x}_2, t+\Delta t)$ separately using the procedures discussed in section 2.1. As before, we develop another approach which does not require the assumption of stationarity or knowledge of the correlation function of the process.

We will use the observed data set ($g_i(p)$) where:

$$g_i(p) = g(p, t_i) \quad (2.16)$$

Using equation (1.5) we note that:

$$\langle g_i(p)g_j(p) \rangle = F_f(p, t_i - t_j) \quad (2.17)$$

Implicit in equation (2.17) is the assumption that the differencing procedure has removed any nonstationary characteristics of f .

We form a linear estimate of $g(p, t+\Delta t)$ as follows:

$$\hat{g}(p, t+\Delta t) = \vec{a} \cdot \vec{g} \quad (2.18)$$

and optimize the estimate by requiring that:

$$\langle [g(p, t+\Delta t) - \vec{a} \cdot \vec{g}] \vec{g} \rangle = \vec{0}. \quad (2.19)$$

Multiplying and taking the expectation gives:

$$\left[\begin{array}{l} F_f(p, t+\Delta t-t_1) - (a_1 D_f(p) + a_2 F_f(p, t_2-t_1) + \dots + a_n F_f(p, t_n-t_1)) \\ F_f(p, t+\Delta t-t_2) - (a_1 F_f(p, t_1-t_2) + a_2 D_f(p) + \dots + a_n F_f(p, t_n-t_2)) \\ \vdots \\ F_f(p, t+\Delta t-t_n) - (a_1 F_f(p, t_1-t_n) + a_2 F_f(p, t_2-t_n) + \dots + a_n D_f(p)) \end{array} \right] = \vec{0} \quad (2.20)$$

where $D_f(p)$ is the spatial structure function of f .

Comparing equations (2.20) and (2.7) we see that they are identical except that in equation (2.20) the hyperstructure function, F , and the structure function, D , have replaced the correlation function, C . It is important to emphasize that F and D can be determined through time domain averages since the differencing procedure creates a process which is stationary, at least for some values of p and Δt . Thus equation (2.20) can be solved since $F_f(p, t_i - t_j)$ can be determined, whereas neither equation (2.6) nor equation (2.7) can be solved since the C_f 's cannot be determined through time domain averages. Once again we note that the problems associated with having a process with large variances are suppressed in equation (2.20). In the next section we will apply the optimum linear estimate to the reduction of anisoplanatic errors.

3.0 THE OPTIMUM LINEAR ESTIMATE FOR THE POINT AHEAD ANGLE

First we derive the anisoplanatic error, then we derive the estimate for reducing it.

3.1 Derivation of the Spatial-Angular Structure Function

We define the spatial-angular structure function, denoted as $H_\phi(\vec{p}, \vec{\theta})$, as follows:

$$H_\phi(\vec{p}, \vec{\theta}) = \langle \{ [\phi(\vec{x}_1, \vec{\psi}_1) - \phi(\vec{x}_2, \vec{\psi}_1)] - [\phi(\vec{x}_1, \vec{\psi}_2) - \phi(\vec{x}_2, \vec{\psi}_2)] \}^2 \rangle \quad (3.1)$$

where: $\vec{\theta} = \vec{\psi}_1 - \vec{\psi}_2$ and $\vec{p} = \vec{x}_1 - \vec{x}_2$ (3.2)

$H_\phi(\vec{p}, \vec{\theta})$ is the mean square phase difference between two points in the aperture plane at two different zenith angles. Thus, $H_\phi(\vec{p}, \vec{\theta})$ quantifies the anisoplanatic error.

Figures 1a, b and c illustrate the nomenclature used in equation (3.1). As shown in figures 1b and c, the phase difference between points \vec{x}_1 and \vec{x}_2 will in general be different for different zenith angles due to atmospheric distortion. This is what creates the anisoplanatic error. It can be shown that equation (3.1) can be written as (HANSON, D.W., 1981):

$$H_\phi(\vec{p}, \vec{\theta}) = 2.91 k^2 (\sec \psi)^2 p^{5/3} \int dh C_n^2(h) \{ 1 + (zh)^{5/3} - (1/2) [1 + 2zh \cos \alpha + (zh)^2]^{5/6} - (1/2) [1 - 2zh \cos \alpha + (zh)^2]^{5/6} \} \quad (3.3)$$

where: ψ is the zenith angle;

k is the wave number (i.e., $2\pi/\lambda$);

λ is the wavelength of the optical signal;

C_n^2 is the refractive index structure parameter;

$$z = (\theta \sec \psi)/p; \quad (3.4)$$

h is the vertical distance (i.e., altitude) above the ground transmitter; and

α is the angle between \vec{p} and $\vec{\theta}$.

Equation (3.3) is the basic result of this section. It determines the anisoplanatic error in terms of the propagation path. In general, the integral must be evaluated using numerical techniques for a particular $C_n(h)$ profile.

3.2 Reduction of the Anisoplanatic Error

We wish to reduce the anisoplanatic error given by H_ϕ . We pause briefly to recapitulate that our knowledge of the additive phase noise is limited. What we know about the process is its structure function, its hyperstructure function, and its spatial-angular structure function. These equations are all developed based on the assumption that the turbulence is Kolmogorov. Thus for these equations to be valid the separation between the propagation paths in figure 1 must be within the inertial subrange.

Finally, the last assumption that we must make is the so called Taylor's hypothesis, also called the frozen flow theory. This theory assumes that in the time scales of interest the elements of turbulence remain fixed in shape (i.e., "frozen"). Time variations in the turbulence-induced aberrations are assumed to be caused by the wind transporting the "frozen" turbulence pattern through the propagation path.

The ambient winds along a propagation path from ground to space have varying speeds and directions as a function of altitude. Thus for a system with a fixed propagation path the turbulence pattern would be moving in a random fashion and no prediction would be possible. For a near earth satellite, however, the slew rate of the line of sight (i.e., ψ) will cause the propagation path to cut through the atmosphere, thus producing a pseudo-wind. If the speed of the pseudo-wind predominates over the natural winds at all altitudes, then the turbulence pattern at each altitude will appear to move at the same angular velocity. For a satellite at an altitude of 200 km the slew rate of the line of sight is approximately 0.039 rad/sec near zenith. The tangential velocity at altitude h is thus:

$$V = (0.039) h \text{ m/sec} \quad (3.5)$$

In the lower altitudes, wind speeds are usually under 8 m/sec. Thus for $h > 200$ m the pseudo-wind will predominate over the ambient winds. The typical maximum windspeed, 100 m/sec, usually occurs at about 12 km. At 12 km, the pseudo-windspeed is 468 m/sec, thus the pseudo-wind easily predominates at the higher altitudes. Thus there is a direct relationship between time and the angle moved at each height of turbulence, for low earth orbiting satellites. This allows us to translate an observation over a certain time interval to an observation over a corresponding angle, and thus, allows use of equation (2.13). Therefore, the optimum linear estimate for the point ahead angle, θ , is given by:

$$g(\vec{p}, \vec{\psi}, \vec{\theta}) = \vec{a} \cdot \vec{g} \quad (3.6)$$

where: all angles are coplanar, and;

\vec{a} is determined by solving:

$$\begin{bmatrix} F_{\phi}(\vec{p}, \vec{\psi} + \vec{\delta} - \vec{\psi}_1) - (a_1 F_{\phi}(\vec{p}, \vec{\theta}) + a_2 F_{\phi}(\vec{p}, \vec{\psi}_2 - \vec{\psi}_1) + \dots + a_n F_{\phi}(\vec{p}, \vec{\psi}_n - \vec{\psi}_1)) \\ F_{\phi}(\vec{p}, \vec{\psi} + \vec{\delta} - \vec{\psi}_2) - (a_1 F_{\phi}(\vec{p}, \vec{\psi}_1 - \vec{\psi}_2) + a_2 F_{\phi}(\vec{p}, \vec{\theta}) + \dots + a_n F_{\phi}(\vec{p}, \vec{\psi}_n - \vec{\psi}_2)) \\ \vdots \\ F_{\phi}(\vec{p}, \vec{\psi} + \vec{\delta} - \vec{\psi}_n) - (a_1 F_{\phi}(\vec{p}, \vec{\psi}_1 - \vec{\psi}_n) + a_2 F_{\phi}(\vec{p}, \vec{\psi}_2 - \vec{\psi}_n) + \dots + a_n F_{\phi}(\vec{p}, \vec{\theta})) \end{bmatrix} = 0 \quad (3.7)$$

Equations (3.6) and (3.7) are the basic result of this section. In the next section we will evaluate the anisoplanatic error for a typical case and determine how much this error can be reduced through utilization of the optimum estimate.

4.0 EVALUATION OF THE PERFORMANCE OF THE OPTIMUM ESTIMATOR

In this section we will obtain numerical results to determine how well the optimum estimator performs. First we evaluate the error without the estimate and then the error with the estimate.

4.1 Magnitude of the Anisoplanatic Error

The anisoplanatic error is given by equation (3.3). To evaluate the integral a profile of turbulence, i.e., C_n^2 as a function of h , must be selected. The most extensive measurements of the strength of turbulence as a function of altitude have been made at the ARPA Maui Optical Station. The model of C_n^2 versus h derived from those measurements is shown in figure 2. This model will be used to evaluate the performance of the optimum estimator. Once we know what to use for C_n^2 in equation (3.3) we can perform a numerical integration. This numerical integration was accomplished using a computer program adapted from Fried (FRIED, D.L., 1977).

For a typical case of $p = 1$ m; $\alpha = 0$; $\psi = 0$; and a point ahead angle, $\theta = 50$ urad; we get:

$$F_{\phi}(1.50 \text{ } \mu\text{rad}) = 4.78 \quad \text{rad}^2 \text{ at } \lambda = .55 \text{ } \mu\text{m} \quad (4.1)$$

This is obviously a significant error. It corresponds to an rms error of approximately $.35 \lambda$ which is about 3.5 times greater than the total wavefront error typically budgeted for all error sources in an optical system. It is this unacceptably large anisoplanatic phase error which generates the requirement for the separation between the reference beacon and the receiver.

4.2 Reduction of the Anisoplanatic Error Through Use of the Optimum Linear Estimate

Before evaluating the error in the estimate we must stop to realize that equations (3.6) and (3.7) only provide the optimum estimate for the selected observed data set ($g_i(\vec{p})$). The equations do not tell us how to select the elements of the set. We will thus evaluate the performance of the estimation procedure for different angular spacings. We will compare the error for each of the optimum estimates to select which elements should be chosen for inclusion in ($g_i(\vec{p})$).

First we use equation (3.7) to find \vec{a} for each ($g_i(\vec{p})$), then we find the mean square error using:

$$\langle e^2 \rangle = \langle [g(\vec{p}, \vec{\psi} + \vec{\delta}) - \hat{g}(\vec{p}, \vec{\psi} + \vec{\delta})]^2 \rangle \quad (4.2)$$

Before we can solve equation (3.7) we must evaluate the F_{ϕ} 's. It can be shown that (HANSON, D.W., 1981):

$$F_{\phi}(\vec{p}, \vec{\delta}) = (2.91/2) k^2 p^{5/3} (\sec \psi) [2I_2 - I_1] \quad (4.3)$$

where: I_1 is the integral in equation (3.3); and

$$I_2 = \int C_n^2(h) dh \quad (4.4)$$

To determine the performance of the estimation procedure as a function of the look-back angle, θ_L , where:

$$\theta_L = n(\psi_i - \psi_{i+1}) \quad (4.5)$$

we choose $n = 2$, $p = 1$ m, $\psi = \alpha = 0$, and let:

$$0.05 < (\theta_L/\theta) < 1 \quad (4.6)$$

for values of θ between 5 and 50 urad. In figure 3 we plot the reduction in mean square error achieved by the estimate as a function of the ratio of θ_L to θ . From figure 3 we see that the performance of the estimate is not a strong function of this ratio.

In figure 4 we plot the maximum reduction in mean square error, for $n = 2$, for each point ahead angle of figure 3. The estimate is seen to give reasonable performance (i.e., 20% improvement) for point ahead angles less than 8 urad, while providing very marginal

performance for a point ahead angle of 50 urad.

5.0 DISCUSSION AND CONCLUSIONS

5.1 Discussion of results

The data in figure 3 shows that the performance of the estimate is not a strong function of the look back angle. We believe that this is a result of the fact the phase aberrations are mostly linear, and that a good estimate of this component can be made over a wide range of look back angles. One would also expect that the estimate would provide better results for small point ahead angles, as shown in figure 4, since for small angles there is better correlation between the measured data and the desired data than there is for larger angles. We believe that the magnitude of the improvement shown in figure 3 is significant as discussed in the next section.

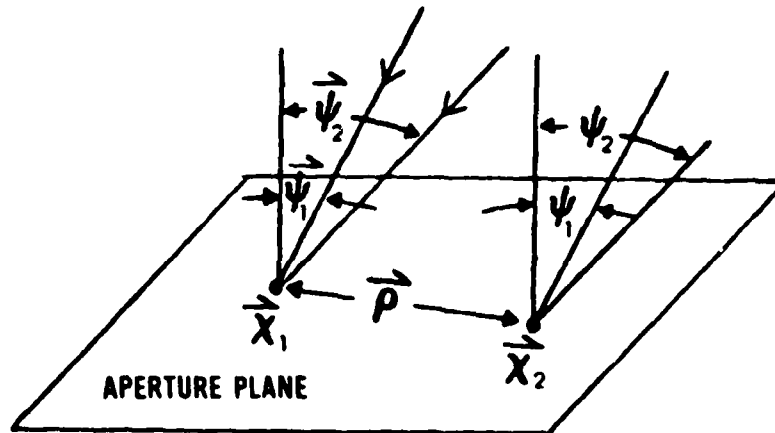
5.2 System Implications

Using equation (3.3) we see that the mean square wavefront error for a station keeping error of 5 urad is $.145 \text{ rad}^2$, at a wavelength of $.5 \mu\text{m}$. This corresponds to an rms wavefront error of $.06\lambda$, which is a reasonable budget for the station keeping error, since an optical system with $.1\lambda$ rms wavefront error is considered a good system.

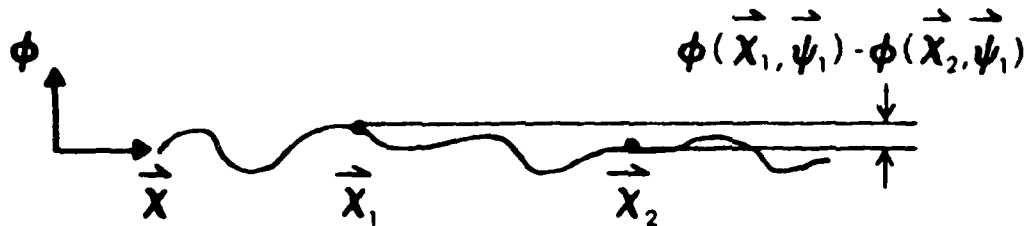
We can interpret the point ahead angle in figure 3 to be the station keeping error allowable between the beacon and the desired receiver. Thus, through utilization of the estimation process developed in this paper the allowable station keeping error can be increased by approximately 15% while maintaining the same wavefront error. Although this increase seems small, it is truly significant since it could extend the lifetime of a system costing 100's of millions of dollars, with a very nominal investment in signal processing electronics. Alternatively the weight of the propellant required to maintain the station keeping could be reduced by 15%. Since almost all space systems have difficulty meeting the design goals for system weight, use of the developed estimation procedure could make the difference between meeting or not meeting the desired system weight goals. Different systems may require varying station keeping requirements. In general, the more stringent the station keeping specification, the more the benefit from the estimation procedure developed herein.

It is important to point out that the data needed to obtain this optimum linear estimate, i.e., the F_{ϕ} 's in equation (3.7), are already available in current adaptive optical systems. No a priori knowledge of the turbulence profile, or any other atmospheric characteristic, is required.

TWO TYPICAL POINTS IN THE APERTURE PLANE RECEIVING OPTICAL SIGNALS FROM TWO TYPICAL ZENITH ANGLES



OPTICAL PHASE AS A FUNCTION OF LOCATION IN THE APERTURE PLANE FOR ZENITH ANGLE $\vec{\psi}_1$



OPTICAL PHASE AS A FUNCTION OF LOCATION IN THE APERTURE PLANE FOR ZENITH ANGLE $\vec{\psi}_2$

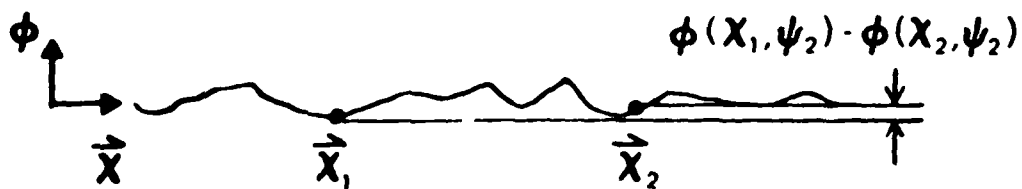


FIGURE 1 ANISOPLANATIC PHASE ERROR

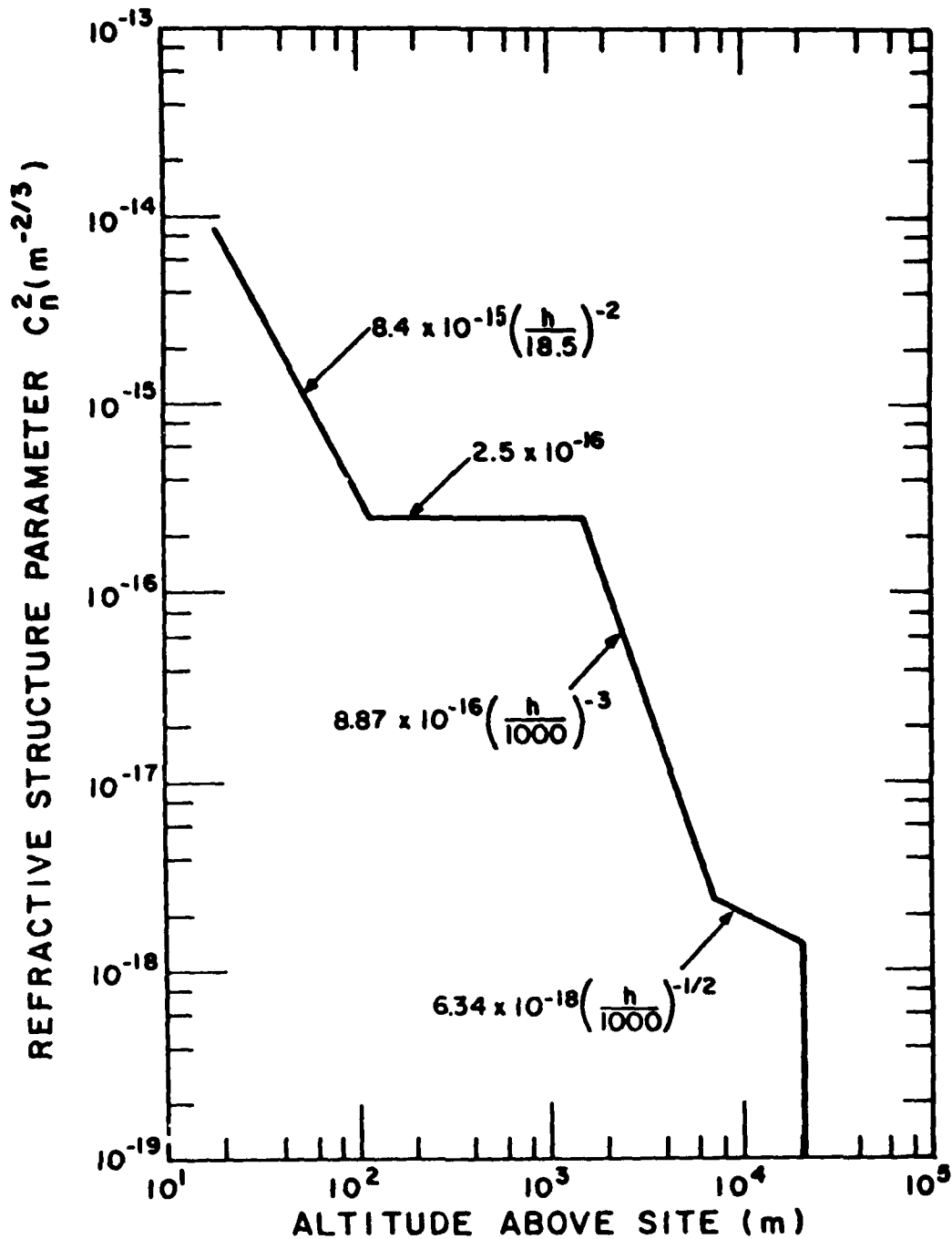
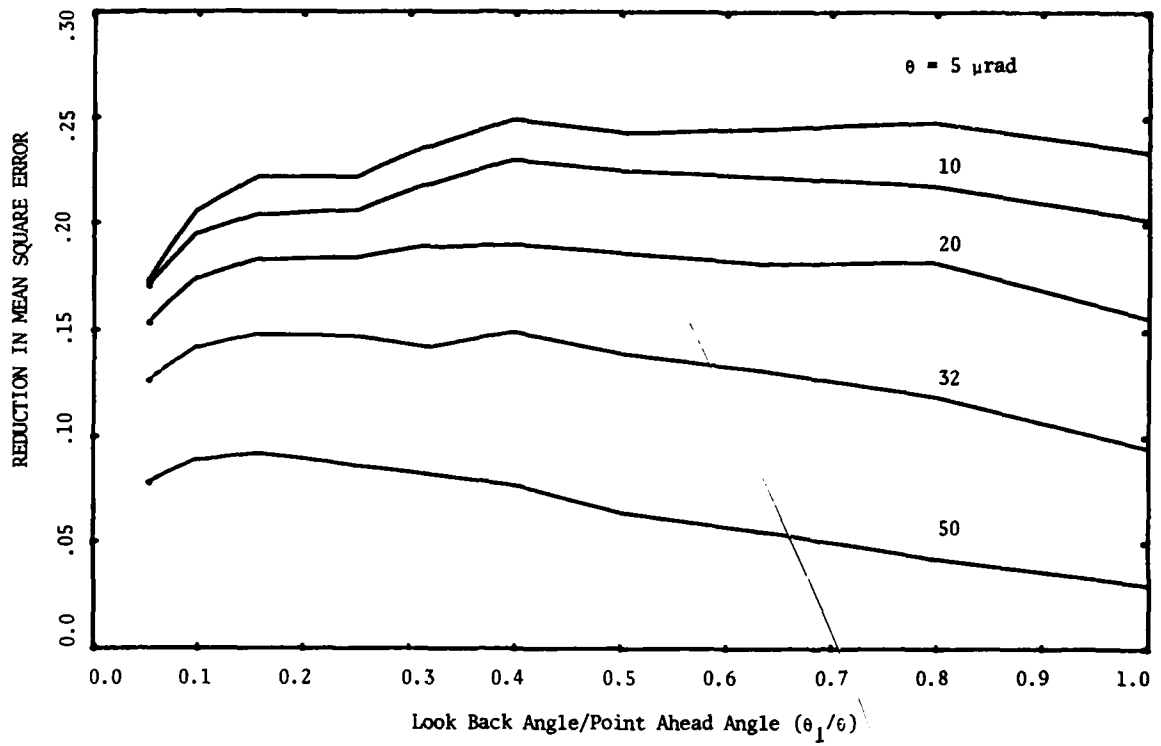
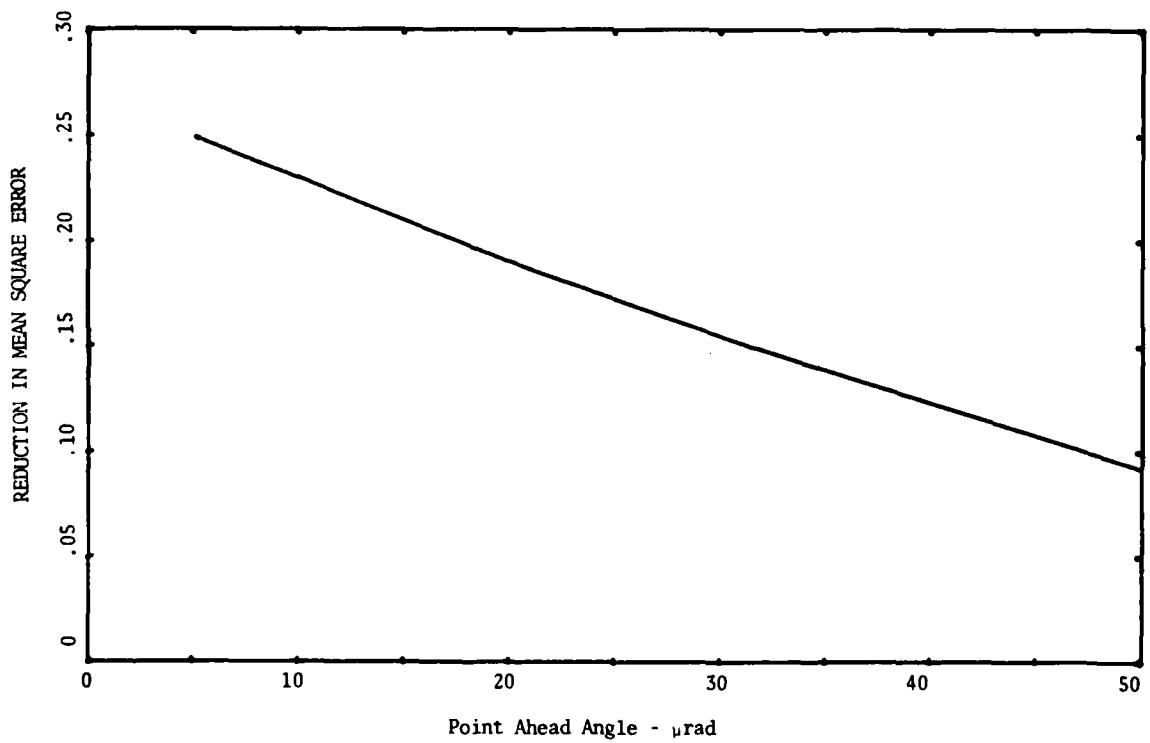


FIGURE 2 MODEL TURBULENCE PROFILE

FIGURE 3 PERFORMANCE OF THE OPTIMUM LINEAR ESTIMATE FOR $n=2$ FIGURE 4 PERFORMANCE OF THE OPTIMUM LINEAR ESTIMATE FOR $n=2$

PHASE MEASUREMENT SYSTEMS FOR ADAPTIVE OPTICS

James C. Wyant
Chris L. Koliopoulos
Optical Sciences Center
University of Arizona
Tucson, Arizona 85721

SUMMARY

This paper describes and compares two basic categories of phase measurement systems for adaptive optics: sensors that measure the wavefront directly and slope measurement sensors. Both self-referencing and non-self-referencing wavefront sensors are discussed and interferometric and geometrical slope sensors are compared. The conclusion is reached that of the phase measurement systems studied to date the lateral shear interferometer and the nutating Hartmann sensor are of the most general use due to their high efficiency and simplicity, however there is a whole class of optical tracking sensors that appear promising for use as phase measurement systems for adaptive optics applications, which warrant future study.

1. INTRODUCTION

The heart of any adaptive optics system is the phase measurement system, generally referred to as the wavefront sensor. The purpose of this paper is to describe and compare the different categories of wavefront sensors and to point out the relative advantages and disadvantages of each.

Wavefront sensors can be divided into two broad categories: 1) sensors that measure the wavefront directly and 2) sensors that measure the slope of the wavefront from which the wavefront is determined by an integration process. Direct measurement wavefront sensors can be further divided into two categories: 1) those requiring an external reference beam and 2) self-referencing sensors. Wavefront sensors requiring an external reference beam have limited use in adaptive optics. Self-referencing wavefront sensors are convenient to use, however they are always extremely light inefficient. Slope sensors, which are the most commonly used wavefront sensors in adaptive optics, can also be divided into two categories: 1) interferometric sensors and 2) geometrical sensors. The interferometric sensors are generally of the lateral shear type and the geometrical sensors are generally of the Hartmann type. While at first glance these two sensors appear quite different, they are rather similar in nature and performance as will be illustrated in this paper. Slope sensors are not limited to lateral shear interferometers and Hartmann sensors, but rather any tracking sensor can be used as a slope sensor for an adaptive optics system.

All the interferometric sensors described in this paper have a common feature in that the phase of the interference pattern is measured electronically. For this reason, the initial part of this paper describes electronic phase measurement techniques.

2. ELECTRONIC PHASE MEASUREMENT

Electronic phase measurement techniques for interferometric applications fall into two general categories: 1) sensors for which the phase difference between the two interfering beams is changed at a constant continuous rate in time, producing a frequency difference between the two beams and 2) sensors for which the phase difference between the two interfering beams is changed in discrete steps in time. Interferometers using phase measurement techniques of the first type given above are often called heterodyne or AC interferometers, while interferometers using the second type of phase measurement technique given above are called phase-shifting or phase stepping interferometers.

Figure 1 shows various techniques that can be used as a frequency shifter in a heterodyne interferometer. For example, if the reference mirror in the interferometer moves at a velocity V , the frequency of the light reflected at normal incidence is frequency shifted an amount $2V/\lambda$. Likewise, if circularly polarized light is transmitted through a rotating half-wave plate, the frequency of the transmitted light is changed an amount equal to twice the rotation rate of the half-wave plate.¹ A convenient way to implement this polarization frequency shifter is to place a fixed quarter-wave plate and a rotating quarter-wave plate in the reference arm of the interferometer so both quarter-wave plates are used in double pass. If the first quarter-wave plate is properly oriented it converts linearly polarized light into circularly polarized light. Since the rotating quarter-wave plate is used in double pass it acts as a rotating half-wave plate which frequency shifts the light transmitted through it, and the stationary quarter-wave plate converts the circularly polarized light back to linearly polarized light. The principal difficulty in using rotating half-wave and quarter-wave plates is that for reasonable rotation rates it is not possible to obtain a frequency shift much larger than 1 or 2 KHz.

A diffraction grating can also be used as a frequency shifter since it shifts the frequency of the N th order by an amount NV/f , where V is the velocity component of the grating perpendicular to the grating lines and f is the spatial frequency of the grating. Equivalently, the frequency shift is equal to N times the number of grating lines that pass a given point per second. Note that, for a grating, the frequency shift is independent of wavelength. An acousto-optic Bragg cell frequency-shifts the diffracted light in the same way as a moving diffraction grating. In this case the traveling acoustic wave serves as the moving grating. The frequency shift of the first diffracted order is equal to the frequency used to drive the Bragg cell, independent of the wavelength of the light.

Although numerous phase-measurement techniques exist, we will limit our discussion to three techniques: 1) zero-crossing, 2) phase-lock, and 3) N-bucket.

In the zero-crossing technique a clock starts when the reference signal passes through zero, and stops when the test signal passes through zero. The ratio of the time the clock runs to the period of the signal gives the phase difference between the two signals. In practice, the sinusoidal signals are greatly amplified to yield a square wave to improve the zero-crossing detection. The phase measurement is performed modulo 2π .

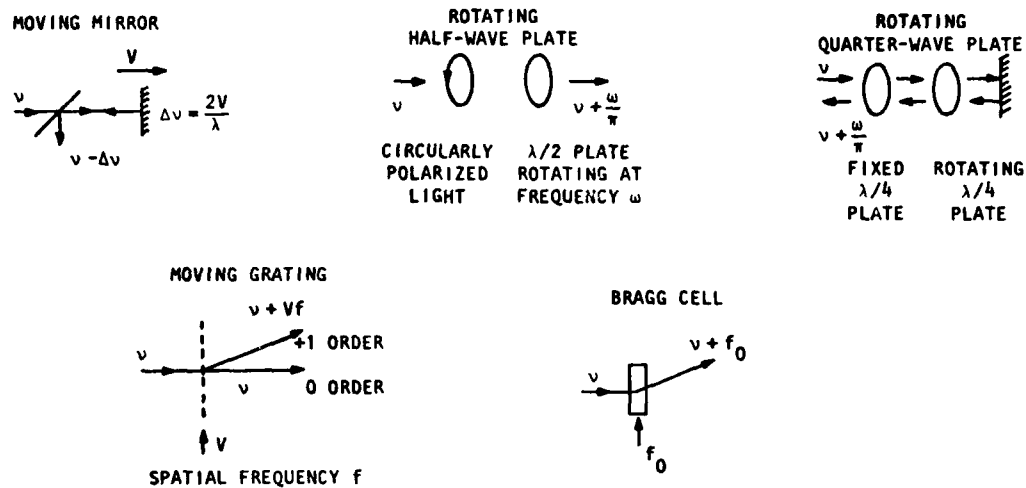


Figure 1. Phase-shifting techniques.

In the phase-lock technique the phase difference between the two interfering beams is dithered, for example by use of a piezoelectric transducer mounted on a mirror. In addition to the high-frequency phase dither, a low-frequency phase shifter is required. If $\delta(t) = A \sin \omega t$ is the high-frequency phase dither, $I_1(x,y)$, $I_2(x,y)$ are the intensities of the two interfering beams, and $\delta(x,y)$ is the phase being measured, then the detected signal can be written

$$\begin{aligned} I(x,y;t) &= I_1(x,y) + I_2(x,y) + 2\sqrt{I_1(x,y)I_2(x,y)} \cos[\delta(x,y) + A \sin \omega t] \\ &= I_1 + I_2 + 2\sqrt{I_1 I_2} \{ \cos \delta(x,y) [J_0(A) + 2J_2(A) \cos 2\omega t + \dots] \\ &\quad - \sin \delta(x,y) [2J_1(A) \sin \omega t + 2J_3(A) \sin 3\omega t + \dots] \} \end{aligned} \quad (1)$$

where J_n is the n^{th} -order Bessel function.

If, by use of the low-frequency phase shifter, $\delta(x,y)$ is made equal to $n\pi$, then $\sin \delta(x,y)$ equals zero and the amplitude of the signal at the frequency of the fundamental dither frequency will be zero. By measuring the phase shift required to make $\sin \delta(x,y) = 0$, which can be achieved for example by measuring the voltage applied to a piezoelectric transducer used to move a mirror, the phase $\delta(x,y)$ can be determined. This phase-lock technique is commonly used in multi-dither COAT (coherent optical adaptive techniques) systems.²

In the so-called N-bucket technique the period of the sinusoidal signal produced by the interference of the two beams of different optical frequencies is broken into subperiods. For example, in the four bucket method, each period of the sinusoidal signal is broken into four quarter-periods. If A, B, C, and D are the number of photons detected during the first, second, third, and fourth quarter-periods, respectively, the relative phase ϕ of the signal is given by

$$\tan(\phi + 45) = \frac{A - C}{B - D}, \quad (2)$$

where the phase is measured with respect to the beginning of the quarter-period. The measurement is modulo 2π if the signs of numerator and denominator are accounted for. It can be shown that the "bucket" technique works as long as the period of the sinusoidal signal is broken into three or more equal subperiods. If three quarter periods are used the phase is given by

$$\tan(\phi + 45) = \frac{A - C}{2B - (A + C)}. \quad (3)$$

In a phase shifting interferometer a moving mirror, a rotating half- or quarter-wave plate, or a moving grating can be moved in discrete steps to give discrete phase shifts. Likewise, an E-O modulator can be used to produce discrete phase shifts.

Eq. (4) gives the irradiance that would be obtained at four different phase steps separated by 90° .

$$\begin{aligned} I_1 &= I_0 + I_0 \gamma \cos(\phi) \\ I_2 &= I_0 - I_0 \gamma \sin(\phi) \\ I_3 &= I_0 - I_0 \gamma \cos(\phi) \\ I_4 &= I_0 + I_0 \gamma \sin(\phi) \end{aligned} \quad (4)$$

From Eq. (4) it follows that the phase, ϕ , is given by

$$\phi = \tan^{-1} \left\{ \frac{I_4 - I_2}{I_1 - I_3} \right\} \quad (5)$$

If only three phase steps separated by 90° are used it follows from Eq. (4) that

$$\phi = \tan^{-1} \left\{ \frac{I_1 + I_3 - 2I_2}{I_1 - I_3} \right\} \quad (6)$$

It is not necessary that the phase step be 90° . If I_n is the intensity of the interference pattern obtained by stepping the phase an amount $n(2\pi/N)$, the phase ϕ can be determined by using Eq. (7).³ In this case the resulting intensity I_n is multiplied by a cosine and sine and summed and ratioed to give the tan of the phase difference ϕ . This method is equivalent to synchronous detection techniques in communication theory.

$$\tan \phi = \frac{\sum_{n=1}^N \{I_n \sin[n(2\pi/N)]\}}{\sum_{n=1}^N \{I_n \cos[n(2\pi/N)]\}} \quad (7)$$

A good feature of phase shifting techniques is that they can be used with solid state detector arrays such as photodiode or CCD arrays. An irradiance distribution can be measured then the detector can be read out and the output stored in memory. The phase difference between the two interfering beams can be changed an appropriate amount such as 90° and the detector can be read out again. This can be repeated for three or more times and then the phase distribution can be calculated. With a CCD array the N-bucket technique can be used as well as the phase shifting technique. The signal is integrated for a quarter-period, then very rapidly the integrated signal is switched out of the detector sites. The detector continues to integrate for another quarter period while the detector is read out. At the end of the second quarter-period the integrated signal is again very rapidly switched out of the detector sites and the process is repeated. If the signal level is sufficiently high, data can be taken at megahertz rates.

The use of solid state detector arrays offers large density of detector elements in a small package, integration of high frequency irradiance noise, and a parallel in-serial out philosophy which reduces electronic processing to an absolute minimum. Complex algorithms can readily be encoded in digital logic.

3. DIRECT MEASUREMENT OF WAVEFRONT

If an external reference beam is available probably the best instrument for measuring the wavefront directly is the Twyman-Green interferometer. Unfortunately, for most adaptive optics systems a reference wavefront is not available, and a self-referencing wavefront sensor is required. Two such self-referencing interferometers are the radial shear interferometer and the Smartt interferometer.

A radial shear interferometer is illustrated in Figure 2. The wavefront being measured is interfered with an expanded version of itself. If the expansion or magnification ratio is sufficiently large, the wavefront of the expanded beam can be thought of as being a constant over the region of overlap with the wavefront being measured. Thus, the interference pattern gives us the wavefront directly. Any of the electronic phase measurement techniques mentioned above can be used to determine the phase distribution.

A second self-referencing interferometer is the Smartt point diffraction interferometer (PDI) illustrated in Figure 3. In the PDI the wavefront being measured is focused onto a plate containing a small pinhole of diameter smaller than $1/2$ the Airy disk diameter that would be obtained if the focused beam had no aberration.⁴ The plate has a partially transmitting coating that transmits between 0.1 and 1% of the incident light. The light diffracted by the pinhole serves as a spherical reference wavefront which interferes with the attenuated beam passing through the plate. The resulting interference pattern gives directly the wavefront aberrations. To obtain maximum fringe contrast, the plate attenuation should be selected such that the diffracted spherical wave and the attenuated transmitted beam have the same intensity.

The PDI can be modified as illustrated in Figure 4 so electronic phase measurement techniques can be used. Now the pinhole is made through a piece of birefringent material such as mica. The thickness of the birefringent material is selected such that it acts as a half-wave plate and it is oriented so as to rotate the direction of polarization of the incident light 90° . Thus the diffracted spherical wave and the directly transmitted wave have orthogonal polarization. An E-0 modulator can be used to shift the relative phases of the beams. Likewise, a stationary quarter-wave plate and a rotating half-wave plate can be used to produce either a relative phase shift or a relative frequency shift between the two beams as described above.

A problem with the PDI is that if beam jitter is present the focused beam will move around relative to the pinhole, and the amount of light in the diffracted spherical beam will vary. Figure 5 shows a modified PDI that does not have this problem. In this interferometer the beam is defocused on the small disk used to produce a spherical wavefront for the reference surface, thus allowing for beam wander of the input beam. The larger the defocused spot, the larger the tilt can be before the fringe contrast changes. Of course the larger the defocused spot the less light we have in the reference beam. For example, for a tilt tolerance of ± 10 fringes, and a reflecting spot diameter of $1/2$ the Airy disk diameter, the reference beam will contain about 0.2% of the incident light.

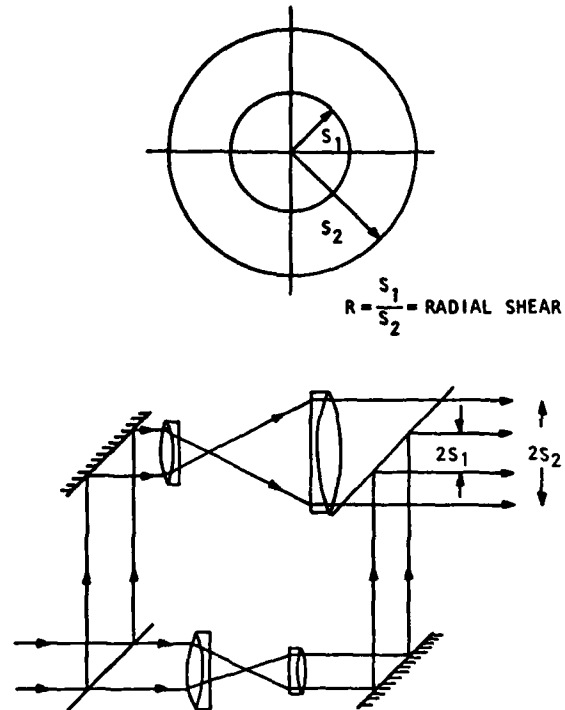


Figure 2. Radial Shear Interferometer.

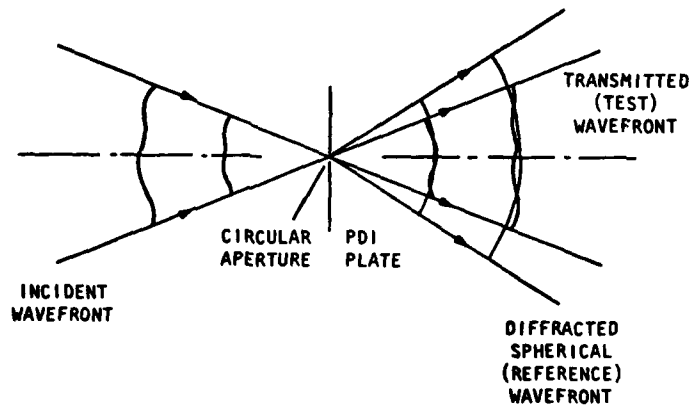


Figure 3. Smartt point diffraction interferometer.

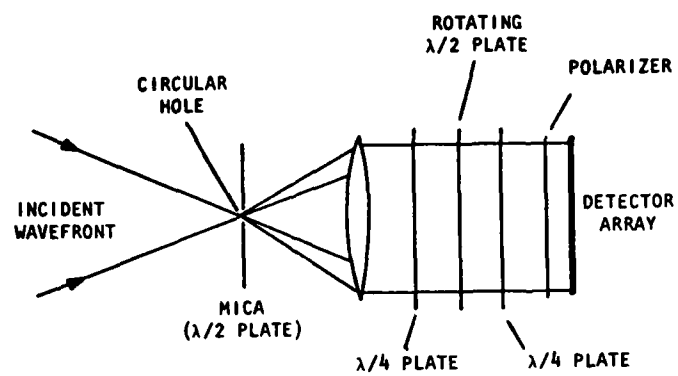


Figure 4. Point diffraction interferometer modified so electronic phase measurement techniques can be used.

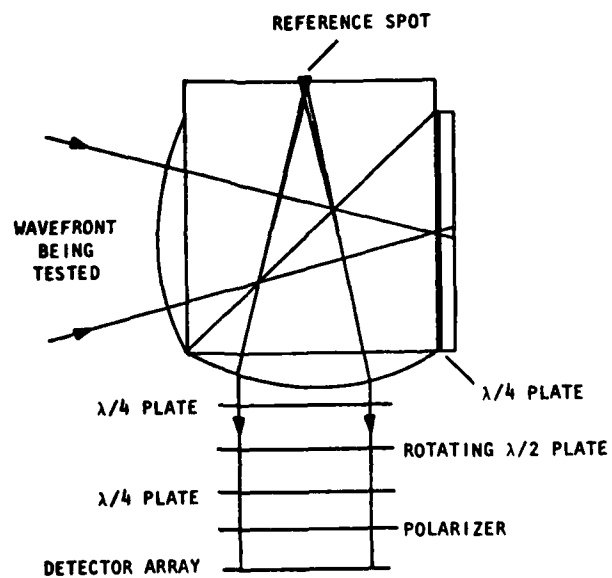


Figure 5. Modified PDI.

It should be noted that the two sides of the polarization cube are made slightly unequal so the reference spot and focused spot in the test arm of the interferometer appear to be the same distance from the output side of the cube when the light falling on the reference spot is suitably defocused. If this condition is not satisfied, the two interfering beams would have a different radius of curvature and defocus fringes would result.

It should also be mentioned, that while the interferometer has been modified so reasonable tilt does not cause a degradation in the contrast of the interference fringes, as the tilt of the input beam changes, the number of fringes in the interferogram does change. That is, the interferometer does correctly measure the amount of tilt in the wavefront.

A major problem with all self-referencing wavefront measurement interferometers is that they are not light efficient. For example, in the radial shear interferometer one beam is expanded a sufficient amount such that the phase distribution across the region of the beam used to form the interferogram is uniform. The amount of beam magnification required to obtain a sufficiently uniform phase across the interference region of course depends upon the amount of aberration present. A reasonable area magnification is generally at least 100. Since the two interfering beams should have roughly the same irradiance over the overlap region this means that in a typical radial shear interferometer 1% or less of the light is utilized.

Similar light in-efficiencies occur in the point diffraction interferometer. As mentioned above, to match beam intensities the plate has a partially transmitting coating that transmits only 0.1 to 1% of the incident light. So, again, 1% or less of the light is utilized. The PDI modified so beam jitter does not introduce interference contrast variations is even less light efficient. For this reason, these self-referencing interferometers find application with laser-based systems.

4. SLOPE MEASUREMENT

The wavefront phase distribution can also be measured indirectly by measuring the slope of the wavefront and using an integration process to calculate the wavefront phase itself. Slope measurement instruments fall into two main categories: 1) interferometric and 2) geometric tests. The most common interferometer for measuring wavefront slope is the lateral shear interferometer and the most common geometric slope measuring instrument used in adaptive optics is the Hartmann sensor, although there are many geometrical optical trackers which can also be used.

In a lateral shear interferometer (LSI) the pupil wavefront is interferometrically compared with a shifted version of itself. Interference fringes exist where these two pupil images overlap, and the position or phase of these fringes gives the average wavefront slope in the shear direction over the shear distance.

Two interferograms having shear in orthogonal directions are required to determine the wavefront. During the past several years improved techniques have been developed for obtaining the wavefront from the slope data obtained directly from the LSI, which is commonly called the wavefront difference function.⁵ It has been shown that the rms error in the wavefront is approximately equal to the rms error in the wavefront difference function multiplied by the ratio of the detector spacing to the shear distance.⁶

A convenient and the most popular LSI in adaptive optics systems is the radial Ronchi grating shown in Figure 6.⁷ In the Ronchi grating LSI the light is focused onto the grating. The interference of the 0 and the +1 orders gives a lateral shear interferogram, as does the interference of the 0 and -1 order, the +1 and -1, +3 and 0, etc. (Note that for a 50% duty cycle grating the even orders will be missing.) Because of the interference of the many different orders, the Ronchi ruling does not serve as a good LSI if the fringes are viewed visually. However, as a heterodyne interferometer it works superbly. The reason is as follows: If the grating is rotated, the different diffracted orders are frequency shifted an amount equal to the number of grating lines passing a given point times the order number. If the frequency shift of the first order is ν , then the frequency shift of the third order is 3ν , and -1 is $-\nu$, the zero order is 0, etc. The irradiance of the interference pattern produced by any two orders will vary sinusoidally at a frequency equal to the difference frequency between the two diffracted orders. It thus follows that if the even orders are absent, the only two interference patterns whose irradiance varies sinusoidally with time at frequency ν are the interference patterns resulting from the interference of the 0 and +1 and 0 and -1 orders. If the electronics used to measure the phase uses filters that pass only frequencies near ν , the other interference patterns will not be detected. Thus, we are left with only two lateral shear interferograms that contain approximately 45% of the incident light. A complete analysis shows that since the amount of shear is the same for the two interferograms, for most instances the measured data are the same as if only a single lateral shear interferogram were present. It can be shown that the resulting filtered signal detected by the detector is given by

$$I_s(x,y;t) = I_0 \left(\frac{1}{2} \right) + \frac{2}{\pi} I_0 \left\{ \cos \left[\Delta \phi'(x,y) + \frac{\Delta^3 \phi'''(x,y)}{6} + \frac{\Delta^5 \phi^V(x,y)}{120} - \omega t \right] \right\} \\ \left\{ \cos \left[\frac{\Delta^2}{2} \phi''(x,y) + \frac{\Delta^4}{24} \phi^{IV}(x,y) + \dots \right] \right\} . \quad (8)$$

Δ is the shear between the 0 and first order and the wavefront phase, $\phi(x,y)$ is equal to $(2\pi/\lambda)W(x,y)$, where $W(x,y)$ is the optical path length variation relative to a reference sphere. The modulation frequency ω is equal to $2\pi(\nu/d)$, where ν is the grating velocity for a point a distance r from the grating center and d is the grating line spacing for this point. Note that for a radial grating ν/d is independent of the position on the grating.

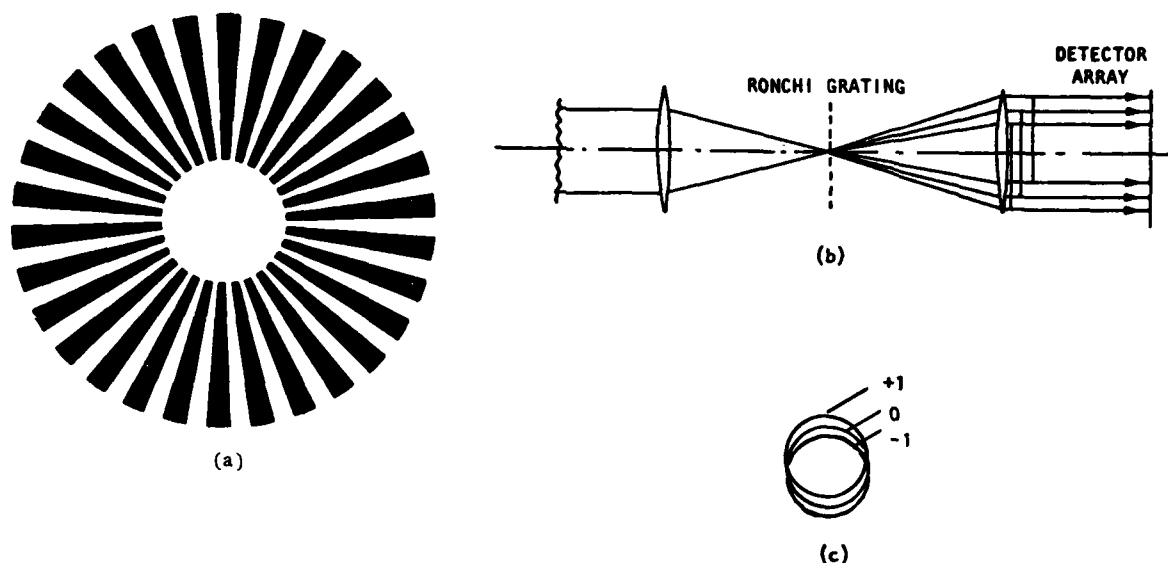


Figure 6. Radial Ronchi grating lateral shear interferometer.

(a) Radial Ronchi grating, (b) wavefront imaged on grating, (c) lateral sheared images showing 0, +1, and -1 diffraction orders.

It is of interest to note that while the above result is based upon a diffraction analysis, a purely geometrical approach gives a similar result for the fundamental frequency signal if derivatives of $\phi(x,y)$ of order higher than one are set equal to zero. Thus, for very small shear, i.e., a coarse Ronchi ruling, a geometrical analysis and a diffraction analysis give essentially the same result. For this reason the Ronchi grating LSI is often called a chopper.

A good feature of the Ronchi grating LSI, as well as of several other grating LSI's, is that they work well with white light. First, the modulation frequency ω depends only upon the grating velocity and period, and it is completely independent of wavelength. Second, the shear Δ is proportional to wavelength, which at first thought appears bad; however, this means that $\Delta\phi'(x,y) = 2\pi W(x,y)/\lambda$ is independent of wavelength as long as the optical path difference, $W(x,y)$ is not a function of wavelength. Thus, as long as the shear is sufficiently small, the signal is independent of the wavelength. For most practical applications, as long as the shear is not more than approximately 10% of the pupil diameter, wavelength effects can be neglected. A shear of 10% of the pupil diameter corresponds to a grating spacing of approximately four times the Airy disk diameter.

Another good feature of most grating LSI's, including the Ronchi grating LSI, is that they work reasonably well with an incoherent extended light source. For a given number of received photons, the wavefront phase measurement error does depend upon the size of the extended source; however, the larger number of photons from an extended source eases the effect of increased size. If the shear is half the aperture diameter required to resolve the light source, for circular or square objects the measurement accuracy is independent of the object size and the only characteristics of the object influencing accuracy is radiance.⁶

If N is the radiance of a circular or square light source, T is the transmission of the entire optical path, ρ is the responsivity of the photodetector, τ is the total integration time, and the effective aperture of each detector is equal to the detector spacing, in which case all the available light is used, for photon-limited operation, $\partial\theta$, the error in the measured wavefront error is given by

$$\partial\theta = \frac{(1.1 \times 10^{-9})}{\lambda(N T \rho \tau)^{1/2}} \quad (9)$$

if the shear is set equal to half the aperture diameter required to resolve the light source.⁶ With a radial Ronchi grating LSI the amount of shear can be optimized by varying the radial position on the grating at which the light is focused.

The basic principle of a Hartmann sensor used to measure wavefront slope error is illustrated in Figure 7. In the Hartmann sensor the wavefront disturbance being measured is imaged onto a lens array. If the incoming wavefront were perfect, each lens would focus the light at its own null position. Local slope variations across the wavefront, however, displace the foci from their ideal positions. This image displacement is directly related to the slope error in the wavefront and can be measured with a quadrant detector. If the geometry of the lens array is not precisely known, it can be calibrated by illuminating it with a wavefront of known high quality. Since in general an AC signal is preferred to a DC signal, it is common to nutate the angle of the beam incident upon the lens placed in front of the detector elements. Now the signal coming out of each detector element is time varying at a known rate, and improved measurement accuracy is obtainable.

The signals obtained using a nutating Hartmann sensor can be understood by looking at Figure 8. If no slope error is present the light spot focused on the quadrant sensor travels in a circle of radius a centered at the center of the quadrant sensor. Figure 8b shows the signal produced by the sum of detector elements 1 and 4, 2 and 3, 1 and 2, and 3 and 4. Since the focused spot spends equal time focused on each detector element all signals have the same time width. However, if a $+x$ slope error is present the focused spot will spend more time on detector elements 1 and 4 than on elements 2 and 3 and the signals out of elements 1 and 4 and 2 and 3 will be as shown in Figure 8c. Likewise, a slope error in the y direction will cause the pulses given by the sum of detectors 1 and 2 and detectors 3 and 4 to have unequal length. Thus, by measuring the relative pulse length both x and y slope errors can be measured.

Most likely for future Hartmann sensors rather than using a separate quadrant detector at the focus of each lens, a CCD array will be used as the detector. Four adjacent detector elements will act as quad detector and while all detectors can be used in parallel, they can be read out in serial, and thus simplify the sensor electronics. Breadboard systems have been demonstrated using this approach.

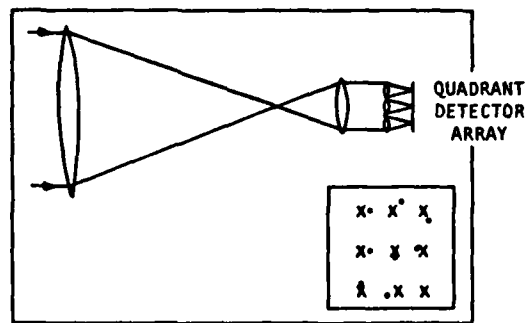


Figure 7. In a Hartmann test, displacement of an image yields wavefront-slope error.

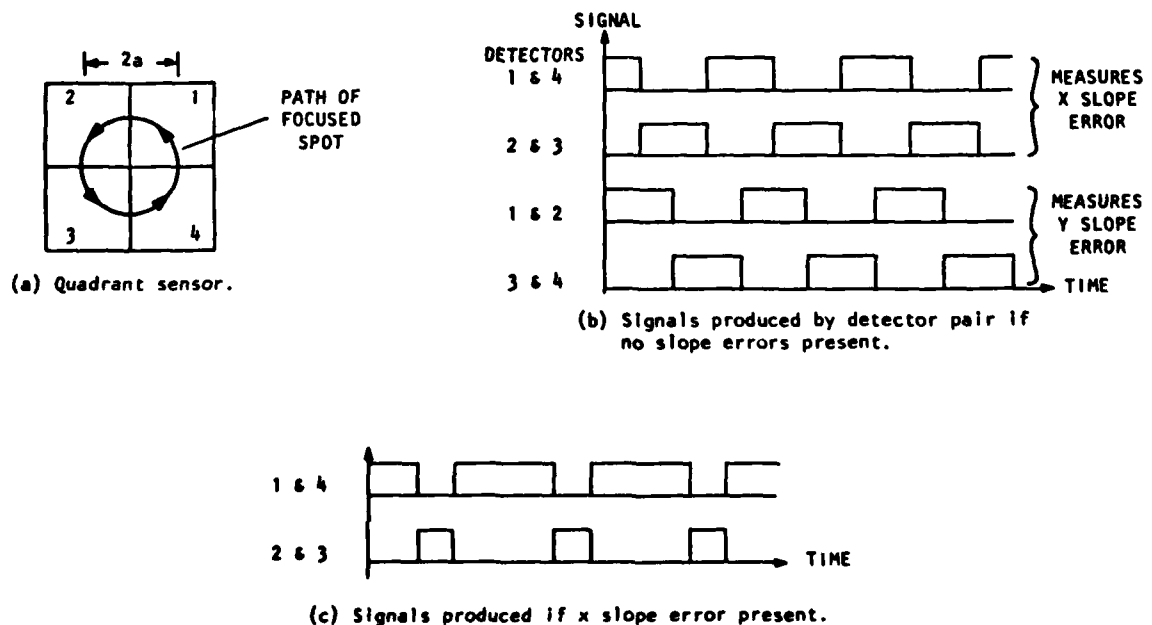


Figure 8. Signals produced by nutating Hartmann sensor.

The shot-noise-limited performance of the Hartmann test is

$$\Delta\theta = \frac{\pi}{\sqrt{P_i}} \quad (10)$$

where $\Delta\theta$ is the rms error in measuring the phase tilt across a single element of the Hartmann sensor and P_i is the number of photons detected by the detector placed behind each lens in the array. Since the rms wavefront-phase error is approximately equal to the rms wavefront-phase tilt across each aperture, the error is approximately equal to π divided by the square root of the number of photons detected by each sensor element, and is independent of the aperture size. It is assumed that the pupil area of each sensing element is sufficiently small that the object cannot be resolved by a single lenslet.

It is interesting to note while we have been discussing the use of a radial grating lateral shear interferometer (chopper) and the Hartmann sensor as wavefront sensors for adaptive optics, they can also be thought of as trackers. That is, they are measuring the direction of the light beam coming into the optical system. The only difference between using these sensors as wavefront sensors rather than trackers is that when they are used as wavefront sensors the optical system's aperture is broken up into many small sub-apertures and the wavefront sensor is working as a tracker for each of these sub-apertures. Thus, trackers and wavefront sensors are really equivalent and any tracker can also be used as a phase sensor. To first order, geometric optical analysis can be used but a complete analysis usually reveals error producing effects. All of these wavefront sensors can be scaled for use in the visible or infrared.

Over the years many trackers have been studied and references 8 and 9 give a summary of the most useful trackers. Probably many of these trackers should be studied in more detail to see if there is not one that would make a better phase sensor than either the radial grating lateral shear interferometer or the Hartmann sensor. One such sensor which looks promising in that it has high efficiency, requires fewer detector elements than the lateral shear interferometer or Hartmann sensor, provides AC operation and variable sensitivity and can work with broad-band extended sources is the Quadrant Reticle Wavefront Sensor (QRWS).

The QRWS operates upon the wavefront to be analyzed in the image plane. The reticle shown in Figure 9 is placed in the image plane of an optical system. The reticle consists of alternating opaque and clear quadrants, hence the name. The optical system and operation of the QRWS is shown in Figure 10. Following the optical wavefront through the system; the input beam is reflected off a nutating mirror upon which is imaged the wavefront disturbance. Assuming the nutating mirror is at the front focus of lens 1, the Fourier transform of the wavefront disturbance is incident upon the quadrant reticle. Due to the nutating mirror, this focused spot describes a circular path on the reticle. The light that is transmitted by the reticle is then passed through lens 2 which re-images the wavefront disturbance onto a detector array. Although the focused spot moves in a circle, the re-imaged pupil is motionless, however, there is an AC modulation of the light incident on the detector due to the focused spot being obstructed by the opaque quadrants as it moves in its circular path. It is this modulation that provides information as to the wavefront slope in each sub-aperture of the pupil as defined by the detector array.

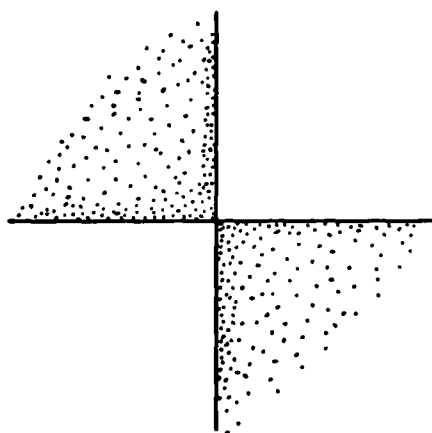


Figure 9. Quadrant reticle.

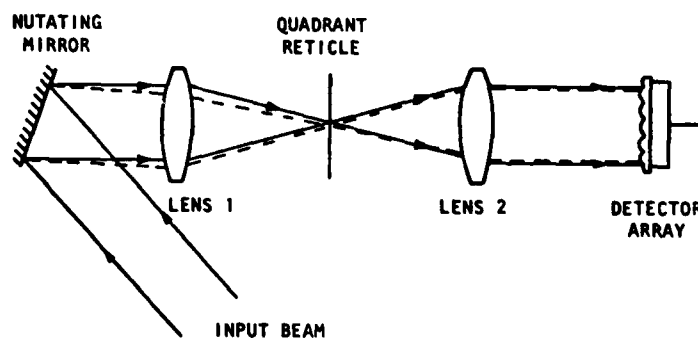


Figure 10. Quadrant Reticle Wavefront Sensor.

The signals produced by the QRWS are similar to the signals produced by the nutating Hartmann sensor. To see this in detail, several examples will be given, based upon a simple geometrical analysis.

The Quadrant Reticule Wavefront Sensor can simply be used as a tracker; that is, the overall tilt across the whole pupil can be obtained. Assume a point source is to be used and no aberrations present. As depicted in Figure 11a, the image of the point source is shown tracing a circular path centered on the axis or center of symmetry of the reticle. The output signal from all the detectors are the same and are as shown. Since the spot spends equal time in each quadrant of the reticle, the electronic waveform is of equal duration on and off.

If now there is a displacement of the point source in the y-direction, the center of the circular path is no longer at the center of symmetry of the reticle pattern and therefore the image spends differing times in the quadrants as it moves about its path. The signal waveform also reflects this by showing a variation in the pulse width and pulse timing (Figure 11b). Similarly a displacement of the point source in the x-direction produces a variation in pulse width and timing (Figure 11c). By comparing these signals to a reference source that is used to drive the nutating mirror the x and y displacements can be obtained.

This is the basis of wavefront sensing of slope errors in each sub-aperture of the pupil. By dividing the re-imaged pupil into sub-apertures through the use of a detector array, the signal waveform of each detector can be observed and compared to the reference signal to obtain the slope across that sub-aperture.

Assume now that there exists a slope error across a sub-aperture in the pupil and a point source is used. As shown in Figure 12, the slope in the sub-aperture causes a fraction of the light to be displaced from the image of the point source. As the image moves in its circular path due to the nutating mirror, the signal that is detected at the re-imaged sub-aperture with the slope error reflects the displacement similar to the previous examples of overall tilt sensing. The larger the slope error, the farther away from the center of symmetry the image due to that sub-aperture lies, the larger the difference in pulse width between the detected signal and the reference signal. Thus it can be seen that this sensor is capable of a wide dynamic range.

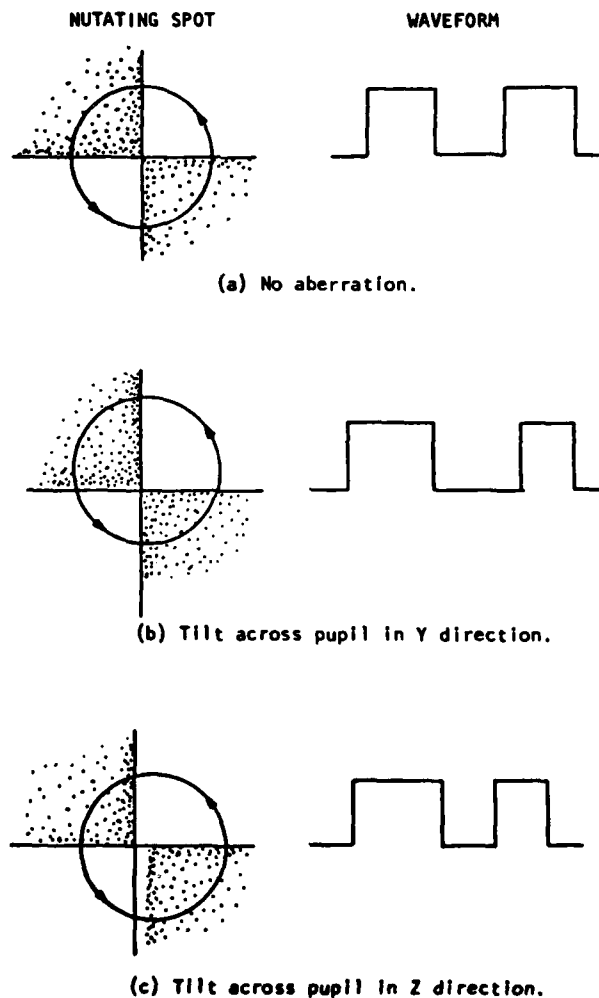


Figure 11. Quadrant reticle wavefront sensor used as a tracker.

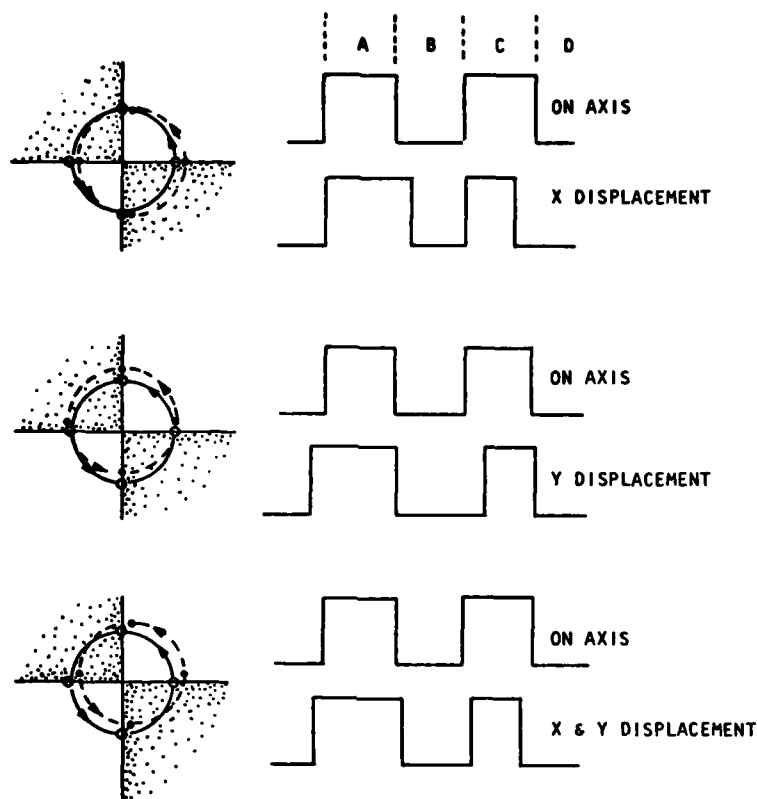


Figure 12. Slope signals obtained at a sub-aperture.

Thus the important advantage of the Quadrant Reticle Wavefront Sensor is the ability to sense x and y slope errors within a sub-aperture with only one detector. This reduces the total number of detectors needed for a system, which reduces cost, size, and complexity, while increasing reliability. As an example, the ITEK Real-Time Atmospheric Compensation System which uses a radial grating lateral shear heterodyne interferometer requires 2 sixteen element detector arrays, one for sensing x slope error and one for y slope errors. Using the QRWS, only twelve detectors are required to sense both x and y slopes, not 32 (Figure 13). Note also that this sensor uses 50% of the light in transmission, and if a reflective reticle is used instead of an opaque reticle, 100% of the light is used. Thus depending on the application, a large reduction in detector elements can be obtained. Sensitivity to slope errors can be changed by changing the nutation amplitude which changes the radius of the circular path taken by the image. Unlike the radial grating interferometer which requires the physical radial motion of the gratings, the QRWS can change its sensitivity by simply applying a different voltage to the PZT driven nutating mirror. This can be adjusted in both x and y drives.

It is seen that the Quadrant Reticle Wavefront Sensor offers a simple solution to wavefront sensing and tracking. Many of the features of the Radial Grating Shearing Interferometer and the nutating Hartmann sensor are combined in the QRWS to produce what may be a sensor which has all the advantages of both sensors but none of their individual disadvantages. There may be other trackers which can be used as even better wavefront sensors.

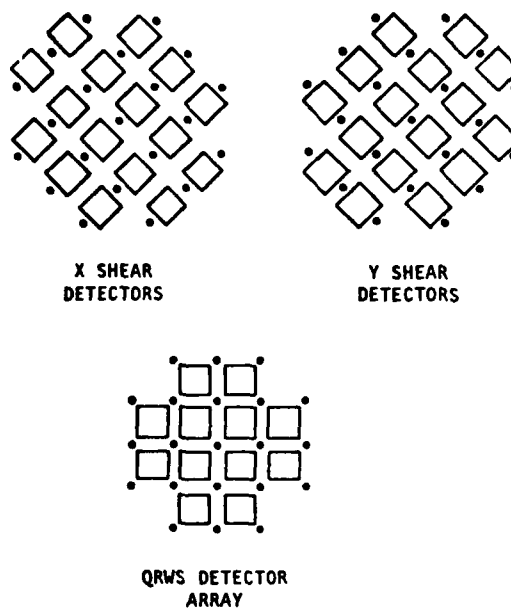


Figure 13. Detector reduction of QRWS over the radial grating shearing interferometer. (The spots are actuator points, squares are detectors measuring slope across a sub-aperture.)

5. CONCLUDING REMARKS

Wavefront sensing is a necessary tool for providing informational feedback in adaptive optical systems. By choosing the appropriate form of the sensor, complexity can be reduced through considerations of light availability and use of solid state integrating detector arrays, among other things. Wavefront sensors can provide accurate wavefront information with a wide variety of light sources, coherent or incoherent. As system complexity increases, a hierarchy of sensors will be used to provide specific functions from simple but high speed tilt (tracking) and focus measurement, to phasing of segments, to high spatial resolution figure sensing. By understanding the fundamental principles of interferometry and wavefront sensing, the designer can choose the appropriate sensor for the task.

6. REFERENCES

1. Robert Crane, *Appl. Opt.* **8**, 538-542 (1969).
2. J.E. Pearson, R.H. Freeman, and H.C. Reynolds, Jr. in *Applied Optics and Optical Engineering*, R.R. Shannon and J.C. Wyant, Eds. (Academic Press, New York, 1979) Vol. 7, pp. 275-281.
3. J.H. Bruning et al., *Appl. Opt.* **13**, 2693 (1974).
4. C. Koliopoulos et al., *Opt. Lett.* **3**, 118 (1978).
5. M.P. Rimmer, *Appl. Opt.* **13**, 623 (1974).
6. J.C. Wyant, *Appl. Opt.* **14**, 2622 (1975).
7. Chris L. Koliopoulos, *Appl. Opt.* **19**, 1523 (1980).
8. Special issue on optical tracking, *Appl. Opt.* **5**, (1966).
9. Gordon Gerson and Arthur Rue in *The Infrared Handbook*, W.L. Wolfe and G.J. Zissis, Eds. (Office of Naval Research, Dept. of the Navy, Washington, D.C., 1978), pp. 22-1 - 22-108.

ADAPTIVE OPTICAL SYSTEMS USING DISCRETE COMPONENTS

John W. Hardy
 Itek Optical Systems
 10 Maguire Road
 Lexington, Massachusetts 02173

ABSTRACT

This paper discusses the present state of development in adaptive optical systems in which the major functions of wavefront sensing, computation, and wavefront correction are performed by discrete components. Most current adaptive systems are of this type, sharing the common feature that they possess a finite number of degrees of freedom. The operating principles and performance of the most important adaptive optical devices developed during the last few years are described, including wavefront sensors, detector arrays, electronic data processors, and deformable mirrors. Typical system configurations for compensated imaging and laser beam control are described. Limitations of discrete technology at the device and system level are reviewed. The paper concludes with an assessment of the directions in which adaptive optical systems may evolve.

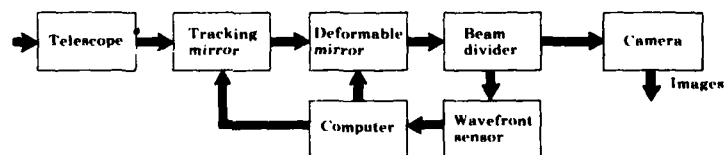
1. INTRODUCTION

Adaptive optical systems have been developed for a variety of applications during the last decade. These applications include figure control of large optical mirrors, laser beam pointing and focusing, image compensation for ground based telescopes, and wavefront compensation of high energy laser beams. The purpose of these systems is to minimize the effects of random disturbances which degrade optical wavefront quality, such as vibration, temperature changes, and atmospheric turbulence.

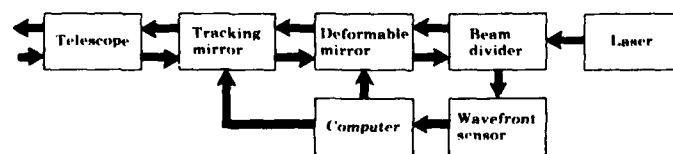
Most adaptive systems built to date have employed discrete optical and electronic components to perform the basic functions of wavefront sensing and wavefront compensation. Two typical system configurations are shown in Fig. 1. The purpose of the compensated imaging system in Fig. 1 is to eliminate the effects of atmospheric turbulence on the images of distant objects, such as astronomical objects or satellites observed by ground-based telescopes. Light reflected from the object is analyzed in real time by the wavefront sensor to determine the instantaneous wavefront aberrations. The required wavefront compensation is computed and control signals are sent to the active mirrors to close the adaptive loop, minimizing the wavefront errors at the wavefront sensor. A beam divider splits off part of the light to form the compensated image.

The purpose of the laser system in Fig. 1 is to concentrate the radiated energy on a distant target through a turbulent propagation path. The phase conjugation system shown operates in a similar way to compensated imaging, using radiation from the target to measure the wavefront distortion. The outgoing beam is precompensated with the same wavefront, and by the principle of optical reciprocity, after traversing the turbulent path in the reverse direction, it will be sharply focused upon reaching the target.

As a consequence of their discrete structure, most existing adaptive optics systems have a limited number of degrees of freedom, often less than 100. Future ground-based optical systems for surveillance, communications, and defense may employ large apertures which will require thousands of degrees of freedom. It is therefore appropriate to review the state of the art of discrete adaptive optics components to determine their limitations in terms of hardware and performance and to investigate approaches which will remove these limitations. In the discussion that follows, the emphasis will be on adaptive systems designed to compensate for high-speed, high-order optical wavefront disturbances such as those produced by mechanical vibration, atmospheric turbulence, and instabilities within a laser resonator because these error sources produce the maximum stress in terms of speed and number of degrees of freedom.



(a) Compensated imaging



(b) Laser communication and laser beam control

Fig. 1 Adaptive optics systems

The three most important parameters determining the design and complexity of discrete adaptive systems are:

- Number of degrees of freedom
- Wavefront correction range
- Temporal frequency response.

The number of degrees of freedom can be equated to the number of independent modes or zones to be compensated in the wavefront, which is usually a function of the aperture size.

The wavefront correction range and temporal frequency response requirements are governed largely by the severity of the environmental effects to be compensated.

For a wavefront propagating through Kolmogorov turbulence, the variance in phase between two points is proportional to $(d/r_0)^{5/3}$ where d is the separation between the points, and r_0 is the turbulence coherence length. The importance of r_0 is that it provides a convenient parameter defining the strength of turbulence in a propagation path, from which the required actuator spacing and compensation range of an adaptive compensator can be derived. At visible wavelengths, typical values for r_0 , up-looking through the earth's atmosphere to space, range between about 2 and 20 cm. The value of r_0 scales as the 6/5 power of the wavelength.

The spatial frequencies of the wavefront disturbance normally range from an inner scale of a few millimeters to an outer scale of several meters. Thus, to measure and compensate an atmospherically distorted wavefront exactly requires the adaptive optical devices to have spatial resolution in the order of hundreds of cycles per meter. For a 1-meter aperture, this would imply between 10^4 and 10^6 discrete zones. Fortunately, the error due to matching the wavefront does not become significant until the zone spacing becomes comparable with the coherence length r_0 . It is this fact that allows good performance to be obtained from adaptive systems, even with a limited number of degrees of freedom (Hardy, J.W., 1978).

The shape of an optical wavefront may be represented in two different ways: (1) using an array of independent localized zonal functions, or (2) using a set of orthogonal whole-aperture modal functions. Main characteristics of these two approaches are summarized in Fig. 2. Analytically, the two systems are equivalent in terms of the number of degrees of freedom required to specify a given wavefront to a certain precision. However, there are major practical differences especially in the implementation of wavefront sensors and compensation devices.

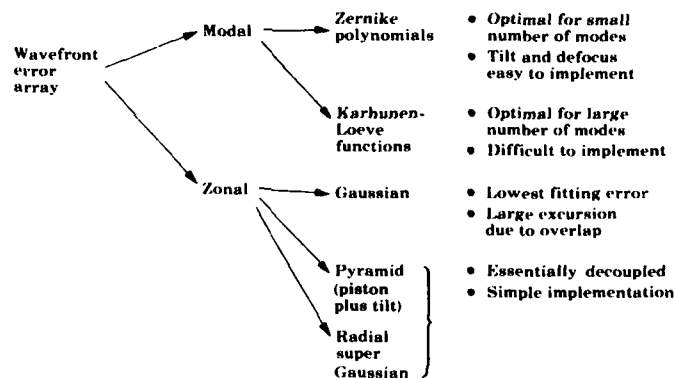


Fig. 2 Wavefront compensation strategies

All practical wavefront sensors and most deformable mirrors use the zonal approach. With zonal mirrors, the main variable is the shape of the influence function of each zone, which determines the wavefront fitting error. Mirrors with very stiff actuators, such as piezoelectric devices, generally have compact influence functions which have little cross-coupling and allow simple implementation. The lowest fitting error is achieved with Gaussian influence functions which, however, spread over adjacent zones and therefore necessitate more complex computations to take account of the cross-coupling.

For modal compensation, the well-known Zernike polynomials, which correspond to systematic optical aberrations such as defocus and astigmatism encountered in conventional optical components, may be employed; for turbulence compensation these are optimal only for a small number of modes. A more general set of functions, the Karhunen-Loeve (Wang, J.Y., 1978), can be optimized for turbulence compensation with apertures of any size. Consequently, at the present time modal compensation is restricted to small apertures with few degrees of freedom, while large apertures employ zonal compensation.

The wavefront correction range and temporal frequency response requirements for adaptive optical systems vary greatly according to the application, as depicted in Fig. 3. These requirements primarily affect the adaptive servo loop, specifically the measurement (integration) time, computation time, and the dynamic range and bandwidth of the wavefront correction device. Also shown on Fig. 3 are typical capabilities of three different types of deformable mirror. It can be seen that the frequency and range requirements of current adaptive systems are well covered by the available devices. We now consider in more detail the basic components used in discrete adaptive systems.

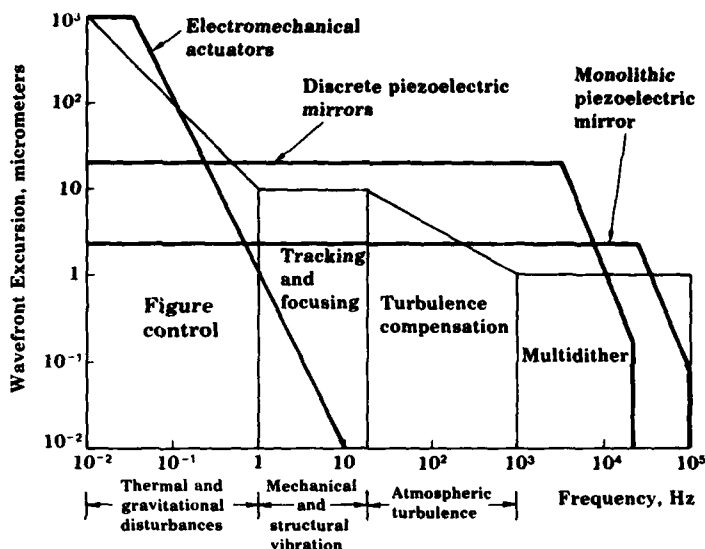


Fig. 3 Requirements for adaptive optics systems

2. WAVEFRONT SENSORS

It is not possible directly to measure the phase of an optical wavefront, as no existing detectors will respond to the temporal frequencies involved ($\approx 5 \times 10^{14}$ Hz). Three techniques are commonly employed to overcome this problem:

1. Measurements can be made on the intensity distribution of the image produced by the entire wavefront.
2. A reference wavefront of the same or slightly different wavelength is combined with the wavefront to be measured to produce interference fringes which can then be detected by conventional photoelectric (intensity) detectors.
3. The wavefront slope of small zones of the wavefront may be independently measured. This can be achieved by using a shearing interferometer or by dividing up the aperture and measuring the position of the image produced by each zone (the Hartmann test). Each of these three approaches has its own advantages and disadvantages. For example, image-plane measurements are useful in high-power systems especially when a non-linear effect (thermal blooming) is present. The well-known multidither adaptive system is an example of this approach. However, the photon efficiency of this technique is inversely proportional to the number of degrees of freedom, resulting in low efficiency for large apertures. For this reason it is not suitable for compensated imaging.

Coherent detection requires the use of a local phase reference, and its unambiguous range of phase measurement is restricted to $\pm\pi$ rad. Such detection systems are useful at longer laser wavelengths (3 to 12 μm) where the dynamic range is compatible with atmospheric phase variations.

Wavefront slope measurement is an extremely useful and versatile approach, as it may be used with either coherent or incoherent light, is highly efficient, and allows an unrestricted dynamic range. Its main drawback is that the wavefront must be reconstructed from the individual slope measurements. This is no problem for small apertures, but may be a factor in very large systems.

Two specific approaches to wavefront slope measurement will now be described.

Hartmann Sensor

The Hartmann sensor (shown schematically in Fig. 4) is based on the well-known Hartmann test for checking the figure of large optical objectives. The wavefront is divided into a number of zones, usually contiguous and of equal size. The light from each zone is brought to a separate focus and the position of the centroid of each image is measured in two dimensions by a photoelectric device. These position measurements reveal the mean wavefront slope over each zone. Residual wavefront curvature over each zone is not measured, and in fact degrades the signal-to-noise ratio. To obtain the highest signal-to-noise ratio, the photoelectric detector for each zone should consist of an array of elements with a matched filter detection system. In practice, useful performance can be obtained with a simple quadrant detector for each zone.

The main problem with the Hartmann sensor is to achieve and maintain the necessary alignment precision between the optical subaperture and the detectors, which is on the order of 1 μm at visible wavelengths. A secondary problem is to balance the photoelectric response of the detector elements and direct-current offsets in the amplifiers.

Solutions to these problems are: first, to use a local (laser) source which forms a common reference for all detectors (Schmutz, L.E., 1979); and second, to nutate the input optical beam, using an offset rotating mirror or a two-axis mirror driven with sine and cosine orthogonal inputs, to generate alternating-current signals from each detector which can be processed with a high degree of precision.

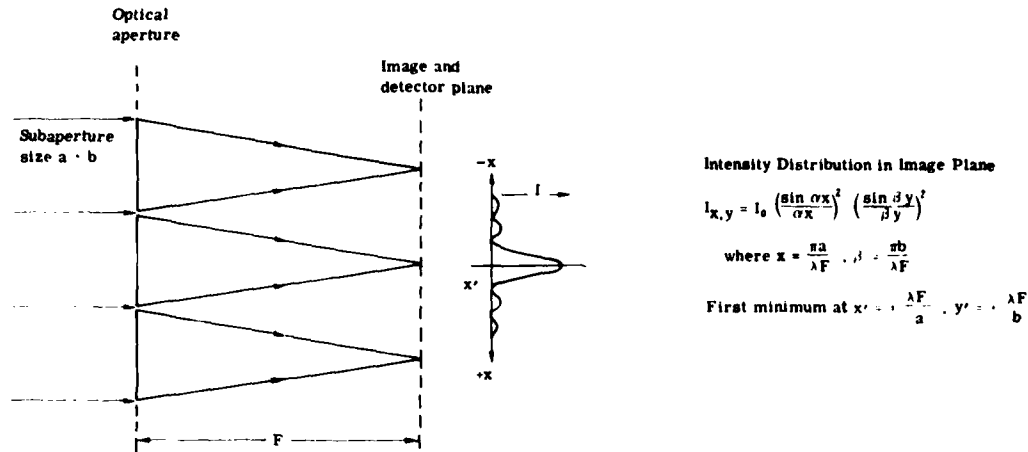


Fig. 4 Imaging Hartmann sensor model. The effective range of tilt measurement for a point reference source corresponds to a wavefront tilt of ± 1 wavelength across each subaperture.

Shearing Interferometer

In a shearing interferometer, the wavefront to be measured is amplitude-divided into two components which are mutually displaced and recombined with each other to generate an interference pattern. If the path lengths of the two beams are equal, then fringes are generated even with an incoherent light source, because light from each element of the source interferes with a (displaced) duplicate of itself.

There are several methods of producing sheared wavefronts. One of the most useful is a Ronchi grating located at the focus of the beam, as shown in Fig. 5. The grating produces multiple displaced images of the incident wavefront corresponding to the odd-order sidebands. The shear distance, s , defined as the displacement between the zero-order and first-order sidebands, is equal to $\lambda \nu F$ where ν is the grating frequency and F the focal distance. The phase difference between the sheared wavefronts is

$$\phi = \alpha \frac{s}{\lambda}$$

where α is the average wavefront slope over the distance s .

Because s is proportional to λ , the measured phase difference of the interfering sidebands is directly proportional to the wavefront slope, independent of λ . This phase difference may be measured by moving the grating and using an array of photoelectric detectors to sense the intensity changes in each zone of the wavefront. If the grating velocity is V , the modulation frequency generated by grating motion is:

$$\omega_0 = V \cdot \nu$$

The electrical signal at one detector output is

$$I_{jk} = A \left[\frac{1}{2} + \gamma \frac{2}{\pi} \cos (\omega_0 t + \phi_{jk}) \right]$$

where γ is the contrast or modulation of the interference pattern. The phase of this electrical signal may be extracted by multiplying it by a reference signal $\cos \omega_0 t$ obtained directly from the grating motion. In this way an array of electrical voltages is obtained, each one proportional to the slope of the optical wavefront in the corresponding zone of the aperture. In practice, rotating gratings with radial (sunburst) patterns are employed to shear the wavefront in two orthogonal directions to provide two orthogonal sets of slope measurements from which the wavefront itself may be reconstructed (Hardy, J.W., 1977).

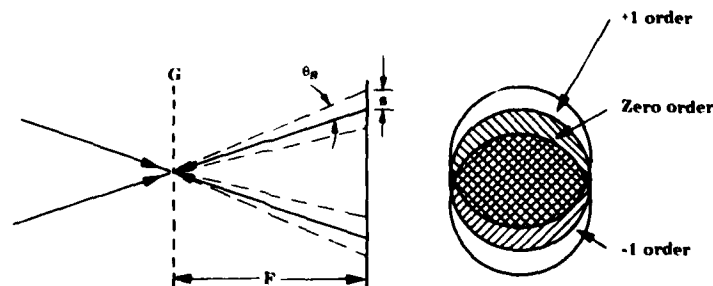


Fig. 5 Shearing interferometer using a Ronchi grating

Some further insight into the operation of this wavefront sensor can be gained by considering the grating as a chopping reticle located at the image of the reference source. If we consider the aperture of the optical system as being divided into many zones, each corresponding to one detector element in the array, then each zone will produce an image of the reference object at the grating. A wavefront tilt across one zone will displace that image so that it is chopped either earlier or later depending on the direction of tilt. The chopped light from each zone is picked up by the corresponding detector element and converted into an electrical signal. The time difference between each signal and a fixed reference is measured electrically to provide an output proportional to the wavefront tilt in each zone.

From this viewpoint, certain similarities between the grating shearing interferometer (SI) and the Hartmann sensor become apparent. The main difference is that the SI requires only one critical component (the grating) which operates on all zones of the aperture simultaneously, obviating the need for auxiliary alignment sources, whereas the Hartmann sensor has two critical components (the subaperture lens and detector) for each zone.

The grating shearing interferometer can be made to measure large wavefront slopes unambiguously by using a small shear distance which is obtained with a large grating spacing. The radial grating makes possible a variable-shear interferometer in which the low spatial frequency at maximum radius provides a large dynamic range for initial closing of the adaptive loop, while the high spatial frequency at minimum radius provides the high sensitivity required to obtain small residual wavefront errors during normal operation.

Detector Arrays

Interferometric and slope-measurement wavefront sensors require detector arrays to convert the interference pattern intensity variations into electrical signals that can be analyzed to yield the required phase or slope data. The requirements on detectors for wavefront sensing are quite different from those of normal imaging systems. For example, the number of resolution elements is relatively small (usually less than 1,000), the frame rate is very high (over 1,000 frames per second) and photon-noise limited operation is often required.

Because of these requirements, discrete detector arrays are employed rather than scanned image tubes. Photomultiplier tube arrays have been employed in several state-of-the-art wavefront sensors. End-on photomultipliers of half-inch diameter can be packed together with their associated signal conditioning electronics to form a compact and efficient detector array. To obtain the maximum photon efficiency, the detector plate is split into contiguous zones using a fly's eye lens array. An advantage of this arrangement is that each tube can be individually replaced without disturbing the rest of the array.

For very large arrays, even small photomultipliers become unwieldy and more compact devices must be found. For laser wavefront sensors operating at relatively high power, silicon or other semiconductor diodes can be employed. For photon-limited operation, intensified diode arrays appear to be feasible (Alting-Mees, H.R., 1979).

Wavefront Reconstruction

All slope-measuring wavefront sensors require a reconstruction operation to recover the wavefront itself. Normally, two orthogonal wavefront slope measurements are made for each actuator location; in other words, there are twice as many measurements as unknowns so that a least-squares fit can be performed with beneficial effects on error propagation.

The reconstruction operation can be performed either numerically in a digital computer or in hardware using an analog computer. Fig. 6 shows several reconstruction strategies that have been used or proposed (Hudgin, R.H., 1977) (Herman, J., 1980; Southwell, W.H., 1980). These are all based on orthogonal x- and y- slope measurements, but the arrangement of the measuring zones with respect to each other and to the actuator locations is different in each case. Because of edge effects, the number of independent slope measurements for a given number of actuators, N^2 , varies considerably for small apertures, but for large N , the number of measurements required converges to $2N^2$ in each case. The error propagation, defined as the least-squares wavefront error divided by the mean square error in the slope measurement, can be made less than unity by using the appropriate algorithm.

Array	Number of Gradient Measurements, M	Error Propagation (minimum norm)			
		3 · 3 Array M	Array E_p	10 · 10 Array M	Array E_p
Shearing Interferometer (Hudgin, Herrmann)	$2N(N-1)$	12	0.43	180	0.67
Hartmann (Fried, Herrmann)	$2N(N-1)'$	8	0.96	162	1.42
Hartmann (Southwell)	$2N^2$	18	0.25	200	0.58

Minimum norm least-squares error: $\sigma^2 = \sigma^2 E_p$
 σ^2 = mean square error of gradient measurements
 E_p = error propagator

Fig. 6 Wavefront reconstruction strategies

The wavefront reconstruction algorithm used with shearing interferometer wavefront sensors is shown in Fig. 7, and is based on the rule that the wavefront value at any point is equal to the average of the adjacent values plus the average of the measured phase differences. The computation itself can be done faster in hardware than in software, and in fact lends itself to a simple analog implementation (Hardy, J. W., 1977).

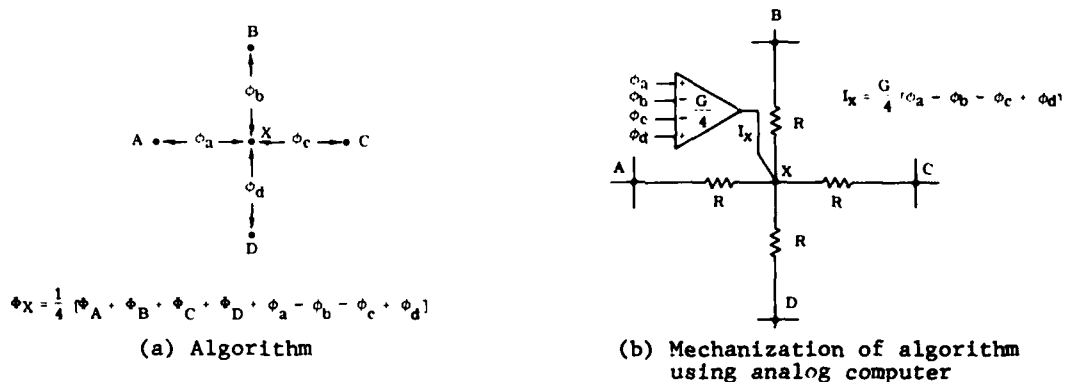


Fig. 7 Wavefront reconstruction algorithm

3. WAVEFRONT CORRECTION DEVICES

The phase of a wavefront can be controlled either by changing the velocity of propagation or by changing the optical path length. The former is achieved by varying the refractive index of a medium, while the latter is implemented by moving a reflective surface such as a mirror or by a moving grating as in a Bragg cell.

At the present time, reflective devices are the most successful and widely used wavefront correctors. Bragg cells have been used at infrared wavelengths. Refractive devices have not been successful because of the difficulty of inducing sufficiently large changes of refractive index in devices of practical size.

Other problems with refractive wavefront correctors are spectral absorption and the difficulty of obtaining uniformity in transmission. Most of these problems are avoided with reflecting type wavefront correctors. Mirror coatings are available with high optical efficiencies over wide spectral ranges from ultraviolet to far infrared. Because the optical path is confined to one side of the mirror surface, a great variety of substrate materials and methods of deforming the mirror are available. Finally, the wavefront deformation is a true optical path length change, independent of wavelength.

The regimes in which active mirrors operate may be separated in terms of wavefront correction range and frequency response have been shown in Fig. 3.

Because of the greatly differing operational requirements as well as the difference in physical size, each regime has its own special set of technical problems and solutions. To meet these varying requirements, the following basic types of active mirrors, shown schematically in Fig. 8, have been developed:

1. Segmented mirrors
 - a. Piston only
 - b. Piston plus tilt
2. Continuous thin-plate mirrors
 - a. Discrete position actuators
 - b. Discrete force actuators
 - c. Bending moment actuators
3. Monolithic mirrors
4. Membrane or pellicle mirrors.

We will now consider each type of active mirror and its associated actuators and control system in more detail.

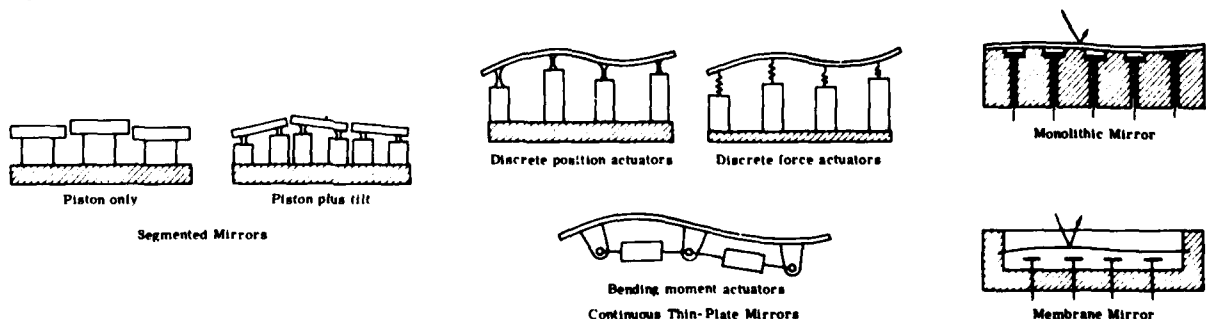


Fig. 8 Types of active mirrors

3.1 Segmented Mirrors

Small piston-type segmented mirrors have been used for generation of multidither tagging signals and for correction of atmospheric turbulence. These mirrors employ cylindrical piezoelectric position actuators and are capable of a deflection of several micrometers with useful bandwidths of over 1 KHz.

From the optical design point of view, the use of segments providing both piston and tilt capability is preferable to piston-only correction because fewer segments are required to match a given wavefront. The total number of actuators or degrees of freedom is essentially the same in each case.

For small and medium sized apertures, up to a few meters in diameter, the use of segmented mirrors is giving way to continuously deformable mirrors.

The prime application of segmented mirrors is in very large arrays which must of necessity be assembled out of a large number of separate components each of which may be over a meter in diameter.

Each segment of such an array is supported at three points by actuators, which may be shared with adjoining segments, giving three degrees of freedom which may be thought of as the average position of the surface (the piston component) plus tilt components in two orthogonal directions.

The shape of each segment is expected to remain constant (e.g., a section of a sphere or paraboloid) during normal operation, thereby setting requirements on rigidity. Light weight is also advantageous for most applications. While early segmented mirrors used solid glass segments, the trend now is toward light weight fabrication using a thin faceplate supported by a ribbed or box-like backing structure.

Edge matching of the segments is an important requirement in astronomical mirrors used in wide spectral bands, and special sensors are used for this purpose. Large segmented arrays are being designed with an expected figure error of less than 0.1 μm (Mast, T., 1980).

3.2 Deformable Thin-Plate Mirrors

For active mirrors in the medium size range from about 10 cm up to 2 or 3 m in diameter, the continuous thin-plate type with discrete actuator has reached the highest stage of development.

Deformation of a thin plate requires the application of an array of forces, usually, but not necessarily, applied at discrete points. The spacing of actuators depends on the spatial frequency of the expected mirror deformations; at least two actuators per deformation wavelength are generally required. While an array of discrete actuators can always be adjusted to produce zero mean figure error, there is a residual ripple which causes an rms surface error, the magnitude of which can be reduced by closer spacing of actuators.

The actuator forces may either be applied normal to the mirror surface reacting against a common backing plate or they may be applied as sets of equal and opposite bending moments to the mirror itself, in which case no external reaction is generated. Within these two distinct approaches to mirror deformation there are several variations. In the first group, using normal forces, we can make a distinction between "position" actuators whose stiffness is greater than that of the mirror itself, and "force" actuators whose stiffness is less than that of the mirror. The position actuator is the natural one to use when there is little reaction from the mirror, as for example when separate segments are used, but it has two serious drawbacks when used with thin plates. The first difficulty is that high stiffness is required not only in the actuators, but also in the backing plate. To operate as a position actuator with a deflection error of, say, 10 percent, it is necessary for the actuator and the backplate to be 10 times stiffer than the mirror; this requirement implies a massive and heavy structure, which may negate the advantages of active control. The second problem is that any deflections in the backing plate due to gravity, structural, or thermal effects are efficiently transferred to the faceplate. While such motion can be sensed and corrected in an active optical system, it does consume part of the dynamic range of the actuator and should be minimized as far as possible.

For these reasons, large thin-plate mirrors generally use force actuators, which act through a spring. In small mirrors, such as the example shown in Fig. 9, provision of the necessary backplate stiffness and stability is not a great problem.

Active area diameter	165 mm
Surface deformation	$\pm 8 \mu\text{m}$ for $\pm 1.500 \text{ V}$
Response function	Zero at adjacent actuator
Surface figure	0.22 μm peak-to-peak (non-energized)
Frequency response	> 1 KHz
Overall diameter	250 mm
Weight	12 Kg



Fig. 9 37-actuator deformable mirror

In the second group of bending moment actuators, the moments may be applied at discrete points using posts or levers attached to the mirror, or may be applied as distributed forces over areas of the mirror.

In summarizing the characteristics of thin-plate deformable mirrors, two main items stand out:

1. The actuator influence functions are normally wide, extending out to the first or second ring of surrounding actuators so that in a hexagonal array, 6 to 18 adjacent actuators are affected. This interaction must be taken into account in the design of the control system.
2. A thin-plate mirror is subject to numerous mechanical resonant modes, the frequencies and amplitudes of which depend on the actuator design and damping.

These characteristics are of greater importance in high-bandwidth mirrors than in large mirrors used for figure control. As the operating frequency gets higher, the problem of obtaining stable operation of a multichannel interacting control system with additional phase shifts due to faceplate resonances becomes severe. For high-bandwidth operation, interaction and resonance problems are greatly reduced in the monolithic active mirrors described next.

3.3 Monolithic Active Mirrors

The concept involved in monolithic active mirrors is to use a homogeneous block of material for the mirror substrate in which local deformations can be induced and controlled by external means. In effect, the functions of the faceplate, actuators, and backplate are all combined in one monolith.

Devices of this type have good mechanical properties, such as stiffness, stability, and shock resistance, making them more tolerant to an operational environment than conventional active devices assembled out of a multiplicity of parts.

The monolithic piezoelectric mirror (MPM) was developed at Itek (Feinleib, J., 1974; Everson, J.H., 1978), and has proved to be admirably suited for correction of atmospheric wavefront distortion at visible wavelengths. The basic construction of an MPM employs a circular slab of lead zirconate titanate (PZT) piezoelectric ceramic typically 5 to 10 cm in diameter and 1.2 to 2.5 cm thick. An array of electrodes is located at the top surface. A control voltage is applied to each, using the electrode at the base of the slab as a common reference. A thin glass plate bonded to the top surface is optically polished and aluminized to form the reflecting surface.

The MPM has the following characteristics:

1. When voltages are applied to the electrodes, the piezoelectric deformation occurs close to the top surface.
2. The induced deformations are localized in the vicinity of the activated electrode.
3. The coupling between neighboring electrodes can be adjusted close to zero by varying the geometry of the electrodes.
4. There is no measurable bending of the block when voltages are applied to the electrodes.

The sensitivity of practical devices is in the range of 0.25 to 0.5- μm surface deflection per KV, depending on the type of PZT material. The maximum interelectrode voltage is limited by the depolarization field, which is typically 1.5KV/mm.

Some control can be obtained over the sensitivity and the shape of the influence function by varying the electrode configuration and the glass thickness.

A typical MPM response function is shown in Fig. 10.

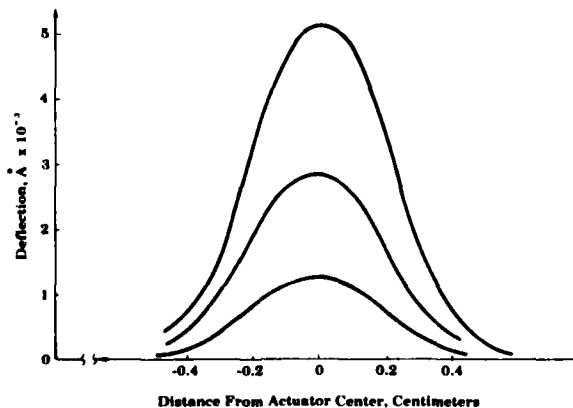


Fig. 10 MPM response function. Interactuator spacing is 3.8 mm.

The frequency response of MPM devices is extremely good, being limited primarily by the natural modes of the PZT block which, because of its large thickness-to-diameter ratio, occur at high frequencies. Typical devices have a flat response to over 10 KHz and have been operated at discrete frequencies as high as 60 KHz, although such frequencies can excite resonant modes.

A typical MPM and its frequency response are shown in Fig. 11, and interferograms depicting the surface deformations achievable are shown in Fig. 12.

Because of the small interaction between actuators, the compensating networks usually required with thin plate mirrors are not necessary with MPM's, resulting in some simplification of hardware. However, MPM actuator sensitivity is lower than with discrete PZT actuators, requiring higher driving voltages.

Experimental MPM's have been built with 300 active elements within a 75-mm diameter.

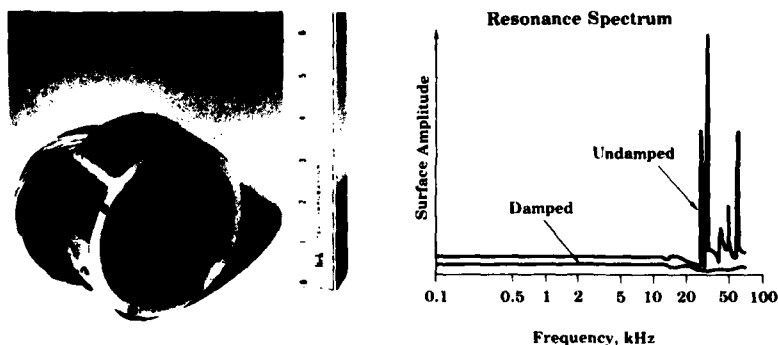


Fig. 11 Typical MPM and frequency response



Fig. 12 Controlled surface deformation of an MPM

3.4 Membrane Mirrors

A membrane is distinguished from a thin plate by having no inherent stiffness so that tension must be applied to maintain flatness: relatively small forces are required to obtain the deflections necessary for optical wavefront correction.

The use of membranes as high-bandwidth, high-order active mirrors has been pioneered at Perkin-Elmer (Grosso, R.P., 1977). The metal membrane is typically 0.5 to 1.0 μm thick and is positioned between a transparent electrode carrying a bias voltage V_B and an array of electrodes, to each of which is applied the bias voltage plus a signal voltage V_S . The membrane is at ground potential, and experiences no net force so long as $V_S = 0$. When a signal voltage is applied to one actuator, a deflection is produced, centered around that actuator. The membrane is operated at low air pressure (2 torr) to obtain a favorable compromise between sensitivity (which is maximized in vacuum), and membrane resonant frequency which is at a minimum in vacuum. The incident light beam passes through the sealing window and the transparent electrode before being reflected off the membrane. In one experimental device using electrostatic actuators with a 50-mm-diameter membrane, a deflection of 0.15×10^{-6} was obtained for $V_B = 200$ V and $V_S = 100$ V.

4. SYSTEM CONSIDERATIONS

The overall system design of discrete-component adaptive optics systems is well understood, even though it involves a large number of parameters, many of which can only be specified statistically. Some parameters (notably those describing atmospheric turbulence) change rapidly over a wide range, making real-time control over certain system parameters necessary to optimize performance.

Performance analysis of adaptive systems operating at energy levels where non-linear effects such as thermal blooming are insignificant, is straightforward. The theoretical capabilities and limitations of these systems are consequently well defined.

In contrast, the hardware for discrete component systems is still in a state of evolution and has not yet reached the maturity of the systems concepts.

A current problem in adaptive system design is how to utilize the available hardware in the most effective way, taking into account factors such as technical risk, cost, and reliability; a discussion of this topic is, however, outside the scope of the paper. In this section we will concentrate on the major considerations which determine the performance of adaptive systems operating in a linear regime.

The main parameters influencing the performance of discrete component phase-conjugate adaptive optics systems are identified in Fig. 13. Radiation from the reference source encounters wavefront disturbances in the propagation path, reaches the wavefront corrector and then travels to the wavefront sensor, where electrical signals defining the wavefront error are generated. The electrical data are fed through a processor which provides spatial and temporal smoothing before being applied to the wavefront corrector to close the feedback loop. The main sources of error in this model are: (1) wavefront fitting error σ_F , which depends on how closely the wavefront corrector can match the actual wavefront error; (2) detection error σ_D , which is essentially the reciprocal of the signal-to-noise ratio of the wavefront error output; and (3) prediction error σ_T , which is due to the time delay between the measurement of a wavefront error and its correction.

The overall residual wavefront error variance is given by:

$$\sigma_R^2 = \sigma_F^2 + \sigma_D^2 + \sigma_T^2$$

The residual error computed in this way defines the on-axis quality of the compensated image of a distant source.

Using the principle of optical reciprocity, this residual error also defines the beam quality of radiation reaching the target from an outgoing laser beam precompensated by the deformable mirror, using radiation received from the target for measurement. In this case, the laser beam is assumed initially perfect and no thermal blooming effects are included.

In the case of off-axis images, an additional error due to anisoplanatism must be included. A similar error occurs when a transmitted laser beam is slewed to track a moving target. If the target has a velocity component V across the line of sight, then the angle between the light received from the target (used for measurement) and the direction of the transmitted beam must be $2V/C$. When this angle is comparable with the isoplanatic angle of the propagation path, then an isoplanatic error is introduced.

In Fig. 13, the source is defined by its radiance and its angular subtense α ; for an unresolved source, only the radiant intensity would be specified. The optical effects of the propagation path can be described by three parameters: the transverse coherence length, r_0 , the isoplanatic angle, θ_0 , and the characteristic temporal bandwidth, f_0 . The parameters r_0 and θ_0 are governed by the distribution of the refractive index structure C_N^2 along the propagation path, while f_0 is largely determined by crosswind velocities and angular slewing rates. It should be noted that these three parameters are integrated values for the entire propagation path.

Wavefront and overall tilt angle excursions for $r_0 = 10$ cm (moderate turbulence) and $r_0 = 5$ cm (high turbulence) are shown in Fig. 14. For small apertures, it can be seen that most of the wavefront disturbance is overall tilt, or angle-of-arrival variation, which can be removed with a two-axis mirror, thereby considerably reducing the excursion required on the deformable mirror. Corresponding power spectra for a single point on the wavefront with and without overall tilt removed and the overall tilt spectrum itself are shown in Fig. 15 for a typical observatory site with $r_0 = 10$ cm.

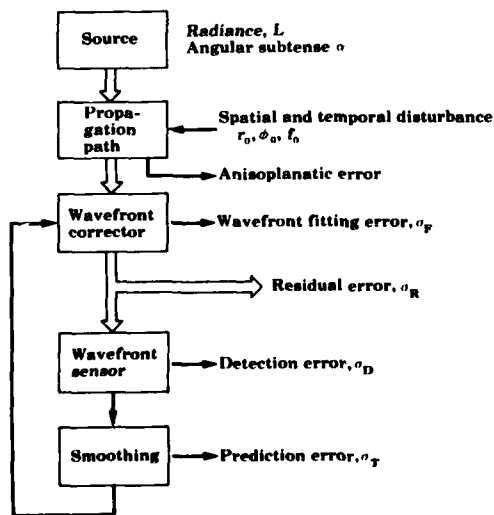


Fig. 13 Compensation loop parameters for discrete phase-conjugation system

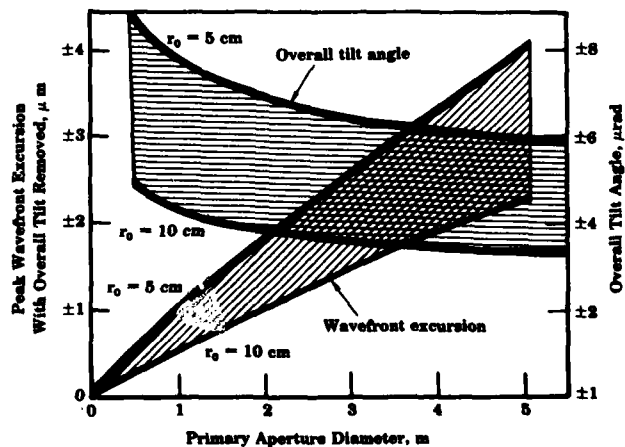


Fig. 14 Wavefront and overall tilt angle excursions due to atmospheric turbulence

The isoplanatic angle θ_0 is determined by the turbulence strength far from the compensated telescope aperture and is particularly small with uniform turbulence such as that occurring in a horizontal path. The isoplanatic angle up-looking through the entire earth's atmosphere at the zenith, specified as the angle at which the wavefront phase error is 6.88 rad^2 at a wavelength of $0.5 \text{ } \mu\text{m}$, is generally in the range 3 to 6 arc-sec.

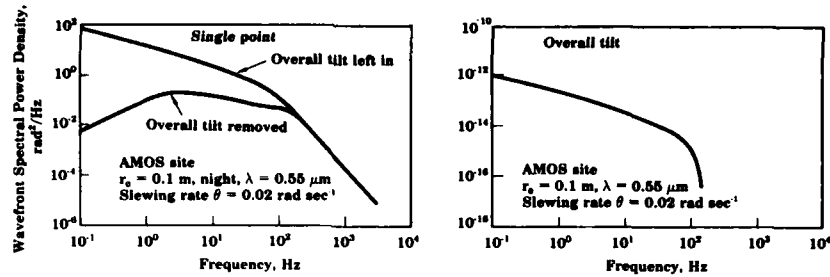


Fig. 15 Turbulence power spectra

The wavefront corrector must be capable of removing the wavefront excursions generated by the propagation path. For a discrete actuator deformable mirror, this implies three major requirements:

1. The surface excursion of the mirror must be compatible with the requirements of Fig. 14.
2. The frequency response of the mirror must be compatible with the power spectra shown in Fig. 15.
3. The number of actuators must be sufficient to keep the wavefront fitting error within the assigned budget.

The wavefront fitting error depends both on the wavefront statistics and on the mirror response function. For Kolmogorov turbulence compensated by a monolithic piezoelectric mirror, the fitting error is given by (Hudgin, R. H., 1977)

$$\sigma_F^2 = 0.01 \left(\frac{D}{Nr_0} \right)^{5/3} \text{ waves}^2$$

where D is the diameter of the compensated aperture and N is the number of zones across the diameter.

Fig. 16 shows the relationship between D and N for a fitting error of $\sigma_F = 0.05$ wave for different values of r_0 corresponding to average turbulence for a vertical path looking through the atmosphere at wavelengths of 0.25, 0.50, and 3.8 μm . The number of zones or actuators required becomes a practical problem for discrete systems with large apertures at visible and UV wavelengths.

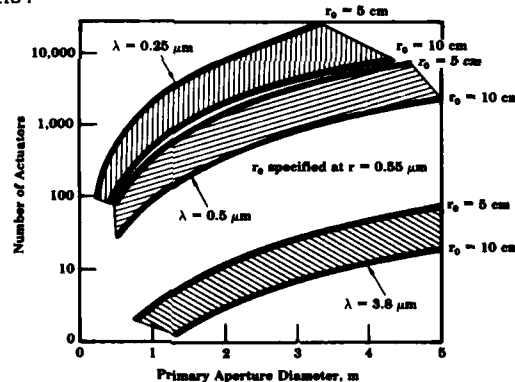


Fig. 16 Number of actuators required to achieve a fitting error of 0.05 wave with zonal compensation

Wavefront sensors contain many practical sources of measurement error such as optical aberrations and alignment which can be minimized by good engineering. However, there is one fundamental limitation which cannot be avoided, namely the noise produced by detection of the radiation from the reference source. At infrared wavelengths, this is primarily electrical noise. At visible and ultraviolet wavelengths, individual photons can be detected, so the noise is then due to fluctuations in the photon arrival rate. For a shearing interferometer operating at visible wavelengths, the detection error variance is given by

$$\sigma_D^2 = \frac{1}{2\pi^2 \gamma^2 S^2 P} \text{ waves}^2 \text{ per aperture zone}$$

where

- γ = modulation (contrast) of reference source
- S = shear distance
- P = photons detected per unit area per measurement time

Note that the detection error depends on the shear distance but not on the actual size of each zone. The zone size influences the wavefront fitting error, σ_F . Minimization of the detection error requires the product $\gamma^2 S^2$ to be maximized. In a shearing interferometer, γ is generally a function of S , so that control of the shear distance, which is easily achieved with the radial-grating interferometer, is essential to performance optimization when P is small.

The prediction error σ_T is a function of the time required to measure and compensate the wavefront error in relation to the characteristic change time of the disturbance. The prediction error increases as the integration time of the adaptive loop increases, as shown in Fig. 17a. However, a longer integration time allows more photons to be collected, so the detection error decreases with longer integration time. The optimum integration time, t_1 , is that which minimizes the detector plus prediction errors. The total wavefront error will decrease with increasing reference source brightness until the fitting error becomes dominant as shown in Fig. 17b.

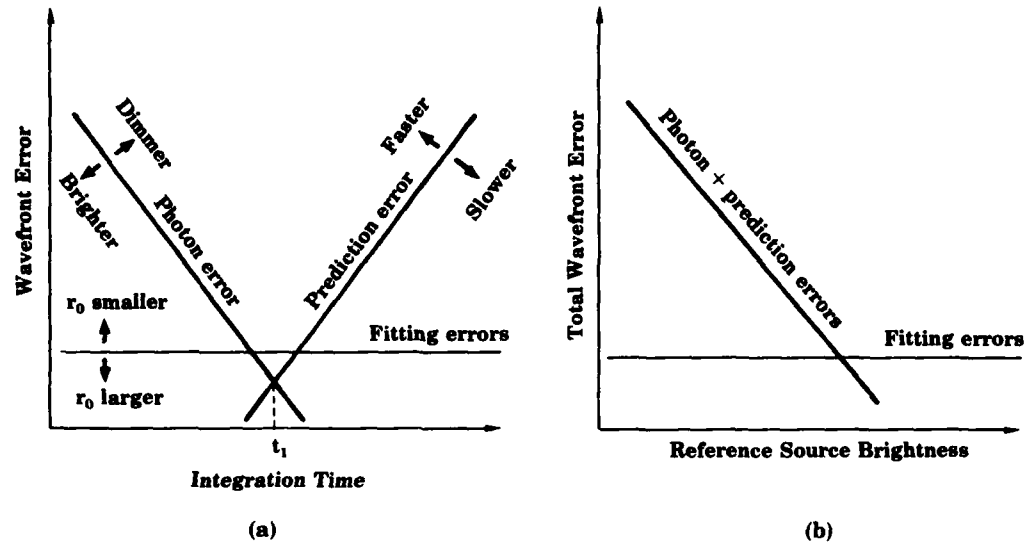


Fig. 17 Wavefront error components

Many systems problems remain to be solved in adaptive optics, the most troublesome of which is anisoplanatism. In the context of compensated imaging, atmospheric anisoplanatism limits the field of view that can be compensated by a single device (such as a deformable mirror) to a few arc-sec. In laser systems transferring power to moving targets, the angle by which the beam must be pointed ahead to offset the round-trip time of the radiation may be greater than the isoplanatic patch, resulting in a considerable reduction (or even nullification) of the wavefront compensation.

One final aspect of discrete adaptive optics systems will be considered: cost versus performance. The main factor influencing the cost of a discrete adaptive system is the number of actuators, N^2 . Typical values of N for several different wavelengths have been shown in Fig. 16 as a function of telescope aperture.

Because adaptive optics systems are still in the development stage, a large part of their cost now consists of engineering and design work. If these initial development costs are considered as non-recurring, the cost of future discrete systems will be of the form $C_A = (A + BN^2)$, where A is the cost of items such as the optics, mechanical structure, and control systems which are almost independent of the telescope aperture size, and B is the cost per actuator of the replicated hardware, mostly electronics. The expected cost of future discrete adaptive systems is shown in Fig. 18, using values of $A = 5 \times 10^5$ and $B = 5 \times 10^3$ in 1980 dollars.

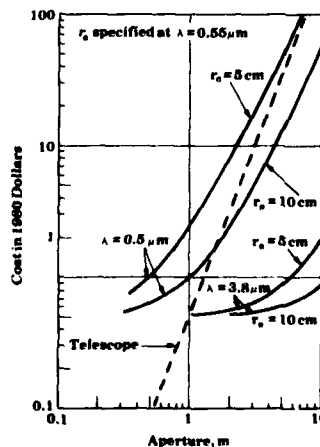


Fig. 18 Expected cost of discrete adaptive optics systems

The cost of conventional telescopes, including the dome and peripherals, is also shown in Fig. 18, using the relation $C_m = 0.5 D^{2.6}$ in 1980 dollars (Meinel, A. B., 1977). The cost of a discrete adaptive system, based on the above assumptions, is seen to be generally comparable with that of the telescope, except for very small apertures. Because of the difference in exponents, the relative cost of the adaptive system actually decreases as the telescope size increases.

The question of cost-effectiveness must be approached with some care, because alternative methods of achieving equivalent performance are not necessarily available. In the case of imaging systems, it is not clear that any alternative exists for compensating ground-based telescopes against atmospheric turbulence. For astronomical purposes, various forms of interferometry have shown promising results with slowly changing objects, but these techniques have yet to be proved effective with rapidly moving objects such as satellites. The one clear alternative is to put a telescope into orbit; the cost of NASA's 2.4-m space telescope is already in excess of \$200 million, excluding the shuttle launch.

For laser beam energy transfer between earth and space, the only alternatives to adaptive wavefront control are, first, the brute force approach of increasing the laser power to overcome the losses, or, second, to place the laser transmitter in orbit. Both of these alternatives are likely to be much more expensive than an adaptive optics system.

5. CONCLUSIONS

The discrete approach to adaptive wavefront compensation has proven feasibility. It enables random wavefront distortion that degrades the performance of optical systems to be neutralized with a hardware complexity comparable with that of the optical systems it is supporting. In comparison with the alternatives, adaptive wavefront compensation appears to be the most cost-effective solution to many current imaging and laser power transfer problems.

Future technology may allow the sequential functions of wavefront measurement and compensation to be implemented by a single integrated device with spatial resolution determined by the structure of the material itself, rather than by an array of discrete devices. Such a solution has already been found for phase conjugation using non-linear physical processes in gases and crystals. Such devices implement the wavefront compensation required for an optical beam to retrace its path through a turbulent medium and regain its original form. The application of these systems is restricted to scenarios in which coherent radiation emanates from a point source at or near the target, propagates through a randomly perturbed medium to a collector, is reflected by the conjugate mirror, and is then retransmitted at high power through the same medium to focus at or near the original source. The conjugate mirror required for this task has a surface deviation exactly equal to that of the incident wavefront. Its effect is to reverse the direction of propagation of the wavefront without changing its shape. For image compensation, the required function may be termed a "half conjugator" in which an initially distorted waveform is flattened by the adaptive mirror. The development of fully integrated "half conjugators" would remove many of the constraints of discrete devices and would constitute a major advance in adaptive optics.

REFERENCES

1. Altling-Mees, H.R., Wenzel, H.A., Beaver, E.A., and Shannon, J.L., 1979, Space Telescope Digicon, Proc. SPIE, vol. 203, p 12-20.
2. Everson, J.H., 1978, New Developments in Deformable Surface Devices, SPIE, vol. 141, p 11-19.
3. Feinleib, J., Lipson, S.G., and Cone, P.F., 1974, Monolithic Piezoelectric Mirror for Wavefront Correction, Appl. Phys. Lett., vol. 25, p 311-313.
4. Grosso, R.P., and Yellin, M., 1977, The Membrane Mirror as an Adaptive Optical Element, J. Opt. Soc. Am., vol. 67, p 399-406.
5. Hardy, J.W., 1978, Active Optics: A New Technology for the Control of Light, Proc. IEEE, Vol. 66, p 651-697.
6. Hardy, J.W., Lefebvre, J.E., and Koliopoulos, C.L., 1977, Real Time Atmospheric Compensation, J. Opt. Soc. Am., vol. 67, p 360-369.
7. Hermann, J., 1980, Least-Squares Wavefront Errors of Minimum Norm, J. Opt. Soc. Am., vol. 70, p 28-35.
8. Hudgin, R.H., 1977, Wavefront Reconstruction for Compensated Imaging, J. Opt. Soc. Am., vol. 67, p 375-378.
9. Hudgin, R.H., 1977, Wavefront Compensation Error due to Finite Corrector Element Size, J. Opt. Soc. Am., vol. 67, p 393-395.
10. Mast, T., and Nelson, J., 1980, Figure Control for a Segmented Telescope Mirror, Conference Proceedings on Optical and Infrared Telescopes for the 1990's, Kitt Peak National Observatory, p 508.

11. Meinel, A.B., 1977, An Overview of the Technological Possibilities of Future Telescopes, Proceedings of the ESO Conference on Optical Telescopes of the Future, Geneva, p 13-26.
12. Schmutz, L.E., Bowker, J.K., Feinleib, J., and Tubbs, S., 1979, Integrated Imaging Irradiance (I^3) Sensor, SPIE, vol. 179, p 76-80.
13. Southwell, W.H., 1980, Wavefront Estimation from Wavefront Slope Measurements, J. Opt. Soc. Am., vol. 70, p 998-1006.
14. Wang, J.Y., and Markey, J.K., 1978, Modal Compensation of Atmospheric Turbulence Phase Distortion, J. Opt. Soc. Am., vol. 68, p 78-87.

SUMMARY OF SESSION VI

ADAPTIVE OPTICS

by

Mr Donald W. Hanson

The design and performance of adaptive optical systems used to reduce the degrading effects of atmospheric turbulence is dependent on several key turbulence parameters : the phase coherence length ; the isoplanatic angle ; and the temporal bandwidth of the aberrations. Further measurements are required to establish nominal values of these parameters.

Nonlinear optics has the potential for providing excellent adaptive optics performance. However, there are applications (e.g., white light imaging) where nonlinear optics cannot be used. In addition, application of nonlinear optics technology in systems does not appear likely in the near future. Therefore, technology development should continue in the area of discrete wavefront correctors and wavefront sensors to increase the number of degrees of freedom in each while reducing cost and complexity.

The subject of thermal blooming at visible wavelengths is not well understood. Research into the atmospheric absorption mechanisms at visible wavelengths is required. The interaction between scintillation of the laser beam and thermal blooming needs to be established since phase compensation for thermal blooming may not be effective if there is a strong interaction. It would be desirable to obtain simplified analytical results which could then be checked with more rigorous computer simulations.

It would be desirable to improve the accuracy of analyses which are used to predict the performance of adaptive optical systems. Currently analyses are adequate for top level system design, more accurate analytical results required for detailed design tradeoffs. Existing computer simulations would be useful in validating the analytical results.

Anisoplanatic errors can significantly reduce the performance of both imaging and communication adaptive optical systems. Further research is required to reduce the effects of anisoplanatic errors on system performance for all applications.

QUESTIONS AND COMMENTS
ON SESSION VI

ADAPTIVE OPTICS

- Paper 43 : Resolving power evaluation of optical adaptive systems through the atmosphere.

Dr. Greenwood : I think it might be useful for those in the audience who are interested in this work to take a look at the paper I have written in the Journal of optical society about two or three years ago where much of that methodology has been given.

Dr. J. Vernin : Why do you use Karman spectrum instead of Kolmogorov spectrum ?

Dr. A. Consortini : The question of Dr. Vernin gives me the opportunity to discuss a problem in which we have been involved from many years.

The Karman model represents a complete Kolmogorov spectrum, so that it would be more appropriate to refer to it as Karman-Kolmogorov model.

Recall that, according to Kolmogorov, the structure function D of, say, the temperature or refractive index fluctuations, depends on r in different ways in the three different regions $r \ll \lambda_0$ (where $D \propto r^2$), $\lambda_0 \ll r \ll L_0$ (where $D \propto r^{2/3}$) and $r \gg L_0$. The Karman model satisfies the $2/3$ law in the $\lambda_0 < r < L_0$ region and saturates for $r \gg L_0$. The modified Karman model correctly describes also the behaviour in the range $r \ll \lambda_0$. The modified Karman model is therefore a continuous mathematical function which correctly describes the behaviour of the structure function given asymptotically by the Kolmogorov theory in the three different regions.

The spectrum $\phi_{nT}(\kappa) = 0.033 C_n^2 \kappa^{-11/3} e^{-\kappa^2/\kappa_m^2}$ which is generally referred to as Kolmogorov spectrum (or $2/3$ law in terms of structure function) would be applicable if L_0 would be infinite. In both case $\phi_{nT} \rightarrow \infty$ for $\kappa \rightarrow 0$. It has been noted that the region $r > L_0$ is an inhomogeneous and anisotropic region so that it is difficult to give a behaviour of the structure function there. However, assuming a saturating behaviour takes at least into account the physical fact that the fluctuations due to turbulence at two points, a distance r apart, become uncorrelated when the distance is larger than L_0 . Correspondingly the spectrum tends to a finite value for $\kappa \rightarrow 0$. On the contrary the spectrum ϕ_{nT} diverges for $\kappa \rightarrow 0$ and the corresponding structure function diverges for $r \rightarrow \infty$, which corresponds to fluctuations more and more correlated. Of course in the region $\kappa \gg \kappa_m$ the two spectra become practically equal. However this does not mean at all that the two spectra are equivalent when they are used in the theory of propagation, for deriving the fluctuations of a wave which has travelled a path through the turbulence. For instance, we have shown that the behaviour of the spectrum for $\kappa < \kappa_m$ plays a role in the structure function of phase fluctuations over a wavefront after propagating a distance through the atmosphere, not only for points at distances $r > L_0$, but also for points at distance $r < L_0$. This fact has a consequence, for example, in the determination of the parameters of the turbulence from propagation experiments.

For a more detailed discussion on these problems see e.g. : A. Consortini, L. Ronchi ("Some Comments on the Theory of e.m. Propagation in a Turbulent Atmosphere") Lettere al Nuovo Cimento Serie I 2, 683, 21 November 1969 ; R. F. Lutomirski and H. T. Yura J. Opt. Soc. Am. 59, 319, 69 ; A. Consortini, L. Ronchi Lettere al Nuovo Cimento 3, 571, 1972 ; A. Consortini, L. Ronchi Applied Optics 11, 1205, 1972.

- Paper 8 : Détermination des performances d'un système COAT en régime de poursuite.

Dr. E. Spitz : Le fait que le miroir est brisé irrégulièrement. Est-ce-que cela donne des directions parasites de réception éventuellement ?

Mr. G. Roger : Bien sûr. Il y a des précautions à prendre sur l'intervalle entre les miroirs, sur la disposition des miroirs. On a les mêmes phénomènes qu'avec les antennes, dans le domaine radio.

- Paper 45 : Adaptive optics for thermal blooming

Question : You spoke of introducing a phase lag in demodulating the multidither signal. I assume that what is meant is that there is a phase lag in the dither signal. To take it out, you need a lead rather than a lag, but that this lead is, in effect, provided by putting a lag on the demodulation reference signal. Is this correct ?

Dr. W. P. Brown : Its a lag in the demodulation, in the referenced signal for the demodulation.

- Paper 47 : Reduction of anisoplanatic errors.

Dr. J. Vernin : Why don't you use the Hufnagel model in your computation ?

Mr. D. W. Hanson : As shown in a previous paper (Hanson D. W. temperature turbulence measurements at AMOS", AGARD C. P. 238, 44-1, 1978) we have not found good agreement between measured data and the Hufnagel model.

- Paper 48 : Phase measurement systems for adaptive optics

- Dr. E. Spitz : When you have got several sources and not only one. The tracking system doesn't work any more ? For example the Hartman's method wouldn't work ?
- Dr. J. C. Wyant : If the sources are incoherent with respect to each other, the tracking system will in many situations still work. However, if the sources are coherent with respect to each other, the tracking system will not perform properly.

LIST OF ATTENDEES

AARONS, J. Dr	Senior Scientist, Air Force Geophysics Lab., Hanscom AFB, Bedford, MA 01731, US
ALBRECHT, Dr-Ing.	FGAN, Konigstrasse 2, 5307 Wbg. Werthoven, GE
ANDERSON, R. Mr	Code 8113, Naval Ocean Systems Center, 271 Catalina Blvd., San Diego, CA 92152, US
AUSTIN, R.W.	Visibility Laboratory, Scripps Institution of Oceanography, La Jolla, CA 92037, US
BAKKER, T. Ir.	Physics Laboratory TNO, P.O. Box 96864, 2509 JG The Hague, NE
BELROSE, J. Dr	Communications Research Centre, Dept. of Communications, P.O.Box 11490, Station H, Ottawa K2H 8S2, CA
BERTRAND, P. Dr	E.T.C.A. CTME/OP, 16 bis Ave., Prieur de la Cte d'Or, 94114 Arcueil, FR
BISSONNETTE, L. Dr	DEF. RES. EST VALCARTIER, P.O. Box 8800 Courcelette, Quebec, GOA IRO, CA
BLIZARD, M. Dr	Office of Naval Research, NSTL Station, MS 39529, US
BLYTHE, J.H. Dr	Marconi Research Laboratories, West Hanningfield Road, Great Baddow, Chelmsford, Essex, CM2 8HN, UK
BOGENBERGER, R. Mr	MBB, Abt. FE 324, Postfach 801160, 8000 Muenchen 80, GE
BROWN, W.P.	Hughes Research Laboratories, 3011 Malibu Canyon Rd., Malibu, CA 91367, US
BURNHAM, R. Dr	Laser Physics Branch, Naval Research Lab., Code 6540, Washington DC 20375, US
CARNEVALE, Prof.	Istituto di Ricerca sulle Onde, Elletromagnetiche del C.N.R., Via Panciatchi, 64, 50127 Firenze, IT
CARSWELL, A.I.	Dept. of Physics, York University, 4700 Keele St., M3J 1P3, Downsview, Ontario, CA
COLEMAN, I.	Bartlett Systems, Inc., Box 126, Woody Creek, CO 81656, US
CONSORTINI, A. Dr	Istituto di Ricerca sulle Onde Elletromagnetiche del C.N.R. (IROE), Via Panciatchi 64, 50127 Firenze, IT
COOPER, A.W. Dr	Naval Postgraduate School, Monterey, CA 93940, US
COYNE, V.J. Mr	Chief, Strategic Surveillance Branch, Surveillance Division, Rome Air Development Center/OCS, Griffiss AFB, N.Y.13441, US
CRITTENDEN, E.C.	Optical Propagation Group Code 61Ct, Dept. of Physics & Chemistry, Naval Postgraduate School, Monterey, CA 93940, US
CROSIGNANI, B. Dr	Fibre Optics Laboratory, Fondazione Ugo Bordoni, Via le Europa 160, 00100 Roma, IT
DAVIDSON, K.L.	Dept. of Meteorology, Naval Postgraduate School, Monterey, CA 93940, US
DEGGES, T.C.	Visidyne Inc. MA, 5 Corporate PL. S. Bedford St., Burlington, MA 01803, US
DI PORTO, Mr	Fondazione Ugo Bordoni, Roma, IT
FAIRALL, C.W.	BDM Corp., Monterey, CA, US
FLOOD, W. Dr	Department of the Army, US Army Research Office, P.O.Box 12211, Research Triangle Pk, NC 27709, US
FORNGES, D. Dr	Bundesstelle für Fernheldestatistik, Wannetstrasse 10, D-8035 Gauting, GE
FRIED, D.L. Dr	Optical Sciences Company, P.O. Box 446, Placentia, CA 92670, US
GIULIANO, C.R.	Hughes Research Laboratories, 3011 Malibu Canyon Rd., Malibu, CA 91367, US
GREENWOOD, Dr	MIT/Lincoln Laboratory, P.O. Box 73, Lexington, MA, US
GRIGSBY, S.H. L/Cdr.	Naval Sea Systems Command, PMS-405, Washington DC 20362, US

HALLEY, Mr	12 rue du Dr. Kurzenne, 78350 Jouy en Josas, FR
HANSON, D.W.	Dept. of Air Force, Hqs. RADC (AFSC), Electro-Optics Section (OCSE), Griffiss Air Force Base, Rome, New York 13441, US
HARRIS, J.M. Dr	Exxon Production Research Co., P.O. Box 2189 M/S N 299 B, Houston, Texas 77001, US
HERING, W.S. Mr	Visibility Laboratory, Scripps Institution of Oceanography, University of California, San Diego, La Jolla, CA 92093, US
HESS, K.	ITT Dept. BS/FZW (Research Centre), SEL Research Centre, Hellmuth - Hirth Str. 42, 7000 Stuttgart 40, GE
HINCKLEY, D. Dr	Jet Prop. Lab., Mail Stop 180-701, California Institute of Technology, 4800 Oak Grove Drive, Pasadena, CA 91109, US
HODARA, H. Dr	Vice President, Tetra Tech. Inc., 630 North Rosemead Blvd., Pasadena, CA 91107, US
HONEY, R.C. Dr	SRI International, Menlo Park, CA 94025, US
HOSTETTER, G.R.	GTE Sylvania Inc., P.O. Box 188, Mountain View, CA 94042, US
HUIGNARD, J.P. Dr	B.P. No.10, Thomson-CSF, Domaine de Corbeville, Orsay 91401, FR
ISHIMARU, A. Prof.	Dept. of Electrical Eng. FT/10, University of Washington, US
JACKSON, J.E.	Dept. E413, Bldg. 81, McDonnell Douglas Astronautics Co. St. Louis Division, St. Louis, MO 63166. US
JOHNSON, R.W. Mr	Visibility Lab.(P003), Univ. of California at San Diego, Scripps Institution of Oceanography, La Jolla, CA 92093, US
JONES, W. Mr	Research & Development Center, General Electric Co., Schenectady, NY 12345, US
JOYNES, G.M.S. Dr	Group Leader, Plessey Electronic Systems Research, Southleigh Park House, Havant, Hants, PO9 2PE, UK
KARR, T. Dr	Lockheed Palo Alto Research Labs., 3251 Hanover St., Palo Alto, CA 94304, US
KARRAS, T.W. Dr	Mgr., Laser Research & Dev., General Electric Co., Space Division, Rm. M9515, P.O.Box 8555, Philadelphia, PA 19101, US
KOHNLE, A. Dr	FFO, Schloss Kressbach, D-7400 Tubingen 1, GE
KUSTERS, E.R. Dr	German Military Geophysical Office, Mont Royal, D-5580 Traben-Trarbach, GE
LANGE-HESSE, G. Dr rer. nat.	Dipl. Phys. Max-Planck-Institut für Ionosphären-Physik, D-3411 Lindau/Harz, GE
LEE, G.M. Dr	McDonnell-Douglas, 4 Twin Oaks Lane, Ladue, MO 63124, US
LUTOMIRSKI, R.F.	Pacific Sierra Research, 1456 Cloverfield Rd., Santa Monica, CA 90404, US
MACGREGOR, A.D. Dr	Marconi Avionics Ltd., Christopher Martin Rd., Basildon, Essex SS14 3EL, UK
MILNE, E. Mr	Naval Postgraduate School, Monterey, CA 93940, US
MOORADIAN, G.C. Dr	Code 811, Naval Ocean Systems Center, 271 Catalina Blvd., San Diego, CA 92151, US
MOORE, C.A. Dr	SRI International, Menlo Park, CA 94025, US
NORTHFIELD, J. Mr	British Aerospace, Manor Rd., Hatfield, Hertfordshire AL10 9LL, UK.
PAK, H. Mr	Oregon State Univ., Oregon, US
PARKER, J.C. Mr	Mgr., Special Systems E.O.D., Ferranti Ltd., Robertson Ave., Edinburgh EH11 1PX, UK
POURNY, J.C. Mr	Ecole Polytechnique, E.N.S.T.A. Batterie de l'Yvette LOA, 91128 Palaiseau, FR
RODEBACK, Mr	Naval Postgraduate School, Monterey, CA 93940, US
ROGER, G.	Laboratoire de Marcoussis, CGE, Route de Nozay, 91460 Marcoussis, FR
ROGGE, J. Mr	Kon. Mil. Academie, Technische Studi, Kasteelplein 10, Postbus 90, 154, 4800 RG Breda, NE
ROPER, Dr	R.S.R.E., St. Andrews Rd., Great Malvern, Worcs., UK
ROSENBERG, W. Dr	Lockheed Research Labs., 3251 Hanover Street, Palo Alto, CA 94304, US

SCHEGGI, A.M. Prof. Istituto di Ricerca sulle Onde, Eletromagnetiche del C.N.R., Via Panciatchi, 64, 50127 Firenze, IT

SCHIMITSCHEK, E. Dr Code 2500, Naval Ocean Systems Center, 271 Catalina Blvd., San Diego, CA 92152, US

SECHAUD, Mr D.R.E.T., 26 Boulevard Victor, 75015 Paris, FR

SHAPIRO, J.H. Prof. Dept. Elec. Eng. & Computer Sc., Massachusetts Inst. of Technology, Rm 36-477, Cambridge, MA 02139, US

SIMPSON, J. Mr Scripps Institution of Oceanography, University of California, San Diego, La Jolla, CA 92093, US

SOICHER, H. Dr USA Comm. Res. & Dev. Command, CENCOMS DRDCO-COM-RH-5, Fort Monmouth, N.J. 07703, US

SPITZ, E. Dr Directeur du Laboratoire Central de Recherches de Thompson CSF, B.P. No.10 Domaine de Corbeville, 91401, Orsay, FR

SPRENKELS, C. Ir. Colonel d'Aviation Commandant 22 Log W, Quartier Roi Albert I, rue de la Fusee 70, B-1130 Bruxelles, BE

STAIR, A.T. AFGL/OPR-1, Optical Physics, Air Force Geophysics Lab., Hanscom AFB, MA 01731, US

STOTTS, L. Code 8113, Naval Ocean Systems Center, San Diego, CA 92152, US

TITLE, A.M. Dr Lockheed Research Labs., 3251 Hanover Street, Palo Alto, CA 94304, US

TITTERTON, P.J. Dr GTE Sylvania, P.O. Box 188, Mountain View, CA 94042, US

TITUS, J. Mr SSG Inc., 150 Bear Hill, Waltham, MA 02154, US

TUCKER, S. Dr United States

TZOAR, N. Prof. Dr. Dept. of Physics, City College of N.Y., 138 Street & Convent Ave., New York, NY 10031, US

UTLAUT, W.F. Dr U.S. Dept. of Commerce, Natl. Telecommunications & Inf. Ad., (NTIA), 325 Broadway, Boulder, Colorado 80303, US

VALTEAU, A. Mr ETCA CTME/OP, 16 bis Ave., Prieur de la Cote d'Or, 94114 Arcueil, FR

VERNIN, J. E.R.A. No. 669 du CNRS, Departement d'Astrophysique I.M.S.P., Univ. de Nice - Parc Valrose, 06034 Nice Cedex, FR

WELLS, W.H. Tetra Tech., Inc., 630 North Rosemead Blvd., Pasadena, CA 91107, US

WERNER, C. German Aerospace Res. Establishment, DFVLR, Institute of Optoelectronics, D-8031 Oberpfaffenhofen/Wesslg, GE

WHITE, M.B. Dr Scientific Dept. Naval Res., Bldg. 114 Section D, 666 Summer St., Boston, MA 00210, US

WILLIAMS, J. Prof. U.S. Naval Academy, Oceanography Dept., Annapolis, MD 21402, US

WYANT, J.C. Mr University of Arizona, Tucson, Arizona, US

YURA, H.T. Dr The Aerospace Corp., P.O. Box 92957, Los Angeles, CA 90009, US

ZACHOR, A.S. Atmospheric Radiation Consultants, 59 High St., Acton, MA 01720, US

ZANEVELD, J.R.V. Mr Oregon State Univ., Oregon, US

REPORT DOCUMENTATION PAGE

1. Recipient's Reference	2. Originator's Reference	3. Further Reference	4. Security Classification of Document
	AGARD-CP-300	ISBN 92-835-0295-7	UNCLASSIFIED
5. Originator	Advisory Group for Aerospace Research and Development North Atlantic Treaty Organization 7 rue Ancelle, 92200 Neuilly sur Seine, France		
6. Title	SPECIAL TOPICS IN OPTICAL PROPAGATION		
7. Presented at	the 28th Meeting of the Electromagnetic Wave Propagation Panel held in Monterey, California, USA, 6-10 April 1981.		
8. Author(s)/Editor(s)	P. Halley	9. Date	July 1981
10. Author's/Editor's Address	12 rue du Docteur Kurzenne 78350 Jouy en Josas, France	11. Pages	434
12. Distribution Statement	This document is distributed in accordance with AGARD policies and regulations, which are outlined on the Outside Back Covers of all AGARD publications.		
13. Keywords/Descriptors	Optical communication Light transmission Optical properties	Marine atmospheres Upper atmosphere	
14. Abstract	<p>These Proceedings consist of the 42 papers and the discussions presented at the 28th Meeting of the Electromagnetic Wave Propagation Panel in Monterey. There are 8 papers on Propagation Effects in Air and Sea Water; 10 on Recent Atmospheric and Sea Measurements; 5 on Upper Atmosphere Effects: Theory and Experiments; 6 on Non-Linear Optics; 7 on Novel Communication Techniques and Devices; and 6 on Adaptive Optics.</p>		

<p>AGARD Conference Proceedings No.300 Advisory Group for Aerospace Research and Development, NATO SPECIAL TOPICS IN OPTICAL PROPAGATION Edited by P.Halley Published July 1981 434 pages</p> <p>These Proceedings consist of the 42 papers and the discussions presented at the 28th Meeting of the Electromagnetic Wave Propagation Panel in Monterey. There are 8 papers on Propagation Effects in Air and Sea Water; 10 on Recent Atmospheric and Sea Measurements; 5 on Upper Atmosphere Effects: Theory and Experiments; 6 on Non-Linear Optics; 7 on Novel Communication Techniques and Devices; and 6 on Adaptive Optics.</p> <p>P.T.O.</p>	<p>AGARD-CP-300</p> <p>Optical communication Light transmission Optical properties Marine atmospheres Upper atmosphere</p>	<p>AGARD Conference Proceedings No.300 Advisory Group for Aerospace Research and Development, NATO SPECIAL TOPICS IN OPTICAL PROPAGATION Edited by P.Halley Published July 1981 434 pages</p> <p>These Proceedings consist of the 42 papers and the discussions presented at the 28th Meeting of the Electromagnetic Wave Propagation Panel in Monterey. There are 8 papers on Propagation Effects in Air and Sea Water; 10 on Recent Atmospheric and Sea Measurements; 5 on Upper Atmosphere Effects: Theory and Experiments; 6 on Non-Linear Optics; 7 on Novel Communication Techniques and Devices; and 6 on Adaptive Optics.</p> <p>P.T.O.</p>	<p>AGARD-CP-300</p> <p>Optical communication Light transmission Optical properties Marine atmospheres Upper atmosphere</p>
<p>AGARD Conference Proceedings No.300 Advisory Group for Aerospace Research and Development, NATO SPECIAL TOPICS IN OPTICAL PROPAGATION Edited by P.Halley Published July 1981 434 pages</p> <p>These Proceedings consist of the 42 papers and the discussions presented at the 28th Meeting of the Electromagnetic Wave Propagation Panel in Monterey. There are 8 papers on Propagation Effects in Air and Sea Water; 10 on Recent Atmospheric and Sea Measurements; 5 on Upper Atmosphere Effects: Theory and Experiments; 6 on Non-Linear Optics; 7 on Novel Communication Techniques and Devices; and 6 on Adaptive Optics.</p> <p>P.T.O.</p>	<p>AGARD-CP-300</p> <p>Optical communication Light transmission Optical properties Marine atmospheres Upper atmosphere</p>	<p>AGARD Conference Proceedings No.300 Advisory Group for Aerospace Research and Development, NATO SPECIAL TOPICS IN OPTICAL PROPAGATION Edited by P.Halley Published July 1981 434 pages</p> <p>These Proceedings consist of the 42 papers and the discussions presented at the 28th Meeting of the Electromagnetic Wave Propagation Panel in Monterey. There are 8 papers on Propagation Effects in Air and Sea Water; 10 on Recent Atmospheric and Sea Measurements; 5 on Upper Atmosphere Effects: Theory and Experiments; 6 on Non-Linear Optics; 7 on Novel Communication Techniques and Devices; and 6 on Adaptive Optics.</p> <p>P.T.O.</p>	<p>AGARD-CP-300</p> <p>Optical communication Light transmission Optical properties Marine atmospheres Upper atmosphere</p>

Papers and Discussions presented at the 28th Meeting of the Electromagnetic Wave Propagation Panel held in Monterey, California, USA, 6-10 April 1981.

Papers and Discussions presented at the 28th Meeting of the Electromagnetic Wave Propagation Panel held in Monterey, California, USA, 6-10 April 1981.

ISBN 92-835-0295-7

ISBN 92-835-0295-7

Papers and Discussions presented at the 28th Meeting of the Electromagnetic Wave Propagation Panel held in Monterey, California, USA, 6-10 April 1981.

Papers and Discussions presented at the 28th Meeting of the Electromagnetic Wave Propagation Panel held in Monterey, California, USA, 6-10 April 1981.

ISBN 92-835-0295-7

ISBN 92-835-0295-7

B22
4

AGARD

NATO  OTAN

7 RUE ANCELLE · 92200 NEUILLY-SUR-SEINE
FRANCE

Telephone 745.08.10 · Telex 610176

DISTRIBUTION OF UNCLASSIFIED AGARD PUBLICATIONS

AGARD does NOT hold stocks of AGARD publications at the above address for general distribution. Initial distribution of AGARD publications is made to AGARD Member Nations through the following National Distribution Centres. Further copies are sometimes available from these Centres, but if not may be purchased in Microfiche or Photocopy form from the Purchase Agencies listed below.

NATIONAL DISTRIBUTION CENTRES

BELGIUM

Coordonnateur AGARD - VSL
Etat-Major de la Force Aérienne
Quartier Reine Elisabeth
Rue d'Evere, 1140 Bruxelles

CANADA

Defence Science Information Services
Department of National Defence
Ottawa, Ontario K1A 0K2

DENMARK

Danish Defence Research Board
Østerbrogades Kaserne
Copenhagen Ø

FRANCE

O.N.E.R.A. (Direction)
29 Avenue de la Division Leclerc
92320 Châtillon sous Bagneux

GERMANY

Fachinformationszentrum Energie,
Physik, Mathematik GmbH
Kernforschungszentrum
D-7514 Eggenstein-Leopoldshafen 2

GREECE

Hellenic Air Force General Staff
Research and Development Directorate
Holargos, Athens

ICELAND

Director of Aviation
c/o Flugrad
Reykjavik

ITALY

Aeronautica Militare
Ufficio del Delegato Nazionale all'AGARD
3, Piazzale Adenauer
Rom./EUR

LUXEMBOURG

See Belgium

NETHERLANDS

Netherlands Delegation to AGARD
National Aerospace Laboratory, NLR
P.O. Box 126
2600 A.C. Delft

NORWAY

Norwegian Defence Research Establishment
Main Library
P.O. Box 25
N-2007 Kjeller

PORTUGAL

Direcção do Serviço de Material
da Força Aérea
Rua da Escola Politécnica 42
Lisboa
Attn: AGARD National Delegate

TURKEY

Department of Research and Development (ARGE)
Ministry of National Defence, Ankara

UNITED KINGDOM

Defence Research Information Centre
Station Square House
St. Mary Cray
Orpington, Kent BR5 3RE

UNITED STATES

National Aeronautics and Space Administration (NASA)
Langley Field, Virginia 23365
Attn: Report Distribution and Storage Unit

THE UNITED STATES NATIONAL DISTRIBUTION CENTRE (NASA) DOES NOT HOLD STOCKS OF AGARD PUBLICATIONS, AND APPLICATIONS FOR COPIES SHOULD BE MADE DIRECT TO THE NATIONAL TECHNICAL INFORMATION SERVICE (NTIS) AT THE ADDRESS BELOW.

PURCHASE AGENCIES

Microfiche or Photocopy

National Technical
Information Service (NTIS)
5285 Port Royal Road
Springfield
Virginia 22161, USA

Microfiche

Space Documentation Service
European Space Agency
10, rue Mário Nikis
75015 Paris, France

Microfiche

Technology Reports
Centre (DTI)
Station Square House
St. Mary Cray
Orpington, Kent BR5 3RF
England

Requests for microfiche or photocopies of AGARD documents should include the AGARD serial number, title, author or editor, and publication date. Requests to NTIS should include the NASA accession report number. Full bibliographical references and abstracts of AGARD publications are given in the following journals:

Scientific and Technical Aerospace Reports (STAR)
published by NASA Scientific and Technical
Information Facility
Post Office Box 8757
Baltimore/Washington International Airport
Maryland 21240, USA

Government Reports Announcements (GRA)
published by the National Technical
Information Services, Springfield
Virginia 22161, USA



Printed by Technical Editing and Reproduction Ltd
Harford House, 7-9 Charlotte St, London W1P 1HD

ISBN 92-835-0295-7